Growing two-dimensional boron *pp. 1468 & 1513*

Managing biological risk *p. 1471*

Algal toxin alters spatial memory *p. 1545*

Science

$10
18 DECEMBER 2015
sciencemag.org

AAAS

CONTENTS

18 DECEMBER 2015 • VOLUME 350 • ISSUE 6267

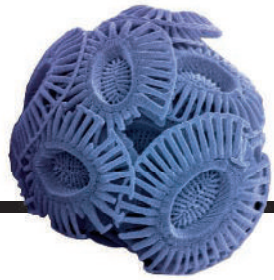

1466, 1530, & 1533
Oceanic plankton shifts

SPECIAL SECTION

Breakthrough of the Year

WINNER

1456 Making the cut

1457 People's choice

RUNNERS-UP

1458 A big year for small worlds

1459 Kennewick Man's kin

1459 Reproducibility in psychology

1460 *Homo naledi* comes out of the dark

1460 Deep mantle plumes rise to the test

1461 A vaccine against Ebola

1462 Yeast engineered to brew opioids

1462 Lymphatic vessels: The brain's well-hidden secret

1463 Quantum weirdness confirmed

OTHER FEATURES

1461 Scorecard for 2015

1464 Areas to watch in 2016

1464 Breakdown of the year: Assault on the past

1465 Breakdown runners-up

ON THE COVER

Cheap, widely available, and easy to use, the genome editing system called CRISPR earned *Science*'s 2015 Breakthrough of the Year laurels for many great feats and some controversial ones—including the alteration of DNA in human embryos. See page 1456.
Illustration: Davide Bonazzi/@SalzmanArt

SEE ALSO
▸ EDITORIAL P. 1445 ▸ PODCAST ▸ VIDEO

NEWS

IN BRIEF

1446 News at a glance

IN DEPTH

1449 EARTH'S LAKES ARE WARMING FASTER THAN ITS AIR
First ever global survey reveals summer lake temperatures rising at an alarming rate *By E. Kintisch*

1450 CARBON TRACKERS COULD HELP BOLSTER CLIMATE VOWS
Projects lay groundwork for a global greenhouse monitoring system
By W. Cornwall

1451 Inside the Paris climate deal
By W. Cornwall

1452 HUMAN IMPACTS ON ECOSYSTEMS BEGAN THOUSANDS OF YEARS AGO
Early humans broke up existing networks of plants and animals
By E. Pennisi

1453 CAMEL VACCINE OFFERS HOPE TO STOP MERS
Vaccinated animals shed less virus, but is that good enough to prevent human outbreaks? *By K. Kupferschmidt*
▸ HAAGMANS *ET AL.* 10.1126/science.aad1283; SABIR *ET AL.* 10.1126/science.aac8608

1454 NSF LOOKS FOR NEW CONTRACTOR TO FINISH TROUBLED OBSERVATORY
Reboot sought for management of ecology network *By J. Mervis*

1455 TB CAMPAIGN STEPS UP
HIV-style activism marks effort to "end" TB by 2030 *By J. Cohen*

INSIGHTS

PERSPECTIVES

1466 ADRIFT IN AN OCEAN OF CHANGE
Rising temperatures and ocean acidification drive changes in phytoplankton communities *By M. Vogt*
▸ REPORTS PP. 1530 & 1533

1468 DISCLOSING BORON'S THINNEST SIDE
Borophene—stable, single-atom-thick layers of boron—displays remarkable properties *By H. Sachdev*
▸ REPORT P. 1513

1470 JOSEPHSON CONTACTS OF NEUTRAL STRONGLY INTERACTING FERMIONS
Contacts between superconductors are explored via their ultracold atomic gas analogs *By W. Belzig*
▸ REPORTS PP. 1498 & 1505

1471 A MORE SYSTEMATIC APPROACH TO BIOLOGICAL RISK
Management of emerging risks in life science and technology requires new leadership and a sober assessment of the legacy of Asilomar
By M. J. Palmer et al.

1473 QUESTIONABLE POLICY FOR LARGE CARNIVORE HUNTING
U.S. wolf-hunting policies do not align with ecological theory or data
By S. Creel et al.

1476 SULFATE TO GO
A trisulfide intermediate is key to microbial sulfur reduction *By G. Fritz and P. M. H. Kroneck*
▸ REPORT P. 1541

1477 OPTING IN OR OUT OF THE NETWORK
Does learning commit neurons that are predisposed to recruitment to a memory network? *By K. C. Martin and E. M. Schuman*

1478 DESIGNER CELLS FINELY TUNED FOR THERAPY
Cells are engineered for on-demand control of psoriasis *By J. Di Domizio and M. Gilliet*
▸ *SCIENCE TRANSLATIONAL MEDICINE* RESEARCH ARTICLE BY L. SCHUKUR *ET AL.*

BOOKS *ET AL.*

1480 BRAIN STORMS
By J. Palfreman, reviewed by O. M. Smith

1481 THE HUNT FOR VULCAN
By T. Levenson, reviewed by M. Livio

1481 WONDER
Reviewed by O. M. Smith

Published by AAAS

CONTENTS

18 DECEMBER 2015 • VOLUME 350 • ISSUE 6267

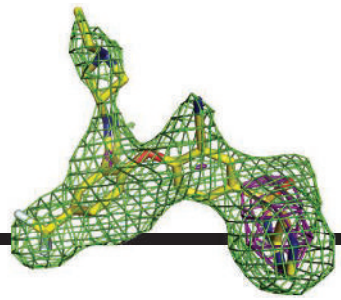

1491 & 1492
Specific targeting of a channel involved in pain perception

LETTERS

1482 RETRACTION
By Y. H. Wang et al.

1482 EDITORIAL EXPRESSION OF CONCERN
By M. McNutt

1482 PREVENTING TROPICAL MINING DISASTERS
By D. P. Edwards and W. F. Laurance

1482 THE GLOBAL WARMING HIATUS'S IRRELEVANCE
By M. F. Wehner and D. R. Easterling

1483 TECHNICAL COMMENT ABSTRACTS

RESEARCH

IN BRIEF

1487 From *Science* and other journals

REVIEW

1490 ELECTRON MICROSCOPY
Opportunities and challenges in liquid cell electron microscopy *F. M. Ross*
REVIEW SUMMARY; FOR FULL TEXT: dx.doi.org/10.1126/science.aaa9886

RESEARCH ARTICLES

STRUCTURAL BIOLOGY

1491 Structural basis of Nav1.7 inhibition by an isoform-selective small-molecule antagonist *S. Ahuja* et al.
RESEARCH ARTICLE SUMMARY; FOR FULL TEXT: dx.doi.org/10.1126/science.aac5464

1492 Structure of the voltage-gated calcium channel $Ca_v1.1$ complex *J. Wu* et al.
RESEARCH ARTICLE SUMMARY; FOR FULL TEXT: dx.doi.org/10.1126/science.aad2395

1493 GENOMIC EVOLUTION
Genomic islands of speciation separate cichlid ecomorphs in an East African crater lake *M. Malinsky* et al.

REPORTS

1498 QUANTUM SIMULATION
Connecting strongly correlated superfluids by a quantum point contact *D. Husmann* et al.
▸ PERSPECTIVE P. 1470; REPORT P. 1505

1501 ULTRAFAST DYNAMICS
Direct observation of collective modes coupled to molecular orbital–driven charge transfer *T. Ishikawa* et al.

1505 QUANTUM SIMULATION
Josephson effect in fermionic superfluids across the BEC-BCS crossover *G. Valtolina* et al.
▸ PERSPECTIVE P. 1470; REPORT P. 1498

1508 ENERGY STORAGE
Nitrogen-doped mesoporous carbon of extraordinary capacitance for electrochemical energy storage *T. Lin* et al.

1513 NANOMATERIALS
Synthesis of borophenes: Anisotropic, two-dimensional boron polymorphs *A. J. Mannix* et al.
▸ PERSPECTIVE P. 1468

1516 BATTERIES
Visualization of O-O peroxo-like dimers in high-capacity layered oxides for Li-ion batteries *E. McCalla* et al.

1521 PLANT SYMBIOSES
Rice perception of symbiotic arbuscular mycorrhizal fungi requires the karrikin receptor complex *C. Gutjahr* et al.

1525 NEURODEVELOPMENT
Loss of motoneuron-specific microRNA-218 causes systemic neuromuscular failure *N. D. Amin* et al.

1530 PHYTOPLANKTON
Millennial-scale plankton regime shifts in the subtropical North Pacific Ocean *K. W. McMahon* et al.
▸ PERSPECTIVE P. 1466; REPORT P. 1533

1533 MARINE CALCIFERS
Multidecadal increase in North Atlantic coccolithophores and the potential role of rising CO_2 *S. Rivero-Calle* et al.
▸ PERSPECTIVE P. 1466; REPORT P. 1530

1537 PALEOCEANOGRAPHY
Dynamical excitation of the tropical Pacific Ocean and ENSO variability by Little Ice Age cooling *G. T. Rustic* et al.

1541 MICROBIAL METABOLISM
A protein trisulfide couples dissimilatory sulfate reduction to energy conservation *A. A. Santos* et al.
▸ PERSPECTIVE P. 1476

1545 ECOTOXICOLOGY
Algal toxin impairs sea lion memory and hippocampal connectivity, with implications for strandings *P. F. Cook* et al.

1548 MEMBRANE REMODELING
Structure and membrane remodeling activity of ESCRT-III helical polymers *J. McCullough* et al.

1552 EVOLUTIONARY GENETICS
An essential cell cycle regulation gene causes hybrid inviability in *Drosophila* *N. Phadnis* et al.

DEPARTMENTS

1445 EDITORIAL
Breakthrough to genome editing
By Marcia McNutt
▸ BREAKTHROUGH OF THE YEAR SECTION P. 1456

1578 WORKING LIFE
Beetle horns and book writing
By Elizabeth Pennisi

Science Staff 1444
AAAS News & Notes 1485
New Products 1557
Science Careers 1558

SCIENCE (ISSN 0036-8075) is published weekly on Friday, except the last week in December, by the American Association for the Advancement of Science, 1200 New York Avenue, NW, Washington, DC 20005. Periodicals mail postage (publication No. 484460) paid at Washington, DC, and additional mailing offices. Copyright © 2015 by the American Association for the Advancement of Science. The title SCIENCE is a registered trademark of the AAAS. Domestic individual membership and subscription (51 issues): $153 ($74 allocated to subscription). Domestic institutional subscription (51 issues): $1282; Foreign postage extra: Mexico, Caribbean (surface mail) $55; other countries (air assist delivery) $85. First class, airmail, student, and emeritus rates on request. Canadian rates with GST available upon request, GST #1254 88122. Publications Mail Agreement Number 1069624. **Printed in the U.S.A.**
Change of address: Allow 4 weeks, giving old and new addresses and 8-digit account number. **Postmaster:** Send change of address to AAAS, P.O. Box 96178, Washington, DC 20090–6178. **Single-copy sales:** $10.00 current issue, $15.00 back issue prepaid includes surface postage; bulk rates on request. **Authorization to photocopy** material for internal or personal use under circumstances not falling within the fair use provisions of the Copyright Act is granted by AAAS to libraries and other users registered with the Copyright Clearance Center (CCC) Transactional Reporting Service, provided that $30.00 per article is paid directly to CCC, 222 Rosewood Drive, Danvers, MA 01923. The identification code for *Science* is 0036-8075. *Science* is indexed in the *Reader's Guide to Periodical Literature* and in several specialized indexes.

Published by AAAS

Science

AAAS

1200 New York Avenue, NW, Washington, DC 20005
Bateman House, 82-88 Hills Road, Cambridge, UK CB2 1LQ

Editor-in-Chief Marcia McNutt

Executive Editor Monica M. Bradford **News Editor** Tim Appenzeller

Managing Editor, Research Journals Katrina L. Kelner

Deputy Editors Barbara R. Jasny, Andrew M. Sugden(UK), Valda J. Vinson, Jake S. Yeston

Research and Insights

SR. EDITORS Caroline Ash(UK), Gilbert J. Chin, Lisa D. Chong, Julia Fahrenkamp-Uppenbrink(UK), Pamela J. Hines, Stella M. Hurtley(UK), Paula A. Kiberstis, Marc S. Lavine(Canada), Kristen L. Mueller, Ian S. Osborne(UK), Beverly A. Purnell, L. Bryan Ray, Guy Riddihough, H. Jesse Smith, Jelena Stajic, Peter Stern(UK), Phillip D. Szuromi, Brad Wible, Nicholas S. Wigginton, Laura M. Zahn **ASSOCIATE EDITORS** Brent Grocholski, Keith T. Smith, Sacha Vignieri **ASSOCIATE BOOK REVIEW EDITOR** Valerie B. Thompson **ASSOCIATE LETTERS EDITOR** Jennifer Sills **CHIEF CONTENT PRODUCTION EDITOR** Cara Tate **SR. CONTENT PRODUCTION EDITOR** Harry Jach, Lauren Kmec **CONTENT PRODUCTION EDITORS** Jeffrey E. Cook, Chris Filiatreau, Cynthia Howe, Barbara P. Ordway, Catherine Wolner **SR. EDITORIAL COORDINATORS** Carolyn Kyle, Beverly Shields **EDITORIAL COORDINATORS** Ramatoulaye Diop, Joi S. Granger, Lisa Johnson, Anita Wynn **PUBLICATIONS ASSISTANTS** Aneera Dobbins, Jeffrey Hearn, Dona Mathieu, Le-Toya Mayne Flood, Shannon McMahon, Scott Miller, Jerry Richardson, Rachel Roberts(UK), Alice Whaley(UK), Brian White **EXECUTIVE ASSISTANT** Anna Bashkirova **ADMINISTRATIVE SUPPORT** Janet Clements(UK), Lizanne Newton(UK), Maryrose Madrid, Laura-Nadine Schuhmacher (UK, Intern), Alix Welch (Intern), John Wood(UK)

News

NEWS MANAGING EDITOR John Travis **INTERNATIONAL EDITOR** Richard Stone **DEPUTY NEWS EDITORS** Daniel Clery(UK), Robert Coontz, Elizabeth Culotta, David Grimm, David Malakoff, Leslie Roberts **CONTRIBUING EDITOR** Martin Enserink(Europe) **SR. CORRESPONDENTS** Jeffrey Mervis, Elizabeth Pennisi **NEWS WRITERS** Adrian Cho, Jon Cohen, Jennifer Couzin-Frankel, Carolyn Gramling, Eric Hand, Jocelyn Kaiser, Catherine Matacic, Kelly Servick, Robert F. Service, Erik Stokstad(Cambridge, UK), Emily Underwood **INTERNS** Hanae Armitage, Emily DeMarco, Annick Laurent, Laura Olivieri, Juan David Romero **CONTRIBUTING CORRESPONDENTS** Michael Balter(Paris), John Bohannon, Ann Gibbons, Mara Hvistendahl, Sam Kean, Eli Kintisch, Kai Kupferschmidt(Berlin), Andrew Lawler, Christina Larson(Beijing), Mitch Leslie, Charles C. Mann, Eliot Marshall, Virginia Morell, Dennis Normile(Tokyo), Heather Pringle, Tania Rabesandratana(London), Gretchen Vogel(Berlin), Lizzie Wade(Mexico City) **CAREERS** Donisha Adams, Rachel Bernstein **COPY EDITORS** Julia Cole, Jennifer Levin (Chief) **ADMINISTRATIVE SUPPORT** Jessica Williams

Executive Publisher Rush D. Holt

Publisher Kent R. Anderson **Chief Digital Media Officer** Rob Covey

BUSINESS OPERATIONS AND PORTFOLIO MANAGEMENT DIRECTOR Sarah Whalen **BUSINESS SYSTEMS AND FINANCIAL ANALYSIS DIRECTOR** Randy Yi **MANAGER OF FULFILLMENT SYSTEMS** Neal Hawkins **SYSTEMS ANALYST** Nicole Mehmedovich **ASSISTANT DIRECTOR, BUSINESS OPERATIONS** Eric Knott **MANAGER, BUSINESS OPERATIONS** Jessica Tierney **BUSINESS ANALYSTS** Cory Lipman, Cooper Tilton, Celeste Troxler **FINANCIAL ANALYST** Robert Clark **RIGHTS AND PERMISSIONS ASSISTANT DIRECTOR** Emilie David **PERMISSIONS ASSOCIATE** Elizabeth Sandler **RIGHTS, CONTRACTS, AND LICENSING ASSOCIATE** Lili Kiser

MARKETING DIRECTOR Elise Swinehart **ASSOCIATE DIRECTOR OF ACQUISITION AND RETENTION** Julianne Wielga **MARKETING ASSOCIATE** Elizabeth Sattler **SR. MARKETING EXECUTIVE** Jennifer Reeves **ASSOCIATE DIRECTOR, CREATIVE SERVICES** Tzeitel Sorrosa **ART ASSOCIATE** Seil Lee **JR. ART ASSOCIATE** Kim Huynh **ASSISTANT COMMERCIAL EDITOR** Selby Frame **MARKETING PROJECT MANAGER** Angelissa McArthur **PROGRAM DIRECTOR, AAAS MEMBER CENTRAL** Peggy Mihelich **FULFILLMENT SYSTEMS AND OPERATIONS** membership@aaas.org **MANAGER, MEMBER SERVICES** Pat Butler **SPECIALISTS** LaToya Casteel, Terrance Morrison, Latasha Russell **MANAGER, DATA ENTRY** Mickie Napoleoni **DATA ENTRY SPECIALISTS** JJ Regan, Brenden Aquilino, Fiona Giblin

DIRECTOR, SITE LICENSING Tom Ryan **DIRECTOR, CORPORATE RELATIONS** Eileen Bernadette Moran **SR. PUBLISHER RELATIONS SPECIALIST** Kiki Forsythe **PUBLISHER RELATIONS MANAGER** Catherine Holland **PUBLISHER RELATIONS, EASTERN REGION** Keith Layson **PUBLISHER RELATIONS, WESTERN REGION** Ryan Rexroth **SALES RESEARCH COORDINATOR** Aiesha Marshall **MANAGER, SITE LICENSE OPERATIONS** Iquo Edim **SENIOR PRODUCTION SPECIALIST** Robert Koepke **SENIOR OPERATIONS ANALYST** Lana Guz **FULFILLMENT ANALYST** Judy Lillibridge **ASSOCIATE DIRECTOR, MARKETING** Christina Schlecht **MARKETING ASSOCIATES** Thomas Landreth, Isa Sesay-Bah

WEB TECHNOLOGIES SR. DEVELOPER Chris Coleman **DEVELOPERS** Dan Berger, Jimmy Marks, Ryan Jensen **SR. PROJECT MANAGER** Trista Smith

MULTIMEDIA DIRECTOR OF ANALYTICS Enrique Gonzales **SR. WEB PRODUCER** Sarah Crespi **WEB PRODUCER** Alison Crawford **VIDEO PRODUCER** Nguyen Nguyen **SOCIAL MEDIA PRODUCER** Brice Russ

DIRECTOR OF OPERATIONS PRINT AND ONLINE Lizabeth Harman **DIGITAL/PRINT STRATEGY MANAGER** Jason Hillman **QUALITY TECHNICAL MANAGER** Marcus Spiegler **PROJECT ACCOUNT MANAGER** Tara Kelly **DIGITAL PRODUCTION MANAGER** Lisa Stanford **ASSISTANT MANAGER DIGITAL/PRINT** Rebecca Doshi **SENIOR CONTENT SPECIALISTS** Steve Forrester, Antoinette Hodal, Lori Murphy, Anthony Rosen **CONTENT SPECIALISTS** Jacob Hedrick, Kimberley Oster

DESIGN DIRECTOR Beth Rakouskas **DESIGN EDITOR** Marcy Atarod **SENIOR DESIGNER** Garvin Grullón **DESIGNER** Chrystal Smith **GRAPHICS MANAGING EDITOR** Alberto Cuadra **SENIOR SCIENTIFIC ILLUSTRATORS** Chris Bickel, Katharine Sutliff **SCIENTIFIC ILLUSTRATOR** Valerie Altounian **SENIOR ART ASSOCIATES** Holly Bishop, Nathalie Cary, Preston Huey **SENIOR PHOTO EDITOR** William Douthitt **PHOTO EDITORS** Leslie Blizard, Christy Steele

DIRECTOR, GLOBAL COLLABORATION, CUSTOM PUBLICATIONS, ADVERTISING Bill Moran **EDITOR, CUSTOM PUBLISHING** Sean Sanders: 202-326-6430 **ASSISTANT EDITOR, CUSTOM PUBLISHING** Tianna Hicklin: 202-326-6463 **ADVERTISING MARKETING MANAGER** Justin Sawyers: 202-326-7061 science_advertising@aaas.org **ADVERTISING MARKETING ASSOCIATE** Javia Flemmings **ADVERTISING SUPPORT MANAGER** Karen Foote: 202-326-6740 **ADVERTISING PRODUCTION OPERATIONS MANAGER** Deborah Tompkins **SR. PRODUCTION SPECIALIST/GRAPHIC DESIGNER** Amy Hardcastle **PRODUCTION SPECIALIST** Yuse Lajiminmuhip **SR. TRAFFIC ASSOCIATE** Christine Hall **SALES COORDINATOR** Shirley Young **ASSOCIATE DIRECTOR, COLLABORATION, CUSTOM PUBLICATIONS/CHINA/TAIWAN/KOREA/SINGAPORE** Ruolei Wu: +86-186 0082 9345, rwu@aaas.org **COLLABORATION/ CUSTOM PUBLICATIONS/JAPAN** Adarsh Sandhu + 81532-81-5142 asandhu@aaas.org **EAST COAST/E. CANADA** Laurie Faraday: 508-747-9395, FAX 617-507-8189 **WEST COAST/W. CANADA** Lynne Stickrod: 415-931-9782, FAX 415-520-6940 **MIDWEST** Jeffrey Dembski: 847-498-4520 x3005, Steven Loerch: 847-498-4520 x3006 **UK EUROPE/ASIA** Roger Goncalves: TEL/FAX +41 43 243 1358 **JAPAN** Katsuyoshi Fukamizu(Tokyo): +81-3-3219-5777 kfukamizu@aaas.org **CHINA/TAIWAN** Ruolei Wu: +86-186 0082 9345, rwu@aaas.org

WORLDWIDE ASSOCIATE DIRECTOR OF SCIENCE CAREERS Tracy Holmes: +44 (0) 1223 326525, FAX +44 (0) 1223 326532 tholmes@science-int.co.uk **CLASSIFIED** advertise@sciencecareers.org **U.S. SALES** Tina Burks: 202-326-6577, Nancy Toema: 202-326-6578 **SALES ADMINISTRATOR** Marci Gallun **EUROPE/ROW SALES** Axel Gesatzki, Sarah Lelarge **SALES ASSISTANT** Kelly Grace **JAPAN** Hiroyuki Mashiki(Kyoto): +81-75-823-1109 hmashiki@aaas.org **CHINA/TAIWAN** Ruolei Wu: +86-186 0082 9345 rwu@aaas.org **MARKETING MANAGER** Allison Pritchard **MARKETING ASSOCIATE** Aimee Aponte

AAAS BOARD OF DIRECTORS RETIRING PRESIDENT, CHAIR Gerald R. Fink **PRESIDENT** Geraldine (Geri) Richmond **PRESIDENT-ELECT** Barbara A. Schaal **TREASURER** David Evans Shaw **CHIEF EXECUTIVE OFFICER** Rush D. Holt **BOARD** Bonnie L. Bassler, May R. Berenbaum, Carlos J. Bustamante, Stephen P.A. Fodor, Claire M. Fraser, Michael S. Gazzaniga, Laura H. Greene, Elizabeth Loftus, Mercedes Pascual

SUBSCRIPTION SERVICES For change of address, missing issues, new orders and renewals, and payment questions: 866-434-AAAS (2227) or 202-326-6417, FAX 202-842-1065. Mailing addresses: AAAS, P.O. Box 96178, Washington, DC 20090-6178 or AAAS Member Services, 1200 New York Avenue, NW, Washington, DC 20005

INSTITUTIONAL SITE LICENSES 202-326-6730 **REPRINTS:** Author Inquiries 800-635-7181 **COMMERCIAL INQUIRIES** 803-359-4578 **PERMISSIONS** 202-326-6765, permissions@aaas.org **AAAS Member Services** 202-326-6417 or http://membercentral.aaas.org/discounts

Science serves as a forum for discussion of important issues related to the advancement of science by publishing material on which a consensus has been reached as well as including the presentation of minority of conflicting points of view. Accordingly, all articles published in *Science*—including editorials, news and comment, and books reviews—are signed and reflect the individual views of the authors and not official points of view adopted by AAAS or the institutions with which the authors are affiliated.

INFORMATION FOR AUTHORS See pages 678 and 679 of the 6 February 2015 issue or access www.sciencemag.org/about/authors

SENIOR EDITORIAL BOARD

Robert H. Grubbs, *California Institute of Technology,* **Gary King,** *Harvard University*
Susan M. Rosenberg, *Baylor College of Medicine,* **Ali Shilatifard,** *Northwestern University*
Feinberg School of Medicine, **Michael S. Turner**, *U. of Chicago*

BOARD OF REVIEWING EDITORS (Statistics board members indicated with **(S)**)

Adriano Aguzzi, *U. Hospital Zürich*
Takuzo Aida, *U. of Tokyo*
Leslie Aiello, *Wenner-Gren Foundation*
Judith Allen, *U. of Edinburgh*
Sonia Altizer, *U. of Georgia*
Sebastian Amigorena, *Institut Curie*
Kathryn Anderson, *Memorial Sloan-Kettering Cancer Center*
Meinrat O. Andreae, *Max-Planck Inst. Mainz*
Paola Arlotta, *Harvard U.*
Johan Auwerx, *EPFL*
David Awschalom, *U. of Chicago*
Clare Baker, *University of Cambridge*
Jordi Bascompte, *University of Zurich*
Facundo Batista, *London Research Inst.*
Ray H. Baughman, *U. of Texas, Dallas*
David Baum, *U. of Wisconsin*
Carlo Beenakker, *Leiden U.*
Kamran Behnia, *ESPCI-ParisTech*
Yasmine Belkaid, *NIAID, NIH*
Philip Benfey, *Duke U.*
Stephen J. Benkovic, *Penn State U.*
May Berenbaum, *U. of Illinois*
Gabriele Bergers, *U. of California, San Francisco*
Bradley Bernstein, *Massachusettes General Hospital*
Peer Bork, *EMBL*
Bernard Bourdon, *Ecole Normale Supérieure de Lyon*
Chris Bowler, *École Normale Supérieure*
Ian Boyd, *U. of St. Andrews*
Emily Brodsky, *U. of California, Santa Cruz*
Ron Brookmeyer, *U. of California Los Angeles* **(S)**
Christian Büchel, *U. Hamburg-Eppendorf*
Joseph A. Burns, *Cornell U.*
Carter Tribley Butts, *U. of California, Irvine*
Gyorgy Buzsaki, *New York U. School of Medicine*
Blanche Capel, *Duke U.*
Mats Carlsson, *U. of Oslo*
Ib Chorkendorff, *U. of Denmark*
David Clapham, *Children's Hospital Boston*
David Clary, *U. of Oxford*
Joel Cohen, *Rockefeller U., Columbia U.*
James J. Collins, *MIT*
Robert Cook-Deegan, *Duke U.*
Alan Cowman, *Walter & Eliza Hall Inst.*
Robert H. Crabtree, *Yale U.*
Roberta Croce, *Vrije Universiteit*
Janet Currie, *Princeton U.*
Jeff L. Dangl, *U. of North Carolina*
Tom Daniel, *U. of Washington*
Frans de Waal, *Emory U.*
Stanislas Dehaene, *Collège de France*
Robert Desimone, *MIT*
Claude Desplan, *New York U.*
Ap Dijksterhuis, *Radboud U. of Nijmegen*
Dennis Discher, *U. of Pennsylvania*
Gerald W. Dorn II, *Washington U. School of Medicine*
Jennifer A. Doudna, *U. of California, Berkeley*
Bruce Dunn, *U. of California, Los Angeles*
William Dunphy, *Caltech*
Christopher Dye, *WHO*
Todd Ehlers, *U. of Tuebingen*
David Ehrhardt, *Carnegie Inst. of Washington*
Tim Elston, *U. of North Carolina at Chapel Hill*
Gerhard Ertl, *Fritz-Haber-Institut, Berlin*
Barry Everitt, *U. of Cambridge*
Ernst Fehr, *U. of Zurich*
Anne C. Ferguson-Smith, *U. of Cambridge*
Michael Feuer, *The George Washington U.*
Toren Finkel, *NHLBI, NIH*
Kate Fitzgerald, *U. of Massachusetts*
Peter Fratzl, *Max-Planck Inst.*
Elaine Fuchs, *Rockefeller U.*
Daniel Geschwind, *UCLA*
Karl-Heinz Glassmeier, *TU Braunschweig*
Ramon Gonzalez, *Rice U.*
Julia R. Greer, *Caltech*
Elizabeth Grove, *U. of Chicago*
Nicolas Gruber, *ETH Zurich*
Kip Guy, *St. Jude's Children's Research Hospital*
Taekjip Ha, *U. of Illinois at Urbana-Champaign*
Christian Haass, *Ludwig Maximilians U.*
Michael Hasselmo, *Boston U.*
Martin Heimann, *Max-Planck Inst. Jena*
Yka Helariutta, *U. of Cambridge*
James A. Hendler, *Rensselaer Polytechnic Inst.*
Janet G. Hering, *Swiss Fed. Inst. of Aquatic Science & Technology*
Kai-Uwe Hinrichs, *U. of Bremen*
Kei Hirose, *Tokyo Inst. of Technology*
David Hodell, *U. of Cambridge*
David Holden, *Imperial College*
Lora Hooper, *UT Southwestern Medical Ctr. at Dallas*
Raymond Huey, *U. of Washington*
Auke Ijspeert, *EPFL Lausanne*
Steven Jacobsen, *U. of California, Los Angeles*
Kai Johnsson, *EPFL Lausanne*
Peter Jonas, *Inst. of Science & Technology (IST) Austria*
Matt Kaeberlein, *U. of Washington*
William Kaelin Jr., *Dana-Farber Cancer Inst.*
Daniel Kahne, *Harvard U.*
Daniel Kammen, *U. of California, Berkeley*
Masashi Kawasaki, *U. of Tokyo*
V. Narry Kim, *Seoul National U.*
Joel Kingsolver, *U. of North Carolina at Chapel Hill*
Robert Kingston, *Harvard Medical School*
Etienne Koechlin, *Ecole Normale Suprieure*
Alexander Kolodkin, *Johns Hopkins U.*
Leonid Kruglyak, *UCLA*
Thomas Langer, *U. of Cologne*
Mitchell A. Lazar, *U. of Pennsylvania*
David Lazer, *Harvard U.*
Thomas Lecuit, *IBDM*
Virginia Lee, *U. of Pennsylvania*
Stanley Lemon, *U. of North Carolina at Chapel Hill*
Ottoline Leyser, *Cambridge U.*
Wendell Lim, *U.C. San Francisco*
Marcia C. Linn, *U. of California, Berkeley*
Jianguo Liu, *Michigan State U.*
Luis Liz-Marzan, *CIC biomaGUNE*
Jonathan Losos, *Harvard U.*
Ke Lu, *Chinese Acad. of Sciences*
Christian Lüscher, *U. of Geneva*
Laura Machesky, *CRUK Beatson Inst. for Cancer Research*
Anne Magurran, *U. of St. Andrews*
Oscar Marin, *CSIC & U. Miguel Hernández*
Charles Marshall, *U. of California, Berkeley*
C. Robertson McClung, *Dartmouth College*
Graham Medley, *U. of Warwick*
Tom Misteli, *NCI*
Yasushi Miyashita, *U. of Tokyo*
Mary Ann Moran, *U. of Georgia*
Richard Morris, *U. of Edinburgh*
Alison Motsinger-Reif, *NC State U.* **(S)**
Thomas Murray, *The Hastings Center*
James Nelson, *Stanford U. School of Med.*
Daniel Neumark, *U. of California, Berkeley*
Kitty Nijmeijer, *U. of Twente*
Pär Nordlund, *Karolinska Inst.*
Helga Nowotny, *European Research Advisory Board*
Ben Olken, *MIT*
Joe Orenstein, *U. of California Berkeley & Lawrence Berkeley National Lab*
Harry Orr, *U. of Minnesota*
Andrew Oswald, *U. of Warwick*
Steve Palumbi, *Stanford U.*
Jane Parker, *Max-Planck Inst. of Plant Breeding Research*
Giovanni Parmigiani, *Dana-Farber Cancer Inst.* **(S)**
Donald R. Paul, *U. of Texas, Austin*
John H. J. Petrini, *Memorial Sloan-Kettering Cancer Center*
Samuel Pfaff, *Salk Institute for Biological Studies*
Joshua Plotkin, *U. of Pennsylvania*
Albert Polman, *FOM Institute AMOLF*
Philippe Poulin, *CNRS*
Jonathan Pritchard, *Stanford U.*
David Randall, *Colorado State U.*
Colin Renfrew, *U. of Cambridge*
Felix Rey, *Institut Pasteur*
Trevor Robbins, *U. of Cambridge*
Jim Roberts, *Fred Hutchinson Cancer Research Ctr.*
Barbara A. Romanowicz, *U. of California, Berkeley*
Amy Rosenzweig, *Northwestern University*
Jens Rostrup-Nielsen, *Haldor Topsoe*
Mike Ryan, *U. of Texas, Austin*
Mitinori Saitou, *Kyoto U.*
Shimon Sakaguchi, *Kyoto U.*
Miquel Salmeron, *Lawrence Berkeley National Lab*
Jürgen Sandkühler, *Medical U. of Vienna*
Alexander Schier, *Harvard U.*
Randy Seeley, *U. of Cincinnati*
Vladimir Shalaev, *Purdue U.*
Robert Siliciano, *Johns Hopkins School of Medicine*
Denis Simon, *Arizona State U.*
Uri Simonsohn, *U. of Pennsylvania*
Alison Smith, *John Innes Centre*
Richard Smith, *U. of North Carolina* **(S)**
John Speakman, *U. of Aberdeen*
Allan C. Spradling, *Carnegie Institution of Washington*
Jonathan Sprent, *Garvan Inst. of Medical Research*
Eric Steig, *U. of Washington*
Paula Stephan, *Georgia State U. and National Bureau of Economic Research*
Molly Stevens, *Imperial College London*
V. S. Subrahmanian, *U. of Maryland*
Ira Tabas, *Columbia U.*
Sarah Teichmann, *Cambridge U.*
John Thomas, *North Carolina State U.*
Shubha Tole, *Tata Institute of Fundamental Research*
Christopher Tyler-Smith, *The Wellcome Trust Sanger Inst.*
Herbert Virgin, *Washington U.*
Bert Vogelstein, *Johns Hopkins U.*
Cynthia Volkert, *U. of Göttingen*
Douglas Wallace, *Dalhousie U.*
David Wallach, *Weizmann Inst. of Science*
Ian Walmsley, *U. of Oxford*
Jane-Ling Wang, *U. of California, Davis*
David A. Wardle, *Swedish U. of Agric. Sciences*
David Waxman, *Fudan U.*
Jonathan Weissman, *U. of California, San Francisco*
Chris Wikle, *U. of Missouri* **(S)**
Ian A. Wilson, *The Scripps Res. Inst.* **(S)**
Timothy D. Wilson, *U. of Virginia*
Rosemary Wyse, *Johns Hopkins U.*
Jan Zaanen, *Leiden U.*
Kenneth Zaret, *U. of Pennsylvania School of Medicine*
Jonathan Zehr, *U. of California, Santa Cruz*
Len Zon, *Children's Hospital Boston*
Maria Zuber, *MIT*

BOOK REVIEW BOARD

David Bloom, *Harvard U.,* **Samuel Bowring,** *MIT,* **Angela Creager,** *Princeton U.,*
Richard Shweder, *U. of Chicago,* **Ed Wasserman,** *DuPont*

EDITORIAL

Breakthrough to genome editing

A, T, G, C: the alphabet code for the nucleotides that are the building blocks of life. Minor, but consequential, changes in this DNA coding can change gene function. Researchers have long sought better ways to edit the genetic code in cultured cells and laboratory organisms to silence, activate, or change targeted genes to gain a better understanding of their roles. This, in turn, could open the door to beneficial applications, from ecological to agricultural to biomedical. Over the years, several editing methods have been developed, but they have suffered from a lack of specificity, difficulty in assembling the molecular constituents, or concerns about off-target effects. Recently, accomplishments in genome editing across biological disciplines have been so remarkable that the method known as clustered regularly interspaced short palindromic repeats—or CRISPR—is *Science*'s 2015 Breakthrough of the Year (see p. 1456).

"...CRISPR is poised to revolutionize research..."

The 2015 advances using CRISPR that warrant this recognition have been on multiple fronts. Researchers have now delivered on the method's promise to, for example, disable retroviruses encoded in the pig genome that had posed a safety concern for organ transplantation from pigs to humans. Concurrently, CRISPR was used to develop a potent gene drive, a system that allows the rapid transmission of an introduced gene throughout insect populations faster than natural selection would permit. CRISPR should make it easier to study human genetic diseases, because it can quickly create cell and animal models for study and for the testing and screening of drugs. For certain diseases, genome editing of somatic cells may lead to potential therapy. Because CRISPR is poised to revolutionize research, the international community gathered earlier this month to address the implications of this technique for modifying human germ cells and embryos, articulating guidelines that clarify the ethical bounds for researchers, funders, and publishers.

Many other achievements in 2015 gave CRISPR tough competition. One that came too late to be considered is last week's agreement in Paris by nearly 200 nations on a pact to fight climate change. Of those that made the short list, most notable are the stunning images from the New Horizons mission as it swept past Pluto; the mission is *Science*'s "People's Choice" for the Breakthrough. Also startling was the discovery that the mammalian lymphatic system extends the immune system's reach into the brain, opening up possible new routes to treatment. In a form of modern-day alchemy, yeast was engineered to produce opiates. We gained experimental confirmation of the correlation in the quantum state of two widely separated particles, a process called "entanglement." Improvements in seismic imaging provided long-sought confirmation of the existence of mantle plumes, responsible for midplate volcanoes such as Hawaii. Our line of defense against Ebola virus has been bolstered with the successful development of a vaccine. Psychologists led the charge in research reproducibility. And affirming that there is still serendipity in science, a new member of the human family was revealed from a hidden cave in South Africa harboring 1500 human fossils. DNA sequencing has now settled the origin of Kennewick Man: Native American, with Asian ancestors.

Choosing the Breakthrough is easy when new research resolves a long-standing question, such as the experimental confirmation of the Higgs particle in 2012. More commonly, the road to success is marked by glimmers of hope, setbacks, and uncertainty as to whether time will prove the value of a new finding or technique. *Science* has been tracking genome editing since the initial successes with zinc fingers; in 2012, we named transcription activator–like effector nucleases (TALENS) as a runner-up Breakthrough. By 2013, researchers were embracing CRISPR, enough so that it too was a runner-up Breakthrough. The Breakthrough nod in 2013 went to cancer immunotherapy, still in early clinical trials at the time. Our hope is that in 2 years' time, CRISPR will have brought to many diverse fields in biology the enduring level of excitement and optimism that immunotherapy has brought to cancer patients.

– Marcia McNutt

Marcia McNutt
Editor-in-Chief
Science *Journals*

IMAGES: (RIGHT) STACEY PENTLAND PHOTOGRAPHY; (INSET) DAVIDE BONAZZI/@SALZMANART

10.1126/science.aae0479

Published by AAAS

NEWS

> “It’s just worthless words. There’s no action, just promises. As long as fossil fuels appear to be the cheapest fuels out there, they will continue to be burned.”
>
> Columbia University climate scientist **James Hansen** to *The Guardian* on last week’s global deal for cutting carbon emissions.

IN BRIEF

Syrian refugees struggle with TB

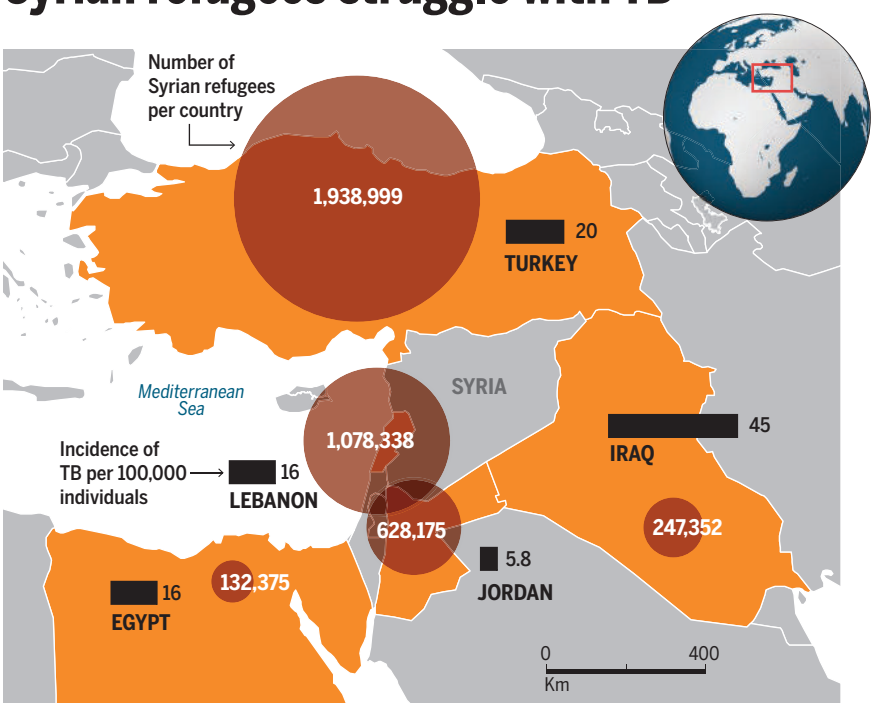

Lebanon, Jordan, and Iraq are struggling to detect and treat tuberculosis (TB) in the nearly 2 million refugees who have fled to these countries from Syria. “The national TB programs operating in conflict-affected regions are strained and they need help,” Aleksandar Galev of the International Organization for Migration explained last week at the 46th Union World Conference on Lung Health. In Lebanon, which hosts half the refugees, more than 20% of those diagnosed with active TB cases are “lost to follow-up” and don’t complete the 6-month treatment needed for a cure. “The refugees move from country to country and even across the seas,” said Galev, who is based in Amman. But this shouldn’t deter countries from taking Syrian refugees, says Gilles Cesari of the Global Fund to Fight AIDS, Tuberculosis and Malaria in Geneva, Switzerland. “The refugees are not vectors of disease,” says Cesari, who stresses that their TB rates are much lower than those of hard-hit populations in sub-Saharan Africa and Asia. “They’re just at a greater risk of being sick because of poor nutrition, being tired and on the move, and living with many people in one room.”

MAP: ADAPTED FROM ALEKSANDAR GALEV/INTERNATIONAL ORGANIZATION FOR MIGRATION BY A. CUADRA/*SCIENCE*

AROUND THE WORLD

NIH to unveil strategic plan

BETHESDA, MARYLAND | The National Institutes of Health (NIH) this week was on track to release its first agency-wide strategic plan in more than 20 years. (It had not been released by the time *Science* went to print.) The plan, previewed in draft form last week, describes four objectives: advancing opportunities by funding basic and applied science, setting priorities, enhancing stewardship, and “managing for results.” Among other changes, the plan ends a tradition of setting aside 10% of NIH’s budget for AIDS research. It further pledges to improve how the agency looks at the public health burden of a disease to guide funding. It also lays out several bold goals for 2020, such as a universal influenza vaccine that works against all virus strains.

New drug from GM chicken eggs

SILVER SPRING, MARYLAND | The U.S. Food and Drug Administration (FDA) last week approved Kanuma, a new drug produced in the eggs of genetically engineered chickens. The drug treats lysosomal acid lipase (LAL) deficiency, a rare genetic disorder that prevents the body from breaking down fat and typically causes fatal organ damage in infants. Alexion Pharmaceuticals of Cheshire, Connecticut, modified chickens to produce a human form of LAL, which can be extracted from egg whites and given to patients as an intravenous infusion. The chickens were approved separately from the drug by FDA’s Center for Veterinary Medicine.

Mexico approves dengue vaccine

MEXICO CITY | Mexico last week became the first country to approve a vaccine for dengue fever, a mosquito-borne disease that causes excruciating muscle and joint pain and kills more than 10,000 people every year. The new vaccine—developed by Sanofi Pasteur—targets each of four distinct virus serotypes. In clinical trials, the vaccine reduced the incidence of severe dengue, which sometimes results

Published by AAAS

The Dawn Jewel, *Chlorocypha aurora*, is a new species that may live only in one river in Cameroon.

African dragonfly boom

They call themselves "bionauts"—explorers not of space, but of life on Earth. In one fell swoop, a team of three naturalists has added 60 new species of dragonfly and damselfly to the 700 previously known in Africa. Worried that increasing development was threatening the insect's freshwater habitat, Klaas-Douwe Dijkstra, a systematist at the Naturalis Biodiversity Center in Leiden, the Netherlands, along with a high school teacher and a former mining mechanic, spent 15 years tracking down as many species on the African continent as they could. "We want to wow the world with so many new dragonflies but also deliver them to the doormats of those who care most about them," Dijkstra says. Describing so many new species at once required a special 230-page issue of *Odonatologica*, a journal devoted to the large, delicate, long-winged insects. http://scim.ag/dragonflyboom

when patients are infected a second time with a different serotype. But the vaccine provided limited protection against dengue serotype 2, a common version of the virus. Despite that shortcoming, the approval is "a milestone in our efforts to prevent and control dengue," says Duane Gubler of the Duke-NUS Graduate Medical School in Singapore. Sanofi is awaiting approval in several other countries.

The most dangerous pathogens

GENEVA, SWITZERLAND | The World Health Organization (WHO) last week released a short list of the world's most dangerous pathogens—eight viruses "likely to cause severe outbreaks in the near future," for which few or no medical countermeasures exist. The list, which includes viruses causing Ebola, Marburg, severe acute respiratory syndrome, Middle East respiratory syndrome, Nipah, Lassa fever, Rift Valley fever, and Crimean Congo hemorrhagic fever, is part of a push to develop vaccine and drug candidates for dangerous emerging pathogens before a major outbreak. "Many of these diseases have not received the funding or the attention they require," says Cathy Roth, a science policy adviser at WHO. Three other diseases were ranked as "serious": chikungunya, severe fever with thrombocytopaenia syndrome, and Zika. http://scim.ag/WHOpathogens

Ebola virus (red) in an infected African monkey.

Dutch get open access

THE HAGUE, NETHERLANDS | A standoff between Dutch universities and publishing giant Elsevier ended last week with a compromise: Elsevier says it will allow 30% of Dutch research in its 2500 journals to be free to the public by 2018. "It's not the 100% that I hoped for," says Gerard Meijer, the president of Radboud University in Nijmegen, the Netherlands, and the lead negotiator on the Dutch side. "But this is the future. No one can stop this anymore." The agreement follows a year of negotiations between the publisher and a coalition of 14 Dutch universities. http://scim.ag/ElsevierOpenAccess

NIH to end monkey experiments

WASHINGTON, D.C. | The National Institutes of Health (NIH) decided last week to phase out controversial monkey experiments at its Poolesville, Maryland, facility. The work—which includes separating young rhesus macaques from their mothers, measuring their addiction to alcohol, and monitoring their long-term stress levels—has been the target of an intense campaign by People for the Ethical Treatment of Animals, but the agency says the group had nothing to do with its decision. Rather, NIH says the facility had become too expensive to maintain. About 300 monkeys will leave the lab for other facilities over the next 3 years, where they may still be used in research. http://scim.ag/Poolesville

PHOTOS: (TOP TO BOTTOM) JENS KIPPING; NIAID/FLICKR

Published by AAAS

NEWSMAKERS

Biodefense lab overseer out

The head of a federal program that oversees safety and security at U.S. labs that work with risky pathogens has been replaced. Since 2006, **Robbin Weyant** had directed the Atlanta-based U.S. Centers for Disease Control and Prevention's (CDC's) Division of Select Agents and Toxins (DSAT), which regulates labs working with viruses, bacteria, and toxins that could be used as bioweapons. Last week, *USA Today* reported that on 9 November, Weyant moved to a different position at CDC. Weyant's departure comes in the wake of several high-profile mishaps with select agents, including mistaken shipments of live anthrax from CDC and an Army lab. CDC's Daniel Sosin is now acting director of DSAT.

Two of the seven pups developed in vitro.

FINDINGS

First 'test tube puppies'

Dogs' reproductive systems are so quirky that researchers have been trying to produce puppies through artificial fertilization since the 1970s without success. But now, scientists have used a new set of techniques to give rise to the world's first "test tube puppies," a litter of beagles and beagle mixes. To bring the new litter into the world, researchers collected mature eggs from the canine equivalent of the fallopian tubes—a trickier prospect than collecting them from ovaries (as is done in humans). Once they had the eggs, the team experimented with different conditions for fertilization and incubation, finally coaxing seven embryos to grow in a surrogate mother hound, they reported last week in *PLOS ONE*. The pups, now 5 months old and thriving with their adoptive human families, could offer hope for endangered species like red wolves and African wild dogs, the researchers write. Dog in vitro fertilization could also be used to study heritable traits and diseases, many of which are shared by dogs and humans.

NSF says Antarctica's McMurdo Station is long overdue for an overhaul.

Overhaul in the works for aging U.S. Antarctic station

The U.S. National Science Foundation (NSF) is planning a $300 million overhaul of McMurdo Station, the biggest of its three Antarctic research stations. The redesign, called the Antarctic Infrastructure Modernization for Science, would replace and reconfigure various scientific, operational, and logistics support facilities at McMurdo as part of a larger plan to upgrade all Antarctic stations. NSF's Office of Polar Programs presented its latest draft at a 4 December meeting of the National Academies' Polar Research Board. The planned redesign is in response to a 2012 report by a blue-ribbon panel convened to study NSF's science facilities on the southernmost continent. Funding would come from NSF's Major Research Equipment and Facilities Construction account, and not from its $300 million annual budget for Antarctic logistics and infrastructure. The overhaul, which is to have no direct impact on ongoing scientific activities, would start in fiscal year 2019 and take about 8 years. **http://scim.ag/McMurdoStation**

BY THE NUMBERS

6 million

Number of pregnancies in the United States in 2010, the lowest annual tally since 1976, the Centers for Disease Control and Prevention reported last week. Girls under 14 saw the biggest decline in pregnancy rate.

$1 billion

Amount of money Silicon Valley investors—including SpaceX's Elon Musk—have committed to OpenAI Inc., a nonprofit firm whose stated goal is to "advance digital intelligence in the way that is most likely to benefit humanity," not shareholders.

213

Number of "unequivocal" references to Bob Dylan's lyrics snuck into biomedical papers by authors at the Karolinska Institute since 1970. The references were the result of a long-running bet among the scientists (*The BMJ*).

PHOTOS: (TOP TO BOTTOM) MIKE CARROLL/CORNELL UNIVERSITY COLLEGE OF VETERINARY MEDICINE; ©DAVID HOSKING/ALAMY STOCK PHOTO

Published by AAAS

Lake ice—shown on Russia's Lake Baikal—shields water from warming air.

CLIMATE

Earth's lakes are warming faster than its air

First ever global survey reveals summer lake temperatures rising at an alarming rate

By **Eli Kintisch**, *in San Francisco, California*

The world's lakes are warming faster than both the oceans and the air around them, a global survey of hundreds of lakes shows. The rapid temperature rise could cause widespread damage to lake ecosystems, say scientists who presented the findings this week at the American Geophysical Union meeting here. The global effects could be even more serious, because higher lake temperatures could trigger the conversion of billions of tons of carbon stored in lake sediments to methane and carbon dioxide (CO_2), in a feedback effect that could accelerate global warming.

The temperature increase—a summertime warming of about a third of a degree per decade over 25 years—is "pretty modest," says lake biologist Peter Leavitt of the University of Regina in Canada, who did not participate in the study. "But you don't need 2° to 3° increases in lake temperatures to have profound impacts."

Many studies have shown that individual lakes are warming up in the summer. (Scientists rarely track lake temperatures in winter, when ice makes measurements more challenging.) The new study encompassed 235 lakes around the world, combining measurements by hand, which reach the depths of lakes, with satellite readings, which provide global coverage of lake surfaces. Over the study's time period, between 1985 and 2009, a few lakes cooled whereas others warmed sharply. On average, lakes warmed 0.34°C per decade, more than twice the 0.12°C warming per decade measured in the oceans over a similar period.

That the oceans lag isn't unexpected, given their enormous mass, says Catherine O'Reilly, lead author on the study, which involved 64 scientists collecting data on six continents. But many lakes are warming even faster than surface air temperatures, which rose an average of 0.25°C per decade between 1979 and 2012. "I would have expected that, on average, lakes would be warming more slowly than air," says O'Reilly, a freshwater ecologist at Illinois State University in Normal.

A shorter ice season because of warmer winters may help explain why. "Normally, ice is a good insulator protecting lakes from atmospheric heating," Leavitt says. With ice melting earlier, lake water is exposed to warm spring air for longer. That probably explains why lakes that normally freeze in winter are warming by 0.48°C per decade, about twice as fast as lakes that don't freeze.

Another factor that may be accelerating the lake warming is a decline in cloudiness in some temperate areas, due at least in part to climate change. Clearer air allows more sunlight to strike lakes' surfaces. And as lakes soak up more heat from the sun and the air, their waters become more stratified, with the less dense warm water floating on top of more dense cold water. The stratification prevents deep, cold waters from mixing into surface layers and cooling them in summer.

The rapid summertime warming bodes ill for lake species. Freshwater fish that like the cold, such as lake trout, could suffer. So could species that rely on increasingly threatened lake ice. The Baikal seal in Russia's Lake Baikal gives birth on the ice, points out biologist Stephanie Hampton of Washington State University, Pullman. Adds O'Reilly: "Large changes in our lakes are not only unavoidable, but are probably already happening."

Meanwhile, in warmer places, Leavitt says, "strong stratification and warm surface waters are the recipe for blooms of noxious and possibly toxic cyanobacteria, particularly in regions where agriculture and urbanization have fertilized the lakes and estuaries."

Warming lakes may have global implications as well, say the researchers, whose study appears this week in *Geophysical Research Letters*. As aquatic organisms die, their carbon-rich remains fall into the water column, where they can be stored in sediments or broken down by microorganisms into gases. "Lakes are already massive furnaces for processing terrestrial organic matter" and creating greenhouse gasses, Leavitt says. "Warming these regions further is likely to increase their role in combusting carbon to CO_2." ■

PHOTO: © OLGA KAMENSKAYA/NATURE PICTURE LIBRARY/CORBIS

Published by AAAS

CLIMATE

Carbon trackers could help bolster climate vows

Projects lay groundwork for a global greenhouse monitoring system

By **Warren Cornwall**

In May, China's statistical agency quietly raised estimates of how much coal the nation has burned since 2000. That little bit of bookkeeping had big implications. It amounted to as much as 900 million metric tons of additional carbon dioxide (CO_2) emitted annually in recent years, more than the total yearly emissions of Germany. It also underscored the challenge of knowing what many countries are really pumping into the atmosphere.

After negotiators left Paris last week with vows to curb the world's climate pollution (see box, p. 1451), officials will want to know whether countries are living up to their promises. The Paris meeting addressed part of the puzzle: greenhouse gas accounting, including mechanisms for auditing emissions reports. But scientists are also in the early stages of deploying systems they hope could buttress international agreements by closely tracking greenhouse gas emissions in the air, rather than on paper.

Space-borne sensors are watching the ebb and flow of carbon around the globe, and a few experimental, city-scale monitoring systems are up and running. Ultimately, a network of instruments on satellites, commercial jets, smokestacks, and communications towers could deliver a detailed, nearly instantaneous picture of emissions in a country, city, or even a neighborhood: a global weather system for greenhouse gases.

"A carbon weather service is probably the best example of where we probably ought to get in the future," says Riley Duren, an engineer at NASA's Jet Propulsion Laboratory in Pasadena, California. He heads the Megacities Carbon Project, which is building a first-generation system in Los Angeles, California. The idea got a boost earlier this year when the United Nations World Meteorological Organization (WMO) endorsed the creation of the Integrated Global Greenhouse Gas Information System, to promote networks for tracking greenhouse gases.

Today, the clearest data on CO_2 are the atmospheric concentrations measured at more than 40 stations around the world. Emissions for countries or cities are estimated by adding up reams of statistics about fuel consumption, deforestation, electricity generation, and other activities.

Many developed countries have honed these inventories over years of practice under the Kyoto, Japan, climate treaty. But much less is known about emissions in the developing world, which today account for an estimated 60% of climate pollution. In October, the European Union's earth observation agency, Copernicus, warned that such uncertainties "could undermine the credibility and the stability of future climate agreements."

The projects now underway in the skies and on the ground could eventually help officials determine whether their neighbors are meeting their promises and whether their own strategies are producing results. "Our goal is to say: 'Your emission reduction policies seem to be consistent with what we see in the atmosphere, although it looks like your efforts in transportation are having a bigger impact than the energy sector,'" says James Butler, director of the global monitoring division at the National Oceanic and Atmospheric Administration's Earth System Research Laboratory in Boulder, Colorado.

Cities, where a majority of human-caused greenhouse gases originate, are serving as testing grounds. Over the last 5 years, Indianapolis, Boston, Los Angeles, and Paris have been outfitted with equipment to track their carbon emissions. A similar network is being built around Washington, D.C., and it may eventually be extended up the East Coast to Boston, says James Whetstone, a scientist and manager at the National Institute of Standards and Technology in Gaithersburg, Maryland, which is helping fund several of the U.S. projects.

Los Angeles illustrates both the potential and the challenges. Today, 13 devices mounted high on tall buildings and cellphone and radio towers constantly measure CO_2 across an area of 17,000 square kilometers. Some also track methane, a potent heat-trapping gas. Atop nearby Mount Wilson, a device scans the basin every 90 minutes, detecting the gases' infrared signature. Airplanes zero in on hot spots identified by the stationary instruments. NASA's Orbiting Carbon Observatory-2 (OCO-2) satellite periodically surveys the city for a big-picture snapshot. The data

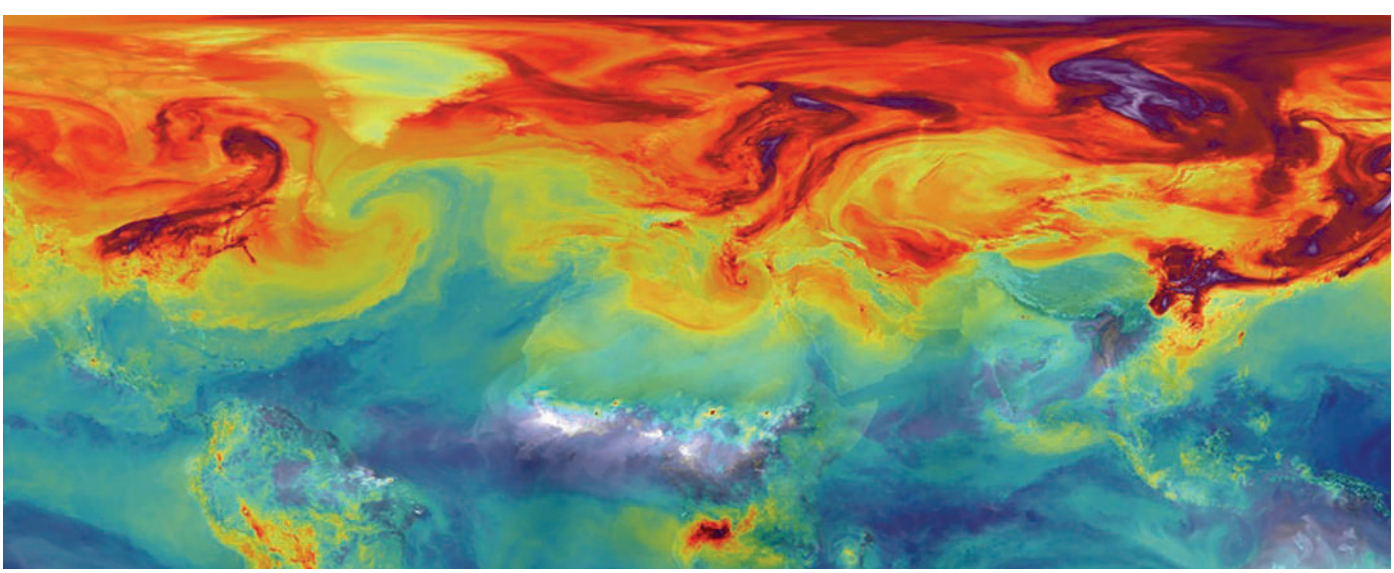

A simulation shows high CO_2 levels over Northern Hemisphere continents. New monitoring efforts aim to keep tabs on regional emissions.

IMAGE: NASA/GSFC

Published by AAAS

are combined with computer models of wind patterns and a detailed inventory of carbon-generating activity such as traffic.

The result is an emerging picture of how the region "breathes" greenhouse gases. The work has already helped scientists pinpoint larger-than-expected methane plumes from a landfill and an oil field. The scientists also plan to monitor the impact of new efforts to cut emissions from traffic congestion, and to check large industrial facilities to see whether they're meeting state greenhouse gas targets.

But the project is a long way from producing something as reliable and rapidly updated as weather reports, Duren says. It's tricky to model how winds come off the Pacific Ocean and interact with the surrounding mountains. Data on sources such as fuel use get outdated quickly. The tower network has gaps, and OCO-2 is better at tracking global flows of carbon than at measuring human-caused emissions on the scale of a city.

The agency's OCO-3 satellite, delayed by funding cuts, could take more detailed measurements, and the European Union's Copernicus agency is in discussions about launching powerful carbon-monitoring equipment on a satellite. Even better results could come from geostationary satellites that could park over a continent, providing a continuous view, Duren says. But no country is currently trying to put one into space.

In Indianapolis, where a similar project has been underway since 2010 and where wind patterns are less complex, CO_2 measurements for the city are now hedged with a "less than 20%" uncertainty, says Ken Davis, an atmospheric scientist at Pennsylvania State University, University Park, who is leading the work. "The technology, I would argue, is ready," he says.

Yet, so far, such carbon monitoring data aren't a key part of international climate policies. A state department official at the Paris talks says that although the technologies could be useful, they "aren't being considered as part of multilateral agreements."

That's a challenge for Phil DeCola, a former NASA scientist and White House science adviser who is chairman of the WMO greenhouse gas tracking project. "I don't want to be responsible for another grand research strategy for the circular file of posterity," says DeCola, who is also chief science officer for Sigma Space Corporation, a satellite instrument maker in Lanham, Maryland. At the Paris conference, he tried to interest smaller emitters, like cities or private industries, in developing tracking systems. "The bottom line is we can produce useful information. But will the information be used?" ■

Warren Cornwall is a freelance writer in Bellingham, Washington.

PHOTO: AP PHOTO/MICHEL EULER

Inside the Paris climate deal

When French foreign minister Laurent Fabius gaveled the Paris climate summit to a close on 12 December, the world was left with a mixture of hope and uncertainty.

Known as the 21st Conference of the Parties, or COP21, the meeting ended with a deal among 195 nations to curb global temperature increases by slowing the rise in greenhouse gas levels. It broke down the long-standing division between developed countries and developing countries that had stalled previous tries at a deal. And it created a timetable for nations to ratchet up their efforts. "It has the elements to be transformational," says Kelly Levin, senior associate at the World Resources Institute, a Washington, D.C.–based think tank.

Yet the individual national climate plans offered in the run-up to the meeting could still result in as much as 3.5°C of warming by 2100. Developed countries skirted demands for firmer commitments of money to help poorer nations build economies minus fossil fuels. Much of the agreement's promise hinges on fine print to be hammered out in the coming years. And the provisions for individual nations to curb emissions further—crucial if the world is to limit warming to 2°C or less—has limited legal bite.

Here are some key phrases from the deal, and what they really mean:

"Well below 2°C" At the 2009 Copenhagen climate meeting, countries agreed on a target of keeping temperatures to no more than 2°C above preindustrial levels. In Paris, countries calling themselves the "most vulnerable"—such as Pacific island nations—pressed for a goal of 1.5°C. They almost got there. The agreement aims at "well below" 2°C, and a promise to "pursue efforts" to cap the warming at 1.5°C.

"Achieve a balance" The deal calls for the rise in atmospheric greenhouse gas concentrations to effectively stop in the second half of the century. At that point, any further emissions would need to be canceled out with "sinks" such as expanding forests that suck up carbon dioxide.

"Every 5 years" Countries are expected to submit new, more ambitious plans every 5 years, beginning in 2020, rather than every 10 years as some major emitters including India reportedly wanted.

"Technology development" The deal emphasizes the importance of developing and spreading new low-emissions technology. At the conference, 20 countries including the United States, China, and a number of European countries vowed to double clean energy R&D spending over 5 years. A private initiative headlined by Microsoft founder Bill Gates will also push for new technology.

"Mobilizing climate finance" Developed countries previously promised $100 billion per year in public and private funding to help developing countries adapt to climate change and build low-carbon economies. In Paris, some developing countries pushed for a legally binding commitment. The deal says the richest countries will set a new funding target by 2025. But the details are in the subsidiary text, not the actual agreement.

"Enhanced transparency" All countries will have to submit regular inventories of their emissions. The reports will have to meet certain accounting standards, and be subjected to "expert review."

"Loss and damage" Poor countries most vulnerable to the impacts of climate change have pressed for developed countries to recognize their losses, and acknowledge legal responsibility. They got the recognition. But the final agreement cautions that it "does not involve or provide a basis for any liability or compensation."

"55%" Although delegates from all nations attending the conference agreed to the deal, it won't take effect until after next April—and only if at least 55 countries representing at least 55% of global greenhouse gas emissions have formally signed it. ■

–W. C.

Published by AAAS

Landscapes carved by humans, as seen on the California-Arizona border, may disrupt species associations.

PHOTO: GOOGLE IMAGES

PALEOECOLOGY

Human impacts on ecosystems began thousands of years ago

Early humans broke up existing plant and animal networks, perhaps boosting extinction risks

By **Elizabeth Pennisi**

Silicon Valley entrepreneurs boast about how disruptive their creations are, from cellphones to Uber. But in a global sense, humans' most disruptive technologies may have been born millennia ago, when our ancestors began to plant crops and cross the globe. Just in the past 150 years, humans have taken such a toll on Earth's status quo that some researchers say we have ushered in a new geological time period: the Anthropocene. But scientists are now suggesting a new dimension to human impacts, one that began many thousands of years ago. Long before the Industrial Age, humans had broken up relationships among plants and animals that had been stable for millions of years, S. Kathleen Lyons, a paleoecologist at the Smithsonian National Museum of Natural History in Washington, D.C., and her colleagues report this week in *Nature*.

The work, based on an analysis of species distributions, "gives us an idea of how far we've already come in changing the planet," says Anthony Barnosky, a paleobiologist at the University of California (UC), Berkeley.

The paper also suggests that extinction isn't the only marker of ecological disruption. It and other recent findings "show how major shifts in the diversity of life are not only quantified by the number of species, but by changes in entire ecological communities," says Nick Haddad, an environmental scientist at North Carolina State University in Raleigh. "They elevate the disastrous consequences of the sixth mass extinction"—the one happening now.

Researchers have debated when human impacts became dramatic enough to mark the start of the Anthropocene. Some pinpointed the start of the Industrial Age, with its accelerated population growth, habitat and species loss, and rising carbon dioxide levels. Others have suggested that human-caused disruption began much earlier, when we became superpredators, able to take all kinds of prey, or when we began farming (*Science*, 7 October 2011, p. 32).

The new data imply an early start to the human-dominated era. As part of the Evolution of Terrestrial Ecosystems Program at the Smithsonian Institution, paleontologists and ecologists pooled 172 data sets on the species present in specific regions and time periods, mostly in North America, spanning the past 300 million years. Lyons and her colleagues assessed how tightly linked species were in these assemblages, analyzing how often about 350,000 pairs of species appeared together, as compared with the clustering seen in a randomly generated assemblage. Pairs of species that clumped together more often than by chance presumably shared resources, and the persistence of these relationships likely stabilizes a community, Lyons says.

Since 300 million years ago, an average of 64% of the nonrandom pairs appeared together and qualified as aggregations, they report. In North America, for example, the now-extinct dire wolf (famous pets in the *Game of Thrones* TV series) and giant ground sloth persisted as a pair, likely connected as predator and prey; bog lemmings and chipmunks were also found together, likely because of common habitat preferences. But a big shift occurred, roughly about 6000 years ago and certainly within the last 10,000 years: Only 37% of the nonrandom pairs of species living now are aggregations. At first, even Lyons's team doubted this result. "It took 2 years to convince ourselves that [the result] was real," she recalls.

Others now are confident as well. "A strength of the paper is the diversity of data sets (mammals, pollen, and plant macrofossils)," emailed Jennifer Marlon, a Yale University environmental scientist. Agrees team member Jessica Blois, a paleoecologist at UC Merced: "The pattern isn't seen in just one system or one time, but emerges across both plants and animals." Even across some ancient mass extinctions, such as that at the end of the Cretaceous Period, species tended to aggregate more than they do now, although the fossil data weren't detailed enough to clearly reveal ecosystem structure during such extinctions, Lyons says.

The loss of species aggregations was not seen during other periods of major climate changes. But by 6000 years ago, humans were migrating around the world; in North America, some had started to settle down and practice agriculture. If the loosening of ecosystem associations is a uniquely human effect, then "the processes that are going on now with humans in the picture are fundamentally different than the processes that have gone on before," says Erle Ellis, an ecologist at the University of Maryland, Baltimore County. "There are going to be a lot of people thinking about this for a while." ■

Published by AAAS

INFECTIOUS DISEASE

Camel vaccine offers hope to stop MERS

Vaccinated animals shed less virus, but is that good enough to prevent human outbreaks?

By **Kai Kupferschmidt**

Last week, scientists and clinicians met at the World Health Organization (WHO) to draw up a list of the most dangerous emerging human pathogens (see p. 1447). One entry on that list needed no debate: Middle East respiratory syndrome (MERS) virus. Since it was discovered in 2012, the camel-borne virus has sickened more than 1200 people in the Middle East and killed more than 500 of them. Scientists worry that the slow-burning epidemic could turn into a global pandemic if the virus changes.

Researchers are hard at work on candidate vaccines for people. But to stamp out the virus before it escalates into an emergency, says Christian Drosten, a virologist at the University of Bonn in Germany, "the best strategy is trying to suppress circulation of the virus in camels." Online in *Science* this week, a team reports encouraging results for one candidate camel vaccine. "This is an extremely important paper," Drosten says, though he warns that the vaccine's effect—reducing the level of virus shed by the animals—may not be enough to stop MERS's circulation. Nor is it clear whether the vaccine gives lasting protection or whether camel owners will accept vaccinating against a disease that causes hardly any symptoms in the animals. "Each of these are potential deal breakers," says MERS researcher Kevin Olival of EcoHealth Alliance in New York City.

The MERS virus is a cousin of the one causing severe acute respiratory syndrome (SARS), which spread around the world in 2003, killing hundreds of people. MERS hasn't yet made a major impact outside the Middle East, however; it seems to infect humans lower in the respiratory tract than SARS, making it harder to transmit from one person to the next. Travelers have brought the virus to countries outside the Middle East more than a dozen times, but only in South Korea did it touch off a large outbreak. (Thirty-six people died.)

Studies pinpoint dromedary camels as the reservoir harboring the pathogen, but it is still unclear how exactly people get infected. Answering even basic questions has been complicated by a shortage of labs able to study such a dangerous pathogen in these large animals and a lack of cooperation from Saudi Arabia, the country that has borne the brunt of MERS.

For the new study, Bart Haagmans of Erasmus MC in Rotterdam, the Netherlands, and colleagues immunized four camels with a modified pox virus known as MVA, engineered to include the spike protein that MERS viruses carry on the surface. At the Centre for Research into Animal Health in Barcelona, Spain, the animals were vaccinated with a shot into the neck plus a spray into the nose. A booster was given after 4 weeks. When the camels were exposed to the MERS virus 3 weeks later, nonvaccinated animals got the mild symptoms typically seen: a slight rise in body temperature and a runny nose. Vaccinated animals were protected from those symptoms, and they harbored far less virus.

A runny camel nose may betray an infection with the MERS virus.

PHOTO: HAAGMANS *ET AL.*/*SCIENCE*

MVA might be attractive to camel owners because it should also protect against camel pox, a far more serious threat to the animals than MERS. Yet camel vaccines face a stumbling block illustrated by another study published online in *Science* this week. By analyzing 97 genomes of the MERS virus collected from camels in Saudi Arabia, a team shows that several different MERS lineages are circulating in the camel population, which might limit a vaccine's effectiveness. "This, coupled with all the local and international movements of dromedary camels, shows that it might be more complex than just rolling out a dromedary camel vaccination campaign," says Vincent Munster, a virologist at the Rocky Mountain Laboratories of the National Institute of Allergy and Infectious Diseases in Hamilton, Montana. Improving infection control in hospitals hosting MERS patients might be a better way to forestall future outbreaks like the one in South Korea, he says.

Still, to prepare for the worst-case scenario, scientists are moving vaccine candidates into human trials. The MVA vaccine will be tested in a phase I trial to start in Hamburg, Germany, next year, says its developer, Gerd Sutter of Ludwig Maximilian University of Munich in Germany. Another vaccine candidate, based on the DNA sequence for the spike protein, will also be tested soon. The companies sponsoring the vaccine have received approval for a trial in the United States, says David Weiner from the University of Pennsylvania, who helped develop the vaccine. If phase I trials go well, the big question will be who to target in a phase II trial, Sutter says. "Everybody agrees that health care workers are at risk. But then it gets difficult. Should we vaccinate anyone who is in contact with camels? How do you start to define that group?"

Human trials are getting more funding than further camel tests, in part because scientists have less experience with camels, and working with the animals isn't easy. Haagmans's group resorted to using young camels from the Canary Islands for its vaccine trial. The animals were small enough to fit into the biosafety facilities in the Spanish lab, and they could be shipped to Barcelona without crossing any borders.

In the end, the political rationale may also be stronger for a human vaccine, Drosten says. "Just imagine if there is a really big outbreak of MERS tomorrow and the vaccine candidates are not ready. It would be Ebola all over again." ■

Published by AAAS

ECOLOGY

NSF looks for new contractor to finish troubled observatory

Reboot sought for management of ecology network after delays, cost overruns, and disputes

By **Jeffrey Mervis**

The problems keep mounting for an ambitious effort to monitor changing ecosystems across the United States. The National Science Foundation (NSF) has fired the organization building its National Ecological Observatory Network (NEON), ecology's pioneering foray into big science. But that's only the first step in NSF's attempt to finish construction and operate the troubled project.

"NEON comes with lots to fix and lots of visibility, with no room for further error," says Joel Widder of Federal Science Partners, a small Washington, D.C.–based lobbying shop. NSF will look for another contractor to complete the project, which aims to monitor environmental changes at dozens of sites representing 20 different ecosystems across the United States. But the new management will face problems ranging from a poisoned relationship with the scientific community and disagreements with NSF to cost overruns and siting troubles. "The new entity has to be ready to deal with all of that," Widder says.

Last week, NSF officials wrote to NEON Inc. that they have "minimal confidence" in the Boulder, Colorado–based organization's ability to complete the $434 million project and operate it once construction is finished. The decision was not unexpected: In August, NSF shrunk NEON's size and scope because of a projected $80 million overrun and repeatedly missed deadlines. On 1 December NEON Inc. submitted a revised construction and operating plan that projected additional costs and a further delay of 2 years, according to NSF officials, which precipitated NSF's decision.

"Responsible stewardship requires the immediate pursuit of other management options … and we have begun that effort," James Olds, head of NSF's biology directorate, wrote in an 11 December letter to NEON Inc.'s CEO, Eugene Kelly, and the chairman of its board, Arizona State University, Tempe, biologist James Collins.

NEON Inc. has managed to alienate much of the U.S. ecological community since taking on the project in 1987. The position of chief scientist has been a revolving door, as leading researchers joined the project with high hopes only to flee after feeling that their authority had been curtailed and their advice ignored (*Science*, 25 September, p. 1436). Earlier this year the project's scientific advisory board threatened to resign en masse after members felt they were wasting their time.

An outside scientific panel asked to assess the smaller NEON network told NSF last month that any further reductions would jeopardize its ability to monitor biodiversity, climate change, and land use patterns over several decades. Olds says that "NSF is dedicated to ensuring that further rescoping of the NEON project will not occur," and Kelly reiterated that message in an email to some 400 NEON Inc. staffers, promising them "the observatory will be built … [and] further rescoping will not occur."

But observers say the new contractor will be hard-pressed to get the project's projected 81 sites up and running by the end of 2017, the projected completion date, without additional funds. One challenge affecting costs and schedules has been getting approval from landowners to set up NEON equipment on their property and obtaining the necessary permits to conduct research on those sites. Another challenge has been standardizing approaches and technologies so that they can be used at all sites. A long-running dispute between NEON Inc. and NSF officials about when sites are ready to be commissioned has also affected the bottom line. Project managers say operating funds should be used once all the equipment at a site is operating, but NSF says construction is completed only when the data being generated are ready for researchers to download.

Scientists formerly with the project say the current team of researchers, engineers, and support staff is capable of completing the project if given the freedom to do their jobs. "My hope is that NSF and the new NEON leadership put science back at the forefront and allow the staff to fully spread their wings," says Scott Ollinger, an ecologist who spent one frustrating year as NEON's chief scientist before returning to the University of New Hampshire, Durham, in 2014.

NSF also has to get its house in order, says David Schimel, NEON Inc.'s founding CEO and later chief scientist, who left the project in 2012. In addition to disputing NSF's definition of a completed site, NEON Inc. has accused the agency of micromanaging decisions on staffing, materials, and procedures. "The NEON team has ample ecological experience and expertise, but they need NSF's respect and support to make the decisions needed to succeed," says Schimel, now at NASA's Jet Propulsion Laboratory in Pasadena, California. "Presumably NSF will also streamline and professionalize its oversight to enable such an effort." ■

One of the towers at a NEON site in northern Virginia.

PHOTO: TREVOR FROST

Published by AAAS

Cape Town streets filled with 1000 protesters who demanded more be done to end TB.

PHOTO: MARCUS ROSE/THE UNION

INFECTIOUS DISEASE

Campaign against TB steps up its ambitions

HIV-style activism marks effort to "end" TB by 2030

By **Jon Cohen**, *in Cape Town, South Africa*

Observers of the traditionally staid Union World Conference on Lung Health could be forgiven for thinking they had stepped into an international HIV/AIDS gathering. This year's meeting, held here last week, included a massive street march, impassioned pleas from people living with the disease, and speeches from the South African minister of health and the head of the Global Fund to Fight AIDS, Tuberculosis (TB) and Malaria. Behind the theater was a striking new pledge. Just before the conference opened, representatives from 30 countries signed on to a new Global Plan to End TB that calls for ramping up the response to the ancient scourge—which killed 1.5 million people in 2014—over the next 5 years and halting it by 2030.

That goal, spearheaded by the Stop TB Partnership, a nonprofit in Geneva, Switzerland, is all the more ambitious given the meager resources devoted to the disease. The global plan calls for spending a total of $58 billion over the next 5 years—far more than the $6.7 billion spent in 2015—with $9 billion devoted to R&D. A report from the Treatment Action Group, a New York City–based nonprofit, calculates that some 100 funders spent a total of $674 million last year on TB R&D; in comparison, the U.S. National Institutes of Health alone invested $3 billion in HIV/AIDS R&D in 2014. Funding would have to jump dramatically, says the Stop TB Partnership, to meet its definition of "ending" TB by 2030: reducing global incidence from more than 130 people per 100,000 today to 10 per 100,000.

Funding aside, the TB campaign has a major advantage over HIV/AIDS: The disease can be cured, and better drugs and diagnostics are in the offing. "It's ridiculous that we're not eliminating tuberculosis," said the Global Fund's director, Mark Dybul. "Imagine if in the AIDS world we had a drug that was curative in 6 months. You think we'd be accepting a 1.5% decline per year in new infections or the slow pace of scale-up of treatments?"

The new movement is "positioning TB for the first time in the same conversation as HIV," says Lucica Ditiu, head of the Stop TB Partnership. That's fitting: *Mycobacterium tuberculosis* and HIV feed off each other, with TB being the No. 1 cause of death in people who have AIDS. Many of the challenges each disease presents are similar, too. One-third of the estimated 9.6 million people who develop active cases of TB each year do not know they have the disease, and patients have difficulty adhering to their treatments, fueling increases in drug resistance and transmission.

At the meeting, TB activists complained that the rollout of promising new drugs against both multidrug-resistant (MDR) and the even more intractable extensively drug-resistant (XDR) strains of *M. tuberculosis* has been "sluggish at best," as Yale University TB researcher Gerald Friedland put it. For resistant strains, the standard treatment course takes 2 years and includes injections that can cause serious side effects. Hopes were high in 2012 when Janssen Pharmaceutica in Beerse, Belgium, announced in 2012 that it had won "conditional approval" from regulatory agencies for a powerful new oral drug, bedaquiline. The approval was based on small-scale trials, and Janssen promised to launch a formal efficacy trial and explore the possibility of cutting treatment time to 9 months.

That large trial has yet to launch, and, as Doctors Without Borders complained, the drug is registered in only seven of 27 countries that have a high burden of MDR and XDR TB. So far fewer than 3000 patients have received it.

Otsuka Pharmaceutical, a Japanese company, took heat for providing its new drug, delamanid, to only 200 people under compassionate use provisions while completing its own efficacy trial, projected to end in 2017. Ample supplies exist of a third novel drug, linezolid, which was approved in 2000 to treat severe, non-TB infections that are antibiotic resistant—but it's expensive.

In South Africa, new tools are already aiding the fight. The country is rapidly adopting the highly touted GeneXpert machine, which determines within a few hours whether sputum samples contain genetic material from *M. tuberculosis*. Unlike standard tests, it detects MDR TB as well as drug-susceptible TB. South Africa has doubled the number of MDR TB patients diagnosed in the past 3 years.

Very sick AIDS patients with TB sometimes test negative on all tests because they produce very little sputum or have scant *M. tuberculosis* in samples. "Our hospitals in Africa are inundated with these people and we can't make the diagnosis," says pulmonologist Keertan Dheda. His team at the University of Cape Town in South Africa has proposed a simple and cheap solution: a urine test that is commercially available and sells for $3.50. These patients, possibly because they have TB in their kidneys, spill a glycolipid from *M. tuberculosis* into their urine. Dheda and his colleagues showed for the first time in a controlled study that adding the urine test to standard diagnostics saved a significant number of AIDS patients near death.

Dheda hopes to develop a TB urine test that can detect a half-dozen other biomarkers of *M. tuberculosis* his lab discovered last year. Says Dheda: "What I'd like to see one day is a simple urine test for TB that you can buy at a pharmacy, just like they have for HIV." ■

Published by AAAS

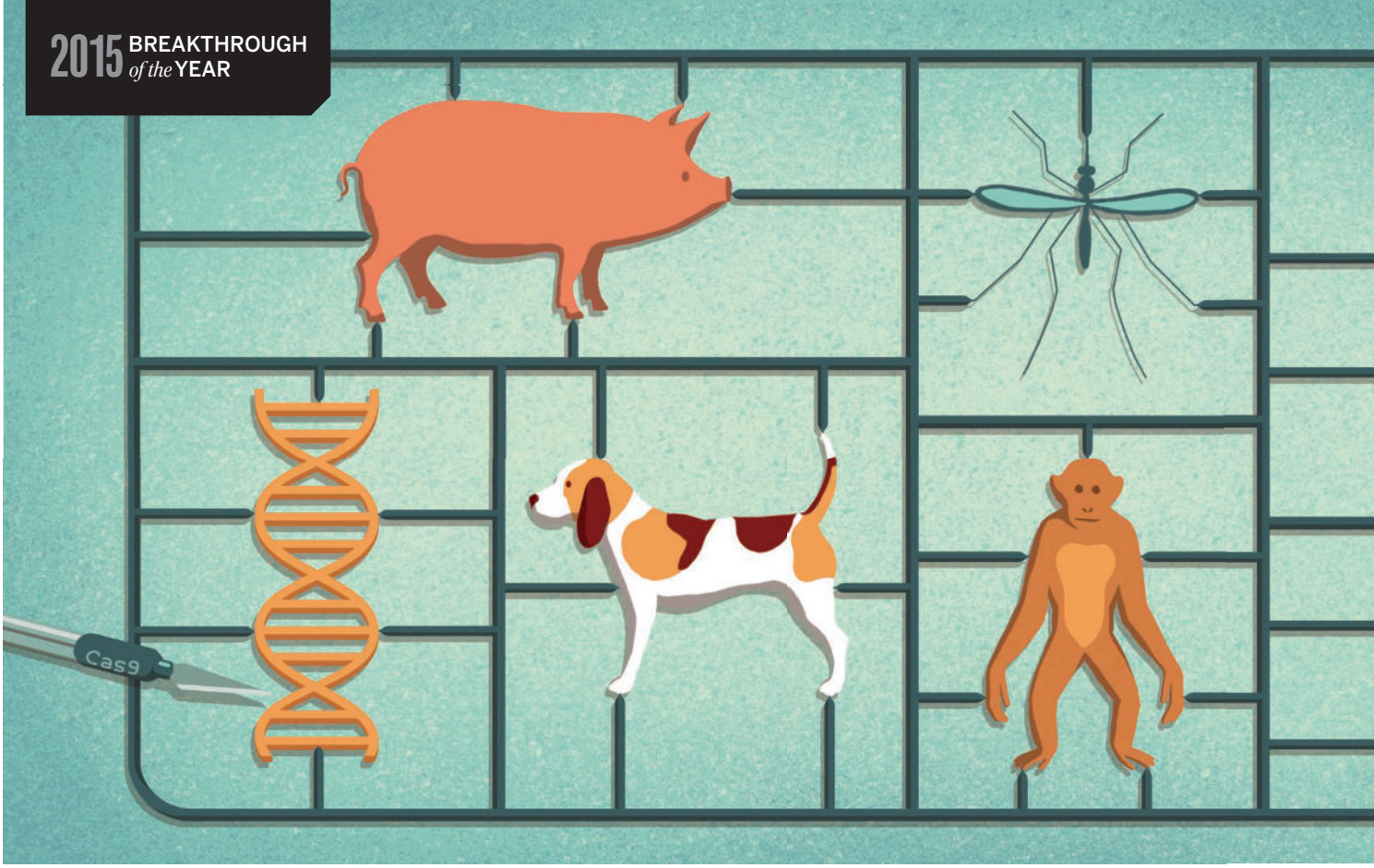

Making the cut

CRISPR genome-editing technology shows its power

By **John Travis**

It was conceived after a yogurt company in 2007 identified an unexpected defense mechanism that its bacteria use to fight off viruses. A birth announcement came in 2012, followed by crucial first steps in 2013 and a massive growth spurt last year. Now, it has matured into a molecular marvel, and much of the world—not just biologists—is taking notice of the genome-editing method CRISPR, *Science*'s 2015 Breakthrough of the Year.

CRISPR has appeared in Breakthrough sections twice before, in 2012 and 2013, each time as a runner-up in combination with other genome-editing techniques. But this is the year it broke away from the pack, revealing its true power in a series of spectacular achievements. Two striking examples—the creation of a long-sought "gene drive" that could eliminate pests or the diseases they carry, and the first deliberate editing of the DNA of human embryos—debuted to headlines and concern. Each announcement roiled the science policy world. The embryo work (done in China with nonviable embryos from a fertility clinic) even prompted an international summit this month to discuss human gene editing. The summit confronted a fraught—and newly plausible—prospect: altering human sperm, eggs, or early embryos to correct disease genes or offer "enhancements." As a genetic counselor quipped during the discussion: "When we couldn't do it, it was easy to say we shouldn't."

What sets CRISPR apart? Its competitors—designer proteins called zinc finger nucleases and TALENs—also precisely alter chosen DNA sequences, and several companies are already exploiting them for therapeutic purposes in clinical trials. But CRISPR has proven so easy and inexpensive that Dana Carroll of the University of Utah, Salt Lake City, who spearheaded the development of zinc finger nucleases, says it has brought about the "democratization of gene targeting." Quoted in a recent issue of *The New Yorker*, bioethicist Hank Greely of Stanford University in Palo Alto, California, compares CRISPR to the Model T Ford: far from the first automobile, but the one whose simplicity of production, dependability, and affordability transformed society. "Any molecular biology lab that wants to do CRISPR can," says Harvard University's George Church, whose lab was one of the first to show that it efficiently edits human and other eukaryotic cells.

Already, the nonprofit group Addgene has distributed about 50,000 plasmids—circlets of DNA—containing genetic code for the two basic components of CRISPR, the "guide RNA" used to target a specific DNA sequence and the DNA-cutting enzyme, or nuclease, usually one called Cas9. "It's going to be like PCR, a tool in the toolbox," says Jennifer Doudna of the University of California, Berkeley, whose group, in collaboration with one led by Emmanuelle Charpentier, now at the Max Planck Institute for Infection Biology in Berlin, published the first report

ILLUSTRATION: DAVIDE BONAZZI/@SALZMANART

Published by AAAS

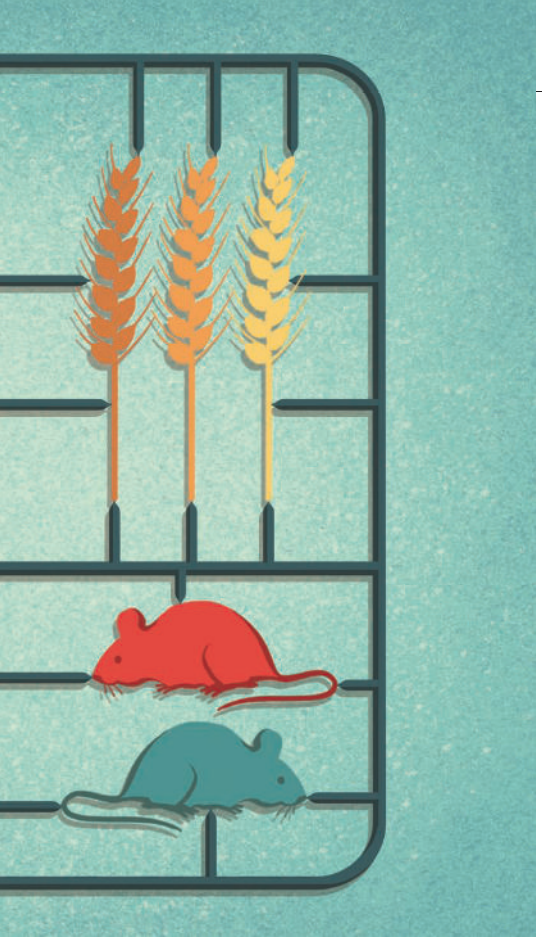

CRISPR's ability to edit DNA has helped scientists create a menagerie of genetically new organisms.

that CRISPR could cut specific DNA targets.

Their work grew out of a surprising observation that bacteria could remember viruses. Looking for a mechanism, researchers found remnants of genes from past infections, sandwiched between odd, repeated bacterial DNA sequences—the "clustered regularly interspaced short palindromic repeats" that give CRISPR its name. The viral scraps serve as an infection memory bank: From them, bacteria create guide RNAs that can seek out the DNA of returning viruses before chopping up the viral genes with a nuclease. Once this mechanism was understood, Doudna and Charpentier, among others, raced to adapt it to editing DNA in higher organisms.

A torrent of applications followed. One of them—the CRISPR-powered gene drive—is a case study in the power, and potential risks, of genome-editing technology. In 2003, Austin Burt, an evolutionary biologist at Imperial College London, envisioned attaching a gene for a desired trait to "selfish" DNA elements that could copy themselves from one chromosome spot to another. That would bias the offspring of a parent carrying the trait to inherit it, quickly spreading it throughout a population. Earlier this year, a U.S. team adapted CRISPR to just that purpose, succeeding well beyond the original vision.

In a method ominously dubbed "mutagenic chain reaction," the researchers drove a pigmentation trait in lab-grown fruit flies to the next generation with 97% efficiency. They then teamed up with another research group to create a gene drive that, unleashed in a lab population of mosquitoes, spread genes that prevent the insects from harboring malaria parasites. Weeks later, working with another malaria-carrying mosquito, Burt and colleagues reported the same thing with genes that rendered the females infertile and could quickly wipe out a population. Debates are now erupting over the benefits and ecological risks of releasing such insects into the wild—and whether gene drives could also thwart invasive species such as Asian carp and cane toads, or combat other animal-borne pathogens such as the one causing Lyme disease.

In other labs, researchers harnessed the technique to create a growing menagerie of genetically engineered animals and plants: extra-muscular beagles, pigs resistant to several viruses, and wheat that can fend off a widespread fungus. Longer-lasting tomatoes, allergen-free peanuts, and biofuel-friendly poplars are all on the drawing board. Depending on how it's wielded, CRISPR can do its work without leaving any foreign DNA behind, unlike earlier techniques for genetically modifying organisms, which poses a challenge for regulations based on the presence of foreign DNA.

There is much, much more. By making "dead" versions of Cas9, scientists eliminated CRISPR's DNA-cutting ability but preserved its talent for finding sequences. Tack molecules onto Cas9 and CRISPR suddenly becomes a versatile, precise delivery vehicle. Several groups, for example, have outfitted dead Cas9s with various regulatory factors, enabling them to turn almost any gene on or off or subtly adjust its level of activity. In one experiment this year, a team led by another CRISPR pioneer, Feng Zhang of the Broad Institute in Cambridge, Massachusetts, targeted the 20,000 or so known human genes, turning them on one by one in groups of cells to identify those involved in resistance to a melanoma drug.

ON OUR WEBSITE

For more on the Breakthrough of the Year, including a video and a podcast, go to http://scim.ag/breakthru15.

The biomedical applications of CRISPR are just starting to emerge. Clinical researchers are already applying it to create tissue-based treatments for cancer and other diseases. CRISPR may also revive the moribund concept of transplanting animal organs into people. Many people feared that retroviruses lurking in animal genomes could harm transplant recipients, but this year a team eliminated, in one fell swoop, 62 copies of a retrovirus's DNA littering the pig genome. And the international summit saw many discussions of CRISPR's promise for repairing genetic defects in human embryos, if society dares to cross what many regard as an ethical threshold and alter the human germline.

In short, it's only slightly hyperbolic to say that if scientists can dream of a genetic manipulation, CRISPR can now make it happen. At one point during the human gene-editing summit, Charpentier described its capabilities as "mind-blowing." It's the simple truth. For better or worse, we all now live in CRISPR's world.

People's choice

Visitors to *Science*'s website voted on our 10 Breakthrough finalists. Their top picks:

1. Pluto **35%**
2. CRISPR **20%**
3. Lymphatic system in the central nervous system **15%**
4. Ebola vaccine **10%**
5. (Tie) Psychology replication/ quantum entanglement **6%**

For the second year in a row, the public weighed in through the Internet, voting for its top discovery while the Breakthrough team was hammering out its choices. High on the list, the results mirrored *Science* staffers' own deliberations. CRISPR surged to an early lead, as high-profile meetings and magazine articles focused public attention on the genome-editing technique. Pluto, a media darling in July when the New Horizons probe swooped past it en route to points beyond, was a distant second.

But the dwarf planet rallied, as New Horizons scientists blitzed Twitter with get-out-the-vote tweets. When the final returns were in, Pluto finished comfortably ahead of CRISPR in the popular vote.

Further down the list, it was a bad year for old bones. *Homo naledi* (a new human species!) finished in seventh place, and Kennewick Man, the ancient Native American whose DNA was recently sequenced, was dead last. Better luck next time, O my people.

Published by AAAS

Close-ups of Pluto revealed mountains of water ice lodged in vast plains of frozen nitrogen.

A big year for small worlds

It was the year of the dwarf planet. Two NASA spacecraft, two encounters, two fuzzy orbs that bloomed in vivid detail before robotic eyes. In March, Dawn went into orbit around Ceres, the largest object in the asteroid belt. And in July, New Horizons zoomed past Pluto, one of the largest objects in the Kuiper belt.

At Pluto, scientists found a place sculpted both in the present day, by the extreme seasons of an elliptical orbit and a 248-year-long year, and billions of years ago, as the dwarf planet cooled and cracked. Scaly textures in a veneer of nitrogen frost bore witness to patterns of sublimation and deposition, as the thin atmosphere breathed through cycles of expansion and collapse. Mountains of water ice towered above smooth plains, jumbled together as if ancient tectonic forces had pushed them across a sea of soft nitrogen ice like drifting icebergs. Two mountains with deep holes in their middles may have been "cryovolcanoes" spewing ice from a warmer interior.

Ceres, closer to the sun, was shaped by different forces. Dark as asphalt, its surface has been brutalized by impacts. Above mysterious bright spots in some of its impact craters floats a haze of dust and water vapor—a hint that Ceres is "outgassing" like a comet on its last legs. Dawn also found ammonia, typical of comets, in surface minerals, adding to the evidence that Ceres is actually a giant dead comet that began its life in the outer solar system, closer to Pluto (see Scorecard, p. 1461). This month, Dawn lowered itself to its final, lowest, mapping orbit, less than 380 kilometers above the surface.

A third small body awaits, as New Horizons heads toward a 2019 rendezvous with a Kuiper belt object called 2014 MU69. After that, New Horizons will glide on, exiting the solar system in a few decades, while Dawn will orbit Ceres for centuries or more.

—Eric Hand

PHOTO: NASA/JOHNS HOPKINS UNIVERSITY APPLIED PHYSICS LABORATORY/SOUTHWEST RESEARCH INSTITUTE

Corrected 17 December 2015; see full text.

Published by AAAS

DNA from Kennewick Man showed that modern Native Americans are his descendants.

Kennewick Man's kin

From the beginning, the bones of the so-called Kennewick Man have sparked contention. Since the 8500-year-old skeleton was discovered on the shore of the Columbia River in Kennewick, Washington, in 1996, anthropologists have debated its relationship to today's Native Americans. Meanwhile, local tribes, regarding "The Ancient One" as an ancestor, have demanded that he be handed over to them and ceremonially reburied. In 2004, the U.S. government granted researchers permission to study the skeleton.

This year, the story took an ironic twist, when experts in ancient DNA succeeded in sequencing Kennewick Man's nuclear genome. The result: The Ancient One is closely related to at least one of the five Washington area tribes that originally fought to reclaim him. More important to scientists, the genome confirms earlier findings, based on DNA from even older human remains, that today's Native Americans are direct descendants of Asian peoples who crossed the Bering land bridge at least 15,000 years ago. Thus, Kennewick Man's genome contradicts suggestions that today's Native Americans stem from later migrants, as well as claims that the first Americans came from Europe rather than Asia.

In a dispute often portrayed as pitting science against cultural traditions, it appears that the Native Americans—who are now renewing their efforts to have The Ancient One turned over to them—may well have had science on their side all along. —*Michael Balter*

Reproducibility in psychology

5

This year caps a transformation for psychological science. The field was mired in scandal just a few years ago. But a band of revolutionaries is turning psychology into a beacon for scientific reproducibility.

Concerns that false positive results might be common in psychology, where studies often involve small numbers of subjects and statistically weak effects, boiled over in 2011. The scandal spurred psychologists to clean up their field—both by replicating key studies and by creating new models of scholarly publication and peer review to restore confidence in published research.

The first crop of replications, in 2013, brought reassuring news: Ten of 13 experiments obtained the same results as the original study. Last year, however, an even larger replication—involving nearly 100 researchers around the world repeating 27 published psychological experiments—proved painful: Not only did about one-third of the follow-up studies fail to replicate, but some of the original authors felt unfairly singled out.

Undaunted, this year the replicators pulled off the biggest do-over yet. In a report published in *Science* in August, 270 psychologists orchestrated a repeat of 100 studies published in three top journals. On the downside, only 39% passed the test. But this time, the process went so smoothly that psychology journal editors announced that the publication of direct replications should become routine.

The innovation that may have the largest effect on the rest of science, however, lies in the design of the replication efforts. The researchers followed a procedure called preregistration, publishing the methods and rationale of each study before the experiments were undertaken. Then they reported the results and statistical analysis no matter what the outcome. That prevents researchers from teasing out positive results from their data or leaving negative results unpublished. If everyone followed that protocol, false positives might all but disappear from journals. —*John Bohannon*

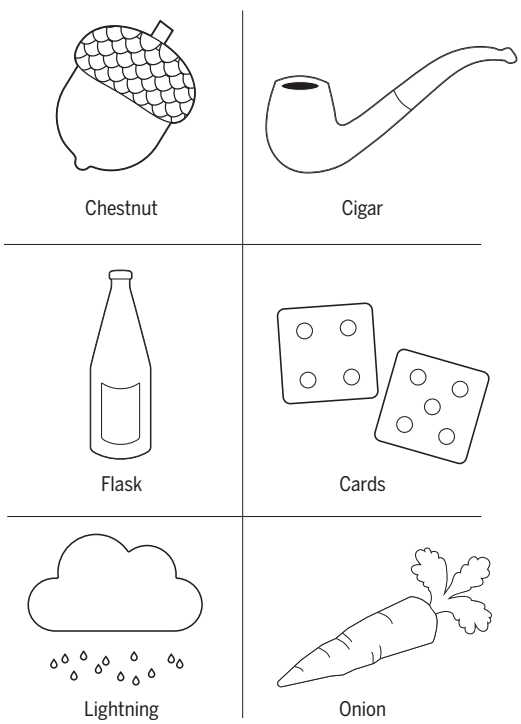

According to the theory of priming, these words change how quickly you can name the images. But the effect has been difficult to reproduce.

CREDITS: (PHOTO) CHIP CLARK, SMITHSONIAN INSTITUTION; (GRAPHIC) G. GRULLÓN/*SCIENCE*

Corrected 17 December 2015; see full text.

Published by AAAS

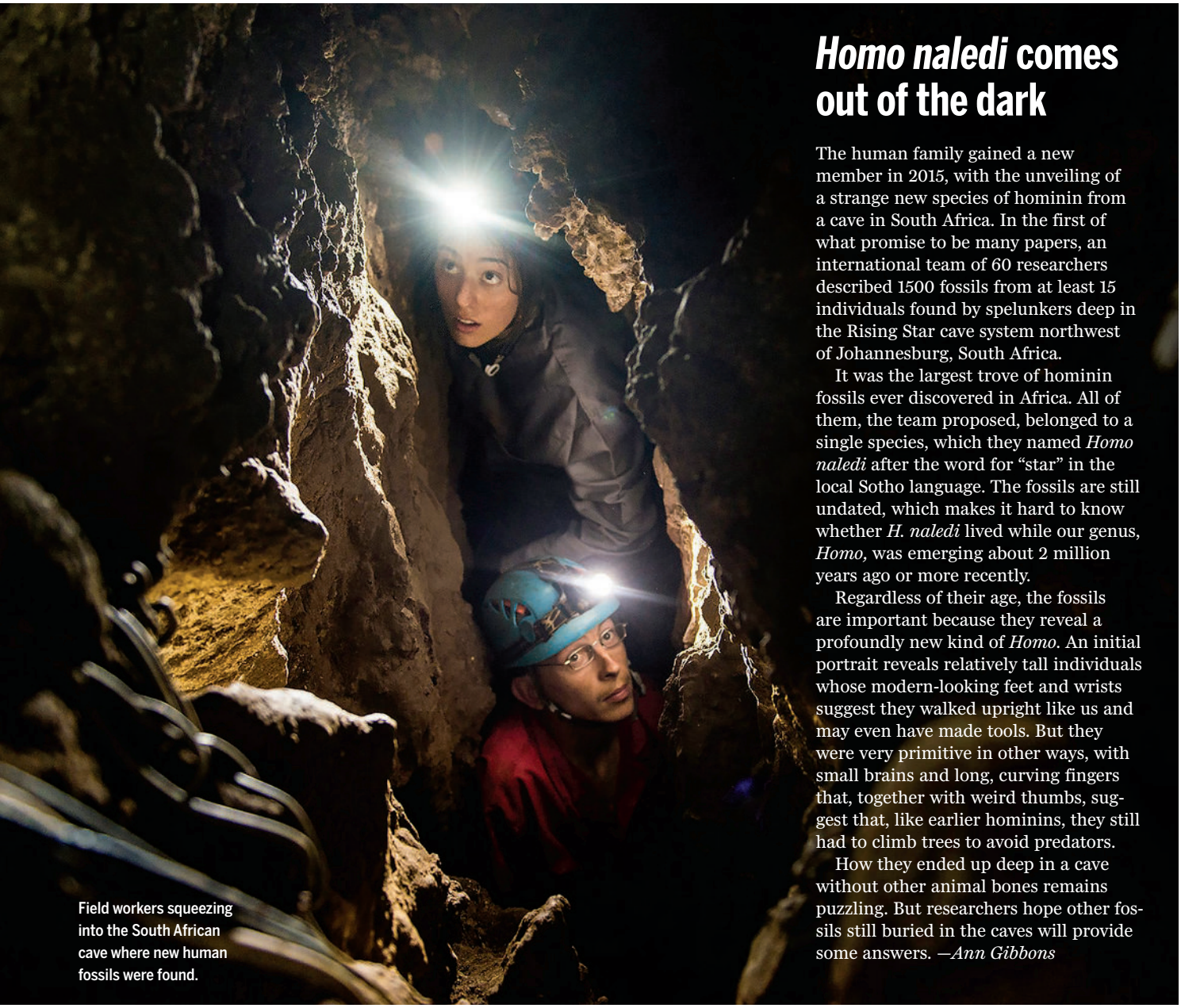

Field workers squeezing into the South African cave where new human fossils were found.

PHOTO: ROBERT CLARK/NATIONAL GEOGRAPHIC

Homo naledi comes out of the dark

The human family gained a new member in 2015, with the unveiling of a strange new species of hominin from a cave in South Africa. In the first of what promise to be many papers, an international team of 60 researchers described 1500 fossils from at least 15 individuals found by spelunkers deep in the Rising Star cave system northwest of Johannesburg, South Africa.

It was the largest trove of hominin fossils ever discovered in Africa. All of them, the team proposed, belonged to a single species, which they named *Homo naledi* after the word for "star" in the local Sotho language. The fossils are still undated, which makes it hard to know whether *H. naledi* lived while our genus, *Homo,* was emerging about 2 million years ago or more recently.

Regardless of their age, the fossils are important because they reveal a profoundly new kind of *Homo*. An initial portrait reveals relatively tall individuals whose modern-looking feet and wrists suggest they walked upright like us and may even have made tools. But they were very primitive in other ways, with small brains and long, curving fingers that, together with weird thumbs, suggest that, like earlier hominins, they still had to climb trees to avoid predators.

How they ended up deep in a cave without other animal bones remains puzzling. But researchers hope other fossils still buried in the caves will provide some answers. —*Ann Gibbons*

Deep mantle plumes rise to the test

Island chains like Hawaii are a clue to Earth's deep stirrings: plumes of hot rock percolating up from its interior. As a tectonic plate crawls over a plume and volcanic eruptions spew material onto the plate, island after island takes shape over geological time.

But for more than 40 years, there has been a debate as hot as the plumes themselves. Do plumes stretch nearly 3000 kilometers down to the base of Earth's rocky mantle? Or could they be fed by shallower reservoirs of magma? To find out, researchers have used seismic waves from earthquakes—which bend and change speed as they encounter boundaries—to probe the mantle like a CT scan. But the images of the deep earth have been frustratingly fuzzy.

Now, geophysicists can see down more clearly, and lo: They have found 28 plumes, stretching all the way to the core. The new studies rely on a computer-intensive technique called "whole waveform tomography," which yields the highest resolution images ever of Earth's interior. Whereas previous studies only used the initial bursts of energy from an earthquake, the new ones now incorporate information from all the squiggles in a seismogram.

The plumes, as thick as 800 kilometers, are three times fatter than theorized, so models of how Earth's core is cooling will need some rethinking. Geophysicists hope the new technique will eventually reveal other details of Earth's interior, including the diving slabs of subducting ocean crust and their presumed resting place in deep mantle "graveyards." —*Eric Hand*

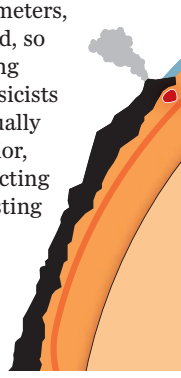

Corrected 17 December 2015; see full text.

Published by AAAS

A study led by the World Health Organization showed that a new vaccine protects against Ebola.

CREDITS: (PHOTO) SEAN HAWKEY; REUTERS/BRIAN SNYDER; (GRAPHIC) A. CUADRA/*SCIENCE*

A vaccine against Ebola

4

The unprecedented campaign to develop drugs and vaccines to fight the Ebola epidemic yielded disappointingly few tangible results. But one potential game changer in future outbreaks emerged in 2015. An Ebola vaccine developed by scientists at the Public Health Agency of Canada—known to work in monkeys, and adopted by the Merck pharmaceutical company at the height of last year's epidemic—proved remarkably successful in a clinical study in Guinea led by the World Health Organization.

Because the trial was launched after the epidemic had begun to dwindle, the vaccine—an innocuous livestock virus with an Ebola surface protein stitched in—was tested in a highly unusual ring vaccination strategy that maximized the chance of detecting an effect. That gamble paid off: A paper published online in *The Lancet* on 31 July showed Merck's vaccine to be between 75% and 100% protective. Another leading vaccine candidate, developed by GlaxoSmithKline, was tested in a traditional setup that ran out of cases and failed to show efficacy.

Regulators such as the European Medicines Agency will need more data before they can give the vaccine their blessing. But Ebola flares up every few years, and even without formal approval, the shots will probably be deployed in the next outbreak on an experimental basis. They may help prevent the West African tragedy from ever happening again. —*Martin Enserink*

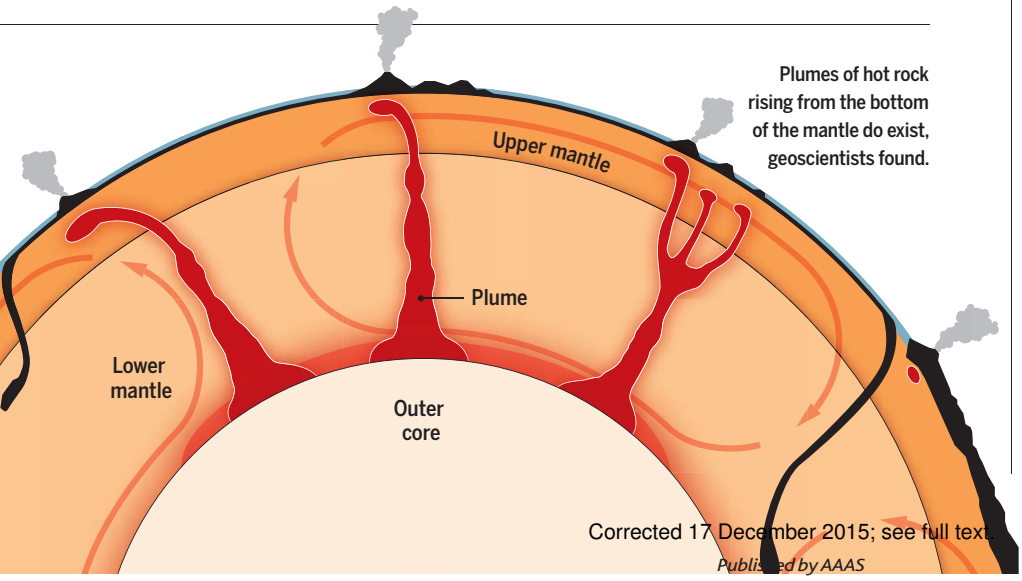

Plumes of hot rock rising from the bottom of the mantle do exist, geoscientists found.

Scorecard for 2015

In every Breakthrough section, staff members record scientific developments they think we'll be talking about in the next year. Our forecasts for 2015 turned out fairly well; next year's are on p. 1464.

ARCTIC SEA ICE

Scientists are still debating whether—and, if so, how—warming in the Arctic and dwindling sea ice influence extreme weather events at midlatitudes. Model limitations, scarce data on the warming Arctic, and the inherent variability of the systems make answers elusive. But a flurry of studies, workshops, and meetings over the past year is ramping up the hunt for an atmospheric link.

SOLAR SYSTEM HISTORY

Could the dwarf planets Ceres and Pluto be twins separated at birth? Scientists have long suspected that Ceres, closer in composition to icy Pluto and its ilk, may be something of an interloper in the asteroid belt. In December, NASA's Dawn spacecraft provided evidence: Mixed with Ceres's surface minerals is ammonia, a compound that could have been stable only in the colder reaches of the outer system. Either the ammonia reached Ceres early on in a fusillade of small impactors, or Ceres formed in the outer solar system and was flung inward to its current locale, perhaps because of the gravitational disruptions of a wandering Jupiter.

LHC RESTART

As expected, after 2 years of repairs, the world's largest atom-smasher, Europe's Large Hadron Collider (LHC), ran at close to its design energy instead of the half-energy that it had coasted at from 2010 to 2013. However, the LHC collected less than half the data envisioned. The hunt for new particles should heat up in the next few years. The future of accelerator-based particle physics may hinge on its success.

COMBINED IMMUNOTHERAPY

Last year we had our eyes on cancer drug combinations that relied at least partly on immunotherapy, using the immune system to target tumors. That research continues to flourish, but there aren't many hard results yet. Still, in September the U.S. Food and Drug Administration approved a combination of two immunotherapy treatments, ipilimumab and nivolumab, for advanced melanoma, and there are hints that some patients respond better to certain combinations still in trials. Keep an eye out in 2016 for more findings in this very active field.

Corrected 17 December 2015; see full text.
Published by AAAS

Engineered microbes (yellow) may help produce safer painkillers.

Yeast engineered to brew opioids

This year, biologists in the United States engineered yeast to convert sugar into the makings of opioid painkillers. The feat of biosynthesis, once unique to opium poppies, might lead to better pharmaceuticals—or, more darkly, to home-brewed morphine and heroin.

In a bioengineering tour de force, the researchers altered yeast to express an additional 21 genes. Those genes originally came from a diverse set of species, including three types of poppies, a plant called Goldthread, bacteria, and even a rat. The result was an organism that could turn sugar into thebaine, normally derived from poppies—the precursor of synthetic painkillers such as

Lymphatic vessels: The brain's well-hidden secret

To anatomists who thought they had the body's systems mapped out, this summer's discovery was like sighting a new continent. An unexpected finding revealed that the lymphatic system—a web of vessels that helps clear waste and transport immune cells in the body—extends into the brain instead of stopping in the neck as most scientists had assumed.

More than 2 centuries ago, an Italian physician, Paolo Mascagni, proposed that the brain has the same lymphatic plumbing as the rest of the body. His claim was largely ignored, but this year, researchers exploring the role of immune cells in the brains of mice spotted a suspiciously well-organized set of T cells in an outer layer of the brain. Nearby vessels seemed to be guiding the cells, and biomarkers showed that the mystery tubes were extensions of the mouse's lymphatic system. Since then, tissue evidence has suggested that human brains harbor similar vessels.

3

Tucked away in the meninges, the outermost layer covering the brain, the well-hidden vessels may offer insights into how the immune system and brain interact. Scientists had thought that brains had their own, self-contained immune defenses, sealed off from the rest of the body. The discovery—or rediscovery—of a physical link could open new avenues for exploring neurodegenerative and neuroinflammatory diseases like Alzheimer's, multiple sclerosis, and meningitis. But researchers say that for now, their top priority is fathoming the basic structure and function of the newly discovered network. —*Hanae Armitage*

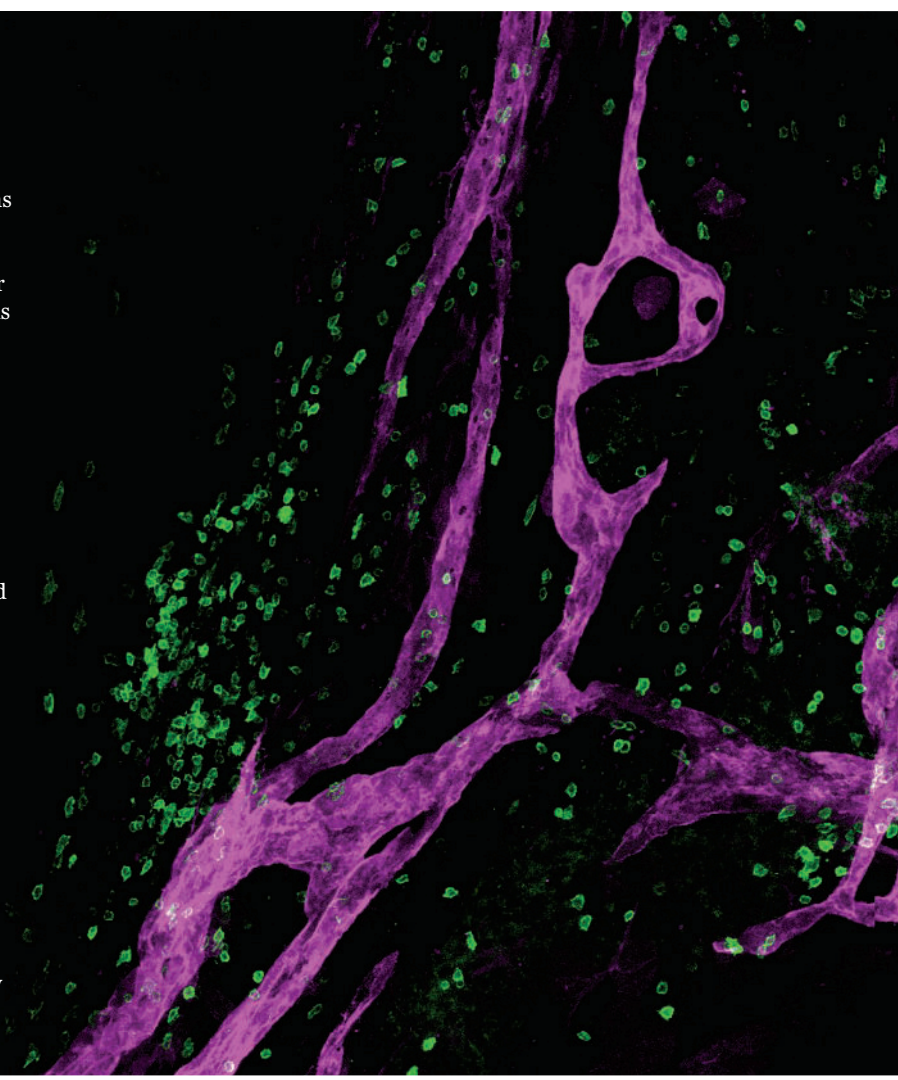

Corrected 17 December 2015; see full text.

Published by AAAS

hydrocodone and oxycodone. With two additional genes, the yeast could make hydrocodone as well.

The U.S. team and others had previously engineered different yeast strains to carry out either the first or second half of this complex pathway. This year, they took the final steps: performing a single chemical transformation to link the two halves, and putting all the genes together in one strain of yeast.

The newly engineered yeasts are far from efficient: Producing one dose of painkiller would probably take thousands of liters of culture. (Reassuringly, the researchers found that a home-brew setup couldn't make enough opioid to be detectable.) Medicinal chemists are now working to increase the yeasts' output and trying to tweak their biochemistry to produce safer, more effective drugs. *—Robert F. Service*

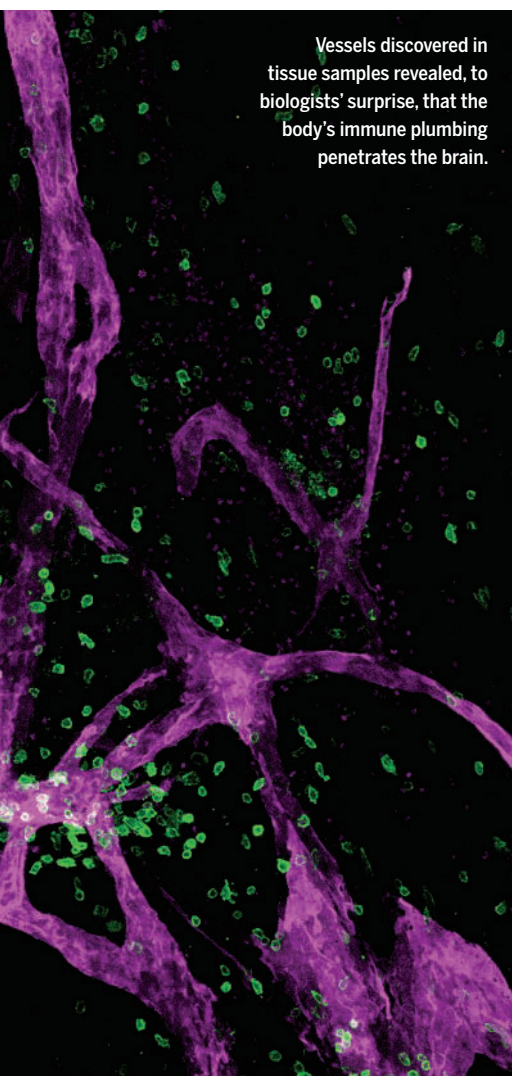

Vessels discovered in tissue samples revealed, to biologists' surprise, that the body's immune plumbing penetrates the brain.

PHOTOS: (CLOCKWISE FROM TOP LEFT) WILLIAM DELOACHE AT UC BERKELEY; © 1982–2015 CERN; JONATHON KIPNIS AND ANTOINE LOUVEAU/UNIVERSITY OF VIRGINIA

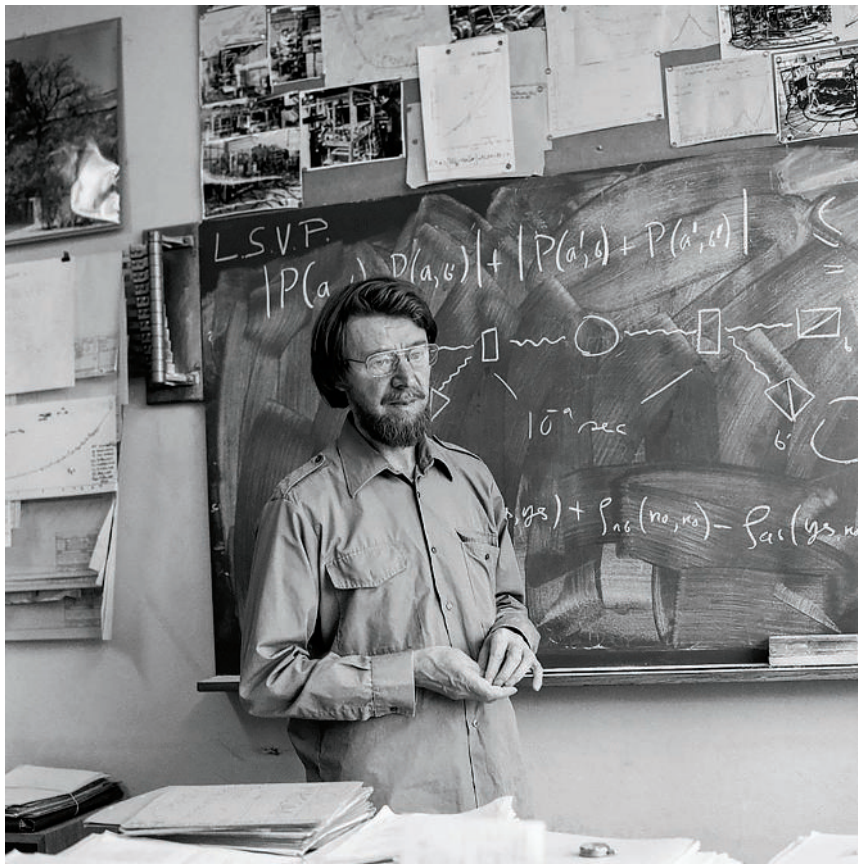

John Bell's 50-year-old quantum acid test confirmed that the world is stranger than Einstein thought.

5 Quantum weirdness confirmed

It may be the strangest idea in quantum mechanics: Measuring the property of one quantum particle, such as a photon, can instantly determine the state of another quantum particle, even if it's light-years away. Albert Einstein balked at such "spooky action at a distance" because it seemed to clash with his postulate that nothing can travel faster than light. But this year, many researchers say, physicists in the Netherlands demonstrated beyond a reasonable doubt that such remote influence exists.

The strange quantum linkage is called entanglement. When particles are entangled, their states are completely uncertain but nonetheless correlated. For example, an electron can be prepared so that if you measure it, you'll have a 50% chance of finding it spinning in one direction, and a 50% chance of finding it spinning the opposite way. But you can entangle two such electrons so that if you measure the state of the first one and find it spinning one way, you will know instantly that the state of the other photon has "collapsed" to the opposite spin.

Einstein and others hoped particles like electrons would turn out to harbor "local hidden variables" that determine each entangled particle's state from the beginning, eliminating the need for any kind of remote influence. In 1964, the U.K. theorist John Bell realized that subtle statistical measurements could reveal whether hidden variables were at work.

Earlier versions of Bell's test jibed with the quantum theory and not with hidden variables, but technical loopholes left room for doubt. This year's experiment—which entangled electrons 1.3 kilometers apart—closes the loopholes and drives a stake through local hidden variables. The result won't surprise many physicists, but it could pave the way for exotic technologies such as a quantum Internet.

It also leaves relativity intact, in spite of Einstein's fears. As Bell noted when he first proposed the test, even though the "action at a distance" happens instantaneously, it can't be used to send signals faster than light. *—Adrian Cho*

Corrected 17 December 2015; see full text.

Published by AAAS

Areas to watch in 2016

News writers live partly in the future. They may not know exactly what lies ahead, but, like old-time whalers, they do keep a sharp eye on the horizon. Here are a few items on the Breakthrough team's "watch list" for the next year.

FALLING BODIES

French researchers plan to launch a satellite that in the next 2 years will recreate in space possibly the most famous experiment that never happened. Most likely, Galileo didn't really drop balls made of two different materials from the Leaning Tower of Pisa—his legendary demonstration that all objects accelerate at the same rate under the pull of gravity. However, physicists with MicroSCOPE (an acronym for the French equivalent of the Drag-Compensated Microsatellite for the Observation of the Equivalence Principle) actually will test whether two free-falling cylinders of different materials, titanium and platinum-rhodium, experience a different pull from Earth's gravity and orbit at ever-so-slightly different heights. Any difference would violate the equivalence principle, which says that gravitational mass equals inertial mass and lies at the heart of Einstein's general theory of relativity. The experiment's a long shot, but a fun one.

WHO LET THE DOGS IN?

Could 2016 be the year we finally figure out where dogs came from? For decades, scientists have debated where and when wolves were domesticated into our canine pals. The proposed epicenters range from Europe to Asia, and the time frames span 15,000 to more than 30,000 years ago. In 2013, the major warring factions declared a truce and began pooling their resources and scouring the globe for every ancient wolf and dog specimen they could get their hands on. Now, they may be close to a definitive answer, one that could solve one of the greatest mysteries of domestication. One of the collaboration's leaders says significant findings should come next year.

GRAVITATIONAL WAVES

Newly upgraded detectors could finally give physicists a glimpse of gravitational waves: ripples in space and time set off by, say, two neutron stars spiraling into each other. This year, scientists with the Laser Interferometer Gravitational-Wave Observatory (LIGO) completed rebuilds of their kilometers-long facilities in Livingston, Louisiana, and Hanford, Washington, to make them up to 10 times more sensitive than when they ran from 2002 to 2010. LIGO took 3 months' worth of data this year. However, the physicists are still tuning up their detectors and will make a longer data run later next year. Meanwhile, European researchers plan to bring their upgraded VIRGO detector near Pisa, Italy, on line. Scientists say that when LIGO and VIRGO reach their design sensitivities in a few years, they are virtually certain to pick up a passing ripple. With luck, they might see one sooner.

Dogs evolved from wolves, but where and when? We may soon know.

Breakdown of the Year: Assault on the past

For 2000 years, the imposing colonnades of the great temple of Baal rose from the desert in the ancient city of Palmyra, in today's Syria. The temple's friezes recorded the story of this ancient crossroads of East and West, and had weathered centuries of conflict, from the warrior queen Zenobia's ill-fated rebellion against Rome to two world wars. But in August 2015, a lethal combination of 21st century explosives and a twisted, 7th century worldview erased that history, when the group known as the Islamic State (IS) group deliberately blew up the temple.

"Palmyra symbolizes everything that extremists abhor—cultural diversity, dialogue between cultures, the encounter of peoples of all origins in this caravan city between Europe and Asia," UNESCO Director-General Irina Bokova said in October, after the group, also known as Daesh, felled the ancient city's iconic Arch of Triumph.

Palmyra, a UNESCO World Heritage Site, was but one of the archaeological wonders that suffered this year as the IS group rampaged through parts of Syria and Iraq, brutalizing local populations and destroying their culture, including archaeological sites. What wasn't destroyed was often plundered and sold, lost either way to humanity and to archaeological research. "I believe [it] is the worst cultural heritage crisis since World War II," says Michael Danti, academic director at the Cultural Heritage Initiative of the American Schools of Oriental Research.

The region is the birthplace of some of humanity's greatest innovations—among them the first agricultural societies, the first writing, and the first empires; it's also home to major World Heritage Sites from later periods. So archaeologists were horrified when, in February, the IS group released a video of men taking sledgehammers to statues in the Mosul Museum in northern Iraq, and drilling away the features of a great winged bull, a Neo-Assyrian sculpture dating to the 8th century B.C.E. In early April, the group

PHOTOS: (LEFT TO RIGHT) EHLERS/ISTOCKPHOTO; JAMES L. STANFIELD/NATIONAL GEOGRAPHIC CREATIVE

Published by AAAS

The 1800-year-old Roman Arch of Triumph in Palmyra, Syria, is gone—demolished by the Islamic State group.

destroyed monuments and bulldozed ruins in the World Heritage Site of Hatra, Iraq, then raced on to do the same at Nimrud, an ancient Assyrian city and also a World Heritage Site. Claiming to wish to "purify" the region of anything "un-Islamic," the militants have also systematically destroyed countless smaller sites, including mosques, churches, and shrines that testify to the diversity of religions both now and in ancient times.

Many of the major sites had previously suffered looting and collateral damage from conflict. But the IS group treated them as targets in a campaign of cultural cleansing. At major sites, explosions were set off as scripted performance pieces, with the release of photos and videos timed for maximum public relations value. Meanwhile, the group has set up industrial-scale looting operations to dig up and sell artifacts, which provide a sizable portion of its income. Satellite images show looters' holes pocking key sites, signaling a loss of priceless archaeological knowledge.

In May, in a raid in eastern Syria, U.S. special forces killed a militant known as Abu Sayyaf who was apparently deeply involved in the antiquities trade. They found a cache of archaeological objects, including coins, suggesting large-scale looting. Some turned out to be fakes, but others still bore inventory numbers from an Iraqi museum. Much of the looting has been market-driven, Danti says, with Hellenistic, Roman, and Byzantine periods especially targeted.

In Palmyra, the IS group wove the attacks on archaeology into its brutal treatment of locals. The group executed 50 captured soldiers in the ancient city's amphitheater and tied captives to columns, then exploded the columns. The group also beheaded Khaled al-Asaad, an 82-year-old Syrian archaeologist who had spent his life studying and protecting Palmyra's ruins. Many other Iraqis and Syrians have risked and lost their lives to protect sites.

UNESCO and several partners now have a program to put 5000 cameras on the ground to document threatened sites and artifacts, including many in the Middle East. Agencies are also working to reduce the trade in looted objects. Another program, run by the University of Pennsylvania Museum of Archaeology and Anthropology and partner institutions, has trained Iraqi locals to protect threatened sites and swiftly pack up artifacts, employing techniques last widely used during WWII. When the conflict raged around the Ma'arra museum outside Aleppo in June, its delicate frescoes had been sandbagged and mostly survived—a minor victory in a terrible year for world heritage. —*Elizabeth Culotta*

Breakdown runners-up

SEXISM IN SCIENCE

This year exposed an underbelly of sexist attitudes in science. In April, a Twitterstorm erupted when a reviewer for *PLOS ONE* suggested that what two (female) scientists really needed to improve their paper was a male co-author. Twitter exploded again in June, when Nobel laureate Tim Hunt told an audience that when women are in the lab, "you fall in love with them and they fall in love with you," although many defenders argued that his remarks were a failed joke. Then in October, prominent University of California, Berkeley (UC), astronomer Geoff Marcy was found to have repeatedly violated the university's sexual harassment policy over a decade, groping, kissing, and touching female students. Despite the bad news barrage, the revelations had a salutary effect: *PLOS ONE* removed the reviewer and editor involved, and women countered Hunt under the hashtag #distractinglysexy, posting photos of themselves doing science bedecked in field and lab gear. As for Marcy, the national tide of outrage proved too great, and he resigned from the UC system on 14 October.

THIRTY METER TELESCOPE

This year, a project to build the largest optical telescope on U.S. soil collided head-on with the rights and beliefs of indigenous people.

The builders of the Thirty Meter Telescope (TMT) got an inkling of trouble in October 2014, when protesters disrupted the project's groundbreaking ceremony on the Hawaiian mountain of Mauna Kea. The mountain is considered sacred in the Hawaiian religion, and—although 13 telescopes already crowd the summit—opponents claim the enormous TMT would desecrate it.

Since March 2015, protesters have been blocking construction crews from reaching the site, and dozens have been arrested. A 1-week halt in construction has grown into an indefinite hiatus. Then, in December, Hawaii's Supreme Court ruled that the TMT's construction permit was invalid because opponents hadn't been given time to make their case before it was awarded in 2011—a setback that could delay construction for years. The outlook for the telescope—meant to deliver some of the clearest ever views of the cosmos—appears distinctly cloudy.

Published by AAAS

INSIGHTS

How microbes reduce sulfur p. 1476 ▸

Memory networks p. 1477

PERSPECTIVES

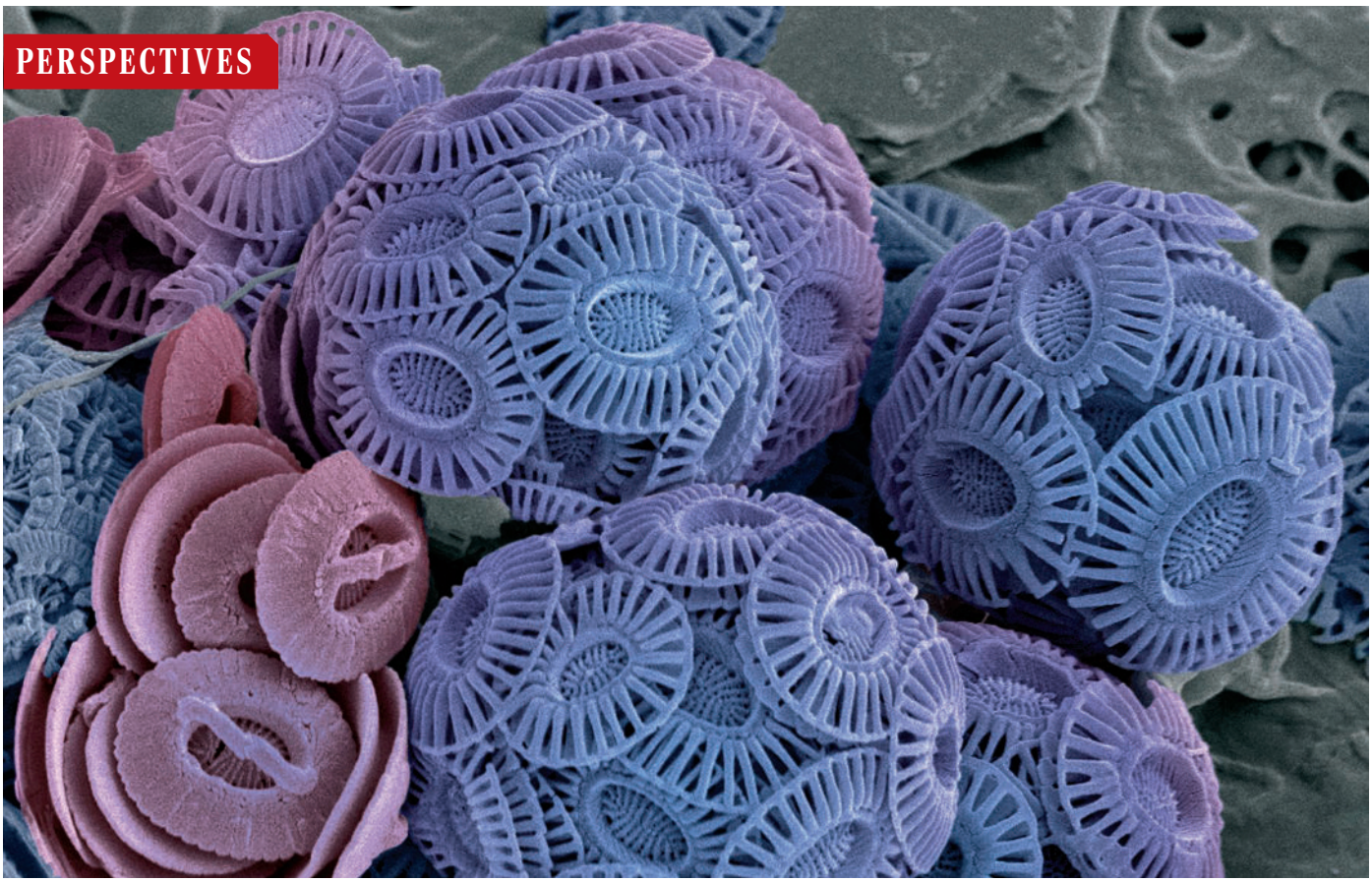

Climate-related phytoplankton habitat shifts. Colored scanning electron micrograph of the calcium carbonate shells of coccolithophores. Each plate is about ~2.5 μm wide. Ranges and abundances of this and other phytoplankton groups shift with changing ocean conditions.

PHOTO: STEVE GSCHMEISSNER/SCIENCE SOURCE

ECOLOGY

Adrift in an ocean of change

Rising temperatures and ocean acidification drive changes in phytoplankton communities

By **Meike Vogt**

Phytoplankton communities play a key role in the global biogeochemical cycling of many essential chemical elements by fixing carbon, nitrogen, and other nutrients into their biomass. If today's oceans were devoid of life, atmospheric CO_2 concentrations would be much higher than currently observed. As marine biologists strive to uncover present plankton distribution and diversity (*1*, *2*), evidence is accumulating that phytoplankton assemblages are already being affected by global change (*3*). In this issue, Rivero-Calle *et al.* (page 1533) (*4*) and McMahon *et al.* (page 1530) (*5*) use observational records of phytoplankton communities from two ocean basins to document climate-related shifts in phytoplankton communities and their environmental drivers on time scales of several decades to millennia (see the figure). The results may have implications for future ocean carbon uptake and storage.

In the realm of phytoplankton, the Who's Who is of critical importance to ecosystem function. Different phytoplankton groups have evolved various physiological strategies that allow them to thrive in marine environments ranging from freezing, nutrient-rich polar waters to warm, nutrient-poor subtropical ocean deserts. Their extensive functional diversity allows them to differentially influence global biogeochemical cycles through a variety of cellular processes that transform, store or metabolize nutrients such as nitrogen, phosphorus and carbon. For example, coccolithophores build calcium carbonate shells, influencing the ocean's carbonate chemistry and carbon export patterns (*4*). Diazotrophs fix atmospheric nitrogen during growth, thus increasing the ocean's nutrient reservoirs, marine productivity, and the efficiency of carbon export (*5*). As the climate changes,

Published by AAAS

the ranges and abundances of these and other functional groups of phytoplankton will shift. The consequences for marine ecosystem functioning and global biogeochemical cycles are as yet poorly quantified.

Despite the importance of these functional groups, little is known about their past and present distributions (*6*). Few long-term time series of pelagic phytoplankton community composition exist, because phytoplankton sampling is costly and laborious and many ocean regions are vast and remote. Laboratory studies often focus on monocultures of a few strains and thus cannot fully capture ecosystem responses, in which physiological changes at the individual level are inextricably linked to changes in the relative fitness of different taxa in a changing environment.

Shedding light on the drivers and consequences of past changes in phytoplankton communities may help us to understand their responses to future climate change. Rivero-Calle *et al.* combine long-term monitoring data with a sophisticated statistical modeling approach to show that coccolithophore abundance has increased significantly over the past five decades in the North Atlantic. They suggest that CO_2 is the primary driver of this pattern.

A preceding study based on a similar statistical model and a subset of the same dataset recorded similar coccolithophore trends, but identified temperature rather than pCO_2 as the main driver of the increase (*7*). Given that CO_2 and temperature simultaneously affect phytoplankton growth and competition, isolating their individual effects on phytoplankton physiology and competition is challenging at the ecosystem level.

Rivero-Calle *et al.* use a synthesis of published coccolithophore growth rates as a function of CO_2 and temperature to disentangle the effect of both drivers. They show that changes in temperature alone are too small to explain the magnitude of the change in coccolithophore prevalence, but that the increase is consistent with a higher growth rate due to the effect of CO_2. Linking basin-scale ecological changes to physiological changes at the cell level, this innovative study provides new evidence for a substantial reorganization of North Atlantic phytoplankton communities.

The North Atlantic is not the only basin experiencing major phytoplankton regime shifts. McMahon *et al.* reveal three different plankton regimes that succeeded each other over the past millennium in the North Pacific subtropical gyre. The authors analyzed the elemental composition of the skeletons of long-lived deep-sea corals. The skeletons record the coral's past diet of phytoplankton detritus and serve as a long-term archive of the surface phytoplankton community composition. Each regime shift identified by McMahon *et al.* coincided with major climatic changes. With the onset of the industrial era, the plankton community transitioned from a mixed community of eukaryotes and non-nitrogen–fixing cyanobacteria to one characterized by an increased contribution of diazotrophs.

McMahon *et al.* attribute the trend in diazotroph abundance to increasing sea surface temperature, stratification, and decreasing nutrient availability but do not rank these environmental drivers and do not discuss CO_2. Laboratory studies have shown that the growth of nitrogen-fixing cyanobacteria is favored under high-CO_2 conditions (*8*). Over the past millennium, changes in ocean pCO_2 were small and thus unlikely to drive the documented regime shifts, but global warming and ocean acidification may well act in

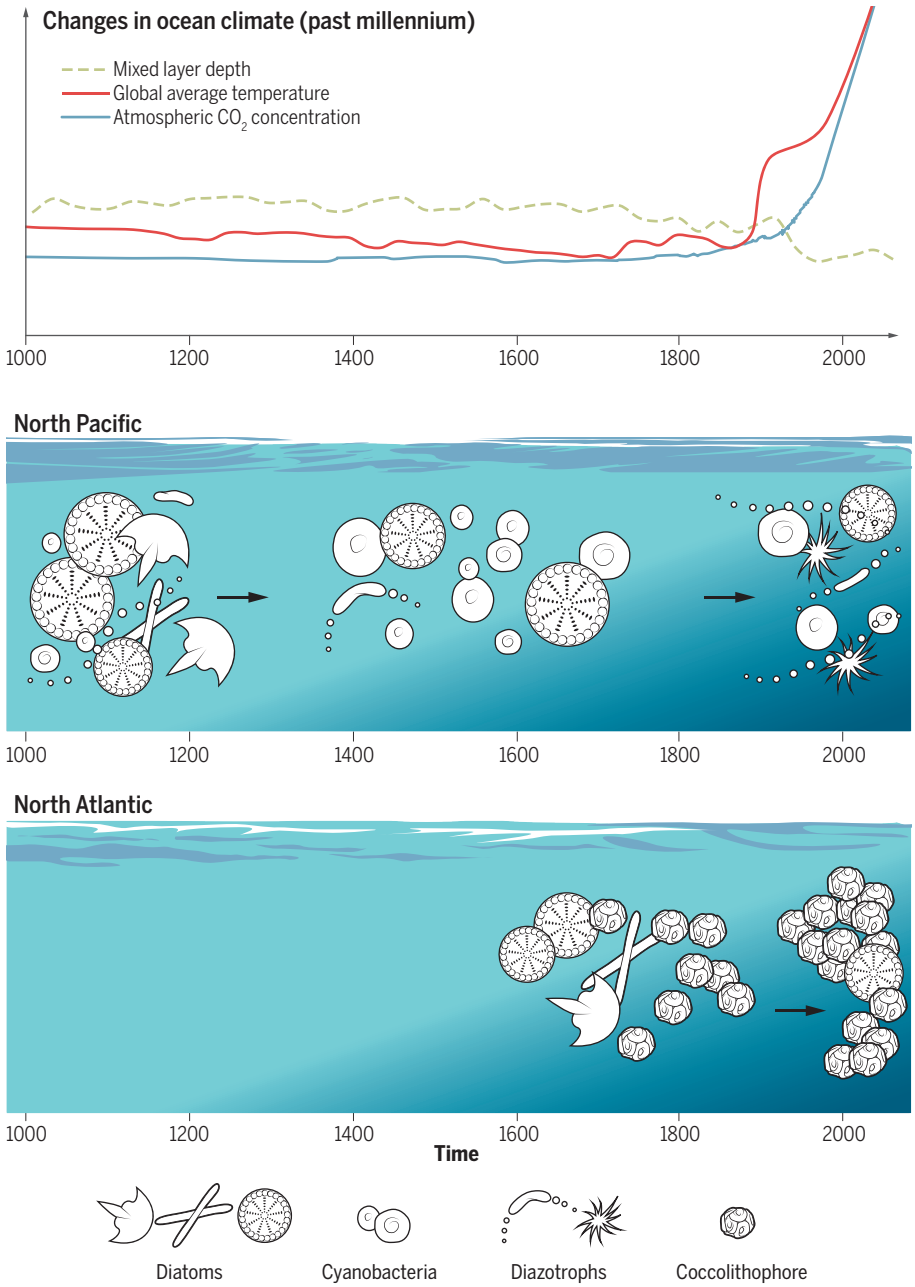

Phytoplankton trends. With rising CO_2 concentrations and temperatures, McMahon *et al.* find evidence of subtropical North Pacific phytoplankton communities shifting from non-nitrogen fixing to nitrogen-fixing, cyanobacteria-dominated phytoplankton communities during the past millennium. In the North Atlantic, Rivero-Calle *et al.* detect an increase in the relative abundance of coccolithophores in temperate and subtropical phytoplankton communities over recent decades.

ILLUSTRATION: P. HUEY/*SCIENCE*

Institute for Biogeochemistry and Pollutant Dynamics, ETH Zurich, Zurich, Switzerland. E-mail: meike.vogt@env.ethz.ch

Published by AAAS

concert to restructure future Pacific phytoplankton communities.

A recent modeling study lends further support to the suggestion that CO_2 might equal or even outrank temperature in its potential to alter future phytoplankton communities. Using a complex global marine ecosystem model, Dutkiewicz *et al.* simulated phytoplankton community structure under global warming and ocean acidification over the 21st century (*9*). Differing growth responses of the phytoplankton types to increased pCO_2 caused substantial shifts in simulated phytoplankton communities, with global increases in both coccolithophore and diazotroph biomass.

Regardless of the main drivers, the species and regime shifts in the phytoplankton communities are likely to alter ocean biogeochemistry. Yet, the relationships between community structure and ocean biogeochemistry are poorly understood, and current evidence suggests that they will depend on the spatiotemporal scales at which they are considered. For example, several long-term studies have reported a negative correlation between past coccolithophore calcification rates and CO_2 levels (*10*, *11*). However, a short-term laboratory study simulating future conditions has identified a few coccolithophore species with impressive adaptive capabilities, providing a compensation mechanism for rising CO_2 (*12*).

As climate change is altering marine ecosystems at an unprecedented rate, research efforts must address the link between marine ecosystem function and phytoplankton biogeography. Further insight will require integration of in situ, satellite, and palaeoceanographic observations with laboratory studies and modeling. Data limitation continues to be the most pressing problem for monitoring large-scale species and regime shifts. Even though the environment in which they live will undergo substantial changes, phytoplankton evolved billions of years ago and are likely to stay afloat in the changing seas. The question is how higher trophic level organisms, such as us, will deal with changes in the services that plankton ecosystems provide. ■

REFERENCES

1. C. de Vargas *et al.*, *Science* **348**, 1261605 (2015).
2. S. Sunagawa *et al.*, *Science* **348**, 6237 (2015).
3. P. Reid *et al.*, *Nature* **391**, 546 (1998).
4. S. Rivero-Calle *et al.*, *Science*, **350**, 1533 (2015).
5. K. W. McMahon *et al.*, *Science* **350**, 1530 (2015).
6. E. Buitenhuis *et al.*, *Earth Sys. Sci. Data* **5**, 227 (2013).
7. G. Beaugrand *et al.*, *Nat. Climate Change* **3**, 263 (2013).
8. D. Hutchins *et al.*, *Nat. Geosci.* **6**, 790 (2015).
9. S. Dutkiewicz *et al.*, *Nat. Climate Change* **5**, 1002 (2015).
10. S. O'Dea *et al.*, *Nat. Commun.* **5**, 5363 (2014).
11. L. Beaufort *et al.*, *Nature* **476**, 80 (2011).
12. L. Schlüter *et al.*, *Nat. Climate Change* **4**, 1024 (2014).

10.1126/science.aad6946

MATERIALS SCIENCE

Disclosing boron's thinnest side

Borophene—stable, single-atom-thick layers of boron—displays remarkable properties

By **Hermann Sachdev**[1,2]

Current research on two-dimensional (2D) materials like graphene, boronitrene layers, phosphorene, silicene, or transition-metal dichalcogenides is focused on the tuning of their electronic and photonic properties combined with high-quality film syntheses. Major goals are the fabrication of (semi)-conducting films for nanoscale electronic devices and applications to improve the performance of energy conversion and storage systems (*1*–*4*). The mechanical properties of graphene and MoS_2 are also being considered for their nano- and mesoscale tribological aspects (*5*). On page 1513 of this issue, Mannix *et al.* (*6*) report on the formation of atomically thin boron films—borophene—by the evaporation and deposition of boron on a Ag(111) surface. The position of boron in the periodic system, between metallic beryllium and nonmetallic carbon, classifies it as a semimetal. Boron displays a pronounced ability to form not only strong covalent two-center-two-electron bonds, but also stable electron-deficient three-center-two-electron bonds. This results in a manifold of 3D cluster patterns for the solid-state structures of elemental boron polymorphs. The strong covalent bonds are responsible for boron and structurally related borides being hard materials. Also, no other p-block element shows a similar complexity of chemical bonding, which is as well displayed within the cluster chemistry of boron hydrides and carboranes (*7*).

"...single and multiple borophene layers offer a broad perspective for the development of nanoscale electronic devices..."

Mannix *et al.* characterized the boron monolayers by scanning tunneling microscopy and low-energy electron diffraction and found that they display a remarkable similarity to a model for "borophene," a quasiplanar molecular compound consisting of a B_{36} cluster of boron atoms (*8*). The dominant pattern of this molecular structure exhibits a hexagonal array of boron atoms with an additional boron atom located centrally within each B_6 hexagon. Because no alloying with the underlying silver substrate is observed, the single atom thick layer of boron can be considered as a novel 2D boron polymorph. Owing to the strong covalent interactions within this 2D borophene layer, the structure resembles a missing link between fully covalent bound 2D materials (graphene, boronitrene layers, phosphorene) and support-stabilized semimetallic films of single atomic thickness like silicene and germanene.

Depending on the relative orientation of the boron monolayer to the Ag(111) substrate and the deposition conditions, different domain structures can be distinguished. These structures can be derived from a corrugated hexagonal array of boron atoms, with additional boron atoms located above each center of a six-membered ring (see the figure), with distortions imposed by the substrate symmetry leading to ribbonlike structural features (*6*). Like benzene (C_6H_6) for graphene, a B_7 molecular cluster (being formed by boron evaporation and stable as per calculations) can be formally regarded as an elemental structure of the borophene layer.

In situ electronic characterization by scanning tunneling spectroscopy reveals anisotropic metallic characteristics, with the electronic conductivity correlating to the chainlike superstructures according to density-of-state calculations. Borophene layers are more stable than silicene layers, owing to the strong covalent interactions of boron atoms by multicenter electron-deficient bonds, but still display a considerable reactivity, e.g., toward oxygen. The borophene structure could be successfully stabilized with a Si/SiO_x buffer layer for exposure at ambient conditions, as indicated by transmission electron microscopy.

These films give rise to considerable toughness, in addition to their structural and electronic properties. Calculations reveal an in-plane Young's modulus in correlation with the experimentally observed structural anisotropy of the boron epilayer (398 GPa·nm

[1]*Max Planck Institute for Polymer Research, Ackermannweg 10, D-55128 Mainz, Germany.* [2]*Technische Universität Kaiserslautern, Abt. Mechanische Verfahrenstechnik/Particle Process Engineering, Gottlieb-Daimler-Straße Geb. 44, D-67663 Kaiserslautern, Germany. E-mail: sachdev@mpip-mainz.mpg.de; hermann.sachdev@mv.uni-kl.de*

Published by AAAS

concert to restructure future Pacific phytoplankton communities.

A recent modeling study lends further support to the suggestion that CO_2 might equal or even outrank temperature in its potential to alter future phytoplankton communities. Using a complex global marine ecosystem model, Dutkiewicz *et al.* simulated phytoplankton community structure under global warming and ocean acidification over the 21st century (*9*). Differing growth responses of the phytoplankton types to increased pCO_2 caused substantial shifts in simulated phytoplankton communities, with global increases in both coccolithophore and diazotroph biomass.

Regardless of the main drivers, the species and regime shifts in the phytoplankton communities are likely to alter ocean biogeochemistry. Yet, the relationships between community structure and ocean biogeochemistry are poorly understood, and current evidence suggests that they will depend on the spatiotemporal scales at which they are considered. For example, several long-term studies have reported a negative correlation between past coccolithophore calcification rates and CO_2 levels (*10*, *11*). However, a short-term laboratory study simulating future conditions has identified a few coccolithophore species with impressive adaptive capabilities, providing a compensation mechanism for rising CO_2 (*12*).

As climate change is altering marine ecosystems at an unprecedented rate, research efforts must address the link between marine ecosystem function and phytoplankton biogeography. Further insight will require integration of in situ, satellite, and palaeoceanographic observations with laboratory studies and modeling. Data limitation continues to be the most pressing problem for monitoring large-scale species and regime shifts. Even though the environment in which they live will undergo substantial changes, phytoplankton evolved billions of years ago and are likely to stay afloat in the changing seas. The question is how higher trophic level organisms, such as us, will deal with changes in the services that plankton ecosystems provide. ■

REFERENCES

1. C. de Vargas *et al.*, *Science* **348**, 1261605 (2015).
2. S. Sunagawa *et al.*, *Science* **348**, 6237 (2015).
3. P. Reid *et al.*, *Nature* **391**, 546 (1998).
4. S. Rivero-Calle *et al.*, *Science*, **350**, 1533 (2015).
5. K. W. McMahon *et al.*, *Science* **350**, 1530 (2015).
6. E. Buitenhuis *et al.*, *Earth Sys. Sci. Data* **5**, 227 (2013).
7. G. Beaugrand *et al.*, *Nat. Climate Change* **3**, 263 (2013).
8. D. Hutchins *et al.*, *Nat. Geosci.* **6**, 790 (2015).
9. S. Dutkiewicz *et al.*, *Nat. Climate Change* **5**, 1002 (2015).
10. S. O'Dea *et al.*, *Nat. Commun.* **5**, 5363 (2014).
11. L. Beaufort *et al.*, *Nature* **476**, 80 (2011).
12. L. Schlüter *et al.*, *Nat. Climate Change* **4**, 1024 (2014).

10.1126/science.aad6946

MATERIALS SCIENCE

Disclosing boron's thinnest side

Borophene—stable, single-atom-thick layers of boron—displays remarkable properties

By **Hermann Sachdev**[1,2]

Current research on two-dimensional (2D) materials like graphene, boronitrene layers, phosphorene, silicene, or transition-metal dichalcogenides is focused on the tuning of their electronic and photonic properties combined with high-quality film syntheses. Major goals are the fabrication of (semi)-conducting films for nanoscale electronic devices and applications to improve the performance of energy conversion and storage systems (*1*–*4*). The mechanical properties of graphene and MoS_2 are also being considered for their nano- and mesoscale tribological aspects (*5*). On page 1513 of this issue, Mannix *et al.* (*6*) report on the formation of atomically thin boron films—borophene—by the evaporation and deposition of boron on a Ag(111) surface. The position of boron in the periodic system, between metallic beryllium and nonmetallic carbon, classifies it as a semimetal. Boron displays a pronounced ability to form not only strong covalent two-center-two-electron bonds, but also stable electron-deficient three-center-two-electron bonds. This results in a manifold of 3D cluster patterns for the solid-state structures of elemental boron polymorphs. The strong covalent bonds are responsible for boron and structurally related borides being hard materials. Also, no other p-block element shows a similar complexity of chemical bonding, which is as well displayed within the cluster chemistry of boron hydrides and carboranes (*7*).

"...single and multiple borophene layers offer a broad perspective for the development of nanoscale electronic devices..."

Mannix *et al.* characterized the boron monolayers by scanning tunneling microscopy and low-energy electron diffraction and found that they display a remarkable similarity to a model for "borophene," a quasiplanar molecular compound consisting of a B_{36} cluster of boron atoms (*8*). The dominant pattern of this molecular structure exhibits a hexagonal array of boron atoms with an additional boron atom located centrally within each B_6 hexagon. Because no alloying with the underlying silver substrate is observed, the single atom thick layer of boron can be considered as a novel 2D boron polymorph. Owing to the strong covalent interactions within this 2D borophene layer, the structure resembles a missing link between fully covalent bound 2D materials (graphene, boronitrene layers, phosphorene) and support-stabilized semimetallic films of single atomic thickness like silicene and germanene.

Depending on the relative orientation of the boron monolayer to the Ag(111) substrate and the deposition conditions, different domain structures can be distinguished. These structures can be derived from a corrugated hexagonal array of boron atoms, with additional boron atoms located above each center of a six-membered ring (see the figure), with distortions imposed by the substrate symmetry leading to ribbonlike structural features (*6*). Like benzene (C_6H_6) for graphene, a B_7 molecular cluster (being formed by boron evaporation and stable as per calculations) can be formally regarded as an elemental structure of the borophene layer.

In situ electronic characterization by scanning tunneling spectroscopy reveals anisotropic metallic characteristics, with the electronic conductivity correlating to the chainlike superstructures according to density-of-state calculations. Borophene layers are more stable than silicene layers, owing to the strong covalent interactions of boron atoms by multicenter electron-deficient bonds, but still display a considerable reactivity, e.g., toward oxygen. The borophene structure could be successfully stabilized with a Si/SiO_x buffer layer for exposure at ambient conditions, as indicated by transmission electron microscopy.

These films give rise to considerable toughness, in addition to their structural and electronic properties. Calculations reveal an in-plane Young's modulus in correlation with the experimentally observed structural anisotropy of the boron epilayer (398 GPa·nm

[1]*Max Planck Institute for Polymer Research, Ackermannweg 10, D-55128 Mainz, Germany.* [2]*Technische Universität Kaiserslautern, Abt. Mechanische Verfahrenstechnik/Particle Process Engineering, Gottlieb-Daimler-Straße Geb. 44, D-67663 Kaiserslautern, Germany. E-mail: sachdev@mpip-mainz.mpg.de; hermann.sachdev@mv.uni-kl.de*

Published by AAAS

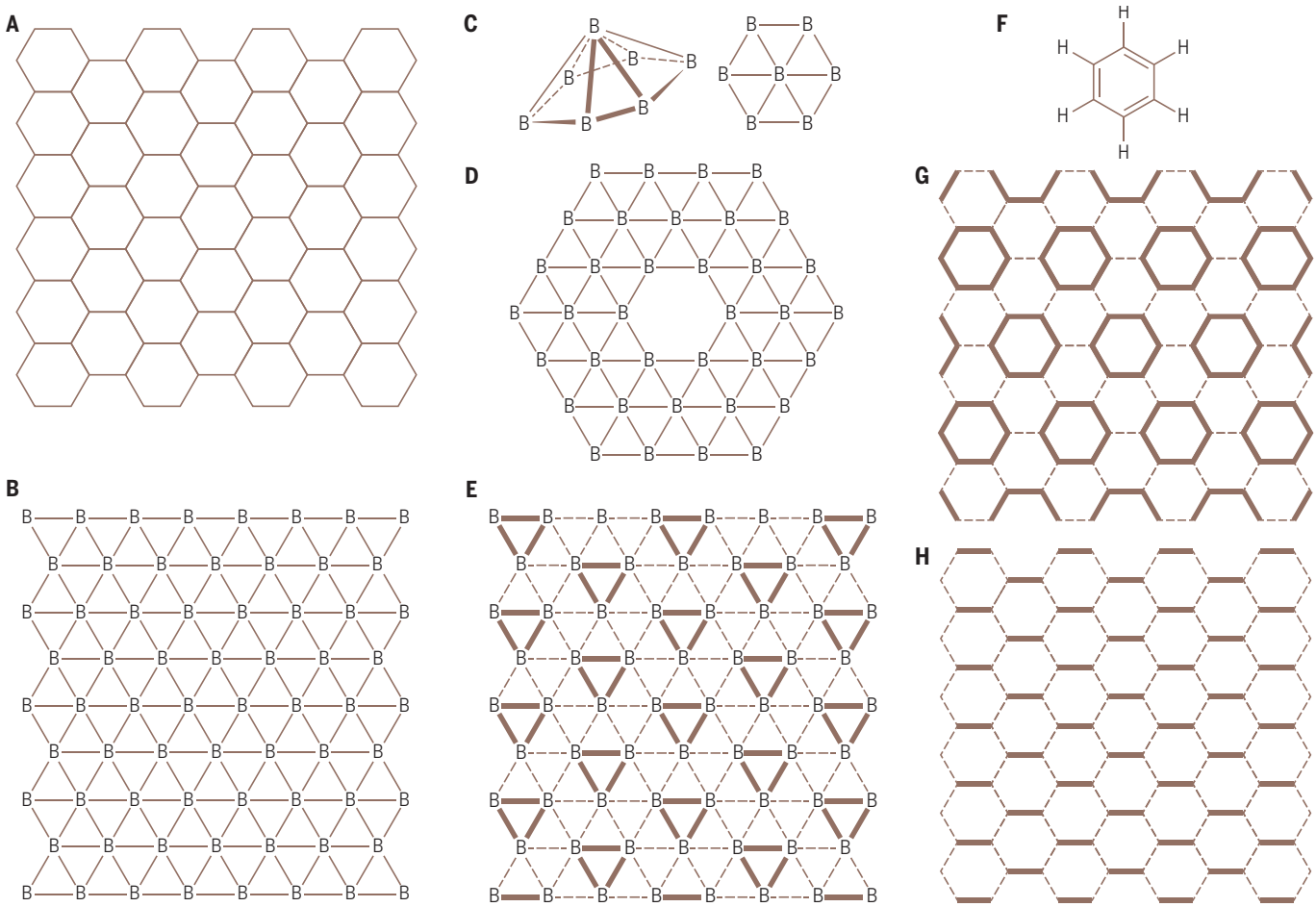

Aufbau principle for graphene and borophene layers. (**A** and **B**) Depiction of how transition-metal (111) surfaces template the arrangement of molecular building blocks for (A) graphene and (B) borophene layers. (**C**) Top and side view of a B7 cluster as a constituting unit for (**D**) a B36 borophene molecule. (**E**) A borophene layer from B3 molecular fragments. (**F**) Benzene (C6H6) as molecular building block for (**G**) graphene. (**H**) Graphene from C2 molecular fragments (*9*). If only B7 clusters are considered responsible for borophene layer growth without further fragmentation, a defective structure must result, for reasons of symmetry (C, D, and G). (The lines resemble atom connectivitiy, not chemical bonds.)

along *a* axis and 170 GPa·nm along *b* axis), which rivals those determined for graphene (340 GPa·nm).

The properties of the borophene layers described by Mannix *et al*. cannot be provided by any other substance from the current set of 2D materials. Thus, superstructured single and multiple borophene layers offer a broad perspective for the development of nanoscale electronic devices with metal, semimetal, or nonmetal interfaces involving electronic, photonic, and spintronic aspects of quantum confinement, as well as issues related to atomic-level tribology for nano- and micromechanical devices (*5*, *10*).

The borophene sheets are grown by physical vapor deposition, a process that does not provide a uniform molecular growth species, but a variety of molecular boron clusters as per the applied thermodynamic parameters. This variety of growth species can lead to additional grain boundaries and layer defects. For an up-scaling of this atomic layer deposition process, it will be beneficial to shift the current reaction conditions toward more moderate parameters. Although involving a highly reactive boron chemistry, chemical precursor approaches can offer access to the growth of borophene or heteroelement-substituted borophene layers by chemical vapor deposition or to molecular bottom-up syntheses of carbon- and nitrogen-doped borophene layers. This will require a boron chemistry being able to provide precursors containing, e.g., stable B_3 units (see the figure), or small heteroboranes (with heteroelements like C, N, O, or Si) to anchor functional groups on the borophene layer surface, or compounds resulting from a combination of the cluster chemistry of boron with the chemistry of polycyclic aromatic hydrocarbons. The borophene layer is still reactive enough to enable its chemical and electronic modification with covalent bound functional groups or by coverage with metals. Thus, future research will explore how the electronic performance can be tuned by grafting functional groups on the borophene layer or by interactions of the boron atoms with different substrates or additional epilayers above the borophene layer. These approaches can help to enhance the accessibility of this interesting type of 2D material for nanoscale boron or boride layers and layers of hard materials for electronic, magnetic, photonic, and mechanical device technologies (*11*, *12*). With all these aspects, borophene layers have the potential to play a key role in future 2D materials research and within the growing field of boron-based nanomaterials. ■

ILLUSTRATION: P. HUEY/*SCIENCE*

REFERENCES AND NOTES

1. S. Balendhran *et al.*, *Small* **11**, 640 (2015).
2. S. Berner *et al.*, *Angew. Chem. Int. Ed.* **46**, 5115 (2007).
3. H. Sachdev *et al.*, *Diamond Relat. Mater.* **19**, 1027 (2010).
4. J. Cai *et al.*, *Nature* **466**, 470 (2010).
5. J. C. Spear *et al.*, *Nano Today* **10**, 301 (2015).
6. A. J. Mannix *et al.*, *Science* **350**, 1513 (2015).
7. M. Driess, H. Noeth, Eds., *Molecular Clusters of the Main Group Elements* (Wiley-VCH, Weinheim, Germany, 2008).
8. Z. A. Piazza *et al.*, *Nat. Commun.* **5**, 3113 (2014).
9. F. Mueller *et al.*, *Small* **5**, 2291 (2009).
10. A. D. Franklin *et al.*, *Science* **349**, aab2750 (2015).
11. J. B. Levine *et al.*, *Adv. Funct. Mater.* **19**, 3519 (2009).
12. M. Herrmann *et al.*, *Int. J. Refract. Metal. Hard. Mater.* **39**, 53 (2013).

ACKNOWLEDGMENTS

Dedicated to the memory of Heinrich Noeth.

10.1126/science.aad7021

Published by AAAS

QUANTUM SIMULATION

Josephson contacts of neutral strongly interacting fermions

Contacts between superconductors are explored via their ultracold atomic gas analogs

By **Wolfgang Belzig**

Ultracold atoms have proven to be versatile tools for simulating quantum many-body states that are impossible to solve numerically. In two papers in this issue, by Husmann *et al.* (*1*) on page 1498 and Valtolina *et al.* (*2*) on page 1505, the physics of junctions between superconductors of strongly interacting lithium-6 fermions is explored in the regime between a Bardeen-Cooper-Schrieffer (BCS) state of loosely bound Cooper pairs and a Bose-Einstein condensate formed from diatomic molecules. These results demonstrate the potential for using ultracold atoms to explore the physics of novel quantum phases, even for systems out of equilibrium.

A supercurrent—a dissipationless electric current—can flow through a junction between two massive superconducting electrodes. This observation allowed the quantum nature of the superconducting state to be probed. Prime examples are the so-called Josephson effects (*3*), which were first seen experimentally in tunnel junctions between superconducting metals. The first effect concerns the supercurrent that flows in equilibrium, and in particular depends on the difference in quantum-mechanical phase ϕ of the macroscopic wave function ψ describing the superconductors. This effect is due to so-called Andreev bound states in the junction carrying a phase-dependent current (*4*). The second Josephson effect is related to a nonequilibrium state between two superconductors created by a difference in chemical potential μ. In that case, oscillating currents, as well as a dissipative direct current (dc), are set up. The dissipation mechanism is then explained by the transition between the Andreev states. The states carry oscillating currents in opposite directions, and the time-dependent phase causes transitions, which result in dissipation (*5, 6*).

The experiments of Husmann *et al.* and Valtolina *et al.* explore the physics of Josephson junctions in a new regime of interactions that can be reached only in ultracold gases. These superfluids are not simple BCS superconductors that can be described by an effective low-energy mean-field theory with well-defined quasiparticles (and hence Andreev bound states). Because of the strong interactions, the pairing energy is of the same order as the Fermi energy, so this simple picture may not apply.

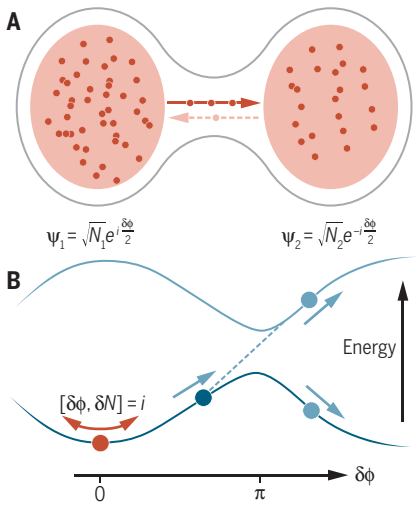

Following supercurrent flow. The Josephson effect describes the equilibrium current between two superconductors, which depends on the quantum-mechanical phase difference $\delta\phi$ as $I(\delta\phi) = I_c \sin(\delta\phi)$. The critical current I_c depends on the properties of the junction, e.g., shown in (**A**) as a constriction connecting the superfluid reservoirs with N_1 and N_2 particles, respectively. At low temperatures, particles transfer predominantly according to the phase difference, here from left to right. Only a small fraction of particles move in the opposite direction. (**B**) If the phase difference and the particle number difference are only weakly excited, they oscillate out of phase as the conjugate variables of a harmonic oscillator (lower left side). The situation changes drastically if a nonequilibrium situation is established in the form of a difference in chemical potential μ. According to the second Josephson relation, $d\delta\phi/dt = 2\delta\mu/\hbar \rightarrow \delta\phi(t) = \delta\phi_0 + 2\delta\mu t/\hbar$, a phase difference develops in time, resulting in an oscillating current. The time dependence leads to transitions between the current-carrying states shown in the right side that cause a dissipative dc current.

Valtolina *et al.* studied the oscillating difference in particle number N between the reservoirs (see the figure). The number difference is the conjugate variable to the phase difference of the superconductors, so they oscillated with a phase difference of $\pi/2$. The authors cleverly detect both quantum observables in the same system, and by repeating the experiment many times, they observed the phase-shifted oscillations. They could then deduce the system parameters that depend on the interaction strength.

Husmann *et al.* established a steady-state nonequilibrium situation in which a dissipative current flowed by creating a quantum point contact of lithium-6 atoms that transports atom pairs between the reservoirs. In a superconductor, such currents arise from the switching betweeen oppositely flowing alternating currents caused by the voltage-induced time evolution of the quantum-mechanical phase. On average, a dc current appears, which in combination with the voltage, results in a dissipative current. Microscopically, the switches can be understood by considering the Andreev bound states in the junction, which appear in pairs carrying current in opposite directions, and μ acting as a voltage. Because of their energy difference, they are differently occupied in a thermal equilibrium state with a stationary phase, so a net dc supercurrent flows. However, the time-dependent phase difference leads to transitions between the states favoring a directed current on average.

Both experiments explore the dependence of the effective parameters describing the junction by varying either the temperature or the interaction strength that can be conveniently tuned by sweeping a magnetic field through a so-called Feshbach resonance. These findings are not yet explained quantitatively by full theoretical calculations. An experimental challenge is to detect signatures of the Andreev bound states (*7*), to better connect strongly interacting superconductivity with Andreev physics (*8*).

The experiments by Husmann *et al.* and Valtolina *et al.* can be considered as quantum simulators (*9*) because a classical computer simulation of 10^5 interacting fermions as used in the experiments is impossible with today's computers. In future, it will be interesting to explore the role of Andreev reflection and bound states in such novel superconductors, as well the quantum dynamics of those junctions, for example, with time-dependent fields. ■

Department of Physics, University of Konstanz, Konstanz, Germany. E-mail: wolfgang.belzig@uni-konstanz.de

REFERENCES

1. D. Husmann *et al.*, *Science* **350**, 1498 (2015).
2. G. Valtolina *et al.*, *Science* **350**, 1505 (2015).
3. B. D. Josephson, *Phys. Lett.* **1**, 251 (1962).
4. J.-D. Pillet *et al.*, *Nat. Phys.* **6**, 965 (2010).
5. D. Averin, A. Bardas, *Phys. Rev. Lett.* **75**, 1831 (1995).
6. J. Cuevas, A. Martín-Rodero, A. Levy Yeyati, *Phys. Rev.* B **54**, 7366 (1996).
7. L. Bretheau *et al.*, *Nature* **499**, 312 (2013).
8. T. M. Klapwijk, S. A. Ryabchun, *JETP* **119**, 997 (2014).
9. S. Lloyd, *Science* **273**, 5278 (1996).

10.1126/science.aad6876

ILLUSTRATION: P. HUEY/*SCIENCE*

Published by AAAS

A more systematic approach to biological risk

Management of emerging risks in life science and technology requires new leadership and a sober assessment of the legacy of Asilomar

By **Megan J. Palmer[1], Francis Fukuyama[2,3], David A. Relman[1,3,4,5*]**

On 29 October 2015, the White House issued a memorandum to agencies with its plans to enhance U.S. biosafety and biosecurity. This memo identifies important gaps and constructive steps, but it grafts recommendations onto inadequate institutional structures and fails to address underlying systemic needs.

The memorandum was a response to a series of events, including U.S. laboratories' mishandling of pathogens. In the summer of 2014, U.S. labs were in the spotlight over mishandling of anthrax, smallpox, and avian flu. In 2015, live anthrax shipments from U.S. defense labs and an investigative report revealed pervasive and long-standing gaps in oversight of work with deadly pathogens, including inadequate systems of reporting and accountability for lab accidents (*1*–*5*). Meanwhile, "gain-of-function" experiments with viral pathogens are back at the center of an international debate over whether certain research poses unjustifiable public safety and security risks (*6*, *7*). The Ebola outbreak drove home the potential public health consequences of infectious agents, irrespective of whether they originate inside or outside the lab. The debate has widened as other dual-use experiments and technologies, such as gene drives, are pursued (*8*, *9*).

POLICY

The nature of these events varied, but the responses to them were all similarly reactive and shortsighted: temporarily stop research and shut down labs, as well as conduct narrow reviews of specific programs and standard protocols. The White House laudably recognized the need for a more systematic approach to biological safety and security. However, its recommendations again place additional oversight responsibilities onto existing institutional structures (*10*). Inadequate processes for assessing the significance of risks have hindered efforts to develop sustained and coordinated plans. The default response has been a narrow treatment of individual incidents rather than a proper diagnosis and a more expansive and proactive approach to a systemic problem.

Our strategies and institutions for managing biological risk in emerging technologies have not matured much in the last 40 years. With the advent of recombinant DNA technology, scientific leaders resorted to halting research when confronted with uncertainty and public alarm about the risks of their work. To determine a framework for managing risk, they gathered at the now-fabled 1975 Asilomar meeting. Their conclusions led to the recombinant DNA guidelines still used today, and Asilomar is often invoked as a successful model for scientific self-governance.

However, Asilomar's legacy has some negative aspects. Like most scientists today, participants at Asilomar had little expertise in and appreciation for institutions that manage risk. Some scientists were shocked to discover the liabilities of their work and their wide disagreements on how to assess risk (*11*, *12*). Organizers focused on safety and sidelined what they deemed to be social, ethical, and political topics, such as security and human modification issues. Asilomar created risky expectations: that leading biological scientists are best-suited for and wholly capable of designing their own systems of governance and that emerging issues can be treated as primarily technical matters.

The world has changed since 1975. The challenges remain just as much social as they are technical in nature but the scope and scale of biological science and technology have changed dramatically. Strategies for balancing benefits and risks must now reach a practitioner community proliferating globally. The increased ease of reading and writing genetic information means that securing materials in a handful of established labs is not feasible.

Unfortunately, today's leadership on biological risk reflects Asilomar's risky legacy: prioritizing scientific and technical expertise over expertise in governance, risk management, and organizational behavior. Political leaders have largely ceded a strategic leadership role, with the analysis of emerging issues of biological risk captured by the largest scientific funding agency for biological research: the U.S. National Institutes of Health. For example, NIH is now leading the U.S. federal risk-benefit analysis of so-called gain-of-function research. It is a one-off study, with very limited scope and timelines, conducted through a process that is tightly controlled by an institution with a clear conflict of interest (*13*, *14*). This and other related studies on emerging biotechnology risks, such as the National Academies of Science investigations of gene editing and gene drives, underrepresent expertise on governance in favor of technical expertise.

This is a worrisome precedent for such

[1]*Center for International Security and Cooperation, Stanford University, Stanford, CA, USA.* [2]*Center on Democracy, Development, and the Rule of Law, and Freeman Spogli Institute for International Studies, Stanford University, Stanford, CA, USA.* [3]*Department of Microbiology and Immunology, Stanford University, Stanford, CA, USA.* [4]*Department of Medicine, Stanford University, Stanford, CA, USA.* **Corresponding author. E-mail: relman@stanford.edu*

ILLUSTRATION: JOHN HOLCROFT

Published by AAAS

studies, the purpose of which, in part, is to offer conceptual approaches to risk management (*15*, *16*). Leadership biased toward those that conduct the work in question can promote a culture dismissive of outside criticism and embolden a culture of invincibility. We need to develop leadership that represents and integrates technical and social expertise. Leaders must instill safety and security as core missions driving the work of scientific and political institutions. By supporting work to identify and mitigate risks, acknowledging failure and uncertainties, and facilitating participation of diverse experts, they can empower organizations to respond to new challenges.

Although enlightened leadership is vital, regulatory oversight is critical to modifying behavior. Effective oversight institutions must have the expertise to assess and adapt performance metrics, the incentives (requirements and rewards) for reporting, and the authority to impose meaningful penalties when standards are not met. Institutional Biosafety Committees currently provide some local oversight but have limited expertise in biosecurity and risk. The Recombinant DNA Advisory Committee and National Science Advisory Board for Biosecurity (NSABB) lack the independence and authority to enforce rules. Embedding these boards within NIH also creates conflicts of interest that can lead to disenfranchisement when problems arise such as occurred following the NSABB's initial recommendations on publication of avian influenza gain-of-function research (*16*). The Office of Science and Technology Policy (OSTP) and the Presidential Commission for the Study of Bioethical Issues (PCSBI) have a great deal of expertise but no authority to regulate behavior. Currently, oversight relies on few enforcement mechanisms outside of revoking or creating barriers to public funding—an indirect and limited approach that does not apply to private entities. Fines can be effective, but only if enforced and tied to specific performance expectations. Reputation is also an important motivator; public reporting of performance (good and bad) is an underutilized tool to improve behavior and enhance accountability.

Unfortunately, metrics and processes for monitoring the performance of our biological safety and security regimes are currently underdeveloped. Mere collection of accident data is not sufficient—at present, lack of errors is considered proof of success, and little forecasting is done to predict future failures. Recognizing a long-standing gap, the U.S. Government Accountability Office (GAO) has suggested that a single federal entity oversee high-containment labs and perform periodic strategic assessment. In order to scale its efforts and adapt over time, such an entity must prioritize public reporting. A lack of transparency in risk-management processes undermines the ability to evaluate substantive claims and solicit input and expertise to inform the design of improved strategies. The current review by the U.S. Federal Select Agent Program, although commendable in emphasizing transparency, does not provide a compelling management plan.

Expertise and precedents across other high-risk, high-consequence activities may suggest lessons for institutions that manage biological risk. In transportation, the Interstate Commerce Commission (ICC) was created to regulate railroads; when trucking needed to be regulated, responsibility was also given to the ICC with the rationale that both crossed state lines. This was a mistake, since there were conflicts of interest between the rail and trucking industries. It thus made sense with the advent of aviation for Congress to give authority to a new, independent regulator, the Federal Aviation Administration (FAA). The National Transportation Safety Board (NTSB) was also created to provide independent investigative functions. The FAA and NTSB were able to design mechanisms through which pilots and controllers could note unsafe conditions, near misses, and accidents, and were able to protect those who reported unsafe conditions.

"to mature and learn, oversight institutions must approach governance as a long-term strategic challenge"

In the nuclear power industry, the Nuclear Regulatory Commission (NRC) was created as an independent and powerful authority, and the industry also formed the Institute of Nuclear Power Operations (INPO) as an independent nonprofit organization to provide standards for, and assessment of, the safety of nuclear plants. Although issues remain, the shared oversight structure between INPO and NRC evolved to resolve conflicting interests and to enhance communication and expertise as compared with the predecessor, the Atomic Energy Commission.

To respond to today's challenges and to prepare for the future, scientific and political leaders must work together to cultivate social expertise alongside technical know-how. A key step is for scientific and political leaders (i) to acknowledge the insufficiencies in our current institutions and risk-management strategies, (ii) to position public safety and security as drivers of ongoing research, and (iii) to create institutional structures that can anticipate and adapt. In the United States, the reviews of biosafety and biosecurity systems conducted by the Federal Expert Security Advisory Panel and the National Science and Technology Council highlight the unnecessary complexity of the process require to reconcile and enforce recommendations. The White House memo clarified some immediate responsibilities but did not resolve long-term issues with overlapping jurisdictions. Although competing perspectives are critical to exposing emerging issues, centralized facilitation is needed. Our consultations with colleagues in other countries indicate that they face similar problems with multiple chains of command. Agreements, such as the Biological Weapons Convention, rely on state-based programs to ensure compliance and updating of safety and security standards, so effective national leadership is essential.

In terms of organization, countries should create permanent, credible national-level oversight and standard-setting bodies that work in partnership through international entities. The International Civil Aviation Organization of the United Nations is an example of the latter; it coordinates state-based programs and adopts standards for global civil aviation. In biotechnology, the mandate should extend beyond health to recognize significant drivers in other domains, such as the production of chemicals, materials, and food. In the United States, the Executive Office of the President could create a high-ranking government official position, such as a special assistant to the president, and a coordinating committee, responsible for anticipating and managing risks associated with biotechnology (*17*). This committee would be independent from, but work in partnership with, funding bodies like NIH and organizations with overlapping roles in biological risk management, including the Department of Homeland Security, Department of Health and Human Services (DHHS), U.S. Department of Agriculture, and Department of Defense (DOD). Rather than acting as a command-and-control czar, this official and committee should facilitate information-sharing and build processes for accountability and harmonization across agencies. This should include assessing the creation of entities like the NTSB that can provide independent performance reporting and the complementary removal of unnecessary or duplicative functions from other agencies. There is precedent for the role of special adviser (*17*), but such a role and a single lead for oversight and strategy have since been rebuked by OSTP and national security staff (*5*). We believe such responses indicate a lack of appetite for acknowledging and ad-

Published by AAAS

dressing underlying issues. Alternatives, such as creating a new position within OSTP, are insufficient to navigate complex interagency chains of command.

Last, to mature and learn, oversight institutions must approach governance as a long-term strategic challenge in need of management and research, as well as the involvement of the general public. Investing in interdisciplinary research centers is one way to bring focus to critical risk governance topics like leadership, organization, and learning in a future of distributed biological knowledge and technology. If we do not address the foundational challenge of emergent technologies and biological risk properly, we should expect reactive and poorly conceived restrictions on potentially beneficial research, as well as many more normal "accidents" with increasingly consequential risks to people and the environment, as biotechnology proliferates globally. ■

REFERENCES AND NOTES

1. White House, "Next steps to enhance biosafety and biosecurity in the United States" [memo] (White House, Washington, DC, 2015).
2. White House, "Enhancing biosafety and biosecurity in the United States" [memo] (White House, Washington, DC, 2015).
3. A. Young, N. Penzenstadler, *USA Today*, 28 May 2015; http://bit.ly/SecretBiolabs.
4. Committee for Comprehensive Review of DoD Laboratory Procedures, Processes, and Protocols Associated with Inactivating *Bacillus anthracis Spores*, "Review Committee report: Inadvertent live shipment of live *Bacillus anthracis* spores by DoD" (DOD, Washington, DC, 2015); http://bit.ly/ShipmentSafety.
5. GAO, *Preliminary Observations on Federal Efforts to Address Weaknesses Exposed by Recent Safety Lapses* (GAO, Washington, DC, 2015); www.gao.gov/assets/680/671679.pdf.
6. F. Sharples *et al.*, *Potential Risks and Benefits of Gain-of-Function Research: Summary of a Workshop* (National Academies Press, Washington, DC, 2015).
7. H. V. Fineberg, *Science* **347**, 929 (2015).
8. K. A. Oye *et al.*, *Science* **345**, 626 (2014).
9. O. S. Akbari *et al.*, *Science* **349**, 927 (2015).
10. U.S. Government, *United States Government Policy for Institutional Oversight of Life Sciences Dual Use Research of Concern* (Government Printing Office, Washington, DC, 2014); www.phe.gov/s3/dualuse/Documents/durc-policy.pdf.
11. M. Rogers, *Roll. Stone* **187**, 37 (1975).
12. S. Wright, *Perspect. Biol. Med.* **44**, 235 (2001).
13. OSTP, DHHS, *U.S. Government Gain-of-Function Deliberative Process and Research Funding Pause on Selected Gain-of-Function Research Involving Influenza, MERS, and SARS Viruses* (OSTP, DHHS, Washington, DC, 2014); www.phe.gov/s3/dualuse/Documents/gain-of-function.pdf.
14. White House, "Doing diligence to assess the risks and benefits of life sciences gain-of-function research" [blog] (White House, Washington, DC, 2014); http://bit.ly/DiligentAssess.
15. M. Lipsitch, D. A. Relman, *Foreign Aff.*, 31 August 2015; https://www.foreignaffairs.com/articles/2015-08-31/new-game-new-rules.
16. D. A. Relman, *J. Infect. Dis.* **209**, 170 (2014).
17. K. W. Bernard, *Biosecur. Bioterror.* **11**, 157 (2013).

ACKNOWLEDGMENTS

The authors thank S. Falkow, D. Endy, A. Zegart, S. Sagan, K. Bernard, K. Oye, S. Weiss-Evans, C. Perrow, S. Hecker, and L. Eden for helpful discussions. D.A.R. is a former member of the NSABB. F.F. was a member of the President's Council on Bioethics.

10.1126/science.aad8849

Where next? Survival and reproduction of wolves in the Northern Rockies have declined.

PHOTO: © DESIGN PICS INC/ALAMY STOCK PHOTO

CONSERVATION POLICY

Questionable policy for large carnivore hunting

U.S. wolf-hunting policies do not align with ecological theory or data

By **Scott Creel,[1,2]* Matthew Becker,[2] David Christianson,[3] Egil Dröge,[1] Neil Hammerschlag,[4] Matt W. Hayward,[5] Ullas Karanth,[6] Andrew Loveridge,[7] David W. Macdonald,[7] Wigganson Matandiko,[1] Jassiel M'soka,[1,8] Dennis Murray,[9] Elias Rosenblatt,[1] Paul Schuette[10]**

Terrestrial large carnivores are in rapid global decline, with consequences for ecosystem structure and function. Among drivers of these declines, legal hunting is unique because it is intentional and thus relatively easily controlled. Although regulated carnivore hunting potentially reduces conflict and provides revenue for conservation, it can also drive population declines (*1*–*5*).

POLICY Some policies regulating carnivore hunting address negative effects on demography and population dynamics, but others do not. Here, we use wolf harvesting in the western United States to illustrate four aspects of policy that do not align well with ecological theory and data, and we suggest resolutions.

Policies regulating human effects on lions, cougars, leopards, and tigers have responded to research by moving to better evaluate and mitigate demographic costs (*1*, *2*, *5*, *6*). For example, policies for lions (*Panthera leo*) include temporary hunting closures to allow population recovery (*5*) and reduced quotas with sex- and age-limited harvesting (*2*). Nonetheless, hunting policies for large carnivores still often suffer from a lack of science-based guidance. For example, policies for harvest of wolves (*Canis lupus)* in the Northern Rocky Mountains Distinct Population Segment (NRM DPS) suggest that annual harvest of up to 50% of the population has little or no effect on dynamics. Wolves were reintroduced in the mid-1990s, and the NRM DPS grew steadily until 2009 (see the chart, part A). Legal hunting began immediately after removal of the Endangered Species Act (ESA)

Published by AAAS

Temporal trends in dynamics of wolves. In the original NRM DPS, data were reported by state (ID, Idaho; MT, Montano; WY, Wyoming; or all three states) or regional boundaries (NWMT, Northwest Montana; GYA, Greater Yellowstone Area; CID, Central Idaho), in USFWS population recovery reports (*18*). See SM for details. (**A**) Population counts since wolf reintroduction in the mid-1990s, described by USFWS as minimum number known alive. Red line denotes the onset of legal hunting. Ordinate is $\log_{10}$ scaled. (**B**) Human offtake causes wolf survival rates to decline in an additive manner, with little evidence of compensation. Each point represents 1 year (*8*), and shading shows 95% confidence intervals. The red line denotes completely additive mortality. (**C**) Recent data (*10*) confirm the prior conclusion (*3*) that anthropogenic mortality has an additive (rather than compensatory) effect on annual population growth rates (λ), and that anthropogenic mortality above ~25% typically yields a declining population with $\lambda < 1$. Each point represents 1 year (1998–2014), and shading shows 95% confidence intervals. (**D**) Total anthropogenic mortality has increased substantially since the onset of hunting [denoted with red line as in (A)], doubling within the original NRM DPS between 2010 and 2013, coincident with a shift from steady population growth to gradual decline. Total anthropogenic mortality combines sport hunting with other direct human killing, primarily in response to predation on livestock, and expresses it as a proportion of the population count.

protections in 2008, occurred in 3 of the 5 years considered here (2009–10 and 2011–13), and continues today. A recent review of current policies by the U.S. Fish and Wildlife Service (USFWS) concluded that harvesting "has not increased any risk" to the NRM DPS (*7*).

Several patterns in the data used to draw these conclusions call them into question (see the chart). We analyze previously published results and information directly reported in USFWS species recovery reports [see supplementary materials (SM)], which have been used as the basis for delisting and increasingly heavy harvest. The issues identified by this analysis are not unique to wolves, and the recommendations that it yields are relevant to other large carnivores.

SIZE, STRUCTURE, DYNAMICS. For wolves (and most other large carnivores), adult mortality rates are low in the absence of human offtake (*8*), which leaves little scope for hunting to substitute for other causes of death (compensatory mortality) (*8*, *9*). Hence, adult mortality rates increase in an additive, nearly one-to-one manner as human offtake increases (see the chart, part B) (*3*, *8*).

Increased adult mortality was correlated with a decrease in wolf pack size since the onset of legal hunting in Montana and Idaho, where pack size declined by 29 to 33% between 2008 and 2013 (*10*). Beyond reducing group size, harvesting mortality can also disrupt social organization (*3*, *4*), and both

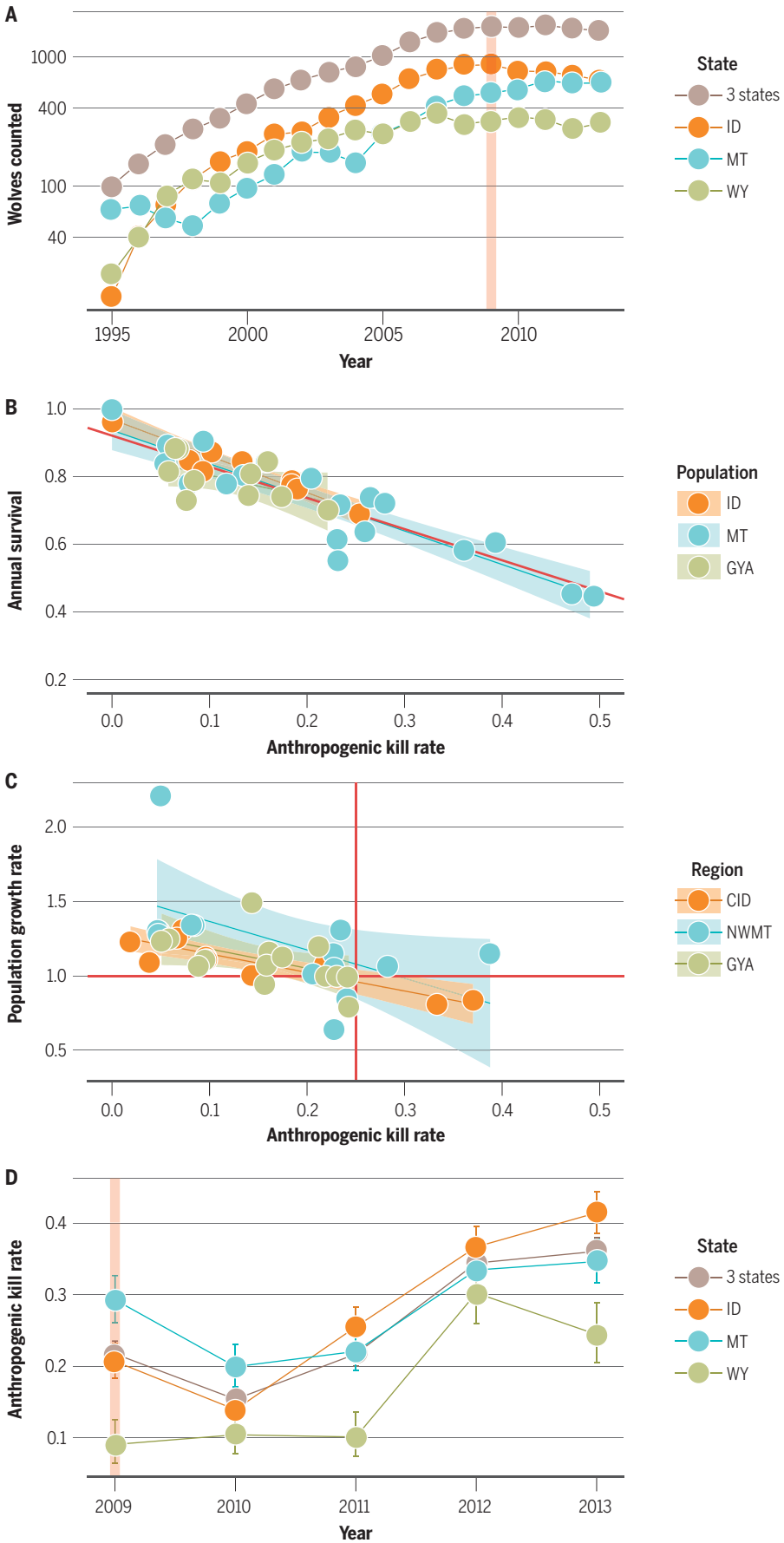

GRAPHS: P. HUEY/*SCIENCE*

Published by AAAS

effects can reduce juvenile survival and recruitment (addition to the population, which depends on litter size and juvenile survival). Pup survival in 10 Idaho packs decreased from 60% in years without hunting to 38% in years with hunting (*11*). Direct trapping or shooting of pups could explain only 27% of this decrease, with the rest attributed to disruption of pack size and social organization (*11*). Recruitment showed a similar decrease in years with hunting, dropping from 3.2 to 1.6 pups recruited per pack (*11*).

Because the population growth rate (λ) is equal to the sum of the adult survival rate and per-capita recruitment, reduced local population growth is inevitable when adult survival and juvenile recruitment decline (see the chart, part C). The mean annual survival of NRM wolves before legal hunting was 0.75 [95% confidence interval (CI) of 0.728 to 0.772] (*12*), so population decline would be expected if recruitment fell below 0.25 recruits per individual (*13*). The mean pack size and recruits per pack reported for Idaho (*10*, *11*) suggest that recruitment dropped below this threshold by 2013, to 0.20 recruits per individual. This would predict population decline even if harvest mortality was completely compensatory. This prediction is corroborated by a 25% decrease in the number of wolves harvested in Idaho and Montana in 2013 (*10*, *14*), despite extended hunting seasons and liberalized hunting limits that have increased the proportion of the population killed (see the chart, part D), a pattern that is commonly taken to indicate that harvest is driving a decline.

BOUNDARIES, DETECTION, GOALS. Several lessons can be learned by considering discrepancies between our analysis and the recent USFWS review concluding that policy has not increased risk to these populations. These lessons are broadly applicable to other exploited carnivores.

Effects of a policy must be considered within the area to which it applies. Carnivore distributions do not follow political borders, but hunting policies do. The relatively constant number of wolves within the entire NRM DPS has been taken as evidence that state-level policies do not increase risk for NRM wolves. However, the DPS originally included only Montana, Idaho, and Wyoming, and has expanded to include wolves in Washington and Oregon. If one evaluates a state's policies by examining effects within its borders, it is reasonable to conclude that risks have increased in some cases. To illustrate, International Union for Conservation of Nature Red List Criterion C1 classifies a population segment as endangered if it holds fewer than 2500 individuals and has declined by ≥20% in <5 years. In Idaho, delisting and subsequent legal harvest produced a 22.4% decline in population counts from 2008 to 2013 (from 849 to 659) (*10*). With no stated population target (other than avoiding relisting under the ESA), current policy does not adequately define a shut-off for this decline.

Evaluation of effects on populations must consider sampling design and effort to control for effects on detection. First, when sampling effort and population counts change in parallel, there is reason to believe that trends in the counts might not describe true dynamics. For example, while the Idaho population count decreased 22.4% from 2008 to 2013, the Montana count increased comparably (see the chart, part A) (*10*), a surprising result given reported decreases in survival (*8*) and reproduction (*11*). During this period, Montana added additional staff and volunteers to monitor the wolf population and initiated a program to gather sightings from the public (eventually with >80,000 reports annually) (*10*). Second, the USFWS evaluation of wolf population trends (*7*) incorrectly asserts that these counts represent "the absolute minimum number of wolves alive." In Idaho, which holds the largest segment of the NRM DPS, tabulated counts are adjusted by substituting mean pack size for smaller pack counts that might have been incomplete (74% of packs in 2013) and then multiplying the adjusted count by 1.125 to account for unseen wolves suspected to be living outside of packs (*10*). Consequently, the Idaho estimate is ~1.75 times the number of individuals known to be alive, and the biggest increase in the minimum estimated NRM DPS occurred in 2006 with the adoption of this method. Recent studies of lions and tigers illustrate the importance of population monitoring that accounts for sampling effort and detection (*5*, *6*).

"policies for harvest of wolves in the Northern Rocky Mountains...suggest that annual harvest of up to 50% of the population has little or no effect...."

Policy cannot ignore the distinction between local compensation and immigration from an external source population. The suggestion that wolves "can apparently withstand human-caused mortality of 28 to 50% without declining" (*15*) derives from studies [e.g., (*16*, *17*)] in which an external source population was available to provide immigrants to offset local losses (*13*). For lions, harvest mortality outside of national parks affects population dynamics within adjacent parks (*4*, *5*). A clear focus on the distinction between true compensation and source-sink dynamics would improve policy.

Clearly defined, quantitative policy goals are needed for science-based evaluation. Such goals require consideration of population viability and sustainable offtake based on robust science by using all available data. Policies for hunting of wolves in the NRM do not specify maximum harvest or targets for population size or growth (other than avoiding decline sufficient to trigger relisting under the ESA). Well-regulated hunting of large carnivores can yield costs and benefits for conservation but requires attention to both. ■

[1]Montana State University, Bozeman, MT 59717, USA. [2]Zambian Carnivore Programme, Mfuwe, Zambia. [3]University of Arizona, Tucson, AZ 85721, USA. [4]University of Miami, Miami, FL 33149, USA. [5]Bangor University, Bangor, LL57 2UW, UK. [6]Wildlife Conservation Society, Bangalore, Karnataka 560 070, India. [7]WildCRU, Oxford University, Recanati-Kaplan Centre, Oxfordshire OX13 5QL, UK. [8]Zambia Wildlife Authority, Chilanga, Zambia. [9]Trent University, Peterborough, Ontario K9J 7B8, Canada. [10]State University of New York College of Environmental Science and Forestry, Syracuse, NY 13210, USA. *Corresponding author. E-mail: screel@montana.edu

REFERENCES AND NOTES

1. H. S. Cooley *et al.*, *Ecology* **90**, 2913 (2009).
2. K. Whitman *et al.*, *Nature* **428**, 175 (2004).
3. S. Creel, J. J. Rotella, *PLOS ONE* **5**, e12918 (2010).
4. A. J. Loveridge *et al.*, *Biol. Conserv.* **134**, 548 (2007).
5. E. Rosenblatt *et al.*, *Biol. Conserv.* **180**, 176 (2014).
6. K. U. Karanth *et al.*, *Anim. Conserv.* **6**, 141 (2003).
7. M. D. Jiminez, *U.S. Fish and Wildlife Service Review of the 2013 Wolf Population in the NRM DPS* (USFWS, Helena, MT, 2014).
8. D. L. Murray *et al.*, *Biol. Conserv.* **143**, 2514 (2010).
9. A. M. Sparkman *et al.*, *PLOS ONE* **6**, e20868 (2011).
10. USFWS *et al.*, *Northern Rocky Mountain Wolf Recovery Program 2013 Interagency Final Report* (USFWS Ecological Services, Helena, MT, 2014).
11. D. E. Ausband *et al.*, *Anim. Conserv.* **18**, 415 (2015).
12. D. W. Smith *et al.*, *J. Wildl. Manage.* **74**, 620 (2010).
13. The relation between λ and anthropogenic mortality has been debated (*3*, *17*). Recruitment is collinear with anthropogenic mortality (*3*, *11*) and is a direct, additive component of λ. Thus, its inclusion as a predictor of λ is not statistically valid and would produce biased estimates of the relation between λ and human offtake. Analyses with this problem [e.g., (*17*)] have been used to suggest that annual harvest rates of 50% or more are sustainable for wolves.
14. Oregon and Washington do not yet allow hunting. Wyoming's wolf management plan was challenged in court, and the state's regulations for wolf hunting were only implemented briefly in 2008 and then again in 2012. Thus, data are not yet available to assess the consequences of the policy that Wyoming has proposed, which would allow unlimited year-round hunting in most of the state, as with coyotes.
15. Idaho Wolf Conservation and Management Plan (Idaho Department of Fish and Game, Boise, ID, 2015); www.fishandgame.idaho.gov/public/wildlife/wolves/?getPage=161.
16. L. G. Adams *et al.*, *Wildl. Monogr.* **170**, 1 (2008).
17. J. A. Gude *et al.*, *J. Wildl. Manage.* **76**, 108 (2012).
18. Endangered Species, Western Gray Wolf (USFWS, 2015); www.fws.gov/mountain-prairie/es/grayWolf.php.

SUPPLEMENTARY MATERIALS

www.sciencemag.org/content/350/6267/1473/suppl/DC1

10.1126/science.aac4768

Published by AAAS

MICROBIOLOGY

Sulfate to go

A trisulfide intermediate is key to microbial sulfur reduction

By **Günter Fritz**[1] *and* **Peter M. H. Kroneck**[2]

Sulfate-reducing microorganisms are ubiquitous and play a central role in the global cycling of carbon and sulfur. They conserve energy through dissimilatory reduction of sulfate to sulfide (DSR), one of the oldest and most prominent microbial metabolic pathways on Earth. Sulfite is a crucial intermediate in the DSR pathway. On page 1541 of this issue, Santos *et al.* (*1*) identify another key intermediate: a protein-based trisulfide that couples the reduction of sulfite to energy conservation (see the figure, left panel).

Among the nonmetallic elements essential for life, sulfur stands out because of its astounding chemical versatility (*2*). It plays a critical role in biochemistry as a structural and redox-active element and carbon carrier, and has been proposed to be a key element in the origin of life (*3*). Its tendency to form chain and ring polymers reflects the remarkable strength of the S–S bond. One of the most common sulfur compounds is sulfate (SO_4^{2-}), an energy-rich molecule that is, however, chemically inert. To use this energy source, microorganisms must invest adenosine 5′-triphosphate (ATP) to form adenosine 5′-phosphosulfate (APS); APS is then reduced to sulfite (SO_3^{2-}), followed by the six-electron reduction of sulfite to sulfide (S^{2-}). It is this last reaction step that releases the most energy (*4*, *5*).

The three key enzymes of the DSR pathway are ATP sulfurylase, APS reductase, and dissimilatory sulfite reductase (DsrAB). Unlike the respiratory complexes found in other microbes (and also in mitochondria), these enzymes are not integral membrane proteins and do not pump protons or other ions across the membrane. This raises the question of how the reduction of sulfate to sulfide is coupled to the generation of the chemiosmotic gradient that is required to drive ATP synthesis and other essential processes in the living cell. Genomic data reveal that sulfate-reducing microorganisms contain a set of membrane-bound redox proteins that are closely related to the energy-conserving complexes in methanogens (*6*). In particular, proteins related to the heterodisulfide reductase of methanogens are part of these complexes. Thus, sulfur redox chemistry is likely to also play a key role in energy conservation during DSR.

DsrAB has a tetrameric $\alpha_2\beta_2$ architecture, with a catalytic site consisting of a siroheme coupled to a [4Fe-4S] cluster by a cysteine sulfur bridge (*7*) (see the figure, right panel). Sulfite reductases with such catalytic centers also play a role in the biosynthesis of amino acids and cofactors (*8*). Early in vitro experiments with purified DsrAB and in vivo studies with growing cultures suggested that both thiosulfate (SSO_3^{2-}) and trithionate ($^-O_3SSSO_3^-$) are reaction intermediates during sulfite reduction. However, these studies could not rule out the possibility that thiosulfate and trithionate are a by-product of catalysis, not true reaction intermediates.

Important insight came from a comparison of the DsrAB active sites from the thermophilic archaeon *Archaeoglobus fulgidus* (*7*) and two different *Desulfovibrio* species. Sulfite coordinated to the siroheme Fe center through its sulfur atom in all three cases. However, the DsrAB enzyme of *A. fulgidus* has a large cavity open to the solvent. This allows more than one sulfite molecule to access the active site. Sulfur-oxygen reaction intermediates can thus readily react with a second sulfite to form thiosulfate or trithionate.

In the *Desulfovibrio* enzyme structures, the protein DsrC closes the opening seen in the *A. fulgidus* enzyme. It thereby blocks binding of further sulfite to the active site. The C-terminal arm of the DsrC protein, which harbors a conserved cysteine, extends toward the siroheme–[4Fe-4S] catalytic site (see the figure, right panel). This arrangement suggests that the cysteine of

[1]*Institute for Neuropathology, University of Freiburg, 79106 Freiburg, Germany.* [2]*Department of Biology, University of Konstanz, 78457 Konstanz, Germany. E-mail: guenter.fritz@uniklinik-freiburg.de; peter.kroneck@uni-konstanz.de*

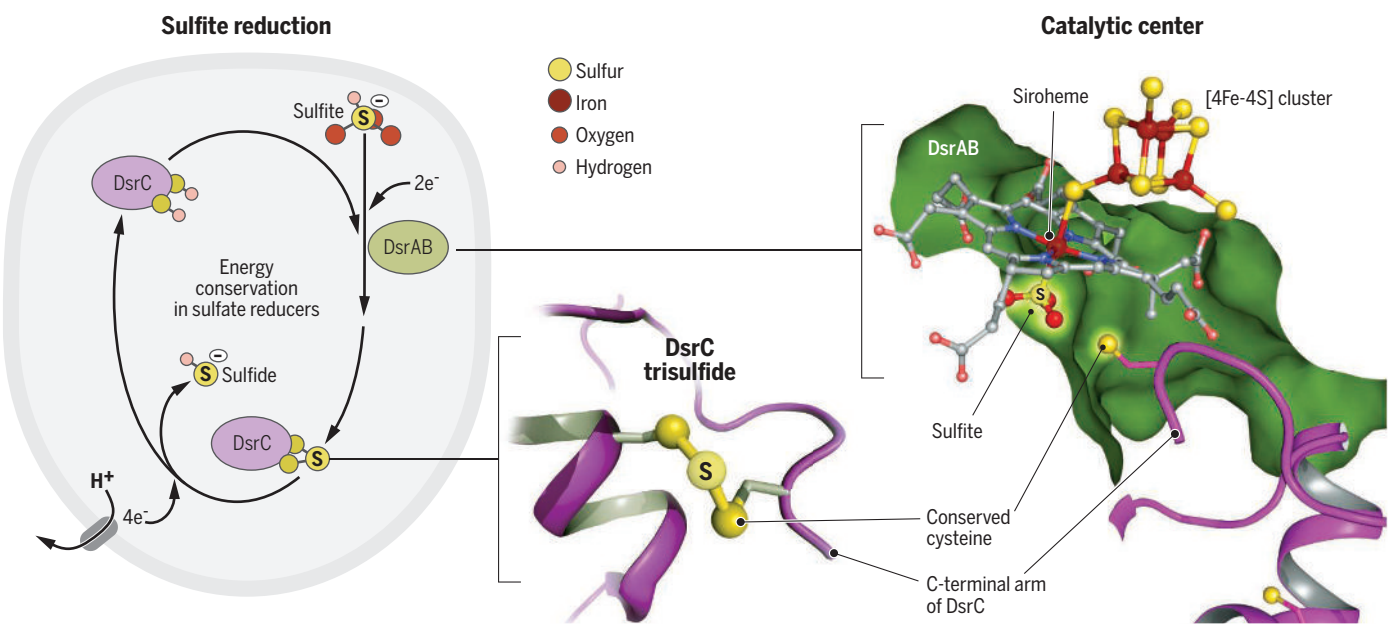

ILLUSTRATION: K. SUTLIFF/*SCIENCE*

Mechanism of dissimilatory sulfite reduction and energy coupling by a protein trisulfide. (**Left**) Dissimilatory reduction of sulfite by the enzyme DsrAB leads to the formation of the DsrC trisulfide discovered by Santos *et al*. It links the exergonic reaction of sulfite-to-sulfide reduction to energy conservation in sulfate-reducing bacteria. (**Middle**) Model of the DsrC trisulfide in the structure of *Archaeoglobus fulgidus* DsrC (*12*) (PDB 1SAU). (**Right**) The coupled siroheme–[4Fe-4S] catalytic site of DsrAB binds sulfite (SO_3^{2-}) through its sulfur atom to the siroheme iron center (*4*) (PDB 3MM5). The C-terminal arm of the DsrC protein extends with the conserved cysteine toward the bound sulfite to pick up the reduced sulfur-oxygen intermediate (*10*, *11*).

Published by AAAS

the C-terminal arm and a further cysteine of DsrC in close proximity are involved in reduction of sulfite to sulfide. However, the exact reaction mechanism has remained unresolved (*9*–*11*).

Santos *et al.* now use an array of elegant biochemical, genetic, and physiological in vitro and in vivo experiments, in combination with mass spectrometry, to show that the DsrC protein is a co-substrate for sulfite reduction by DsrAB. They reveal that a sulfite-derived, zero-valent sulfur bridges the two conserved cysteine residues of the DsrC protein during sulfite reduction. In the first step of trisulfide synthesis, the coupled siroheme–[4Fe-4S] catalytic site of DsrAB receives two electrons from a reductant of unknown identity. Sulfite then binds to siroheme and gets reduced to an S(1+) intermediate; the latter leaves the iron coordination sphere and finally ends on DsrC, forming a protein-based trisulfide (see the figure, middle panel).

Deletion of the gene encoding DsrC is lethal for the microorganisms; hence, DsrC is vital for catalysis and energy conservation. The trisulfide is presumably reduced at a membrane-bound complex and sulfide is liberated as a product. In this way, the reduction of sulfite in the cytoplasm can be efficiently coupled to energy conservation at the membrane.

The discovery of the trisulfide in DsrC as the product of sulfite reduction represents major progress in understanding microbial sulfur conversion. It redefines the in vivo redox chemistry of DsrAB and links the energy-providing redox reactions to the generation of a chemiosmotic gradient. This finding moves the sulfate reducers a bit closer to the methanogens, underscoring the similarities of anaerobic respiration among these organisms and pointing to their common ancient origin. Researchers should now have a closer look at the membrane protein complexes involved. Knowing the stoichiometry of ions translocated across the membrane per electron transferred will be crucial for understanding the bioenergetics of DSR. Moreover, the electron donors for DsrAB and for the other enzymes of DSR have not yet been identified. ■

REFERENCES

1. A. A. Santos *et al.*, *Science* **350**, 1541 (2015).
2. H. Beinert, *Eur. J. Biochem.* **267**, 5657 (2000).
3. C. Huber, G. Wächtershäuser, *Science* **276**, 245 (1997).
4. K. Parey *et al.*, *Metallomics* **5**, 302 (2013).
5. R. K. Thauer *et al.*, *Bacteriol. Rev.* **41**, 100 (1977).
6. F. Grein *et al.*, *Biochim. Biophys. Acta* **1827**, 145 (2013).
7. A. Schiffer *et al.*, *J. Mol. Biol.* **379**, 1063 (2008).
8. B. R. Crane, E. D. Getzoff, *Curr. Opin. Struct. Biol.* **6**, 744 (1996).
9. T. F. Oliveira *et al.*, *J. Struct. Biol.* **164**, 236 (2008).
10. T. F. Oliveira *et al.*, *J. Biol. Chem.* **283**, 34141 (2008).
11. Y. C. Hsieh *et al.*, *Mol. Microbiol.* **78**, 1101 (2010).
12. G. J. Mander *et al.*, *FEBS Lett.* **579**, 4600 (2005).

10.1126/science.aad8139

NEUROSCIENCE

Opting in or out of the network

Does learning commit neurons that are predisposed to recruitment to a memory network?

By **K. C. Martin**[1] *and* **E. M. Schuman**[2]

Plasticity, a general feature of all nervous systems, is essential for the survival of organisms, allowing them to respond and adapt to their environment through the processes of learning and memory. Even relatively simple forms of learning, such as habituation (a reduction in responsiveness to stimuli that have no immediate consequences) or sensitization (an increase in overall responsiveness following an arousing stimulus), involve changes in neural gene transcription and protein translation, and the modification of neuronal connections (synapses) and neural networks (*1*). In a recent study, Hill *et al.* (*2*) examined the mechanisms that underlie the sensitization of a swimming response in the marine mollusk *Tritonia*. The authors propose that memories are stored as an expansion in the number of neurons in networks that underlie behavior, presumably to enhance responsiveness to other potential stimuli in the environment. But is this simply too simple a model?

> ***"...'nonsynaptic' mechanisms ...occur together with synaptic changes in... learning..."***

Hill *et al.* made use of a voltage-sensitive dye that allowed them to monitor, simultaneously, the activity of ~66 neurons in the pedal ganglion, the neurons that control *Tritonia*'s escape swim response (*2, 3*). For many rhythmic motor behaviors like swimming, the neural activity that drives and sustains these behaviors involves central pattern-generating circuits and "bursting"—clusters of action potentials elicited with a relatively high frequency—that entrain and drive downstream neurons in the network. Following a sensitizing stimulus (shock to the pedal nerve), the onset latency for the *Tritonia* swim motor program is reduced, indicating that the system exhibits sensitization (*4, 5*). Hill *et al.* examined the contribution of individual neurons to this program before, during, and after sensitization. The authors built upon earlier identification of neurons within the pedal ganglion that contribute to the swim motor program with different propensities to burst—reliable bursters, variable bursters, and nonbursters (*3*). By monitoring the activity of each class of neuron, they observed that after sensitization, an increased number of neurons exhibited reliable bursting behavior due to the conversion of some neurons from variable or nonbursting to reliable bursting phenotypes (see the figure). Dissipation of sensitization was accompanied by a return to the original network size. Remarkably, however, the constituent neurons in each class of the network (reliable bursters, variable bursters and nonbursters) following loss of sensitization were different from those observed before sensitization, indicating that the swim motor program is encoded by a dynamic network rather than by a fixed network of specific neurons.

To identify the cellular mechanisms that drive the reorganization observed during sensitization, Hill *et al.* focused on neurons containing the neurotransmitter serotonin that constitute part of the swim central pattern generator (*6*). Not only did stimulation of these neurons decrease the latency of the swim motor program (consistent with sensitization), but application of serotonin to the pedal ganglion decreased latency and increased the number of reliable burster neurons in the swim motor program network. As such, activation of a small number of serotonergic neurons was sufficient to implant a "false sensitization memory" in the system.

The findings of Hill *et al.* add to a rich history of discoveries about the mechanisms of learning and memory in invertebrate "simple systems." Although these systems contain a relatively small number of neurons, they undergo multiple and robust forms of learning. Two features contribute to the experimental tractability of these simple systems: The neurons are often identifiable from animal to animal; and isolated preparations of these neurons undergo forms of plasticity that mirror learning in the animal. These features facilitate the delineation of circuits underlying

[1]*Department of Biological Chemistry, David Geffen School of Medicine at University of California, Los Angeles, 695 Charles East Young Drive South, Los Angeles, CA, USA.* [2]*Max Planck Institute for Brain Research, Max von Laue Strasse 4, 60438 Frankfurt, Germany. E-mail: kcmartin@mednet.ucla.edu; erin.schuman@brain.mpg.de*

Published by AAAS

Sensitization and shuffling. The 66 neurons recorded in *Tritonia*'s pedal ganglion that control the swim motor program are present in three different classes. During sensitization to a stimulus and memory formation, neurons presumably predisposed to recruitment move into the reliably bursting class. After loss of sensitization, the number of neurons in each class returns to the naïve state, but the constituent neurons are different.

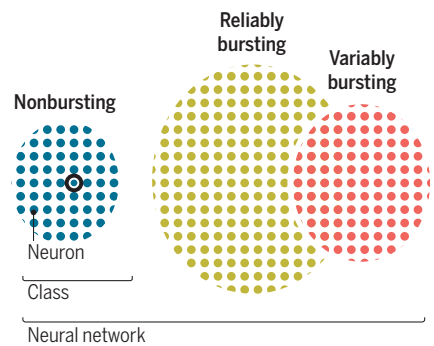

behavioral modification, and become even more powerful when combined, as by Hill *et al.*, with the use of voltage-sensitive dyes to monitor, simultaneously, the activity of many neurons in a circuit.

The conclusion from Hill *et al.* is that neurons are predisposed to join a given network, and that learning, acting via neuromodulation, commits these predisposed neurons to the network. This relatively "simple" idea is contrasted with the prevailing view that memories are stored as activity-dependent changes in synaptic strength and number, or synaptic plasticity. However, just as simple systems generate complex behaviors from a small number of neurons and circuits, they also do so using multiple mechanisms. Although studies in the marine mollusk *Aplysia californica* have emphasized the importance of changes in synaptic strength and number in mediating learning, including sensitization (*7*), other studies in *Aplysia* and the related mollusk *Hermissenda* have identified "nonsynaptic" mechanisms, including changes in excitability that occur together with synaptic changes in both nonassociative and associative forms of learning (*8, 9*). A remarkable set of studies on a central pattern generator in another invertebrate "simple system," the crustacean stomatogastric ganglion, has revealed tremendous functional variability in neuronal networks, emerging from activity-dependent changes in synaptic strength and excitability (*10*). The findings of Hill *et al.* are indeed reminiscent of the work on the lobster, which established that neurons switch allegiance from one motor pattern to another under neuromodulatory control (*11*). This indicated that the same circuit elements can be recombined in numerous ways, to generate behavioral flexibility.

Hill *et al.*'s framework of synaptic plasticity opposed to network expansion, and of changes in synaptic strength opposed to alterations in neuronal excitability, is simply too simple. The authors do not explore the mechanisms by which the bursting profile of the individual neurons within the network are altered. Changes in bursting behavior could be elicited by changes in intrinsic ionic conductances, but also could be mediated by alterations in excitatory and/or inhibitory transmission in the network. Indeed, the two mechanisms often co-occur (*10*). For example, the usual line-up of ion channels that alter excitability in neuronal processes can also change the properties of axon terminal depolarization and repolarization, resulting in changes in the kinetics and amount of neurotransmitter released. Thus, it's more likely that both mechanisms, and not any single mechanism, are operative, a conclusion often reached in arguments about mechanism in neurobiology. ■

REFERENCES

1. E. R. Kandel, Y. Dudai, M. R. Mayford, *Cell* **157**, 163 (2014).
2. E. S. Hill *et al.*, *Curr. Biol.* **25**, 2879 (2015).
3. E. S. Hill *et al.*, *PLOS One* **7**, e40579 (2012).
4. G. D. Brown *et al.*, *Behav. Neurosci.* **110,** 478 (1996).
5. W. N. Frost, C. L. Brandon, D. L. Mongeluzi, *Neurobiol. Learn. Mem.* **69**, 126 (1998).
6. P. A. Getting *et al.*, *J. Neurophysiol.* **44**, 151 (1980).
7. C. H. Bailey, E. R. Kandel, *Prog. Brain Res.* **169**, 179 (2008).
8. E. M. Schuman, G. A. Clark, *J. Neurosci.* **14**, 1613 (1994).
9. R. D. Hawkins, J. H. Byrne, *Cold Spring Harb. Perspect. Biol.* **7**, a021709 (2015).
10. A. Destexhe, E. Marder, *Nature* **431**, 789 (2004).
11. E. Marder, *Neuron* **76**, 1 (2012).

10.1126/science.aad9467

SYNTHETIC BIOLOGY

Designer cells finely tuned for therapy

Cells are engineered for on-demand control of psoriasis

By **Jeremy Di Domizio** *and* **Michel Gilliet**

The use of disease-specific molecular markers to select the appropriate treatment and dosing regimen is at the essence of precision medicine and represents a major research initiative for the years to come (*1*). A recent study by Schukur *et al.* (*2*) provides a major conceptual advance in this arena, particularly in the treatment of chronic inflammatory diseases. The study shows that synthetic biology can be used to generate cells that selectively respond to a combination of cytokine signals, providing therapeutic output that is disease-specific and related to disease activity. The findings hold great promise for treating psoriasis and other chronic-relapsing inflammatory diseases, including Crohn's disease and rheumatoid arthritis.

Psoriasis is a chronic-relapsing T cell–mediated inflammatory disease of the skin characterized by scaly red plaques that can cover large surfaces of the human body (*3–5*). These plaques are triggered by aberrantly activated dendritic cells that produce the cytokines tumor necrosis factor (TNF) and interleukin-23 (IL-23). These cytokines favor the generation of T helper cell 17 (T_H17) cells, which release the proinflammatory cytokines IL-17 and IL-22 that contribute to disease pathogenesis. The elucidation of immune pathways in psoriasis has led to the development of biologics that target and inhibit these pathogenic cytokines. Blockade of TNF, IL-23p40, and IL-17 by biologics is currently part of the strategic arsenal to treat moderate to severe psoriasis, but it has limitations. Dosing regimens are typically continued for long periods of time regardless of clinical activity of the disease. Because the targeted cytokines are also involved in antimicrobial defense, these standard dosing regimens result in

Department of Dermatology, University Hospital of Lausanne CHUV, Lausanne, Switzerland. E-mail: michel.gilliet@chuv.ch

ILLUSTRATION: V. ALTOUNIAN/*SCIENCE*

Published by AAAS

an increased risk for infections. The design of flexible anti-inflammatory therapies that are stopped during remissions and reinitiated in a disease-specific manner early during flares remains a major challenge in precision medicine.

Schukur *et al*. take on this challenge using synthetic biology. The authors engineered human embryonic kidney cells into cytokine "converter" cells that selectively detect the combination of TNF and IL-22, a specific biomarker for psoriatic inflammation. In response to this detection, the designer cells are activated to release the cytokines IL-4 and IL-10, which dampen the inflammation and allow the control of psoriasis.

How is the conversion from a proinflammatory input to an anti-inflammatory output achieved in the converter cell? TNF receptor signaling in the converter cell is artificially coupled to IL-22 receptor (IL-22R) signaling through the expression of a synthetic nuclear factor kappa B–responsive promoter that controls the expression of IL-22RA subunit. As a result, the detection of TNF drives the expression of a functional IL-22R, which is required to sense the presence of IL-22. The IL-22R signaling pathway itself is rewired to a transcription factor called signal transducer and activator of transcription 3 (STAT3), and a synthetic STAT3-responsive promoter drives the expression of IL-4 and IL-10. Thus, TNF and IL-22 signaling are artificially linked together, providing an AND gate logic in which both signals are required to activate the synthetic cell and to convert the proinflammatory cytokine input into the production of anti-inflammatory cytokines.

Schukur *et al* tested the therapeutic potential of the synthetic cytokine converter cells in an established experimental mouse models of psoriasis (*6*). Converter cells were encapsulated into an alginate-based biomaterial with an optimal pore size for cytokine diffusion, but lacking immunogenicity [the biomaterial had been successfully used in clinical trials of type I diabetes (*7*)]. The encapsulated converter cells were then implanted into the peritoneum of mice bearing psoriasis-like skin lesions induced by topical imiquimod treatment. Converter cells were found to detect circulating TNF and IL-22 that originates from established psoriatic skin plaques and to attenuate disease severity through the production of IL-4 and IL-10. Converter cells were also activated in response to the blood of psoriatic patients with severe skin disease, suggesting a potential therapeutic applicability of converter cells in humans. Interestingly, converter cells also effectively suppressed the development of psoriasis in a prophylactic model in which the engineered cells were implanted in mice before the induction of psoriasis. Thus, the converter cells appear highly sensitive in that they can detect very low concentrations of circulating proinflammatory cytokines even before the development of overt skin disease.

"...cytokine converter cells can be fine-tuned, depending on the need ('on demand')."

A major advantage of synthetic cytokine converter cells is that therapy is only delivered when inflammation is of psoriatic origin. Indeed, unrelated inflammatory processes, including bacterial or viral infections, were unable to activate converter cells because of the lack of the simultaneous presence of proinflammatory TNF and IL-22. Converter cells also ensure that therapy is provided only when the disease is active. Indeed, converter cell activity is abolished (switched OFF) upon withdrawal of TNF, IL-22, or both. By contrast, converter cell activity can be fully restored (switched ON) by addition of TNF and IL-22. Importantly, low proinflammatory cytokine input yields low anti-inflammatory cytokine output, indicating that the activity of cytokine converter cells can be fine-tuned, depending on the need ("on demand"). The engineered cells also allow a continuous delivery of therapeutic doses of anti-inflammatory IL-4 and IL-10. This is a great advantage over the need for daily injection of recombinant cytokines, which have a short half-life. This characteristic has precluded their development as therapeutic agents despite the antipsoriatic efficacy of both IL-4 and IL-10 in phase 2 clinical trials (*8, 9*)

Future studies that identify other cytokine combinations characteristic of chronic-relapsing inflammatory diseases could point to markers of early disease activity that are distinguishable from infections or unrelated inflammatory responses. Yet, many important questions need to be addressed before the synthetic designer cells can enter clinical testing. These include the type of cells to be used for the synthetic design (most likely autologous cells), the heterogeneity of patient-specific responses, the dosing performance, the location of implantation, and the type of encapsulation that requires it to be retrievable. Overcoming these translational hurdles may provide great advances in precision medicine and lead to new treatment modalities for psoriasis and other chronic inflammatory disorders. ■

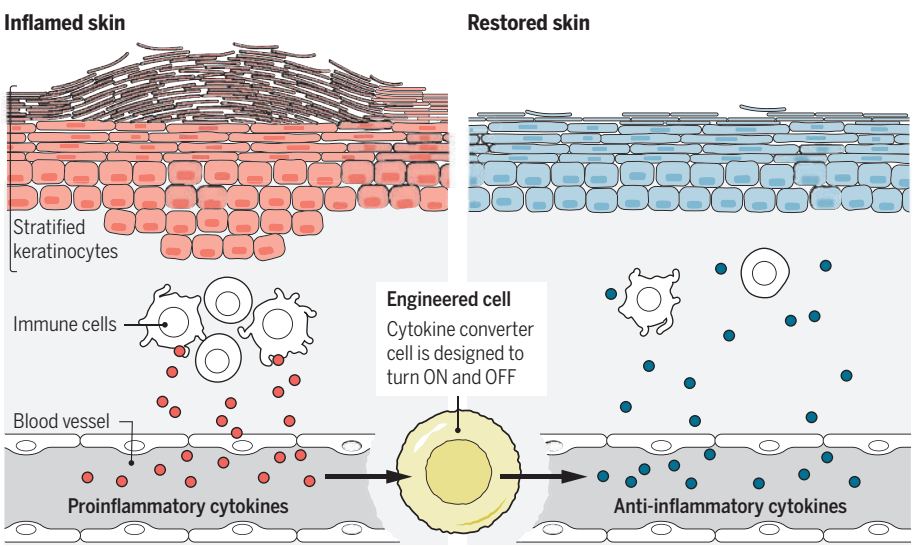

On-demand design. Cells are engineered to detect psoriasis-associated cytokines and produce anti-inflammatory cytokines in response. These cytokine converter cells are encapsulated in a biomaterial that allows their vascularization and prevents rejection by the host (a mouse model of psoriasis). They are turned ON when a psoriasis flare occurs and turned OFF when inflammation ceases, allowing precise fine-tuning of therapy.

ILLUSTRATION: V. ALTOUNIAN/*SCIENCE*

REFERENCES

1. F. S. Collins, H. Varmus, *N. Engl. J. Med.* **372**, 793 (2015).
2. L. Schukur, B. Geering, G. Charpin-El Hamri, M. Fussenegger, *Sci. Transl. Med.* **318**, ra201 (2015).
3. M. A. Lowes, A. M. Bowcock, J. G. Krueger, *Nature* **445**, 866 (2007).
4. F. O. Nestle, D. H. Kaplan, J. Barker, *N. Engl. J. Med.* **361**, 496 (2009).
5. C. E. Griffiths, J. N. Barker, *Lancet* **370**, 263 (2007).
6. B. Flutter, F. O. Nestle, *Eur. J. Immunol.* **43**, 3138 (2013).
7. D. Jacobs-Tulleneers-Thevissen *et al*., *Diabetologia* **56**, 1605 (2013).
8. K. Ghoreschi *et al*., *Nat. Med.* **9**, 40 (2003).
9. K. Asadullah *et al*., *Arch Dermatol.* **135**, 187 (1999).

10.1126/science.aad9464

Published by AAAS

BOOKS *et al.*

NEUROSCIENCE

A patient's progress

Diagnosed at age 60, a journalist sets out to learn all he can about Parkinson's disease

By **Orla M. Smith**

They say that each event that happens to you prepares you for the next step on life's journey. The award-winning journalist Jon Palfreman, best known for his 1986 Nova documentary, *The Case of the Frozen Addict*, is likely to agree with this. As he meticulously researched the story of six young heroin addicts who suddenly developed severe Parkinson's disease after ingesting a bad batch of heroin, little did he know that several decades later he, too, would be diagnosed with this disease. *Brain Storms* is Jon Palfreman's frank autobiography about life after his diagnosis and his quest to learn everything possible about this incurable neurodegenerative disorder.

The book opens in June 2012 with Palfreman visiting his longtime collaborator, Bill Langston, who discovered that the "frozen addicts" had unwittingly ingested MPTP, a neurotoxin contaminant in the synthetic heroin that they had purchased on the street. As Palfreman reminisces with Langston, he reveals his own diagnosis and his determination to conquer the disease. He weaves personal anecdotes throughout the book as he discusses the history, pathogenesis, and treatment of Parkinson's disease, as well as new treatments on the horizon. Along the way, we are introduced to a colorful cast of characters: dedicated research scientists, caring physicians, and a panoply of courageous patients from all walks of life.

Starting with the discovery of the disease by James Parkinson in 1817, we learn about the French physician Jean-Martin Charcot, who, in the 1860s, codified the classic motor symptoms (tremor, rigidity, and slowness of movement) and gave Parkinson's disease its name. Fast forward to the 1950s, when Arvid Carlsson showed that dopaminergic neuron loss caused the disease's motor symptoms, work that would later earn him a Nobel Prize.

A decade later came the development of the current mainstay treatment, L-dopa, a precursor molecule that is broken down into dopamine in the brain. But L-dopa is far from a perfect solution. At best, it temporarily relieves the motor symptoms of the disease. At worst, it can cause debilitating side effects, becomes less effective over time, and, ultimately, fails to mitigate the loss of dopaminergic neurons. In the 1990s, researchers identified mutations in the α-synuclein gene in patients with a rare familial form of Parkinson's disease. The misfolding of mutant α-synuclein protein results in sticky aggregates that are a principal component of Lewy bodies, a pathological hallmark of the disease.

A key question that readers will be asking is whether a cure, or at least a disease-modifying therapy, is close at hand. Palfreman discusses several innovative treatments that have been tested over the past two decades, including fetal cell transplants to replace lost neurons and gene therapy to provide nourishing growth factors that could sustain the dwindling population of dopaminergic neurons. Unfortunately, as Palfreman explains, neither approach has garnered clinical success. He also delves into a number of other important advances, including the discovery and use of deep brain stimulation for control of motor symptoms and the serendipitous discovery of one of the newest drug candidates, NPT088, an efficient disruptor of α-synuclein clumps, which is awaiting approval for entry into clinical trials.

One of the most compelling aspects of this book is Palfreman's conversations with other Parkinson's patients. There is the modern dancer Pamela Quinn, who has put her years of dance training to excellent use by teaching her fellow patients tricks to initiate and control their erratic movements. Then there is Tom Isaacs, diagnosed at the age of 27, who walked around the coastline of Great Britain (4500 miles) over 365 days, raising $350,000 for Parkinson's research.

Palfreman also discusses the vital contributions of charities and foundations launched by patients, including the eponymous Michael J. Fox Foundation. The MJFF has aggressively funded crucial large multicenter projects such as the Parkinson's Progression Markers Initiative, which aims to identify biomarkers of the earliest stages of the disease.

This book tackles the scientific and medical complexity of Parkinson's disease in a clear writing style with accurate scientific content that should be easy to assimilate for the informed reader. In true journalistic fashion, no scientific fact is too difficult to explain and no scientific detail too uninteresting to discuss. With 7 million Parkinson's patients worldwide and 1 million in the United States alone, not to mention their families and caregivers, there will certainly be a plentiful audience for this well-written and informative book.

Stimulating electrodes implanted deep in the brain can sometimes mitigate Parkinson's symptoms that are not adequately controlled with medication.

CREDIT: BURGER/PHANIE

Brain Storms
The Race to Unlock the Mysteries of Parkinson's Disease
Jon Palfreman
Scientific American/Farrar, Straus and Giroux, 2015. 283 pp.

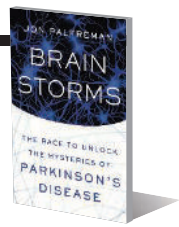

The reviewer is at Science Translational Medicine, *AAAS, Washington, DC 20005, USA.*

10.1126/science.aad5574

Published by AAAS

ASTROPHYSICS

The planet that wasn't there

The planet Vulcan wasn't just demoted, it was debunked

By **Mario Livio**

In 2015, we are celebrating the 100th anniversary of Einstein's theory of general relativity—a theory that transformed spacetime from a mere backdrop for cosmic events into a major player in modern physics. This occasion provides author Thomas Levenson with an excellent opportunity to describe some of the fascinating historical circumstances that led to the birth of this elegant and incredibly successful theory.

The story of the planet Vulcan, whose existence, although never confirmed, was once considered a foregone conclusion, is one of the most colorful examples of a scientific misstep that, in a somewhat convoluted fashion, paved the way for an astonishing intellectual revolution. Levenson's book beautifully captures the drama of the tireless search for this celestial object, which—according to the Newtonian gravitational theory that was prevailing at the time—had to exist. In doing so, it concisely and lucidly provides the necessary details for appreciating Einstein's monumental achievement.

When the orbit of Uranus was found to deviate from the predictions of Newtonian gravity in the mid-19th century, mathematician Urbain Le Verrier postulated the existence of a never-before-seen planet that perturbed Uranus's orbit. His mathematical prediction eventually led to the discovery of the planet Neptune, supporting Newton's theory of gravity and validating what was later dubbed by physicist Eugene Wigner "the unreasonable effectiveness of mathematics." When it was discovered that the precession of the orbit of Mercury did not conform to Newton's theory of gravitation, Le Verrier suggested the presence of a putative planet that was given the name Vulcan.

Levenson's fascinating description of the searches for, and false detections of, this "planet," read like a fast-paced thriller. We learn that, despite the initial enthusiasm for Vulcan, eventually the observations fairly conclusively showed that such a planet did not exist, and from around 1878 almost all astronomers abandoned the idea that a previously unseen object existed between Mercury and the Sun.

What then, was causing Mercury's anomalous precession? In November 1915, Einstein unveiled his theory of general relativity. Among other explanations, the theory perfectly elucidated Mercury's unusual orbit. His predictions concerning the bending of light by the Sun's mass were confirmed by two British astronomers in May 1919, striking the final blow to the planet Vulcan.

Levenson's book also emphasizes important lessons from the rich and complex history and philosophy of science. First, it drives home the fact that no scientific theory has an absolute and permanent value. Rather, every claim is provisional. As new results become available, theories have to be modified or are altogether refuted. Second, referring to the many false "detections" of Vulcan, Levenson insightfully writes, "It's so damn easy to see what one wants or expects to find." Indeed, a recent study that sought to replicate 100 experimental and correlational studies published in three major psychology journals in 2008 demonstrated that, although 97% of the original studies claimed to have produced significant results, only 36% of the replications did (*1*).

The tale of Vulcan is strikingly similar to the current searches for dark matter, the evidence for which comes entirely from its gravitational influence. The spatial distribution of dark matter can be inferred and mapped in detail through the effect of gravitational lensing—the distortion and magnification of the light from distant objects by intervening gravitating masses—one of the predictions of Einstein's general relativity.

Despite extensive searches, the actual constituents of dark matter remain elusive. This frustrating situation has led a few theorists to propose that dark matter in fact does not exist and that we need to modify our theory of gravity (namely, general relativity). Most astronomers argue, however, that if a large number of astronomical phenomena can be fully explained by matter that by definition does not emit any light, then we should not rush to the conclusion that an entirely new theory is needed. As in the case of Vulcan, future observations and experiments will show which of these two opinions will turn out to be correct.

The Hunt for Vulcan
Thomas Levenson
Random House, 2015.
247 pp.

REFERENCES AND NOTES

1. Open Science Collaboration, Estimating the reproducibility of psychological science. *Science* **349**, aac4716 (2015).
10.1126/science.aad4438

The reviewer is an astrophysicist and the author of Brilliant Blunders *(Simon & Schuster, New York, 2013). E-mail: dr.mario.livio@gmail.com*

CREDIT: COURTESY CONDUIT GALLERY. PHOTO BY RON BLUNT

EXHIBITION

Wonder
Renwick Gallery of the
Smithsonian American Art Museum,
Washington, D.C.
Through 10 July 2016.

Standing inside a nest made of woven willow branches, there is no doubt why birds have chosen such intricate creations to call home. This installation is part of the new environmentally themed exhibition that heralds the opening of the elegantly refurbished Renwick gallery. Highlights include a bright pink room (think cochineal dye) studded from floor to ceiling with intricate patterns created by pinning thousands of insects to the walls. John Grade's *Middle Fork (Cascades)* is a replica of a 150-year-old hemlock tree from the Cascade Mountains reassembled from half a million tiny pieces of reclaimed cedar. Suspended horizontally from the ceiling, the tree gently sways as though alive. *Wonder* is a visual feast and a must see. – *Orla M. Smith*

10.1126/science.aad9003

Published by AAAS

LETTERS

Edited by **Jennifer Sills**

Retraction

IN THE REPORT "Observation of chiral currents at the magnetic domain boundary of a topological insulator" (*1*), we reported the observation of a chiral current in a topological insulator/ferromagnetic insulator heterostructure. The measurement used a superconducting quantum interference device (SQUID) to detect an ac magnetic field that we believed was produced by a current flowing in the sample. Depending on the conductivity of various layers of the sample, a similar signal can arise when electric coupling causes a vertical oscillation of the SQUID in the spatially varying magnetic field produced by the magnetism of the sample. We and collaborators have subsequently shown that the magnitude, shape, frequency dependence, and backgate-voltage dependence of the signal can be explained by the electric coupling artifact (*2*). Although this does not rule out the presence of chiral edge states in these samples, we cannot state that we have observed them. Thus, we must retract our results. This artifact does not affect other papers that used similar methods to image current in nonmagnetic samples.

Y. H. Wang,[1,2]* J. R. Kirtley,[1] F. Katmis,[3,4] P. Jarillo-Herrero,[4] J. S. Moodera,[3,4] K. A. Moler[1,2]*

[1]Department of Physics and Applied Physics, Stanford University, Stanford, CA 94305, USA. [2]Stanford Institute for Materials and Energy Sciences, SLAC National Accelerator Laboratory, Menlo Park, CA 94025, USA. [3]Francis Bitter Magnet Laboratory and Plasma Science and Fusion Center, Massachusetts Institute of Technology, Cambridge, MA 02139, USA. [4]Department of Physics, Massachusetts Institute of Technology, Cambridge, MA 02139, USA.

*Corresponding author. E-mail: wangyhv@stanford.edu (Y.H.W.); kmoler@stanford.edu (K.A.M.)

REFERENCES

1. Y. H. Wang *et al.*, *Science* **349**, 948 (2015); published online 13 August 2015 (10.1126/science.aaa0508).
2. E. M. Spanton *et al.*, "Electric coupling in scanning SQUID measurements" (2015); http://arxiv.org/abs/1512.03373.

Editorial expression of concern

IN THE 29 May 2015 issue, *Science* published the Research Article "The protein LEM promotes CD8$^+$ T cell immunity through effects on mitochondrial respiration" by I. Okoye *et al.* (*1*). On 23 October 2015, *Science* published a Correction to two of the figures in the Okoye *et al.* paper (*2*). An investigation into potential errors in the paper is being undertaken by Imperial College London, UK. In light of the continuing investigation, *Science* is publishing this Editorial Expression of Concern to alert our readers to the fact that questions have been raised about the validity of findings in the Okoye *et al.* paper.

Marcia McNutt

Editor-in-Chief

Published online 10 December 2015; 10.1126/science.aae0548

REFERENCES

1. I. Okoye *et al.*, *Science* **348**, 995 (2015).
2. *Science* **350**, aad6462 (2015).

Preventing tropical mining disasters

MINING FOR FOSSIL fuels and minerals is penetrating into many of the world's most remote and biologically important tropical forests. In the Amazon, there are some 53,000 active mining leases (*1*), and hundreds of billions of dollars in new mines are planned across the Congo basin (*2*). But are extractive industries in the tropics investing sufficiently to prevent environmental disasters?

The urgency of this question is underscored by a recent disaster at the Samarco iron ore mine in Minas Gerais, Brazil. Tailing-pond dams burst on 5 November, disgorging 50 million cubic meters of mineral sludge into the Rio Doce. Hundreds of kilometers of river have been polluted, with potentially devastating long-term consequences for aquatic wildlife and hundreds of thousands of local inhabitants, who formerly relied on the river for water and fisheries (*3*). A disaster of this magnitude in a remote tropical forest would cause a catastrophic loss of hyperdiverse forest, and endanger indigenous tribes.

In tropical wet environments, huge quantities of rain can fall in short timespans. Tropical mines therefore require specially designed tailing ponds and infrastructure that can withstand massive influxes of water, but the engineering is often inadequate. This appears to have been the case in the Samarco disaster.

Although many nations require mining corporations to pay a bond to be held in escrow for future clean-ups, it is unclear how often or effectively this is being enforced in tropical developing nations. However, prevention is far better than cure. We urgently need a global framework to police the construction, management, and

PHOTO: AP PHOTO/FELIPE DANA

maintenance of key infrastructure in tropical mines. Given that tropical nations are hungry for mining-tax revenues and mining corporations (including Vale, the joint owner of Samarco) are often major contributors to political parties, there will be temptations to overlook these urgent safeguards (*4*).

We propose an independent global authority to fulfill this critical role. Such an authority must be able to temporarily close failing or high-risk mines, and must have mechanisms for reporting to relevant stock exchange listings and financial institutions. Without independently verified security, there is an escalating risk of environmental catastrophe in the world's tropical regions.

David P. Edwards[1]* and William F. Laurance[2]

[1]Department of Animal and Plant Sciences, University of Sheffield, S10 2TN, UK. [2]Centre for Tropical Environmental and Sustainability Science, and College of Marine and Environmental Sciences, James Cook University, Cairns, QLD 4878, Australia.

*Corresponding author. E-mail: david.edwards@sheffield.ac.uk

REFERENCES

1. N. Alexander, *The Emerging Multi-polar World Order: Its Unprecedented Consensus on a New Model for Financing Infrastructure Investment and Development* (Heinrich Böll Foundation North America, 2014).
2. D. P. Edwards *et al.*, *Conserv. Lett.* **7**, 302 (2014).
3. H. Escobar, *Science* **350**, 1138 (2015).
4. W. F. Laurance, *New Scientist*, **16 August**, 16 (2008).

The global warming hiatus's irrelevance

IN 2009, WE argued that short periods of warming or cooling in the observed global average temperature were inconsequential to conclusions about either the existence or magnitude of anthropogenic climate change (*1*). Natural variations on interannual and interdecadal time scales are combined with the effect of human-forcing factors in the observational record, and it came as no surprise that warming of the climate system is episodic and interspersed

Published by AAAS

A girl runs between mattresses inside a sports arena where residents are taking refuge after being displaced by bursting dams in Minas Gerais, Brazil.

with stagnant and even cooling periods.

This point appears to be completely lost in the ongoing public controversy surrounding the recent study by Karl *et al.* (*2*), which found that errors in previous estimates of the global surface air temperature were largely responsible for the so-called hiatus in warming since the late 1990s. The current public debate concerning the Karl *et al.* study is completely disconnected from the most important matter at hand: The human burning of fossil fuels, and the resulting emission of CO_2, has long-term consequences on the entire climate system. How much future warming is realized at the end of the century depends far more on human behavior than it does on modes of natural variability (*3*).

Scientifically, a hiatus in global mean temperature increase provides an opportunity to more fully understand energy transport in the climate system, particularly during periods where natural variability dominates [e.g., (*4*)], and the role of variations in climate forcing factors, both natural (*5*, *6*) and human (*7*). Evidence of the hiatus led the Intergovernmental Panel on Climate Change to slightly decrease the estimated lower bound (*8*) of the response of global mean temperature to a specified change in greenhouse gases, but the upper bound estimate remains unchanged (*9*).

As we cautioned in 2009, "Claims that global warming is not occurring that are derived from a cooling observed over such short time periods ignore…natural variability and are misleading" (*1*). We are disheartened by the abundance of misleading statements about climate change, justified by a temporary variation in the rate of global mean temperature increase, whether they be alarmist or denialist. To more fully understand the human signal amidst the natural noise, we must take the long view. In that sense, whether or not the early 21st century global warming hiatus existed is not important.

Michael F. Wehner[1] and David R. Easterling[2]*

[1]Lawrence Berkeley National Laboratory, Berkeley, CA 94720, USA. [2]Center for Weather and Climate, NOAA's National Centers for Environmental Information, Asheville, NC 28801, USA.

*Corresponding author. E-mail: David.Easterling@noaa.gov

REFERENCES

1. D. R. Easterling, M. F. Wehner, *Geophys. Res. Letts.* **36**, L08706 (2009).
2. T. R. Karl *et al.*, *Science* **348**, 1469 (2015).
3. E. Hawkins, R. Sutton, *Bull. Amer. Meteor. Soc.* **90**, 1095 (2009).
4. G. A. Meehl, *Nat. Clim. Change* **4**, 898 (2014).
5. S. Solomon *et al.*, *Science* **333**, 866 (2011).
6. B. D. Santer *et al.*, *Geophys. Res. Lett.* **42**, 500 (2015).
7. L. J. Wilcox *et al.*, *Environ. Res. Lett.* ***8***, *024033* (2013).
8. A. Otto *et al.*, *Nature Geosci.* **6**, 415 (2013).
9. M. Huber, R. Knutti, *Nat. Geosci.* **7**, 651 (2014).

ACKNOWLEDGMENT

The views expressed here are those of the authors and do not necessarily reflect the U.S. Department of Energy, the National Oceanic and Atmospheric Administration, or their subsidiary organization. Support for M.F.W. is provided by the Regional and Global Climate Modeling Program of the Office of Biological and Environmental Research in the Department of Energy Office of Science under contract number DE-AC02-05CH11231.

TECHNICAL COMMENT ABSTRACTS

Comment on "Dilution limits dissolved organic carbon utilization in the deep ocean"

Nianzhi Jiao, Louis Legendre, Carol Robinson, Helmuth Thomas, Ya-Wei Luo, Hongyue Dang, Jihua Liu, Rui Zhang, Kai Tang, Tingwei Luo, Chao Li, Xiaoxue Wang, Chuanlun Zhang

Arrieta *et al.* (Reports, 17 April 2015, p. 331) propose that low concentrations of labile dissolved organic carbon (DOC) preclude prokaryotic consumption of a substantial fraction of DOC in the deep ocean and that this dilution acts as an alternative mechanism to recalcitrance for long-term DOC storage. Here, we show that the authors' data do not support their claims.
Full text at http://dx.doi.org/10.1126/science.aab2713

Response to Comment on "Dilution limits dissolved organic carbon utilization in the deep ocean"

Jesús M. Arrieta, Eva Mayol, Roberta L. Hansman, Gerhard J. Herndl, Thorsten Dittmar, Carlos M. Duarte

Our recent finding that dilution limits dissolved organic carbon (DOC) utilization in the deep ocean has been criticized based on the common misconception that lability equates to rapid and complete utilization. Even when considering the redefinition of recalcitrant DOC recently proposed by Jiao *et al.*, the dilution hypothesis best explains our experimental observations.
Full text at http://dx.doi.org/10.1126/science.aac7249

Published by AAAS

TECHNICAL COMMENT

OCEAN CHEMISTRY

Comment on "Dilution limits dissolved organic carbon utilization in the deep ocean"

Nianzhi Jiao,[1,2]* Louis Legendre,[3]* Carol Robinson,[4]* Helmuth Thomas,[5]* Ya-Wei Luo,[1,2] Hongyue Dang,[1,2] Jihua Liu,[2,6] Rui Zhang,[1,2] Kai Tang,[1,2] Tingwei Luo,[1,2] Chao Li,[7] Xiaoxue Wang,[8] Chuanlun Zhang[9]

Arrieta *et al*. (Reports, 17 April 2015, p. 331) propose that low concentrations of labile dissolved organic carbon (DOC) preclude prokaryotic consumption of a substantial fraction of DOC in the deep ocean and that this dilution acts as an alternative mechanism to recalcitrance for long-term DOC storage. Here, we show that the authors' data do not support their claims.

The mechanisms controlling the reactivity/recalcitrance continuum of dissolved organic carbon (DOC) in the nutrient-rich deep ocean remain a "recalcitrant" problem due to the complexity of the underlying biogeochemical interactions and the limitations of current methods (*1*). The experimental study by Arrieta *et al.* (*2*) claims to provide new evidence for the existence of labile DOC that behaves as recalcitrant DOC (RDOC) when its concentration is below the threshold for prokaryotic utilization. The publication of Arrieta *et al.*'s data (*2*) is timely given that a recent review article (*3*) proposed that there are two categories of RDOC in the ocean: RDOC that consists of compounds occurring at concentrations below the uptake thresholds of prokaryotes [concentration-constrained ($RDOC_c$)] and RDOC that is recalcitrant in a given biogeochemical context [environmental context-dependent ($RDOC_t$)]. Dilute labile DOC *sensu* Arrieta *et al.* (*2*) is the same as $RDOC_c$ (*3*).

Arrieta *et al.* (*2*) tested experimentally the null hypothesis that "no significant increase in prokaryotic growth should be detectable when increasing DOC concentrations." Their enrichment experiments showed increased prokaryotic growth, consistent with the dilution hypothesis. However, if low concentrations did limit prokaryotic growth in Arrieta *et al.*'s (*2*) incubations, then the corollary of their hypothesis should also hold—i.e., the prokaryotic consumption of DOC should be related to the DOC concentration. We therefore reanalyzed the data of Arrieta *et al.* (*2*) to test the null hypothesis that no significant increase in DOC consumption by prokaryotes should be detectable when increasing DOC concentrations. Plotting the authors' incubation measurements from Stations K, L, and N (data from Station M were anomalous due to a second phase of intense growth) shows, first, that the relative fraction of DOC consumed by prokaryotes is below 6% in each of the assays and, second, that this fraction is independent of the DOC enrichment (2×, 5×, or 10×) (Fig. 1). The lack of rejection of our null hypothesis indicates the inconsistency of Arrieta *et al.*'s data with the dilution hypothesis.

Arrieta *et al.* (*2*) also based their conclusion that dilute labile DOC is a substantial fraction of DOC in the deep ocean on the results of specific growth rate experiments, in which they used population growth kinetics to estimate the minimum concentration of DOC required for growth of deepwater prokaryotic communities [figure 2, figure S3, and table S2 in (*2*)]. However, the minimum concentration of bulk DOC required for growth of a prokaryotic community cannot be equated with the threshold values of availability of single DOC compounds. Instead, the dilution hypothesis as formulated by Arrieta *et al.* (i.e., most organic substrates in the deep ocean are labile but cannot be used by prokaryotes at concentrations below the levels matching the energetic investment required for their uptake and degradation) suggests that at steady state, and neglecting abiotic processes that could transform DOC, the supply of individual dilute labile DOC compounds is balanced by prokaryotic uptake to just below their respective uptake thresholds. This is illustrated in Fig. 2, which shows that, if low concentrations of individual labile DOC compounds had indeed prevented prokaryotic utilization in the deep-water samples, then the consumption of bulk DOC should have increased substantially with higher DOC enrichments, but it did not (Fig. 1). The majority (~94%) of bulk DOC remained at the end of the incubations (Fig. 1), which is not consistent with the dilution hypothesis and is thus in contradiction of Arrieta *et al.*'s (*2*) conclusion that their figures 1 and 2 "validated the dilution hypothesis

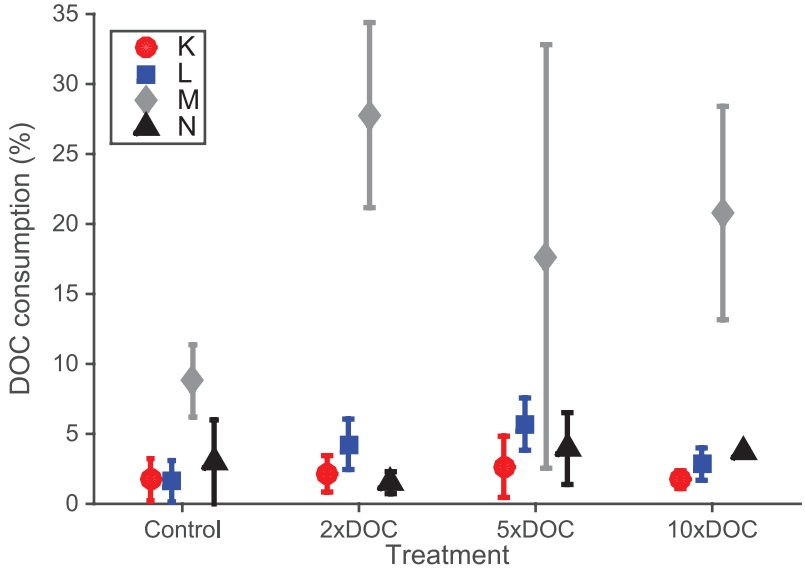

Fig. 1. DOC consumption as a function of DOC enrichment (data from Arrieta *et al.*). Apart from Station M, which is anomalous, all the data from Stations K, L, and N show that only <6% of the DOC is consumed regardless of enrichment (2×, 5×, and 10×), and the remaining >94% is not used.

[1]State Key Laboratory of Marine Environmental Sciences, Xiamen University, China. [2]Institute of Marine Microbes and Ecospheres, Xiamen University, China. [3]Sorbonne Universités, UPMC Université Paris 06, CNRS, Laboratoire d'Océanographie de Villefranche, Observatoire Océanologique, 06230 Villefranche-sur-Mer, France. [4]School of Environmental Sciences, University of East Anglia, Norwich Research Park, Norwich, UK. [5]Department of Oceanography, Dalhousie University, Halifax, Nova Scotia, Canada. [6]Institute of Marine Science and Technology, Shandong University, China. [7]State Key Laboratory of Biogeology and Environmental Geology, China University of Geosciences, Wuhan 430074, China. [8]South China Sea Institute of Oceanology, Chinese Academy of Sciences, Guangzhou, China. [9]Tongji University, Shanghai, China.
***Corresponding author. E-mail: jiao@xmu.edu.cn (N.J.); legendre@obs-vlfr.fr (L.L.); carol.robinson@uea.ac.uk (C.R.); helmuth.thomas@posteo.org (H.T.)**

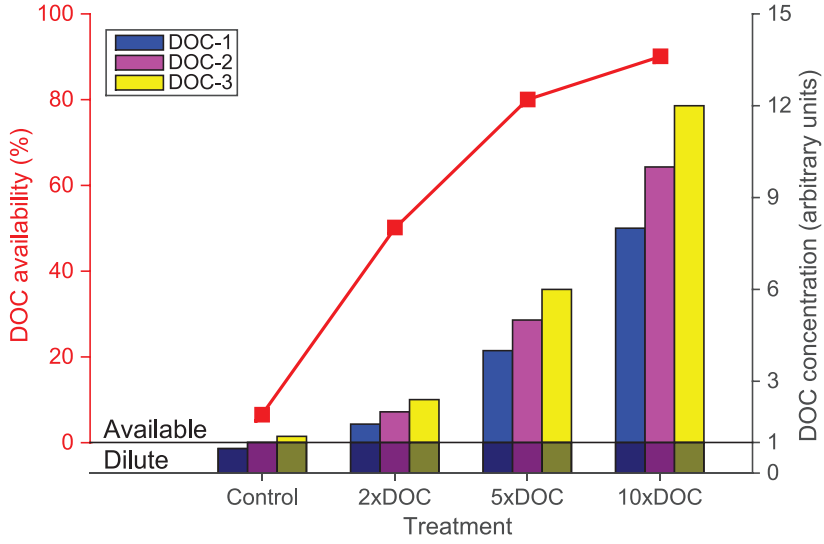

Fig. 2. The expected increase in DOC availability with increasing DOC enrichment in a scenario where the availability of labile DOC to prokaryotes is limited by dilution. It is assumed here that labile DOC compounds in the deep ocean are at three concentration levels (DOC-1, below uptake threshold; DOC-2 at threshold; and DOC-3, above threshold), and the threshold is set at a concentration of 1 (arbitrary units). This thought experiment reveals that the availability of labile DOC increases rapidly with increasing enrichment, so that an increasing proportion of labile DOC in the incubations should be taken up by the prokaryotes, which is contrary to what is observed in Fig. 1.

tested, showing that dilution limits C utilization in the deep ocean."

One possibility that could explain these contradictory interpretations of Arrieta *et al.*'s data is that the increased prokaryotic growth in the enrichment experiments did not reflect a release of dilution limitation by the enrichments. Some labile DOC compounds may have been in the original sample, and their concentrations accordingly increased with the bulk DOC enrichment. Hence, although the measured prokaryotic growth increased with DOC enrichment, the proportion of total DOC consumed (DOC consumption, %) did not (Fig. 1). This possibility is consistent with the fact that prokaryotes grew in most of the controls [in figure 1 and figure S2 in (*2*) , prokaryotic abundance typically doubled over 10 to 20 days in controls at 10 of the 14 stations]. Other potential labile DOC sources in the incubations include viral lysis (*4*), chemolithoautotrophic activities (*5*, *6*), and grazing by protists (*7*), which are independent of enrichment. This could explain Arrieta *et al.*'s Fourier-transform ion cyclotron resonance mass spectrometry (FT-ICR-MS) data, which showed generation of new DOC compounds during the incubations but no correlation between the numbers of compounds utilized and the enrichments. In fact, at one of the two stations sampled, Station P, more compounds were utilized in the controls than in the 5× enrichment (i.e., *1753* versus *936*, respectively) (*2*).

The use of novel technical and analytical approaches by Arrieta *et al.* (*2*) to experimentally study the prokaryotic uptake of deep-ocean DOC provides a renewed perspective on investigating the availability and recalcitrance of the huge inventory of DOC in the deep ocean, an enigma that was first highlighted in the seminal study of Barber in 1968 (*8*). However, as is often the case, probing the natural environment with advanced techniques (including here solid phase extraction of organic compounds and FT-ICR-MS) leads to new questions instead of simple testing of initial hypotheses. In the present case, although Arrieta *et al.*'s experiments (*2*) were inconclusive with regard to the dilution hypothesis, they lead the way to test this hypothesis in the future and provide new evidence for the microbial generation of $RDOC_t$ in deep oceanic waters (*1*, *9*).

REFERENCES AND NOTES

1. N. Jiao *et al.*, *Nat. Rev. Microbiol.* **8**, 593–599 (2010).
2. J. M. Arrieta *et al.*, *Science* **348**, 331–333 (2015).
3. N. Jiao *et al.*, *Biogeosciences* **11**, 5285–5306 (2014).
4. M. G. Weinbauer, F. Chen, S. W. Wilhelm, Virus-mediated redistribution and partitioning of carbon in the global oceans, in *Microbial Carbon Pump in the Ocean*, N. Jiao, F. Azam, S. Sanders, Eds. (*Science*/AAAS, Washington, DC), pp. 54–56 (2011).
5. M. Hügler, S. M. Sievert, *Ann. Rev. Mar. Sci.* **3**, 261–289 (2011).
6. D. A. Stahl, J. R. de la Torre, *Annu. Rev. Microbiol.* **66**, 83–101 (2012).
7. S. L. Strom, R. Benner, S. Ziegler, M. J. Dagg, *Limnol. Oceanogr.* **42**, 1364–1374 (1997).
8. R. T. Barber, *Nature* **220**, 274–275 (1968).
9. O. J. Lechtenfeld, N. Hertkorn, Y. Shen, M. Witt, R. Benner, *Nat. Commun.* **6**, 6711 (2015).

ACKNOWLEDGMENTS

This study was supported by the Ministry of Science and Technology of the People's Republic of China (2013CB955700 to N.J.) and the National Natural Science Foundation of China (91428308 to N.J.; 41476093 to Y.-W.L.; and 91328209 to H.D.).

18 May 2015; accepted 11 November 2015
10.1126/science.aab2713

TECHNICAL RESPONSE

OCEAN CHEMISTRY

Response to Comment on "Dilution limits dissolved organic carbon utilization in the deep ocean"

Jesús M. Arrieta,[1,2]* Eva Mayol,[2] Roberta L. Hansman,[3] Gerhard J. Herndl,[3,4] Thorsten Dittmar,[5] Carlos M. Duarte[1,2]

Our recent finding that dilution limits dissolved organic carbon (DOC) utilization in the deep ocean has been criticized based on the common misconception that lability equates to rapid and complete utilization. Even when considering the redefinition of recalcitrant DOC recently proposed by Jiao *et al*., the dilution hypothesis best explains our experimental observations.

A large reservoir of DOC preserved within the deep oceanic water masses has been termed "refractory" or "recalcitrant" in the bulk of the scientific literature. Recalcitrant DOC is defined as "resistant to rapid microbial degradation" (*1*) or "resistant to microbial utilization" (*2*), which implies that the intrinsic properties of these substrates make them unavailable to oceanic microbes. In a recent study (*3*), we tested the alternative hypothesis that the dilution of the different constituents of DOC, rather than their chemical properties, limits DOC utilization in the deep ocean (*4*). Our results show that a substantial part of the deep-sea DOC pool is labile (i.e., available to the in situ microbial community) but that the low individual concentrations of its many constituents slow down the overall rates of utilization. Jiao *et al.* (*5*) recently redefined recalcitrant DOC (RDOC) as consisting of two pools: $RDOC_c$, comprising labile compounds that are too diluted to be efficiently utilized by bacteria (the same mechanism that we demonstrate) and $RDOC_t$, consisting of labile compounds that cannot be used by the actual microbial community in their environmental context. Our study does not rule out the existence of recalcitrant molecules, which would be impossible to test experimentally for each of the thousands of different compounds present. Yet, Jiao *et al.* (*5*) implicitly deny the existence of structurally recalcitrant molecules in the DOC pool because none of the RDOC fractions in their new definition is inherently "recalcitrant." Thus, Jiao *et al.* (*5*) concur with our assertion that much of the deep-oceanic DOC is not intrinsically recalcitrant as defined in the bulk of existing literature (*1*, *2*, *6*, *7*).

In their Comment, Jiao *et al.* (*8*) argue that our data do not support the dilution hypothesis because increasing the DOC concentrations in our experiments did not result in a much higher percentage of DOC utilization. They also model the DOC pool as an even mixture of compounds present at three concentration levels. Based on this crude model, they estimate that DOC availability should increase on average from 6 to 90% when increasing the bulk DOC concentration by a factor of 10 if all of the DOC were labile. Consequently, and based on the fact that the fraction of carbon utilized at the end of our experiments did not exceed 6% in most cases, Jiao *et al.* (*8*) estimate that labile carbon represents at most 6% of the total DOC and conclude that the remaining 94% must be recalcitrant or, according to their new definition of recalcitrant DOC, context-recalcitrant DOC.

Unfortunately, their model is flawed by the underlying misconception that lability implies immediate and complete utilization regardless of concentration. Thus, they assume that the amount of DOC consumed at the end of the experiments represents the total amount of labile DOC present over threshold concentrations. This naïve expectation assumes that 40 days suffice to utilize all the labile DOC in the samples and that the utilization of a given substrate is either inhibited or proceeds at maximum speed, in contrast with the well-established concentration-dependent model of microbial substrate utilization (*9*). A more likely scenario, consistent with microbial substrate uptake kinetics, is that in the deep ocean, DOC utilization will be relatively slow, limited by molecular diffusion, with uptake systems operating well below their maximum velocity at the low end of the Monod curve. Our experimental data indicate that labile DOC was not used completely at the end of the experiment and that substantial DOC consumption occurred after no apparent increase in cell abundance was detectable (*3*). Although our experiment was designed to test the growth response of bacteria and not to estimate the total amount of labile DOC, a more realistic estimation of what happened in our experiment can be obtained by using rates of utilization rather than final concentrations.

To better illustrate these processes, we performed a simulation in which utilization was solely limited by concentration (Fig. 1A). Total consumption rates were higher with increasing concentrations; however, substrate consumption did not decrease down to the control levels after 1 year. The percentage of DOC utilized did increase with increasing concentrations, but very slowly. The total DOC utilized after 40 days equaled 2.1, 2.6, 3.7 and 5.3% of the initial concentration for controls, two-, five- and tenfold concentrated treatments (Fig. 1B), respectively—well within the range of our observations but probably not enough to allow significant statistical comparisons given the scatter associated with a 40-day incubation experiment. Hence, this simulation demonstrates that the small proportion of DOC used in our experiments is consistent with the dilution hypothesis, although complete consumption of labile substrates would take much longer, as it does in the deep ocean. Thus, the use of short-term incubation experiments to quantify the amount of labile DOC present in natural samples proposed by Jiao and colleagues leads to wrong conclusions (*8*). The corollary of the dilution hypothesis—that prokaryotic consumption is related to DOC concentration—still holds because both microbial growth and total substrate consumption markedly increased in concentrated samples as compared with controls, clearly demonstrating that concentration limited prokaryotic growth. Jiao *et al.* (*8*) argue that the growth observed in our experiments could be due to a small amount of labile DOC already detectable in the unamended controls, implicitly admitting that growth (and therefore DOC consumption) was limited by concentration, at least for this small fraction of DOC that they estimate to be 6% of the bulk concentration. Yet, consumption was detected across thousands of different compounds in both controls and concentrated samples (*3*), which probably comprise a much higher proportion of the total DOC. Thus, a large fraction of the DOC compounds (and of the bulk DOC) in our samples was neither intrinsically recalcitrant nor context-recalcitrant (there was no difference in "biogeochemical context" between treatment and controls, apart from DOC concentration), and dilution remains the mechanism that best explains our results. The fact that we detected utilization of fewer compounds in the concentrated treatment in one of the experiments does not make these molecules less labile.

Jiao *et al.* also argue that other sources of labile materials—such as chemolithoautotrophy, grazing, and viral lysis—may have played a role; however,

[1]Red Sea Research Center, Division of Biological and Environmental Sciences and Engineering, King Abdullah University of Science and Technology, Thuwal 23955-6900, Saudi Arabia. [2]Department of Global Change Research, Institut Mediterrani d'Estudis Avançats (IMEDEA), Consejo Superior de Investigaciones Científicas (CSIC)/Universidad de las Islas Baleares (UIB), 07190 Esporles, Spain. [3]Department of Limnology and Bio-Oceanography, Division Bio-Oceanography, University of Vienna, Althanstrasse 14, 1090 Vienna, Austria. [4]Department of Biological Oceanography, Royal Netherlands Institute for Sea Research (NIOZ), 1790AB Den Burg, Netherlands. [5]Research Group for Marine Geochemistry (ICBM-MPI Bridging Group), Institute for Chemistry and Biology of the Marine Environment (ICBM), Carl von Ossietzky University Oldenburg, Germany.
***Corresponding author. E-mail: jesus.arrieta@kaust.edu.sa**

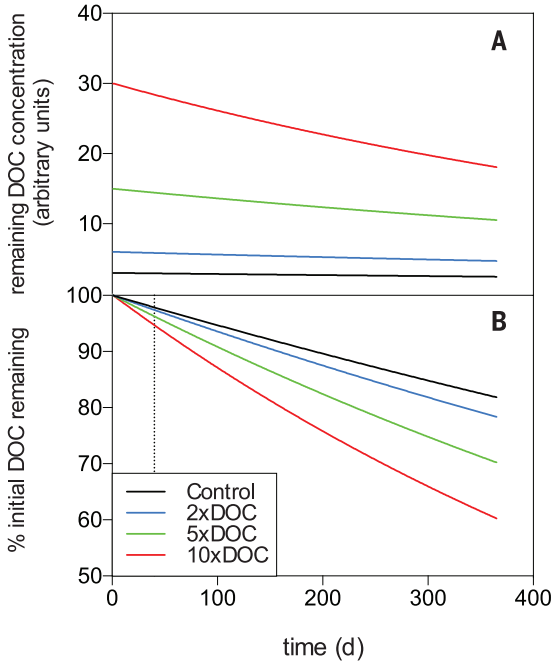

Fig. 1. Expected DOC utilization as a function of DOC enrichment in a scenario where utilization is limited by dilution. We started our simulation with three different DOC concentration levels in each sample (0.8, 1, and 1.2 arbitrary units in the control and the corresponding two-, five- and tenfold initial concentrations, respectively) for consistency with the model of Jiao *et al*. (*8*). The rate of utilization for each DOC pool was calculated as a function of substrate concentration and cell abundance, assuming a specific substrate affinity of 1×10^{-11} (L cell^{-1} day^{-1}) and using the maximum cell abundances observed in experiment N for each treatment (55, 67, 97, and 139 × 10^6 prokaryotes L^{-1} for the controls, two-, five- and tenfold DOC treatments, respectively). The average specific substrate affinity was estimated from the 2% decrease in DOC concentration observed in control treatments of experiments K to N after 40 days. Our calculated utilization rates are proportional to substrate concentration, and we have assumed one average affinity for all the substrates. Thus, our model does not change if we use one or many substrates, and therefore only bulk DOC concentrations are presented. This simplified model also assumes that all of the bacteria present were able to utilize all of the substrates present with the same average affinity and is likely to result in an overestimation of utilization rates as compared with the real world scenario involving a diverse microbial community feeding on a very diverse molecular mixture of DOC, including a large range of concentrations and affinities. Despite these limitations, this is a more realistic approach that more closely resembles the processes measured in our experiments, as well as those occurring in the deep ocean. (**A**) Bulk consumption of DOC over time. Increasing substrate concentration tenfold results in a much higher bulk consumption rate; however, labile substrates are not brought down to the initial levels after 1 year of incubation. (**B**) Percentage of substrate remaining over 1 year of incubation. At least 95% of the initial substrate remains unused after 40 days (dotted line) of microbial consumption, even in the most concentrated treatments. We assumed that utilization rates increase constantly with concentration, and this is only valid at the low end of the Monod model. If substrate concentrations reached saturation levels in the more concentrated treatments, as observed in our experiments, the differences between the percentage of utilization in concentrated versus control treatments would be even smaller.

it is unclear how chemolithoautotrophy would be enhanced by increasing DOC concentrations. Increases in grazing and viral lysis are incidentally derived from enhanced bacterial growth caused by higher DOC concentrations but are not the primary factor fueling bacterial growth.

Our results indicate that apparent recalcitrance is largely related to low substrate concentrations. Thus, deep-oceanic microbes may not be functioning as a carbon pump (*2*, *8*), transforming labile DOC into recalcitrant compounds prone to accumulate in the ocean but rather as efficient degraders of a vast array of compounds, even at very low, growth-limiting concentrations. Microbial production of persistent DOC by mechanisms other than substrate dilution remains to be demonstrated, although recent reports suggest that this contribution may be minor (*10*).

REFERENCES AND NOTES

1. D. A. Hansell, *Ann. Rev. Mar. Sci.* **5**, 421–445 (2013).
2. N. Jiao *et al*., *Nat. Rev. Microbiol.* **8**, 593–599 (2010).
3. J. M. Arrieta *et al*., *Science* **348**, 331–333 (2015).
4. H. W. Jannasch, *Limnol. Oceanogr.* **12**, 264–271 (1967).
5. N. Jiao *et al*., *Biogeosciences* **11**, 5285–5306 (2014).
6. H. Ogawa, Y. Amagai, I. Koike, K. Kaiser, R. Benner, *Science* **292**, 917–920 (2001).
7. R. L. Sinsabaugh, S. Findlay, in *Aquatic Ecosystems* (Academic Press, Burlington, MA, 2003), pp. 479–498.
8. N. Jiao *et al*., *Science* **350**, 1483 (2015).
9. J. Monod, *Annu. Rev. Microbiol.* **3**, 371–394 (1949).
10. H. Osterholz, J. Niggemann, H.-A. Giebel, M. Simon, T. Dittmar, *Nat. Commun.* **6**, 7422 (2015).

ACKNOWLEDGMENTS

This is a contribution to the MALASPINA Expedition 2010 project, funded by the CONSOLIDER-Ingenio 2010 program of the Spanish Ministry of Economy and Competitiveness (ref. CSD2008-00077).

21 June 2015; accepted 11 November 2015
10.1126/science.aac7249

Sandbags protect 3rd- to 5th-century C.E. mosaics at the Ma'arra Mosaic Museum in the Syrian city of Maarat al-Numaan.

PHOTO: PENN CULTURAL HERITAGE CENTER AT THE UNIVERSITY OF PENNSYLVANIA MUSEUM

Scientists work to save antiquities from Islamic State destruction

Western scholars and their Syrian and Iraqi colleagues are using technological tools to document and protect a vanishing cultural heritage

By **Earl Lane**

In the summers of 2009 and 2010, Katharyn Hanson was working in the Syrian city of Raqqa as a University of Chicago doctoral student in archaeology. Just down the street from her lodgings were the revered tombs of three medieval Islamic prophets. Today, those tombs have been obliterated and the ground on which they stood graded to remove all evidence of their existence.

Such targeted destruction by the Islamic State or ISIS, which occupies Raqqa as its headquarters city, is meant to both terrify the local population and rob it of its cultural heritage, said Hanson, a visiting scholar for the AAAS Geospatial Technologies Project and a postdoctoral fellow at the Cultural Heritage Center of the University of Pennsylvania Museum.

While ISIS has drawn worldwide condemnation for blowing up the temple of Baalshamin in the ancient city of Palmyra this summer and for destroying other historical sites in that city and elsewhere, such actions involve more than smashing structures the group deems idolatrous. They strike at the heart of the religious pluralism that marked Syria and Iraq for centuries, Hanson said, and erase physical manifestations of a people's history. Once lost, that cultural heritage can be irreplaceable, she said.

In a 10 November colloquium at AAAS, Hanson spoke movingly of the need to preserve and protect Syria's antiquities. For Hanson, it is a personal as well as a professional imperative. She has worked closely with Syrian and Iraqi specialists who face tremendous peril in their efforts to protect historic sites not only from the symbolic atrocities of ISIS but also the general chaos that accompanies armed conflict.

Hanson noted that cultural sites in Syria and Iraq had been threatened well before ISIS arrived on the scene. Since the 2011 beginning of the Syrian civil war, she said, troops of the Bashar al-Assad regime routinely have been embedded at cultural sites that often occupy the high ground. Iraqi troops and Shia militias have scribbled graffiti on a historic spiral minaret in Samarra, Iraq, and displaced persons have been living within fragile Byzantine ruins northwest of Aleppo, Syria.

Looting of historic sites also has been rampant, with ISIS selling permits to locals who want to engage in the practice. Iraq's U.N. ambassador has said that ISIS earns up to $100 million annually from looting and trafficking of antiquities to support its terrorism. Satellite images analyzed by AAAS have shown the extent of such looting, with some sites, such as one in Apamea, Syria, so pockmarked with pits and tunnels dug by looters that they appear as though they have been carpet-bombed.

"To an archaeologist, this is painful to see," Hanson said. The activity "rips up the stratigraphy" of the site, the crucial geological record that specialists used to date materials and provide historical context. Accustomed to working in the region as a field archaeologist, Hanson said it has been frustrating to now view some sites only via satellite photos. In the case of looting, it can

Published by AAAS

Tools to help save a culture

Satellite and drone imagery—The AAAS Geospatial Technologies Project has produced several lengthy reports documenting damage or destruction at important cultural heritage sites in Syria and Iraq, showing the scope of the problem and confirming reports from sources on the ground. The project is exploring the possibility of using aerial drones to get an even closer look at looting and other threats to critical sites. Drones have been used by other specialists in a "Follow the Pots" project to monitor looting at an Early Bronze Age cemetery in Fifa, Jordan.

A 3D reconstruction of the Iraqi Nirgul Tablet. The original artifact was destroyed by ISIS.

Time-series analyses—By analyzing multiple satellite images over time, researchers can spot physical changes in the historic structures of interest and also detect the arrival of trucks and bulldozers that could be a warning of imminent destruction to come. The method has been used to document the status and subsequent destruction of sites such as the tombs of Uwais al-Qarani, Obay ibn Qays, and Ammar ibn Yasir in the Raqqa neighborhood where Hanson lived. Time-series analysis also has been used to document the destruction of Armenian cultural artifacts in Azerbaijan between 1998 and 2005, Hanson said.

High-resolution scans—Specialists have been creating 3D reproductions of endangered, damaged, or destroyed artifacts. One effort, called Project Mosul, is collecting imagery of materials in the Mosul Museum that were destroyed by ISIS fighters in February. These cyber archaeologists are using file photographs and even videos and pictures taken by tourists to digitally reconstruct lost objects. The Mosul team also has been collecting images of historic buildings destroyed by a devastating earthquake in Nepal in April in hopes of helping to rebuild the Durbar Square area of Kathmandu.

Archival documentation—The German Archaeological Institute and the Museum of Islamic Art in Berlin have undertaken a joint effort to digitize paper records of numerous research projects conducted in Syria over the years under the auspices of the Syrian Directorate-General of Antiquities and Museums. Such documentation is essential to protect important archival data and to help experts better evaluate the current status of Syria's imperiled cultural heritage.

be nearly impossible, she said, to determine from overhead images just what artifacts have been stolen or damaged.

Still, Hanson and other western specialists have remained very much engaged with the region and their Iraqi and Syrian colleagues. They are using scientific methods and technological tools to document and better understand the ongoing loss of cultural heritage and prevent further destruction if possible. Hanson traveled to Erbil, Iraq, twice this year to conduct training sessions for local antiquities specialists, helping to update them on methods to do site assessment and risk management for artifacts under threat. "There are some incredible conservation efforts being done quietly" in the region, Hanson said.

The Safeguarding the Heritage of Syria and Iraq (SHOSI) Project—a collaborative effort by AAAS, the University of Pennsylvania, the Smithsonian Institution, The Day After Association (a Syrian-led civil society group), and others—stabilized an ancient wall mosaic at the Ma'arra Museum outside Aleppo and placed sandbags in front of it for protection. When the museum was bombed in June, allegedly by the Assad regime, the mosaic survived.

Beyond efforts to document the status of endangered sites, Hanson said, there is a critical need to restrict the illicit trade in antiquities from Syria and Iraq. That was one focus of a 28 October panel discussion on Capitol Hill, organized by the University of Pennsylvania Museum in conjunction with AAAS, the Smithsonian Institution, and the U.S. Committee of the Blue Shield, a nonprofit organization committed to the protection of cultural property worldwide during armed conflict.

Speakers at the event, hosted by Sen. Bob Casey (D–PA), called for the Senate to pass a bill, cosponsored by Casey and already approved in the House, to impose restrictions on the import of illicit Syrian artifacts.

"In Syria, cultural heritage is part of everyday life," said Salam Al Kuntar, former deputy director of Syria's Department of Excavation and Archaeological Research. "It's not something that belongs to the past." Emphasizing the ongoing importance of sites that have been destroyed or looted by the Islamic State group, she noted that these "living historical landscapes" are "embedded in our identities as Syrians and Iraqis." ■

(Andrea Korte contributed to this story.)

AAAS 2016 ANNUAL MEETING
GLOBAL SCIENCE ENGAGEMENT
FEBRUARY 11-15 · WASHINGTON, DC

Science is a global endeavor—from the challenges that it seeks to solve to the partners who come together to meet these challenges. Today's researchers, entrepreneurs, educators, and policy-makers must work across national boundaries to address food and water security, infectious disease and health, climate change, and energy issues. In February 2016, thousands of scientists, engineers, and others will convene in Washington, D.C., to discuss their successes, goals, and expectations in international scientific collaboration. Visit the 2016 Annual Meeting website at **meetings.aaas.org** to see the full program of scientific symposia, lectures, career workshops, and free public events like Family Science Days.

PHOTO: PROJECTMOSUL.ORG

Published by AAAS

RESEARCH

The making of two-dimensional boron sheets

Mannix et al., *p. 1513*

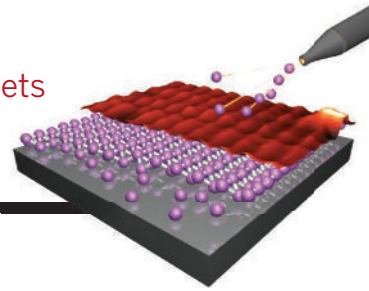

IN *SCIENCE* JOURNALS

Edited by **Stella Hurtley**

Large frugivores, like these Seychelles flying foxes, are important for tropical forest carbon storage

TROPICAL ECOSYSTEMS

Faunal loss reduces tropical forest carbon

Losing large fruit-eating animals from tropical forests disproportionally affects carbon stocks. Bello *et al.* modeled the loss of carbon associated with large tropical trees that depend on large vertebrates for seed dispersal and regeneration. As well as reducing deforestation and promoting reforestation, key ecological interactions need to be taken into account to achieve full tropical forest carbon storage. — TEL

Sci. Adv. 10.1126. sciadv.1501105 (2015).

MARINE CALCIFERS

Passing an acid test

Calcifying marine organisms will generally find it harder to make and maintain their carbonate skeletons as increasing concentrations of atmospheric CO_2 acidify the oceans. Nevertheless, some types of organisms will be damaged more than others, and some may even benefit from higher CO_2 levels. Coccolithophores are a case in point, because their photosynthetic ability is strongly carbon-limited. Rivero-Calle *et al*. show that the abundance of coccolithophores in the North Atlantic has increased by up to 20% or more in the past 50 years (see the Perspective by Vogt). Thus, this major phytoplankton functional group may be able to adapt to a future with higher CO_2 concentrations. — HJS

Science, this issue p. 1533; see also p. 1466

GRAFT REJECTION

Friendly fire from organ failure

These days organ transplantation may seem like a routine procedure, but rejection of the donated organ still poses a substantial risk. Autoantibodies contribute to rejection, but how these autoantibodies are generated remains unclear. Dieudé *et al.* found that exosome-like vesicles derived from apoptotic endothelial cells stimulated autoantibody production in mice, which increased graft rejection. These vesicles contained active 20S proteasome core complexes; proteasome inhibition decreased both vesicle immunogenicity and graft rejection in transplanted mice. Circulating exosome-like vesicles and increased anti-autoantibody titers were also observed in mouse models of vascular injury, suggesting that the same organ failure that necessitates the transplant might increase the risk of rejection. — ACC

Sci. Transl. Med. **7**, 318ra200 (2015).

ENERGY STORAGE

Store more energy with a touch of nitrogen

In contrast to batteries, capacitors typically can store less power, but they can capture and release that power much more quickly. Lin *et al*. fabricated a porous carbon material that was then doped with nitrogen. This raised the energy density of the carbon more than threefold—an increase that was retained in full capacitors, without losing their ability to deliver power quickly. — MSL

Science, this issue p. 1508

ULTRAFAST DYNAMICS

The making of a molecular movie

Phase transitions familiar from everyday life, such as boiling or melting, are caused by changing the temperature. In the laboratory, however, researchers can also change the phase of a material by shining intense light on it. During such transitions,

PHOTO: © BLICKWINKEL/ALAMY STOCK PHOTO

Published by AAAS

changes occur in both the electronic and lattice structure of the material. Ishikawa *et al*. used ultrafast optical and electron diffraction probes to monitor both types of change simultaneously during a photo-induced phase transition in a molecular crystal. The resulting molecular movies showed expansion of the intermolecular distance, flattening of the molecules, and tilting of molecular dimers. — JS

Science, this issue p. 1501

GENOMIC EVOLUTION

Cichlids diverge within a crater lake

It is not clear how populations diversify and new species form at the genomic level, especially when they coexist in the same location. Malinsky *et al*. investigated how two ecomorphs of cichlid fish in a small lake in Tanzania are diversifying relative to each other. Although there is gene flow between the two forms, major regions of genetic divergence, known as genomic islands, separate the populations. Within these islands, the authors found genes likely to be associated with mate choice, supporting the idea that genetic changes related to breeding preferences are the first to diverge during speciation. — LMZ

Science, this issue p. 1493

Astatotilapia calliptera – a cichlid fish

NEURODEVELOPMENT

The makings of motor neuron disease

Developing motor neurons link the muscles to the central nervous system. Amin *et al*. found that microRNA-218 (miR-218) was expressed in developing motor neurons and repressed a wide network of genes whose expression typifies other sorts of neurons. Mice lacking miR-218 died at birth with symptoms characteristic of human motor neuron diseases. — PJH

Science, this issue p. 1525

ECOTOXICOLOGY

Red tides make dinner hard to find

Domoic acid (DA) is a neurotoxin produced by marine algae. When present in large amounts, it is harmful to marine organisms and to humans. Cook *et al*. tested California sea lions being treated at a marine mammal rescue facility. Animals that had evidence of exposure to DA had lesions in their hippocampus and displayed reduced performance on spatial memory tasks. Because such tasks are essential to foraging in a marine environment, increasing exposure to DA may be contributing to increasing sea lion strandings. — SNV

Science, this issue p. 1545

MEMBRANE REMODELING

ESCRTs work in two very different ways

The so-called ESCRT proteins are involved in the budding of vesicles into the lumen of endosomes and in virus budding. These reactions involve the formation of a cytoplasm-filled neck that spirals of the ESCRTs help to seal. McCullough *et al*. now show that ESCRTs can also promote the scission of membrane tubules with the completely opposite topology. ESCRT-III and IST1 ESCRT subunits form spirals on the outside of membrane tubules and so can mediate the budding of tubules and vesicles into the cytosol. Relatively minor structural rearrangements were required to turn ESCRT function on its head. — SMH

Science, this issue p. 1548

IN OTHER JOURNALS

Edited by **Sacha Vignieri** *and* **Jesse Smith**

A 2011 tornado in Nebraska

CELL MIGRATION

Moving forward by localized translation

Proper development and morphogenesis requires many cells to coordinate movements that are influenced by local forces, or from the migration of cells under their own power. In mesenchymal cell migration, actin filaments at the front push the cell forward while the back portion is retracted. By comparing mRNA localization and translation rate in the forward-located protrusions relative to trailing section, Mardakheh *et al*. identify the mechanism by which front-back cell asymmetry is maintained. Protein translation in the front of the cell is critical to stabilize the protrusion and produce the cell's polarized morphology. Analyses reveal specific cis-regulatory mRNA UTR motifs and RNA-binding proteins, such as the exosome core complex, as important for cell migration asymmetry. – BAP

Dev. Cell. **35**, 344 (2015).

PLANETARY SCIENCE

What counts as a planet?

In 2006, the International Astronomical Union formally defined the term "planet" in such a way that bodies such as Pluto, Ceres, and Eris do not qualify. The definition was controversial, partly because the criteria are somewhat subjective and cannot be directly applied to planets around other stars (exoplanets). Margot has proposed an alternative objective mathematical definition of a planet. Within our solar system, the calculation clearly separates the eight planets from all other bodies. It can also be calculated from data that are already available for 99% of known exoplanets. It remains to be seen whether the new metric will catch on. — KTS

Astron. J. arXiv:1507.06300 (2015).

POLITICAL SCIENCE

Predicting protests via tweets

Although many investigations have attempted to link the use

PHOTOS (LEFT TO RIGHT) KEVIN BAUMAN; © MIKE HOLLINGSHEAD/CORBIS

Published by AAAS

PHOTO: EYE OF SCIENCE/SCIENCE SOURCE

TORNADO FORECASTING

Gaining momentum for anticipating storms

Tornados cause many deaths and costly damage to property every year, so being able to predict them farther in advance could save both human lives and money. Gensini and Marinaro show that that tornadoes are more likely to occur when the base state of atmospheric angular momentum is low and less likely to occur when it is high. Differences in atmospheric angular momentum, expressed as the global wind oscillation, can explain nearly an order of magnitude of variability in boreal spring tornado occurrence in the United States during the period from 1994 to 2013. This observation thereby suggests a pathway to better springtime tornado forecasting. — HJS

Mon. Weather Rev. 10.1175/MWR-D-15-0289.1 (2015).

of social media with protests, they have usually been based on events occurring in one country. Steinert-Threlkeld *et al.* collected nearly 14 million tweets and protest records from 16 countries in the Middle East and North Africa from 1 November 2010, through 31 December 2011, which includes the period of the Arab Spring protests. They studied the coordination of tweets (i.e., the progressive use of smaller numbers of protest-related hashtags by multiple users) and found that increased coordination was strongly associated with increased protests the next day. This was not the result of a few highly tweeted events or a few digital activists or international attempts to draw attention to the events. — BJ

EPJ Data Sci. 10.1140/epjds/s13688-015-0056-y (2015).

LIPID BIOCHEMISTRY

A parasite's phospholipid

The phospholipid repertoire used in animal cell membranes is surprisingly limited, but another candidate has emerged. During investigations on virulence in the ubiquitous animal and human protist parasite *Toxoplasma gondii*, Arroyo-Olarte *et al.* identified phosphatidylthreonine (PtdThr) as an abundant constituent. A small evolutionary accident seems to have allowed *T. gondii* to become parasitic by shifting from phosphatidylserine- to phosphatidylthreonine-based membranes. Although mutant parasites lacking PtdThr can replicate, they are paralyzed and neither able to enter nor exit host cells. PtdThr mutants provoke strong immune responses and look promising as vaccine candidates. Because the synthetic enzyme PtdThr synthase was also characterized, there is scope for drug interventions too. — CA

PLOS Biol. 10.1371/journal.pbio.1002288 (2015).

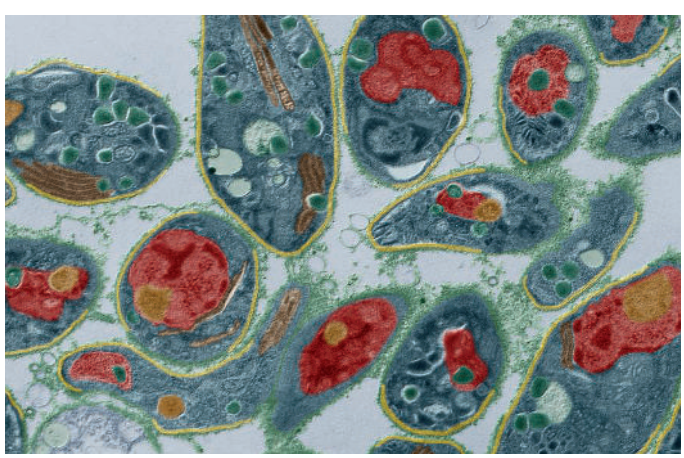

Evolution of a new phospholid led *Toxoplasma gondii* to parasitism

PSYCHOLOGY

Reading minds across the ocean

Natives of different cultures often have trouble figuring out what the other believes—a sought-after experience for the traveler visiting faraway lands, yet a hindrance for the immigrant adjusting to her new environment. Perez-Zapata *et al.* identify a high-level contributory factor by presenting social and cognitive scenarios to Australians (in English) and to Chileans (in Spanish). The cognitive scenarios depicting activities involving either Australians or Chileans were understood equally well by natives of both countries. In contrast, Australians more accurately inferred what one Australian believed about another Australian in comparison to a conversation between two Chileans; likewise, Chileans found it easier to read the minds of other Chileans. — GJC

Cognition **146**, 410 (2016).

POLICY EXPERIMENT

Cashing in on clean air

Exposure to air pollution early in life could undermine earnings as an adult. Isen *et al.* studied 5.7 million people born in hundreds of counties across the United States, within a few years before and after those counties reduced ambient levels of total suspended particulates (TSPs) under the Clean Air Act (CAA) in the early 1970s. U.S. Census Bureau data were used to link date and location of birth with labor market outcomes decades later. Although those born 1 to 3 years before the CAA improvements still enjoyed cleaner air beginning at ages one to three, they were exposed to more pollutants from conception until age one. Compared to them, those born after the CAA induced a 10% decline in TSP levels earned roughly 1% more at age 30, possibly due to improved cognitive ability and health. — BW

J. Polit. Econ., http://faculty.haas.berkeley.edu/rwalker/research/caalongtermhealth.pdf (2015).

Published by AAAS

ALSO IN *SCIENCE* JOURNALS

Edited by **Stella Hurtley**

NANOMATERIALS

Borophene: Boron in two dimensions

Although bulk allotropes of carbon and boron differ greatly, small clusters of these elements show remarkable similarities. Boron analogs of two-dimensional carbon allotropes such as graphene have been predicted. Now Mannix *et al*. report the formation of two-dimensional boron by depositing the elemental boron onto a silver surface under ultrahigh-vacuum conditions (see the Perspective by Sachdev). The graphene-like structure was buckled, weakly bonded to the substrate, and metallic. — PDS

Science, this issue p. 1513; see also p. 1468

ELECTRON MICROSCOPY

Advances in seeing small things

Electron microscopes, particularly those with aberration correction, can view materials at the subnanometer scale. Additional improvements make it possible to obtain images at lower electron doses, thus minimizing the damage to the sample. However, for a number of materials, particularly those of biological origin, samples need to be imaged in solution. Ross reviews recent advances that have made it possible to do liquid cell electron microscopy, which opens up the possibility of studying problems such as the changes inside a battery during operation, the growth of crystals from solution, or biological molecules in their native state. — MSL

Science, this issue p. 1490

STRUCTURAL BIOLOGY

A channel involved in pain perception

Voltage-gated sodium (Nav) channels propagate electrical signals in muscle cells and neurons. In humans, Nav1.7 plays a key role in pain perception. It is challenging to target a particular Nav isoform; however, arylsulfonamide antagonists selective for Nav1.7 have been reported recently. Ahuja *et al*. characterized the binding of these small molecules to human Nav channels. To further investigate the mechanism, they engineered a bacterial Nav channel to contain features of the Nav1.7 voltage-sensing domain that is targeted by the antagonist and determined the crystal structure of the chimera bound to an inhibitor. The structure gives insight into the mechanism of voltage sensing and will enable the design of more-selective Nav channel antagonists. — VV

Science, this issue p. 1491

INFLAMMATION

Limiting inflammation in obesity

Obese individuals have increased circulating levels of inflammatory cytokines produced by adipose tissue macrophages. Velmurugan *et al*. found that adipose tissue macrophages from obese mice had decreased levels of the gasotransmitter H_2S, increased calcium signaling, and increased production of proinflammatory cytokines. H_2S inhibited a calcium channel, which resulted in reduced calcium entry into macrophages. Thus, inflammatory stimuli lead to the depletion of H_2S in adipose tissue, which exacerbates inflammatory responses by resident adipose tissue macrophages. — JFF

Sci. Signal. **8**, ra128 (2015).

STRUCTURAL BIOLOGY

A complex channel comes into focus

Voltage-gated calcium (Cav) channels are activated in response to membrane potential to initiate calcium-mediated signaling pathways and are associated with diseases such as cardiac arrhythmia and epilepsy. Cav1.1 couples changes in membrane potential to cardiac muscle contraction. It comprises a core subunit and three auxiliary subunits. Wu *et al*. isolated the Cav1.1 complex from rabbit skeletal muscle and determined its structure by single-particle electron cryomicroscopy using direct electron detection and advanced image processing. The detailed architecture of the pseudotetrameric eukaryotic Cav channel in complex with its auxiliary subunits provides an important framework for understanding the function and disease mechanisms of related channels. — VV

Science, this issue p. 1492

PLANT SYMBIOSES

Early stages of a beneficial relationship

Plants benefit from widespread symbiosis with arbuscular mycorrhizal fungi. This symbiosis between plant and fungus aids plants in capturing mineral and micronutrients from the soil. Gutjahr *et al*. have now identified a component of an intracellular receptor, the hydrolase DWARF 14 LIKE, required in rice roots for initiating the symbiosis. A similar receptor detects karrikins in smoke that signal opportunity for fireweed to grow after a forest fire. — PJH

Science, this issue p. 1521

QUANTUM SIMULATION

Simulating electronic transport with atoms

Two superconductors connected by a bridge made out of nonsuperconducting material form a so-called Josephson junction (see the Perspective by Belzig). Valtolina *et al*. replaced the superconductors with two reservoirs of a superfluid Fermi gas and connected them by a weak link to allow atoms to move from one side to the other. Then they made one reservoir more populated than the other and studied the ensuing dynamics as a function of interaction strength between the atoms. In a related experiment, Husmann *et al*. kept the interaction strength at its maximum, but varied the temperature and the properties of the link. As temperature increased, the superfluid disappeared and thermal transport took over. — JS

Science, this issue p. 1495, p. 1505; see also p. 1407

BATTERIES

Peering into cathode layered oxides

The quest for better rechargeable batteries means finding ways to pack more energy into a smaller mass or volume. Lithium layered oxides are a promising class of materials that could double storage capacities. However, the design of safe and long-lasting batteries requires an understanding of the physical and chemical changes that occur during redox processes. McCalla *et al*. used a combination of experiments and calculations to understand the formation of O-O dimers, which are key to improving the properties of these cathode materials. — MSL

Science, this issue p. 1516

PHYTOPLANKTON

Community changes centuries in the making

How might climate change affect the base of the marine food chain? Phytoplankton, the foundation of the marine ecosystem, depend on ambient oceanographic conditions such as temperature, salinity, and nutrient availability, which affect ocean chemistry and isotopic distributions. McMahon *et al*. report carbon isotopic composition changes in the North Pacific Ocean over the past 1000 years,

Published by AAAS

which reflect changes in the community composition of phytoplankton in the region (see the Perspective by Vogt). An ongoing trend toward greater prevalence of nitrogen-fixing cyanobacteria that began 100 years ago might lead to a more efficient carbon pump and remove increasing amounts of CO_2 from the atmosphere. — HJS

Science, this issue p. 1530; see also p. 1466

PALEOCEANOGRAPHY

East joins West to complete a picture

How have eastern equatorial Pacific sea surface temperatures varied over the past 1000 years? Today, the tropical Pacific Ocean has a large influence on global climate, through processes such as El Niño. Researchers would thus like to know how the ocean varied in the past. Although good records exist from the western ocean, the same has not been true for the eastern side. Rustic *et al*. analyzed marine sediments recovered from near the Galapagos Islands. They conclude that the tropical Pacific Ocean changed state about 500 years ago, near the transition between the warm Medieval Climate Anomaly and the cold Little Ice Age. — HJS

Science, this issue p. 1537

MICROBIAL METABOLISM

Sulfate reduction via a trisulfide

Microorganisms can respire sulfur compounds in the absence of oxygen, eventually leading to the production of hydrogen sulfide. This ancient metabolism is common in modern anoxic environments, but the enzymatic pathways aren't yet fully resolved. Through in vivo and in vitro experiments, Santos *et al*. clarify the enzymology of the sulfate reduction pathway in both bacteria and archaea (see the Perspective by Fritz and Kroneck). Reduction of the sulfite intermediate results in the linkage of two cysteine residues to a third sulfur atom from sulfite, forming a trisulfide product. Because the reduction of sulfite conveys a strong isotopic signature on sulfur in the environment, isotope fractionation models should account for this additional step. — NW

Science, this issue p. 1541; see also p. 1476

EVOLUTIONARY GENETICS

Essential genes and species incompatibilities

Crosses between two fruit fly species, *Drosophila melanogaster* and *D. simulans*, result in hybrid progeny that are all female. Although some of the genes responsible for this species barrier are known, the full complement of molecular determinants that lead to inviable males has remained mysterious. Phadnis *et al.* used mutagenesis and a sequencing-based genomic screen to link hybrid inviability to the cell cycle. The inviable males result from an interaction between three genes, one of which is essential, which precluded its identification with standard genetic screens. This strategy to identify speciation genes can be applied to other model and nonmodel systems. — LMZ

Science, this issue p. 1552

Published by AAAS

REVIEW SUMMARY

ELECTRON MICROSCOPY

Opportunities and challenges in liquid cell electron microscopy

Frances M. Ross

BACKGROUND: Transmission electron microscopy offers structural and compositional information with atomic resolution, but its use is restricted to thin, solid samples. Liquid samples, particularly those involving water, have been challenging because of the need to form a thin liquid layer that is stable within the microscope vacuum. Liquid cell electron microscopy is a developing technique that allows us to apply the powerful capabilities of the electron microscope to the imaging and analysis of liquid specimens. We can examine liquid-based processes in materials science and physics that are traditionally inaccessible to electron microscopy, and image biological structures at high resolution without the need for freezing or drying. The changes that occur inside batteries during operation, the attachment of atoms during the self-assembly of nanocrystals, and the structures of biological materials in liquid water are examples in which a microscopic view is providing unique insights.

ADVANCES: The difficulty of imaging water and other liquids was recognized from the earliest times in the development of transmission electron microscopy. Achieving a practical solution, however, required the use of modern microfabrication techniques to build liquid cells with thin but strong windows. Usually made of silicon nitride on a silicon support, these liquid cells perform two jobs: They separate the liquid from the microscope vacuum while also confining it into a layer that is thin enough for imaging with transmitted electrons. Additional functionality such as liquid flow, electrodes, or heating can be incorporated in the liquid cell. The first experiments to make use of modern liquid cells provided information on electrochemical deposition, nanomaterials synthesis, diffusion in liquids, and the structure of biological assemblies. Materials and processes now under study include corrosion, biomolecular structure, bubble dynamics, radiation effects, and biomineralization. New window materials such as graphene can improve resolution, and elemental analysis is possible by measuring energy loss or x-ray signals. Advances in electron optics and detectors, and the correlation of liquid cell microscopy data with probes such as fluorescence, have increased the range of information available from the sample. Because the equipment is not too expensive and works in existing electron microscopes, liquid cell microscopy programs have developed around the world.

ON OUR WEB SITE

Read the full article at http://dx.doi.org/10.1126/science.aaa9886

OUTLOOK: Liquid cell electron microscopy is well positioned to explore new frontiers in electrochemistry and catalysis, nanomaterial growth, fluid physics, diffusion, radiation physics, geological and environmental processes involving clays and aerosols, complex biomaterials and polymers, and biological functions in aqueous environments. Continuing improvements in equipment and technique will allow materials and processes to be studied under different stimuli—for example, in extreme temperatures, during gas/liquid mixing, or in magnetic or electric fields. Correlative approaches that combine liquid cell electron microscopy with light microscope or synchrotron data promise a deeper study of chemical, electrochemical, and photochemical reactions; analytical electron microscopy will provide details of composition and chemical bonding in water; high-speed and aberration-corrected imaging extend the scales of the phenomena that can be examined. As liquid cell microscopy becomes more capable and quantitative, it promises the potential to extend into new areas, adopt advanced imaging modes such as holography, and perhaps even solve grand challenge problems such as the structure of the electrochemical double layer or molecular movements during biological processes. ■

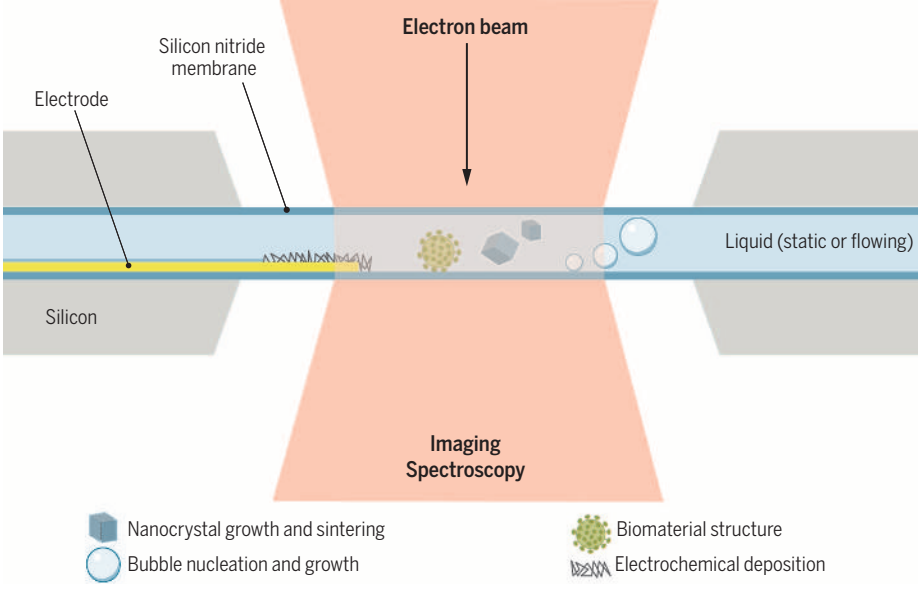

Schematic diagram of a liquid cell for the transmission electron microscope and its application for imaging phenomena in materials science, life science, and physics. The liquid cell is made from two vacuum-tight electron transparent membranes. In this diagram the membranes are made of silicon nitride (blue) on a silicon support (gray), although other materials are possible. A spacer layer (not shown) keeps the membranes at a controlled separation of about 100 nm to 1 μm. The cell is filled with the liquid of interest, and the liquid may be flowed using an external pump (not shown). The electron beam (pink) passes through the membranes and liquid to allow recording of images, movies, or spectroscopic data for compositional analysis. Several possible experiments are illustrated: growth of nanocrystals in solution, nucleation and growth of bubbles, imaging biological structures such as viruses in liquid water, and imaging electrochemical processes at an electrode (yellow) that is built into the liquid cell. The dimensions of the electron beam and the nanoscale objects are exaggerated for clarity.

The list of author affiliations is available in the full article online.
*Corresponding author. E-mail: fmross@us.ibm.com
Cite this article as F. M. Ross, *Science* 350, aaa9886 (2015). DOI: 10.1126/science.aaa9886

REVIEW

ELECTRON MICROSCOPY

Opportunities and challenges in liquid cell electron microscopy

Frances M. Ross

Transmission electron microscopy offers structural and compositional information with atomic resolution, but its use is restricted to thin, solid samples. Liquid samples, particularly those involving water, have been challenging because of the need to form a thin liquid layer that is stable within the microscope vacuum. Liquid cell electron microscopy is a developing technique that allows us to apply the powerful capabilities of the electron microscope to imaging and analysis of liquid specimens. We describe its impact in materials science and biology. We discuss how its applications have expanded via improvements in equipment and experimental techniques, enabling new capabilities and stimuli for samples in liquids, and offering the potential to solve grand challenge problems.

Transmission electron microscopy (TEM) is a constantly evolving characterization technique that offers atomic-level information on the structure and chemical composition of materials. In materials design, TEM plays a central role by helping to establish structure-property relationships and defect structures. In biology, it provides high-resolution information on biological cells and their components. In physics, time-resolved imaging can probe processes such as phase transformations and directly correlate a material's response to an applied stimulus. TEM is carried out using samples that are stable in the vacuum environment of the microscope and thin enough (e.g., below 100 nm) to give reasonable resolution in images formed by transmitted electrons. However, these requirements have meant that TEM is generally incompatible with liquids, particularly those such as water that have a high vapor pressure.

We describe here a development in TEM that provides the ability to image samples that contain liquids, most importantly water. The difficulty of imaging liquids lies in separating the liquid from the microscope vacuum while achieving a controlled liquid geometry that is thin enough for reasonable image resolution. The solution was understood early on in the development of electron microscopy, but the goal was achieved only when modern microfabrication techniques were used to build thin windows of silicon nitride with a controlled submicrometer separation, between which the liquid could be confined (*1*). This "closed" liquid cell was rapidly developed to include electrodes and flow capabilities and interfaced to the microscope with dedicated sample holders.

The first experiments to make use of these modern liquid cell designs addressed questions in electrochemical deposition, nanomaterials synthesis, diffusion in liquids, and the structure of biological assemblies. The results, reviewed in (*1*), demonstrated the ability of the liquid cell to probe areas that had traditionally been inaccessible to electron microscopy, and in doing so to achieve useful and unique information. The scope of liquid cell electron microscopy has increased rapidly (*2*, *3*). Materials and processes now under study include corrosion, biomolecular structure and dynamics, bubble motion, radiation effects, and biomineralization. Beyond straightforward imaging modes, it is possible to carry out elemental analysis through energy loss or x-ray signals. Advances in electron optics and detectors are now being applied to reduce the electron dose needed and improve the resolution of the images. Finally, correlative techniques, in which electron microscopy signals are combined with other probes such as fluorescence microscopy or synchrotrons, are starting to examine the relationship between function and structural, chemical, and electronic properties. Because processes and structures in liquids are important over such a broad set of scientific and technological areas, the ability to apply the powerful capabilities of TEM to liquid samples promises exciting possibilities for solving grand challenges in materials science, self-assembly, electrochemistry, geology, biology, physics of fluids, and other fields.

The rapidly developing liquid cell microscopy technique

The early pioneers of transmission electron microscopy were interested in imaging water for both materials science and biological applications and made remarkable progress, given the challenges of observing even solid samples with the microscopes of the time (*4*, *5*). Two techniques were developed for getting water into the electron microscope while still maintaining a good enough vacuum to operate the electron source. Both are in use today. One approach (*6*) is to use differential pumping to enable a high enough pressure at the sample region to allow water droplets to condense. This "open cell" approach became highly successful in environmental scanning electron microscopy (ESEM) (*7*, *8*). The TEM community appeared less interested in open cells for water, perhaps because the droplet geometry was not controlled and the maximum pressure was limited. However, liquid droplets in open cells have recently regained popularity in TEM (*9*) for electrochemistry involving low vapor pressure ionic liquids, driven by a need to understand materials transformations during Li-ion battery operation (*10*, *11*).

The second approach is closed-cell electron microscopy (*12*, *13*) (Fig. 1A). Enclosing water between two electron transparent windows circumvented the limited maximum pressure of the open cell (*5*), but the resolution was reduced by the thick windows used—nitrocellulose (collodion) was the best material available—and it was difficult to control the window separation. The recent surge of interest in liquid cell microscopy can be attributed to the relative ease of building closed liquid cells using modern microfabrication techniques. The initial liquid cells were homemade, somewhat unreliable, and sealed the liquid hermetically with glue (*14*), but closed liquid cells and the associated TEM equipment are now simpler to use and available commercially.

Almost all microfabricated liquid cells use silicon nitride as the window material. To fabricate windows that are electron transparent yet can withstand the 1-atm pressure difference between the cell interior and the microscope vacuum, a thin film of silicon nitride is deposited onto a silicon wafer and the silicon is etched from the back to form windows with dimensions around 100 μm. The wafer is diced into chips, each containing a window; two such chips are placed face to face, with a spacer material between. This confines the liquid within a thin layer, forming the basic overall design for most closed liquid cells.

To complete the liquid cell (*1*), the chips may be glued, wafer-bonded, or squeezed by clamping in the holder using small o-rings. The spacer may be a solid layer with a channel, or spherical particles. The liquid may be inserted through an entry port etched into one chip (*14*–*18*) or flowed in through the gap between the chips (*19*). Electrodes can be patterned lithographically inside the closed cell and controlled by an external potentiostat (*14*). In each design, the electrode materials and geometry can be customized for the particular applications (*14*, *16*, *18*, *20*–*22*). A heating element (*23*) or cooling capability (*24*) can be integrated, and the silicon nitride surfaces can be patterned or chemically modified to enable reactions with species in solution (*25*–*28*). Careful assembly procedures and cleaning are necessary (*29*). The sample holder is a key part of the liquid cell experiment, and its function extends beyond simply holding the cell securely. It carries the electrical connections between electrode or heater elements and their external controllers. In many designs, it also

IBM T. J. Watson Research Center, 1101 Kitchawan Road, Yorktown Heights, NY 10598, USA.
E-mail: fmross@us.ibm.com

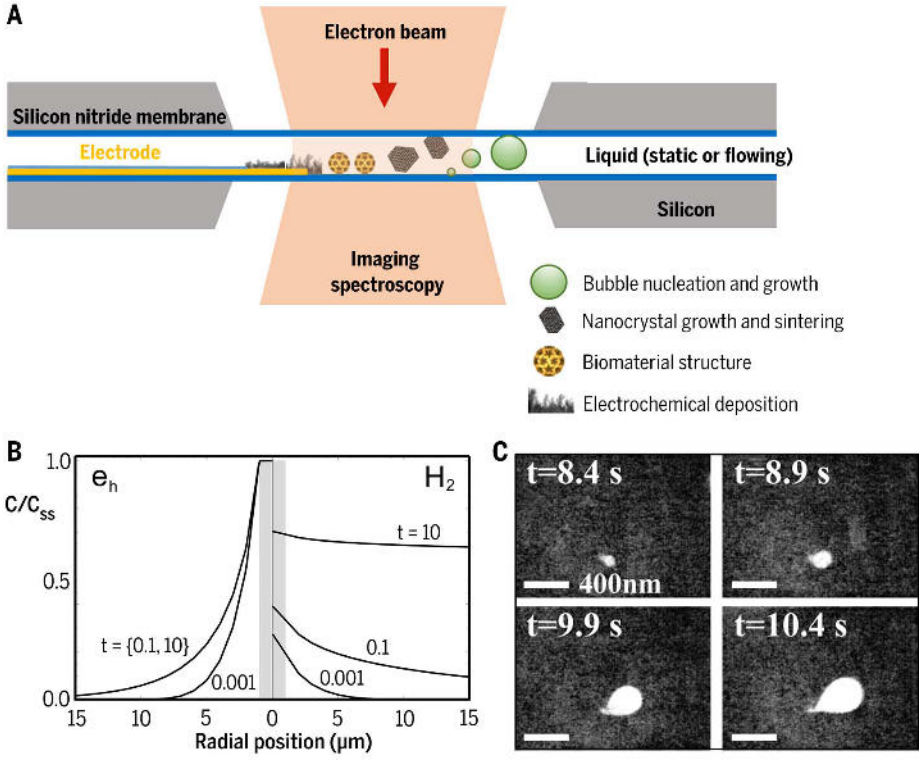

Fig. 1. The liquid cell microscopy technique. (**A**) Schematic diagram of the liquid cell and its application for imaging phenomena in materials science, life science, and physics. The dimensions of the electron beam and the nanoscale objects are exaggerated for clarity. (**B**) The predicted concentration due to radiolysis, C, normalized by the steady-state concentration C_{SS} of H_2 (right) and hydrated electrons e_h (left) in and around an irradiated area of radius 1 μm (gray stripe) as a function of distance from the beam center at various times in seconds. (**C**) Image series showing heterogeneous nucleation, growth, detachment, and migration of radiolytic hydrogen bubbles formed during TEM imaging at 300 keV, beam current < 1 nA and beam radius ~2 μm. Relative times are shown in seconds. [(B) and (C) adapted with permission from (*39*) Copyright 2014, American Chemical Society]

provides the vacuum seal by clamping the chips and supplies the liquid through inlet and outlet tubes driven by a syringe pump. Flow enables exciting possibilities of replenishing or changing the solution chemistry while imaging (*15*, *19*, *30*).

One of the key ongoing developments in closed liquid cell microscopy is the use of a wider range of TEM capabilities. Initially, liquid cell data was recorded using conventional bright-field TEM or high-angle annular dark-field (HAADF) scanning TEM (STEM) imaging modes. The main decision was whether to record single images, often appropriate for imaging biological structures, or movies of dynamic materials processes, at 30 images per second or whatever the dose rate permits. A wider range of microscopy modes is now common, including dark-field and high-resolution TEM and aberration-corrected imaging (*31*, *32*). Analytical microscopy, both electron energy-loss spectroscopy (EELS) (*32*, *33*) and x-ray energy dispersive spectroscopy (XEDS) (*34*), is also being applied in liquid cell experiments.

There are two main limitations of liquid cell electron microscopy, image resolution and electron beam effects. Low image resolution is an obvious problem in many liquid cell experiments. Resolution is lost through multiple scattering of the electrons in both the liquid layer and the window material. The liquid layer is usually thicker than desired, especially toward the center of the window, because the windows bulge outward due to the pressure difference between the interior of the cell and the microscope vacuum. To control the deflection, one can fabricate long thin windows or narrow channels (*17*); join the windows with posts (*16*); or use thicker, stiffer membranes with small thin regions for imaging (*35*). Reducing window separation improves resolution, but we can not decrease the liquid thickness arbitrarily and still expect the liquid cell experiment to be a faithful representation of a "real" phenomenon (*9*). For example, Brownian motion may differ in ultrathin liquid layers as we discuss below. In electrochemical growth, where diffusion gradients control the kinetics of processes such as deposition, thin liquid layers, may produce results that are different from bulk, making it necessary to calculate the effects of the limited volume (*36*).

On the other hand, reducing the window thickness improves image quality without affecting the physics of the process under study. The thinnest window material is graphene. High-resolution images can be obtained through liquid droplets that are placed on a supported graphene membrane, then encapsulated by a second membrane placed on top (*37*). By using graphene to cover channels in a thicker material, more complex graphene liquid cell designs can be developed (*38*).

The second major limitation of liquid cell microscopy is the effect of the electron beam. At the energies used in electron microscopy, the beam causes radiolysis of liquids, including water (Fig. 1, B and C). For the conditions appropriate to TEM, calculations show that within seconds, radiolysis products reach equilibrium concentrations in the irradiated region (*39*, *40*) (Fig. 1B). These concentrations depend on dose rate, illuminated area, liquid thickness, and total liquid volume, and can affect the structure or process under study. Radiolytically produced hydrogen gas can exceed its solubility limit and form bubbles (*39*) (Fig. 1C), which alter the liquid geometry. Hydrogen ions can change the solution pH (*40*). The highly reactive hydrated (or solvated) electron can drive beam-induced growth of metallic nanoparticles by reducing metallic cations in aqueous salt solutions (*41*), allowing possibilities for beam writing (*39*, *42*). In combination, radiolytic species can have complex effects (*40*).

Much work needs to be done to understand electron-beam effects in solutions with multiple dissolved species, as well as in nonaqueous solutions such as ionic liquids. However, existing knowledge of radiation physics can be a guide, and it has already been shown that electron-beam effects can be mitigated with scavenging strategies (*43*). As microscopists become increasingly familiar with beam effects in liquids, the low-dose techniques developed for biological cryo-electron microscopy are becoming standard, and the benefits of high-sensitivity detectors in reducing the dose required per image are being exploited.

Liquid cell microscopy for materials science, life science, and beyond

Modern microfabricated liquid cells were first used for electrochemical experiments, recording movies of metal deposition onto electrode surfaces and correlating the images with electrochemical parameters, voltage and current (*14*, *36*, *44*, *45*). The synthesis of nanoparticles in solution was a second key materials area. The electron beam both triggers growth and allows imaging of the growing and moving nanocrystals (*41*, *46*). In the biological arena, it was quickly realized that, remarkably, few nanometer-size Au labels on biological structures could be resolved even through several micrometers of water (*47*). Here, we describe highlights of recent results in these areas and in new fields such as biomineralization, the imaging of unlabeled biostructures, bubble dynamics, corrosion, and phase transformations.

Electrochemistry

The importance of liquid cell microscopy to electrochemistry is that liquid cell experiments enable us to relate the structural and compositional changes that take place to the electrochemical

signature. Other techniques do not probe electrochemical processes with the same combination of temporal and spatial resolution (*9*, *14*, *22*). The outcome can be a detailed test of growth mechanisms and information on the phenomena controlling key processes such as corrosion or battery cycling.

Understanding growth instabilities

Refining electrochemical growth models is an exciting opportunity for liquid cell microscopy. Initial experiments followed electrodeposition of individual copper nuclei on gold electrodes (*14*, *36*, *44*, *45*). On further deposition, a polycrystalline film grows over the electrode and then grows beyond it. Understanding the physics governing the morphology of the growth front is essential for controlling the structure and composition of deposited materials. Dynamic observations are helpful because models of solid-liquid interface stability are generally limited to steady-state conditions. Recently, growth instabilities and dendrite formation have been imaged in systems relevant to battery development (*18*, *20*, *40*, *48*–*50*). Quantitative measurements of the evolution of the growth front allow us to understand and control growth front stability through additives or pulse deposition (*51*). Power laws can be obtained for the development of roughness, and local measures such as growth rate at each point on the dendrite are accessible (*48*). Because diffusion fields play such a key role in electrochemical growth, a key advance has been the demonstration that, under certain circumstances, it is possible to image the distribution of ions in solution through their scattering of transmitted electrons (*20*).

Reactions in battery anodes, cathodes, and electrolytes

Interfacial electrochemical reactions control the transport of charge and mass in batteries and energy conversion systems. Liquid cell microscopy enables direct imaging of key phenomena during battery operation. The technique has already produced promising results relevant to Li-ion batteries, for both the key electrode materials and the electrolyte. Adaptation of existing techniques for a wider range of materials—for example, air-sensitive electrolytes—and improved experimental design for quantitative, sensitive (nanoampere) electrochemical measurement (*50*, *52*) are important for these experiments, as is a detailed understanding of the effect of the electron beam on electrochemical measurements.

In electrode materials, dramatic structural and chemical changes take place during cycling. Incorporation of Li changes the volume of some anode materials by hundreds of percent. This volume change can be imaged—for example, in Si in the form of a nanowire attached to a liquid cell electrode (*53*). The lithiation kinetics in this fully surrounded nanowire differ from those in nanowires that are in contact with electrolyte only at one end (*9*, *10*), illustrating the role of diffusion through the electrolyte. Chemical changes in electrode materials during cycling are also accessible. The progress of lithium transport across individual particles in a $LiFePO_4$ cathode material, resolved using EELS (*33*), is shown in Fig. 2A.

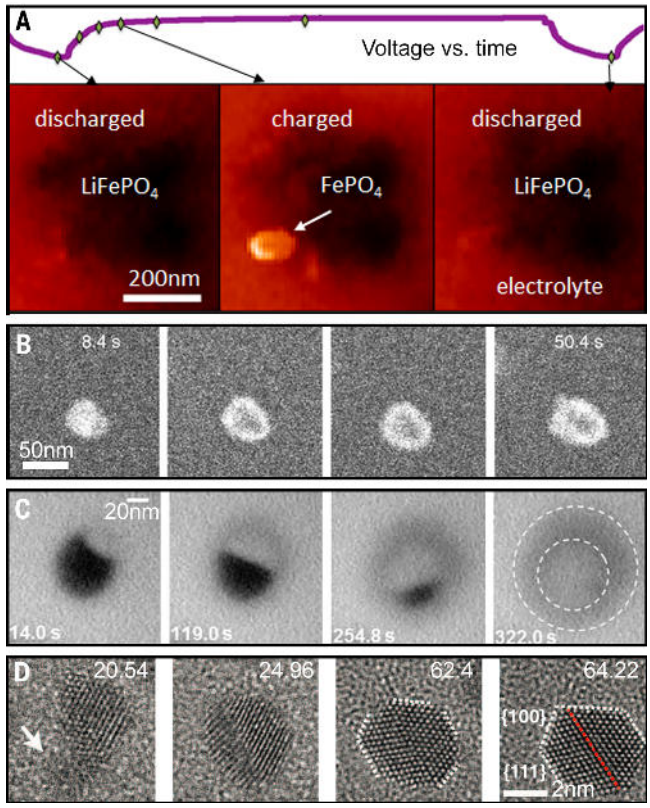

Fig. 2. Liquid processes in nanostructured materials. (**A**) The progress of lithium transport across individual particles as voltage is varied during cycling of a $LiFePO_4$ particle-based cathode material deposited by slurry printing onto a glassy carbon working electrode. Voltage versus time is shown, and 5-eV energy-filtered maps show delithiated $FePO_4$ as bright regions. [Reprinted with permission from (*33*). Copyright 2014, American Chemical Society] (**B**) Galvanic replacement of an Ag particle by Pd in 50-μM aqueous $PdCl_2$ solution imaged in dark-field STEM at 6 e^- $Å^{-2}$ s^{-1}; frame time, 8.4 s; electron dose per image, 52 e^- $Å^{-2}$. Images are shown at 8.4, 16.8, 25.2, and 50.4 seconds. [Reprinted by permission from (*43*). Copyright 2014, Macmillan Publishers Ltd.] (**C**) The formation of a hollow void in an oxidized Bi nanoparticle via the Kirkendall effect, dominated by nonuniform diffusion of bismuth. Relative times are shown in seconds. [Reprinted with permission from (*74*). Copyright 2013, American Chemical Society.] (**D**) High-resolution view in a graphene liquid cell of the sintering of two particles (smaller one arrowed), conversion of the grain boundary into a planar twin boundary, and evolution toward a hexagonal shape consistent with the Wulff construction. [Reprinted with permission of AAAS from (*37*)]

Battery electrolytes also undergo key changes during cycling: They break down and form a solid electrolyte interphase (SEI) composed of inorganic and organic electrolyte by-products. Understanding the formation of this layer could help improve Li-ion battery safety and cycle life. The structural morphology and evolution of the SEI has recently been observed (*54*) on highly oriented pyrolitic graphite, cut and joined onto a liquid cell electrode. The use of a three-electrode cell allowed correlation between the onset potential for the electrolyte solvent reduction and the SEI nucleation and growth.

Future battery progress relies on how well one can simulate a "real" battery—in other words, incorporate arbitrary anode and cathode materials in an appropriate geometry, include a reference electrode for quantitative measurements, and surround it all with liquid electrolyte. The development of ways to place nanoparticles, blocks, or strips of materials onto liquid cell electrodes is key (*33*, *52*, *53*), as is the availability of electrode materials such as glassy carbon (*33*). Electron-beam effects can be strong in battery experiments and may even indicate parameters of electrolyte stability (*55*).

Corrosion and related phenomena

The ability to relate nanoscale microstructural features of corrosion, such as pit formation, with macroscopic, electrochemical parameters is an important motivation for using liquid cell microscopy in understanding corrosion processes. Localized corrosion occurs through breakdown of the protective oxide film on stainless steel and aluminum or titanium alloys, due to aggressive species such as Cl^-. Liquid cell movies can show the initiation of pitting when metals such as Cu and Al are exposed to salt solutions, with or without an applied potential (*56*, *57*). This allows measurement of the kinetics and dependence of corrosion morphology on solution concentration. Corrosion mechanisms are often investigated by measuring a Tafel plot—i.e., the current due to dissolution of the material versus the applied voltage. Such data can be obtained using a liquid cell that contains a thin metal film deposited over the window, with a second electrode nearby (*57*). A wider range of materials can be examined using an approach similar to that described above for batteries: cutting out a lamella of the material of interest and welding it

to the liquid cell electrode (58). If beam effects can be understood (56), the liquid cell technique can provide a unique link between electrochemical parameters and structural change.

Nanoparticle nucleation, growth, and coalescence

Liquid cell TEM has been used successfully to study colloidal nanoparticle formation, and from the earliest observations it was clear that high spatial and temporal resolution provide opportunities for understanding growth mechanisms, diffusion, and coalescence. The scope of nanoparticle experiments has been augmented by improvements in resolution and by the introduction of heating, which has allowed a greater range of synthesis techniques to be addressed.

Growth and etching mechanisms

Metal nanoparticles nucleate and grow when metal ions in solution are reduced by radiolytic hydrated electrons. This beam-induced growth is relevant to real life because irradiation is often used to form particles with a narrow size distribution and without using surfactants. Liquid cell movies allow quantitative measurements of individual particles as they grow, providing a direct view of the mechanisms at work (Fig. 2). Initial experiments (41) showed previously unrecognized growth pathways for Pd nanoparticles, and were able to distinguish the mechanisms of monomer attachment and coalescence. Beam-induced growth has since been observed in other systems (37, 59–61), including multicomponent materials such as core-shell (62) and alloy (63) particles. Measurements as a function of dose rate (64) show the circumstances under which diffusion or attachment control growth. To obtain the highest-quality data from these growth experiments, it is important to improve the time resolution using fast detectors and to track as many particles as possible. Thus, a key advance is data compression and the development of automated video-analysis techniques (67) that can identify simultaneously operating growth mechanisms (64). As well as visualizing the formation of compact nanoparticles, beam-induced growth experiments also show how templates can alter nanoparticle nucleation (66), how beam-induced growth can form extended structures like dendrites (67, 68), and how patterned deposits can be made by rastering the beam (39, 42). Liquid cell microscopy can also image corrosive dissolution of nanoparticles (69, 70). The balance between oxidizing and reducing species produced by radiolysis can lead to situations in which the beam intensity controls particle stability (40, 71).

Growth during heating

With the development of heating capabilities, reactions can be driven by temperature rather than the electron beam, to probe other methods of nanoparticle synthesis and structural modification. Examples include hydrothermal precipitation of ZnO, achieved using a thermal reservoir outside the microscope (72), and nucleation of particles by laser heating (73). Complex phenomena can be visualized, such as Kirkendall voids formed by oxidizing Bi nanoparticles at elevated temperature (74) (Fig. 2C) and oscillatory growth of Bi nanoparticles exchanging material on heating (75).

Factors determining particle shape

As liquid cell resolution improves through the use of aberration correction and high-speed imaging (31) or graphene windows (37), it becomes possible to determine the nature and evolution of nanoparticle facets (31, 60) (Fig. 2D). Such experiments show how surfactants control which facets form (60) and how they may alter facet growth rates, even breaking the surface energy minimization rule so that growth does not follow the Wulff plot (31).

Dynamics of coalescence

As particles coalesce in solution into larger assemblies, liquid cell microscopy provides a remarkable view of the processes at work. Observing the dynamic motions and rotations of particles as they approach provides direct information on interparticle forces (59, 76, 77). Coalescence appears to take place on preferred planes (37). Particles may approach multiple times until they rotate into registry and snap together (77). Defect formation during coalescence can be imaged (Fig. 2D), as can structural rearrangements after coalescence. When multiple particles assemble, superlattices or diffusion-limited aggregates may form, and aggregation parameters (62, 78) and orientational order parameters of superlattices (79) can be measured. A common theme, of importance to synthesis and biomineralization, is the rich variety of growth pathways possible; it becomes clear that the final shape of a particle assembly alone provides only limited information on its formation mechanism.

Phase transformations in liquids

Electron microscopy has a distinguished history in exploring phase transformations and reactions in solids (2). The recent development of heating and cooling in liquid cells allows temperature, the key thermodynamic parameter, to be controlled, and therefore a range of transformations to be accessed.

Heating water nucleates bubbles, and their nucleation, growth, and stability can be measured and compared with thermodynamic models (23). Localized heating is achieved via Joule strips made of Pt lines, and the temperature gradients can in principle be modeled. Heating via an external reservoir results in more uniform temperature; laser heating (73), through a fiberoptic or port on the column, enables rapid temperature changes. Given the variety of heating methods, experiments can be optimized for the phenomenon under study, suggesting rich future possibilities.

Cooling allows ice to form from liquid water (provided beam-induced heating is minimized). Solidification of saline solutions containing Au nanoparticles (24)—using a cold finger in contact with the liquid cell—has provided insights into the competition between hexagonal and cubic ice nucleation and growth as a function of temperature, as well as particle rejection and occlusion as the ice advances (Fig. 3A). These types of experiments yield information that is complementary to what can be obtained from cold-stage experiments in ESEM and TEM in which water (80) (Fig. 3B) or ice (81) condense from vapor.

The physics of fluids at the nanoscale

Fluid physics is another area where our understanding can benefit from observations at nanometer length scales and especially at improved temporal resolution. Liquid cell microscopy can show how water moves at small length scales, how nanoscale bubbles move in water, and how nanoscale objects move within thin water films.

It is easy (often unavoidable) to form bubbles by radiolysis of the water in a liquid cell (39, 40, 82). As a large bubble forms, water recedes across the silicon nitride windows and leaves a thin wetting layer. Voids form in this layer, and their growth or shrinkage depends on size (83). Ultrathin droplets form, as do more complex structures that are thought to be caused by droplet charging (84). The droplets move with a stick-slip appearance, demonstrating the importance of interfacial interactions to nanoscale fluidity (84). Small bubbles in comparably thick liquid films drift up thickness gradients, and this motion can be modeled by considering the effects of trijunction forces (85).

The nucleation and motion of small droplets and the movement of bubbles in confined volumes is important in a range of fields, including catalysis, cavitation and lubrication, degassing of fluids, and boiling. Recent experiments have therefore examined liquid dynamics in other constrained geometries. Cylinders can be made from carbon nanotubes (86) or by using a graphene stack that curls into scrolls around the liquid (87). This provides the opportunity to observe bubble dynamics, condensation, and other processes in restricted volumes and offers the useful option of imaging parallel to the liquid/solid interface (Fig. 3B).

Particle motion in response to liquid motion (46) is readily observed from liquid cell experiments. Brownian motion can also be quantified. Nanoparticles in thin layers move much more slowly than expected for a bulk liquid (78, 88–90); the discrepancy can be 7 to 9 orders of magnitude. Such highly damped diffusive movement is helpful for recording images, but it is unexpected based on calculations of water in pores (91). If this damping arises from interactions between particle and substrate, it may be worth exploring other window materials (37).

Environmental and biological mineralization

The mechanisms that control key biological and environmental processes, such as mineral formation, are not well understood, partly due to the difficulty of making observations with appropriate resolution during growth. Liquid cell microscopy provides information on aggregation

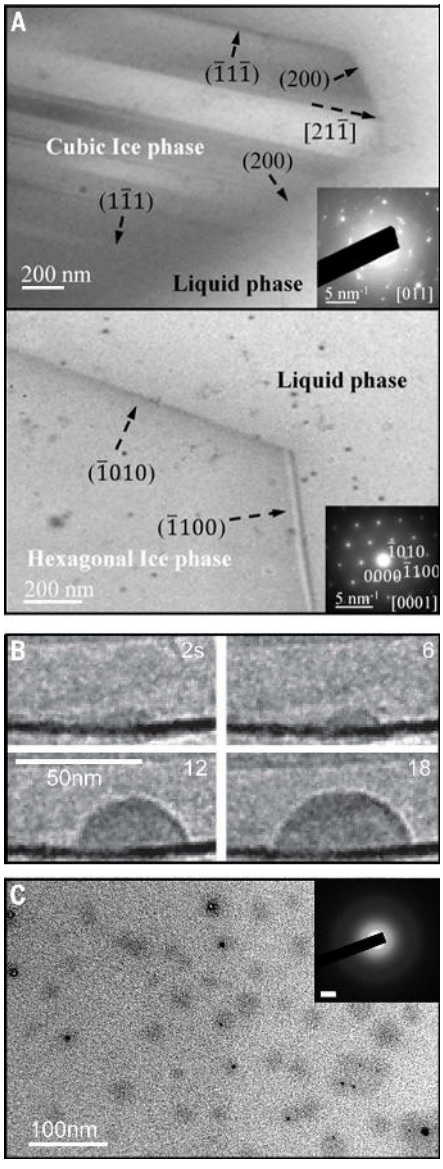

Fig. 3. Phase transformations. (**A**) Ice crystallizing from saline solution at 245 and 260 K (upper and lower images) showing the competition between different solid phases, identified by diffraction. [From (*24*). Copyright Microscopy Society of America, 2014] (**B**) A nanodroplet within a graphene nanochannel scroll imaged after the times shown. The hemispherical cap-shaped droplet condenses and grows on the wall. [Reproduced from (*87*) with permission from The Royal Society of Chemistry] (**C**) Amorphous $CaCO_3$ nucleation (dark points) within an organic matrix containing Ca-polystyrene sulphonate globules (larger patches). Nucleation sites are within the organic matrix, with an amorphous structure seen in diffraction data (inset). [Reprinted by permission from (*95*), Macmillan Publishers Ltd, copyright 2015]

processes, an example being the geological material iron oxyhydroxide (*77*). Key biomineralization questions can be examined, such as the effect of organic materials on nucleation pathways (*92*–*95*). Figure 3C (*95*) illustrates how, by binding calcium, organic additives bias calcium carbonate nucleation toward the amorphous phase rather than a crystalline phase. These experiments illustrate an innovative design in which CO_2 was diffused through one inlet of a dual-inlet liquid cell holder into a calcium-bearing solution to gradually raise supersaturation. This type of approach may be useful in other materials systems.

Biomineralization can also be investigated in whole (single-cell) organisms. Magnetotactic bacteria construct magnetosomes, chains of magnetite crystals. Correlative liquid cell STEM and fluorescence microscopy (Fig. 4A) explore magnetosome structure in the natural cellular environment (*96*). These images are static, but dynamic information could in principle be obtained if the dose can be kept low. The success of liquid cell microscopy in imaging systems containing both soft macromolecular matrices and hard mineral constituents suggests that the technique will be applicable to many key biomineralization processes.

Liquid cell microscopy for life science

Microscopy has been a driver for discovery in life science. Fluorescence microscopy can image specific proteins at up to 10-nm resolution if superresolution techniques are used and can image protein dynamics and interactions in fixed or living cells. Electron microscopy can offer higher resolution on material that is encased in amorphous ice at cryogenic temperature or on dried or embedded material at room temperature. Correlative light and electron microscopy uses the strengths of both techniques to provide detailed structural and functional information. Unfortunately, the resolution benefits of electron microscopy are associated with the challenge of preserving the material during conventional sample preparation. Dehydration or freezing changes the structure and, of course, removes the possibility of making dynamic observations or imaging living cells. The pioneering demonstrations that labeled biological structures can be resolved through micrometers of water using STEM (*47*, *97*), and that biological processes can be stimulated in situ by injecting nutrients (*30*), showed that liquid cell microscopy can provide high-resolution information while circumventing some of the sample preparation issues. Liquid cell TEM is therefore positioned well as a complement to conventional light and electron microscopy methods to address the complexity of biological materials.

Whole cells and live cells

The ability to image nanoparticle labels through thick liquid enables the study of cell structure and function. Cells can be grown on an electron transparent membrane chip, incubated for different times or under varied conditions with labels that tag specific proteins or are taken up by the cells, and then enclosed by adding the top chip. Liquid cell microscopy can visualize the tagged structures or measure particle uptake (*47*, *48*, *98*) (Fig. 4B). Correlative experiments involving fluorescence microscopy (*99*) provide additional information on cell structure and viability. Correlative light and liquid cell microscopy has been used to measure the spatial distribution of a growth factor that is expressed in tumor cells (*100*), finding a nonuniform distribution over the cell membrane that may be relevant to metastasis and drug response. An important step forward for such studies is the statistical information obtained by measuring relatively large numbers of cells in a short time, enabled through optimization of experimental procedures (*101*). The interactions of cell edges with nanoparticles can also be imaged (*102*). Studies of this type may have relevance to safety and dose evaluation for nanoparticle-based drug-delivery vehicles.

If the enclosure has suitable size and surface condition, and if nutrients are supplied, unfixed cultured cells can be kept alive in a liquid cell chamber at room temperature with liquid flow for several hours (*97*, *103*). But is it possible for cells to remain alive while images are recorded? Although unfixed cells can be imaged, it appears that they are not viable after even one image is recorded (*103*), even with liquid flow to provide nutrients and perhaps remove radiolysis products and heat during imaging. The dose delivered in one image is typically above the lethal dose. There is much ongoing interest in establishing whether tolerable doses exist for in vivo liquid cell microscopy (*96*, *103*); it may be possible to study certain biochemical processes, as it appears that the speed of cell death depends on the region of the cell that is imaged.

Tracking motion in labeled biological systems

It is possible to visualize certain biological functions by tracking the movements of the labels attached to them. An interesting example (*30*) is the movement of the myosin head in response to adenosine triphosphate (ATP). These experiments involve synthetic myosin muscle filaments, labeled with Au particles and placed on one surface of a large liquid cell chamber filled with saturated air. ATP is injected through a capillary, diffusing to the sample through the surface liquid layer and stimulating a several-nanometer filament movement. Labels can also be attached to smaller biomolecules such as DNA. The motion of pairs of gold nanoparticles tethered by a single piece of double-stranded DNA gives information on DNA configuration under the electron beam (*104*).

Imaging unlabeled biostructures, soft materials, and dynamical phenomena

Under favorable conditions, biomolecules and macromolecular assemblies can be imaged without the use of nanoparticle labels and at relatively low dose. Favorable imaging conditions include the lowest possible liquid and window thickness and a strategy for minimizing motion blur during image acquisition. One approach is to closely encase the material with graphene,

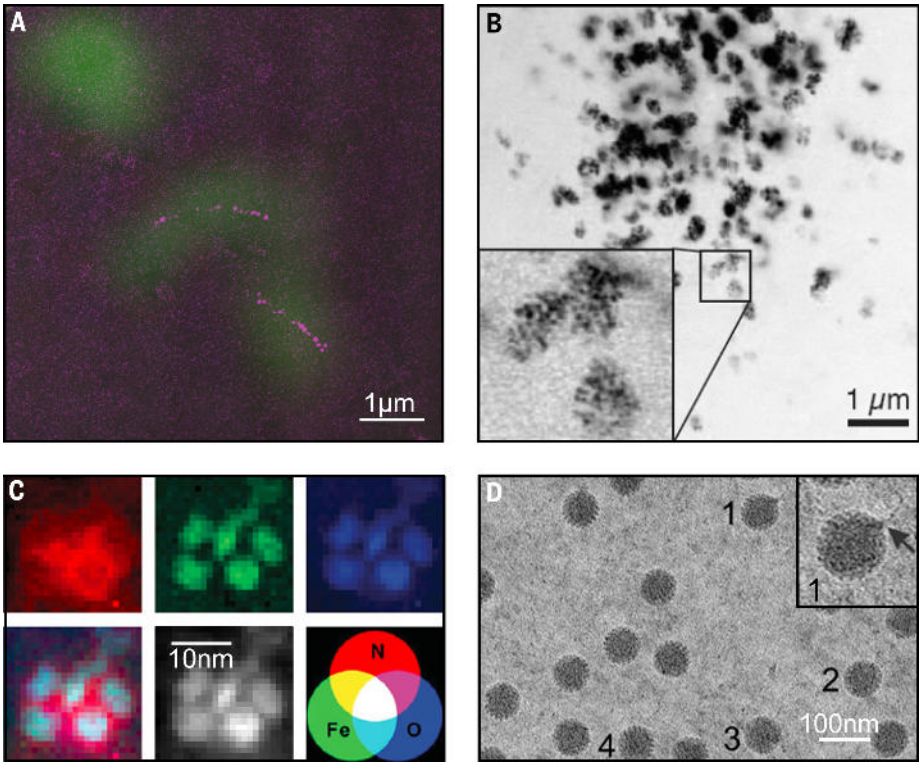

Fig. 4. Biological structures and processes. (**A**) Superimposed fluorescence and STEM images of two viable cells of ***Magnetospirillum*** *magneticum*. The magnetosome chains appear in purple. Scale bar, 1 mm. [From (*96*). Reprinted by permission from Macmillan Publishers Ltd., copyright 2014] (**B**) Live whole COS7 cells during nanoparticle take-up, imaged 24 hours after their incubation with serum-protein coated 30-nm Au nanoparticles. The particles were found in a dense, three-dimensional cluster of vesicles. The inset represents a processed image of the indicated region, with individual particles visible within the vesicles. [Reprinted from (*97*)] (**C**) Compositional maps for N, Fe, and O obtained for ferritin molecules in water sandwiched between graphene sheets with 1-nm resolution. A composite map (see color chart) and a HAADF image are also shown. The raw data are filtered to improve signal to noise. The protein shell of ferritin is clearly resolved and the iron valence identified as 3+. [Reprinted with permission from (*107*)] (**D**) Double-layered particles, the structures into which rotavirus transforms on invading a host cell, imaged while actively transcribing mRNA. The particles are tethered to SiN microchips, and ATP was added to enable transcription. Single-stranded mRNA is seen around several viral capsids (1 to 4 and inset). [From (*27*), Copyright Royal Society of Chemistry, 2015]

minimizing the membrane thickness and the volume of surrounding liquid (*105*, *106*). Another approach is to use patterned silicon nitride substrates with microwells that control the liquid thickness (*25*, *26*) and additionally to tether biostructures by functionalizing the substrate (*26*–*28*).

Such improvements can result in high-quality imaging of biomaterials and soft materials in the liquid state. High-contrast materials, such as the magnetosomes mentioned above (*96*), ferritin molecules (*107*) (Fig. 4C), and micelles containing heavy metals (*108*), are readily imaged to show their overall structure. Analytical techniques can provide composition and bonding, as has been shown for ferritin using EELS (*107*), and dynamics can be studied, as has been shown for Pt-containing micelles (*108*). However, even low-atomic-number materials are visible using liquid cell microscopy. Liposomes and polymers have been imaged (*109*, *110*) to provide shape and size in water, a useful comparison with cryoelectron microscopy results. In addition, more complex biostructures can be imaged. For example, the acrosomal process, a membrane that extends from sperm heads, has an appearance in the liquid cell that is consistent with that in cryoelectron microscopy (*28*). Protein crystals have been imaged at 2.7-nm resolution with a cumulative electron dose of 3500 electrons per nm^2 (*28*). The combination of TEM and fluorescence microscopy has been used to determine the spatial distributions and interactions of subcellular organelles, such as the cytoskeleton and its contact with adjacent cells (*111*). Finally, Fig. 4C shows a viral pathogen imaged at ~3-nm resolution in the process of transcribing RNA (*27*). With image processing, these data are sensitive to rearrangements in the internal structure of the virus during RNA synthesis. Tests for viability are important in evaluating experiments involving dynamic biochemical processes (*27*).

Because liquid cell electron microscopy is a new technique, it is important to validate all of its results by comparison with cryoelectron microscopy and to establish radiation damage criteria. However, these recent advances provide encouragement that liquid cell microscopy might complement cryoelectron microscopy, fluorescence, and diffraction techniques in providing static and dynamic imaging of biological systems in water, fulfilling the critical need to develop real-time, high-resolution imaging tools for life sciences.

Future prospects

Geological materials such as clays

The hydration of clay minerals is important for soil properties, in developing building materials, and in mining activities. Microsopy of clay minerals in a controlled environment that includes liquid water should provide new information on the pathways by which the key structural transformations occur. Early research in this area (*5*, *112*) on the hydration of Portland cement was hampered by the lack of a reliable method for handling water in situ. Modern liquid cells have a greater chance of producing quantitative results in, for example, imaging the behavior of the swelling clays (montmorillonites or bentonites) in fluids of different compositions. Hydration behavior in confined volumes is well suited for liquid cell experiments and could provide information relevant to oil sand extraction. Many minerals with hydrated and anhydrous varieties have commercial value, and others cause problems when they change state. There appears to be no shortage of interesting questions in this area.

Extreme temperature and pressure geological processes

Conventional liquid cells can withstand pressures of only a few atmospheres (*20*). How far we can push this upper pressure limit depends on the mechanical properties of the windows. Inorganic fluids confined in liquid cells at high pressures can perhaps provide nanoscale insights into geological processes such as hydrothermal reactions relevant to crystal growth, nanostructure synthesis, fuel production, or volcanic activity. The nature of many hydrothermal chemical reactions is difficult to assess, and nanoscale in situ observations could provide new insights. At low temperatures, the structure and stability of methane clathrates could be a useful field of study.

Atmospheric aerosols

Environmental TEM provides valuable information for understanding the behavior and properties of atmospheric particles (*113*). However, its use is limited at high relative humidities, in particular the extreme of complete saturation. The full ability to control the water environment is relevant to cloud formation, where saturation and supersaturation values are high. We could imagine, for example, subjecting various types of common atmospheric particles to water and liquids with different salinities and

observe phase changes during cooling at controlled rates.

Biominerals

The recent results described above suggest further applications in a wider range of mineral systems and environments, including those involving organic components. Multiple mineral phases and reaction pathways are a common characteristic, and comparing different systems would allow an understanding of the principles that determine which pathway will be followed and how nucleation can be directed with control over phase, orientation, and location.

Physics of fluids

A grand challenge for understanding interfacial fluids has been the difficulty of imaging liquid/solid interfaces with good time and space resolution (*114*). Given the improvements in liquid cell microscopy resolution and detector sensitivity, we anticipate that studies over the next few years should illuminate features of the liquid/solid interface such as ordering, the hydration layer, and the double layer, and provide direct observations of phase transitions. Diffusion through liquids is important in catalysis, battery operation, biomaterials, and tribology. With the development of low-temperature imaging, it could be exciting to examine liquids such as nitrogen or even helium, and solvents such as liquid ammonia.

Electrochemistry in more complex systems

There has been little study of materials other than metals, of codeposition and electroless deposition, or of temperature-dependent electrochemistry. Take, for example, the electrochemically deposited polymers: Polypyrrole is an extensively studied conducting polymer, whose most efficient synthesis method is electropolymerization (*115*). Temperature-dependent electrochemistry, including low-temperature Li-ion battery function, is a critical area. It is possible that molten salt electrochemical reactions relevant to Al refining or the process of stress corrosion cracking could be performed in extreme environments of water and high temperature and pressure.

The electrochemical double layer

A grand challenge for microscopy is to image directly the electrochemical double layer and measure its behavior during electrochemical processes. Its length scale of a few nanometers makes this difficult, but experiments may involve combinations of holography and liquid cell microscopy to probe the double layer at an atomically flat electrode surface.

Magnetic materials

The holography/liquid cell combination provides other fascinating opportunities. One can imagine in situ observation during liquid phase deposition of magnetic materials, simultaneously measuring their developing microstructure and magnetic fields. Magnetic thin films such as the NiFe layers used in magnetic read heads are formed by electroless deposition at moderate temperatures, and understanding film evolution could potentially improve our control of nucleation and domain development. Other areas of application include the interactions of magnetic particles in liquids and the behavior of the surfactant-coated particles within ferrofluids while being magnetized.

Catalysis

Electron microscopy has provided detailed insights into catalysis from gases (*116*, *117*) but is relatively less explored for reactions that form liquids (*118*) or that are catalyzed by liquids (*119*). As liquid geometry and flow become better controlled, we can now envisage liquid cell microscopy of catalyst reactions involving water. Water splitting can be achieved by catalysts driven electrochemically or with light fed through a fiber optic, as already demonstrated in gas-phase catalysis (*117*), and this will likely be a key application area for liquid cell microscopy.

High-speed phenomena

The ability to record liquid cell data at high frame rates expands the range of phenomena that can be addressed and also improves image resolution by reducing motion-induced blur. For even faster processes, though, the technique of dynamic TEM (DTEM) can be adapted for the liquid cell (*82*). A laser hits the sample, supplying heat or optical stimulation, and also triggers a pulse of electrons (delayed by a specified time) that form an image. The time resolution, determined by the length of the pulse, is 1 μs to 1 ns. Microanalysis is possible via energy-filtered TEM through an in-column filter. So far, laser-induced nucleation and growth has been examined at ~10-nm spatial resolution (*73*), and DTEM is likely to have broad application for rapid liquid-mediated reactions.

Imaging whole biological cells

Imaging cells in their native liquid state is already an exciting prospect, offering the possibility of high-resolution information without freezing or drying. It is not yet clear whether live cells can ever be imaged. We need a better understanding of dose effects, through correlative experiments that determine the extent to which biological functions are preserved during imaging. Indeed, irradiation effects on cells (with taken-up nanoparticles, for example) could provide insights into cancer therapies. Because various parts of a cell show different dose tolerances, it may be useful to develop systems with optimized liquid geometry to allow dose-tolerant regions to be imaged with good resolution and minimized dose. To distinguish different components within a cell, the use of mixtures of labels could be explored in liquid cell TEM, as is done for fluorescence microscopy.

The structures of biomaterials and proteins

The current progress in liquid cell microscopy of unlabeled biomaterials, combined with greater use of techniques already developed for cryo-EM—such as low-dose imaging, dose fractionation techniques, and image analysis techniques—suggests that in the future the technique could provide insights into the structure of materials such as block copolymers, protein domains, macromolecule-mediated nanoparticle assembly, and even food materials. The liquid environment may provide a benefit, compared with cryoelectron microscopy, if it can be shown to help move away radiolysis products while preserving structure. In addition, temperature control will prove useful in understanding interactions and processes in these types of materials.

Imaging biological dynamics

Movies of processes such as the dynamics of large proteins, changes in membrane geometry, or the assembly of microfilaments would provide fundamental and practical insights. Prospects for real-time imaging ultimately come down to the dose required per image. Increasing the material contrast reduces the dose required; achieving higher contrast (without using labels or defocus techniques) may require exploring the use of phase plates (*120*) or electron holography (*121*). Temperature-dependent imaging of biological structures and processes could allow optimum temperatures to be chosen for measurements of dynamics and exploration of biological processes under extreme environments. The processes may be triggered by introducing chemicals into the solution flow [as demonstrated in (*30*)] or by laser pumping (as in DTEM) by heating or direct light stimulation. Because biological systems also respond to electromagnetic fields, the use of externally applied fields, with results measured using holography, could be potentially transformative, if issues of dose and the holographic reference beam could be resolved. This could possibly produce charge maps of proteins and show the self-assembly and folding of proteins or the field-induced interactions between individual biomolecules and binding sites. Although some of the above speculations appear far from reality, the recent pace of progress encourages us to expect a strong impact of liquid cell microscopy for understanding biological structures and processes.

The examples described above, covering both current research and future ideas, suggest that liquid cell electron microscopy is well positioned to explore new frontiers in nanomaterial growth, fluid physics, radiation physics, corrosion and electrochemical processes, geological and environmental processes, and biomaterial structure and function. Based on continuing improvements in equipment and experimental capabilities, we anticipate that observations made using liquid cell microscopy can address key materials challenges and provide an exciting view of liquid-phase materials and processes.

REFERENCES AND NOTES

1. N. de Jonge, F. M. Ross, Electron microscopy of specimens in liquid. *Nat. Nanotechnol.* **6**, 695–704 (2011). doi: 10.1038/nnano.2011.161; pmid: 22020120
2. R. Sinclair, In situ high-resolution transmission electron microscopy of material reactions. *Mater. Res. Soc. Bull.* **38**, 1065–1071 (2013). doi: 10.1557/mrs.2013.285

3. H.-G. Liao, K. Niu, H. Zheng, Observation of growth of metal nanoparticles. *Chem. Commun.* **49**, 11720–11727 (2013). doi: 10.1039/c3cc47473a; pmid: 24212413
4. D. F. Parsons, Structure of wet specimens in electron microscopy. Improved environmental chambers make it possible to examine wet specimens easily. *Science* **186**, 407–414 (1974). doi: 10.1126/science.186.4162.407; pmid: 4213401
5. E. P. Butler, K. F. Hale, *Dynamic Experiments in the Electron Microscope* (North-Holland, 1981), Chapter 6.
6. E. Ruska, Beitrag zur uebermikroskopischen Abbildungen bei hoeheren Drucken. *Kolloid Z.* **100**, 212–219 (1942). doi: 10.1007/BF01519549
7. G. D. Danilatos, Review and outline of environmental SEM at present. *J. Microsc.* **162**, 391–402 (1991). doi: 10.1111/j.1365-2818.1991.tb03149.x
8. D. Stokes, *Principles and Practice of Variable Pressure/Environmental Scanning Electron Microscopy (VP-ESEM)* (Wiley, 2008).
9. C.-M. Wang, H.-G. Liao, F. M. Ross, Observation of materials processes in liquids by electron microscopy. *MRS Bull.* **40**, 46–52 (2015). doi: 10.1557/mrs.2014.283
10. J. Y. Huang *et al.*, In situ observation of the electrochemical lithiation of a single SnO_2 nanowire electrode. *Science* **330**, 1515–1520 (2010). doi: 10.1126/science.1195628; pmid: 21148385
11. C. M. Wang *et al.*, In situ transmission electron microscopy and spectroscopy studies of interfaces in Li ion batteries: Challenges and opportunities. *J. Mater. Res.* **25**, 1541–1547 (2010). doi: 10.1557/JMR.2010.0198
12. I. M. Abrams, J. W. McBain, A closed cell for electron microscopy. *Science* **100**, 273–274 (1944). doi: 10.1126/science.100.2595.273; pmid: 17746136
13. D. D. Double, A. Hellawell, S. J. Perry, The hydration of Portland cement. *Proc. R. Soc. London Ser. A* **359**, 435–451 (1978). doi: 10.1098/rspa.1978.0050
14. M. J. Williamson, R. M. Tromp, P. M. Vereecken, R. Hull, F. M. Ross, Dynamic microscopy of nanoscale cluster growth at the solid-liquid interface. *Nat. Mater.* **2**, 532–536 (2003). doi: 10.1038/nmat944; pmid: 12872162
15. C. Mueller, M. Harb, J. R. Dwyer, R. J. D. Miller, Nanofluidic cells with controlled pathlength and liquid flow for rapid, high-resolution in situ imaging with electrons. *J. Phys. Chem. Lett.* **4**, 2339–2347 (2013). doi: 10.1021/jz401067k
16. J. M. Grogan, H. H. Bau, The nanoaquarium: A platform for in situ transmission electron microscopy in liquid media. *J. Microelectromech. Syst.* **19**, 885–894 (2010). doi: 10.1109/JMEMS.2010.2051321
17. E. Jensen, A. Burrows, K. Mølhave, Monolithic chip system with a microfluidic channel for in situ electron microscopy of liquids. *Microsc. Microanal.* **20**, 445–451 (2014). doi: 10.1017/S1431927614000300; pmid: 24717178
18. A. J. Leenheer, J. P. Sullivan, M. J. Shaw, C. T. Harris, A sealed liquid cell for in situ transmission electron microscopy of controlled electrochemical processes. *J. Microelectromech. Syst.* **24**, 1061–1068 (2015). doi: 10.1109/JMEMS.2014.2380771
19. E. A. Ring, N. de Jonge, Microfluidic system for transmission electron microscopy. *Microsc. Microanal.* **16**, 622–629 (2010). doi: 10.1017/S1431927610093669; pmid: 20804635
20. E. R. White *et al.*, In situ transmission electron microscopy of lead dendrites and lead ions in aqueous solution. *ACS Nano* **6**, 6308–6317 (2012). doi: 10.1021/nn3017469; pmid: 22702348
21. B. L. Mehdi *et al.*, In-situ electrochemical transmission electron microscopy for battery research. *Microsc. Microanal.* **20**, 484–492 (2014). doi: 10.1017/S1431927614000488; pmid: 24755142
22. R. R. Unocic *et al.*, Quantitative electrochemical measurements using in situ ec-S/TEM devices. *Microsc. Microanal.* **20**, 452–461 (2014). doi: 10.1017/S1431927614000166; pmid: 24618013
23. E. R. White, M. Mecklenburg, S. B. Singer, S. Aloni, B. C. Regan, Imaging nanobubbles in water with scanning transmission electron microscopy. *Appl. Phys. Express* **4**, 055201 (2011). doi: 10.1143/APEX.4.055201
24. K. Tai, Y. Liu, S. J. Dillon, In situ cryogenic transmission electron microscopy for characterizing the evolution of solidifying water ice in colloidal systems. *Microsc. Microanal.* **20**, 330–337 (2014). doi: 10.1017/S1431927613014128; pmid: 24548432
25. K. Degen, M. Dukes, J. R. Tanner, D. F. Kelly, The development of affinity capture devices-a nanoscale purification platform for biological in situ transmission electron microscopy. *RSC Adv.* **2**, 2408–2412 (2012). doi: 10.1039/c2ra01163h
26. M. J. Dukes *et al.*, Improved microchip design and application for in situ transmission electron microscopy of macromolecules. *Microsc. Microanal.* **20**, 338–345 (2014). doi: 10.1017/S1431927613013858; pmid: 24331164
27. A. C. Varano *et al.*, Visualizing virus particle mobility in liquid at the nanoscale. *Chem. Commun.* **51**, 16176 (2015). doi: 10.1039/c5cc05744b
28. U. M. Mirsaidov, H. Zheng, Y. Casana, P. Matsudaira, Imaging protein structure in water at 2.7 nm resolution by transmission electron microscopy. *Biophys. J.* **102**, L15–L17 (2012). doi: 10.1016/j.bpj.2012.01.009; pmid: 22385868
29. D. B. Peckys, N. de Jonge, Studying the stoichiometry of epidermal growth factor receptor in intact cells using correlative microscopy. *J. Vis. Exp.* **103**, e53186 (2015). doi: 10.3791/53186
30. H. Sugi *et al.*, Direct demonstration of the cross-bridge recovery stroke in muscle thick filaments in aqueous solution by using the hydration chamber. *Proc. Natl. Acad. Sci. U.S.A.* **105**, 17396–17401 (2008). doi: 10.1073/pnas.0809581105; pmid: 18987316
31. H. G. Liao *et al.*, Facet development during platinum nanocube growth. *Science* **345**, 916–919 (2014). doi: 10.1126/science.1253149; pmid: 25146287
32. K. L. Jungjohann, J. E. Evans, J. A. Aguiar, I. Arslan, N. D. Browning, Atomic-scale imaging and spectroscopy for in situ liquid scanning transmission electron microscopy. *Microsc. Microanal.* **18**, 621–627 (2012). doi: 10.1017/S1431927612000104; pmid: 22640968
33. M. E. Holtz *et al.*, Nanoscale imaging of lithium ion distribution during in situ operation of battery electrode and electrolyte. *Nano Lett.* **14**, 1453–1459 (2014). doi: 10.1021/nl404577c; pmid: 24548177
34. E. A. Lewis *et al.*, Real-time imaging and local elemental analysis of nanostructures in liquids. *Chem. Commun.* **50**, 10019–10022 (2014). doi: 10.1039/C4CC02743D; pmid: 24831648
35. J. F. Creemer *et al.*, Atomic-scale electron microscopy at ambient pressure. *Ultramicroscopy* **108**, 993–998 (2008). doi: 10.1016/j.ultramic.2008.04.014; pmid: 18556124
36. A. Radisic, P. M. Vereecken, J. B. Hannon, P. C. Searson, F. M. Ross, Quantifying electrochemical nucleation and growth of nanoscale clusters using real-time kinetic data. *Nano Lett.* **6**, 238–242 (2006). doi: 10.1021/nl052175i; pmid: 16464042
37. J. M. Yuk *et al.*, High-resolution EM of colloidal nanocrystal growth using graphene liquid cells. *Science* **336**, 61–64 (2012). doi: 10.1126/science.1217654; pmid: 22491849
38. V. P. Adiga, G. D. Dunn, A. P. Alivisatos, A. Zettl, Electrically integrated graphene on silicon nitride liquid flow cells for high resolution electron microscopy, U.S. Patent Application Ser. No. 14/817,551. http://ipo.lbl.gov/lbnl2014-129/.
39. J. M. Grogan, N. M. Schneider, F. M. Ross, H. H. Bau, Bubble and pattern formation in liquid induced by an electron beam. *Nano Lett.* **14**, 359–364 (2014). doi: 10.1021/nl404169a; pmid: 24299122
40. N. M. Schneider *et al.*, Electron–water interactions and implications for liquid cell electron microscopy. *J. Phys. Chem. C* **118**, 22373–22382 (2014). doi: 10.1021/jp507400n
41. H. Zheng *et al.*, Observation of single colloidal platinum nanocrystal growth trajectories. *Science* **324**, 1309–1312 (2009). doi: 10.1126/science.1172104; pmid: 19498166
42. M. den Heijer, I. Shao, A. Radisic, M. C. Reuter, F. M. Ross, Patterned electrochemical deposition of copper using an electron beam. *APL Materials* **2**, 022101 (2014). doi: 10.1063/1.4863596
43. E. Sutter *et al.*, In situ liquid-cell electron microscopy of silver-palladium galvanic replacement reactions on silver nanoparticles. *Nat. Commun.* **5**, 4946 (2014). doi: 10.1038/ncomms5946; pmid: 25208691
44. A. Radisic, F. M. Ross, P. C. Searson, In situ study of the growth kinetics of individual island electrodeposition of copper. *J. Phys. Chem. B* **110**, 7862–7868 (2006). doi: 10.1021/jp057549a; pmid: 16610883
45. A. Radisic, P. M. Vereecken, P. C. Searson, F. M. Ross, The morphology and nucleation kinetics of copper islands during electrodeposition. *Surf. Sci.* **600**, 1817–1826 (2006). doi: 10.1016/j.susc.2006.02.025
46. H. Zheng, S. A. Claridge, A. M. Minor, A. P. Alivisatos, U. Dahmen, Nanocrystal diffusion in a liquid thin film observed by in situ transmission electron microscopy. *Nano Lett.* **9**, 2460–2465 (2009). doi: 10.1021/nl9012369; pmid: 19408927
47. N. de Jonge, D. B. Peckys, G. J. Kremers, D. W. Piston, Electron microscopy of whole cells in liquid with nanometer resolution. *Proc. Natl. Acad. Sci. U.S.A.* **106**, 2159–2164 (2009). doi: 10.1073/pnas.0809567106; pmid: 19164524
48. M. Sun, H.-G. Liao, K. Niu, H. Zheng, Structural and morphological evolution of lead dendrites during electrochemical migration. *Sci. Rep.* **3**, 3227 (2013). pmid: 24233151
49. Z. Zeng *et al.*, Visualization of electrode-electrolyte interfaces in $LiPF_6$/EC/DEC electrolyte for lithium ion batteries via in situ TEM. *Nano Lett.* **14**, 1745–1750 (2014). doi: 10.1021/nl403922u; pmid: 24443941
50. B. L. Mehdi *et al.*, Observation and quantification of nanoscale processes in lithium batteries by operando electrochemical (S)TEM. *Nano Lett.* **15**, 2168–2173 (2015). doi: 10.1021/acs.nanolett.5b00175; pmid: 25705928
51. N. M. Schneider *et al.*, Visualization of active and passive control of morphology during electrodeposition. *Microsc. Microanal.* **20**, 1530–1531 (2014). doi: 10.1017/S1431927614009386
52. B. L. Mehdi *et al.*, In-situ electrochemical transmission electron microscopy for battery research. *Microsc. Microanal.* **20**, 484–492 (2014). doi: 10.1017/S1431927614000488; pmid: 24755142
53. M. Gu *et al.*, Demonstration of an electrochemical liquid cell for operando transmission electron microscopy observation of the lithiation/delithiation behavior of Si nanowire battery anodes. *Nano Lett.* **13**, 6106–6112 (2013). doi: 10.1021/nl403402q; pmid: 24224495
54. R. L. Sacci *et al.*, Direct visualization of initial SEI morphology and growth kinetics during lithium deposition by in situ electrochemical transmission electron microscopy. *Chem. Commun. (Camb.)* **50**, 2104–2107 (2014). doi: 10.1039/c3cc49029g; pmid: 24413070
55. P. Abellan *et al.*, Probing the degradation mechanisms in electrolyte solutions for Li-ion batteries by in situ transmission electron microscopy. *Nano Lett.* **14**, 1293–1299 (2014). doi: 10.1021/nl404271k; pmid: 24559146
56. S. W. Chee, D. J. Duquette, F. M. Ross, R. Hull, Metastable structures in Al thin films prior to the onset of corrosion pitting as observed using liquid cell transmission electron microscopy. *Microsc. Microanal.* **20**, 462–468 (2014). doi: 10.1017/S1431927614000221; pmid: 24565052
57. S. W. Chee *et al.*, Studying localized corrosion using liquid cell transmission electron microscopy. *Chem. Commun.* **51**, 168–171 (2015). doi: 10.1039/C4CC06443G; pmid: 25388023
58. X. Zhong, M. G. Burke, S. Schilling, S. J. Haigh, N. J. Zaluzec, Novel hybrid sample preparation method for in situ liquid cell TEM analysis. *Microsc. Microanal.* **20** (suppl. S3), 1514–1515 (2014). doi: 10.1017/S1431927614009301; pmid: 25010485
59. H. G. Liao, L. Cui, S. Whitelam, H. Zheng, Real-time imaging of Pt_3Fe nanorod growth in solution. *Science* **336**, 1011–1014 (2012). doi: 10.1126/science.1219185; pmid: 22628649
60. H. G. Liao, H. Zheng, Liquid cell transmission electron microscopy study of platinum iron nanocrystal growth and shape evolution. *J. Am. Chem. Soc.* **135**, 5038–5043 (2013). doi: 10.1021/ja310612p; pmid: 23477794
61. T. J. Woehl *et al.*, Direct observation of aggregative nanoparticle growth: Kinetic modeling of the size distribution and growth rate. *Nano Lett.* **14**, 373–378 (2014). doi: 10.1021/nl4043328; pmid: 24325680
62. K. L. Jungjohann, S. Bliznakov, P. W. Sutter, E. A. Stach, E. A. Sutter, In situ liquid cell electron microscopy of the solution growth of Au-Pd core-shell nanostructures. *Nano Lett.* **13**, 2964–2970 (2013). doi: 10.1021/nl4014277; pmid: 23721080
63. A. De Clercq *et al.*, Growth of Pt-Pd nanoparticles studied in situ by HRTEM in a liquid cell. *J. Phys. Chem. Lett.* **5**, 2126–2130 (2014). doi: 10.1021/jz500690a; pmid: 26270503
64. T. J. Woehl, J. E. Evans, I. Arslan, W. D. Ristenpart, N. D. Browning, Direct in situ determination of the mechanisms controlling nanoparticle nucleation and growth. *ACS Nano* **6**, 8599–8610 (2012). doi: 10.1021/nn303371y; pmid: 22957797
65. C. Park, T. J. Woehl, J. E. Evans, N. D. Browning, Minimum cost multi-way data association for optimizing multitarget tracking of interacting objects. *IEEE Trans. Pattern Anal. Mach. Intell.* **37**, 611–624 (2015). doi: 10.1109/TPAMI.2014.2346202; pmid: 26353265
66. L. R. Parent *et al.*, Direct in situ observation of nanoparticle synthesis in a liquid crystal surfactant template. *ACS Nano* **6**, 3589–3596 (2012). doi: 10.1021/nn300671g; pmid: 22439964

67. T. Kraus, N. de Jonge, Dendritic gold nanowire growth observed in liquid with transmission electron microscopy. *Langmuir* **29**, 8427–8432 (2013). doi: 10.1021/la401584z; pmid: 23789977
68. G. Zhu *et al*., In situ study of the growth of two-dimensional palladium dendritic nanostructures using liquid-cell electron microscopy. *Chem. Commun.* **50**, 9447–9450 (2014). doi: 10.1039/C4CC03500C; pmid: 24938863
69. Y. Jiang *et al*., In situ study of oxidative etching of palladium nanocrystals by liquid cell electron microscopy. *Nano Lett.* **14**, 3761–3765 (2014). doi: 10.1021/nl500670q; pmid: 24927485
70. J. Wu, W. Gao, H. Yang, J.-M. Zuo, Imaging shape-dependent corrosion behavior of Pt nanoparticles over extended time using a liquid flow cell and TEM. *Microsc. Microanal.* **20**, 1508–1509 (2014). doi: 10.1017/S1431927614009271
71. K. W. Noh, Y. Liu, L. Sun, S. J. Dillon, Challenges associated with in-situ TEM in environmental systems: The case of silver in aqueous solutions. *Ultramicroscopy* **116**, 34–38 (2012). doi: 10.1016/j.ultramic.2012.03.012
72. Y. Liu, K. Tai, S. J. Dillon, Growth kinetics and morphological evolution of ZnO precipitated from solution. *Chem. Mater.* **25**, 2927–2933 (2013). doi: 10.1021/cm303522z
73. J. E. Evans, K. L. Jungjohann, N. D. Browning, I. Arslan, Controlled growth of nanoparticles from solution with in situ liquid transmission electron microscopy. *Nano Lett.* **11**, 2809–2813 (2011). doi: 10.1021/nl201166k; pmid: 21619024
74. K.-Y. Niu, J. Park, H. Zheng, A. P. Alivisatos, Revealing bismuth oxide hollow nanoparticle formation by the Kirkendall effect. *Nano Lett.* **13**, 5715–5719 (2013). doi: 10.1021/nl4035362; pmid: 24131312
75. H. L. Xin, H. Zheng, In situ observation of oscillatory growth of bismuth nanoparticles. *Nano Lett.* **12**, 1470–1474 (2012). doi: 10.1021/nl2041854; pmid: 22313455
76. H. Zheng, U. M. Mirsaidov, L. W. Wang, P. Matsudaira, Electron beam manipulation of nanoparticles. *Nano Lett.* **12**, 5644–5648 (2012). doi: 10.1021/nl302788g; pmid: 23035740
77. D. Li *et al*., Direction-specific interactions control crystal growth by oriented attachment. *Science* **336**, 1014–1018 (2012). doi: 10.1126/science.1219643; pmid: 22628650
78. J. M. Grogan, L. Rotkina, H. H. Bau, In situ liquid-cell electron microscopy of colloid aggregation and growth dynamics. *Phys. Rev. E Stat. Nonlin. Soft Matter Phys.* **83**, 061405 (2011). doi: 10.1103/PhysRevE.83.061405; pmid: 21797362
79. J. Park *et al*., Direct observation of nanoparticle superlattice formation by using liquid cell transmission electron microscopy. *ACS Nano* **6**, 2078–2085 (2012). doi: 10.1021/nn203837m; pmid: 22360715
80. D. Bhattacharya, M. Bosman, V. R. S. S. Mokkapati, F. Y. Leong, U. Mirsaidov, Nucleation dynamics of water nanodroplets. *Microsc. Microanal.* **20**, 407–415 (2014). doi: 10.1017/S1431927614000476; pmid: 24667092
81. C.-Y. Ruan, V. A. Lobastov, F. Vigliotti, S. Chen, A. H. Zewail, Ultrafast electron crystallography of interfacial water. *Science* **304**, 80–84 (2004). doi: 10.1126/science.1094818; pmid: 15064414
82. N. D. Browning *et al*., Recent developments in dynamic transmission electron microscopy. *Curr. Opin. Solid State Mater. Sci.* **16**, 23–30 (2012). doi: 10.1016/j.cossms.2011.07.001
83. U. Mirsaidov, C.-D. Ohl, P. Matsudaira, A direct observation of nanometer-size void dynamics in an ultra-thin water film. *Soft Matter* **8**, 7108–7111 (2012). doi: 10.1039/c2sm25331c
84. U. M. Mirsaidov, H. Zheng, D. Bhattacharya, Y. Casana, P. Matsudaira, Direct observation of stick-slip movements of water nanodroplets induced by an electron beam. *Proc. Natl. Acad. Sci. U.S.A.* **109**, 7187–7190 (2012). doi: 10.1073/pnas.1200457109; pmid: 22517747
85. M. M. Norton, F. M. Ross, H. H. Bau, Nano bubble migration in a tapered conduit in the asymptotic limits of zero capillary and bond numbers: Theory and experiments. *Bull. Am. Phys. Soc.* **60**, H36.00004 (2015). http://meetings.aps.org/Meeting/DFD15/Session/H36.4
86. D. Mattia, Y. Gogotsi, Review: Static and dynamic behavior of liquids inside carbon nanotubes. *Microfluidics Nanofluidics* **5**, 289–305 (2008). doi: 10.1007/s10404-008-0293-5
87. U. Mirsaidov *et al*., Scrolling graphene into nanofluidic channels. *Lab Chip* **13**, 2874–2878 (2013). doi: 10.1039/c3lc50304f; pmid: 23702655
88. E. A. Ring, N. de Jonge, Video-frequency scanning transmission electron microscopy of moving gold nanoparticles in liquid. *Micron* **43**, 1078–1084 (2012). doi: 10.1016/j.micron.2012.01.010; pmid: 22386765
89. E. R. White, M. Mecklenburg, B. Shevitski, S. B. Singer, B. C. Regan, Charged nanoparticle dynamics in water induced by scanning transmission electron microscopy. *Langmuir* **28**, 3695–3698 (2012). doi: 10.1021/la2048486; pmid: 22320230
90. J. Lu, Z. Aabdin, N. D. Loh, D. Bhattacharya, U. Mirsaidov, Nanoparticle dynamics in a nanodroplet. *Nano Lett.* **14**, 2111–2115 (2014). doi: 10.1021/nl500766j; pmid: 24641092
91. P.-A. Cazade, R. Hartkamp, B. Coasne, Structure and dynamics of an electrolyte confined in charged nanopores. *J. Phys. Chem. C* **118**, 5061–5072 (2014). doi: 10.1021/jp4098638
92. S. Kashyap, T. J. Woehl, X. Liu, S. K. Mallapragada, T. Prozorov, Nucleation of iron oxide nanoparticles mediated by Mms6 protein in situ. *ACS Nano* **8**, 9097–9106 (2014). doi: 10.1021/nn502551y; pmid: 25162493
93. M. H. Nielsen, J. R. I. Lee, Q. N. Hu, T. Y. J. Han, J. J. De Yoreo, Structural evolution, formation pathways and energetic controls during template-directed nucleation of $CaCO_3$. *Faraday Discuss.* **159**, 105–121 (2012). doi: 10.1039/c2fd20050c
94. M. H. Nielsen, S. Aloni, J. J. De Yoreo, In situ TEM imaging of $CaCO_3$ nucleation reveals coexistence of direct and indirect pathways. *Science* **345**, 1158–1162 (2014). pmid: 25190792
95. P. J. M. Smeets, K. R. Cho, R. G. E. Kempen, N. A. J. M. Sommerdijk, J. J. De Yoreo, Calcium carbonate nucleation driven by ion binding in a biomimetic matrix revealed by in situ electron microscopy. *Nat. Mater.* **14**, 394–399 (2015). doi: 10.1038/nmat4193; pmid: 25622001
96. T. J. Woehl *et al*., Correlative electron and fluorescence microscopy of magnetotactic bacteria in liquid: Toward in vivo imaging. *Sci. Rep.* **4**, 6854 (2014). doi: 10.1038/srep06854; pmid: 25358460
97. D. B. Peckys, N. de Jonge, Visualizing gold nanoparticle uptake in live cells with liquid scanning transmission electron microscopy. *Nano Lett.* **11**, 1733–1738 (2011). doi: 10.1021/nl200285r; pmid: 21410218
98. E. A. Ring, D. B. Peckys, M. J. Dukes, J. P. Baudoin, N. de Jonge, Silicon nitride windows for electron microscopy of whole cells. *J. Microsc.* **243**, 273–283 (2011). doi: 10.1111/j.1365-2818.2011.03501.x; pmid: 21770941
99. M. J. Dukes, D. B. Peckys, N. de Jonge, Correlative fluorescence microscopy and scanning transmission electron microscopy of quantum-dot-labeled proteins in whole cells in liquid. *ACS Nano* **4**, 4110–4116 (2010). doi: 10.1021/nn1010232; pmid: 20550177
100. D. B. Peckys, U. Korf, N. de Jonge, Local variations of HER2 dimerization in breast cancer cells discovered by correlative fluorescence and liquid electron microscopy. *Sci. Advances* **1**, e1500165 (2015). doi: 10.1126/sciadv.1500165
101. D. B. Peckys, J.-P. Baudoin, M. Eder, U. Werner, N. de Jonge, Epidermal growth factor receptor subunit locations determined in hydrated cells with environmental scanning electron microscopy. *Scientific Reports* **3**, 2626 (2013). doi: 10.1038/srep02626; pmid: 24022088
102. E. S. Pohlmann *et al*., Real-time visualization of nanoparticles interacting with glioblastoma stem cells. *Nano Lett.* **15**, 2329–2335 (2015). doi: 10.1021/nl504481k; pmid: 25734907
103. D. B. Peckys, N. de Jonge, Liquid scanning transmission electron microscopy: Imaging protein complexes in their native environment in whole eukaryotic cells. *Microsc. Microanal.* **20**, 346–365 (2014). doi: 10.1017/S1431927614000099; pmid: 24548636
104. Q. Chen *et al*., 3D motion of DNA-Au nanoconjugates in graphene liquid cell electron microscopy. *Nano Lett.* **13**, 4556–4561 (2013). doi: 10.1021/nl402694n; pmid: 23944844
105. N. Mohanty, M. Fahrenholtz, A. Nagaraja, D. Boyle, V. Berry, Impermeable graphenic encasement of bacteria. *Nano Lett.* **11**, 1270–1275 (2011). doi: 10.1021/nl104292k; pmid: 21271738
106. J. Park *et al*., Direct observation of wet biological samples by graphene liquid cell transmission electron microscopy. *Nano Lett.* **15**, 4737–4744 (2015). doi: 10.1021/acs.nanolett.5b01636; pmid: 26065925
107. C. Wang, Q. Qiao, T. Shokuhfar, R. F. Klie, High-resolution electron microscopy and spectroscopy of ferritin in biocompatible graphene liquid cells and graphene sandwiches. *Adv. Mater.* **26**, 3410–3414 (2014). doi: 10.1002/adma.201306069; pmid: 24497051
108. S. M. Hoppe, D. Y. Sasaki, A. N. Kinghorn, K. Hattar, In-situ transmission electron microscopy of liposomes in an aqueous environment. *Langmuir* **29**, 9958–9961 (2013). doi: 10.1021/la401288g; pmid: 23886420
109. M. T. Proetto *et al*., Dynamics of soft nanomaterials captured by transmission electron microscopy in liquid water. *J. Am. Chem. Soc.* **136**, 1162–1165 (2014). doi: 10.1021/ja408513m; pmid: 24422495
110. F. A. Plamper *et al*., Spontaneous assembly of miktoarm stars into vesicular interpolyelectrolyte complexes. *Macromol. Rapid Commun.* **34**, 855–860 (2013). doi: 10.1002/marc.201300053; pmid: 23508924
111. M. Wojcik, M. Hauser, W. Li, S. Moon, K. Xu, Graphene-enabled electron microscopy and correlated super-resolution microscopy of wet cells. *Nat. Commun.* **6**, 7384 (2015). doi: 10.1038/ncomms8384; pmid: 26066680
112. A. Fukami, K. Fukushima, N. Kohyama, Observation technique for wet clay minerals using film-sealed environmental cell equipment attached to high-resolution electron microscope, in *Microstructure of Fine-Grained Sediments*, R. Bennett *et al*., Eds. (Springer New York, 1991), pp. 321–331.
113. K. Adachi, E. J. Freney, P. R. Buseck, Shapes of internally mixed hygroscopic aerosol particles after deliquescence, and their effect on light scattering. *Geophys. Res. Lett.* **38**, L13804 (2011). doi: 10.1029/2011GL047540
114. P. G. de Gennes, Wetting: Statics and dynamics. *Rev. Mod. Phys.* **57**, 827–863 (1985). doi: 10.1103/RevModPhys.57.827
115. S. Sadki, P. Schottland, N. Brodie, G. Sabouraud, The mechanisms of pyrrole electropolymerization. *Chem. Soc. Rev.* **29**, 283–293 (2000). doi: 10.1039/a807124a
116. S. Helveg *et al*., Atomic-scale imaging of carbon nanofibre growth. *Nature* **427**, 426–429 (2004). doi: 10.1038/nature02278; pmid: 14749826
117. B. K. Miller, P. A. Crozier, Analysis of catalytic gas products using electron energy-loss spectroscopy and residual gas analysis for operando transmission electron microscopy. *Microsc. Microanal.* **20**, 815–824 (2014). doi: 10.1017/S1431927614000749; pmid: 24815065
118. P. L. Gai, Development of wet environment TEM (wet-ETEM) for in situ studies of liquid-catalyst reactions on the nanoscale. *Microsc. Microanal.* **8**, 21–28 (2002). doi: 10.1017/S143192760201005X; pmid: 14710723
119. F. M. Ross, Controlling nanowire structures through real time growth studies. *Rep. Prog. Phys.* **73**, 114501–114522 (2010). doi: 10.1088/0034-4885/73/11/114501
120. R. Danev, K. Nagayama, Transmission electron microscopy with Zernike phase plate. *Ultramicroscopy* **88**, 243–252 (2001). doi: 10.1016/S0304-3991(01)00088-2; pmid: 11545320
121. P. Simon *et al*., Electron holography of biological samples. *Micron* **39**, 229–256 (2008). doi: 10.1016/j.micron.2006.11.012; pmid: 17374487

ACKNOWLEDGMENTS

The research described in this review was partially supported by the National Science Foundation under NSF-GOALI grants DMR-1310639 and CMMI-1129722. I acknowledge A. W. Ellis and M. C. Reuter of IBM for their technical assistance with the development of the liquid cell technique.

10.1126/science.aaa9886

RESEARCH ARTICLE SUMMARY

STRUCTURAL BIOLOGY

Structural basis of Nav1.7 inhibition by an isoform-selective small-molecule antagonist

Shivani Ahuja, Susmith Mukund, Lunbin Deng, Kuldip Khakh, Elaine Chang, Hoangdung Ho, Stephanie Shriver, Clint Young, Sophia Lin, J. P. Johnson Jr., Ping Wu, Jun Li, Mary Coons, Christine Tam, Bobby Brillantes, Honorio Sampang, Kyle Mortara, Krista K. Bowman, Kevin R. Clark, Alberto Estevez, Zhiwei Xie, Henry Verschoof, Michael Grimwood, Christoph Dehnhardt, Jean-Christophe Andrez, Thilo Focken, Daniel P. Sutherlin, Brian S. Safina, Melissa A. Starovasnik, Daniel F. Ortwine, Yvonne Franke, Charles J. Cohen, David H. Hackos,* Christopher M. Koth,* Jian Payandeh*

INTRODUCTION: Voltage-gated sodium (Nav) channels open and close ion-selective pores in response to changes in membrane potential, and this gating underlies the generation of action potentials. Nav channels are large membrane proteins that contain four peripheral voltage-sensor domains (VSD1–4) that influence the functional state of the central ion-conducting pore. Mutations within the nine human Nav channel isoforms are associated with migraine (Nav1.1), epilepsy (Nav1.1–1.3, Nav1.6), pain (Nav1.7–1.9), cardiac (Nav1.5), and muscle paralysis (Nav1.4) syndromes. Accordingly, Nav channel blockers are used for the treatment of many neurological and cardiovascular disorders. These drugs bind within the central pore domain and generally lack isoform selectivity owing to the high sequence conservation found among Nav channels, limiting their therapeutic utility. In this study, we focused on a recently identified class of isoform-selective small-molecule antagonists that target a unique binding site on the fourth voltage-sensor domain, VSD4. Here we report the structural determination of such small-molecule aryl sulfonamide antagonists in complex with human Nav1.7 VSD4. Our studies demonstrate how this important new class of gating modifier engages VSD4 to inhibit Nav channel activity through a "voltage-sensor trapping" mechanism.

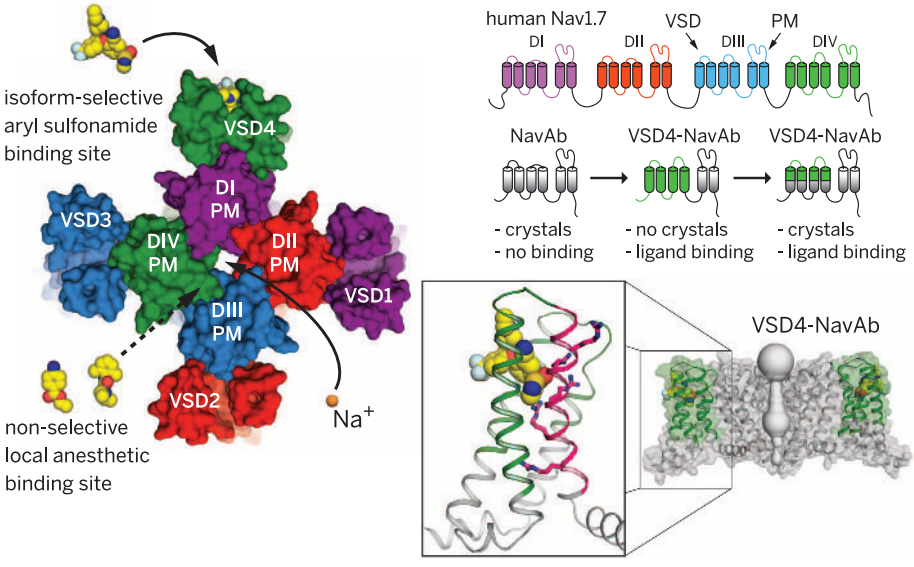

Drug binding sites in sodium channels. (**Left**) Top-view model of human Nav1.7. When open, sodium passes through the channel. Blocking drugs lacking isoform selectivity bind to a conserved site within the central pore. Isoform-selective inhibitors bind to a distinct site on VSD4. (**Right**) Strategy for Nav1.7 crystallography. Portions of Nav1.7 VSD4 were grafted onto a tetrameric channel (NavAb) and crystallized. (**Inset**) Side view of aryl sulfonamide binding site with the S4 helix and arginine gating charges highlighted pink.

RATIONALE: For structural studies, we devised a novel protein-engineering strategy that overcomes the technical complexities of producing full-length human Nav channels. Exploiting the evolutionary relationship between human and bacterial Nav channels, we fused portions of Nav1.7 VSD4 onto the bacterial channel NavAb. Using ligand-binding assays and alanine-scanning mutagenesis, we demonstrated that the antagonist binding site present in the human Nav1.7 channel is preserved within this human VSD4-NavAb chimeric channel. This chimeric construct allowed purification, crystallization, and structure determination of potent aryl sulfonamide antagonists in complex with the human Nav1.7 VSD4 binding site.

RESULTS: Functional studies using patch-clamp electrophysiology revealed that aryl sulfonamide inhibitors bind with high affinity to an isoform-selective and extracellularly accessible site on VSD4. These inhibitors show a high level of state dependence, potently blocking human Nav1.7 only when VSD4 is in its activated conformation. Our crystallographic studies revealed that the anionic warhead from the aryl sulfonamide inhibitors directly engages the fourth gating charge residue (R4) on the voltage-sensing S4 helix, effectively trapping VSD4 in its activated state. Isoform selectivity is achieved by inhibitor interactions with nonconserved residues found on the S2 and S3 transmembrane helices. The drug receptor site is partially submerged within the membrane bilayer, and a peripherally bound phospholipid was observed to form a tripartite complex with the antagonist and channel.

ON OUR WEB SITE

Read the full article at http://dx.doi.org/10.1126/science.aac5464

CONCLUSION: A new crystallization strategy has enabled the structural determination of VSD4 from human Nav1.7 in complex with potent, state-dependent, isoform-selective small-molecule antagonists. Mechanistically, inhibitor binding traps VSD4 in an activated conformation, which stabilizes a nonconductive state of the channel, and likely prevents recovery from inactivation. Unique phospholipid interactions and an exposed inhibitor binding site expand the importance of the membrane bilayer in ion channel biology. We anticipate that these structures will enable drug design efforts aimed at other voltage-gated ion channels and may accelerate the development of new treatments for pain that selectively target Nav1.7. ■

The list of author affiliations is available in the full article online.
*Corresponding author. E-mail: hackos.david@gene.com (D.H.H.); koth.christopher@gene.com (C.M.K.); payandeh.jian@gene.com (J.P.)
Cite this article as S. Ahuja *et al.*, *Science* **350**, aac5464 (2015). DOI: 10.1126/science.aac5464

RESEARCH ARTICLE

STRUCTURAL BIOLOGY

Structural basis of Nav1.7 inhibition by an isoform-selective small-molecule antagonist

Shivani Ahuja,[1]*† Susmith Mukund,[1]* Lunbin Deng,[2]‡ Kuldip Khakh,[3]‡ Elaine Chang,[3]‡ Hoangdung Ho,[1] Stephanie Shriver,[1] Clint Young,[3] Sophia Lin,[3] J. P. Johnson Jr.,[3] Ping Wu,[1] Jun Li,[4] Mary Coons,[1]§ Christine Tam,[1] Bobby Brillantes,[1] Honorio Sampang,[1] Kyle Mortara,[1] Krista K. Bowman,[1] Kevin R. Clark,[5] Alberto Estevez,[1] Zhiwei Xie,[3] Henry Verschoof,[3] Michael Grimwood,[6] Christoph Dehnhardt,[6] Jean-Christophe Andrez,[6] Thilo Focken,[6] Daniel P. Sutherlin,[4] Brian S. Safina,[4] Melissa A. Starovasnik,[1] Daniel F. Ortwine,[4] Yvonne Franke,[1] Charles J. Cohen,[3] David H. Hackos,[2]‖ Christopher M. Koth,[1]‖ Jian Payandeh[1]‖

Voltage-gated sodium (Nav) channels propagate action potentials in excitable cells. Accordingly, Nav channels are therapeutic targets for many cardiovascular and neurological disorders. Selective inhibitors have been challenging to design because the nine mammalian Nav channel isoforms share high sequence identity and remain recalcitrant to high-resolution structural studies. Targeting the human Nav1.7 channel involved in pain perception, we present a protein-engineering strategy that has allowed us to determine crystal structures of a novel receptor site in complex with isoform-selective antagonists. GX-936 and related inhibitors bind to the activated state of voltage-sensor domain IV (VSD4), where their anionic aryl sulfonamide warhead engages the fourth arginine gating charge on the S4 helix. By opposing VSD4 deactivation, these compounds inhibit Nav1.7 through a voltage-sensor trapping mechanism, likely by stabilizing inactivated states of the channel. Residues from the S2 and S3 helices are key determinants of isoform selectivity, and bound phospholipids implicate the membrane as a modulator of channel function and pharmacology. Our results help to elucidate the molecular basis of voltage sensing and establish structural blueprints to design selective Nav channel antagonists.

Voltage-gated sodium (Nav) channels conduct ionic currents that initiate action potentials in neurons and muscle cells. Consequently, Nav channels are the molecular targets of neurotoxins, clinically relevant drugs, and disease-causing mutations (*1*, *2*). Nav and voltage-gated calcium (Cav) and potassium (Kv) channels share a conserved architecture with a central ion-conducting pore module surrounded by four voltage-sensing domains (VSDs) (*2*, *3*). These remarkable proteins open and close ion-selective pores in response to small changes in membrane voltage, and their orchestrated gating underlies the generation of action potentials. In accordance with their specialized role in electrical signaling, Nav channels display rapid activation and fast inactivation properties (*1*, *2*). However, fundamental questions about their structure, pharmacological modulation, and functional relationship with the membrane bilayer persist.

Humans express nine closely related Nav channel isoforms (Nav1.1–1.9) that are differentiated by unique functional characteristics and tissue distribution patterns (*4*). The Nav1.7 channel is found almost exclusively in the peripheral nervous system, where it is highly expressed in olfactory epithelium, sympathetic ganglion, and dorsal root ganglion sensory neurons (*5*). Gain-of-function mutations in Nav1.7 are associated with extreme pain disorders (*6*, *7*), whereas loss-of-function mutations cause congenital insensitivity to pain in individuals who are otherwise free of motor or cognitive impairment (*8*, *9*). These contrasting phenotypes identify Nav1.7 as a key target in the pain perception pathway and have motivated intense efforts to develop selective inhibitors that are expected to overcome the liabilities of current analgesics.

The inherent complexity of mammalian Nav channels limits our ability to pursue crystallographic studies because these proteins contain a large pore-forming α subunit (~2000 residues) that undergoes extensive post-translational modification and associates with auxiliary subunits (*2*–*4*). By contrast, high-resolution structures of the biochemically more tractable homotetrameric Kv and bacterial Nav channels have been determined (*10*–*14*). Compared to Kv1.2 (*11*), the NavAb channel from *Arcobacter butzleri* has revealed distinct structural characteristics suggested to be shared with its human counterparts (*12*, *13*). However, experimental structures of mammalian Nav channels will be essential to understanding their distinctive functions, complex pharmacology, and precise relationship to bacterial Nav channels (*3*).

Architecturally, the α subunit of a mammalian Nav channel contains 24-transmembrane (TM) segments linked in four homologous domains (DI–DIV), where each domain contains six TM segments (S1–S6) (*2*, *4*). The S1–S4 segments form the four peripheral voltage-sensing domains (VSDs), which are distinct in primary sequence (VSD1–4). Each VSD is capable of sensing changes in the membrane voltage by virtue of positively charged arginine residues conserved along the S4 helix, and it is believed that the S4 helix translates within the VSD during voltage sensing (*15*, *16*). The S5 and S6 segments associate to form the ion-conducting pore module (PM) that scaffolds the selectivity filter and holds two pharmacologically important vestibules. The outer vestibule contains the binding sites for pore-blocking neurotoxins like tetrodotoxin (*17*), whereas the inner vestibule houses the therapeutically relevant local anesthetic receptor site (*18*).

All Nav channel inhibitors currently used in the clinic bind within the inner vestibule to prevent sodium conductance (*19*, *20*). Although block is state-dependent and generally thought to stabilize inactivated states of the channel (*21*–*23*), these inhibitors lack molecular selectivity among the Nav1.1–1.9 isoforms owing to the high sequence conservation found within the PM (*3*, *4*). Isoform-selective peptide toxins that target the outer vestibule are known (*24*, *25*), but these inhibitors lack state dependence and are unsuitable for oral dosing. To date, efforts to identify drugs with higher therapeutic index that target a receptor site offering improved isoform selectivity have failed (*26*, *27*). In this respect, peptide toxins that target the VSDs of Nav channels have generated considerable interest because these so-called gating modifiers profoundly affect the activation or inactivation properties of the channel (*28*, *29*), and isoform-selective toxins have been identified (*30*). Unfortunately, gating modifier toxins typically display poor drug-like properties, and clinical efficacy with these VSD-targeting molecules has yet to be demonstrated in humans.

A recent breakthrough study reported an aryl sulfonamide antagonist (PF-04856264) that binds to VSD4 and demonstrates molecular selectivity for human Nav1.7 over a subset of other Nav channel isoforms (*31*). Here, we describe the structural basis of Nav1.7 inhibition by this class of small-molecule antagonist using x-ray crystallography, and thus present important experimental structures of a small-molecule gating modifier in complex with a voltage-gated ion channel. Our study reveals the details of how an isoform-selective

[1]Department of Structural Biology, Genentech Inc., South San Francisco, CA 94080, USA. [2]Department of Neuroscience, Genentech Inc., South San Francisco, CA 94080, USA. [3]Department of Biology, Xenon Pharmaceuticals Inc., Burnaby, British Columbia, V5G 4W8, Canada. [4]Department of Discovery Chemistry, Genentech Inc., South San Francisco, CA 94080, USA. [5]Department of Biochemical and Cellular Pharmacology, Genentech Inc., South San Francisco, CA 94080, USA. [6]Department of Chemistry, Xenon Pharmaceuticals Inc., Burnaby, British Columbia, V5G 4W8, Canada.
*These authors contributed equally to this work. †Present address: Vollum Institute, Portland, OR 97239, USA. ‡These authors contributed equally to this work. §Present address: Caribou Biosciences, Berkeley, CA 94710, USA. ‖Corresponding author. E-mail: hackos.david@gene.com (D.H.H.); koth.christopher@gene.com (C.M.K.); payandeh.jian@gene.com (J.P.)

antagonist binds to VSD4 in a membrane environment to inhibit Nav1.7 (movie 1), and therefore highlights VSDs as untapped potential therapeutic targets (*32*–*34*). To enable these unique mammalian Nav channel crystal structures, we exploited the established portability of VSDs (*11*, *35*–*37*) and the presumed structural relatedness between human and bacterial Nav channels (*3*) to develop a robust protein production and crystallization strategy.

Characterization of small-molecule Nav1.7-selective gating modifiers

To investigate the nature of Nav1.7 inhibition by the aryl sulfonamide class of antagonists like PF-04856264, GX-674, and GX-395 (Fig. 1A) (*31*, *38*), we performed patch-clamp analysis of human Nav channels expressed in human embryonic kidney 293 (HEK293) cells. Using a representative compound of this class, GX-674, and a voltage protocol that allows Nav1.7 current measurements at both hyperpolarizing and depolarizing holding

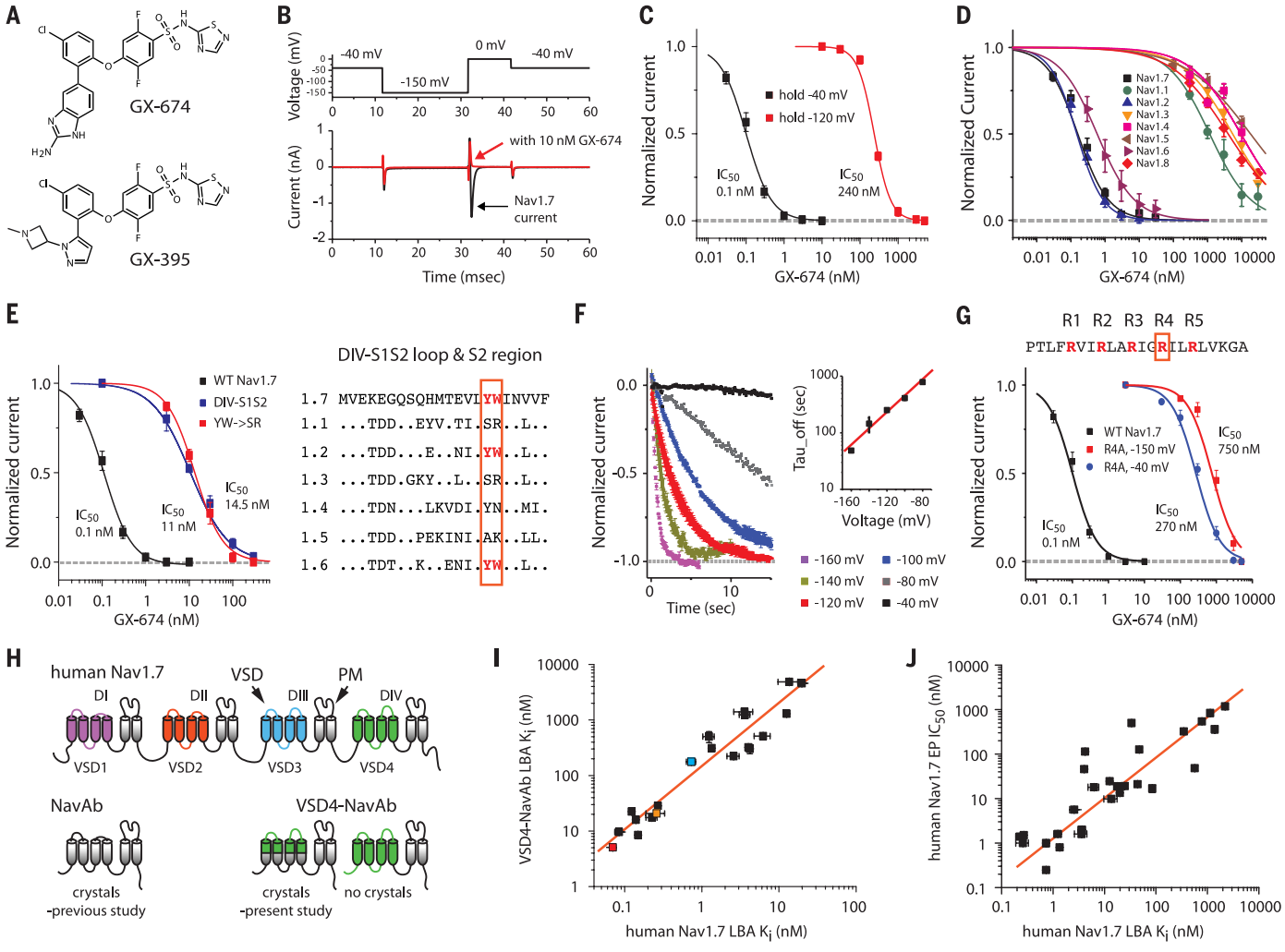

Fig. 1. Aryl sulfonamides inhibit native Nav1.7 and bind to chimeric VSD4-NavAb channels with high affinity. (**A**) Chemical structures of GX-674 and GX-395. GX-674 was found to have favorable properties for easier use in electrophysiological experiments. (**B**) Standard voltage protocol used for IC_{50} studies of human Nav1.7 (see Methods for further details). To enable current measurements at both hyperpolarizing and depolarizing holding voltages, a short 20-ms pulse to –150 mV was used to recover channels from inactivation, followed by a 10-ms pulse to 0 mV to open unblocked channels, which we repeated at 1-Hz frequency. Current traces using this voltage protocol are shown both in the absence (black) and presence (red) of 10 nM GX-674. (**C**) Dose-response curves of GX-674 on human Nav1.7 at holding potentials of –40 and –120 mV. For all electrophysiology data: $n \geq 3$, error bars indicate SEM, and IC_{50}'s are calculated with the Hill function. (**D**) Potency of GX-674 inhibition on a panel of human Nav channels (see Methods for further details). (**E**) A DIV-S1S2-Nav1.1 chimera and Y1537S/W1538R mutants in Nav1.7 VSD4 reduce GX-674 potency compared to wild-type Nav1.7 channels [see (B), holding voltage of –40 mV for each channel]. A sequence alignment between human Nav isoforms shows the S1-S2 loop and extracellular S2 region within VSD4. (**F**) Measurement of the off-rate following complete block with 10 nM GX-674 demonstrates a high degree of voltage dependence. Peak Nav current was measured over time with our standard voltage protocol (B), but at a frequency of 0.2 Hz and with more hyperpolarizing holding voltages as indicated. Time constants are shown in the inset. (**G**) The R1608A (R4A) mutation reduces the potency and state-dependence of block [see (B)]. The amino acid sequence of VSD4 S4 is shown for reference. (**H**) Domain architecture of the human Nav1.7 pore-forming α subunit and the simplier homotetrameric NavAb bacterial channel are illustrated. A schematic of the VSD4-NavAb chimeric channels used in the present study is also shown (sequence details found in fig. S3 and Methods). (**I**) A panel of 20 diverse aryl sulfonamide compounds were studied by radioligand-binding assays using [^{3}H]GX-545 on the native human Nav1.7 channel and the crystallization construct VSD4-NavAb (see fig. S3C and Methods for construct details). Select compounds used throughout this study are highlighted: [^{3}H]GX-545 (red), GX-674 (blue), and GX-936 (orange). The solid line indicates a linear regression to the observed data with a correlation coefficient of 0.956. (**J**) A panel of 28 diverse aryl sulfonamides were studied on the full-length human Nav1.7 channel using either radioligand binding with [^{3}H]GX-545 and automated patch-clamp electrophysiology. The solid line indicates a linear regression to the observed data with a correlation coefficient of 0.868. The full list of compounds used to generate the data presented in (I) and (J) are shown in tables S1 and S2.

voltages (Fig. 1B and fig. S1, A to C), we observed potent inhibition when GX-674 binding was equilibrated at −40 mV [half-maximal inhibitory concentration (IC_{50}) = 0.1 nM; Fig. 1C], a membrane voltage that promotes steady-state inactivation of Nav1.7. By contrast, GX-674 inhibition was weaker by a factor of 2400 at −120 mV (Fig. 1C), a voltage that promotes a resting closed state of the channel. A similar state dependence of block has been observed by local anesthetics that bind within the conserved inner vestibule of Nav channels (*19*), but unlike local anesthetics, GX-674 shows substantial Nav subtype selectivity, inhibiting Nav1.7 with much higher potency than most other Nav isoforms: Nav1.7 ~ Nav1.2 > Nav1.6 >> Nav1.1 > Nav1.8 > Nav1.3 > Nav1.4 ~ Nav1.5 (Fig. 1D). Notably, the potency of GX-674 for Nav1.7 is 100,000 times greater than that of the cardiac isoform Nav1.5 (*4*), which is a desirable property for cardiac safety and a level of selectivity unseen among local anesthetics.

Previous studies have shown that PF-04856264 and related aryl sulfonamides interact with the extracellular surface of VSD4 (*31*). To evaluate this conclusion, we first studied GX-395 (Fig. 1A) and its membrane-impermeant quaternary amine derivative GX-626, and observed that both compounds had similar potency and kinetics of Nav1.7 inhibition when applied extracellularly (fig. S2, A to C). In contrast to the membrane-impermeant local anesthetic QX-314 (*18*), GX-626 failed to inhibit Nav1.7 upon intracellular application (fig. S2D), pointing to an extracellular interaction site on the channel. To further validate the binding site of GX-674, we generated a Nav1.7 chimera in which the extracellular S1-S2 loop region of VSD4 was replaced with Nav1.1 sequence, which resulted in a factor of 100 decrease in potency (Fig. 1E). Indeed, modifying only two residues on the predicted extracellular side of the S2 helix to Nav1.1 or Nav1.3 equivalents (Y1537S/W1538R; Fig. 1E) resulted in a reduction in GX-674 potency by more than a factor of 100, pinpointing important determinants of isoform-selectivity on the extracellular face of VSD4 (fig. S3A). We also found that complete inhibition of Nav1.7 by GX-674 at −40 mV could be subsequently relieved by applying strong hyperpolarizing voltages (Fig. 1F and fig. S1D), suggesting a voltage-dependent deformation of the small-molecule receptor site. Because cysteine accessibility studies have demonstrated that gating charges can translocate from the intracellular side to the extracellular side of VSD4 during activation (*39*), we considered that Nav1.7 inhibition might involve an interaction between the negatively charged aryl sulfonamide warhead (Fig. 1A) and a positively charged S4 arginine side chain (Fig. 1G). Mutagenesis revealed that the R1608A (R4A) substitution decreased GX-674 potency by a factor of 3000 (Fig. 1G), indicating that R4 may translocate into the extracellular cleft of VSD4 during channel activation and make direct contact with GX-674. Consistent with this hypothesis, R4 is necessary for the state dependence of GX-674 inhibition, because this characteristic is almost completely eliminated in the R4A mutant channel (Fig. 1G).

Our data collectively indicate that GX-674 binds to a high-affinity, isoform-selective, and extracellularly accessible site on VSD4. Because GX-674 potently inhibits Nav1.7 only when VSD4 is in an activated conformation (Fig. 1C) and strong hyperpolarizations disrupt the receptor site (Fig. 1F and fig. S1D), we propose that binding of GX-674 opposes VSD4 deactivation. Since VSD4 activation is necessary and sufficient to produce fast inactivation (*16*, *40*), GX-674 binding may promote or stabilize an inactivated state of Nav1.7 through a VSD4-based voltage-sensor trapping mechanism. This mechanism is distinct from the α-scorpion and sea anemone gating modifier toxins that also bind to the surface of VSD4, because these toxins stabilize a deactivated conformation of VSD4 and slow the rate of fast inactivation (*28*, *41*). Moreover, and in contrast to canonical peptide gating modifiers like Protoxin-II that inhibit Nav channels but still allow some level of channel activation (*42*), GX-674 effectively abolishes channel activation between −80 mV and +60 mV when bound to Nav1.7 (fig. S4, A to D).

Protein engineering enables crystallization of Nav1.7 VSD4

To further understand the mechanism by which aryl sulfonamides antagonize Nav channels, we sought to determine crystal structures of human Nav1.7 VSD4 in complex with representative inhibitors. Because VSDs are modular protein domains that can be transferred en masse or in part onto distantly related channels while retaining their functional, pharmacological, and structural properties (*11*, *35*–*37*, *43*), we reasoned that the bacterial NavAb channel might facilitate the expression, purification, and crystallization of VSD4 and overcome the formidable challenges of producing full-length Nav1.7 for crystallization studies. The extracellular VSD loops in existing NavAb structures lack direct crystal contacts (*12*, *13*), suggesting that large sequence changes might be readily tolerated (fig. S5, A and B). The NavAb PM also forms a dominant crystal contact that we hoped would nucleate crystal growth (fig. S5C).

We began by replacing the NavAb VSD with each of the four VSDs from human Nav1.7, leaving the S4-S5 linker and PM of NavAb intact (Fig. 1H and fig. S3B). Because we were unable to record reliable voltage-activated Na^+ currents from these channels, we synthesized a suitable tritiated aryl sulfonamide compound, [^{3}H]GX-545, to enable affinity measurements utilizing radioligand binding assays. Membranes containing the VSD4-NavAb channel bound the [^{3}H]GX-545 radioligand with high affinity [dissociation constant (K_d) = 4 nM], whereas the VSD1, VSD2, and VSD3-NavAb chimeras showed low specific binding (K_d ≥30 nM), comparable to that of the parental NavAb channel (fig. S6). A strong linear correlation was observed between the VSD4-NavAb chimera and the native Nav1.7 channel when comparing the K_i's of 20 structurally diverse GX-series aryl sulfonamide compounds (Fig. 1I and tables S1 and S2). Notably, a strong correlation between functional channel inhibition and radioligand binding was also observed on the native Nav1.7 channel (Fig. 1J and tables S1 and S2), validating our use of [^{3}H]GX-545 binding to assess the degree to which the relevant receptor site is maintained within our chimeric constructs. We conclude that the high-affinity, Nav1.7-selective antagonist receptor site has been preserved within our VSD4-NavAb chimera.

The VSD4-NavAb chimera could be readily purified with a recovery yield of 5 mg/liter from insect cell culture, >1000-fold higher than expected for the native Nav1.7 channel; however, this VSD4-NavAb construct did not yield crystals. We hypothesized that removal of a minor crystal contact (fig. S5B) was precluding crystallization and engineered a channel in which a small intracellular portion of the NavAb VSD was reintroduced. The extracellular portion of VSD4 was left completely intact (Fig. 1H and fig. S3C), and the binding affinity of [^{3}H]GX-545 did not change (K_d = 4 nM; Fig. 1I and fig. S6), critically indicating that the protein engineering required to crystallize this human-bacterial VSD chimera does not perturb the GX-compound receptor site. This hybrid channel crystallized from a phosphatidylcholine-based bicelle system only in the presence of a potent aryl sulfonamide antagonist, and our best diffracting crystals were obtained in complex with GX-936. The GX-936-VSD4-NavAb structure was phased by molecular replacement using the available high-resolution model of NavAb (*12*) and refined to 3.53 Å resolution (table S3), with electron density maps of high quality (fig. S7). Crystal structures of VSD4-NavAb in complex with GX-629 (3.85 Å) and GX-674 (4.5 Å) have also been obtained (tables S1 and S3), and these are both highly similar to the GX-936 complex detailed below (fig. S8).

Structure of Nav1.7 VSD4-NavAb channels in a membrane environment

The VSD4-NavAb chimera displays the domain-swapped arrangement expected for a voltage-gated ion channel (*11*, *12*), and 22 phospholipids are seen bound to the channel, suggesting the maintenance of a native membrane-like environment (fig. S9, A and B). Crystal contacts are not observed between the Nav1.7-substituted portions of VSD4, implying that a relatively unconstrained conformation of the VSD has been captured (fig. S9, C and D). Despite replacing most of the NavAb VSD (Fig. 2A and fig. S3C), surface complementarity with the PM remains high, underscoring the noted sequence conservation between NavAb and human Nav channels (*12*, *13*). As seen in previous NavAb structures (*12*, *13*), the ion-conducting PM of the VSD4-NavAb chimeric channel is closed, consistent with a nonconductive or inactivated state.

During crystallographic refinement, strong residual electron density within the extracellular cleft of VSD4 allowed us to unambiguously position GX-936 (Fig. 2B). Unexpectedly, GX-936 is submerged below the membrane-aqueous interface, and a portion of the compound protrudes into the lipid bilayer (Fig. 2A). To corroborate the binding mode of GX-936, a bromide-substituted derivative (GX-629) was cocrystallized with VSD4-NavAb and analyzed through a single-wavelength anomalous

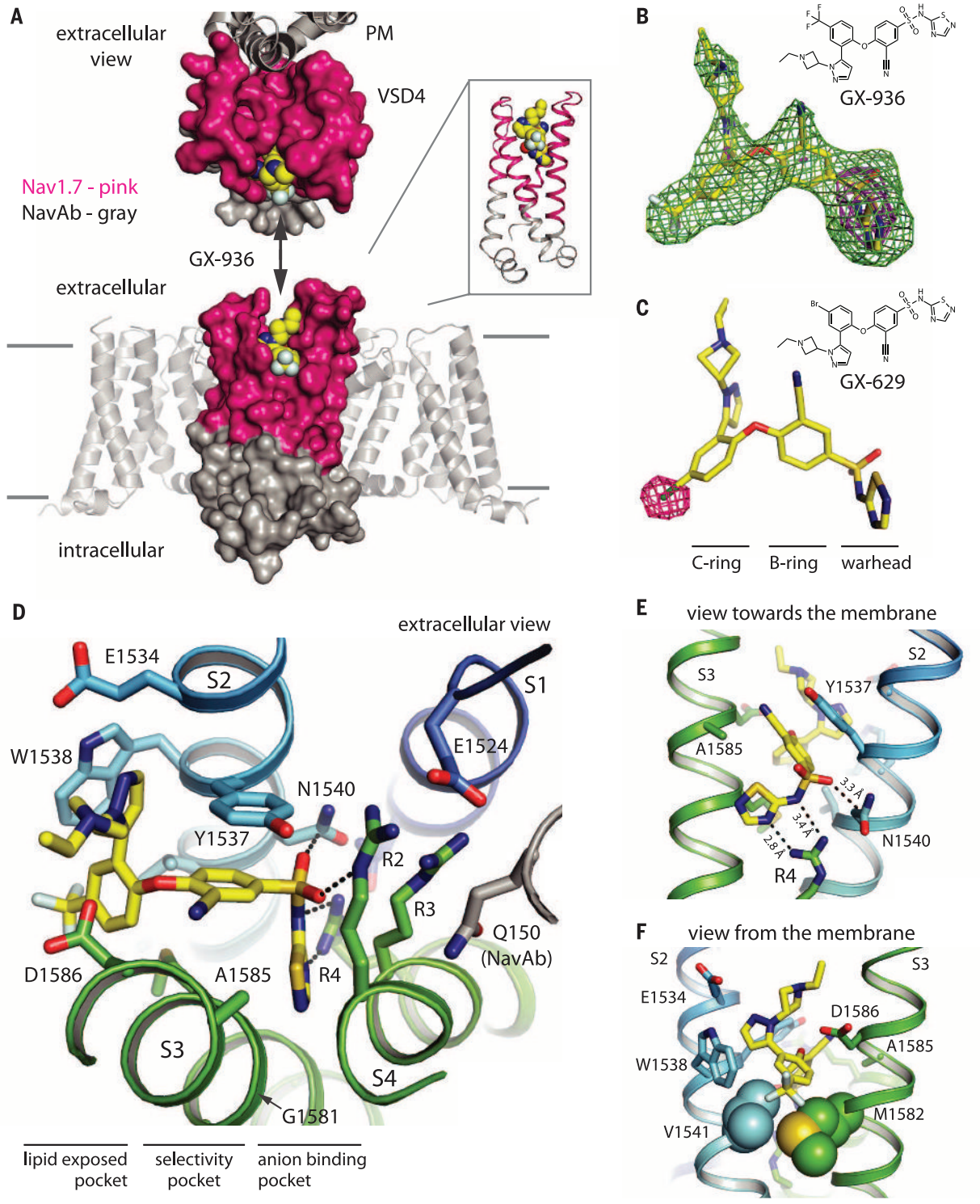

Fig. 2. Crystal structure of the Nav1.7 VSD4-NavAb channel in complex with GX-936. (**A**) A single VSD from the homotetrameric Nav1.7 VSD4-NavAb channel is shown in surface representation with GX-936 rendered in spheres. Grafted portions of human Nav1.7 VSD4 are highlighted in pink (see fig. S3C) and also shown in ribbon representation (inset). (**B**) $F_o - F_c$ map calculated to 3.53 Å before GX-936 was modeled, shown with the final refined coordinates of GX-936. Purple mesh contoured at 5.0 σ; green mesh contoured at 2.75 σ. (**C**) Anomalous difference Fourier map calculated to 3.85 Å from data at the Br absorption edge (λ = 0.9199 Å) contoured at 6 σ shown with the final refined coordinates of GX-629. (**D**) Nav1.7 VSD4 aryl sulfonamide receptor site is shown with select side chains rendered as sticks. Dashed lines represent ionic, hydrogen bonding, and electrostatic interactions between GX-936 and VSD4. Notably, Q150 from the NavAb PM S5 (gray) aligns with Q265 from DI S5 of human Nav1.7. (**E**) Side view highlighting key interactions with the GX-936 warhead. (**F**) V1541 and M1582 side chains forming the hydrophobic floor are shown in sphere representation; view is 180° relative to (E).

dispersion experiment (Fig. 2C). Similarly, a selenomethionine-incorporated protein crystal (4.35 Å) was used to landmark the five newly introduced methionine side chains from Nav1.7 VSD4 found around GX-936 (figs. S3C and S10 and table S3). Overall, these results unequivocally confirm the extracellular accessibility of the aryl sulfonamide binding site on Nav1.7 and the portability of the VSD4 receptor site onto NavAb.

Structural determinants of GX-936 binding to Nav1.7 VSD4-NavAb

Reminiscent of a Venus flytrap, the S1-S2 and S3-S4 helices from VSD4 form a clamshell-like structure that closes over GX-936 (Fig. 2, A and D). Human Nav1.7 residues completely engulf GX-936, whereas not a single NavAb side chain makes contact (Fig. 2A). This key result validates our experimental approach and allows us to define the structural determinants of this isoform-selective receptor site (movie 1). Upon inspection, the binding site of GX-936 and related aryl sulfonamides in Nav1.7 VSD4 can be divided into three regions: an anion-binding pocket, a selectivity pocket, and a lipid-exposed pocket (Figs. 2D and 3A).

The anionic warhead of GX-936 bisects VSD4 and sits deep within the extracellular cleft where the R4 gating charge (R1608) demarks the bottom of the anion-binding pocket (Figs. 2, D and E, and 3A). The guanidinium group of R4 engages the delocalized charge of the aryl sulfonamide thiadiazole headgroup through a bidentate salt bridge, which landmarks the interaction (Fig. 2, D and E). As anticipated by our electrophysiological studies, this pivotal gating charge–warhead interaction can rationalize the state dependence of GX-674 inhibition (Fig. 1, C, F, and G) because R4 will only be exposed to the extracellular side of the VSD when the membrane is sufficiently depolarized (*39*). The R3 gating charge (R1605) lines the front of the anion-binding pocket where its aliphatic portion makes van der Waals contact with GX-936 (Fig. 2D). R2 (R1602) engages the sulfonamide group of GX-936 from above through its ε-nitrogen, and the N1540 side chain (from S2) makes an electrostatic interaction with the adjacent sulfonamide oxygen (Fig. 2, D and E). All of the interactions that pin the anionic warhead into the anion-binding pocket arise from residues that are strictly conserved in human Nav channels (fig. S3A), suggesting that the determinants of Nav1.7 (as well as Nav1.2 and Nav1.6) molecular selectivity stem from elsewhere in the receptor site.

The selectivity pocket in the VSD4 receptor site is lined by the S2 and S3 helices, consistent with physiological studies that point toward the Y1537 and W1538 side chains as major determinants of isoform selectivity (Fig. 1E) (*31*). Y1537 (S2) forms a roof over the benzonitrile ring of GX-936 through a π-stacking interaction, while W1538 (S2) buttresses the pyrazole ring and walls off a portion of the selectivity pocket from the lipid bilayer (Fig. 2, D to F). Underneath GX-936, the V1541 (S2) and M1582 (S3) side chains form a hydrophobic floor that supports the trifluoromethylphenyl and benzonitrile rings through van der Waals contacts (Fig. 2F). Although E1534 (S2) and D1586 (S3) seem poised to make contact with the azetidine group of GX-936, neither side chain forms a direct interaction (≥3.9 Å; Fig. 2, D and F). By contrast, the small side chains of G1581 (S3) and A1585 (S3) provide good complementarity around GX-936 to allow closure of the VSD4 clamshell (Fig. 2, D and E). Consistent with sequence differences between Nav channel isoforms (fig. S3A), these first-shell S2 and S3 residues appear to present the molecular logic for binding specificity of the aryl sulfonamide antagonists to Nav1.7 (Fig. 1, D and E).

A lipid-exposed pocket is found in the VSD4 receptor site where the floor of the aryl sulfonamide-binding site sits 5 to 10 Å below the membrane-aqueous interface, judging by the positions of

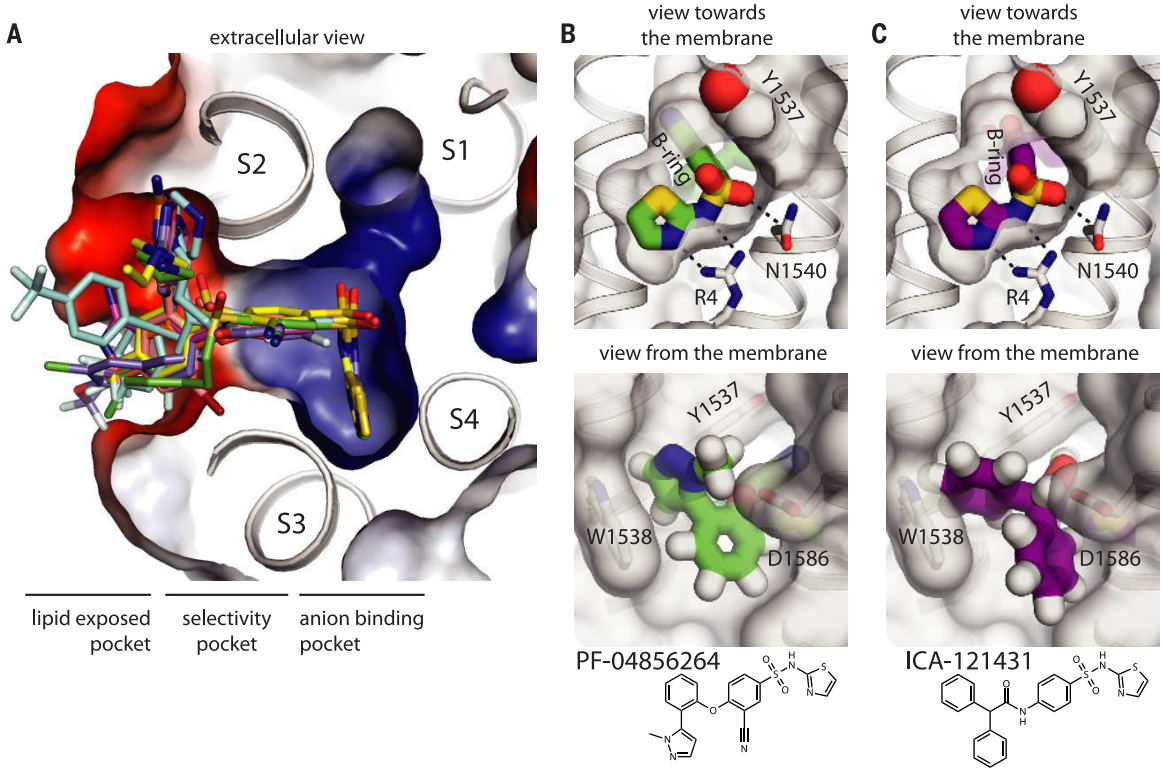

Fig. 3. Determinants of aryl sulfonamide isoform selectivity revealed by docking analyses in Nav1.7 VSD4-NavAb. (**A**) A selection of Nav channel inhibitors of the aryl sulfonamide class (fig. S11) are shown in their lowest-energy docked conformations superimposed onto the experimental coordinates of the GX-936-VSD4-NavAb crystal structure. GX-936 is shown in yellow sticks for reference. An electrostatic surface of the VSD4 binding site is shown: blue, basic regions; red, acidic regions; white, hydrophobic regions. Approximate boundaries of the lipid-exposed pocket, selectivity pocket, and anion-binding pocket are also indicated. The view is sectioned within the plane of the membrane, and bound lipids are omitted for clarity. (**B**) Docking of the Nav1.7 isoform-selective inhibitor, PF-04856264 (green stick representation), shows high correspondence to the position of GX-936 in the x-ray structure. (**C**) Docking of the Nav1.3/Nav1.1 isoform-selective inhibitor ICA-121431 (purple stick representation) indicates that formation of the favorable R4-warhead interaction leads to multiple unfavorable clashes with side chains in the Nav1.7 VSD4 receptor site (Y1537, W1538, and D1586) that are not conserved in Nav1.3/Nav1.1. For clarity, hydrogens are only represented in lower panels in order to best appreciate the fit (B) or steric clashes (C) of the respective compounds shown in this docking analysis.

annular phospholipids bound around the VSD4-NavAb channel (fig. S9, A and B). The trifluoromethylphenyl group of GX-936 points into the lipid-exposed pocket and makes limited protein contact (Fig. 2, A, D, and F, and Fig. 3A), presumably contributing little to the isoform selectivity profile of these antagonists. Direct exposure of GX-936 to the bilayer suggests a possible membrane-access mechanism for inhibitor binding to VSD4, which is intriguing because gating modifier toxins have also been shown to partition into the membrane (*44*–*48*). This result highlights an emerging concept that drugs may gain access to their binding sites on disparate channels or receptors through the membrane bilayer (*12*, *21*, *49*–*53*).

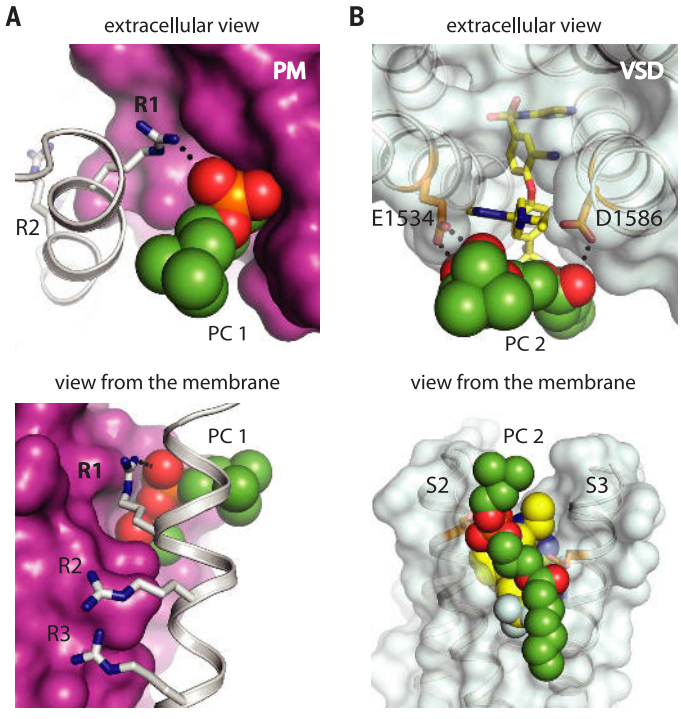

Fig. 4. Membrane phospholipids interact with Nav1.7 VSD4-NavAb and GX-936. (**A**) The R1 gating charge on S4 interacts with a phospholipid (PC1) phosphodiester group, as highlighted by a dashed line (~3.4 Å). The VSD4-NavAb channel was crystallized from a phosphatidylcholine (PC)–based bicelle system, and the extra electron density was well fit by a partial PC molecule (see Methods). (**B**) A partially modeled PC molecule (PC2) is observed beside the S2 and S3 helices. PC2 is coordinated to E1534 in all channel subunits in the asymmetric unit, and putatively coordinated to D1586 in two of the subunits within the asymmetric unit. Good surface complementarity between the PC2 and GX-936 is also observed. GX-936 is shown in yellow stick and sphere representation, and chain B of the VSD4-NavAb channel is shown in this panel.

VSD4 receptor site binding mode informs on selectivity

To explore the generality of the GX-936 binding mode beyond our GX-629 and GX-674 cocrystal structures (fig. S8 and tables S1 and S3), several inhibitors of the aryl sulfonamide class (*31*, *38*) were docked into the x-ray structure (Fig. 3 and fig. S11). For many compounds, including the Nav1.7 isoform-selective PF-04856264 (*31*), docking revealed a similar engagement of the anionic warhead with the R4 gating charge and a nearly perpendicular vector between the aryl sulfonamide moiety and the B-ring (Figs. 2D and 3, A and B, and fig. S11, A to I). These results highlight diverse substituents protruding into the lipid-exposed pocket (Fig. 3A) and suggest that a minimal pharmacophore may be required to engage Nav1.7. Our docking analysis supports the identification of two key selectivity motifs within VSD4 for Nav1.7-isoform–selective inhibitors like GX-674: YWxxV on S2 and GMxxA on S3 (Figs. 1, D and E, and 2, D to F, and fig. S3A). Accordingly, the Nav1.3-selective aryl sulfonamide ICA-121431 (*31*) could not be favorably docked into the Nav1.7 VSD4 receptor site, owing to clashes of this compound's B-ring and bulky biphenyl substitution on the C-ring with side chains from the YWxxV motif on S2 and D1586 on S3, respectively (Fig. 3C and fig. S11J).

Bound phospholipids surround the GX-936-VSD4-NavAb complex

The membrane bilayer has an increasingly recognized role in the function of voltage-gated ion channels, and the phosphodiester-containing headgroups of lipids are essential for voltage-dependent gating (*54*, *55*). We have assigned a

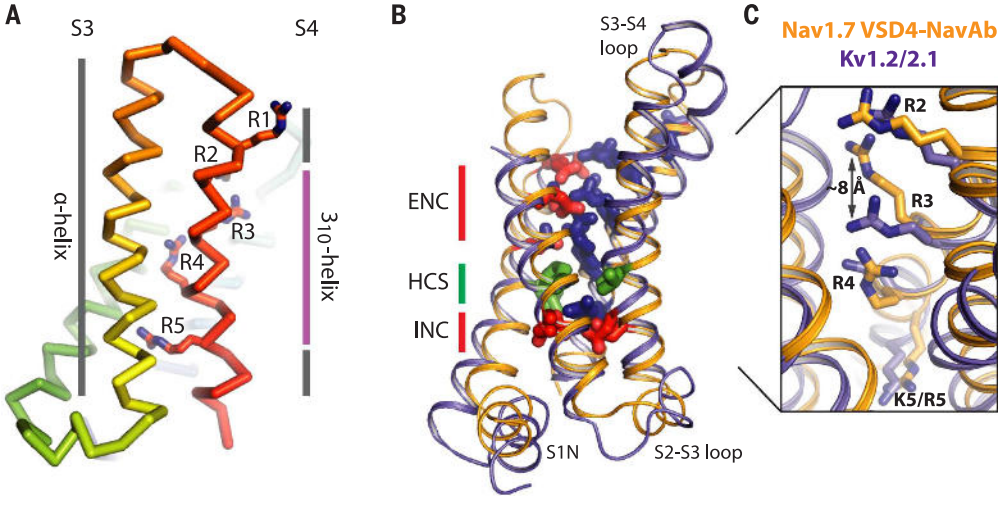

Fig. 5. GX-936 traps Nav1.7 VSD4 in an activated conformation. (**A**) Ribbon diagram representation of VSD4-NavAb highlights a 3_{10}-helical conformation extending across the middle of the S4 segment. By comparison, the S3 helix exists in an entirely α-helical conformation. GX-936 is omitted for clarity. (**B**) Superposition of Nav1.7 VSD4-NavAb (orange) with the rat Kv1.2/2.1 channel VSD (purple; PDB 2R9R) highlights their overall structural likeness and conformational similarity. Gating charges and residues from the conserved extracellular negative charge cluster (ENC), hydrophobic constriction site (HCS), and intracellular negative charge cluster (INC) regions are shown in stick representations and colored purple, red, green, and red, respectively. GX-936 in VSD4 and the S1-S2 loop in Kv1.2/2.1 are omitted for clarity. (**C**) Zoom-in view highlights the close spatial correspondence between gating charges in VSD4-NavAb (orange) and Kv1.2/2.1 (purple).

number of electron densities within the GX-936-VSD4-NavAb structure as phosphatidylcholine (PC) molecules, in part, because this channel was crystallized in the presence of high concentrations of PC (see Methods). We find that the outermost R1 gating charge (R1599) in VSD4 forms an ion-pair interaction with the phosphodiester group of a glycerophospholipid (PC 1) that is nestled between the VSD and PM (Fig. 4A, movie 2, and fig. S9E). Although direct contact between an S4 arginine and a lipid headgroup has not been seen in previous Kv or bacterial Nav channel structures (*10*–*14*), our crystallographic observations clearly support the view that gating charges can make compensating interactions with phospholipids to stabilize different gating states of the VSD and channel (*54*–*56*).

The precise composition of the membrane bilayer also influences Nav channel pharmacology in important ways. Some gating modifier toxins are known to partition into lipid membranes (*44*–*48*), and early reconstitution studies with purified Nav channels established that distinct lipid mixtures are required to recover α-scorpion toxin binding (*57*). Enzymatic removal of sphingomyelin headgroups can also modulate the binding of gating modifier toxins through the disruption of a postulated ternary lipid-toxin-channel complex (*47*). However, it remains unknown if these reports of pharmacological modulation stem from direct or indirect lipid interactions with Nav channels. Here, we find strong electron density, unseen in previous NavAb structures (*12*, *13*), attributed to a bound phospholipid (PC 2) buttressing the GX-936 binding site (Fig. 4B, movie 3, and fig. S9F). This peripherally bound lipid covers ~200 Å^2 of GX-936 surface and forms specific interactions with side chains from the S2 and S3 helices (E1534 and D1586, respectively; Fig. 4B and movie 3). Our experimental observation of a lipid-antagonist-VSD4 ternary complex raises the distinct possibility that membrane lipids can directly modulate the structure and character of the VSD4 receptor site of Nav1.7 within cells.

Small-molecule gating modifiers trap VSD4 in an activated state

Unlike α-scorpion and sea anemone toxins that are known to impair VSD4 activation (*28*, *41*), our functional and structural studies suggest that compounds like GX-674 and GX-936 bind to the activated state of VSD4 (Fig. 1, C, F, and G, and fig. S8). When VSD4 is trapped in this state, four gating charges (R1–R4) are exposed to the extracellular cleft of VSD4, whereas R5 (R1611) remains engaged with the intracellular negative charge cluster (Fig. 5, A and B). A 3_{10}-helical

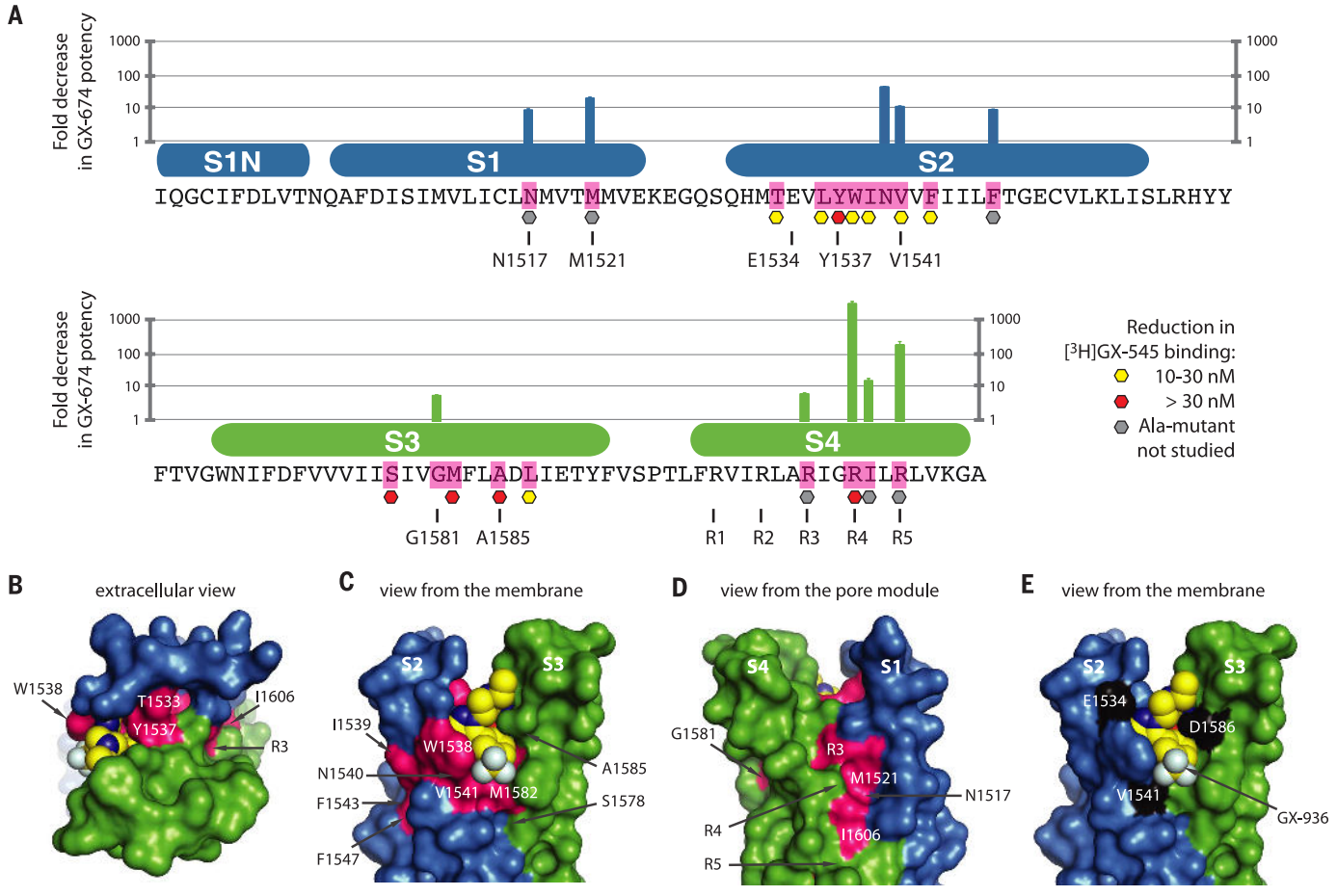

Fig. 6. Structural determinants of aryl sulfonamide binding and selectivity in Nav1.7 VSD4. (**A**) The native Nav1.7 VSD4 sequence is shown with data from a scanning mutagenesis study measured by electrophysiology using GX-674 on full-length human Nav1.7 channels (top, bar graph) or radioligand binding to chimeric VSD4-NavAb channels using [^{3}H]GX-545 (below, hexagonal symbols). Fold-reduction in GX-674 potency is measured relative to wild-type Nav1.7. A1585 was mutated to Phe for the [^{3}H]GX-545 study; and R3 was mutated to Gln for the GX-674 study (because R3A channels failed to generate currents sufficient for study). See Methods for experimental details and fig. S14 to S18 for the full extent of mutations studied. For electrophysiology data: $n \geq 3$; error bars indicate SEM. (**B** to **D**) Residue positions affecting IC_{50} and/or K_d from site-directed mutational scans of native Nav1.7 and chimeric VSD4-NavAb channels, respectively, are highlighted in pink and mapped onto a surface representation of VSD4-NavAb. The S1-S2 region is colored blue, the S3-S4 region is colored green, and GX-936 is shown in yellow sphere representation. (**E**) Three first-shell residues within 5 Å of contact of GX-936 that are not conserved among Nav1.7, Nav1.2, and Nav1.6 channel isoforms are highlighted in black. The similar potencies of GX-674 on the Nav1.7, Nav1.2, and Nav1.6 channel isoforms (Fig. 1D) suggest that these three side-chain positions might be exploited in future structure-based drug design efforts. In Nav1.7, the three residues in question are E1534, V1541, and D1586; whereas the equivalents in Nav1.2 are Asn, Leu, and Glu; and in Nav1.6 are Asn, Leu, and Asp (see fig. S3A).

conformation in S4 spans across R2–R5 (Fig. 5A), allowing these gating charges to form an interlaced interaction network that participates in closure of the VSD4 clamshell around GX-936–like compounds (movie 2).

The presence of a cocrystallized state-dependent inhibitor pharmacologically stabilizes an activated state of the VSD4 structure. Therefore, the pronounced resemblance between inhibitor-bound VSD4 and rat Kv1.2 VSD (*11*), where the spatial correspondence between equivalent gating charges is <1 Å, suggests a ubiquitous pathway for S4 activation (Fig. 5, B and C, and movie 4). Only R3 in VSD4 is laterally displaced to accommodate binding of the GX-936 warhead to R4 (Fig. 5C). Despite limited sequence identity (fig. S3D) or the presence of a small-molecule antagonist (Fig. 2), these structural observations imply that a shared conformation exists in the activated state of mammalian Nav and Kv VSDs (*58*) (movie 4).

Until now, it has been unclear to what extent the bacterial Nav channel VSDs resemble the four mammalian Nav channel VSDs, VSD1–4, because these mammalian VSDs have distinct sequences with unique functions and pharmacology (*16*, *37*, *40*). Superposition of VSD4-NavAb coordinates onto the parental VSD from NavAb (*12*) demonstrates that mammalian and bacterial S1–S4 domains share very similar structures in the activated state (fig. S12). Our VSD4-NavAb structure further reveals an elongation of S3 by three helical turns and other vertebrate-specific elaborations (fig. S12 and movie 4), providing more accurate models of the four mammalian VSDs to interpret physiological data (*59*) and guide drug discovery (fig. S13). Because the VSD4-NavAb protein that we engineered for crystallography is actually a hybrid of human and bacterial components (Fig. 2A and fig. S3), the chimeric nature of this construct confirms the likeness of mammalian and bacterial VSDs since high-affinity radioligand binding is maintained (fig. S6), rather than destroyed.

Mutational analyses of the Nav1.7 VSD4 receptor site

To dissect contributions of aryl sulfonamide binding to the VSD4 receptor site, we performed scanning mutagenesis on the human Nav1.7 channel (figs. S14 to S16). Within the anion-binding pocket, N1540A (S2) and R4A (S4) mutations had the largest effect, reducing GX-674 potency by a factor of 43 and 3000, respectively (Fig. 6, A to D). R3Q (in place of R3A) and R5A reduced GX-674 potency by a factor of 6 and 170, indicating that these gating charges may stabilize the local structure of the S4 (Figs. 5A and 6, A to D, and fig. S16). R1A and R2A did not significantly affect GX-674 potency (fig. S16), suggesting that the observed R1-lipid and R2-sulfonamide oxygen interactions contribute minimally (~3.4 Å; Figs. 2D and 4A). Alanine scanning further revealed 9- to 20-fold effects on GX-674 inhibition for residues that directly or indirectly encase R4 (Fig. 6, A to D, and figs. S14 and S17), underscoring the importance of precisely positioning the R4 side chain. Mutation of R4 to lysine (R4K) decreased GX-674 potency by a factor of 675 (fig. S16), further highlighting the bidentate interaction seen between R4 and the aryl sulfonamide thiadiazole moiety (Fig. 2E). Overall, the potency of Nav1.7 inhibition by this class of molecules is dominated by the R4 gating charge interaction, in line with the voltage dependence required to expose this side chain into the extracellular cleft to engage the anionic warhead (Figs. 1, C, F, and G, and 2, D to F).

To better understand the selectivity pocket within the VSD4 receptor site, we used GX-674 and [^{3}H]GX-545 to assay human Nav1.7 or VSD4-NavAb channels, respectively. V1541A (S2; YWxx**V**) and M1582A (S3; G**M**xxA) mutations decreased antagonist affinity, highlighting the hydrophobic floor in forming an optimal receptor site and pointing to side-chain differences among Nav channel isoforms (Fig. 6, A to E, and fig. S3A). G1581A and A1585F mutations within the S3 **G**Mxx**A** selectivity motif reduced antagonist potency, owing to the introduction of steric hindrance (Fig. 6, A to D); and because equivalent residues in VSD1-3 are larger than alanine, this result can explain the selective targeting of VSD4 by the aryl sulfonamides (figs. S3A and S13). Inhibitor potencies were substantially decreased in both human Nav1.7 and VSD4-NavAb channels when Y1537 and W1538 were simultaneously mutated to their Nav1.1 or Nav1.3 equivalents Y1537S/W1538R (Figs. 1E and 6, A to D, and fig. S18), solidifying the importance of the S2 **YW**xxV motif in determining isoform selectivity of the aryl sulfonamide antagonists. Interestingly, the single mutation Y1537S (as well as Y1537A) increased GX-674 potency and increased the on-rate and off-rate of GX-674 inhibition (fig. S18), suggesting that the bulky tyrosine side chain may restrict access to the binding pocket. Furthermore, the mutation W1538R did not by itself alter GX-674 potency, suggesting that a complex interaction between Y1537, W1538, and GX-674 exists to establish isoform selectivity (fig. S18, A and B).

Mapping the mutations that have effects on antagonist affinity (fig. S17) in combination with VSD4 homology modeling will guide isoform-selective Nav channel inhibitor design efforts. The S2 selectivity motif in Nav1.7 is YWxx**V**, but YWxxL in Nav1.2 and Nav1.6 (Fig. 1E), which together with nearby side-chain differences (Fig. 6E and fig. S3A) provides an opportunity for the development of truly Nav1.7-selective inhibitors. Alternatively, the design of "central nervous system (CNS)–sparing" aryl sulfonamides that target Nav1.7 with only limited isoform-selectivity against Nav1.2 and Nav1.6 (Fig. 1D) might still enable safe and effective treatment for pain, because the dose-limiting side effects of blockers that lack molecular selectivity (*60*) likely involve the Nav1.2 and Nav1.6 channels, which are abundantly expressed in the CNS (*4*).

Discussion

Nav channel inhibitors have traditionally been classified as either functionally selective, where binding is modified by channel gating (e.g., local anesthetics), or molecularly selective, where potency differs among Nav channel isoforms with little interaction from gating (e.g., tetrodotoxin). All clinically used Nav channel inhibitors are functionally selective, where their time- and state-dependence of block favors patterns of electrical activity seen in pathological conditions. Our structural studies define the mechanism of action of a new class of compounds (*31*, *38*) that possess both functional and molecular selectivity, a phenomenon previously unknown among small-molecule ligands of the Nav channel family (*32*–*34*). Inhibition by the aryl sulfonamides is exquisitely sensitive to channel activation, which derives from the requisite movement of the R4 gating charge into the extracellular cleft of VSD4 to form pivotal contacts with the antagonist's anionic warhead. The VSD4 location of the binding site on Nav channels is likely mechanistically meaningful because charge movement of S4 in VSD4 is necessary and sufficient for fast inactivation (*40*). Therefore, by targeting and immobilizing the S4 helix of VSD4, the R4-warhead interaction underlies the voltage-sensor trapping mechanism of Nav channel inhibition by these small-molecule gating modifier antagonists.

We have exploited a bacterial Nav channel to obtain crystal structures of human Nav1.7 VSD4 in complex with potent and isoform-selective small-molecule inhibitors. Our structures reveal the details of a remarkable Nav channel VSD4 receptor site, where residues conserved in all Nav channels are required for high-affinity binding, and side chains from the S2 and S3 helices are key determinants of isoform selectivity. In addition to establishing a close structural relationship between prokaryotic and eukaryotic VSDs, a potential membrane access pathway for small-molecule gating modifiers and roles for phospholipids in modulating Nav channel function have also been noted. Indeed, we have observed a unique phospholipid-antagonist-VSD4 tripartite interaction that may expand the importance of the lipid bilayer in ion channel biology and pharmacology. Ultimately, we anticipate that our new crystallization strategy will form the basis for drug design efforts aimed at other voltage-gated ion channels (*32*–*34*) and hope that the Nav1.7 structures reported here will accelerate the development of superior treatments for pain.

REFERENCES AND NOTES

1. B. Hille, *Ion Channels of Excitable Membranes* (Sinauer, Sunderland, MA, ed. 3, 2001).
2. W. A. Catterall, Structure and function of voltage-gated ion channels. *Annu. Rev. Biochem.* **64**, 493–531 (1995). doi: 10.1146/annurev.bi.64.070195.002425; pmid: 7574491
3. J. Payandeh, D. L. Minor Jr., Bacterial voltage-gated sodium channels (BacNa(V)s) from the soil, sea, and salt lakes enlighten molecular mechanisms of electrical signaling and pharmacology in the brain and heart. *J. Mol. Biol.* **427**, 3–30 (2015). doi: 10.1016/j.jmb.2014.08.010; pmid: 25158094
4. W. A. Catterall, A. L. Goldin, S. G. Waxman, International Union of Pharmacology. International Union of Pharmacology. XLVII. Nomenclature and structure-function relationships of voltage-gated sodium channels. *Pharmacol. Rev.* **57**, 397–409 (2005). doi: 10.1124/pr.57.4.4; pmid: 16382098
5. S. D. Dib-Hajj, Y. Yang, J. A. Black, S. G. Waxman, The Na(V)1.7 sodium channel: From molecule to man. *Nat. Rev. Neurosci.* **14**, 49–62 (2013). doi: 10.1038/nrn3404; pmid: 23232607

6. C. R. Fertleman *et al*., SCN9A mutations in paroxysmal extreme pain disorder: Allelic variants underlie distinct channel defects and phenotypes. *Neuron* **52**, 767–774 (2006). doi: 10.1016/j.neuron.2006.10.006; pmid: 17145499
7. Y. Yang *et al*., Mutations in SCN9A, encoding a sodium channel alpha subunit, in patients with primary erythermalgia. *J. Med. Genet.* **41**, 171–174 (2004). doi: 10.1136/jmg.2003.012153; pmid: 14985375
8. J. J. Cox *et al*., An SCN9A channelopathy causes congenital inability to experience pain. *Nature* **444**, 894–898 (2006). doi: 10.1038/nature05413; pmid: 17167479
9. Y. P. Goldberg *et al*., Loss-of-function mutations in the Nav1.7 gene underlie congenital indifference to pain in multiple human populations. *Clin. Genet.* **71**, 311–319 (2007). doi: 10.1111/j.1399-0004.2007.00790.x; pmid: 17470132
10. Y. Jiang *et al*., X-ray structure of a voltage-dependent K^+ channel. *Nature* **423**, 33–41 (2003). doi: 10.1038/nature01580; pmid: 12721618
11. S. B. Long, X. Tao, E. B. Campbell, R. MacKinnon, Atomic structure of a voltage-dependent K^+ channel in a lipid membrane-like environment. *Nature* **450**, 376–382 (2007). doi: 10.1038/nature06265; pmid: 18004376
12. J. Payandeh, T. Scheuer, N. Zheng, W. A. Catterall, The crystal structure of a voltage-gated sodium channel. *Nature* **475**, 353–358 (2011). doi: 10.1038/nature10238; pmid: 21743477
13. J. Payandeh, T. M. Gamal El-Din, T. Scheuer, N. Zheng, W. A. Catterall, Crystal structure of a voltage-gated sodium channel in two potentially inactivated states. *Nature* **486**, 135–139 (2012). pmid: 22678296
14. X. Zhang *et al*., Crystal structure of an orthologue of the NaChBac voltage-gated sodium channel. *Nature* **486**, 130–134 (2012). pmid: 22678295
15. W. Stühmer *et al*., Structural parts involved in activation and inactivation of the sodium channel. *Nature* **339**, 597–603 (1989). doi: 10.1038/339597a0; pmid: 2543931
16. B. Chanda, F. Bezanilla, Tracking voltage-dependent conformational changes in skeletal muscle sodium channel during activation. *J. Gen. Physiol.* **120**, 629–645 (2002). doi: 10.1085/jgp.20028679; pmid: 12407076
17. B. Hille, The receptor for tetrodotoxin and saxitoxin. A structural hypothesis. *Biophys. J.* **15**, 615–619 (1975). doi: 10.1016/S0006-3495(75)85842-5; pmid: 1148362
18. G. R. Strichartz, The inhibition of sodium currents in myelinated nerve by quaternary derivatives of lidocaine. *J. Gen. Physiol.* **62**, 37–57 (1973). doi: 10.1085/jgp.62.1.37; pmid: 4541340
19. H. A. Fozzard, P. J. Lee, G. M. Lipkind, Mechanism of local anesthetic drug action on voltage-gated sodium channels. *Curr. Pharm. Des.* **11**, 2671–2686 (2005). doi: 10.2174/1381612054546833; pmid: 16101448
20. C. Bagnéris *et al*., Prokaryotic NavMs channel as a structural and functional model for eukaryotic sodium channel antagonism. *Proc. Natl. Acad. Sci. U.S.A.* **111**, 8428–8433 (2014). doi: 10.1073/pnas.1406855111; pmid: 24850863
21. B. Hille, Local anesthetics: Hydrophilic and hydrophobic pathways for the drug-receptor reaction. *J. Gen. Physiol.* **69**, 497–515 (1977). doi: 10.1085/jgp.69.4.497; pmid: 300786
22. B. P. Bean, Nitrendipine block of cardiac calcium channels: High-affinity binding to the inactivated state. *Proc. Natl. Acad. Sci. U.S.A.* **81**, 6388–6392 (1984). doi: 10.1073/pnas.81.20.6388; pmid: 6093100
23. M. C. Sanguinetti, R. S. Kass, Regulation of cardiac calcium channel current and contractile activity by the dihydropyridine Bay K 8644 is voltage-dependent. *J. Mol. Cell. Cardiol.* **16**, 667–670 (1984). doi: 10.1016/S0022-2828(84)80631-8; pmid: 6206231
24. M. J. Wilson *et al*., μ-Conotoxins that differentially block sodium channels $Na_v1.1$ through 1.8 identify those responsible for action potentials in sciatic nerve. *Proc. Natl. Acad. Sci. U.S.A.* **108**, 10302–10307 (2011). doi: 10.1073/pnas.1107027108; pmid: 21652775
25. O. Knapp, J. R. McArthur, D. J. Adams, Conotoxins targeting neuronal voltage-gated sodium channel subtypes: Potential analgesics? *Toxins (Basel)* **4**, 1236–1260 (2012). doi: 10.3390/toxins4111236; pmid: 23202314
26. S. England, D. Rawson, Isoform-selective voltage-gated Na^+ channel modulators as next-generation analgesics. *Future Med. Chem.* **2**, 775–790 (2010). pmid: 21426202
27. C. J. Cohen, Targeting voltage-gated sodium channels for treating neuropathic and inflammatory pain. *Curr. Pharm. Biotechnol.* **12**, 1715–1719 (2011). doi: 10.2174/138920111798357249; pmid: 21466442
28. F. Bosmans, K. J. Swartz, Targeting voltage sensors in sodium channels with spider toxins. *Trends Pharmacol. Sci.* **31**, 175–182 (2010). doi: 10.1016/j.tips.2009.12.007; pmid: 20097434
29. M. de Lera Ruiz, R. L. Kraus, Voltage-Gated Sodium Channels: Structure, Function, Pharmacology, and Clinical Indications. *J. Med. Chem.* **58**, 7093–7118 (2015). doi: 10.1021/jm501981g; pmid: 25927480
30. J. K. Murray *et al*., Engineering potent and selective analogues of GpTx-1, a tarantula venom peptide antagonist of the $Na_v1.7$ sodium channel. *J. Med. Chem.* **58**, 2299–2314 (2015). doi: 10.1021/jm501765v; pmid: 25658507
31. K. McCormack *et al*., Voltage sensor interaction site for selective small molecule inhibitors of voltage-gated sodium channels. *Proc. Natl. Acad. Sci. U.S.A.* **110**, E2724–E2732 (2013). doi: 10.1073/pnas.1220844110; pmid: 23818614
32. K. Padilla, A. D. Wickenden, A. C. Gerlach, K. McCormack, The KCNQ2/3 selective channel opener ICA-27243 binds to a novel voltage-sensor domain site. *Neurosci. Lett.* **465**, 138–142 (2009). doi: 10.1016/j.neulet.2009.08.071; pmid: 19733209
33. A. Peretz *et al*., Targeting the voltage sensor of Kv7.2 voltage-gated K^+ channels with a new gating-modifier. *Proc. Natl. Acad. Sci. U.S.A.* **107**, 15637–15642 (2010). doi: 10.1073/pnas.0911294107; pmid: 20713704
34. N. E. Ottosson *et al*., Resin-acid derivatives as potent electrostatic openers of voltage-gated K channels and suppressors of neuronal excitability. *Sci. Rep.* **5**, 13278 (2015). doi: 10.1038/srep13278; pmid: 26299574
35. Z. Lu, A. M. Klem, Y. Ramu, Ion conduction pore is conserved among potassium channels. *Nature* **413**, 809–813 (2001). doi: 10.1038/35101535; pmid: 11677598
36. A. A. Alabi, M. I. Bahamonde, H. J. Jung, J. I. Kim, K. J. Swartz, Portability of paddle motif function and pharmacology in voltage sensors. *Nature* **450**, 370–375 (2007). doi: 10.1038/nature06266; pmid: 18004375
37. F. Bosmans, M. F. Martin-Eauclaire, K. J. Swartz, Deconstructing voltage sensor function and pharmacology in sodium channels. *Nature* **456**, 202–208 (2008). doi: 10.1038/nature07473; pmid: 19005548
38. U. Norinder, M. E. Ek, QSAR investigation of NaV1.7 active compounds using the SVM/Signature approach and the Bioclipse Modeling platform. *Bioorg. Med. Chem. Lett.* **23**, 261–263 (2013). doi: 10.1016/j.bmcl.2012.10.102; pmid: 23177785
39. N. Yang, A. L. George Jr., R. Horn, Molecular basis of charge movement in voltage-gated sodium channels. *Neuron* **16**, 113–122 (1996). doi: 10.1016/S0896-6273(00)80028-8; pmid: 8562074
40. D. L. Capes, M. P. Goldschen-Ohm, M. Arcisio-Miranda, F. Bezanilla, B. Chanda, Domain IV voltage-sensor movement is both sufficient and rate limiting for fast inactivation in sodium channels. *J. Gen. Physiol.* **142**, 101–112 (2013). doi: 10.1085/jgp.201310998; pmid: 23858005
41. F. V. Campos, B. Chanda, P. S. Beirão, F. Bezanilla, Alpha-scorpion toxin impairs a conformational change that leads to fast inactivation of muscle sodium channels. *J. Gen. Physiol.* **132**, 251–263 (2008). pmid: 18663133
42. R. E. Middleton *et al*., Two tarantula peptides inhibit activation of multiple sodium channels. *Biochemistry* **41**, 14734–14747 (2002). doi: 10.1021/bi026546a; pmid: 12475222
43. K. Takeshita *et al*., X-ray crystal structure of voltage-gated proton channel. *Nat. Struct. Mol. Biol.* **21**, 352–357 (2014). doi: 10.1038/nsmb.2783; pmid: 24584463
44. S. Y. Lee, R. MacKinnon, A membrane-access mechanism of ion channel inhibition by voltage sensor toxins from spider venom. *Nature* **430**, 232–235 (2004). doi: 10.1038/nature02632; pmid: 15241419
45. J. J. Smith, S. Alphy, A. L. Seibert, K. M. Blumenthal, Differential phospholipid binding by site 3 and site 4 toxins. Implications for structural variability between voltage-sensitive sodium channel domains. *J. Biol. Chem.* **280**, 11127–11133 (2005). doi: 10.1074/jbc.M412552200; pmid: 15632158
46. M. Milescu *et al*., Tarantula toxins interact with voltage sensors within lipid membranes. *J. Gen. Physiol.* **130**, 497–511 (2007). doi: 10.1085/jgp.200709869; pmid: 17938232
47. M. Milescu *et al*., Interactions between lipids and voltage sensor paddles detected with tarantula toxins. *Nat. Struct. Mol. Biol.* **16**, 1080–1085 (2009). doi: 10.1038/nsmb.1679; pmid: 19783984
48. K. Gupta *et al*., Tarantula toxins use common surfaces for interacting with Kv and ASIC ion channels. *eLife* **4**, e06774 (2015). doi: 10.7554/eLife.06774; pmid: 25948544
49. S. D. Silberberg, M. Li, K. J. Swartz, Ivermectin interaction with transmembrane helices reveals widespread rearrangements during opening of P2X receptor channels. *Neuron* **54**, 263–274 (2007). doi: 10.1016/j.neuron.2007.03.020; pmid: 17442247
50. R. E. Hibbs, E. Gouaux, Principles of activation and permeation in an anion-selective Cys-loop receptor. *Nature* **474**, 54–60 (2011). doi: 10.1038/nature10139; pmid: 21572436
51. H. Nury *et al*., X-ray structures of general anaesthetics bound to a pentameric ligand-gated ion channel. *Nature* **469**, 428–431 (2011). doi: 10.1038/nature09647; pmid: 21248852
52. M. A. Hanson *et al*., Crystal structure of a lipid G protein-coupled receptor. *Science* **335**, 851–855 (2012). doi: 10.1126/science.1215904; pmid: 22344443
53. Y. Y. Dong *et al*., K2P channel gating mechanisms revealed by structures of TREK-2 and a complex with Prozac. *Science* **347**, 1256–1259 (2015). doi: 10.1126/science.1261512; pmid: 25766236
54. D. Schmidt, Q. X. Jiang, R. MacKinnon, Phospholipids and the origin of cationic gating charges in voltage sensors. *Nature* **444**, 775–779 (2006). doi: 10.1038/nature05416; pmid: 17136096
55. Y. Xu, Y. Ramu, Z. Lu, Removal of phospho-head groups of membrane lipids immobilizes voltage sensors of K^+ channels. *Nature* **451**, 826–829 (2008). doi: 10.1038/nature06618; pmid: 18273018
56. R. K. Hite, J. A. Butterwick, R. MacKinnon, Phosphatidic acid modulation of Kv channel voltage sensor function. *eLife* **3**, e04366 (2014). doi: 10.7554/eLife.04366; pmid: 25285449
57. D. J. Feller, J. A. Talvenheimo, W. A. Catterall, The sodium channel from rat brain. Reconstitution of voltage-dependent scorpion toxin binding in vesicles of defined lipid composition. *J. Biol. Chem.* **260**, 11542–11547 (1985). pmid: 2413014
58. X. Tao, A. Lee, W. Limapichat, D. A. Dougherty, R. MacKinnon, A gating charge transfer center in voltage sensors. *Science* **328**, 67–73 (2010). doi: 10.1126/science.1185954; pmid: 20360102
59. S. A. Pless *et al*., Asymmetric functional contributions of acidic and aromatic side chains in sodium channel voltage-sensor domains. *J. Gen. Physiol.* **143**, 645–656 (2014). doi: 10.1085/jgp.201311036; pmid: 24778431
60. E. Kalso, M. R. Tramèr, H. J. McQuay, R. A. Moore, Systemic local-anaesthetic-type drugs in chronic pain: A systematic review. *Eur. J. Pain* **2**, 3–14 (1998). doi: 10.1016/S1090-3801(98)90041-6; pmid: 10700296

ACKNOWLEDGMENTS

We thank our colleagues in the Structural Biology, Biology, Neuroscience, Discovery Chemistry, Biochemical and Cellular Pharmacology, and Chemistry Departments at Genentech and Xenon for project support. We especially appreciate the efforts of P. Bichler, C. Eigenbrot, W. Wang, P. Lupardus, B. Sellers, R. Mayer, J. Kiefer, T. Maurer, and S. Hymowitz in their support of this project. We acknowledge the European Synchrotron Radiation Facility for provision of synchrotron radiation facilities and thank S. Monac for assistance in using beamline ID29. A portion of this work was carried out with the support of the Diamond Light Source beamline I24, and we thank J. Waterman and A. Dias for assistance. Use of the Stanford Synchrotron Radiation Lightsource SSRL 12-12 at Stanford Linear Accelerator Center National Accelerator Laboratory is supported by the U.S. Department of Energy (DOE), DOE Office of Biological and Environmental Research, National Institutes of Health, and National Institute of General Medical Sciences. The contents of this publication are the responsibility of the authors and do not necessarily represent the views of NIH or National Institute of General Medical Sciences. Reagents used in this study are available under a materials transfer agreement with Genentech. T. Focken is inventor on patent application WO 2013/064984 that covers compounds GX-674, cmp6 (fig. S11), GX-0328, GX-3340, GX-4377, GX-4195, GX-4197, GX-4251, GX-4309, GX-4338, and GX-4375. Xenon Pharmaceuticals additionally holds patent application WO 2013/064983 that covers GX-4314. Structure factors and coordinates for the GX-936-VSD4-NavAb structure have been deposited in the Protein Data Bank with the accession code 5EK0. All authors are employees of Genentech Inc. or Xenon Pharmaceuticals Inc.

SUPPLEMENTARY MATERIALS

www.sciencemag.org/content/350/6267/aac5464/suppl/DC1
Materials and Methods
Figs. S1 to S18
Tables S1 to S3
Chemical synthesis of GX-545, GX-629, GX-674, and GX-936.

10 May 2015; accepted 29 October 2015
10.1126/science.aac5464

RESEARCH ARTICLE SUMMARY

STRUCTURAL BIOLOGY

Structure of the voltage-gated calcium channel $Ca_V1.1$ complex

Jianping Wu,* Zhen Yan,* Zhangqiang Li, Chuangye Yan, Shan Lu, Mengqiu Dong, Nieng Yan†

INTRODUCTION: Voltage-gated Ca^{2+} (Ca_V) channels activate in response to membrane potential changes and initiate Ca^{2+}-mediated cellular signaling cascades. The L-type, high voltage–activated Ca_V channel $Ca_V1.1$ is specialized for the excitation-contraction (E-C) coupling that causes contraction of skeletal muscles in response to changes in membrane potential. The action potential–induced conformational changes of $Ca_V1.1$ activate the type 1 ryanodine receptor (RyR1), which releases Ca^{2+} from the sarcoplasmic reticulum and subsequently triggers muscle contraction. The $Ca_V1.1$ complex consists of the pore-forming subunit α_1 and auxiliary subunits $\alpha_2\delta$, β, and γ that modulate the membrane trafficking, current kinetics, and gating properties of the Ca_V channels. The Ca_V channels represent important drug targets because of their association with diseases such as hypokalemic periodic paralysis, cardiac arrhythmia, and epileptic seizure. The $\alpha_2\delta$-1 subunit is directly targeted by the gabapentinoid drugs used for conditions such as epilepsy and neuropathic pain. In contrast to the homotetrameric Kv channels, the α_1 subunit of eukaryotic Ca_V and Na_V channels consists of one single polypeptide chain that is organized into four repeated domains (I to IV) of six transmembrane helices (S1 to S6). The large size, pseudo-symmetry, and heavy glycosylation of the Ca_V and Na_V channels are major impediments to the use of x-ray crystallography for structural elucidation.

RATIONALE: We purified endogenous $Ca_V1.1$ complex from rabbit skeletal muscle membranes with the use of glutathione *S*-transferase (GST)–fused β_{1a}, which is an exclusive auxiliary subunit of $Ca_V1.1$. Structural determination was achieved using single-particle cryo–electron microscopy (cryo-EM). The structural model was generated by homology modeling, rigid-body docking, and de novo model building. The identification of the four homologous repeats in the α_1 subunit was achieved through analysis of the distinctive extracellular loops of the pore domain, unique sequence patterns, and mass spectrometric analysis of cross-linked samples.

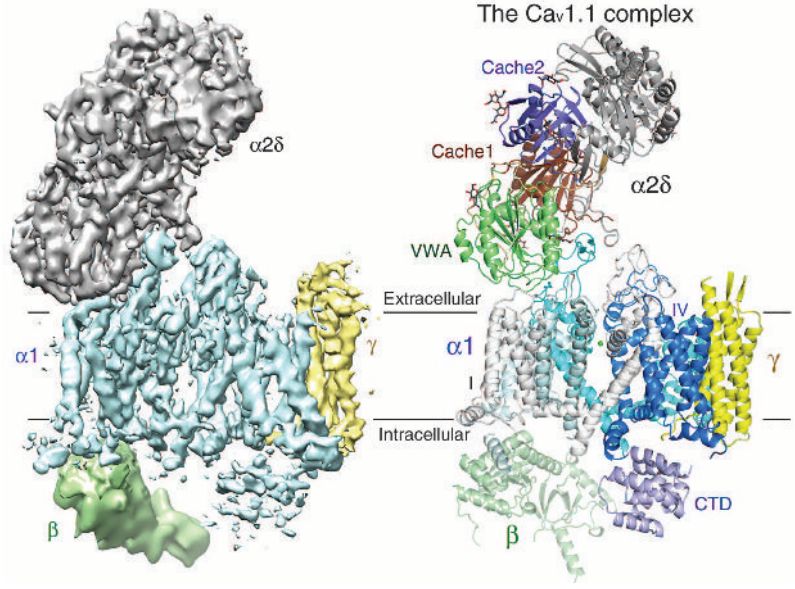

The cryo-EM structure of the rabbit voltage-gated Ca^{2+} channel $Ca_V1.1$ complex at a nominal resolution of 4.2 Å. The overall EM density map on the left is colored according to different subunits. The structure model on the right is domain-colored. The glycosyl moieties are shown as sticks. The putative Ca^{2+} is shown as a green sphere.

RESULTS: The EM density map for the rabbit $Ca_V1.1$ complex was reconstructed to 4.2 Å resolution according to the gold-standard Fourier shell correlation (FSC) 0.143 criterion. The overall structure is approximately 170 Å in height and 100 Å in the longest dimension of the width. The α_1 subunit folds into four homologous repeats, each exhibiting the voltage-gated ion channel fold formed by S1 to S6. The S5 and S6 segments from the four repeats constitute the pore domain, whereas the S1 to S4 segments in each repeat form the voltage-sensing domain (VSD). The four-fold symmetry of the pore domain is disrupted by the distinct extracellular loops (designated L5 loops for those between S5 and the P1 helix, and L6 loops for those connecting the P2 helix and S6) and by the slightly different conformations of the S5 and S6 segments among the four repeats. The $S6_{IV}$ segment is immediately followed by a cytosolic C-terminal domain. The selectivity filter is constituted by the side chains of four critical Glu residues and the carbonyl oxygen atoms of the two preceding residues in each repeat. The clockwise arrangement of the four repeats in the extracellular view may be conserved in all eukaryotic Ca_V and Na_V channels.

ON OUR WEB SITE

Read the full article at http://dx.doi.org/10.1126/science.aad2395

The four transmembrane helix–containing γ subunit, which exhibits structural similarity to claudins, interacts with VSD_{IV}, whereas the cytosolic β subunit is located adjacent to VSD_{II} of α_1. On the extracellular side, the α_2 subunit interacts with the extracellular loops of repeats I to III through its von Willebrand A (VWA) and Cache1 domains. The α_2 residue Arg^{243}, which has been implicated in binding to the drug pregabalin, is in the Cache1 domain and covers a central pocket that may accommodate ligands.

CONCLUSION: Our study reveals the detailed architecture of a pseudo-tetrameric eukaryotic Ca_V channel in complex with its auxiliary subunits. Although molecular understanding of ion selectivity and voltage gating will require improved resolution, the present structural analysis provides an important framework for understanding the function and disease mechanisms of related Ca_V and Na_V channels. The intersubunit interfaces identified in the complex structure provide the basis for molecular interpretation of α_1 modulation by the auxiliary subunits. ■

The list of author affiliations is available in the full article online.
*These authors contributed equally to this work.
†Corresponding author. E-mail: nyan@tsinghua.edu.cn
Cite this article as J. Wu *et al.*, *Science* **350**, aad2395 (2015). DOI: 10.1126/science.aad2395

RESEARCH ARTICLE

STRUCTURAL BIOLOGY

Structure of the voltage-gated calcium channel $Ca_v1.1$ complex

Jianping Wu,[1,2,3]* Zhen Yan,[1,2,3]* Zhangqiang Li,[1,2,3] Chuangye Yan,[1,2,3] Shan Lu,[4] Mengqiu Dong,[4] Nieng Yan[1,2,3]†

The voltage-gated calcium channel $Ca_v1.1$ is engaged in the excitation-contraction coupling of skeletal muscles. The $Ca_v1.1$ complex consists of the pore-forming subunit α_1 and auxiliary subunits $\alpha_2\delta$, β, and γ. We report the structure of the rabbit $Ca_v1.1$ complex determined by single-particle cryo–electron microscopy. The four homologous repeats of the α_1 subunit are arranged clockwise in the extracellular view. The γ subunit, whose structure resembles claudins, interacts with the voltage-sensing domain of repeat IV (VSD_{IV}), whereas the cytosolic β subunit is located adjacent to VSD_{II} of α_1. The α_2 subunit interacts with the extracellular loops of repeats I to III through its VWA and Cache1 domains. The structure reveals the architecture of a prototypical eukaryotic Ca_v channel and provides a framework for understanding the function and disease mechanisms of Ca_v and Na_v channels.

Calcium ions (Ca^{2+}) play a critical role in diverse physiological processes such as contraction, secretion, neurotransmission, gene transcription, and cell death. The cytoplasmic Ca^{2+} concentration is generally maintained at approximately 100 nM, several orders of magnitude lower than extracellular or organellar Ca^{2+} stores. In response to a variety of stimuli, Ca^{2+} is released into the cytoplasm, triggering a cascade of signaling events (*1*–*3*).

Voltage-gated Ca^{2+} (Ca_v) channels activate in response to changes of membrane potential and function upstream of Ca^{2+}-mediated signal transduction (*4*–*8*). The Ca_v channel $Ca_v1.1$, also known as the dihydropyridine receptor (DHPR), is an L-type Ca_v channel specialized for the excitation-contraction (E-C) coupling of skeletal muscles (*9*–*11*). $Ca_v1.1$ is enriched at the transverse tubule of myocytes and controls activation of the type 1 ryanodine receptor (RyR1), which is the high-capacity channel responsible for rapid Ca^{2+} release from the sarcoplasmic reticulum. In contrast to the E-C coupling mechanism in cardiac muscles, where the influx of Ca^{2+} through another L-type Ca_v channel, $Ca_v1.2$, activates the cardiomyocyte-specific RyR2 (known as calcium-induced calcium release), activation of RyR1 is triggered by the action potential–induced conformational changes of $Ca_v1.1$. In this sense, $Ca_v1.1$ functions as the voltage sensor for E-C coupling (*12*–*15*).

$Ca_v1.1$, like other Ca_v channels, consists of a core α_1 subunit and auxiliary subunits $\alpha_2\delta$, β, and γ (*16*, *17*). The pore-forming α_1 subunit, similar to eukaryotic Na_v channels, consists of a single polypeptide chain that is organized into four homologous repeats (I to IV) of six transmembrane helices (S1 to S6). S5, S6, and their intervening segments from each repeat form the ion-conducting pore domain, which is flanked by four voltage-sensing domains (VSDs) constituted by S1 to S4 (*18*–*22*). There are different genes and splicing isoforms for each auxiliary subunit. The extracellular α_2 and the membrane-anchored δ subunits result from proteolytic cleavage of a single gene product and are structurally bound through a disulfide bond. The cytosolic β subunits participate in the interaction between $Ca_v1.1$ and RyR1. The γ subunits comprise four transmembrane helices (TM1 to TM4) with the N and C termini on the cytosolic side. These auxiliary subunits modulate the membrane trafficking, current kinetics, and gating properties of the Ca_v channels and mediate the regulation of the α_1 subunit by a variety of signals (*17*, *23*–*27*).

The Ca_v channels are important drug targets because of their association with diseases such as hypokalemic periodic paralysis, cardiac arrhythmia, and epileptic seizure (*28*). Whereas the α_1 subunit represents the primary site for ligand and toxin binding, the $\alpha_2\delta$-1 subunit is the direct target for the gabapentinoid drugs gabapentin and pregabalin (*29*, *30*).

The crystal structures of β subunits, alone and in complex with the α_1 interaction domain (AID) motif of α_1, were obtained more than a decade ago (*31*–*33*). Other than that, structural information on the eukaryotic Ca_v and Na_v channels remains elusive, except for low-resolution electron microscopic (EM) models (*34*–*38*). Structural interpretation was mostly based on the crystal structures of Kv channels (*19*, *20*), bacterial homologs of Na_v channels Na_vAb (*21*) and Na_vRh (*22*), and an engineered Na_vAb variant that became Ca^{2+}-selective (named Ca_vAb) (*39*). However, all these channels are formed by four identical

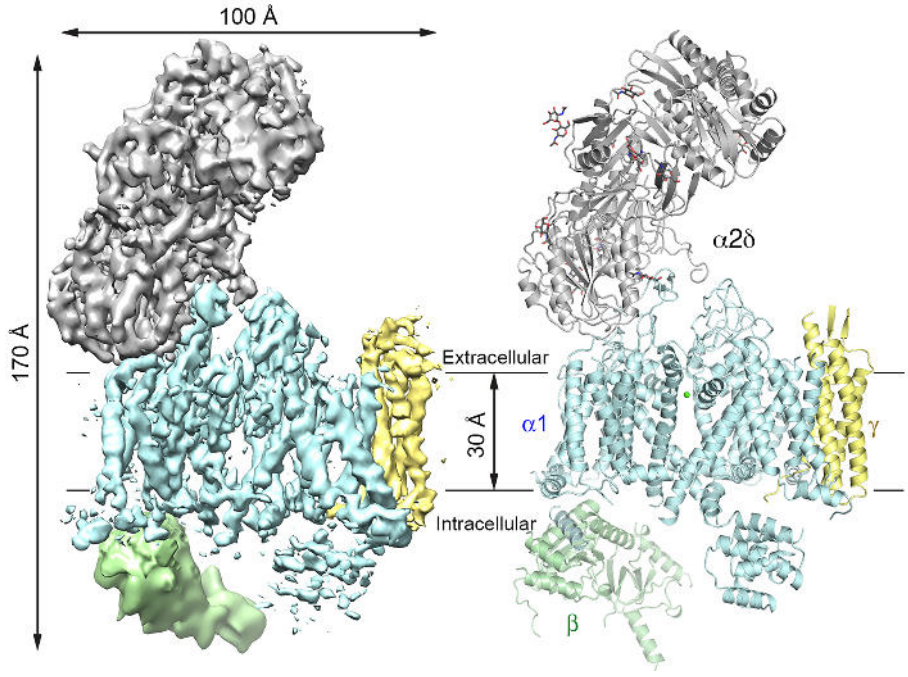

Fig. 1. Overall architecture of the rabbit $Ca_v1.1$ complex. The overall EM density map (left) and structure (right) of the rabbit $Ca_v1.1$ complex. The density corresponding to the β subunit was generated from the 6.1 Å map at a contour level of 0.0135, and the other regions were from the 4.2 Å map at a contour level of 0.0435 in Chimera (*77*). All structure figures were prepared with PyMol (*78*).

[1]State Key Laboratory of Membrane Biology, Tsinghua University, Beijing 100084, China. [2]Tsinghua-Peking Joint Center for Life Sciences, Tsinghua University, Beijing 100084, China. [3]Center for Structural Biology, School of Life Sciences and School of Medicine, Tsinghua University, Beijing 100084, China. [4]National Institute of Biological Sciences, Beijing 102206, China.
*These authors contributed equally to this work.
†Corresponding author. E-mail: nyan@tsinghua.edu.cn

polypeptide chains. They cannot support reliable modeling of the pseudo-tetrameric Ca_v and Na_v channels, nor can they clarify the molecular basis for the interactions between α_1 and the auxiliary subunits. Here, we report the structure of the rabbit $Ca_v1.1$ complex at 4.2 Å resolution determined using single-particle cryo–electron microscopy (cryo-EM).

Structural determination of $Ca_v1.1$

Details of protein preparation and EM data acquisition can be found in figs. S1 to S3 and in Materials and Methods below. Following a strategy similar to that used for purification of endogenous RyR1 (*40*), we used glutathione *S*-transferase (GST)–fused β_{1a}, an exclusive auxiliary subunit of $Ca_v1.1$ among all β isoforms (*25*, *41*), to pull down the $Ca_v1.1$ complex from rabbit skeletal muscle membranes. A variety of detergents and amphipols were screened. After repeated trials, digitonin proved to be the optimal detergent for protein extraction, purification, and cryo-EM data acquisition (fig. S1, A to C). Mass spectrometric (MS) analysis of the purified complex confirmed the presence of all the components of a complete $Ca_v1.1$ complex. By means of direct electron detection and advanced image processing algorithms (*42*, *43*), we were able to reconstruct the three-dimensional structure of the $Ca_v1.1$ complex with an overall resolution of 4.2 Å according to the gold-standard Fourier shell correlation (FSC) 0.143 criterion (Fig. 1, table S1, and figs. S1 and S2).

The transmembrane region was unambiguously identified in the EM density map, owing to the distinctive detergent micelle at low resolution and the characteristic voltage-gated ion channel (VGIC) fold (fig. S3). We were able to build 1224 residues, of which 618 residues have side groups assigned, for the α_1 subunit. The additional four TMs belong to the γ subunit. A predicted structural model of the γ subunit can be fit into the density with slight adjustment. Previous EM imaging with specific antibodies distinguished the extracellular domain from the intracellular ones at approximately 20 Å resolution (*38*). Whereas EM density for the β subunit is largely missing in the 4.2 Å EM map, a "tail" below the TM region corresponding to the previously characterized β subunit was distinguishable in a classification that yielded a 6.1 Å map. Because of the low resolution, the crystal structure of AID-bound $Ca_v\beta_2$ (PDB code 1T0J) was docked into the "tail" density as a rigid body (figs. S2 and S3). Model building of the extracellular $\alpha_2\delta$-1 subunit was aided by homologous structural docking, unique sequence patterns, N-linked glycosylation sites, and MS characterization of the cross-linked complex (Movie 1 and figs. S3 and S4).

In the refined structural model of the $Ca_v1.1$ complex at 4.2 Å resolution, the majority of the four components, α_1, $\alpha_2\delta$-1, γ, and β_{1a}, have been built or docked. Among the 2515 modeled residues, 1123 have side chains assigned (table S2). The overall structure is approximately 170 Å in height and 100 Å in the longest dimension of the width (Fig. 1).

Domain assignment of the α_1 subunit

The lack of EM density for the inter-repeat cytosolic segments made it challenging to distinguish the four homologous repeats in the α_1 subunit. The repeat identification in α_1 was achieved through analysis of the distinctive extracellular loops of the pore domain, unique sequence patterns, and MS analysis of cross-linked samples (Fig. 2A and figs. S4 and S5).

The loops connecting S5 and the P1 helix (designated L5 loops) in repeats I and III are longer than those in the other two repeats (fig. S5B). These two extracellular loops were well resolved in the EM density map, placing repeats I and III on opposite sides. The characteristic sequence Tyr^{971}-Tyr^{972}-Tyr^{973}-Val^{974}-Tyr^{975} in repeat III could be identified in the EM density, thereby distinguishing repeat III from repeat I (fig. S5, B and C). Discrimination of repeats II and IV was facilitated by the distinct lengths of the connecting loops between the P2 helix and S6 (designated L6 loops). The $L6_{IV}$ loop is considerably longer than $L6_{II}$, allowing discrimination of these two repeats (fig. S5, B and D). The structural assignment was supported by cross-linking characterizations (fig. S4). For instance, MS analysis identified the cross-linking between Lys^{976}, a residue on $L5_{III}$ loop of α_1, and Lys^{234} in α_2, which are close to each other in the modeled structure. Finally, the

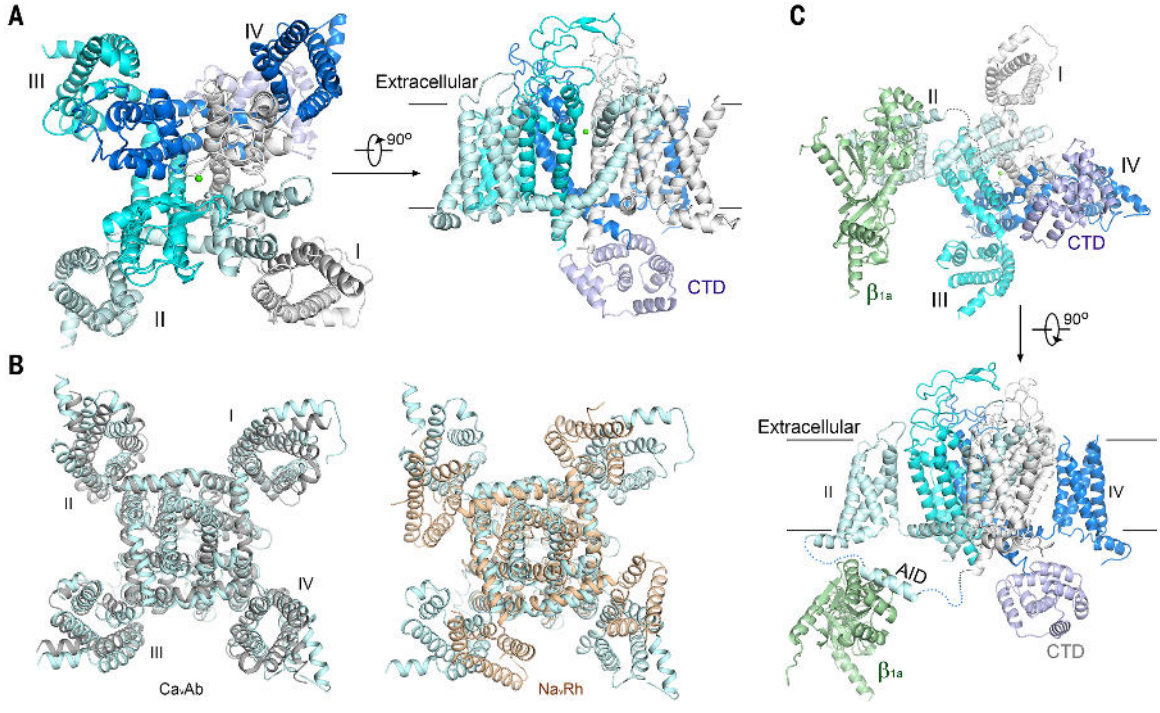

Fig. 2. Structure of the α_1 subunit. (**A**) Repeat assignment of the α_1 subunit. The four homologous repeats of the α_1 subunit exhibit a clockwise arrangement when viewed from the extracellular side. See fig. S5 for evidence in support of such domain assignment. The same color scheme is applied to all the figures where the four repeats need to be distinguished. CTD, C-terminal domain. (**B**) Structural comparison of $Ca_v1.1$ with Ca_vAb and Na_vRh (PDB codes 4MS2 and 4DXW, respectively). A cytosolic view is shown. For visual clarity, the CTD of $Ca_v1.1$ is omitted. Note that when the pore domains are superimposed, there is a subtle counterclockwise rotation of the VSDs of $Ca_v1.1$ relative to those of Ca_vAb, and an approximately 30° clockwise rotation relative to those of Na_vRh in the cytoplasmic view. (**C**) The β_{1a} subunit, which interacts with the intracellular AID motif between repeats I and II, may be adjacent to VSD_{II} of α_1. Because of the low resolution of the EM density corresponding to β_{1a}, the structure of AID-bound β_{2a} (PDB accession code 1T0J) was docked into the density as a rigid body. The location and orientation of β_{1a} and AID shown in the $Ca_v1.1$ complex cannot be regarded as reliable in the present structural model.

EM density between the S6 segment of repeat IV and the C-terminal domain is consecutive, validating the assignment of repeat IV (fig. S5E).

The clockwise arrangement of the four homologous repeats in the extracellular view may be conserved in all eukaryotic Ca_v and Na_v channels (*44*, *45*) (Fig. 2A and fig. S6). Notably, this repeat organization is also consistent with that of the two-pore K^+ channel TRAAK (*46*, *47*), but is different from a bacterial K^+ transporter TrkH (*48*).

In contrast to the well-resolved EM density of the pore domain, the four VSDs exhibit variable density qualities. The S1 to S4 segments in repeats I and IV were well resolved. Densities corresponding to S1 and S4, but not S2 and S3, were recognized in repeat II. Only residual density was found, corresponding to the VSD in repeat III (VSD_{III}). We modeled poly-Ala for VSDs in repeats I and IV, and subsequently docked the VSD models to repeats II and III (fig. S5F). Superimposing the pore domain with those of Ca_vAb and Na_vRh showed a slight counterclockwise rotation of the VSDs of $Ca_v1.1$ relative to those of Ca_vAb and an approximately 30° clockwise rotation relative to those of Na_vRh when viewed from the cytoplasmic side (Fig. 2B).

Two cytosolic domains were discernible in the 6.1 Å map: the β_{1a} subunit and the $S6_{IV}$-connected C-terminal domain, which are located in the vicinity of VSD_{II} and VSD_{IV}, respectively (Fig. 2C). The resolution and map quality of these two domains precluded detailed analysis. Nonetheless, one major question concerning $Ca_v1.1$ is how it translates changes in membrane potential into activation of RyR1. The structural observation that β_{1a} is adjacent to VSD_{II}, which may undergo pronounced conformational changes or domain motions in response to membrane potential fluctuations (*49*, *50*), sheds light on the E-C coupling mechanism.

The pseudo-symmetric pore domain

The pore domain of $Ca_v1.1$ exhibits a pseudo–four-fold symmetry (Fig. 3A). The extracellular L5 and L6 loops of the four repeats have marked differences in primary sequences and show distinct conformations. All these loops are well resolved in the EM densities, indicating relatively stable conformations (Fig. 3B, fig. S1G, and fig. S5, C and D). Although $L5_I$ is longer than $L5_{III}$ in primary sequences, the latter exhibits an extended conformation and protrudes higher into the extracellular space. A pair of antiparallel β strands can be recognized in $L5_{III}$.

The distinctive sequences and conformations of the L5 and L6 loops represent a characteristic feature of eukaryotic Ca_v channels (fig. S6). In the reported VGIC structures, such loops are mostly missing except for RyR1, which has elongated luminal loops between the P-loop and S6 segments (*40*). The luminal loops of RyR1 are highly enriched with negatively charged residues, whereas the L5 and L6 loops of $Ca_v1.1$ have an even distribution of all types of amino acids. The compositional and conformational differences of these loops between RyR1 and $Ca_v1.1$ support their distinct functions. In RyR1, the luminal loops may be responsible for attracting Ca^{2+} ions, whereas in $Ca_v1.1$, the L5 and L6 loops provide the docking site for the α_2 subunit.

In addition to the extracellular loops, the S5 and S6 segments exhibit slightly different conformations (Fig. 3C). When the four repeats are overlaid relative to the selectivity filter (SF), the P1 and P2 helices completely superimpose. In contrast, all the S5 and S6 segments deviate from each other to different extents. The S4 and S5 linker helices, especially that of repeat IV, deviate even more. A kink of the $S6_{IV}$ segment close to the intracellular end results in destruction of symmetry at the activation gate (*51*) (Fig. 3, A and C).

The lack of EM density for the side chains at the inner activation gate prevents an unambiguous assessment of the conformation of the internal gate (*51*). When superimposed relative to the SF, the distance between Cα atoms of repeats I and III at the inner gate is shorter than that of Ca_vAb and Na_vRh whose inner gates are closed, while that between $S6_{II}$ and $S6_{IV}$ is longer owing to the kink in $S6_{IV}$. Interestingly, the interhelix

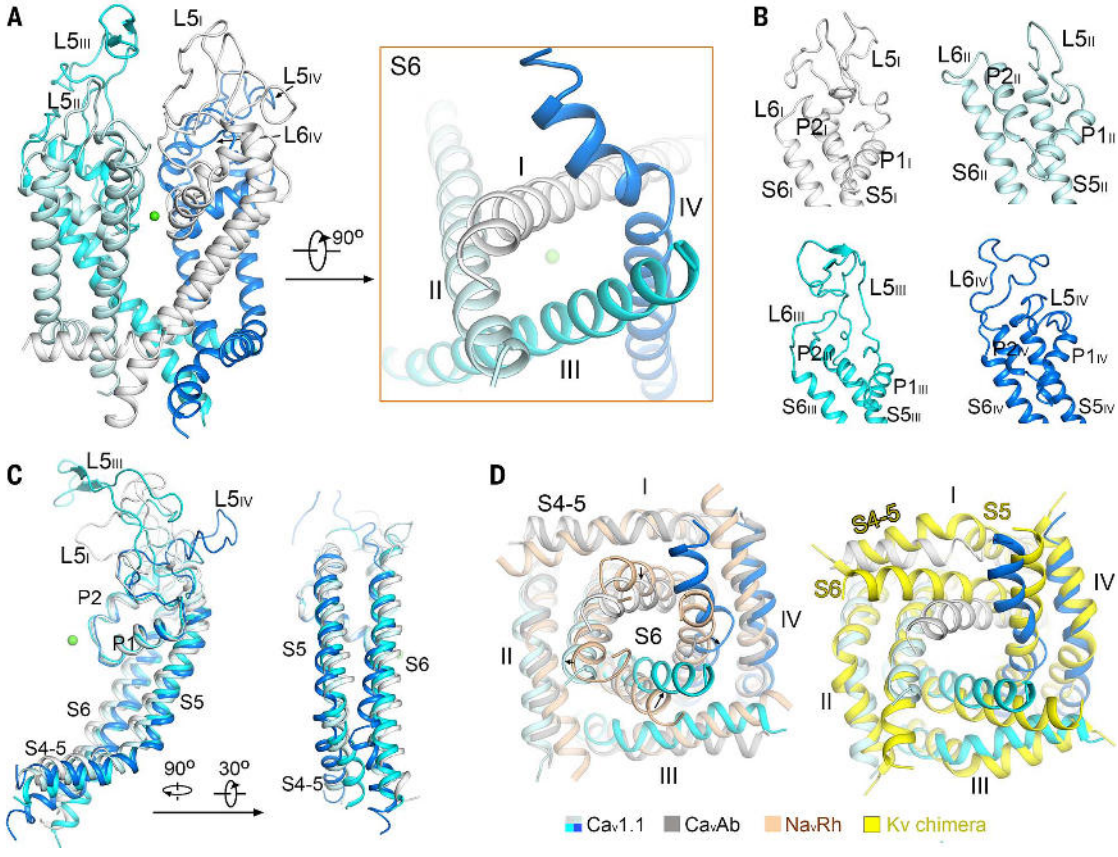

Fig. 3. The pore domain of $Ca_v1.1$. (**A**) The pore domain exhibits a four-fold pseudo-symmetry. The loops between S5 and the P1 helix and between the P2 helix and S6 are designated L5 and L6 loops, respectively. When viewed from the intracellular side, the four-fold symmetry of the activation gate was broken, mainly due to the kink of the $S6_{IV}$ segment. (**B**) The L5 and L6 loops in the four repeats have different lengths and exhibit distinct conformations. (**C**) Comparison of the pore-forming segments of the four repeats. When superimposed relative to the selectivity filter (SF), the S5 and S6 segments of the four repeats exhibit slightly different conformations, further disrupting the perfect symmetry. (**D**) Structural comparison of the pore domains of $Ca_v1.1$, Ca_vAb, Na_vRh, and Kv1.2-2.1 paddle chimera. Shown here are cytoplasmic views. Left: At the inner activation gate, the interhelix distance between $S6_I$ and $S6_{III}$ of $Ca_v1.1$ is shorter, while that between $S6_{II}$ and $S6_{IV}$ is longer than those of Ca_vAb and Na_vRh, resulting in a rectangular contour. Right: Whereas the interhelix distance between $S6_{II}$ and $S6_{IV}$ is similar to that of the paddle chimera (PDB code 2R9R) at the inner gate, that between $S6_I$ and $S6_{III}$ is considerably shorter.

distance between $S6_{II}$ and $S6_{IV}$ of $Ca_v1.1$ is similar to that of the open-channel Kv1.2-2.1 paddle chimera at the inner gate (*20*) (Fig. 3D). Interpretation of the state of the inner gate of $Ca_v1.1$ awaits structures of improved resolution.

The selectivity filter of $Ca_v1.1$

The EM density allows assignment of side groups to the majority of the P1 and P2 helices and the SF (Fig. 4A and fig. S7). As the densities for negatively charged residues are usually missing in EM maps, the side chains of Glu and Asp were modeled, but these cannot be considered reliable. A sphere-shaped density at an inner site of SF was tentatively assigned to Ca^{2+} because protein samples were prepared in the presence of 0.5 mM $CaCl_2$ (fig. S7A).

The SFs of Ca^{2+} conducting channels of the VGIC superfamily, exemplified by TRPV1 (*52*), TRPA1 (*53*), and RyR1 (*40*), show compositional and structural diversity (fig. S8A). Despite the variations in the primary sequences, the backbone configurations of the SF in $Ca_v1.1$ are nearly identical to those of Ca_vAb and Na_vRh (Fig. 4, B and C, and fig. S8B). The SF vestibule is constituted by the side chains of the essential EEEE residues (Glu^{292}, Glu^{614}, Glu^{1014}, and Glu^{1323} in the four repeats, respectively) (*54*–*56*) and the carbonyl oxygen atoms of the two preceding residues including an invariant Thr (Thr^{290}, Thr^{612}, Thr^{1012}, and Thr^{1321}, designated $C{=}O_{lower}$) and the residues that directly follow each of these (Met^{291}, Gly^{613}, Phe^{1013}, and Gly^{1322}, designated $C{=}O_{upper}$) (Fig. 4, B and D). The entrance to the SF vestibule is enriched with polar and negatively charged residues, including Asp^{615} of repeat II and four residues (Asp^{296}, Ser^{618}, Gln^{1018}, and Glu^{1327}) at corresponding positions in the four repeats. These residues may constitute extracellular Ca^{2+} binding site(s) or they may provide the electronegativity to attract cations (Fig. 4, B and D).

Interaction between γ and VSD_{IV}

The EM density corresponding to the γ subunit conforms to the predicted four-TM topology and reveals the interaction between γ and VSD_{IV} of α_1 (Fig. 5A and fig. S9A). Structural prediction with the I-TASSER server (*57*) returned a few models for γ, among which the five top-scored models are almost identical in the transmembrane region and can be fit into the EM density map with minor manual adjustment (fig. S9B). The extended extracellular sequences between TM1 and TM2 were predicted to form a β sheet in all the models (fig. S9B). However, the EM density corresponding to this region is mostly invisible, so that the structure cannot be built. The structure of γ is similar to those of claudin-15 and -19 (fig. S9C) (*58*, *59*), supporting the bioinformatic characterizations that the γ subunits and claudins may have a common evolutionary ancestor (*60*, *61*) (fig. S9D).

In the structure of the $Ca_v1.1$ complex, TM2 and TM3 of γ interact with S3 of VSD_{IV} in α_1 (Fig. 5). The structure provides a molecular explanation for the previous observation that replacement of TM1 and TM2 of γ led to loss of interaction with α_1 (*62*). There might be additional interfaces on the extracellular and intracellular regions that are not discernible in the present structure. Nonetheless, the extensive contact between γ and VSD_{IV} suggests that γ may antagonize Ca^{2+} conductance by modulating the conformational changes of VSD_{IV}. These structural observations also set the foundation for future investigations on the potential regulation of Ca_v channels by claudins and on other functions of the γ proteins (*23*, *24*, *63*, *64*).

The $\alpha_2\delta$-1 subunit

The preprocessed $\alpha_2\delta$-1 polypeptide in rabbit consists of 1106 residues. Proteolytic cleavage occurs after Ala^{960}, resulting in the N-terminal α_2 subunit and the C-terminal δ_1 subunit. As the direct target of pregabalin and gabapentin, the $\alpha_2\delta$-1 subunit has been structurally pursued for years. However, heavy glycosylation has made crystallization challenging. There are 16 predicted N-linked glycosylation sites in the human homolog, 14 on α_2 and

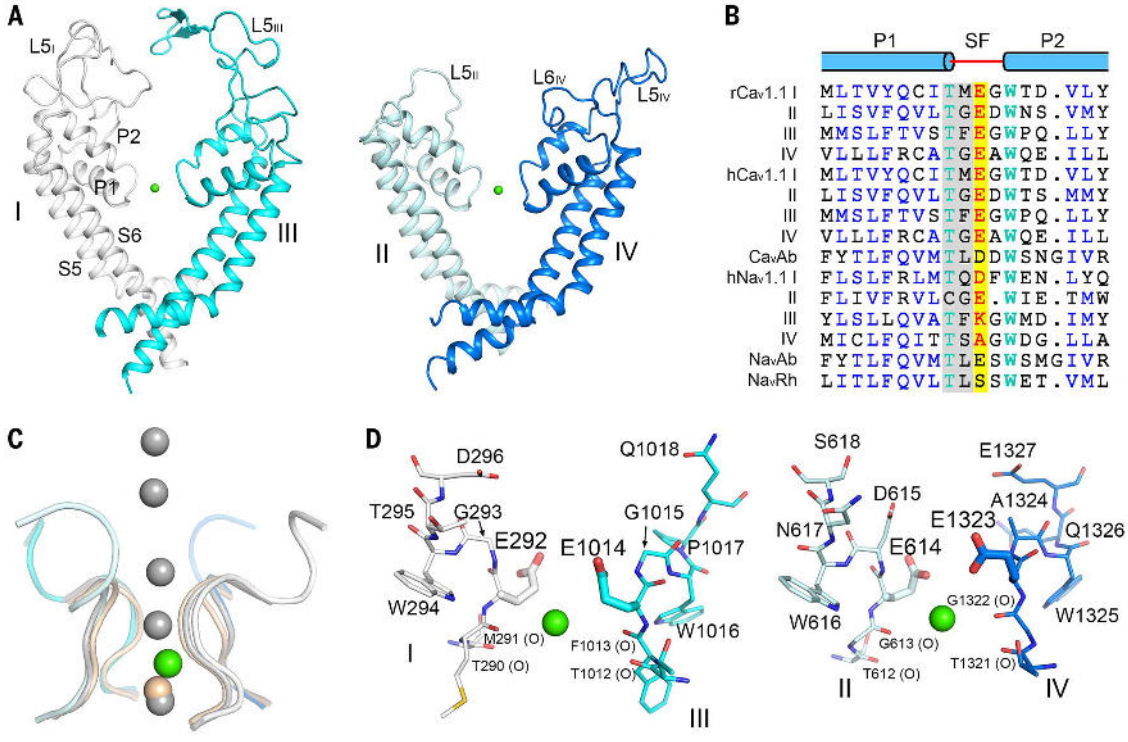

Fig. 4. The selectivity filter of $Ca_v1.1$. (**A**) The structural elements that constitute the ion conduction channel of $Ca_v1.1$. Two diagonal repeats are shown in each panel. Similar to the bacterial homotetrameric Ca_v and Na_v channels, the SF of $Ca_v1.1$ is supported by two pore helices (P1 and P2). A sphere-shaped density was found in the SF vestibule, which was tentatively assigned to a Ca^{2+} ion (green sphere). (**B**) Sequence comparison of the selectivity filter of rat and human $Ca_v1.1$ channels as well as human Nav1.1, Ca_vAb, Na_vAb, and Na_vRh. The residues whose main-chain carbonyl oxygen atoms constitute the SF vestibule are shaded gray. The critical EEEE (Glu^{292}, Glu^{614}, Glu^{1014}, and Glu^{1323}) residues in $Ca_v1.1$ and the corresponding residues in other related channels are shaded yellow. The invariant Trp residues and the highly conserved Thr residues are colored cyan. Abbreviations: A, Ala; C, Cys; D, Asp; E, Glu; F, Phe; G, Gly; H, His; I, Ile; K, Lys; L, Leu; M, Met; N, Asn; P, Pro; Q, Gln; R, Arg; S, Ser; T, Thr; V, Val; W, Trp; Y, Tyr. (**C**) Comparison of the SF vestibule of $Ca_v1.1$ to that of Ca_vAb and Na_vRh. Despite the nonidentical SF sequences among the four repeats of $Ca_v1.1$ and sequence difference from Ca_vAb and Na_vRh, the backbone conformations of the SF segments are nearly identical in these three channels. For visual clarity, only the backbones of SF are shown. The bound Ca^{2+} ions in Ca_vAb, Na_vRh, and $Ca_v1.1$ are colored gray, wheat, and green, respectively. Note that the position of the putative Ca^{2+} ion in $Ca_v1.1$ deviates from those in Ca_vAb and Na_vRh. (**D**) The details of the selectivity filter of $Ca_v1.1$. Because of the limited resolution, the side groups of the key EEEE residues in the SF vestibule are not well resolved. They were modeled to facilitate description. The accurate conformations of the side chains await high-resolution structures.

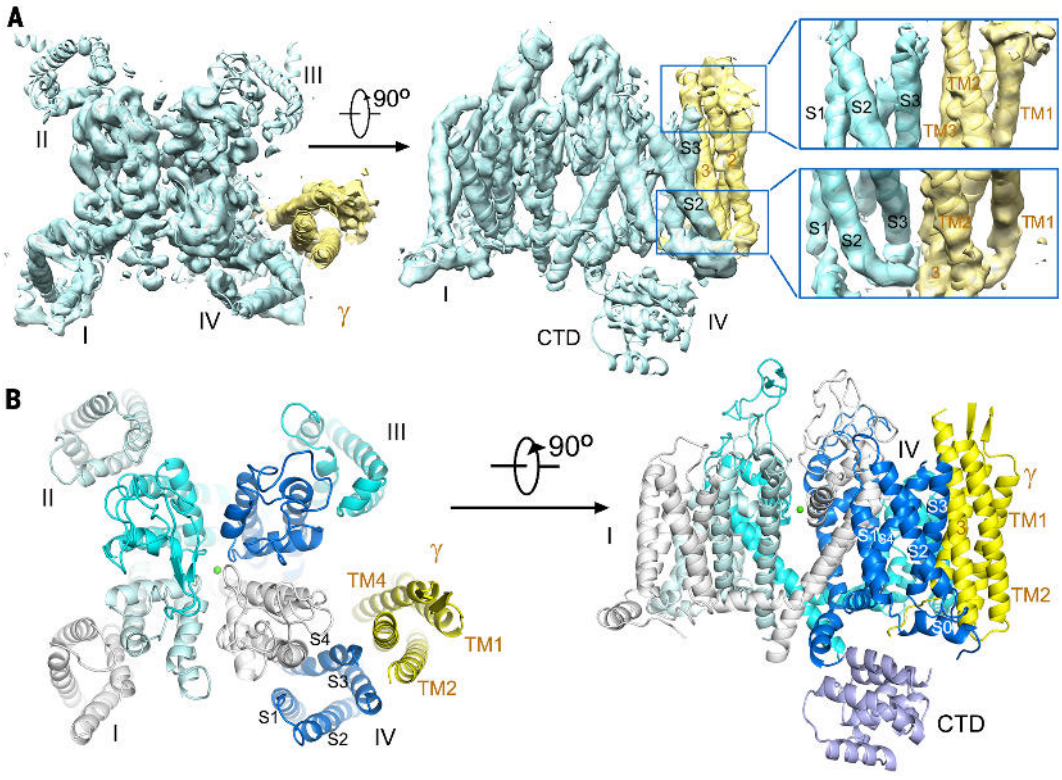

Fig. 5. Interactions between the γ and α_1 subunits. (**A**) The γ subunit contacts the VSD of repeat IV in the α_1 subunit. Density maps were generated in Chimera. (**B**) TM2 and TM3 of the γ subunit appear to mediate the interaction with VSD_{IV} of α_1. [See fig. S9 for details of structural modeling of γ, which resembles claudins (*58*, *59*).]

two on δ_1 (Fig. 6A). These glycosyl groups proved instrumental to the structural determination with moderate-resolution EM density maps.

It was predicted that the α_2 subunit consists of a von Willebrand A (VWA) domain and two Cache domains (*17*, *27*). Sequence similarity with the I-domain of integrin and excellent EM density map led to accurate model building of the α_2-VWA domain (fig. S10, A and B). The metal ion–dependent adhesion site (MIDAS) motif, which modulates the conformational changes of VWA domains upon ion binding, is conserved in the α_2-VWA domain (Fig. 6B and fig. S10A). A hydrophobic residue, Phe^{302}, in the loop between β_6 and α_6 is buried in the pocket in the closed state of the αM integrin I domain, but not in its open state (*65*). In the α_2-VWA structure, despite the lack of the corresponding Phe and the lack of density for a metal ion, the loop is away from the pocket, reminiscent of an open state (Fig. 6B).

After assignment of the VWA domain, we were able to identify the two Cache domains and build the structural model based on the crystal structures of the sensor domain of the *Bacillus subtilis* kinase D (KinD) (*66*) and the Mcp_N and cache domain of methyl-accepting chemotaxis protein (PDB code 3C8C) (fig. S10C). The VWA and the two Cache domains are intertwined in the primary sequences (Fig. 6A). The Cache1 domain is disrupted by the VWA domain (residues 251 to 443). In addition, similar to other tandem Cache domains, the N- and C-terminal segments of one extended helix belong to the Cache2 and Cache1 domains, respectively, and the last β strand in Cache1 is directly connected to the second helix of Cache2 (Fig. 6A). These features suggest that the two Cache domains may be rigid relative to each other. Together, they interact with the VWA domain through an extended and continuous interface (Fig. 6C). The primary sequence of Cache2 is further disrupted by a fragment (residues 521 to 559) whose EM densities are largely missing except for two extended segments that adjoin the Cache2 domain.

Ala substitution of Arg^{217} (the residue was renumbered after removal of the signal peptide) in the mouse α_2 subunit was shown to inhibit binding of pregabalin (*29*). In rabbit, the corresponding residue is Arg^{243}, which demarcates the short helix α_3 and the preceding loop and covers a central pocket of the Cache1 domain (Fig. 6D). The Cache domain is present in diverse bacterial chemotaxis receptors (*66*, *67*). A single point mutation of the conserved Arg (Arg^{131} → Ala) in KinD changed the ligand specificity from pyruvate to acetate (*66*). The structural similarity between α_2-Cache1 and KinD suggests that pregabalin may be accommodated in the pocket of Cache1 and coordinated by Arg^{243} (Fig. 6D and fig. S10C).

The identification of the δ_1 subunit was aided by the disulfide bond. Because the position of Cys^{406} was well defined in the VWA domain, the adjacent density likely belongs to Cys^{1062} in δ_1 and the elongated thread of density likely corresponds to a fragment in the δ_1 subunit (fig. S10D). However, the quality of the density did not support residue assignment. We modeled a poly-Ala chain to indicate its position relative to α_1 and α_2. No density was found in the transmembrane region that may correspond to segment in the δ_1 subunit. The density for the remainder of $\alpha_2\delta$-1 was less well resolved. We thereby modeled poly-Ala to this density.

The EM density map reveals that the α_1 subunit interacts with α_2 mainly through its extracellular loops, particularly the L5 loops of repeats I to III and the intervening loop between S1 and S2 of repeat I (designated $L1\text{-}2_I$ loop) (Fig. 6, B and E). The structure is consistent with a previous observation that the extracellular motif of repeat III associates with α_2 (*68*, *69*). As seen from the EM density, three domains of α_2 contact α_1, including the VWA, Cache1, and the intervening loop of Cache2 (Fig. 6E). The extensive interactions, which may stabilize the extracellular loops of α_1 and give rise to the well-resolved EM densities, provide the molecular basis for the modulation of α_1 by $\alpha_2\delta$-1. In particular, the MIDAS motif is localized immediately above the L1-2 loop in VSD_I (Fig. 6B). Conformational changes of MIDAS can be directly coupled to the modulation of VSD_I. Although Arg^{243} of the Cache1 domain is away from the interface between α_1 and α_2, its preceding loop is involved in the association with $L5_{III}$ of α_1 (Fig. 6, D and F, and fig. S4). It remains to be investigated whether the gabapentinoid drugs may allosterically regulate α_1 through this interface.

Our structural characterizations reveal the detailed architecture of a eukaryotic Ca_v channel in complex with its auxiliary subunits (Fig. 6F and movie S1). Although molecular understanding of ion selectivity and voltage gating will require improved resolution, the present structural analysis provides an important framework for understanding the function and disease mechanisms of related Ca_v and Na_v channels. The intersubunit interfaces identified in the complex structure provide the basis for molecular interpretation of α_1 modulation by the auxiliary subunits.

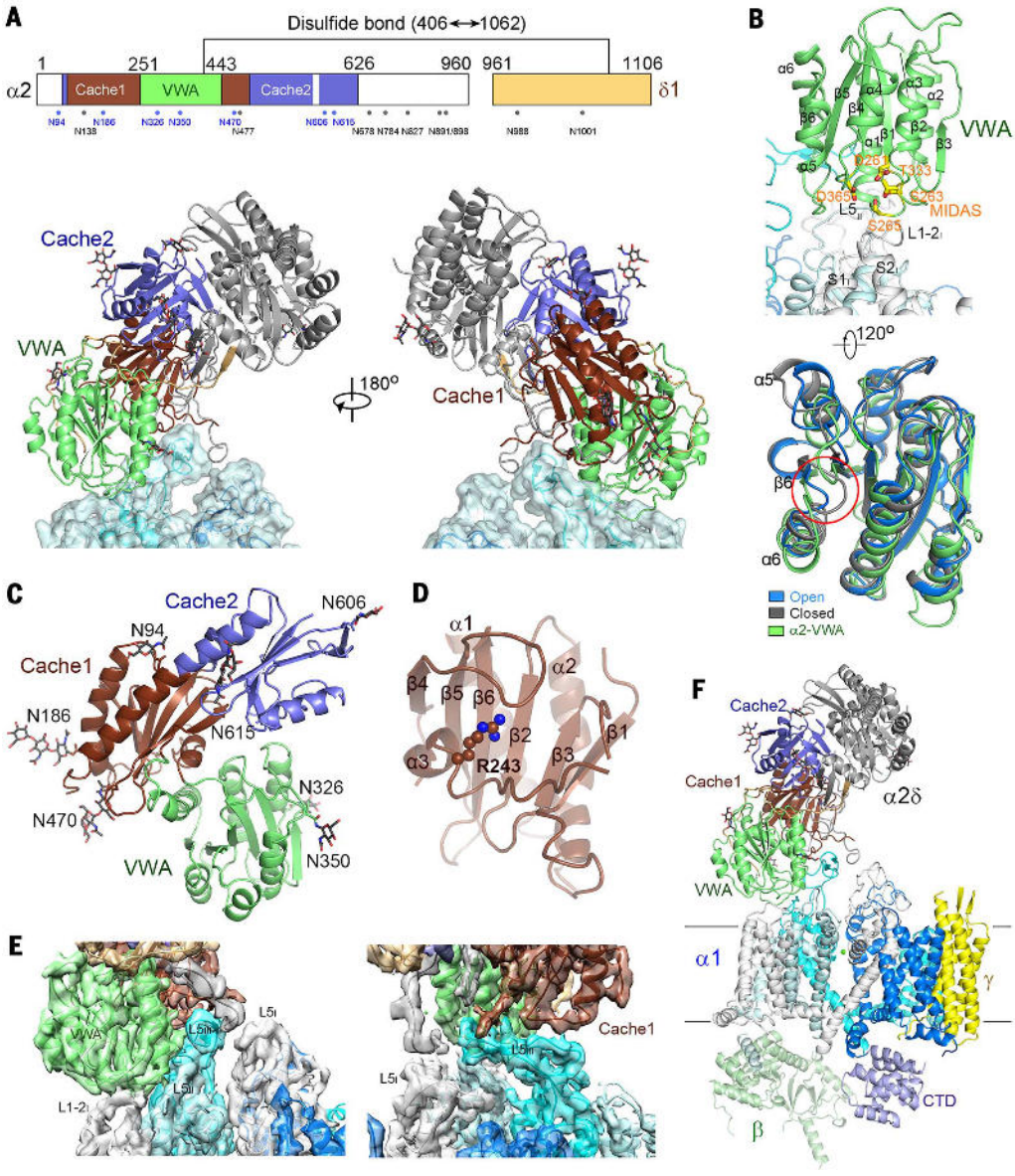

Fig. 6. Structure of the $\alpha_2\delta$-1 subunit. (**A**) Domain organization of the $\alpha_2\delta$-1 subunit. Shown above is a diagram of the domain structures of $\alpha_2\delta$-1. The residues that are glycosylated are indicated by the dots below, blue for structurally identified ones. The α_1 subunit is shown in semitransparent surface view to indicate its relative position to $\alpha_2\delta$-1. The sugar moieties are shown as sticks. (**B**) Structure of the VWA domain. Top: The conserved metal ion–dependent adhesion site (MIDAS) motif, shown as yellow sticks, is located directly above the α_1 subunit. Bottom: The VWA domain may exhibit an open conformation. Shown here are the structural overlay of α_2-VWA subunit (green) with the I-domain of α_M integrin in the open (PDB code 1IDO, colored blue) and closed (PDB code 1JLM, colored gray) conformations. The conformation of the intervening loop (highlighted with red circle) between strand β_6 and helix α_6 suggests that the α_2-VWA may adopt an open state. (**C**) Interaction between the VWA and two Cache domains in α_2. Note that the elongated helix that spans the two Cache domains is a characteristic feature of two tandem Cache domains. The glycosylated residues are labeled. (**D**) Arg^{243}, whose mutation led to reduced pregabalin binding, caps the central pocket of the Cache1 domain. [See fig. S10D for structural comparison with the homologous KinD domain.] Mutation of the corresponding Arg of KinD led to the change of ligand specificity (*66*). (**E**) Interaction between $\alpha_2\delta$-1 and α_1. The semitransparent EM density maps, generated in Chimera, are colored according to domain. (**F**) The detailed structure of the $Ca_v1.1$ complex. The structure is color-coded for the domains discussed in the text.

The structure also provides a foundation for future biophysical and computational characterizations of the Ca_v and Na_v channels.

Materials and methods

Expression and purification of rabbit β_{1a}

The cDNA of the rabbit β_{1a} (Uniprot ID: P19517) was synthesized and codon-optimized for *Escherichia coli* expression. The cDNA was subcloned into the pGEX-4T2 vector (Novagen). GST-fused β_{1a} was overexpressed and purified following similar protocol reported previously (*31*–*33*). Briefly, overexpression of β_{1a} was induced in *E. coli* BL21 (DE3) by 0.2 mM isopropyl-β-D-thiogalactoside when the cell density reached an optical density at 600 nm (OD_{600}) of approximately 1.2. After growth for 12 hours at 18°C, the cells were collected; resuspended in the lysis buffer containing 25 mM Tris-HCl, pH 8.0, and 150 mM NaCl; and disrupted through sonication. Cell debris was removed by centrifugation at 27,000*g* for 1 hour. The supernatant was applied to Glutathione Sepharose 4B resin (GS4B, GE Healthcare) and washed three times with the lysis buffer. The protein was then eluted from GS4B resin with the buffer containing 50 mM Tris-HCl, pH 8.0, 50 mM NaCl, and 10 mM glutathione, and was further purified through an anion-exchange column (Source 15Q, GE Healthcare). The peak fractions were collected and stored at −80°C for future use.

Pull-down of $Ca_v1.1$ complex by GST-β_{1a}

The skeletal muscle membrane from New Zealand white rabbit was collected as described (*40*). The enriched membrane was solubilized at 4°C for 2 hours in buffer containing 20 mM MOPS-Na, pH 7.4, 500 mM NaCl, 0.5 mM $CaCl_2$, 1% (w/v) digitonin (Sigma), protease inhibitor cocktail [2 mM phenylmethylsulfonyl fluoride (PMSF), aprotinin (2.6 μg/ml), pepstatin (1.4 μg/ml), and leupeptin (10 μg/ml)], and excessive purified GST-β_{1a}. After ultracentrifugation at 200,000*g* for 30 min, the supernatant was collected and incubated with GS4B resin at 4°C for 1 hour. The protein-loaded resin was washed three times with buffer containing 20 mM MOPS-Na, pH 7.4, 500 mM NaCl, 0.5 mM $CaCl_2$, 0.1% digitonin, and protease inhibitors. The target protein complex was eluted by the buffer containing 100 mM Tris-HCl, pH 8.0, 200 mM NaCl, 0.5 mM $CaCl_2$, 15 mM reduced glutathione, 0.1% digitonin, and protease inhibitors. After proteolytic removal of the fused GST, the eluent was concentrated and applied to size-exclusion chromatography (Superdex 200, 10/300 GL, GE Healthcare) in buffer containing 20 mM MOPS-Na, pH 7.4, 200 mM NaCl, 0.5 mM $CaCl_2$, 0.1% digitonin, and protease inhibitors. The peak

fractions of target protein complex were pooled and concentrated to about 0.1 mg/ml for EM analysis.

Cross-linking of proteins coupled with mass spectrometry analysis (CXMS)

CXMS samples were prepared following a published protocol (*70*). The purified $Ca_v1.1$ complex proteins were cross-linked using disuccinimidyl suberate (DSS) at room temperature with the protein:DSS (w/w) ratios at 4:1, 2:1, and 1:1 for 1 hour. The reactions were stopped by addition of 20 mM ammonium bicarbonate over 20 min at room temperature. Cross-linked protein samples were separated on a 12% SDS-PAGE gel, stained with Coomassie blue, and washed with ddH_2O. The high molecular weight bands seen only in the cross-linked samples were carefully excised and digested in gel with Lys-C (5 ng/μl) and trypsin (10 ng/μl).

Digested peptides were analyzed on a Q-Exactive mass spectrometer equipped with an easy nano-LC 1000 liquid chromatography system (Thermo-Fisher Scientific). Peptides were desalted on a 75 μm × 6 cm pre-column, which was packed with 10 μm, 120 Å ODS-AQ C18 resin (YMC Co. Ltd., Kyoto). The pre-column was connected to a 75 μm × 10 cm analytical column, which was packed with 1.8 μm, 120 Å UHPLC-XB-C18 resin (Welch Materials Inc., Shanghai). The peptides were separated using a 66-min linear gradient from 5% buffer B (100% acetonitrile, 0.1% formic acid), 95% buffer A (0.1% formic acid) to 30% buffer B, followed by a 5-min gradient from 30% to 80% buffer B and a final 8-min wash with 80% buffer B. The flow rate was 200 nl/min. The MS parameters were as follows: top 15 most intense ions were selected for HCD dissociation; R = 140,000 in full scan, R = 17,500 in HCD scan; AGC targets were 1e6 for FTMS full scan, 5e4 for MS2; minimal signal threshold for MS2 = 4e4; precursors having a charge state of +1, +2, > +6 or unassigned were excluded; normalized collision energy, 30; peptide match, preferred.

To identify cross-linked peptides, the MS data were searched using the pLink search engine (*71*) against a protein database containing the sequences of all the subunits of the $Ca_v1.1$ complex and the proteases used in the digestion. The pLink search parameters were: maximum number of missed cleavages (excluding the cross-linking site) = 3; min peptide length = 4 amino acids; fixed modification = cysteine carbamidomethylation. The search results were filtered by requiring a mass deviation of ≤10 ppm between an observed precursor mass and the mass of the matched peptide or peptide pair (either the monoisotopic or the first, second, third, or fourth isotopic mass), E-value < 0.001, false discovery rate < 0.05, and identification in at least two biological repeats.

Cryo-EM data acquisition

Cryo-EM grids were prepared with Vitrobot Mark IV (FEI). Aliquots (4 μl) of purified $Ca_v1.1$ complex at a concentration of approximately 0.1 mg/ml were placed on the copper grids supported by a thin layer of continuous carbon film estimated to be ~30 Å thick (Zhongjingkeyi Technology Co. Ltd.). Grids were blotted for 2 s and flash-frozen in liquid ethane cooled by liquid nitrogen. Grids were transferred to a Titan Krios (FEI) electron microscope that was operating at 300 kV with a nominal magnification of 22,500. Defocus varied from 2.0 to 3.3 μm. Images were recorded manually using a K2 Summit counting camera (Gatan Co.) in superresolution mode and binned to a pixel size of 1.32 Å. Each image was dose-fractionated to 32 frames with a dose rate of about 8.2 counts per second per physical pixel (~$6.3e^-/s\ Å^2$), resulting a total exposure time of 8 s and 0.25 s per frame. UCSFImage4 was used for all data collection (developed by X.L.).

Image processing

The images were aligned and summed using whole-image motion correction (*42*). The defocus value of each image was determined by CTFFIND3 (*72*). The particles were picked by RELION 1.3 (*43*) and manually checked by removing bad particles. All 2D and 3D classifications and refinements were performed using RELION 1.3.

A total of 1,481,899 particles from 3991 micrographs were selected and reference-free 2D class averaging was performed, yielding 1,367,382 good particles. The previously reported 20 Å cryo-EM reconstruction of $Ca_v1.1$ (EMDB accession 1069) (*38*) was used as starting model. Through 3D classification against the starting model low pass filtered to 60 Å, a random subset of 250,000 particles were classified to generate the most homogeneous class of 82,453 particles. Auto-refinement of this class gave rise to a 3D reconstruction with resolution at 6.7 Å, which showed distinguishable secondary structural elements. The handedness of the map was determined and corrected by comparison with crystal structures of Ca_vAb and Na_vRh and the handedness-corrected map was used as new initial model.

A 3D classification into six classes was then performed for all the 1,367,382 particles. This resulted in three classes with better overall reconstructed features. The three classes were combined into a subset of 872,390 particles (subset 1). The other three classes showed a small "tail" in the cytosolic region reminiscent of the previously reported β (*38*). These classes were combined into a subset of 494,992 particles (subset 2). The auto-refinement of both subsets were performed, yielding two maps with resolution of 5.3 Å and 6.9 Å, respectively (fig. S2). In a subsequent 3D classification run with four classes, an angular sampling of 1.8° was combined with local angular searches around the refined orientations. The most homogeneous class of 353,372 particles from subset 1 was subjected to auto-refinement and resulted in a reconstruction at a resolution of 4.2 Å based on the gold-standard Fourier shell correlation (FSC) 0.143 criterion. Auto-refinement of the best class of the 167,081 particles from subset 2 gave rise to a reconstruction of 6.1 Å. Local resolution was estimated using ResMap (*73*).

Model building and structure refinement

A simplified diagram of the procedure for model building is presented in fig. S3. The model was built in COOT (*74*). The crystal structure of β_2 bound to the alpha-interaction domain (AID) (PDB code 1T0J) was docked into the "tail" density as a rigid body. A crude poly-Ala model for α_1 was generated based on the crystal structures of Na_vRh (PDB code 4DXW) (*22*) and Ca_vAb (PDB code 4MS2) (*39*) by CHAINSAW (*75*). The model was manually adjusted to fit the EM density. Extracellular loops, unique sequence patterns with consecutive aromatic residues, and CXMS analysis were used to distinguish the four homologous repeats (fig. S5). The lack of EM density for the inter-repeat segments made it challenging to assign the four homologous but nonidentical repeats in the α_1 subunit. Theoretically, there can be six spatial arrangements of the four repeats that are allowed by the long intervening sequences (fig. S5A). Previous analysis of the interaction between μ-conotoxin GIIIA and the pore domain of a Na_v channel suggested a clockwise arrangement of the four repeats when viewed from the extracellular surface (*44*, *45*). However, the structure of a K^+ transporter TrkH revealed a counter-clockwise connection in the same view (*48*).

After the assignment of α_1 subunit, the EM density corresponding to four additional transmembrane helices (TM) was clearly identified to be the γ subunit. Structural predication by the I-TASSER server (*57*) gave rise to five models, whose TM regions fit well to the EM map.

Consistent with previous analysis, the bulky extramembrane domain appears to be the extracellular $\alpha_2\delta$-1 subunit. The VWA domain that is located just above the VSD of repeat I was first identified. An atomic model of this domain was derived from the homologous structure of I-domain of the α_M integrin (PDB code 1IDO). Two adjacent domains enriched with beta strands were predicted to be homologous to bacterial chemosensory domains (known as the Cache1 and Cache2 domains). The structural model of these domains was built on the basis of the crystal structures of the sporulation kinase D sensor domain (PDB code 4JGP) and Mcp_N and cache domains of methyl-accepting chemotaxis protein (PDB code 3C8C). The structural models for VWA and the two Cache domains were manually adjusted into the EM density with the reference of unique sequence patterns and predicted N-linked glycosylation sites. Upon assignment of side chains of the VWA domain, the disulfide bond between Cys^{406} of the VWA domain and Cys^{1062} of the δ subunit was identified, which allowed the tracing of an elongated fragment of the δ subunit. Finally, poly-Ala chains were built for the remaining EM density, which should mostly correspond to the α_2 subunit.

Structure refinement was carried out by PHENIX (*76*) in real space with secondary structure and geometry restraint.

REFERENCES AND NOTES

1. S. Ebashi, M. Endo, Calcium ion and muscle contraction. *Prog. Biophys. Mol. Biol.* **18**, 123–183 (1968). doi: 10.1016/0079-6107(68)90023-0; pmid: 4894870
2. S. Miyazaki, Thirty years of calcium signals at fertilization. *Semin. Cell Dev. Biol.* **17**, 233–243 (2006). doi: 10.1016/j.semcdb.2006.02.007; pmid: 16549376

3. D. E. Clapham, Calcium signaling. *Cell* **131**, 1047–1058 (2007). doi: 10.1016/j.cell.2007.11.028; pmid: 18083096
4. P. Fatt, B. Katz, The electrical properties of crustacean muscle fibres. *J. Physiol.* **120**, 171–204 (1953). doi: 10.1113/jphysiol.1953.sp004884; pmid: 13062231
5. M. C. Nowycky, A. P. Fox, R. W. Tsien, Three types of neuronal calcium channel with different calcium agonist sensitivity. *Nature* **316**, 440–443 (1985). doi: 10.1038/316440a0; pmid: 2410796
6. E. A. Ertel *et al*., Nomenclature of voltage-gated calcium channels. *Neuron* **25**, 533–535 (2000). doi: 10.1016/S0896-6273(00)81057-0; pmid: 10774722
7. B. Hille, *Ion Channels of Excitable Membranes* (Sinauer, Sunderland, MA, ed. 3, 2001).
8. A. C. Dolphin, A short history of voltage-gated calcium channels. *Br. J. Pharmacol.* **147** (suppl. 1), S56–S62 (2006). doi: 10.1038/sj.bjp.0706442; pmid: 16402121
9. E. Rios, G. Brum, Involvement of dihydropyridine receptors in excitation-contraction coupling in skeletal muscle. *Nature* **325**, 717–720 (1987). doi: 10.1038/325717a0; pmid: 2434854
10. T. Tanabe *et al*., Primary structure of the receptor for calcium channel blockers from skeletal muscle. *Nature* **328**, 313–318 (1987). doi: 10.1038/328313a0; pmid: 3037387
11. T. Tanabe, K. G. Beam, J. A. Powell, S. Numa, Restoration of excitation-contraction coupling and slow calcium current in dysgenic muscle by dihydropyridine receptor complementary DNA. *Nature* **336**, 134–139 (1988). doi: 10.1038/336134a0; pmid: 2903448
12. B. A. Block, T. Imagawa, K. P. Campbell, C. Franzini-Armstrong, Structural evidence for direct interaction between the molecular components of the transverse tubule/sarcoplasmic reticulum junction in skeletal muscle. *J. Cell Biol.* **107**, 2587–2600 (1988). doi: 10.1083/jcb.107.6.2587; pmid: 2849609
13. B. A. Adams, T. Tanabe, A. Mikami, S. Numa, K. G. Beam, Intramembrane charge movement restored in dysgenic skeletal muscle by injection of dihydropyridine receptor cDNAs. *Nature* **346**, 569–572 (1990). doi: 10.1038/346569a0; pmid: 2165571
14. H. Takekura, L. Bennett, T. Tanabe, K. G. Beam, C. Franzini-Armstrong, Restoration of junctional tetrads in dysgenic myotubes by dihydropyridine receptor cDNA. *Biophys. J.* **67**, 793–803 (1994). doi: 10.1016/S0006-3495(94)80539-9; pmid: 7948692
15. F. Van Petegem, Ryanodine receptors: Allosteric ion channel giants. *J. Mol. Biol.* **427**, 31–53 (2015). doi: 10.1016/j.jmb.2014.08.004; pmid: 25134758
16. W. A. Catterall, Voltage-gated calcium channels. *Cold Spring Harb. Perspect. Biol.* **3**, a003947 (2011). doi: 10.1101/cshperspect.a003947; pmid: 21746798
17. R. A. Bannister, K. G. Beam, $Ca_V1.1$: The atypical prototypical voltage-gated Ca^{2+} channel. *Biochim. Biophys. Acta* **1828**, 1587–1597 (2013). doi: 10.1016/j.bbamem.2012.09.007; pmid: 22982493
18. Y. Jiang *et al*., X-ray structure of a voltage-dependent K^+ channel. *Nature* **423**, 33–41 (2003). doi: 10.1038/nature01580; pmid: 12721618
19. S. B. Long, E. B. Campbell, R. Mackinnon, Voltage sensor of Kv1.2: Structural basis of electromechanical coupling. *Science* **309**, 903–908 (2005). doi: 10.1126/science.1116270; pmid: 16002579
20. S. B. Long, X. Tao, E. B. Campbell, R. MacKinnon, Atomic structure of a voltage-dependent K^+ channel in a lipid membrane-like environment. *Nature* **450**, 376–382 (2007). doi: 10.1038/nature06265; pmid: 18004376
21. J. Payandeh, T. Scheuer, N. Zheng, W. A. Catterall, The crystal structure of a voltage-gated sodium channel. *Nature* **475**, 353–358 (2011). doi: 10.1038/nature10238; pmid: 21743477
22. X. Zhang *et al*., Crystal structure of an orthologue of the NaChBac voltage-gated sodium channel. *Nature* **486**, 130–134 (2012).pmid: 22678295
23. M. G. Kang, K. P. Campbell, γ subunit of voltage-activated calcium channels. *J. Biol. Chem.* **278**, 21315–21318 (2003). doi: 10.1074/jbc.R300004200; pmid: 12676943
24. Z. Andronache *et al*., The auxiliary subunit γ_1 of the skeletal muscle L-type Ca^{2+} channel is an endogenous Ca^{2+} antagonist. *Proc. Natl. Acad. Sci. U.S.A.* **104**, 17885–17890 (2007). doi: 10.1073/pnas.0704340104; pmid: 17978188
25. Z. Buraei, J. Yang, The β subunit of voltage-gated Ca^{2+} channels. *Physiol. Rev.* **90**, 1461–1506 (2010). doi: 10.1152/physrev.00057.2009; pmid: 20959621
26. A. Davies *et al*., Functional biology of the $\alpha_2\delta$ subunits of voltage-gated calcium channels. *Trends Pharmacol. Sci.* **28**, 220–228 (2007). doi: 10.1016/j.tips.2007.03.005; pmid: 17403543
27. A. C. Dolphin, The $\alpha_2\delta$ subunits of voltage-gated calcium channels. *Biochim. Biophys. Acta* **1828**, 1541–1549 (2013). doi: 10.1016/j.bbamem.2012.11.019; pmid: 23196350
28. G. W. Zamponi, J. Striessnig, A. Koschak, A. C. Dolphin, The physiology, pathology, and pharmacology of voltage-gated calcium channels and their future therapeutic potential. *Pharmacol. Rev.* **67**, 821–870 (2015). doi: 10.1124/pr.114.009654; pmid: 26362469
29. F. Bian *et al*., Calcium channel $\alpha_2\delta$ type 1 subunit is the major binding protein for pregabalin in neocortex, hippocampus, amygdala, and spinal cord: An ex vivo autoradiographic study in $\alpha_2\delta$ type 1 genetically modified mice. *Brain Res.* **1075**, 68–80 (2006). doi: 10.1016/j.brainres.2005.12.084; pmid: 16460711
30. Z. Li *et al*., Pregabalin is a potent and selective ligand for $\alpha_2\delta$-1 and $\alpha_2\delta$-2 calcium channel subunits. *Eur. J. Pharmacol.* **667**, 80–90 (2011). doi: 10.1016/j.ejphar.2011.05.054; pmid: 21651903
31. F. Van Petegem, K. A. Clark, F. C. Chatelain, D. L. Minor Jr., Structure of a complex between a voltage-gated calcium channel β-subunit and an α-subunit domain. *Nature* **429**, 671–675 (2004). doi: 10.1038/nature02588; pmid: 15141227
32. Y. H. Chen *et al*., Structural basis of the $\alpha_1\beta$ subunit interaction of voltage-gated Ca^{2+} channels. *Nature* **429**, 675–680 (2004). doi: 10.1038/nature02641; pmid: 15170217
33. Y. Opatowsky, C. C. Chen, K. P. Campbell, J. A. Hirsch, Structural analysis of the voltage-dependent calcium channel β subunit functional core and its complex with the α_1 interaction domain. *Neuron* **42**, 387–399 (2004). doi: 10.1016/S0896-6273(04)00250-8; pmid: 15134636
34. H. Hu *et al*., The molecular architecture of dihydropyrindine receptor/L-type Ca^{2+} channel complex. *Sci Rep* **5**, 8370 (2015). doi: 10.1038/srep08370; pmid: 25667046
35. I. I. Serysheva II, S. J. Ludtke, M. R. Baker, W. Chiu, S. L. Hamilton, Structure of the voltage-gated L-type Ca^{2+} channel by electron cryomicroscopy. *Proc. Natl. Acad. Sci. U.S.A.* **99**, 10370–10375 (2002). doi: 10.1073/pnas.162363499; pmid: 12149473
36. M. C. Wang *et al*., 3D structure of the skeletal muscle dihydropyridine receptor. *J. Mol. Biol.* **323**, 85–98 (2002). doi: 10.1016/S0022-2836(02)00890-2; pmid: 12368101
37. K. Murata, S. Nishimura, A. Kuniyasu, H. Nakayama, Three-dimensional structure of the $\alpha_1\beta$ complex in the skeletal muscle dihydropyridine receptor by single-particle electron microscopy. *J. Electron Microsc.* **59**, 215–226 (2010). doi: 10.1093/jmicro/dfp059; pmid: 19995890
38. M. Wolf, A. Eberhart, H. Glossmann, J. Striessnig, N. Grigorieff, Visualization of the domain structure of an L-type Ca^{2+} channel using electron cryo-microscopy. *J. Mol. Biol.* **332**, 171–182 (2003). doi: 10.1016/S0022-2836(03)00899-4; pmid: 12946355
39. L. Tang *et al*., Structural basis for Ca^{2+} selectivity of a voltage-gated calcium channel. *Nature* **505**, 56–61 (2014). doi: 10.1038/nature12775; pmid: 24270805
40. Z. Yan *et al*., Structure of the rabbit ryanodine receptor RyR1 at near-atomic resolution. *Nature* **517**, 50–55 (2015). doi: 10.1038/nature14063; pmid: 25517095
41. P. A. Powers, S. Liu, K. Hogan, R. G. Gregg, Skeletal muscle and brain isoforms of a β-subunit of human voltage-dependent calcium channels are encoded by a single gene. *J. Biol. Chem.* **267**, 22967–22972 (1992). pmid: 1385409
42. X. Li *et al*., Electron counting and beam-induced motion correction enable near-atomic-resolution single-particle cryo-EM. *Nat. Methods* **10**, 584–590 (2013). doi: 10.1038/nmeth.2472; pmid: 23644547
43. S. H. Scheres, Semi-automated selection of cryo-EM particles in RELION-1.3. *J. Struct. Biol.* **189**, 114–122 (2015). doi: 10.1016/j.jsb.2014.11.010; pmid: 25486611
44. S. C. Dudley Jr. *et al*., μ-Conotoxin GIIIA interactions with the voltage-gated Na^+ channel predict a clockwise arrangement of the domains. *J. Gen. Physiol.* **116**, 679–690 (2000). doi: 10.1085/jgp.116.5.679; pmid: 11055996
45. R. A. Li *et al*., Clockwise domain arrangement of the sodium channel revealed by μ-conotoxin (GIIIA) docking orientation. *J. Biol. Chem.* **276**, 11072–11077 (2001). doi: 10.1074/jbc.M010862200; pmid: 11154701
46. A. N. Miller, S. B. Long, Crystal structure of the human two-pore domain potassium channel K2P1. *Science* **335**, 432–436 (2012). doi: 10.1126/science.1213274; pmid: 22282804
47. S. G. Brohawn, J. del Mármol, R. MacKinnon, Crystal structure of the human K2P TRAAK, a lipid- and mechano-sensitive K^+ ion channel. *Science* **335**, 436–441 (2012). doi: 10.1126/science.1213808; pmid: 22282805
48. Y. Cao *et al*., Crystal structure of a potassium ion transporter, TrkH. *Nature* **471**, 336–340 (2011). doi: 10.1038/nature09731; pmid: 21317882
49. M. O. Jensen *et al*., Mechanism of voltage gating in potassium channels. *Science* **336**, 229–233 (2012). doi: 10.1126/science.1216533; pmid: 22499946
50. X. Zhang, N. Yan, The conformational shifts of the voltage sensing domains between Na_vRh and Na_vAb. *Cell Res.* **23**, 444–447 (2013). doi: 10.1038/cr.2012.158; pmid: 23147793
51. C. Xie, X. G. Zhen, J. Yang, Localization of the activation gate of a voltage-gated Ca^{2+} channel. *J. Gen. Physiol.* **126**, 205–212 (2005). doi: 10.1085/jgp.200509293; pmid: 16129771
52. M. Liao, E. Cao, D. Julius, Y. Cheng, Structure of the TRPV1 ion channel determined by electron cryo-microscopy. *Nature* **504**, 107–112 (2013). doi: 10.1038/nature12822; pmid: 24305160
53. C. E. Paulsen, J. P. Armache, Y. Gao, Y. Cheng, D. Julius, Structure of the TRPA1 ion channel suggests regulatory mechanisms. *Nature* **520**, 511–517 (2015). doi: 10.1038/nature14367; pmid: 25855297
54. J. Yang, P. T. Ellinor, W. A. Sather, J. F. Zhang, R. W. Tsien, Molecular determinants of Ca^{2+} selectivity and ion permeation in L-type Ca^{2+} channels. *Nature* **366**, 158–161 (1993). doi: 10.1038/366158a0; pmid: 8232554
55. P. T. Ellinor, J. Yang, W. A. Sather, J. F. Zhang, R. W. Tsien, Ca^{2+} channel selectivity at a single locus for high-affinity Ca^{2+} interactions. *Neuron* **15**, 1121–1132 (1995). doi: 10.1016/0896-6273(95)90100-0; pmid: 7576655
56. R. K. Cloues, S. M. Cibulsky, W. A. Sather, Ion interactions in the high-affinity binding locus of a voltage-gated Ca^{2+} channel. *J. Gen. Physiol.* **116**, 569–586 (2000). doi: 10.1085/jgp.116.4.569; pmid: 11004206
57. J. Yang *et al*., The I-TASSER Suite: Protein structure and function prediction. *Nat. Methods* **12**, 7–8 (2015). doi: 10.1038/nmeth.3213; pmid: 25549265
58. H. Suzuki *et al*., Crystal structure of a claudin provides insight into the architecture of tight junctions. *Science* **344**, 304–307 (2014). doi: 10.1126/science.1248571; pmid: 24744376
59. Y. Saitoh *et al*., Structural insight into tight junction disassembly by *Clostridium perfringens* enterotoxin. *Science* **347**, 775–778 (2015). doi: 10.1126/science.1261833 pmid: 25678664
60. J. S. Simske, Claudins reign: The claudin/EMP/PMP22/γ channel protein family in *C. elegans*. *Tissue Barriers* **1**, e25502 (2013). doi: 10.4161/tisb.25502; pmid: 24665403
61. Y. Moran, H. H. Zakon, The evolution of the four subunits of voltage-gated calcium channels: Ancient roots, increasing complexity, and multiple losses. *Genome Biol. Evol.* **6**, 2210–2217 (2014). doi: 10.1093/gbe/evu177; pmid: 25146647
62. J. Arikkath *et al*., γ_1 subunit interactions within the skeletal muscle L-type voltage-gated calcium channels. *J. Biol. Chem.* **278**, 1212–1219 (2003). doi: 10.1074/jbc.M208689200; pmid: 12409298
63. R. S. Chen, T. C. Deng, T. Garcia, Z. M. Sellers, P. M. Best, Calcium channel γ subunits: A functionally diverse protein family. *Cell Biochem. Biophys.* **47**, 178–186 (2007). doi: 10.1007/s12013-007-0002-0; pmid: 17652770
64. C. Sager, D. Tapken, S. Kott, M. Hollmann, Functional modulation of AMPA receptors by transmembrane AMPA receptor regulatory proteins. *Neuroscience* **158**, 45–54 (2009). doi: 10.1016/j.neuroscience.2007.12.046; pmid: 18304745
65. J. O. Lee, L. A. Bankston, M. A. Arnaout, R. C. Liddington, Two conformations of the integrin A-domain (I-domain): A pathway for activation? *Structure* **3**, 1333–1340 (1995). doi: 10.1016/S0969-2126(01)00271-4; pmid: 8747460
66. R. Wu *et al*., Insight into the sporulation phosphorelay: Crystal structure of the sensor domain of *Bacillus subtilis* histidine kinase, KinD. *Protein Sci.* **22**, 564–576 (2013). doi: 10.1002/pro.2237; pmid: 23436677
67. V. Anantharaman, L. Aravind, Cache - a signaling domain common to animal Ca^{2+}-channel subunits and a class of prokaryotic chemotaxis receptors. *Trends Biochem. Sci.* **25**, 535–537 (2000). doi: 10.1016/S0968-0004(00)01672-8; pmid: 11084361
68. H. Liu *et al*., Identification of three subunits of the high affinity omega-conotoxin MVIIC-sensitive Ca^{2+} channel. *J. Biol. Chem.* **271**, 13804–13810 (1996). doi: 10.1074/jbc.271.23.13804; pmid: 8662888
69. C. A. Gurnett, R. Felix, K. P. Campbell, Extracellular interaction of the voltage-dependent Ca^{2+} channel $\alpha_2\delta$ and α_1 subunits.

J. Biol. Chem. **272**, 18508–18512 (1997). doi: 10.1074/jbc.272.29.18508; pmid: 9218497
70. K. Coffman *et al.*, Characterization of the Raptor/4E-BP1 interaction by chemical cross-linking coupled with mass spectrometry analysis. *J. Biol. Chem.* **289**, 4723–4734 (2014). doi: 10.1074/jbc.M113.482067; pmid: 24403073
71. B. Yang *et al.*, Identification of cross-linked peptides from complex samples. *Nat. Methods* **9**, 904–906 (2012). doi: 10.1038/nmeth.2099; pmid: 22772728
72. J. A. Mindell, N. Grigorieff, Accurate determination of local defocus and specimen tilt in electron microscopy. *J. Struct. Biol.* **142**, 334–347 (2003). doi: 10.1016/S1047-8477(03)00069-8; pmid: 12781660
73. A. Kucukelbir, F. J. Sigworth, H. D. Tagare, Quantifying the local resolution of cryo-EM density maps. *Nat. Methods* **11**, 63–65 (2014). doi: 10.1038/nmeth.2727; pmid: 24213166
74. P. Emsley, B. Lohkamp, W. G. Scott, K. Cowtan, Features and development of Coot. *Acta Crystallogr. D* **66**, 486–501 (2010). doi: 10.1107/S0907444910007493; pmid: 20383002
75. N. Stein, CHAINSAW: A program for mutating pdb files used as templates in molecular replacement. *J. Appl. Crystallogr.* **41**, 641–643 (2008). doi: 10.1107/S0021889808006985
76. P. D. Adams *et al.*, PHENIX: A comprehensive Python-based system for macromolecular structure solution. *Acta Crystallogr. D* **66**, 213–221 (2010). doi: 10.1107/S0907444909052925; pmid: 20124702
77. E. F. Pettersen *et al.*, UCSF Chimera—a visualization system for exploratory research and analysis. *J. Comput. Chem.* **25**, 1605–1612 (2004). doi: 10.1002/jcc.20084; pmid: 15264254
78. W. L. DeLano, The PyMOL Molecular Graphics System; www.pymol.org (2002).

ACKNOWLEDGMENTS

We thank Xueming Li, Jiawei Wang, and Hongwei Wang for technical discussions; Jianlin Lei, Yanji Xu, Mingfang Wang, and Xiaomei Li for technical support; and Jiao Lin and Guangwen Yang for facility support. We thank the Tsinghua University Branch of China National Center for Protein Sciences (Beijing) for providing facility support. The computation was completed on the "Explorer 100" cluster system of Tsinghua National Laboratory for Information Science and Technology. This work was supported by funds from the Ministry of Science and Technology of China (2015CB9101012014, ZX09507003006) and National Natural Science Foundation of China (projects 31130002 and 31125009). The research of N.Y. was supported in part by an International Early Career Scientist grant from the Howard Hughes Medical Institute and an endowed professorship from Bayer Healthcare. The atomic coordinates of the rabbit $Ca_v1.1$ complex have been deposited in the Protein Data Bank with accession code 3JBR. The 4.2 Å and 6.1 Å EM maps have been deposited in EMDB with accession codes EMD-6475 and EMD-6476, respectively.

SUPPLEMENTARY MATERIALS

www.sciencemag.org/content/350/6267/aad2395/suppl/DC1
Tables S1 and S2
Figs. S1 to S10

14 August 2015; accepted 30 October 2015
10.1126/science.aad2395

RESEARCH ARTICLE

GENOMIC EVOLUTION

Genomic islands of speciation separate cichlid ecomorphs in an East African crater lake

Milan Malinsky,[1,2]† Richard J. Challis,[3]†‡ Alexandra M. Tyers,[3] Stephan Schiffels,[1] Yohey Terai,[4] Benjamin P. Ngatunga,[5] Eric A. Miska,[1,2] Richard Durbin,[1] Martin J. Genner,[6]* George F. Turner[3]*

The genomic causes and effects of divergent ecological selection during speciation are still poorly understood. Here we report the discovery and detailed characterization of early-stage adaptive divergence of two cichlid fish ecomorphs in a small (700 meters in diameter) isolated crater lake in Tanzania. The ecomorphs differ in depth preference, male breeding color, body shape, diet, and trophic morphology. With whole-genome sequences of 146 fish, we identified 98 clearly demarcated genomic "islands" of high differentiation and demonstrated the association of genotypes across these islands with divergent mate preferences. The islands contain candidate adaptive genes enriched for functions in sensory perception (including rhodopsin and other twilight-vision–associated genes), hormone signaling, and morphogenesis. Our study suggests mechanisms and genomic regions that may play a role in the closely related mega-radiation of Lake Malawi.

Understanding the causes and consequences of speciation, including at the genetic level, requires the investigation of taxa at different stages on the speciation continuum (*1*, *2*). East African cichlids have repeatedly undergone rapid adaptive radiation (*3*). The Lake Malawi radiation has generated over 500 species in less than 5 million years, involving divergence in habitat, feeding apparatus, and nuptial color. Thus, these phenomena present an opportunity to observe hundreds of varied, recent, and in some cases ongoing, speciation events (*4*). However, the investigation of early stages of speciation in the large cichlid radiations of Malawi as well as Lakes Tanganyika and Victoria has been hampered by difficulties in identifying sister species relationships, in reconstructing past geographical situations, and in controlling for possible introgression from non-sister taxa (*5*).

During 2011, we conducted a survey (table S1) of fish fauna in six crater lakes in the Rungwe District of Tanzania (Fig. 1A and table S2). In all six lakes, we found endemic haplochromine cichlids of the genus *Astatotilapia*, closely related to *A. calliptera* (Fig. 1A), a species widely distributed in the rivers, streams, and shallow lake margins of the region. Thus, the Rungwe District *Astatotilapia* are close relatives of the of Lake Malawi endemic haplochromine cichlids (*5*).

In Lake Massoko (fig. S1), the benthic zone in deep waters (~20 to 25 m) is very dimly lit and populated by cichlids with phenotypes clearly different from those typical of shallow waters (≲5 m) close to the shore (littoral). Deep-water males are dark blue-black, whereas most males collected from the shallow waters are yellow-green, similar to riverine *A. calliptera* (Fig. 1B, movie S1, and table S3). We also collected small (<65 mm standard length) males that were not readily field-assigned to either ecomorph (*6*). The benthic and littoral morphs are reminiscent of the species pair of *Pundamilia* cichlids from Lake Victoria (*7*), but within a potentially simpler historical and geographical context. Lake Massoko is steep-sided, has a strong thermocline at ~15 m, and an anoxic boundary at ~25 m (*8*). The estimated time of lake formation is ~50,000 years ago (*9*).

Ecomorph separation

To examine relationships between crater lake and riverine *A. calliptera* of southern Tanzania, we obtained restriction site–associated DNA (RAD) data from 30 fish from the Rungwe District and 11 outgroup *Astatotilapia* from the broader Lake Malawi catchment and a neighboring catchment (fig. S2 and table S4). A maximum-likelihood phylogeny constructed on the basis of these data (*6*) demonstrates monophyly of all specimens from Lake Massoko (Fig. 1A). Thus, the RAD phylogeny provides evidence that Massoko morphs might have evolved in primary sympatry, as proposed for crater lake cichlid radiations of Cameroon (*10*) and Nicaragua (*11*).

Morphological analyses of these two color morphs revealed significant differences in head and body shape, body mass, the shape of pharyngeal teeth, and pharyngeal jaw mass [Fig. 1, C to F, and table S5; analysis of covariance (ANCOVA) tests, all $P < 0.001$]. We also found significant differences in stable isotope ratios (Fig. 1G and table S5; ANCOVA test, $P < 0.001$), which are indicative of dietary differences. Together these results demonstrate ecomorph separation and adaptation to different ecological environments.

Whole-genome evidence

To study the genome-wide pattern of Massoko ecomorph divergence and to further clarify its geographical context, we obtained whole-genome sequence data at ~15× coverage for 6 individuals each of the yellow littoral and blue benthic ecomorphs and 16 additional *A. calliptera* from the wider Lake Malawi catchment and two adjacent catchments (fig. S2), supplemented by lower-coverage (~6×) data from 87 specimens from Lake Massoko (25 littoral, 32 benthic, and 30 small unassigned) and 30 individuals from Lake Itamba (Fig. 1A and table S6). Sequence data were aligned to the *Metriaclima zebra* reference assembly (*12*), from which divergence was 0.2 to 0.3%, and variants were called at 4,755,448 sites (1.2 to 1.6 million sites per individual).

A maximum-likelihood phylogeny built from whole-genome sequence data confirmed reciprocal monophyly of *Astatotilapia* within Lakes Massoko and Itamba and revealed the sister group of Massoko fish to be an *A. calliptera* population from the nearby Mbaka River (Fig. 2A). All specimens of the benthic ecomorph formed a monophyletic clade derived from the littoral ecomorph (Fig. 2A). Principal components analysis (PCA) showed strong population structure (Tracy-Widom statistics: $P < 1 \times 10^{-12}$), with benthic and littoral individuals separated by the first eigenvector and forming separate clusters (Fig. 2B). In contrast, within Lake Itamba, PCA did not reveal significant population structure (Tracy-Widom statistics: $P = 0.11$). Individuals from Massoko that were not field-assigned to either of the ecomorphs did not form a monophyletic clade in the phylogeny (Fig. 2A) or a distinct cluster in PCA (Fig. 2B).

Analysis of fine-scale genetic relationships with fineSTRUCTURE (*13*) supports the monophyly of the benthic ecomorph within the littoral, but also suggests that compared with the benthic population, the littoral population has greater coancestry with other *A. calliptera*; in particular with the Mbaka River sample (fig. S3). Therefore, we tested for evidence of secondary gene flow, as seen in cichlid populations from Cameroonian crater lakes (*14*). Under the null hypothesis of no differential gene flow into Massoko, *A. calliptera* from the Mbaka River should share derived alleles equally often with the littoral and with the benthic populations (*15*, *16*). Instead, we found a small excess of shared derived alleles between *A. calliptera* from the Mbaka River and the littoral population,

[1]Wellcome Trust Sanger Institute, Cambridge CB10 1SA, UK. [2]Gurdon Institute and Department of Genetics, University of Cambridge, Cambridge CB2 1QN, UK. [3]School of Biological Sciences, Bangor University, Bangor, Gwynedd LL57 2UW, UK. [4]Department of Evolutionary Studies of Biosystems, SOKENDAI, Kanagawa 240-0193, Japan. [5]Tanzania Fisheries Research Institute, Box 9750, Dar es Salaam, Tanzania. [6]School of Biological Sciences, Life Sciences Building, 24 Tyndall Avenue, University of Bristol, Bristol BS8 1TQ, UK. ***Corresponding author. E-mail: george.turner@bangor.ac.uk (G.F.T.); m.genner@bristol.ac.uk (M.J.G.)** †These authors contributed equally to this work. ‡Present address: Institute of Evolutionary Biology, University of Edinburgh, Charlotte Auerbach Road, Edinburgh EH9 3FL, UK.

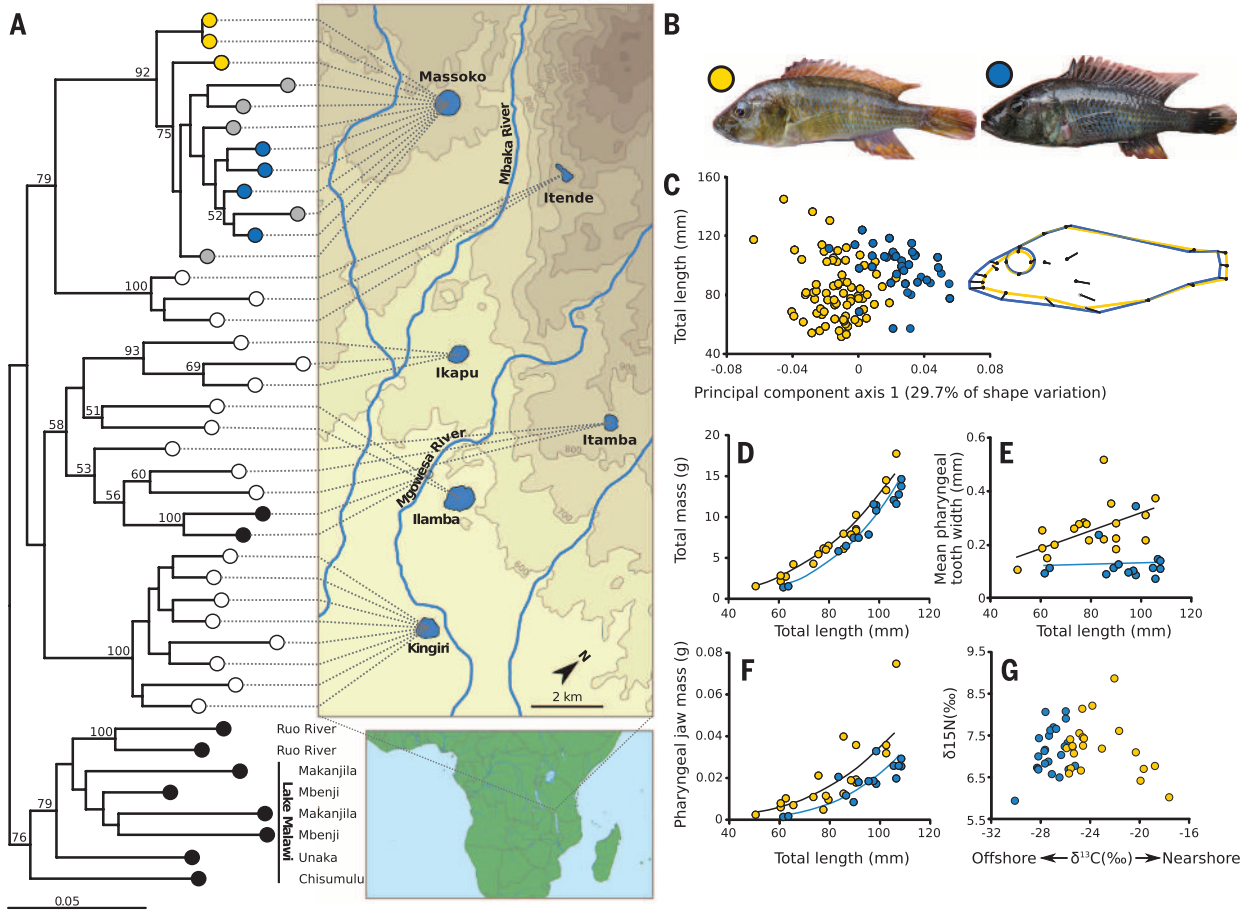

Fig. 1. Cichlid radiation in the crater lakes of southern Tanzania. (**A**) A phylogeny of the crater lake *Astatotilapia* based on reference-aligned RAD data (7906 SNPs across 5010 polymorphic RAD loci). It demonstrates reciprocal monophyly between the populations in each lake except for Itamba, and a close relationship to *A. calliptera* from rivers and from Lake Malawi. Within Lake Massoko, yellow symbols indicate the littoral morph, blue symbols indicate the benthic morph, and gray symbols denote small, phenotypically ambiguous, and thus unassigned individuals. Additional *Astatotilapia* individuals from other crater lakes are denoted by open circles. *A. calliptera* from rivers and Lake Malawi are denoted by black circles. Bootstrap values are displayed for nodes with >50% support. (**B**) Breeding males of the yellow littoral and blue benthic morphs of Lake Massoko. The symbols next to the photographs correspond to symbols used in (C) to (G). (**C** to **F**) Morphological divergence between the two morphs of Lake Massoko. Relative to the littoral morph, the benthic morph has relatively longer head and jaw (C), lower body mass (D), narrower "papilliform" pharyngeal teeth (E), and lighter lower pharyngeal jaws (F). The benthic fish have stable isotope ratios that tend to be more depleted in C^{13} than the littoral fish, indicative of a more offshore-planktonic diet (**G**).

when compared with the benthic population (Patterson's D = 1.1%; 4.86 SD from 0% or $P < 5.8 \times 10^{-7}$) (*6*). The proportion of admixture f with Mbaka was estimated at 0.9 ± 0.2%. This value is low, at a proportion that is approximately half of the Neanderthal introgression into non-African humans (*15*), and cross-coalescence rate analysis with the multiple sequentially Markovian coalescent (MSMC) (*6*, *17*) indicates an average separation time of both Massoko ecomorphs from other *A. calliptera* samples (including the Mbaka River) approximately 10 times earlier than the split between the two ecomorphs (fig. S5). Thus, it is unlikely that a secondary invasion from the neighboring river systems (fig. S11B) contributed to the divergence of the ecomorphs.

We estimated individual ancestries for all Massoko and *A. calliptera* specimens with ADMIXTURE (*6*, *18*) (fig. S4). Focusing on the Massoko samples, 11 of the 31 samples field-assigned as littoral were identified as admixed, with admixture fraction >25% from the benthic gene pool. No individuals identified as benthic were estimated to be admixed to the same extent; therefore, recent gene flow may be biased from deep to shallow waters. Ten of the 30 unassigned individuals were also identified as >25% admixed, whereas the remaining 20 unassigned samples appear to represent subadult individuals of both benthic and littoral ecomorphs (fig. S4A). When additional *A. calliptera* samples were included in ADMIXTURE analysis, a small amount of gene flow into Massoko was apparent with K = 2 ancestral populations (fig. S4C), consistent with the fineSTRUCTURE and Patterson's D results described above. This analysis also suggests similar or even stronger gene flow out of Massoko and into the Mbaka River (fig. S4C).

Islands of speciation

Interestingly, there are no fixed differences between Massoko benthic and littoral ecomorphs. Genome-wide divergence F_{ST} is 0.038, and almost half (47.6%) of the variable sites have zero F_{ST} (table S7). Above the low background, a genome-wide F_{ST} profile shows clearly demarcated "islands" of high differentiation (Fig. 2, C and E). For single sites, the maximum F_{ST} is 13.6 SD above the mean, and 7543 sites have F_{ST} over 6 SD above the mean. In contrast, comparisons of the combined Massoko population and Itamba population revealed a pattern of consistently high F_{ST} across the genome (Fig. 2D) and large variance, making it impossible to detect statistical outliers (Fig. 2E). Similar results were obtained when varying the window size to include 15, 50, 100, or 500 variants (table S7 and figs. S6 and S7).

Comparing observed levels of divergence with neutral coalescent simulations (*6*) under a range of possible demographic models revealed that the top 1% of observed F_{ST} values (approximately $F_{ST} \geq 0.25$) are always higher than the corresponding neutral F_{ST} values from simulations, consistent

with divergent selection acting on approximately this top 1% of variant sites (figs. S8 and S9).

We identified genomic regions with observed benthic-littoral $F_{ST} \geq 0.25$ (i.e., with F_{ST} above maximum levels seen in neutral simulations) (*6*). For this we used windows of 15 variants each, providing a balance between fine genomic resolution and reducing stochastic variation by averaging over variants. Small gaps arising from brief dips of F_{ST} below the threshold were eliminated by merging regions within 10 kb of one another. We found 344 such regions, with total length of 8.1 Mb (~1% of the genome). Next, to focus on the more significant outliers, we narrowed the list down to a set of 98 highly diverged regions (HDRs) for further characterization (table S8) by adding the requirement that at least one 10-kb window must have reached $F_{ST} \geq 0.3$. The HDRs varied in length from 4.4 kb to 285 kb (median, 36.1 kb), with a total length of 5.5 Mb.

A key prediction of speciation with gene flow models is that loci participating in speciation should have both high relative divergence (F_{ST}) and high absolute sequence divergence (d_{XY}) (*19*, *20*). However, previous studies [examined in (*20*)] revealed low d_{XY} and low nucleotide diversity (π) in regions of high F_{ST}. In contrast, we found that d_{XY} in Massoko is significantly higher in HDRs relative to the rest of the genome ($P < 2.2 \times 10^{-16}$, two-tailed Mann-Whitney test; Fig. 3A). In the benthic ecomorph, π in HDRs is not significantly different from the rest of the genome ($P = 0.34$, two-tailed Mann-Whitney test; fig. S10A), and in the littoral ecomorph π in HDRs is elevated ($P = 5.47 \times 10^{-6}$, two-tailed Mann-Whitney test; fig. S10B). Individually, 55 HDRs have d_{XY} above the 90th percentile of the genome-wide distribution. The convergence of F_{ST} and d_{XY} measures in regions of normal π suggests that these 55 "islands of speciation" (table S9) may have been involved in reducing gene flow in sympatry and thereby directly causing speciation to progress. In contrast, loci involved in continuing local adaptation after the ecomorphs split sufficiently to constitute two largely separate gene pools (or during a period of allopatry) would be expected to have elevated F_{ST} but not d_{XY} (*20*).

Another key prediction of speciation with gene flow models is that loci causing speciation should be located in relatively few linked clusters within the genome (*2*, *20*, *21*). Instead of a large number of scattered islands, the theory predicts a smaller number of clusters that grow in size because of the "divergence hitchhiking" process. We tested this prediction using a recently generated linkage map (*22*) and found that at least 27 out of the 55 putative speciation islands are co-localized on five linkage groups (LGs), with 26 of them clustered within their respective LGs (Fig. 3B and table S9). These potential speciation clusters extended for approximately 25 cM on LG5, 40 cM on LG7, 30 cM on LG12, 5 cM on LG20, and 45 cM on LG 23. In total, these regions account for under 7% of the genome, suggesting that divergence hitchhiking may play a role in shaping the observed pattern of genomic differentiation.

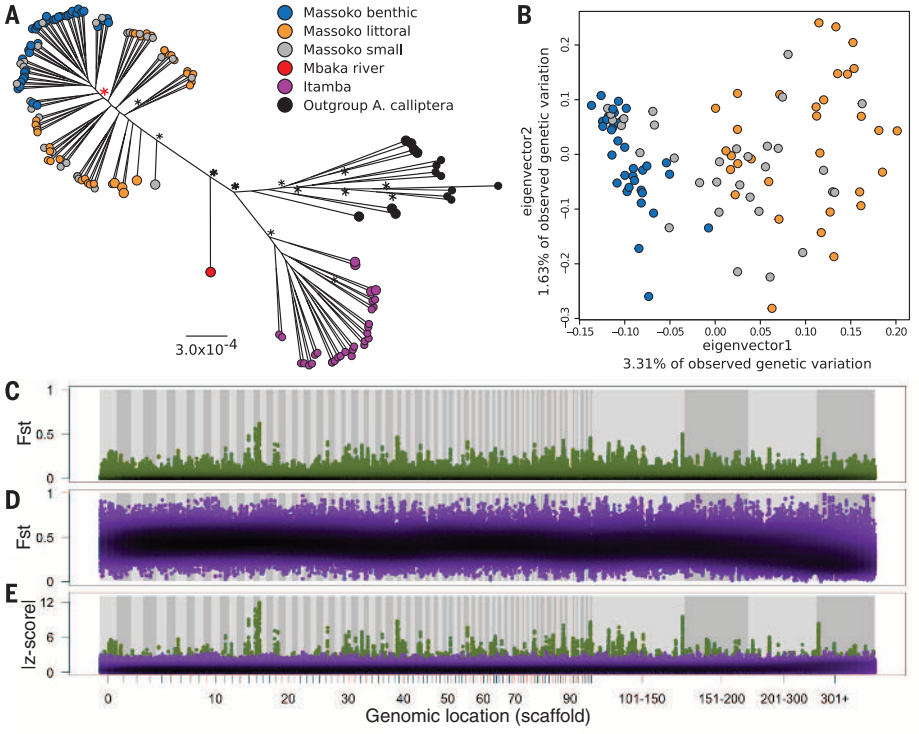

Fig. 2. Whole-genome sequence data. (**A**) A maximum-likelihood whole-genome phylogenetic tree. Black stars indicate nodes with 100% bootstrap support. The red star highlights the branch that separates all the Massoko benthic samples from the rest of the phylogeny (benthic ecomorph individuals are monophyletic in 50% of bootstrap samples). (**B**) PCA of genetic variation within Lake Massoko. (**C** to **E**) Genome-wide pattern of F_{ST} divergence in windows of 15 variants each. Darker color indicates greater density of data points. (C) Divergence between benthic and littoral ecomorphs within Massoko. (D) Divergence between combined Massoko and Itamba populations. (E) Absolute standard scores of Massoko-Itamba divergence (purple) overlaid on divergence between benthic and littoral ecomorphs (green).

Although genomic islands within these clusters are often separated only by a few hundred kilobases, F_{ST} divergence between HDRs generally drops to background levels (Fig. 3D), with one exception on scaffold 88 ,where a broader "continent" of divergence has formed (fig. S11).

Further support for sympatric divergence

We next tested whether the HDRs correlated with the signal of gene flow into Lake Massoko, as identified using the sample from the nearby Mbaka River. Compared with the rest of the genome, the HDRs do not have elevated values of Patterson's D ($P = 0.22$, two-tailed Mann-Whitney test; fig. S12C), nor elevated f statistics, which were recently proposed as an means by which one could identify introgressed loci (*6*, *23*) ($P = 0.08$, two-tailed Mann-Whitney test; fig. S12D). These results suggest that introgression from the Mbaka River did not play a major role in generating the HDRs between the benthic and littoral ecomorphs within Lake Massoko (fig. S12), and strengthen the evidence that the ecomorph divergence has taken place within the lake.

Divergent SNPs associated with mate choice

Many recently diverged taxa, particularly those not geographically isolated, show stronger premating isolation than postmating isolation (*1*, *24*, *25*). We carried out laboratory experiments to test for reproductive isolation resulting from direct mate choice between the Massoko ecomorphs (*6*) (movie S2). Fifty Massoko females were given a choice from 16 males representing the variety of male phenotypes. In parallel, we designed a single-nucleotide polymorphism (SNP) assay with 117 polymorphic sites representing 44 HDRs identified from the first 12 genomes sequenced (table S10).

We genotyped a reference sample of 18 benthic and 16 littoral males, demonstrating that the SNP assay can reliably separate the ecomorphs along the first principal component (PC1) in PCA (Fig. 4A, top). We then genotyped all females and males participating in the mate choice experiments (Fig. 4A, bottom) and calculated an average of the PC1 distances between each female and the males she mated with during the experiment, as assayed by microsatellite paternity analysis (*6*). Compared with expectation under random mating (*6*), females had a moderate, but significant ($P = 4.3 \times 10^{-5}$, paired t test), preference for mating with males more genetically similar to themselves (i.e., closer to them along PC1) (Fig. 4B), demonstrating direct association between HDR variants and mate choice. Assortative mating by genotype was strong among females with

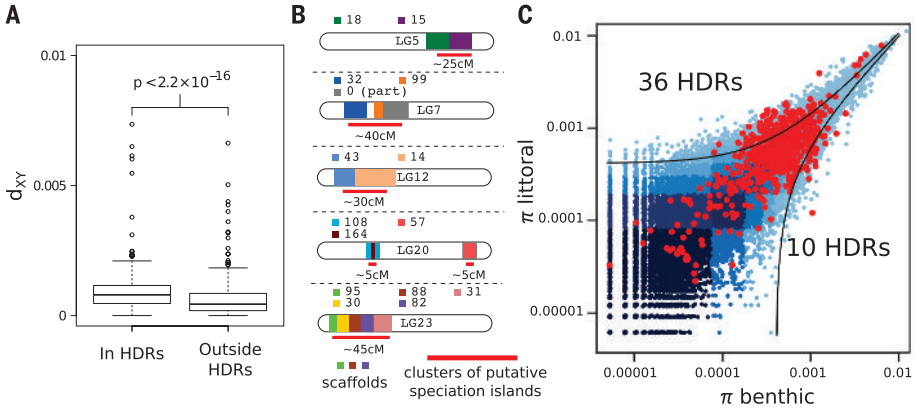

Fig. 3. Islands of speciation between benthic and littoral ecomorphs. (**A**) Elevated d_{XY} in HDRs. (**B**) Clustering of putative speciation islands on five linkage groups. (**C**) Nucleotide diversity (π) within HDRs (red points) and outside HDRs (blue with shading corresponding to density). Each point corresponds to a 10-kb window (therefore, there may be multiple points per HDR). Overall, 95% of observations lie between the two curves ($y = x \pm 4.1 \times 10^{-4}$). Putative sweeps in the benthic ecomorph are in the top left corner, and putative sweeps in the littoral are in the bottom right corner. (**D**) Patterns of F_{ST}, d_{XY}, and π_{diff} in a speciation cluster on scaffold 15.

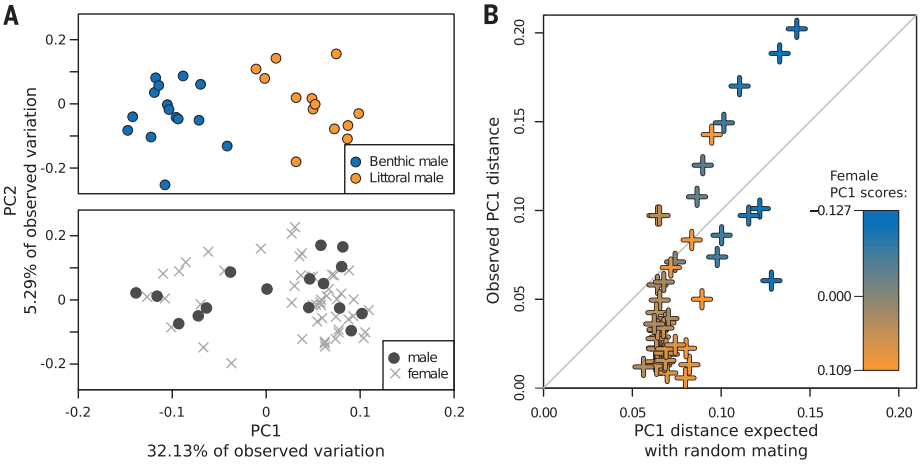

Fig. 4. Mate choice trials. (**A**) PCA based on 117 genotyped SNPs. (Top) The first axis of variation (PC1) in PCA reliably separates benthic and littoral males in a reference sample. (Bottom) PC1 positions of females ($n = 50$) and males ($n = 16$) participating in mate- hoice trials. (**B**) Results: Each point compares the average of absolute PC1 distances between a female and the males she mated with (observed PC1 distance) and all males she could have mated with (expected PC1 distance). Points are colored according to the PC1 score of the female. Females below and to the right of the dashed diagonal line on average mate with males more like themselves in terms of PC1 score than would be true if they mated at random.

positive (littoral) PC1 scores ($P = 5.9 \times 10^{-9}$, paired t test), whereas no assortative mating was detected among females with negative (benthic) PC1 scores (Fig. 4B).

Stronger mating discrimination by ancestral populations as compared to derived ones has been previously found in *Drosophila* and sticklebacks, possibly because low population density after a founder event favors less choosy individuals (*26*). However, it is also possible that the benthic ecomorph mates assortatively only in the deep-water environment; given that our experiments used wide-spectrum lighting characteristic of shallow water. Overall, the moderate assortative mating suggests a role for sexual selection in ecomorph divergence but does not indicate that it is a primary force causing population-wide divergence.

Signals of adaptation

A reduced level of genetic polymorphism in one subpopulation may be indicative of a recent selective sweep. Overall, the magnitude of difference in nucleotide diversity (π) between benthic and littoral ecomorphs (π_{diff}) is significantly higher in the HDRs than in the rest of the genome ($P < 2.2 \times 10^{-16}$, two-tailed Mann-Whitney test; fig. S13A) (*6*). Individually 46 HDRs have π_{diff} above the 95th percentile of the genome-wide distribution and are likely to have been under recent positive selection in one of the two ecomorphs. There is a significant overlap between HDRs with high d_{XY} (putative speciation islands) and HDRs with high π_{diff} (putative recent selective sweeps): 35 of 55 high-d_{XY} islands also have high π_{diff} (fig. S13B; $P = 3 \times 10^{-5}$, hypergeometric test). On the other hand, the 11 putative sweeps that did not lead to elevated d_{XY} are indicative of adaptation not directly involved in reproductive isolation. Reduced nucleotide diversity in high π_{diff} regions, indicative of selective sweeps, was significantly more prevalent in the benthic ecomorph (36 of 46; $P < 1.6 \times 10^{-4}$, two-tailed binomial test; Fig. 3C, top left, and fig. S13C) (*6*), consistent with the benthic ecomorph being derived and undergoing more extensive adaptation. Nevertheless, there are also a few strong outliers, suggesting selective sweeps in the littoral ecomorph (Fig. 3C, bottom right).

Functions of adaptation

To explore the function of candidate adaptive genes, we performed gene ontology (GO) enrichment analysis (*6*) on three sets: (i) genes in candidate islands of speciation ±50 kb (enriched terms in table S11); (ii) genes in all HDRs ±10 kb (table S12); (iii) genes in all HDRs ±50 kb (table S13). Combining results of all three analyses in a network (Fig. 5A) connecting GO terms with high overlap (i.e., they share many genes) revealed clear clusters of enriched terms related to (i) morphogenesis (e.g., cartilage and pharyngeal system development or fin morphogenesis), consistent with morphological differentiation; (ii) sensory systems (e.g., photoreceptor cell differentiation), consistent with previous studies showing the role of cichlid vision in adaptation and speciation (*7*, *27*); and (iii) (steroid) hormone signaling.

We examined in more detail the functions of candidate genes involved in photoreceptor function (table S14) and two highly diverged alleles of the rhodopsin (*rho*) gene in Lake Massoko (alleles H4 and H5, separated by four amino acid changes; $F_{ST} = 0.39$; fig. S14). Blue-shifted rhodopsin absorption spectra are known to play a role in deep-water adaptation (*27*). Therefore, we expressed rhodopsins from H4 and H5 alleles and reconstructed them with 11-*cis*-retinal, measured

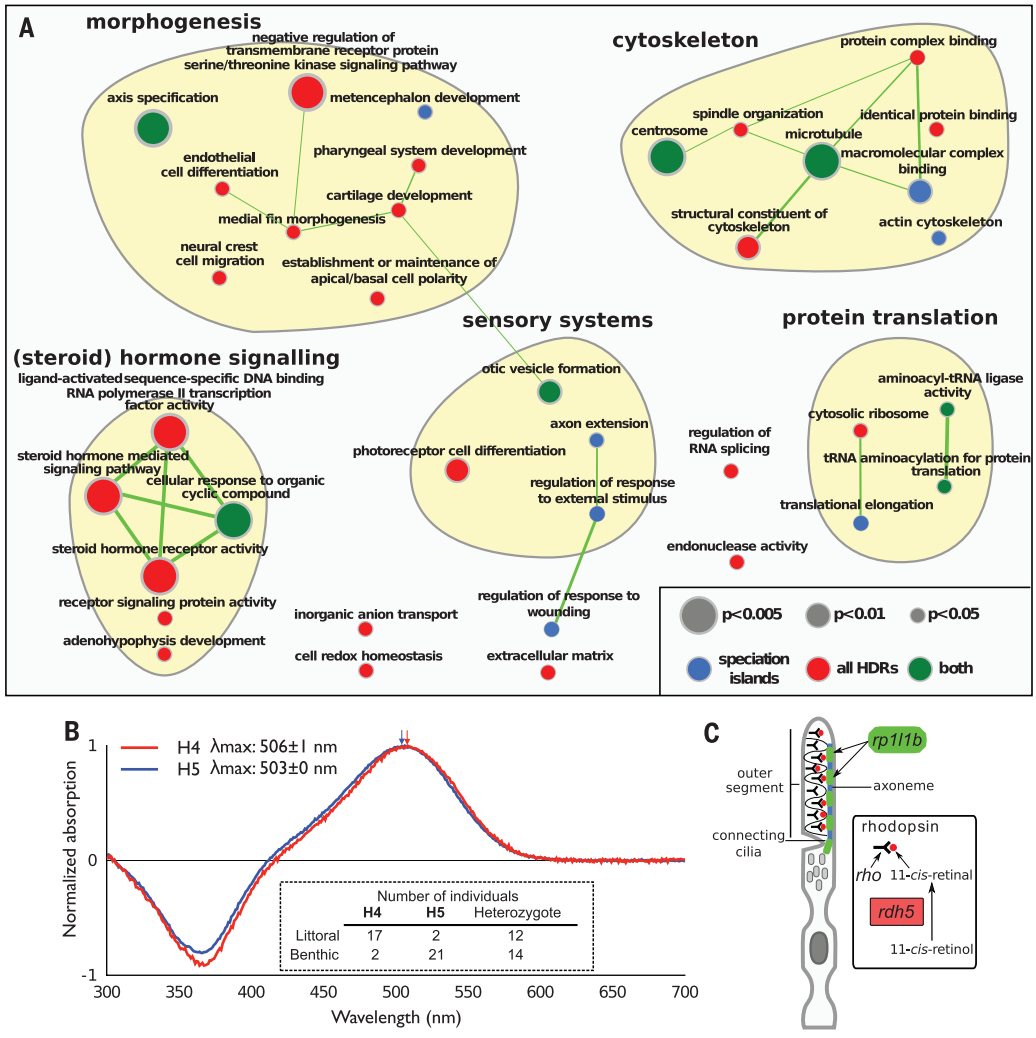

Fig. 5. Characterizing function of genes in HDRs. (**A**) Enrichment map for significantly enriched GO terms. The level of overlap between GO enriched terms is indicated by the thickness of the edge between them. The size of the node indicates the best *P* value for the term, and the color of the node indicates the gene group for which the term was found significant (i.e., has $P < 0.05$ in candidate speciation islands ±50 kb, blue; in all HDRs ±10 kb or ±50 kb, red; or in both groups, green). Broad functional groupings (morphogenesis, sensory systems, etc.) were derived using automatic clustering followed by manual editing. (**B**) The absorption spectrum of the H5 allele of *rho*, more prevalent in the benthic ecomorph, is shifted toward blue wavelengths. (**C**) The joint roles of *rho*, *rdh5*, and *rp1l1b* in photoreceptor rod cells. *rdh5* produces the chromophore 11-*cis*-retinal that binds *rho*, whereas *rp1l1b*, located at the axoneme of the outer segment and connecting cilia, also contributes to photosensitivity.

their absorption spectra (*6*), and demonstrated that the H5 allele, associated with the deep-water benthic ecomorph, has a blue-shifted absorption spectrum (Fig. 5B). The retina-specific retinol dehydrogenase *rdh5* (table S14) produces 11-*cis*-retinal, the visual pigment binding partner of rhodopsin (*28*) and thus is likely to have a direct role in dark adaptation. Finally, a mouse ortholog of *rp1l1b* affects photosensitivity and morphogenesis of the outer segment (OS) of rod photoreceptor cells, locating to the axoneme of the OS and of the connecting cilia (*29*) (Fig. 5C). Together, these results suggest that divergent selection on *rho*, *rdh5*, and *rp1l1b* may facilitate the adaptation of scotopic (twilight) vision to the darker conditions experienced by the benthic ecomorph.

Comparisons to other systems

Overall, our results suggest a pair of incipient species undergoing divergence with gene flow within crater lake Massoko. Their overall level of divergence (F_{ST} = 0.038) is low compared with background F_{ST} observed in other recent studies of speciation with gene flow in *Anopheles* mosquitoes (S and M forms; F_{ST} = 0.21) (*20*), *Ficedula* flycatchers (F_{ST} = 0.36) (*30*), and *Heliconius* butterflies (F_{ST} = 0.18) (*31*), highlighting that we are looking at an early stage of divergence. The MSMC analysis suggests that median effective divergence occurred within the past 500 to 1000 years (~200 to 350 generations), after the separation of lake fish from the Mbaka River population around 10,000 years ago (fig. S5). However, divergence may have started considerably earlier than these times and be masked by subsequent gene flow.

Among populations at similar levels of divergence to that of the Lake Massoko ecomorphs are *Timema* stick insects (F_{ST} = 0.015 for adjacent and F_{ST} = 0.03 for geographically isolated population pairs), in which thousands of regions of moderately elevated divergence were found all across the genome (*32*), and German carrion and Swedish hooded crows (F_{ST} = 0.017), which have strongly diverged with fixed differences, but at fewer than five loci (*33*). In Massoko, we observe an intermediate pattern between these two extremes, with a few dozen moderately elevated islands clustering within the genome, indicating close linkage and no fixed differences. A genome-wide pattern with multiple loci of moderate divergence suggests a genomic architecture similar to the ecological divergence of a sympatric threespine stickleback pair in Paxton Lake, Canada (*34*), and the sympatric divergence of dune-specialist sunflowers, *Helianthus* (*35*).

The ecomorphs of Lake Massoko show clear differences in traits normally associated with adaptive radiation in cichlid fishes, including body shape, pharyngeal jaw morphology, diet, microhabitat preference, retinal pigment sensitivity, male color, and mate preference (*3*, *4*, *11*, *12*, *27*). Therefore, our study suggests processes and specific genomic regions to investigate to determine whether they are involved in speciation events within the great cichlid radiations of Lakes Malawi, Victoria, and Tanganyika.

REFERENCES AND NOTES

1. J. A. Coyne, H. A. Orr, *Speciation* (Sinauer, Sunderland, MA, 2004).
2. J. L. Feder, S. P. Egan, P. Nosil, *Trends Genet.* **28**, 342–350 (2012).
3. C. E. Wagner, L. J. Harmon, O. Seehausen, *Nature* **487**, 366–369 (2012).
4. T. D. Kocher, *Nat. Rev. Genet.* **5**, 288–298 (2004).
5. D. A. Joyce *et al.*, *Curr. Biol.* **21**, R108–R109 (2011).
6. Materials and methods are available as supplementary materials on *Science* Online.
7. O. Seehausen *et al.*, *Nature* **455**, 620–626 (2008).

8. M. Delalande, Hydrologie et géochimie isotopique du lac Masoko et de lacs volcaniques de la province active du Rungwe (Sud-Ouest Tanzanie), www.theses.fr (2008).
9. P. Barker, D. Williamson, F. Gasse, E. Gibert, *Q Res* **60**, 368–376 (2003).
10. U. K. Schliewen, D. Tautz, S. Pääbo, *Nature* **368**, 629–632 (1994).
11. M. Barluenga, K. N. Stölting, W. Salzburger, M. Muschick, A. Meyer, *Nature* **439**, 719–723 (2006).
12. D. Brawand *et al.*, *Nature* **513**, 375–381 (2014).
13. D. J. Lawson, G. Hellenthal, S. Myers, D. Falush, *PLOS Genet.* **8**, e1002453 (2012).
14. C. H. Martin *et al.*, *Evolution* **69**, 1406–1422 (2015).
15. R. E. Green *et al.*, *Science* **328**, 710–722 (2010).
16. E. Y. Durand, N. Patterson, D. Reich, M. Slatkin, *Mol. Biol. Evol.* **28**, 2239–2252 (2011).
17. S. Schiffels, R. Durbin, *Nat. Genet.* **46**, 919–925 (2014).
18. D. H. Alexander, J. Novembre, K. Lange, *Genome Res.* **19**, 1655–1664 (2009).
19. M. A. F. Noor, S. M. Bennett, *Heredity* **103**, 439–444 (2009).
20. T. E. Cruickshank, M. W. Hahn, *Mol. Ecol.* **23**, 3133–3157 (2014).
21. S. Via, *Philos. Trans. R. Soc. London Ser. B* **367**, 451–460 (2012).
22. C. T. O'Quin, A. C. Drilea, M. A. Conte, T. D. Kocher, *BMC Genomics* **14**, 287 (2013).
23. S. H. Martin, J. W. Davey, C. D. Jiggins, *Mol. Biol. Evol.* **32**, 244–257 (2015).
24. T. D. Price, M. M. Bouvier, *Evolution* **56**, 2083–2089 (2002).
25. R. B. Stelkens, K. A. Young, O. Seehausen, *Evolution* **64**, 617–633 (2010).
26. K. Y. Kaneshiro, *Evolution* **34**, 437 (1980).
27. T. Sugawara *et al.*, *Proc. Natl. Acad. Sci. U.S.A.* **102**, 5448–5453 (2005).
28. G. Duester, *Eur. J. Biochem.* **267**, 4315–4324 (2000).
29. T. Yamashita *et al.*, *J. Neurosci.* **29**, 9748–9760 (2009).
30. H. Ellegren *et al.*, *Nature* **491**, 756–760 (2012).
31. N. J. Nadeau *et al.*, *Philos. Trans. R. Soc. London Ser. B* **367**, 343–353 (2012).
32. V. Soria-Carrasco *et al.*, *Science* **344**, 738–742 (2014).
33. J. W. Poelstra *et al.*, *Science* **344**, 1410–1414 (2014).
34. M. E. Arnegard *et al.*, *Nature* **511**, 307–311 (2014).
35. R. L. Andrew, L. H. Rieseberg, *Evolution* **67**, 2468–2482 (2013).

ACKNOWLEDGMENTS

This work was funded by Royal Society–Leverhulme Trust Africa Awards AA100023 and AA130107 (M.J.G., B.P.N. and G.F.T.), Wellcome Trust Ph.D. studentship grant 097677/Z/11/Z (M.M.), Wellcome Trust grant WT098051 (S.S. and R.D.), Wellcome Trust and Cancer Research UK core support and a Wellcome Trust Senior Investigator Award (E.A.M.), Leverhulme Trust Research Fellowship RF-2014-686 (M.J.G.), a University of Bristol Research Committee award (M.G.), a Bangor University Anniversary Ph.D. studentship (A.M.T.), and a Fisheries Society of the British Isles award (G.F.T.). Raw sequencing reads are in the Sequence Read Archive: RAD sequencing (BioProject: PRJNA286304; accession nos. SAMN03768857 to SAMN03768912) and whole-genome sequencing (BioProject PRJEB1254: sample accessions listed in table S16). The RAD-based phylogeny and alignments have been deposited in TreeBase (TB2:S18241). Whole-genome variant calls in the Variant Call Format (VCF), phylogenetic trees, and primer sequences for Sequenom genotyping are available from the Dryad Digital Repository (http://dx.doi.org/10.5061/dryad.770mc). R.D. declares his interests as a founder and non-executive director of Congenica Ltd., that he owns stock in Illumina from previous consulting, and is a scientific advisory board member of Dovetail Inc. We thank R. Schley for generating pharyngeal jaw data; S. Mzighani, J. Kihedu, and the staff of the Tanzanian Fisheries Research Institute for logistical support; A. Smith, H. Sungani, A. Shechonge, P. Parsons, J. Swanstrom, G. Cooke, and J. Bridle for contributions to sampling and aquarium maintenance; the Sanger Institute sequencing core for DNA sequencing; and H. Imai (Kyoto University) for the use of the spectrometer in his laboratory.

SUPPLEMENTARY MATERIALS

www.sciencemag.org/content/350/6267/1493/suppl/DC1
Materials and Methods
Figs. S1 to S16
Tables S1 to S16
References (*36*–*67*)
Movies S1 and S2

11 July 2015; accepted 10 November 2015
10.1126/science.aac9927

REPORTS

QUANTUM SIMULATION

Connecting strongly correlated superfluids by a quantum point contact

Dominik Husmann,[1] Shun Uchino,[2] Sebastian Krinner,[1] Martin Lebrat,[1] Thierry Giamarchi,[2] Tilman Esslinger,[1]* Jean-Philippe Brantut[1]

Point contacts provide simple connections between macroscopic particle reservoirs. In electric circuits, strong links between metals, semiconductors, or superconductors have applications for fundamental condensed-matter physics as well as quantum information processing. However, for complex, strongly correlated materials, links have been largely restricted to weak tunnel junctions. We studied resonantly interacting Fermi gases connected by a tunable, ballistic quantum point contact, finding a nonlinear current-bias relation. At low temperature, our observations agree quantitatively with a theoretical model in which the current originates from multiple Andreev reflections. In a wide contact geometry, the competition between superfluidity and thermally activated transport leads to a conductance minimum. Our system offers a controllable platform for the study of mesoscopic devices based on strongly interacting matter.

The effect of strong interactions between the constituents of a quantum many-body system is at the origin of several challenging questions in physics. Although the ground states of strongly interacting systems are increasingly better understood (*1*), the properties out of equilibrium and at finite temperature often remain puzzling because these are determined by the excitations above the ground state. In laboratory experiments, strongly interacting systems are found in certain materials, as well as in quantum fluids and gases (*1*). In solid-state systems, a conceptually simple and clean approach to probe nonequilibrium physics is provided by transport measurements through the well-defined geometry of a quantum point contact (QPC) (*2*–*4*). Yet, the technical hurdles to realize a controlled QPC between strongly correlated materials pose a big challenge. Ultracold atomic Fermi gases in the vicinity of a Feshbach resonance, in the so-called unitary regime, provide an alternative route to study correlated systems (*5*). Superfluidity has been established at low temperature (*6*), but the finite-temperature properties are only partially understood (*7*–*10*)—a situation similar to the field of strongly correlated materials.

Recent progress in the manipulation of cold atomic gases has enabled the realization of a

[1]Institute for Quantum Electronics, Eidgenössische Technische Hochschule (ETH) Zürich, CH–8093 Zürich, Switzerland. [2]Department of Quantum Matter Physics, Université de Genève, CH-1211 Genève, Switzerland.
*Corresponding author. E-mail: esslinger@phys.ethz.ch

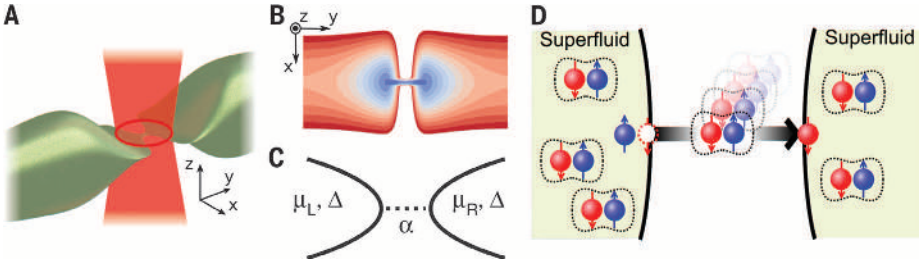

Fig. 1. Concept of the experiment. (**A**) Schematics of the two atom reservoirs (green) connected by a QPC. Two repulsive beams (not shown) confine the center of the cloud in the *x* and *z* directions, and the attractive gate beam (red) propagates along *z* and tunes the density in the QPC. (**B**) Potential landscape in the plane $z = 0$. Close to the QPC, the attractive gate creates areas of high density (blue). (**C**) Theoretical model for the QPC. Both sites of the QPC have a defined atom number, imposing chemical potentials μ_L and μ_R and a pairing gap Δ. The transparency α is an energy-dependent function describing the transmission of single particles from one side to the other. (**D**) Transport via multiple Andreev reflections. Coherent tunneling of pairs allows for the creation and tunneling of a single particle excitation (pair breaking), leading to a dc, even for $\mu_R - \mu_L = \Delta\mu \ll \Delta$.

mesoscopic device featuring quantized conductance between two reservoirs in the noninteracting regime (*11*). We used this technique to create a QPC in a strongly interacting Fermi gas consisting of $1.7(2) \times 10^5$ ^{6}Li atoms in each of the two lowest hyperfine states, in a magnetic field of 832 G, at which the interaction strength diverges owing to a broad Feshbach resonance [numbers in parentheses indicate the uncertainty on the last digit. Here, 1.7(2) means 1.7 ± 0.2]. The atoms form a strongly correlated superfluid, with a pairing gap larger than the chemical potential (*5*). Typical temperatures in the cloud are $T = 100(4)$ nK at a chemical potential of $\mu = 360$ nK $\cdot k_B$, where k_B is the Boltzmann constant. The setup is presented in Fig. 1A (*12*). The QPC is characterized by transverse trapping frequencies of $v_x = 10.0(4)$ kHz and $v_z = 10(3)$ kHz in the x and z direction, respectively. Along the y direction, the curvature of the magnetic field yields an underlying harmonic trap, with a frequency of 31 Hz. An optical attractive "gate" potential is used to tune the chemical potential and the number of channels in the QPC (Fig. 1B) (*12*). This gate potential is formed by a Gaussian beam propagating along z. We prepare two atomic clouds (reservoirs) with an atom number difference ΔN while blocking transport through the QPC with a repulsive laser beam. This results in a chemical potential bias between the two reservoirs $\Delta\mu = f(\Delta N, T/T_F)$, with the Fermi temperature T_F and the function f derived from the equation of state (EoS) of the trapped Fermi gas at unitarity (*8*, *12*).

We opened the QPC and measured ΔN as a function of time t. This evolution is presented in Fig. 2A for various strengths of the gate potential V_G. We observed that ΔN decays from its initial value to zero over a time scale of 0.5 to 1.5 s. The shape of the decay curves deviates from an exponential and is a direct manifestation of a nonlinear relation between ΔN and the atom current (*13*).

We extracted the numerical derivative of these data (*12*), yielding the instantaneous current at a function of $\Delta\mu$ (Fig. 2B). We normalized the current and bias by the strength of the pairing gap Δ using the known relation of Δ with the chemical potential μ for the low-temperature Fermi gas, $\Delta = \eta/\xi \cdot \mu$, with $\eta = 0.44$ being the universal pairing gap (*14*) and $\xi = 0.37$ the universal ground state energy (*8*, *15*) in units of the Fermi energy at zero temperature.

The current-bias characteristics in Fig. 2B are strongly nonlinear for all the choices of V_G, featuring a very strong response at low bias. The high-bias regime approaches a linear dependence with a nonzero intercept on the current axis, marking an excess current that depends on the strength of the V_G. The current is much larger than what is observed for noninteracting atoms (*11*), as observed in earlier measurements on strongly interacting atoms in multimode channels (*16*).

We modeled the experimental system as two superfluid reservoirs connected by a single-particle-hopping mechanism solely characterized by the transparency α of the QPC (Fig. 2, inset) (*17*–*21*). This is motivated by the large proximity effect in superfluids separated by a ballistic normal barrier (*22*). Indeed, we expect a coherence length of $\hbar v_F/k_B T \sim 3$ μm, where $\hbar$ is Planck's constant h divided by 2π, v_F is the Fermi velocity, and T is the temperature of the gas. This is comparable with the half-width half-maximum length of the laser beam creating the channel (3.3 μm). Thus, we approximated the channel with a point-like connection, an approximation suited for the high-transparency regime (*12*). Applying a nonequilibrium Keldysh Green function technique (*23*) in mean-field approximation (*12*), we calculated the theoretical current-bias curves for our experimental parameters. Our model does not explicitly account for any finite size or geometry-dependent effects, which we think of as absorbed in the transparency α.

Because the pairing gap and the EoS of the unitary gas are known a priori, the only free parameter in our model is the transparency α_n for each transverse mode n in the QPC (*12*). The solid lines in Fig. 2B indicate the results with the best fits of α. For the two lowest gate potentials, we obtained good agreement with a single-channel model, whereas for higher gate potentials, three channels are required, which is in agreement with our reference measurement with a weakly interacting Fermi gas (*11*).

The agreement between theory and experiment clarifies the microscopic origin of the current. Thanks to the strongly interacting nature of the system, we have $\Delta\mu \ll \Delta$. In this regime, a current flow is allowed via multiple coherent reflections of quasiparticles between superconducting reservoirs—multiple Andreev reflections, illustrated in Fig. 1D (*18*). In this case, the gap for a single particle transfer can be bridged by the simultaneous, coherent transfer of n pairs if $n\Delta\mu > 2\Delta$, with a probability of order α^{2n}. As is seen in Fig. 2B, the drop of current observed at low bias corresponds to $\Delta\mu \sim \Delta(1 - \alpha)$ (*18*), where the finite transparency α suppresses the corresponding Andreev processes. The dc should become exponentially suppressed in the very-low-bias regime, which is not resolved in the experiment. A situation different to ours occurs in tunnel junctions with much lower transparencies. There, multiple Andreev reflections lead to a succession of sharp conduction peaks at very low bias (*18*). The ac Josephson

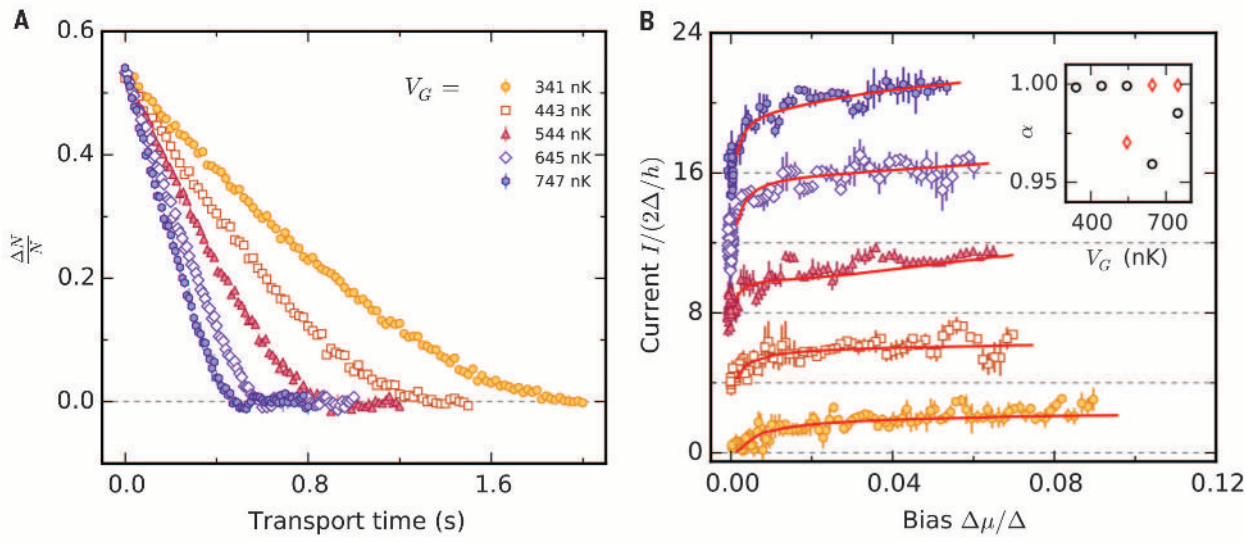

Fig. 2. Nonlinear characteristic of the QPC. (**A**) Time evolution of the particle imbalance $\Delta N/N$ for various values of the gate potential V_G. (**B**) Current-bias characteristics normalized with respect to Δ, the pairing gap. The error bars represent the variation of three averaged data sets. Negative values of the current are artifacts from the numerical derivation process. The red lines indicate the result of Keldysh calculations with the transparency α of the QPC as the only free parameter (*12*). For clarity, the curves are shifted vertically by 4 units. Temperature is 100(4) nK for all data sets. (Inset) Fitted transparency α for the various gate potentials. Black circles refer to the lowest mode, and red diamonds refer to the next two degenerate modes, when present.

current, which is induced by the energy mismatch between the two reservoirs, adds to the dc response (*12*, *24*–*29*) but averages to zero in the dc limit and is therefore not measured in our experiment.

We investigated the current-bias relation as a function of temperature, for a fixed gate potential V_G = 674 nK. To this end, we introduced a controlled heating of both reservoirs before the transport was started using variable-amplitude parametric heating. With this method, we explored a temperature range of 124 to 290 nK, from a deeply superfluid regime up to the superfluid-to-normal transition point. We measured the decay of particle imbalance with increasing temperature and observed a crossover toward exponential decay when temperature is above 145 nK. We extracted the current-bias characteristic (Fig. 3A) using the known finite-temperature EoS of the unitary Fermi gas (*8*, *12*). With increasing temperature, the nonlinearity disappears, and the current globally decreases. We interpret this as the disappearance of the superfluid contribution to transport as temperature is raised.

From these data, the differential resistance R at low bias is estimated by fitting a line to the low-bias region of the curve. The result is presented in Fig. 3B, where the decrease in R is clearly visible as temperature is decreased. We compare this to a model-independent measure of the nonlinearity of the characteristic provided by the χ^2 parameter of an exponential fit to the entire decay curves (*12*). This parameter shoots up for the lowest temperatures, whereas τ, the fitted exponential time scale, drops in close correlation with R.

In the low-temperature regime, nonlinearity is captured by our mean-field model; however,the model fails to reproduce the resistance at high temperature, indicating a breakdown of the mean-field description. In particular, it predicts a resistance in the linear regime given by the noninteracting Landauer formula, whereas the resistance that we measure is one order of magnitude smaller. This constitutes indirect evidence that the high-temperature state of the gas is not a Fermi liquid because Fermi liquid theory leads to the Landauer formula, setting the upper limit for the current carried by an ideal contact. One possible explanation is the presence of superfluid fluctuations, which are expected to be large close to T_C (*30*). Indeed, a one-dimensional Fermi gas held between attractively interacting leads, a prototype of a non-Fermi liquid system (*31*), shows an enhanced conductance (*32*–*34*).

The physical picture emerging from these measurements relies on the finite-temperature properties of the reservoirs. Some of the intrinsic physics of the channel appears when the mode spacing in the QPC is comparable with the temperature range explored. In this situation, several modes are thermally populated (*35*), enhancing transport for increasing temperature and competing with the subsequent reduction of the superfluid current. To show this, we decreased the confinement in the QPC along the x direction to 5 kHz and systematically measured the current at the largest bias as a function of temperature for various gate potentials. The results are shown in Fig. 4A, where the current at high bias normalized to the bias is shown as a function of temperature for various gate potentials. In the linear response regime, this current-bias ratio reduces to the differential conductance.

For large V_G, we observed a decrease of the current with temperature over one order of magnitude. In this superfluid-dominated regime, the pairing gap is large compared with both temperature and level spacing in the QPC, which is analogous to the previous measurements. At low V_G, the pairing gap is small and vanishes upon heating. In this channel-dominated regime, we observed an increase of the normalized current with temperature, which we attribute to thermal activation of transport channels in the QPC. There again, the current in the high-temperature regime is much higher than that predicted by a Fermi-liquid–based Landauer formula.

At equilibrium in the reservoirs, superfluidity is universally related to the local fugacity (*36*) because of the scale invariance of the unitary Fermi gas. This suggests the parameter μ/k_BT as a common dimensionless scale for comparing conductances at various temperatures and V_G. The normalized current is presented in Fig. 4B as a function of μ/k_BT. The data sets showing decreasing current with increasing temperature are

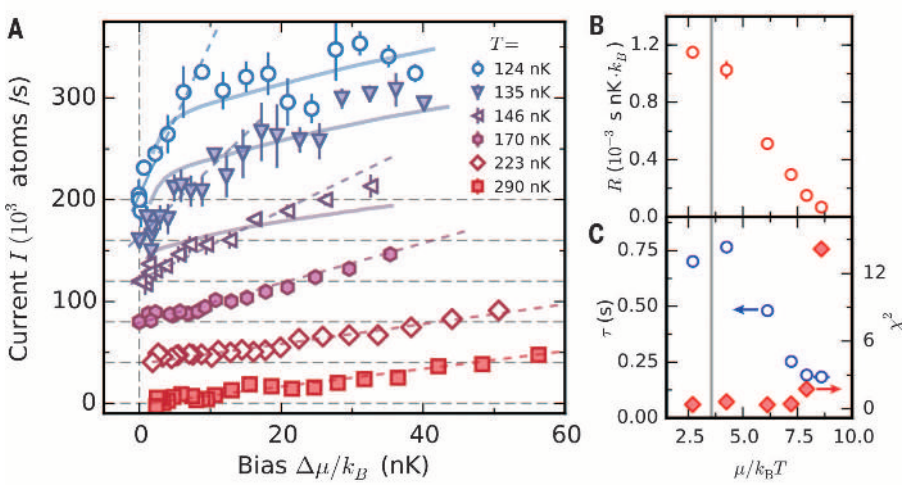

Fig. 3. Finite-temperature transport properties. (**A**) Current-bias curves for various values of the temperature T. For better visibility, the curves have been shifted vertically by 40 units. Solid lines indicate best fits of the Keldysh calculations. Dashed lines are linear fits to the low-bias regime, which yield the differential resistance $R = \Delta\mu/I$ shown in (**B**) as a function of decreasing temperature μ/k_BT. (**C**) Decay time τ of the particle imbalance relaxation (open circles) obtained by fitting decay curves with an exponential; χ^2 of the corresponding exponential fits (solid diamonds) as a function of decreasing temperature μ/k_BT. The colored arrows point to the corresponding y axis. The gray solid line marks the superfluid transition at μ/k_BT_c = 3.56.

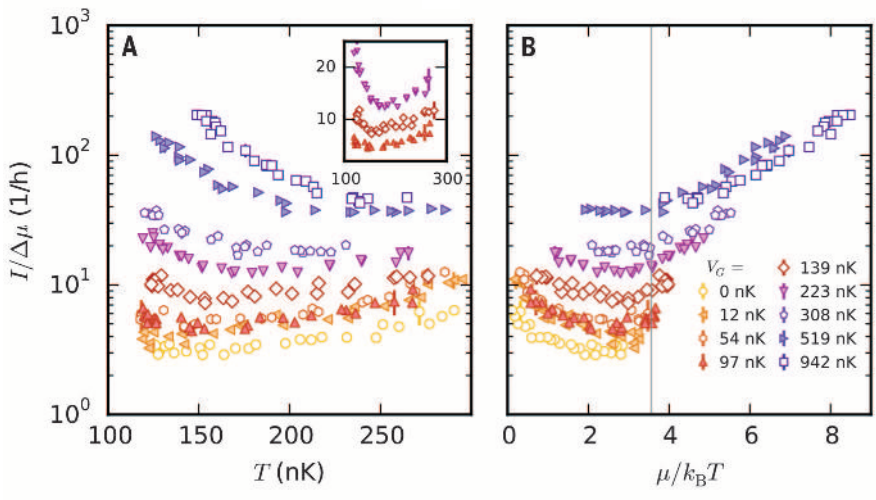

Fig. 4. Competition between superfluidity and thermally activated transport. (**A**) Ratio of current to chemical potential bias as a function of temperature for various values of the gate potential V_G. (Inset) Zoom into the transient region for three selected values of V_G. (**B**) The same data as a function of μ/k_BT. The gray solid line marks the superfluid transition at μ/k_BT_c = 3.56. A few representative error bars are shown.

all grouped in the high-fugacity regime, below the expected superfluid transition point, confirming that this regime is dominated by superfluidity. Conversely, in the low-fugacity regime the current increases with temperature, corresponding to the channel-dominated regime. The crossover takes place close to the same fugacity for all the gate potentials and is close to the universal transition point for the unitary Fermi gas at the center of the cloud. We expect that the exact location of the crossover as well as the conductance at the minimum depend on the details of the channel geometry, such as its energy-dependent mode spacing. In addition, proximity effects should be reduced at high temperature, and one-dimensional physics could emerge in the QPC, making the results dependent on the length of the contact (*37*). Our setup, allowing for a direct and independent control of the geometry, could be used to investigate such effects in future experiments.

REFERENCES AND NOTES

1. A. J. Leggett, *Quantum Liquids: Bose Condensation and Cooper Pairing in Condensed-Matter Systems* (Oxford Univ. Press, 2006).
2. N. van der Post, E. T. Peters, I. K. Yanson, J. M. van Ruitenbeek, *Phys. Rev. Lett.* **73**, 2611–2613 (1994).
3. E. Scheer, P. Joyez, D. Esteve, C. Urbina, M. H. Devoret, *Phys. Rev. Lett.* **78**, 3535–3538 (1997).
4. O. Fischer, M. Kugler, I. Maggio-Aprile, C. Berthod, C. Renner, *Rev. Mod. Phys.* **79**, 353–419 (2007).
5. W. Zwerger, *The BCS-BEC Crossover and the Unitary Fermi Gas*, vol. 836 (Springer Science & Business Media, 2011).
6. M. W. Zwierlein, J. R. Abo-Shaeer, A. Schirotzek, C. H. Schunck, W. Ketterle, *Nature* **435**, 1047–1051 (2005).
7. S. Nascimbène *et al.*, *Phys. Rev. Lett.* **106**, 215303 (2011).
8. M. J. H. Ku, A. T. Sommer, L. W. Cheuk, M. W. Zwierlein, *Science* **335**, 563–567 (2012).
9. Y. Sagi, T. E. Drake, R. Paudel, R. Chapurin, D. S. Jin, *Phys. Rev. Lett.* **114**, 075301 (2015).
10. C. Cao *et al.*, *Science* **331**, 58–61 (2011).
11. S. Krinner, D. Stadler, D. Husmann, J.-P. Brantut, T. Esslinger, *Nature* **517**, 64–67 (2015).
12. Materials and methods are available as supplementary materials on *Science* Online.
13. R. Labouvie, B. Santra, S. Heun, S. Wimberger, H. Ott, *Phys. Rev. Lett.* **115**, 050601 (2015).
14. A. Schirotzek, Y. I. Shin, C. H. Schunck, W. Ketterle, *Phys. Rev. Lett.* **101**, 140403 (2008).
15. G. Zürn *et al.*, *Phys. Rev. Lett.* **110**, 135301 (2013).
16. D. Stadler, S. Krinner, J. Meineke, J.-P. Brantut, T. Esslinger, *Nature* **491**, 736–739 (2012).
17. G. E. Blonder, M. Tinkham, T. M. Klapwijk, *Phys. Rev. B* **25**, 4515–4532 (1982).
18. D. Averin, A. Bardas, *Phys. Rev. Lett.* **75**, 1831–1834 (1995).
19. J. C. Cuevas, A. Martín-Rodero, A. L. Yeyati, *Phys. Rev. B* **54**, 7366–7379 (1996).
20. C. J. Bolech, T. Giamarchi, *Phys. Rev. Lett.* **92**, 127001 (2004).
21. C. J. Bolech, T. Giamarchi, *Phys. Rev. B* **71**, 024517 (2005).
22. A. M. Zagoskin, *Quantum Theory of Many-Body Systems* (Springer, 1998).
23. A. Kamenev, *Field Theory of Non-Equilibrium Systems* (Cambridge Univ. Press, 2011).
24. O. Avenel, E. Varoquaux, *Phys. Rev. Lett.* **60**, 416–419 (1988).
25. J. C. Davis, R. E. Packard, *Rev. Mod. Phys.* **74**, 741–773 (2002).
26. M. Albiez *et al.*, *Phys. Rev. Lett.* **95**, 010402 (2005).
27. A. Ramanathan *et al.*, *Phys. Rev. Lett.* **106**, 130401 (2011).
28. L. J. LeBlanc *et al.*, *Phys. Rev. Lett.* **106**, 025302 (2011).
29. F. Jendrzejewski *et al.*, *Phys. Rev. Lett.* **113**, 045305 (2014).
30. B. Liu, H. Zhai, S. Zhang, *Phys. Rev. A* **90**, 051602 (2014).
31. T. Giamarchi, *Quantum Physics in One Dimension* (Oxford Univ. Press, 2003).
32. D. L. Maslov, M. Stone, *Phys. Rev. B* **52**, R5539–R5542 (1995).
33. I. Safi, H. J. Schulz, *Phys. Rev. B* **52**, R17040–R17043 (1995).
34. V. V. Ponomarenko, *Phys. Rev. B* **52**, R8666–R8667 (1995).
35. J.-P. Brantut *et al.*, *Science* **342**, 713–715 (2013).
36. T.-L. Ho, *Phys. Rev. Lett.* **92**, 090402 (2004).
37. H. P. Büchler, V. B. Geshkenbein, G. Blatter, *Phys. Rev. Lett.* **92**, 067007 (2004).

ACKNOWLEDGMENTS

We acknowledge discussions with C. Berthod, J. von Delft, E. Demler, C. Grenier, P. Törmä, J. Blatter, and M. Zaccanti. We acknowledge financing from Swiss National Center of Competence in Research Quantum Science and Technology, the European Research Council project Synthetic Quantum Many-Body Systems, the EU Seventh Framework Programme project Simulators and Interfaces with Quantum Systems, Swiss National Science Foundation under division II and the Ambizione program, and the Army Research Office–Multidisciplinary University Research Initiative Non-equilibrium Many-body Dynamics grant (W911NF-14-1-0003). Data are available upon request to T.E.

SUPPLEMENTARY MATERIALS

www.sciencemag.org/content/350/6267/1498/suppl/DC1
Materials and Methods
Figs. S1 to S3
References (*38*–*51*)

5 July 2015; accepted 10 November 2015
10.1126/science.aac9584

ULTRAFAST DYNAMICS

Direct observation of collective modes coupled to molecular orbital–driven charge transfer

Tadahiko Ishikawa,[1]* Stuart A. Hayes,[2,3]* Sercan Keskin,[2,3] Gastón Corthey,[2,3] Masaki Hada,[2,4] Kostyantyn Pichugin,[2] Alexander Marx,[2,3] Julian Hirscht,[2,3] Kenta Shionuma,[1] Ken Onda,[4] Yoichi Okimoto,[1] Shin-ya Koshihara,[1,5] Takashi Yamamoto,[6] Hengbo Cui,[7] Mitsushiro Nomura,[7] Yugo Oshima,[7] Majed Abdel-Jawad,[7] Reizo Kato,[7] R. J. Dwayne Miller[2,3,8]†

Correlated electron systems can undergo ultrafast photoinduced phase transitions involving concerted transformations of electronic and lattice structure. Understanding these phenomena requires identifying the key structural modes that couple to the electronic states. We report the ultrafast photoresponse of the molecular crystal $Me_4P[Pt(dmit)_2]_2$, which exhibits a photoinduced charge transfer similar to transitions between thermally accessible states, and demonstrate how femtosecond electron diffraction can be applied to directly observe the associated molecular motions. Even for such a complex system, the key large-amplitude modes can be identified by eye and involve a dimer expansion and a librational mode. The dynamics are consistent with the time-resolved optical study, revealing how the electronic, molecular, and lattice structures together facilitate ultrafast switching of the state.

The photoexcited states of correlated electron systems often bear strong resemblance to the states reached via thermally induced phase transitions. The phenomenon of a photoinduced phase transition (PIPT) is considered to be an important concept to guide further developments for control of material properties (*1*). However, photoexcitation is intrinsically a far-from-equilibrium process, and new phases or hidden states may also appear (*2*) that differ qualitatively from those observed under equilibrium conditions. Optical pump-probe techniques provide access to the electronic states of the system, but to complete our understanding, it is essential to use an additional structural probe to directly observe the atomic rearrangements involved in propagating the structural transition. This requires the additional step of synchronizing the femtosecond optical excitation laser pulses used to trigger the structure change with a high-brightness femtosecond pulsed x-ray or electron source to observe the atomic motions involved on the relevant time scales. Hard x-ray probes have been shown to be capable of resolving coherent phonons in inorganic materials such as bismuth (*3*, *4*) and in perovskites undergoing PIPTs (*5*); more recently, femtosecond gas-phase x-ray diffraction has been used to provide constraints for a theoretical treatment of a ring-opening reaction (*6*).

[1]Department of Chemistry and Materials Science, Tokyo Institute of Technology, 2-12-1 Oh-okayama, Meguro-ku, Tokyo 152-8551, Japan. [2]Max Planck Institute for the Structure and Dynamics of Matter, Center for Free Electron Laser Science, Luruper Chaussee 149, 22761 Hamburg, Germany. [3]Hamburg Centre for Ultrafast Imaging, University of Hamburg, Luruper Chaussee 149, 22761 Hamburg, Germany. [4]JST-PRESTO, Tokyo Institute of Technology, 4259 Nagatsuta, Midori-ku, Yokohama, Kanagawa 226-8502, Japan. [5]JST-CREST, 4-1-8 Honcho, Kawaguchi, Saitama 332-0012, Japan. [6]Graduate School of Science and Engineering, Ehime University, 2-5 Bunkyo-cho, Matsuyama, Ehime 790-8577, Japan. [7]Condensed Molecular Materials Laboratory, RIKEN, 2-1 Hirosawa, Wako, Saitama 351-0198, Japan. [8]Departments of Chemistry and Physics, University of Toronto, Toronto, Ontario M5S 3H6, Canada.
*These authors contributed equally to this work.
†Corresponding author. E-mail: dwayne.miller@mpsd.mpg.de

Electron sources have also been evolving (*7*–*9*), and femtosecond electron diffraction (FED) has been used to capture a variety of phenomena in inorganic lattices, such as the melting of aluminum (*10*) and suppression of charge-density waves in TaS_2 (*11*). Molecular crystals pose even greater challenges for source brightness because of the increased structural complexity and combination of low damage thresholds, low thermal conductivity, limited reversibility, and large unit cell sizes. Reports of ultrafast diffraction experiments on such systems are scarce, but electron density fluctuations have been observed upon intense nonresonant excitation using laser-based x-ray probes (*12*, *13*). Recent studies of $(EDO\text{-}TTF)_2PF_6$ (EDO-TTF = ethylenedioxytetrathiafulvalene) (*14*) and diarylethene ring-closing reaction dynamics (*15*) have demonstrated the ability of electron probes to observe molecular reactions from well-defined excited states using resonant one-photon excitation of the reactive states. This latter work brings to the forefront the challenge of retrieving the atomic motion from an incomplete set of data.

Here, we followed the electronic and molecular dynamics upon photoexcitation of the correlated electron-molecule-lattice system $Me_4P[Pt(dmit)_2]_2$ (Me_4P = tetramethylphosphonium, dmit = 1,3-dithiol-2-thione-4,5-dithiolate) and directly observed how the cooperative motion of a small

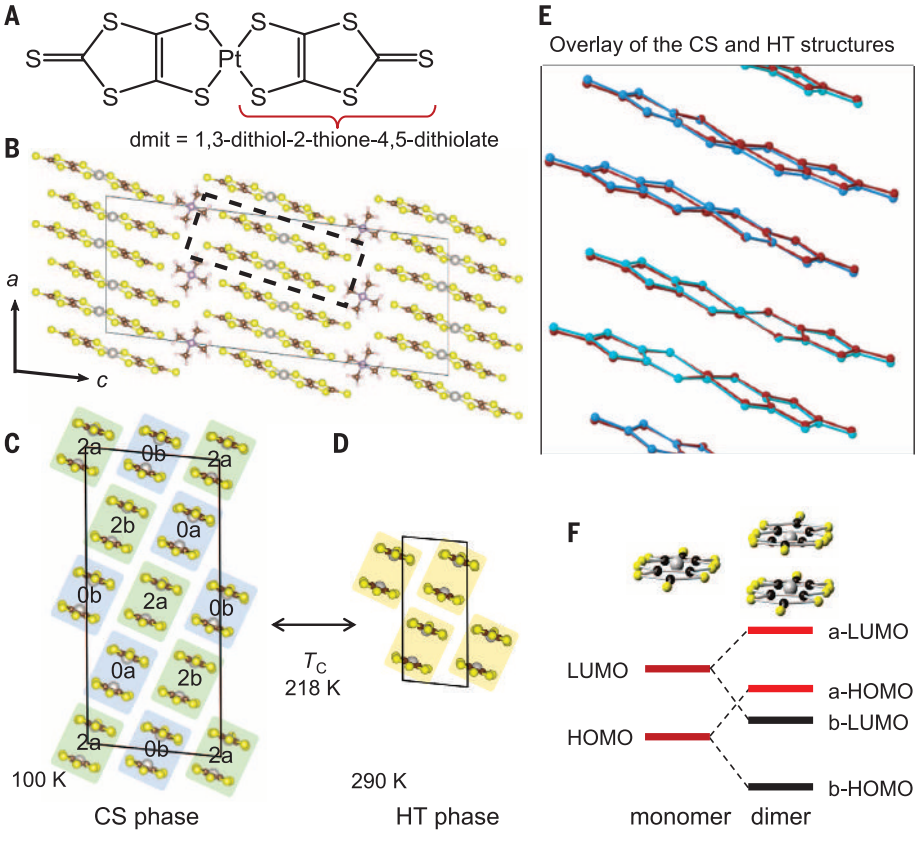

Fig. 1. Chemical and crystal structure. (**A**) Chemical structure of $Pt(dmit)_2$. (**B**) Crystal structure of $Me_4P[Pt(dmit)_2]_2$ viewed along the *b* axis. The dimer unit is surrounded by the thick dashed line. (**C** and **D**) Crystal structure of $Me_4P[Pt(dmit)_2]_2$ viewed along the long molecular axis of $Pt(dmit)_2$ at 100 K [charge-separated (CS) phase] and 290 K [metallic, high-temperature (HT) phase]. 0a, 0b, 2a, and 2b represent the crystallographically independent dimers. (**E**) Overlay of the $Me_4P[Pt(dmit)_2]_2$ molecules in the CS phase (blue for neutral dimer, cyan for divalent dimer) and the HT phase (red). (**F**) Schematic energy level diagram of the molecular orbitals in the $Pt(dmit)_2$ monomer and dimer.

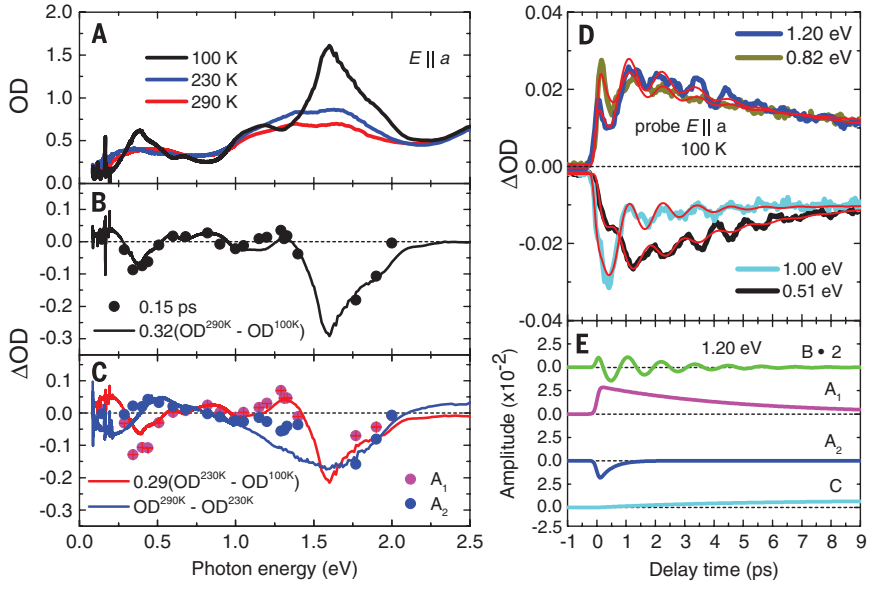

Fig. 2. Ultrafast spectroscopy. (**A**) Temperature dependence of the optical density (OD) spectra of $Me_4P[Pt(dmit)_2]_2$ with polarization along the *a* axis. (**B**) Transient difference in the OD spectrum at 0.15 ps at 100 K (black circles, pump: *E*||*a*, 1.64 × 10^{16} photons/cm^2, 500 Hz; probe: *E*||*a*) and compared with a scaled (0.32) difference spectrum between 290 K (metallic phase) and 100 K (CS phase). (**C**) Spectra of the components of the slow (A_1) and the fast (A_2) relaxation processes from the photo-induced response at 100 K (pink circles, τ = 4.85 ps; blue circles, τ = 0.42 ps); these values are deduced by the fitting procedure (*19*). The red line represents a scaled (0.29) difference OD spectrum between 230 K (metallic phase) and 100 K (CS phase); the blue line represents the difference OD spectrum between 290 and 230 K (both are in the metallic phase). (**D**) Typical temporal profiles of the photoinduced OD change (pump-probe signal; thick colored lines) with various probe photon energies; the fitted curves are shown as thin red lines. (**E**) Temporal profile of the components of the change in OD at 1.2 eV.

number of collective modes leads to transient states similar to those at elevated temperatures, indicating the presence of charge reorganization associated with PIPTs in this type of material. This reduction of a highly multidimensional problem to a few key modes, most strongly coupled to structural transitions (*9*, *14*, *15*), is now directly observable.

$Me_4P[Pt(dmit)_2]_2$ is similar to the compound $Et_2Me_2Sb[Pd(dmit)_2]_2$ (Et_2Me_2Sb = diethyldemethylantimonium), which exhibits a PIPT from a unique charge-separated (CS) phase to an average valence phase, triggered by an intradimer electron excitation (*16*–*18*). $Me_4P[Pt(dmit)_2]_2$ shows a similar CS phase transition, but with a different charge ordering and a higher transition temperature T_c (218 K rather than 70 K), as characterized by resistivity, magnetic susceptibility, and x-ray structural analysis (*19*). The chemical and crystal structures in the high-temperature (HT) phase are shown in Fig. 1, A and B, respectively. The planar $Pt(dmit)_2$ molecules associate into tight dimers and assemble into sheets, which are interleaved with planes of Me_4P cations. Within each $Pt(dmit)_2$ plane, the CS phase transition causes a structural change (Fig. 1, C and D). There are four crystallographically independent dimers in the unit cell of the CS phase, which can be classified into two groups according to the Pt-Pt distances between the molecules: 0a and 0b have a short Pt-Pt spacing of 2.93 Å and are neutral, whereas 2a and 2b are divalent with a charge of –2 and a longer Pt-Pt distance of 3.42 Å. In comparison, the dimers in the HT phase have a charge of –1 and equal Pt-Pt distances, with values of 3.31 Å at 293 K (3.22 Å at 230 K). The neutral and divalent dimers are ordered like a checkerboard in the CS phase, and the breaking of symmetry results in a doubling of the unit cell along both the *a* and *b* axes. A direct comparison between the local structures in the CS and HT phases is shown in Fig. 1E. In the neutral dimer, both the b-HOMO (highest occupied molecular orbital) and b-LUMO (lowest unoccupied molecular orbital) are filled (Fig. 1F), resulting in strong dimerization, but in the anion, the antibonding orbital a-HOMO is also filled, destabilizing the dimer. The relative stability of the CS and HT phases is dependent on a fine balance between this localized effect, interdimer interactions, and long-range Coulomb repulsion (*20*, *21*). The family of dmit salts is therefore considered to be one of the highly correlated electron-molecule-lattice systems.

Figure 2A shows the temperature dependence of the optical density (OD) spectrum of $Me_4P[Pt(dmit)_2]_2$ thin crystals with the polarization of light along the *a* axis. Analogous to the optical conductivity spectra of $Et_2Me_2Sb[Pd(dmit)_2]_2$ (*20*, *22*), we could assign the peak structures in these spectra (*19*) and confirmed that the spectral change was a good representation of the CS phase transition. In addition, the height of the broad peak around 1.5 eV in the HT phase increases with decreasing temperature toward T_c, corresponding to the shortening of the intermolecular distance within the $Pt(dmit)_2$ dimer, which increases the value of the intradimer overlap integral.

We performed time-resolved pump-probe optical spectroscopy and measured the OD changes upon optical excitation using various probe photon energies at 100 K (CS phase). The photon energy of 1.55 eV ($E \| a$) used for the pump matched the intradimer electronic excitation in the neutral dimer. Typical temporal profiles of the pump-probe signal are shown in Fig. 2D along with the fitted curves. The traces also show relaxation-type dynamics and a coherent oscillation. The

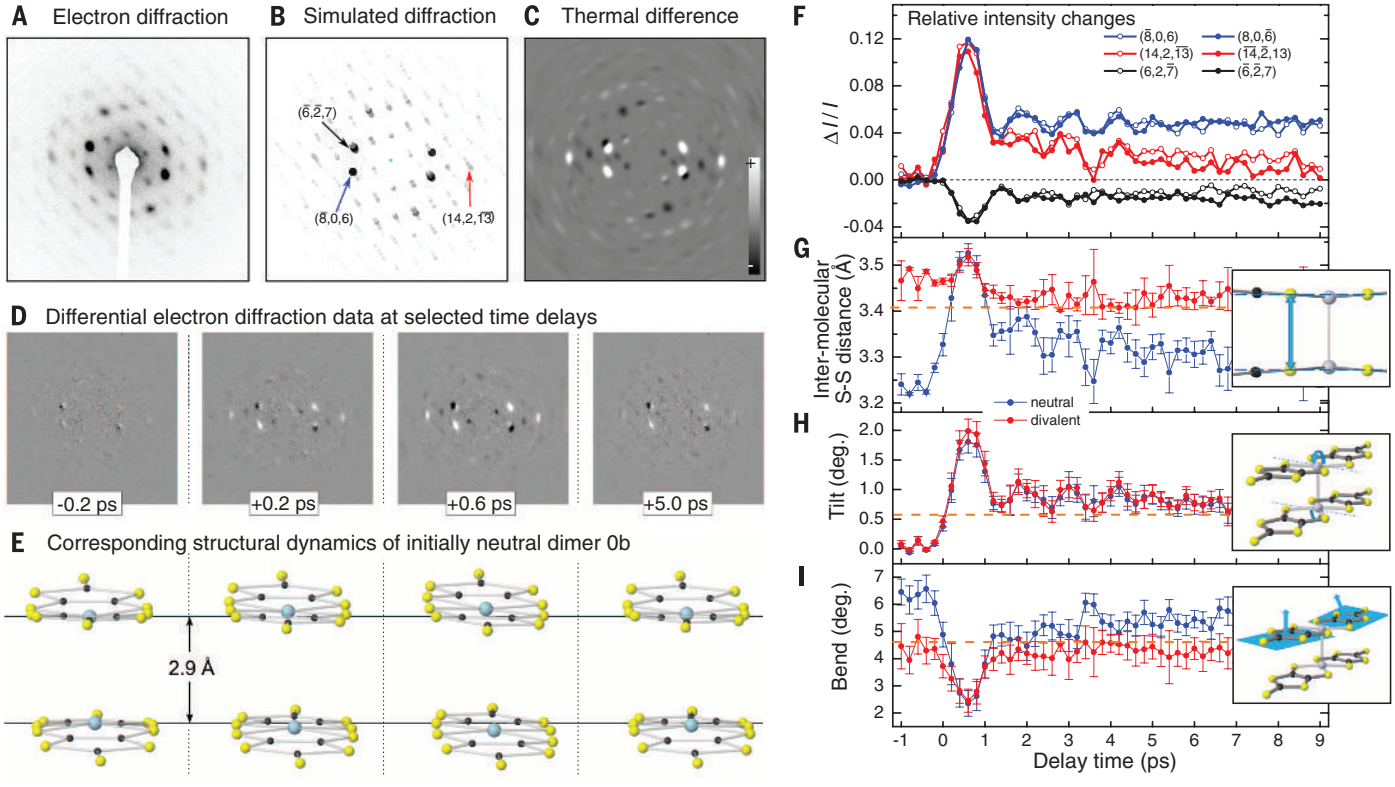

Fig. 3. Femtosecond electron diffraction. (**A**) Experimental diffraction pattern of $Me_4P[Pt(dmit)_2]_2$ at 90 K. (**B**) Simulated diffraction showing the contributions of individual reflections and selected Miller indices. (**C**) Simulated difference pattern for the thermal phase transition: CS phase → HT (metallic) phase, assuming a fixed unit cell. (**D**) Difference FED data [$I^{laser\ on}(t) - I^{laser\ off}$] at the specified time delay, *t*, of the probe electrons with respect to laser excitation. (**E**) A molecular movie of the structural dynamics constructed from the FED data and knowledge of the structures at 100 and 290 K. Snapshots are shown here focusing on one neutral dimer at time points corresponding to the data in (D), with the Pt-Pt distance in the ground state (2.93 Å) shown behind the molecules. (**F**) Temporal profiles of the relative intensity changes of selected diffraction peaks. (**G** to **I**) Dynamics of key structural modes involved in the PIPT for dimers initially neutral (blue) and divalent (red), and compared with the thermal phase transition (dashed orange lines): (G) the intermolecular separation, (H) the tilting of the dimers, and (I) the bend, defined as the angle between the vectors normal to the dmit ligands. Uncertainties were derived from the agreement between models using different input parameters.

temporal dependence of the optical density close to time zero exhibits some variation with energy, especially the data of 1.2 and 0.51 eV compared with the other probe energies, suggesting multiple relaxation pathways. We performed the fitting analysis assuming the summation of two exponential decay–type relaxation processes, one exponentially decayed oscillatory component, and a long-lived component that gradually appears (*19*), as shown in Fig. 2D. Figure 2E shows each fitted component in the 1.2-eV probe data deduced from a global fit to all the data with common relaxation time constants. The two relaxation processes indicate the relaxation of two kinds of photoinduced states. The frequency of the oscillatory component, 0.87 THz, is indicative of a low-energy molecular vibration or lattice phonon mode; this frequency is slightly lower than those observed in other molecular crystals undergoing dimer-Mott (*23*), neutral-ionic (*24*), and spin-crossover photoswitching (*25*, *26*). Figure 2B shows the transient change in the OD spectrum at 0.15 ps after photoexcitation, compared with the difference OD spectrum between 100 and 290 K. The striking similarity suggests the occurrence of a PIPT from the CS phase to a HT-like averaged valence dimer phase. Figure 2C shows the spectra of the photoinduced OD change, which correspond to the slow (τ = 4.85 ps) and the fast (τ = 0.42 ps) relaxation processes, with different spectral shapes. We found that these spectra can be well reproduced by the scaled difference spectra observed at different temperatures for the different phases (red and blue curves in Fig. 2C). The spectrum of the slow relaxation process is similar to that of the thermally induced CS phase transition, whereas the fast relaxation process is similar to the spectral change upon cooling the HT phase. However, the fast relaxation time constant of 0.42 ps is too short to be assigned to a thermal process, and we turn to electron diffraction for more insight into the structural rearrangements accompanying the electronic changes.

The diffraction pattern of thin (<150 nm), crystalline $Me_4P[Pt(dmit)_2]_2$ in the CS phase (90 K), as recorded in our FED instrument, is shown in Fig. 3A. Comparison with the simulated pattern in Fig. 3B reveals that each spot comprises more than one reflection; we attribute this to a combination of the large unit cell size (a = 28.9 Å, b = 12.6 Å, c = 37.4 Å), the finite electron coherence length, and texture of the thin film.

The FED measurements were performed with excitation conditions similar to those of the optical measurements, with excitation of the neutral dimer at a wavelength of 800 nm (1.55 eV) and repetition rate of 250 Hz. The electron probe was generated using a compact electron gun with bunches accelerated to 110 keV, comprising about 4000 electrons and totaling 10^8 electrons per time point measured. The averaged difference images for selected time points are displayed in Fig. 3D. The data immediately preceding excitation (–0.2 ps) are essentially featureless, showing that the structure has relaxed back to the ground state before the excitation pulse arrives at t = 0, whereas the difference images at +0.2 and +0.6 ps show a strong resemblance to the simulated thermal difference pattern (Fig. 3C) (*19*), indicating that the photoinduced structure change is similar to the thermal phase transition, in good agreement with the optical data. After +5.0 ps, the difference pattern retains some similarity to those observed on the subpicosecond time scale, although less pronounced; the dark spots indicate a rise in lattice temperature resulting from redistribution of the absorbed energy into random thermal motion. Quantitative evaluation was performed by integrating the intensities of 40 clearly identifiable spots. A selection of these is shown in Fig. 3F as a function of time. Fitting of the diffraction data using the same functions as for the optical data yielded similar values of the fast time constant of about 0.5 ps, and a frequency of 0.88 THz for the coherent oscillation (*19*), illustrating that the same process is being probed in both the optical and electron diffraction experiments.

A full reconstruction of the atomically resolved dynamics from FED data by direct transfer of the methodology developed for time-resolved crystallography at longer time scales (*27*) would appear to be impossible because of the limited sampling of reciprocal space. Previous studies have approached this problem by searching expected reaction coordinates for maximum correlation between theory and experiment (*14*, *15*); instead, we refined individual atom positions by defining a minimization function that combines the experimental FED data with the known structures involved in the thermal phase transition and using penalty functions to bias the optimization toward chemically reasonable structures (*19*). The additional information stabilized the refinement and enabled us to optimize all atomic coordinates in the asymmetric unit comprising 103 atoms. In this way we could avoid assumptions of specific reaction modes, making the discovery of unexpected structures possible. Movies S1 and S2 show the structural dynamics as observed from different perspectives; snapshots showing one neutral dimer are displayed in Fig. 3E. Three distinct motions can be easily identified from the molecular movies: an expansion of the intermolecular distance in the neutral dimer, flattening of the molecules, and a libration or tilting of all dimers in unison. To discuss the structural dynamics quantitatively, we parameterized these motions along with three additional collective variables: a rotational motion perpendicular to the tilt, and two orthogonal intradimer sliding motions (fig. S5). The temporal profiles of the intermolecular distance, monomer tilt, and bend motions are shown in Fig. 3, G to I.

These photoinduced dynamics can be compared with the structure changes associated with the thermal phase transition, which are represented by the orange dashed lines in Fig. 3, G to I; they can also be understood in terms of the optical data as summarized in Fig. 4. Photoexcitation of the neutral dimer initiates a rapid expansion of the intermolecular distance, which acts as a photoswitch and within 0.5 ps produces a state that is similar to the HT phase at 290 K (Fig. 4B), as seen by the convergence of the parameter values for the neutral and divalent dimers. This is accompanied by a tilting of all dimers, which should be identified as a librational mode of the lattice, because there is no discrimination between the neutral and divalent species. The initial excitation also flattens the $Pt(dmit)_2$ monomers, predominantly in the neutral species. However, this state is unstable and relaxes back to an intermediate structure, with τ = 0.42 ps—a relaxation that appears optically similar to a cooling from 290 K to 230 K (Fig. 4C). The associated structural relaxation is a partial reversal of the initial structure change, with a contraction of the neutral dimer to give an intermolecular distance just below the value of the HT phase at 230 K and a smaller contraction of the divalent dimers to produce a metastable state that is similar to the HT phase. The tilting mode similarly relaxes back to an intermediate value. These fast dynamics are accompanied by a pronounced oscillation with a frequency of 0.87 THz that persists for a few picoseconds, as clearly seen in both the optical and diffraction data. The structural origin deduced from the diffraction studies is related to the lattice libration of the tilting mode (Fig. 4D), as revealed by the especially pronounced oscillation in this degree of freedom (Fig. 3H).

The large unit cell of this system demonstrates that FED can provide insight into complex problems in ultrafast materials science, and suggests the possibility of extension to even larger systems. The method used in the structure determination provides a general approach to FED data analysis that can be applied to any system with a known initial ground-state structure. This approach provides a new window on directly

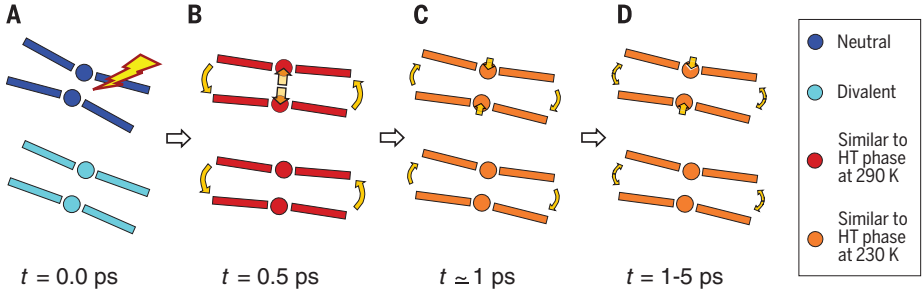

Fig. 4. Summary of the ultrafast dynamics. (**A** to **D**)The solid circles depict Pt atoms; the solid bars are dmit ligands. The color scheme represents the spectroscopic similarity of the excited states to those at thermal equilibrium. The arrows indicate displacements along large-amplitude modes observed by FED.

observing the key modes involved in propagating structural transitions and the enormous simplification this affords in understanding the structural dynamics of complex systems.

REFERENCES AND NOTES

1. K. Nasu, Ed., *Photoinduced Phase Transitions* (World Scientific, 2004).
2. H. Ichikawa *et al.*, *Nat. Mater.* **10**, 101–105 (2011).
3. K. Sokolowski-Tinten *et al.*, *Nature* **422**, 287–289 (2003).
4. D. M. Fritz *et al.*, *Science* **315**, 633–636 (2007).
5. P. Beaud *et al.*, *Nat. Mater.* **13**, 923–927 (2014).
6. M. P. Minitti *et al.*, *Phys. Rev. Lett.* **114**, 255501 (2015).
7. J. C. Williamson, J. Cao, H. Ihee, H. Frey, A. H. Zewail, *Nature* **386**, 159–162 (1997).
8. A. H. Zewail, *Science* **328**, 187–193 (2010).
9. R. J. D. Miller, *Annu. Rev. Phys. Chem.* **65**, 583–604 (2014).
10. B. J. Siwick, J. R. Dwyer, R. E. Jordan, R. J. D. Miller, *Science* **302**, 1382–1385 (2003).
11. M. Eichberger *et al.*, *Nature* **468**, 799–802 (2010).
12. M. Braun *et al.*, *Phys. Rev. Lett.* **98**, 248301 (2007).
13. T. Elsaesser, M. Woerner, *J. Chem. Phys.* **140**, 020901 (2014).
14. M. Gao *et al.*, *Nature* **496**, 343–346 (2013).
15. H. Jean-Ruel *et al.*, *J. Phys. Chem. B* **117**, 15894–15902 (2013).
16. T. Ishikawa *et al.*, *Phys. Rev. B* **80**, 115108 (2009).
17. N. Fukazawa *et al.*, *J. Phys. Chem. C* **117**, 13187–13196 (2013).
18. K. Nishioka, K. Yonemitsu, *J. Phys. Soc. Jpn.* **82**, 094716 (2013).
19. See supplementary materials on *Science* Online.
20. H. Tajima *et al.*, *Solid State Commun.* **79**, 337–341 (1991).
21. M. Tamura, R. Kato, *Chem. Phys. Lett.* **387**, 448–452 (2004).
22. M. Tamura *et al.*, *Chem. Phys. Lett.* **411**, 133–137 (2005).
23. Y. Kawakami *et al.*, *Phys. Rev. Lett.* **103**, 066403 (2009).
24. H. Okamoto *et al.*, *Phys. Rev. B* **70**, 165202 (2004).
25. C. Consani *et al.*, *Angew. Chem. Int. Ed.* **48**, 7184–7187 (2009).
26. M. Cammarata *et al.*, *Phys. Rev. Lett.* **113**, 227402 (2014).
27. I. I. Vorontsov *et al.*, *J. Am. Chem. Soc.* **131**, 6566–6573 (2009).

ACKNOWLEDGMENTS

We thank G. Sciaini and G. Moriena for help constructing the FED apparatus; W. Kazub, M. Lorenc, and A. Moreac for their help in the early stage of the optical study; and T. Tsumuraya for information concerning the band calculation. The electron diffraction work was funded by the Max Planck Society in collaboration with the Centre for Free Electron Laser Science and the Hamburg Centre for Ultrafast Imaging. This work was also partially supported by Grants-in-Aid for Scientific Research (A) (no. 15H02103) from the Ministry of Education, Culture, Supports, Science, and Technology of Japan, and CREST, JST. G.C. thanks the Alexander von Humboldt Foundation for support. M.H. acknowledges the Japan Science Technology Agency (JST), PRESTO, for funding the project "Molecular technology and creation of new functions." The authors declare no conflicts of interest.

SUPPLEMENTARY MATERIALS

www.sciencemag.org/content/350/6267/1501/suppl/DC1
Materials and Methods
Figs. S1 to S24
Tables S1 to S4
Movies S1 and S2
References (*28*–*32*)

14 April 2015; accepted 6 November 2015
10.1126/science.aab3480

QUANTUM SIMULATION

Josephson effect in fermionic superfluids across the BEC-BCS crossover

Giacomo Valtolina,[1,2,3] Alessia Burchianti,[1,2] Andrea Amico,[1,2,4] Elettra Neri,[1,2,4] Klejdja Xhani,[1,2] Jorge Amin Seman,[1]* Andrea Trombettoni,[5] Augusto Smerzi,[1,2,6] Matteo Zaccanti,[1,2] Massimo Inguscio,[2,4,7] Giacomo Roati[1,2]†

The Josephson effect is a macroscopic quantum phenomenon that reveals the broken symmetry associated with any superfluid state. Here we report on the observation of the Josephson effect between two fermionic superfluids coupled through a thin tunneling barrier. We show that the relative population and phase are canonically conjugate dynamical variables throughout the crossover from the molecular Bose-Einstein condensate (BEC) to the Bardeen-Cooper-Schrieffer (BCS) superfluid regime. For larger initial excitations from equilibrium, the dynamics of the superfluids become dissipative, which we ascribe to the propagation of vortices through the superfluid bulk. Our results highlight the robust nature of resonant superfluids.

The Josephson effect (*1*) allows extraction of the most elusive part of the superfluid order parameter, the phase, through a measurable quantity, a particle current (*2*). Furthermore, Josephson dynamics provide fundamental insights into the microscopic properties of superfluids and their robustness against dissipative phenomena (*3*). Since its discovery, the Josephson effect has been demonstrated in a variety of fermionic and bosonic systems (*3*–*12*). However, it has so far eluded observation in Bose-Einstein condensate (BEC)–Bardeen-Cooper-Schrieffer (BCS) crossover superfluids (*13*, *14*) realized by ultracold Fermi gas mixtures close to a Feshbach resonance (*15*, *16*). These systems encompass the two paradigmatic aspects of superfluidity within a single framework: Bose-Einstein condensation of tightly bound molecules and BCS superfluidity of long-range fermion pairs (*13*). Moreover, in the resonant regime, where the pair size is comparable to the interparticle spacing, they show universal properties, exhibiting similarities to other exotic strongly correlated fermionic superfluids, from cuprate superconductors to nuclear and quark matter (*17*, *18*). Here we report on the observation of the Josephson effect in ultracold gases of ^{6}Li atom pairs across the BEC-BCS crossover. Our Josephson junction consists of two superfluid reservoirs, weakly coupled through a thin tunneling barrier. For all interaction regimes, we detected coherent oscillations of both the pair population imbalance $\Delta N = N_L - N_R$ and the

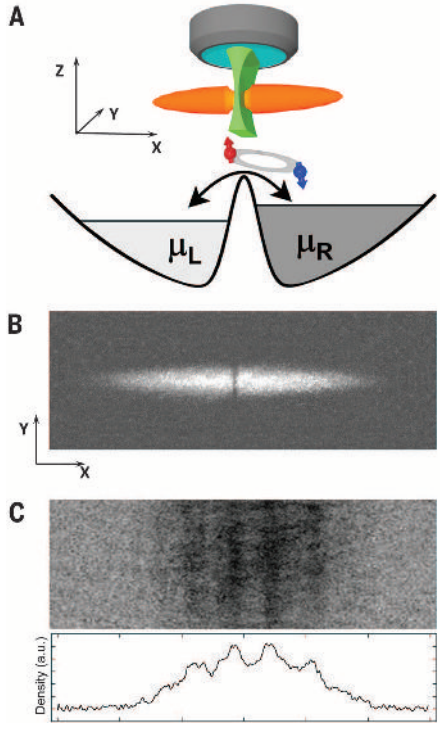

Fig. 1. Josephson junction between two ultracold fermionic superfluids. (**A**) Sketch of the experimental apparatus. The junction is realized by bisecting trapped superfluids of ^{6}Li atom pairs with an optical barrier that is only a few times wider than the correlation length of the system. Red and blue arrows indicate the two different spin components forming the fermionic pairs. The dynamics are monitored by recording the number imbalance and relative phase between the two reservoirs via in situ (**B**) and time-of-flight (**C**) imaging, respectively (a.u., arbitrary units).

[1]Istituto Nazionale di Ottica del Consiglio Nazionale delle Ricerche (CNR), 50019 Sesto Fiorentino, Italy. [2]European Laboratory for Nonlinear Spectroscopy (LENS), 50019 Sesto Fiorentino, Italy. [3]Faculty of Mathematic and Natural Sciences, Scuola Normale Superiore, 56126 Pisa, Italy. [4]Department of Physics and Astronomy, University of Florence, 50019 Sesto Fiorentino, Italy. [5]Istituto Officina dei Materiali del CNR and Scuola Internazionale Superiore di Studi Avanzati, I-34136 Trieste, Italy. [6]Quantum Science and Technology in Arcetri, I-50125 Firenze, Italy. [7]Istituto Nazionale di Ricerca Metrologica, 10135 Torino, Italy.
*Present address: Instituto de Fisica, Universidad Nacional Autonoma de Mexico, Apartado Postal 20-364, 01000 Mexico Distrito Federal, Mexico. †Corresponding author. E-mail: giacomo.roati@ino.it

relative phase $\varphi = \varphi_L - \varphi_R$ across the junction, measured in situ and after time-of-flight expansion, respectively (L, left reservoir; R, right reservoir).

In our experiment, we produced fermionic superfluids of about $N = 10^5$ atom pairs (*21*, *22*), confined in a harmonic potential of frequencies $\omega_x = \omega_0 = 2\pi \times 15$ Hz, $\omega_y = 2\pi \times 150$ Hz, and $\omega_z = 2\pi \times 170$ Hz. To minimize finite temperature effects on the superfluid dynamics, we worked at the lowest detectable temperature, $T/T_F = 0.07 \pm 0.02$, where T_F is the Fermi temperature. This ensured a superfluid fraction around unity for all interaction strengths that we investigated (*22*). The interatomic interaction, parameterized by the s-wave scattering length a, was finely tuned by exploiting a broad Feshbach resonance at 832 G (*15*, *16*). Because strong interactions foster the development of dissipative processes (*19*, *23*), we engineered a thin optical barrier whose width was only a few times larger than the superfluid coherence length of the system that would be expected in the strongly interacting regime (*9*). We realized this set-up by focusing onto the atomic cloud a strongly anisotropic laser beam at 532 nm, which was blue-detuned with respect to the main optical transition of lithium atoms. At the trap center, the beam was Gaussian-shaped, with a $1/e^2$ beam waist of 2.0 ± 0.2 and 840 ± 30 μm along the x and y directions, respectively (Fig. 1A). The repulsive barrier was homogeneous along the y and z axes while bisecting the cloud on the weak x axis in two reservoirs. We parameterized the barrier height with the potential peak V_0, felt by one atom pair, which we adjusted by controlling the power of the barrier beam. The dynamics of the system were then induced as follows: Initially, the trap center was axially displaced with respect to the barrier position (*22*), creating an initial nonzero population imbalance $z_0 = \Delta N/N$ between the two reservoirs. Here, $N = N_L + N_R$ is the sum of the pair populations of the two wells. A nonadiabatic movement of the trap center back onto the barrier position created a nonzero chemical potential difference $\delta\mu_0$, triggering the superfluid dynamics. Initially, we focused our study on the regime of small excitations, working at the lowest detectable initial imbalance $z_0 = 0.03 \pm 0.01$ and for barrier heights V_0 exceeding the bulk chemical potential μ (i.e., barrier heights in the tunneling regime). In such cases, the system Hamiltonian can be written in terms of only two macroscopic dynamically conjugate variables: the relative phase φ and the relative population $\Delta N/2$ (*2*). Generally, for small oscillations, the Hamiltonian reduces to the sum of two energy terms: $E_J\varphi^2/2$ and $(E_C/2)(\Delta N/2)^2$. The first term depends on the Josephson tunneling energy E_J, and it favors the coherent flow of particles through the junction. The second term represents the charging energy E_C, which is the energy cost to add a single pair in one reservoir (*2*, *24*, *25*). Consequently, both the imbalance and the phase undergo harmonic oscillations, out of phase from each other by π/2, at a plasma frequency ω_J that is independent of z_0 and given by

$$\hbar\omega_J = \sqrt{E_C E_J} \qquad (1)$$

where $\hbar$ is the reduced Planck constant.

We confirmed this expectation by studying the evolution of z and φ as functions of time [$z(t)$ and $\varphi(t)$], using absorption images that were recorded in situ and after a time-of-flight expansion, respectively (Fig. 1, B and C). To determine $\varphi(t)$ in the strongly interacting regime, we performed a 200-μs fast ramp to the BEC side of the resonance (*22*, *26*). This reduced the detrimental effects of collisions during the expansion, which would completely wash out the visibility of the interferogram (*27*). Figure 2 shows an example of the evolution of $z(t)$ and $\varphi(t)$ for a molecular BEC and a unitary Fermi gas. In both cases, the two quantities oscillate at the same frequency with a relative phase shift of π/2, within error bars. Our measurement establishes the conjugate nature of the phase and number imbalance, and it provides direct evidence of the macroscopic phase coherence of these systems. Because this behavior is also observed in a resonant superfluid, whose phase can be inferred only after ramping to the BEC limit, we conclude that the magnetic sweep does not appreciably distort the measurement of $\varphi(t)$.

To understand how the Josephson dynamics are influenced by interactions in the BEC-BCS crossover, we extracted the Josephson frequency ω_J by measuring $z(t)$ for a fixed barrier height $V_0 = 1.2 \pm 0.1\ E_F$, at different values of the interaction strength that we parameterized via the

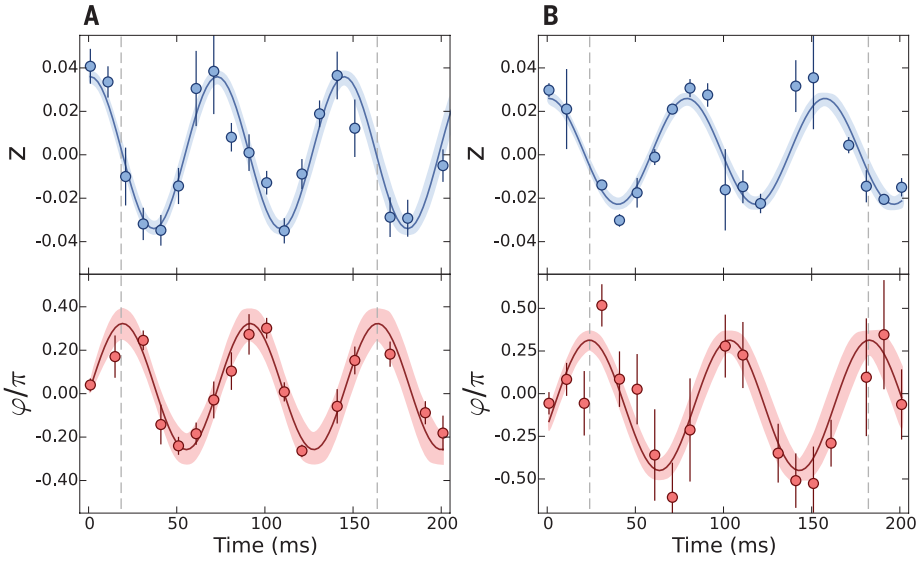

Fig. 2. Josephson oscillations of ultracold Fermi superfluids. (**A**) Time evolution of $z(t)$ (blue) and of $\varphi(t)$ (red) in the BEC limit at $1/k_Fa = 4.3$ and $V_0/\mu = 1.0$. Each data point is the average of at least five independent measurements. Error bars are the corresponding standard deviations. Solid lines are fitted to the data with a sinusoidal function. The oscillation frequencies of $z(t)$ and of $\varphi(t)$ obtained from the fit are 13.9 ± 0.1 and 13.8 ± 0.2 Hz, respectively. The phase shift between the two oscillations is 1.1 ± 0.1 π/2. (**B**) As in (A), but at unitarity for $V_0/\mu = 1.1$. The phase was detected after a rapid sweep to the BEC limit. The extracted oscillation frequencies are 12.8 ± 0.1 and 12.6 ± 0.3 Hz, respectively. The relative phase shift is equal to 1.2 ± 0.2 π/2. The shaded regions reflect the fit uncertainties. Dashed gray lines indicate the times at which the relative phase reaches its maximum value.

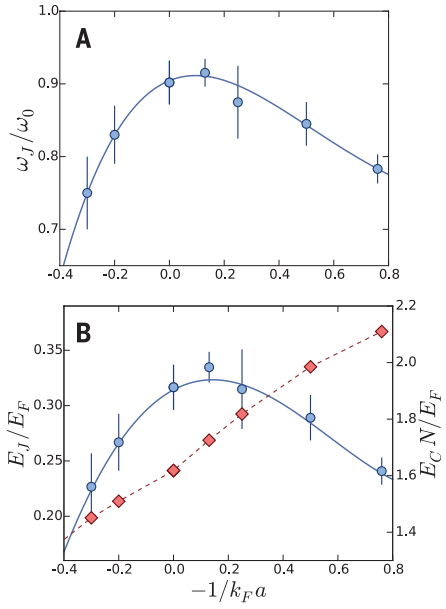

Fig. 3. Plasma frequency and Josephson coupling energy across the BEC-BCS crossover. (**A**) ω_J (blue circles) normalized to the bare trap frequency ω_0 for $V_0/E_F = 1.2 \pm 0.1$, as a function of $1/k_Fa$. The plasma frequency is obtained by fitting $z(t)$ with a sinusoidal function. Error bars indicate the fit uncertainty. (**B**) Calculated charging energy E_C multiplied for the number of pairs N (red solid diamonds), and Josephson coupling energy E_J (blue circles) normalized to the Fermi energy E_F extracted from Eq. 1. In both panels, the curves are guides to the eye.

dimensionless parameter $1/k_F a$. Here, k_F is the modulus of the Fermi wave vector associated to a noninteracting gas of N trapped fermions, whose Fermi energy is given by $E_F = \frac{\hbar^2 k_F^2}{2m} = \hbar\bar{\omega}(6N)^{1/3}$ (m is the mass of one ^{6}Li atom and $\bar{\omega} = (\omega_x\omega_y\omega_z)^{1/3}$). The extracted ω_J exhibits a nonmonotonic evolution across the BEC-BCS crossover (Fig. 3A), with a maximum around the unitary limit. To gain further insights into this trend, by exploiting Eq. 1, we derived E_J from the measured values of ω_J combined with the computed E_C. E_C is related to the inverse of the system compressibility; it was derived from an extended Thomas-Fermi model, based on a generalized Gross-Pitaevskii equation for the pairs wave function that accounts for the correct chemical potential, obtained by means of Monte Carlo calculations across the entire crossover (*22*). Figure 3B shows E_J and $N \times E_C$ normalized to E_F as a function of $1/k_F a$. Whereas E_C increases monotonically moving from the BEC to the BCS regime, E_J reflects the behavior of ω_J, reaching a maximum close to unitarity. Our system qualitatively reproduces the trend for the maximum Josephson current that has been derived from numerical approaches (*28*, *29*), which explicitly account for the composite nature of the superfluid pairs.

For $V_0 \ll \mu$, this behavior can be ascribed to the competition of two different critical velocities (*29*), set by sound and pair-breaking excitations that are predominant on the BEC and BCS sides, respectively (*29*). In turn, our observation in the tunneling regime ($V_0 > \mu$) can be qualitatively understood by considering that, in both the BEC and BCS limits, one expects

$$E_J \sim KN_0 \qquad (2)$$

N_0 is the total number of condensed pairs, and K is the tunneling term that depends on the chemical potential and the barrier properties. In the deep BEC limit, almost all pairs are condensed, so that $N_0 \cong N$ and $E_J \sim KN$ (*24*, *31*). In the BCS limit, $N_0/N \propto \Delta/E_F$, where Δ is the superfluid gap, and Eq. 2 reproduces the Ambegaokar-Baratoff formula at $T = 0$ (*3*). Moving from the BEC to the unitary limit, the increase in E_J (Fig. 3B) is associated with the growth of K. In this regime, N_0 decreases only slightly (*32*), whereas the increase in the interactions makes μ, and hence K, progressively larger. In contrast, toward the BCS limit, μ does not vary much with $k_F a$, whereas N_0 decreases sharply, causing a net reduction of E_J. Even if a microscopic derivation of the dependence of E_J on N_0 is presently missing in the strongly interacting regime, the previous arguments suggest that a maximum E_J should occur close to the unitary limit, in agreement with the experiment.

Our study initially focused on the regime of small excitations, characterizing the Josephson oscillations throughout the BEC-BCS crossover. We next investigated the system's evolution when the dynamics are triggered by larger initial excitations. In our setup, this can be done easily, either by increasing the initial imbalance z_0 at a fixed V_0 or vice versa. Under these conditions, we observed a completely different behavior, in which the transport through the junction turned from coherent to dissipative. As an example, Fig. 4A shows the evolution of $z(t)$ for $z_0 = 0.04 \pm 0.01$ and $V_0/E_F = 2$, at $1/k_F a = 0$. These dynamics strongly contrast with those shown in Fig. 2: The system in Fig. 4A is characterized by a dissipative flow, which tends to irreversibly equilibrate the two reservoirs, similarly to what was reported in (*23*) for crossover superfluids coupled through a mesoscopic channel. In this regime, despite the presence of dissipative processes, the visibility of the observed interference pattern remains high, and we were able to trace the initial evolution of $\varphi(t)$ (Fig. 4A). Again, the dynamics of this observable property differ considerably from those in Fig. 2: $\varphi(t)$ grows linearly in time in Fig. 4A, at a rate much faster than ω_J and comparable to the initial chemical potential imbalance $\delta\mu_0$. This behavior can be explained by the fact that, once the initial charging energy $\frac{1}{8}E_C z_0^2 N^2$ exceeds the Josephson coupling E_J, the phase increases as $\hbar\varphi(t) \sim E_C z_0 N t$ (*24*). After an evolution time on the order of the axial trap period, despite the high contrast of the interferograms in each image, we observed a considerable increase in the shot-to-shot fluctuations, making it difficult to further follow a clear trend in $\varphi(t)$.

To understand how a slow resistive flow can coexist with the phase coherence between the two reservoirs, we investigated the microscopic origin of dissipation in our system. The high visibility of the interference pattern, detected at all evolution times, rules out pair-breaking processes as the origin of the dissipative flow. Rather, our observation recalls the phenomenology typical of neutral superfluid systems, such as liquid helium (*2*, *19*) and atomic BECs (*20*, *33*), in which resistive dynamics are established by phase-slippage processes and vortex nucleation. In fact, the entrance into this "running phase" regime is expected to be accompanied by the nucleation of a vortex within the link region (*19*). A complete phase slip $\varphi = 2\pi$ occurs when the vortex annihilates within the barrier region. This gives rise to the macroscopic quantum self-trapping of the relative population (*22*, *24*). However, this outcome depends on the system configuration, and for $V_0 \sim \mu$, such a topological defect may escape the low-density region (*2*, *19*, *20*) upon entering

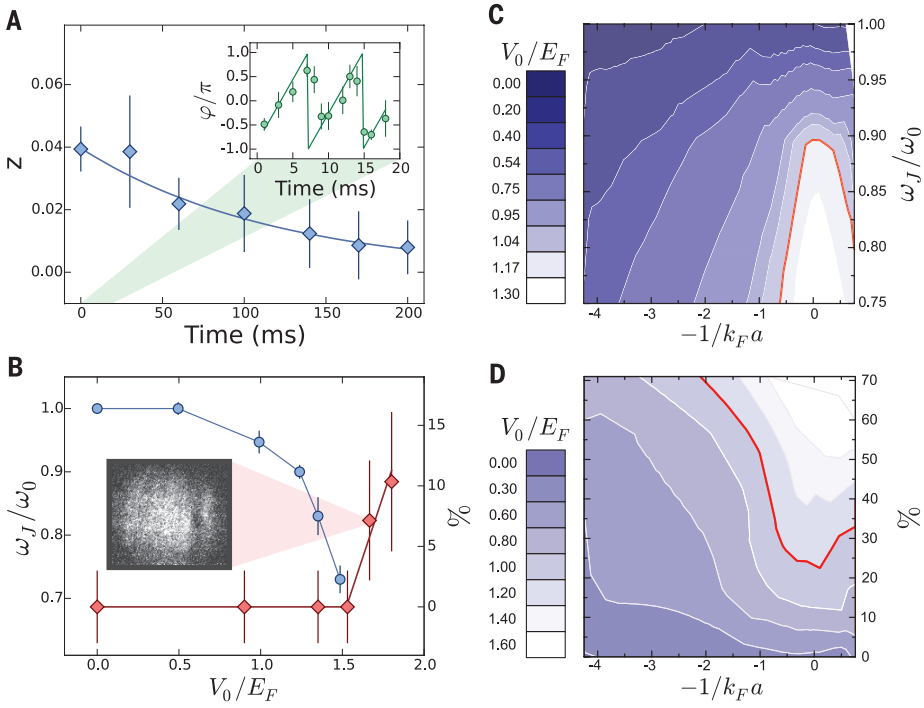

Fig. 4. Onset of dissipative dynamics. (**A**) Time evolution of $z(t)$ at resonance for $V_0/E_F = 2$ and $z_0 = 0.04 \pm 0.01$ (blue diamonds). The solid line is an exponential fit to the data. The inset shows the time evolution of $\varphi(t)$ (green circles) for the same initial parameters. The green solid line is a fit to a sawtooth function. Error bars are 1 SD of five independent measurements. (**B**) Vortex occurrence probability, evaluated over a collection of 40 independent time-of-flight images (red diamonds, right axis), and normalized plasma frequency ω_J/ω_0 (blue circles, left axis) as a function of V_0/E_F at $1/k_F a = 0$, for $z_0 = 0.04 \pm 0.01$. Error bars for the vortex occurrence were obtained using the Wilson score interval. Error bars for ω_J/ω_0 represent the fit uncertainties. The inset shows a typical image of one vortex, recorded after a 10-ms time-of-flight expansion. (**C**) Contour plot of ω_J/ω_0 versus $1/k_F a$ for different V_0/E_F values, which are indicated by the color legend on the left. (**D**) As in (C), but for the probability of vortex occurrence. To speed up the data acquisition, z_0 was set to 0.12 ± 0.02), and the statistics were performed over 20 images. In (C) and (D), the red line highlights the barrier value $V_0/E_F = 1.2$.

the superfluid bulk, before annihilation. The propagation of the vortex through the superfluid bulk acts as a dissipative channel that gives rise to a resistive flow, which leads to an exponential decay of $z(t)$. This mechanism can occur in our crossover superfluids: The three-dimensional character of our junction, combined with the coupling to the transverse modes favored by the strong interparticle interactions, may facilitate the leakage of vortices from the barrier region (*33*).

By performing a statistical study over several time-of-flight images recorded after some time evolution in the trap (*22*), we detected with nonzero probability the presence of topological defects, which appear as density depletions in the expanded clouds (Fig. 4B, inset). By measuring their oscillation period in the trap after switching off the barrier, we identified them as solitonic vortices (*22*, *34*). The intimate connection between the breakdown of the Josephson oscillations and the appearance of vortices is further confirmed by the data shown in Fig. 4B. This figure shows the behavior of the Josephson frequency ω_J at unitarity as a function of V_0, together with the occurrence of defects observed for each V_0 value over a statistical ensemble of 40 images. Vortices appear only in the regime where coherent oscillations are absent ($V_0/E_F > 1.5$). The interconnection between the quench of the coherent dynamics and the vortex nucleation is not peculiar to the unitary point; it extends over the entire BEC-BCS crossover region. This can be observed by comparing Fig. 4C and 4D, where the measured ω_J is contrasted with the vortex occurrence probability, as a function of V_0/E_F and $1/k_Fa$. The trend of the first observable is inversely correlated with the behavior of the second one for all interaction regimes. Figure 4D highlights the robustness of the crossover superfluid, which resists the formation of topological defects while maintaining the highest Josephson frequency. Our results differ from those reported in a study of the limit of vanishingly low barriers ($V_0 \ll \mu$), where phononic excitations and pair-breaking effects, rather than vortices, respectively cause the breakdown of superfluidity in the BEC and BCS sides (*30*).

Our work paves the way for studies of the interplay between elementary and topological excitations in the dissipative dynamics created by varying the height and width of the interwell barrier, and to the measurement of the superfluid gap, in close analogy with tunneling experiments in superconductors (*3*, *18*). Moreover, extending our studies of the tunneling dynamics above the condensation temperature T_C may provide insight into the role of phase fluctuations in the regime where preformed noncondensed pairs appear in the system (*17*).

REFERENCES AND NOTES

1. B. D. Josephson, *Phys. Lett.* **1**, 251–253 (1962).
2. P. W. Anderson, *Rev. Mod. Phys.* **38**, 298–310 (1966).
3. A. Barone, G. Paternò, *Physics and Applications of the Josephson Effect* (Wiley, New York, 1982).
4. K. Sukhatme, Y. Mukharsky, T. Chui, D. Pearson, *Nature* **411**, 280–283 (2001).
5. E. Hoskinson, Y. Sato, I. Hahn, R. E. Packard, *Nat. Phys.* **2**, 23–26 (2006).
6. F. S. Cataliotti *et al.*, *Science* **293**, 843–846 (2001).
7. M. Albiez *et al.*, *Phys. Rev. Lett.* **95**, 010402 (2005).
8. T. Schumm *et al.*, *Nat. Phys.* **1**, 57–62 (2005).
9. S. Levy, E. Lahoud, I. Shomroni, J. Steinhauer, *Nature* **449**, 579–583 (2007).
10. L. J. LeBlanc *et al.*, *Phys. Rev. Lett.* **106**, 025302 (2011).
11. M. Abbarchi *et al.*, *Nat. Phys.* **9**, 275–279 (2013).
12. J. C. Davis, R. E. Packard, *Rev. Mod. Phys.* **74**, 741–773 (2002).
13. A. J. Leggett, *Quantum Liquids: Bose Condensation and Cooper Pairing in Condensed-Matter Systems* (Oxford Univ. Press, Oxford, 2006).
14. W. Zwerger, Ed., *The BCS-BEC Crossover and the Unitary Fermi Gas* (Springer, Heidelberg, Germany, 2012).
15. M. Inguscio, W. Ketterle, C. Salomon, Eds., *Proceedings of the International School of Physics "Enrico Fermi", Course CLXIV*, Varenna, Italy, 20 to 30 June 2006 (IOS Press, Amsterdam, 2008).
16. M. W. Zwierlein, in *Novel Superfluids, Volume 2*, K. H. Bennemann, J. B. Ketterson, Eds. (International Series of Monographs on Physics 157, Oxford Univ. Press, Oxford, 2014), pp. 269–422, and references therein.
17. Q. Chen, J. Stajic, S. Tan, K. Levin, *Phys. Rep.* **412**, 1–88 (2005).
18. S. Hüfner, M. A. Hossain, A. Damascelli, G. A. Sawatzky, *Rep. Prog. Phys.* **71**, 062501 (2008).
19. E. Varoquaux, *Rev. Mod. Phys.* **87**, 803–854 (2015), and references therein.
20. F. Piazza, L. A. Collins, A. Smerzi, *New J. Phys.* **13**, 043008 (2011).
21. A. Burchianti *et al.*, *Phys. Rev. A* **90**, 043408 (2014).
22. Materials and methods are available as supplementary materials on *Science* Online.
23. D. Stadler, S. Krinner, J. Meineke, J. P. Brantut, T. Esslinger, *Nature* **491**, 736–739 (2012).
24. A. Smerzi, S. Fantoni, S. Giovanazzi, S. R. Shenoy, *Phys. Rev. Lett.* **79**, 4950–4953 (1997).
25. I. Zapata, F. Sols, A. J. Leggett, *Phys. Rev. A* **57**, R28–R31 (1998).
26. J. K. Chin *et al.*, *Nature* **443**, 961–964 (2006).
27. C. Kohstall *et al.*, *New J. Phys.* **13**, 065027 (2011).
28. P. Zou, F. Dalfovo, *J. Low Temp. Phys.* **177**, 240–256 (2014).
29. A. Spuntarelli, P. Pieri, G. C. Strinati, *Phys. Rev. Lett.* **99**, 040401 (2007).
30. D. E. Miller *et al.*, *Phys. Rev. Lett.* **99**, 070402 (2007).
31. F. Meier, W. Zwerger, *Phys. Rev. A* **64**, 033610 (2001).
32. G. E. Astrakharchik, J. Boronat, J. Casulleras, S. Giorgini, *Phys. Rev. Lett.* **95**, 230405 (2005).
33. K. C. Wright, R. B. Blakestad, C. J. Lobb, W. D. Phillips, G. K. Campbell, *Phys. Rev. Lett.* **110**, 025302 (2013).
34. M. J. Ku *et al.*, *Phys. Rev. Lett.* **113**, 065301 (2014).

ACKNOWLEDGMENTS

We acknowledge inspiring discussions with F. Dalfovo, A. Recati, and W. Zwerger. We thank C. Fort, A. Trenkwalder, A. Morales, and T. Macrì for collaboration at the initial stage of this work. We especially acknowledge the LENS Quantum Gases group. This work was supported under European Research Council grant no. 307032 QuFerm2D.

SUPPLEMENTARY MATERIALS

www.sciencemag.org/content/350/6267/1505/suppl/DC1
Materials and Methods
Figs. S1 to S7
References (*35*–*49*)

7 July 2015; accepted 13 November 2015
10.1126/science.aac9725

ENERGY STORAGE

Nitrogen-doped mesoporous carbon of extraordinary capacitance for electrochemical energy storage

Tianquan Lin,[1,2] I-Wei Chen,[3] Fengxin Liu,[1] Chongyin Yang,[1] Hui Bi,[1] Fangfang Xu,[1] Fuqiang Huang[1,2]*

Carbon-based supercapacitors can provide high electrical power, but they do not have sufficient energy density to directly compete with batteries. We found that a nitrogen-doped ordered mesoporous few-layer carbon has a capacitance of 855 farads per gram in aqueous electrolytes and can be bipolarly charged or discharged at a fast, carbon-like speed. The improvement mostly stems from robust redox reactions at nitrogen-associated defects that transform inert graphene-like layered carbon into an electrochemically active substance without affecting its electric conductivity. These bipolar aqueous-electrolyte electrochemical cells offer power densities and lifetimes similar to those of carbon-based supercapacitors and can store a specific energy of 41 watt-hours per kilogram (19.5 watt-hours per liter).

Carbon supercapacitors have outstanding attributes of low weight, very fast charging/discharging kinetics, and bipolar operational flexibility. For carbon-based materials, only electrical double-layer capacitance (EDLC) is available; thus, surface area is the key concern. But even at a very large surface area (~2180 to 3100 $m^2\ g^{-1}$), their specific capacitance is still relatively low (~250 $F\ g^{-1}$), which has limited their appeal (*1*–*4*). Meanwhile, graphene has a theoretical EDLC of ~550 $F\ g^{-1}$ (*5*, *6*) because of its extraordinary conductivity and specific surface area (~2630 $m^2\ g^{-1}$). In practice, however, its capacitance has also been limited to ~300 $F\ g^{-1}$, about the same as the best carbon-based EDLC (*2*, *5*–*7*). Therefore, efforts have been made to enable redox reactions in ordered mesoporous carbon (OMC) (*8*, *9*) and conducting polymers by N doping, which via proton incorporation can theoretically endow a capacitance of ~2000 $F\ g^{-1}$

to conducting polymer polyaniline (*10*). Nevertheless, such efforts have failed because conducting polymers are too unstable for practical electrochemical cells, while stable OMC is too resistive to deliver a high capacitance or power.

We demonstrate that N doping can turn inert graphene-like layered carbon into an electrochemically active substance. The preparation method is described in the supplementary materials, starting with a sacrificial mesoporous silica template, which contains self-assembled tubes (*11*) later covered by few-layer carbon. After etching away silica, a self-supported ordered mesoporous few-layer carbon (OMFLC) superstructure in Fig. 1A remained. Various N-doped OMFLC (OMFLC-N) having N incorporated at several OMFLC locations in Fig. 1B were also obtained, some further modified by a HNO_3 oxidation treatment that partially converted N into N–O. This set of OMFLC-N samples (table S1) includes 8.2 atomic percent (at%) N before and after oxidation treatment (samples S1 and S2) and 11.9 at% N before and after treatment (samples S3 and S4). For comparison, an ordered mesoporous (amorphous) carbon and a commercial activated carbon (YP-50, Kuraray Chemical) were also studied. To demonstrate the relevance to practical applications, we further implemented the idea using a simplified, template-free, scalable method producing essentially the same N-doped mesoporous few-layer carbon materials with the same overall performance.

The ordered mesoporous nature of OMC (Fig. 1C) and OMFLC (Fig. 1D) was confirmed by electron microscopy. In both, OMFLC tubes appear as bright strips 4 to 6 nm wide. The tubes are porous, containing pores 1 to 2 nm in diameter (dark regions in strips), and are separated by aligned pore channels (dark regions between strips) of about the same size or diameter. High-resolution imaging of OMFLC's tube walls further revealed graphene-like sheets with ≤5 layers (Fig. 1E). These relatively homogeneous and uniform mesoporous textures were largely preserved in OMFLC-N (fig. S1). The silica tubes in the template are known to form a two-dimensional (2D) hexagonal "crystal" with space group *p6mm* (*11*). The same superstructure was confirmed in OMC, OMFLC, and OMFLC-N by their diffraction patterns (Fig. 1F), which show decreasing peak intensities in the above order, indicating a progressive distortion of the superstructure.

Nitrogen adsorption-desorption suggests a bimodal pore size distribution (Fig. 1G) centered around 1.8 nm and 3.5 to 4.0 nm in all three mesoporous structures. They share similar N_2 adsorption-desorption isotherms with a Langmuir

[1]State Key Laboratory of High Performance Ceramics and Superfine Microstructure and CAS Key Laboratory of Materials for Energy Conversion, Shanghai Institute of Ceramics, Chinese Academy of Sciences, Shanghai 200050, P.R. China. [2]Beijing National Laboratory for Molecular Sciences and State Key Laboratory of Rare Earth Materials Chemistry and Applications, College of Chemistry and Molecular Engineering, Peking University, Beijing 100871, P.R. China. [3]Department of Materials Science and Engineering, University of Pennsylvania, Philadelphia, PA 19104, USA.
*Corresponding author. E-mail: huangfq@mail.sic.ac.cn

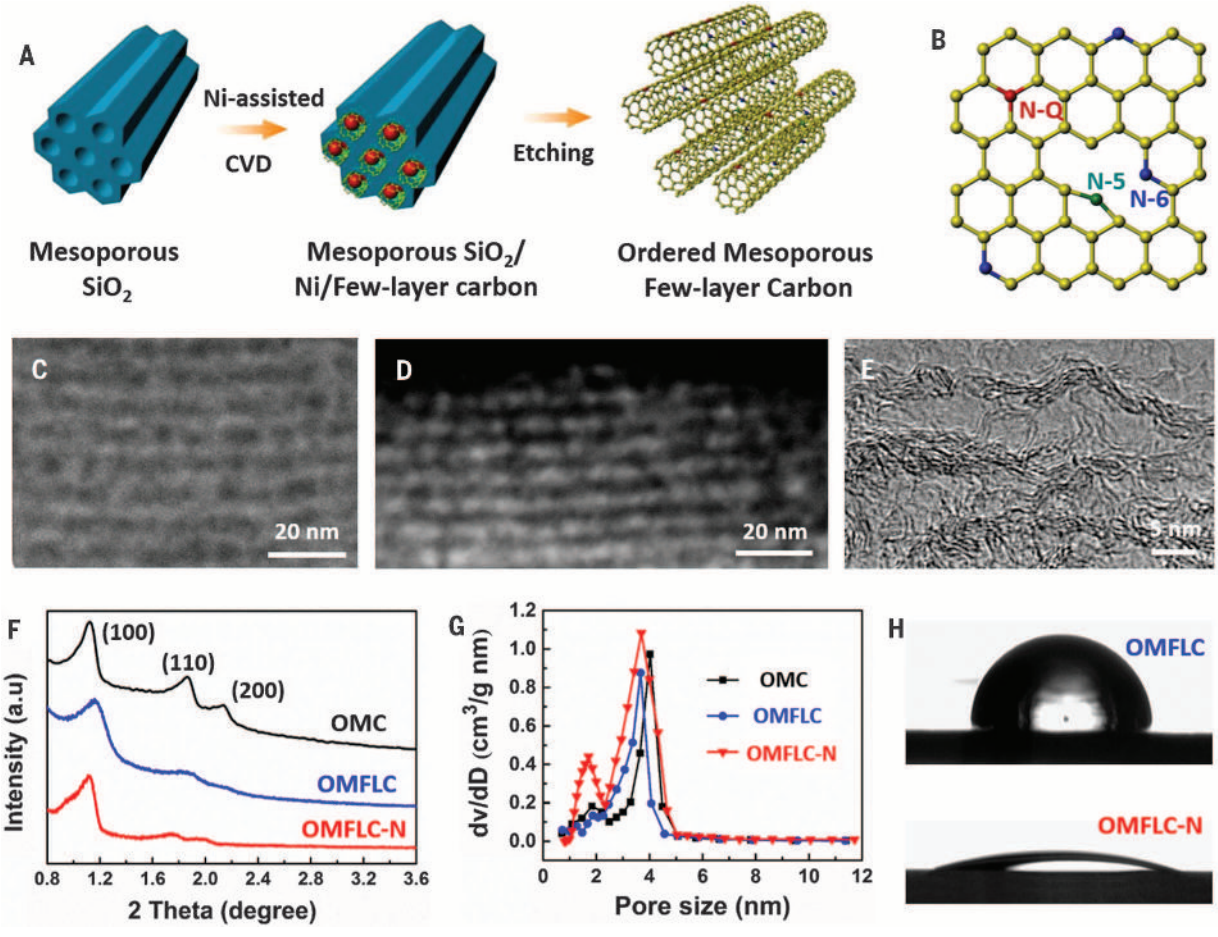

Fig. 1. Structure of N-doped ordered mesoporous few-layer carbon and related materials. (**A**) Fabrication schematic of ordered mesoporous few-layer carbon (OMFLC). (**B**) Possible locations for N incorporation into a few-layer carbon network. (**C** and **D**) High-angle annular dark-field transmission electron microscopy (TEM) images of ordered mesoporous carbon (OMC) (C) and OMFLC (D); dark regions indicate connected pore channels. (**E**) High-resolution TEM image of OMFLC; nanoporous walls consist of few-layered carbon sheets. (**F**) Low-angle x-ray diffraction patterns of OMC, OMFLC, and OMFLC-N (S1), showing characteristic (100), (110), and (200) peaks of hexagonal packing. (**G**) Pore size distributions of OMC, OMFLC, and OMFLC-N (S1). (**H**) Wetting angles of 0.5 M H_2SO_4 droplet on OMFLC (85°) and OMFLC-N (S1) (21°) substrates.

hysteresis (fig. S2A) typical of well-defined mesopores. Among them, OMFLC-N (S1) has the largest surface area (1580 $m^2\ g^{-1}$), the largest total pore volume (2.20 $cm^3\ g^{-1}$), the smallest average pore width (2.25 nm), and the most prominent pores smaller than 2 nm (Fig. 1G). The characteristic Raman 2D band (fig. S2B) verified the formation of local graphene-like structure with ≤5 layers in OMFLC and OMFLC-N.

Local graphene-like structure formation and N doping profoundly altered other physical properties as well. Whereas OMC is clearly an insulator, OMFLC and OMFLC-N display much lower room-temperature resistance with much weaker temperature dependence (fig. S2C), indicating an improvement in the structural order of carbon (*12*). Meanwhile, whereas both OMC and OMFLC are hydrophobic, OMFLC-N is hydrophilic, wetting a 0.5 M H_2SO_4 droplet in Fig. 1H. This is consistent with the zeta potential: Nearly neutral OMFLC (zeta potential = −6 mV, almost the same as OMC's −4 mV) becomes more nucleophilic OMFLC-N (−20 mV) as a result of lone-pair N $2p_z$ electrons; these improved physical properties of OMFLC-N are generally conducive to the supercapacitive performance (see below).

Spectroscopy studies identified C-bonding and N-C locations in the carbon network. The presence of sp^2 bonding expected for graphene and local graphene-like structure was evident from the high ratio of π* bonding to π* + σ* bonding (fig. S3A), giving 98% (±2%) sp^2 bonding in OMFLC versus 86% (±2%) in OMFLC-N, with reference to graphite (100%). Evidence for N substitution in OMFLC-N was also detected (fig. S3B), and the N/O content and bonding of OMFLC-N quantified by x-ray photoelectron spectroscopy (XPS) (fig. S3, C to F, and table S1) provided the following picture: (i) Deconvoluted N 1s XPS contains three characteristic peaks at 398, 400, and 401 eV, corresponding to pyridinic (N-6), pyrrolic (N-5), and graphitic (N-*Q*) nitrogen, respectively, as shown in Fig. 1B (*13*, *14*). (ii) As the N content increases from ~8.2 at% in sample S1 to 11.9 at% in S3, N substitution at "regular" graphitic C sites (N-*Q*) instead of defective sites (N-5 and N-6) becomes more abundant. (iii) Oxidative HNO_3 treatment caused the least stable N-5 to substantially convert to N–O (N associated with an O, shown in fig. S3D at 403.2 eV) (*15*) without affecting the most stable N-*Q*, as suggested by the correlation of N-O percentage (%N-O) to the decrement of N-5 percentage (%N-5), denoted by Δ%N-5 in table S1. (iv) Non–N-*Q* fractions (i.e., %N-5 + %N-6 in table S1) decrease in the order of samples S3, S1, S2, and S4; their redox potentials also increase in the same order.

These redox potentials in aqueous electrolytes were determined in three-electrode electrochemical cells in 0.5 M H_2SO_4 (pH 0) electrolyte using an Ag/AgCl reference electrode and a Pt counter-electrode. The working electrode was prepared by pressing together active-material powders (at a mass loading of 0.5 mg cm^{-2}) and an inactive, highly compressible graphene foam (3D-graphene, specific capacitance = 30 F g^{-1}) without any other additive. In cyclic voltammetry (CV) at 2 mV s^{-1} (Fig. 2A), cells with both OMC and OMFLC working electrodes have nearly rectangular CV curves representative of an ideal efficient EDLC. With OMFLC-N electrodes, the curves may be deconvoluted into (i) a nearly rectangular EDLC-like curve, albeit with a substantially higher charging/discharging current not seen with OMC and OMFLC, and (ii) a set of symmetric Faradaic charging/discharging peaks. In (ii), the charging peaks are located at ~0.25 V to ~0.5 V, increasing in the order of S3, S1, S2, and S4 (S4 data omitted in Fig. 2A but listed in table S1), which is exactly the same order that non–N-*Q* fractions decrease, thus strongly suggesting that the redox potential is related to N-5 and/or N-6. The above shape and symmetry features were maintained when the scan rate increased to 100 mV s^{-1}, as shown for S1 in fig. S4A. This indicates that both EDLC-like and redox reactions have fast charging/discharging kinetics.

To proceed further, we note that pseudocapacitive materials with a pronounced redox peak are usually inefficient electrodes in a symmetric electrochemical cell, which renders the effort of incorporating faradaic capacitance ineffective. This is because a symmetric cell is electrically equivalent to two serial capacitors, C_1 and C_2, so its total capacitance $C_1C_2/(C_1 + C_2)$ is optimized when $C_1 = C_2$. This condition is usually impossible to satisfy at all potentials unless the CV curve is rectangular. We found that the following simple method can overcome this problem, however.

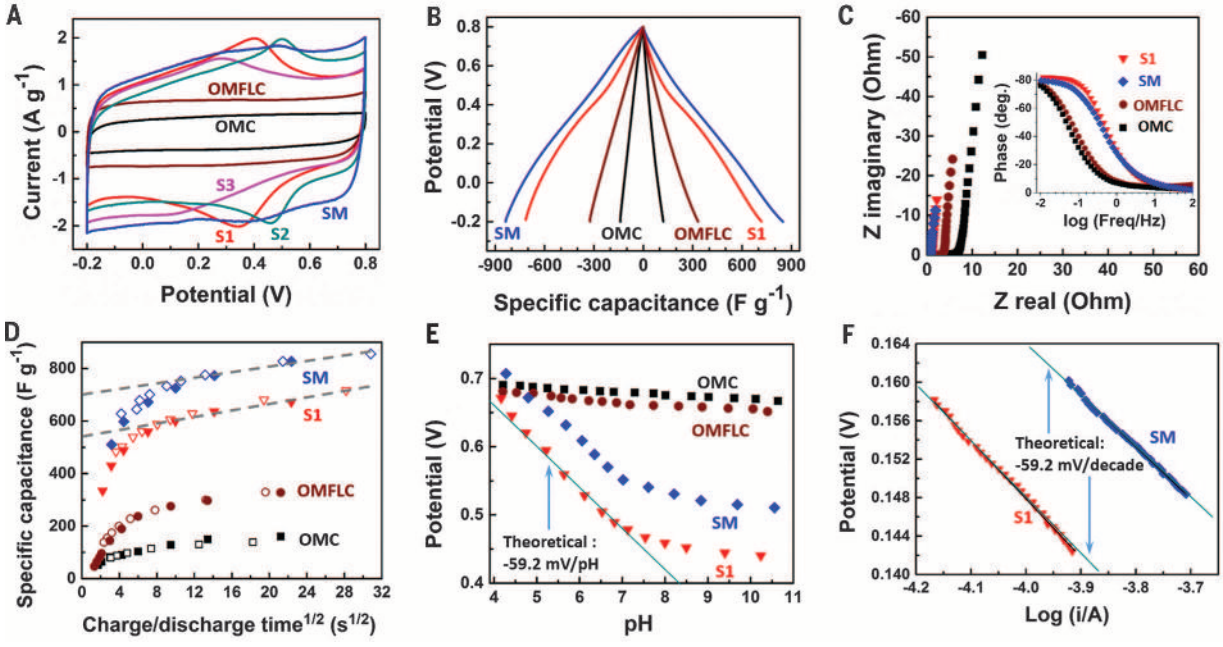

Fig. 2. Electrochemical evaluation. (**A**) Cyclic voltammetry (CV test, at 2 mV s^{-1}) from the first cycle for OMC, OMFLC, and OMFLC-N (S1 to S3) and for mixed OMFLC-N (SM). (**B**) Galvanostatic charge/discharge (CC test at 1.0 A g^{-1}) from the first cycle for OMC, OMFLC, and OMFLC-N (S1 and SM). (**C**) Complex-plane plots of AC impedance. Inset shows phase angle versus frequency. (**D**) Capacity versus square root of half-cycle time. Solid symbols, CV test data from 2 to 500 mV s^{-1}; open symbols, CC test data from 1 to 40 A g^{-1}. Extrapolated intercept capacitance is rate-independent capacitance k_1, the remainder diffusion-controlled capacitance. (**E**) Tafel plots of electrode potential against pH at steady-state current density of 10 μA cm^{-2}. (**F**) Tafel plots of electrode potential against current *i* at pH 6.8 for OMFLC-N (S1 and SM). All potentials are relative to Ag/AgCl reference electrode; all electrolytes except (E) and (F) are 0.5 M H_2SO_4 aqueous solution. In (E) and (F), theoretical slope (−59.2 mV/decade) is shown as a straight line to suggest reasonable agreement with the data (see text).

By mixing three OMFLC-N powders at the ratio of S1:S2:S3 = 0.3:0.3:0.4 to form another OMFLC-N powder (SM), we obtain a new material that is capable of supporting multiple faradaic peaks. It exhibits a rectangular EDLC-like CV curve at a very large current (Fig. 2A)—a feature that should prove useful for constructing high-performance symmetric electrochemical cells. Because this is a qualitatively different CV curve from those of other OMFLC-N electrodes as well as OMC and OMFLC, we made further performance comparisons between SM, S1, OMC, OMFLC, and YP-50.

Consistent with the CV results, all galvanostatic charge/discharge tests (the CC test in Fig. 2B) show symmetric features with a fairly linear slope. A specific capacitance as high as 855 F g^{-1} at a current density of 1 A g^{-1} was obtained for SM, versus 715 F g^{-1} for S1 (fig. S4, C and D) and 175 F g^{-1} for YP-50 (fig. S5). Over a wide range of current densities, SM continued to provide a well-behaving CC curve and high capacitance (fig. S4, E and F), achieving 615 F g^{-1} at 40 A g^{-1}, which is much higher than known EDLC and quite comparable to the capacitance of transition metal–oxide faradaic pseudocapacitors (*16*–*18*).

Electrochemical impedance spectroscopy (Fig. 2C, enlarged in fig. S6A) found OMFLC-N (S1) to have the lowest equivalent series resistance of ~0.8 ohms, better than that of OMFLC and OMC. This may be attributed to better wetting on OMFLC-N, which lowers the interface resistance, because OMFLC has at least comparable, if not lower, resistivity than OMFLC-N (fig. S2C). The >45° (negative) phase angle of both OMFLC-N (S1 and SM; inset of Fig. 2C) at relatively high frequencies confirms their capacitive behavior at fast rates. Specifically, the frequency (of −45°) when the resistance and reactance have equal magnitudes is 0.48 Hz for OMFLC-N, giving a relaxation time ($\tau_0 = 1/f_0$) of 2.1 s.

The CV and CC tests are in broad agreement with each other when compared at the same half-cycle time T as seen in Fig. 2D, which also provides insight into the charging/discharging kinetics. (In the CV test, T is the time to sweep over the voltage window. In the CC test, it is the time to discharge.) In general, the capacitance C may contain a rate-independent component k_1 (classically attributed to EDLC) and a diffusion-limited component controlled by the scanning rate, $v = T^{-1}$, taking the form (*19*, *20*)

$$C = k_1 + k_2 v^{-1/2} \quad (1)$$

In Fig. 2D, the $k_2 v^{-1/2}$ term represents the long-T data, which extrapolate to k_1 at the $T^{1/2} = v^{-1/2} = 0$ intercept. (In the CV test, Fig. 2D reduces to the standard C-$v^{-1/2}$ plot in fig. S6B, from which one can also obtain k_1.) Apparently, k_1 dominates in OMFLC-N, exceeding 700 F g^{-1} in SM and 545 F g^{-1} in S1. Dominance of rate-independent capacitances is common for EDLC, but it nevertheless holds here in redox reactions of the above materials because (i) OMFLC is a low-dimensional, fast-conducting, high-surface-area, few-layered material, and (ii) OMFLC-N is mesoporous (fig. S1) and hydrophilic (Fig. 1H). Therefore, they allow facile reactions both outside and inside the few-layer carbon tubes, as well as across the tube thickness.

The data from the slowest, near-equilibrium tests allowed us to construct the Tafel plots in Fig. 2, E and F, to compare the energetics of faradaic reactions and reveal a fundamental difference between OMFLC-N and OMC or OMFLC. For both S1 and SM, the potential required to sustain a constant current density of 10 μA cm^{-2} from pH 4.0 to 7.0 (Fig. 2E) lies close to the theoretical Tafel line with a slope of 2.3 × *RT/F* (−59.2 mV/pH) (*21*). Likewise, measuring the potential required for different current densities (Fig. 2F) at pH 6.8 gives again a slope in close coincidence with 2.3 × *RT/F*. Because both sets of Tafel lines imply a one-electron reaction, the pH dependence must arise from the concurrent incorporation of one proton and one electron. In contrast, for OMC and OMFLC, the slope is very

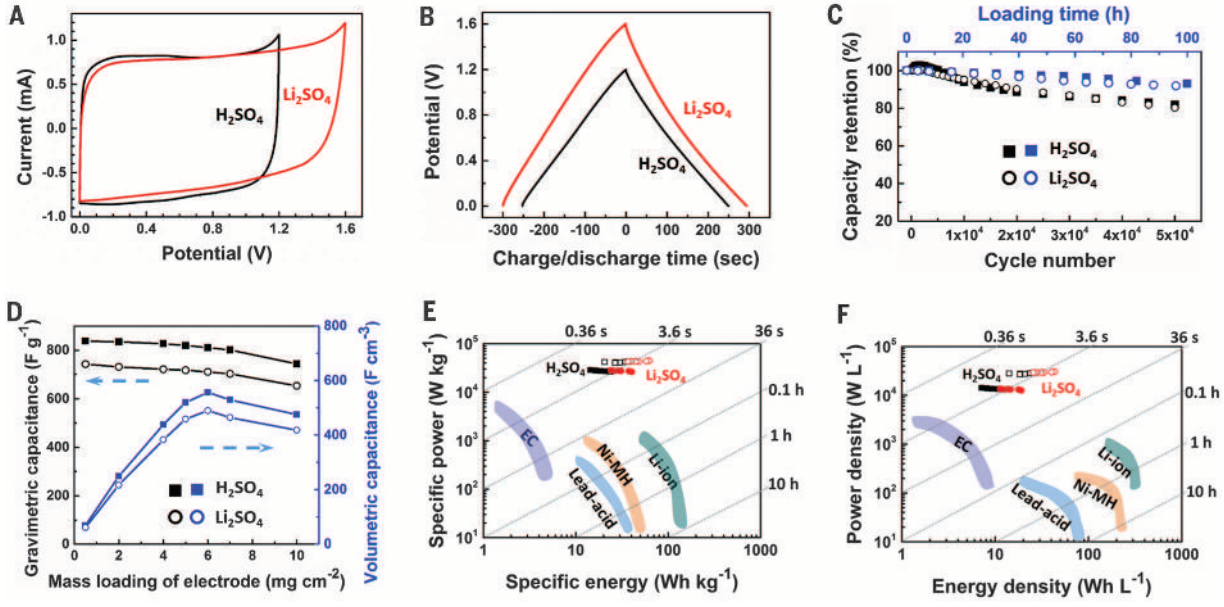

Fig. 3. Electrochemical performance of symmetric cells. OMFLC-N SM cathode and anode were used in two aqueous electrolytes, 0.5 M H_2SO_4 (pH 0) and 2 M Li_2SO_4 (pH 1.8). (**A**) Cyclic voltammetry from the first cycle at 2 mV s^{-1} scan rate. (**B**) Galvanostatic charge/discharge curves from the first cycle at 1 A g^{-1}. (**C**) Symmetric electrochemical cell devices retain >92% after 100 hours of sustained loading (blue symbols, upper scale) at 1.2 V (in 0.5 M H_2SO_4) and 1.6 V (in 2 M Li_2SO_4), and retain >80% of their initial response after 50,000 cycles (black symbols, lower scale) from 0 to same peak voltages in two electrolytes. (**D**) Gravimetric (left) and volumetric (right) capacitance (at 1 A g^{-1}) of symmetric electrochemical cell device (counting electrode weight and volume only) versus areal mass loading of OMFLC-N SM in two aqueous electrolytes. (**E**) Ragone plot of specific energy versus specific power for OMFLC-N SM symmetric devices (counting all-device weight) using 0.5 M H_2SO_4 (solid squares) and 2 M Li_2SO_4 (solid circles) electrolytes, as well as several standard devices: electrochemical capacitors (EC) (*2*, *28*), lead-acid batteries (*1*, *26*), nickel metal-hydride batteries (*27*), and lithium-ion batteries (*28*). Data counting electrode mass only are shown as open symbols. (**F**) Ragone plots of energy density versus power density for OMFLC-N SM packaged symmetric devices (counting all-device volume) using 0.5 M H_2SO_4 (solid squares) and 2 M Li_2SO_4 (solid circles) electrolytes, as well as several standard devices as in (E). Data counting electrode volume only are shown as open symbols. Dotted lines in (E) and (F) are current drain time, calculated by dividing specific energy by specific power.

flat, suggesting little redox activity. Recalling that the redox potential decreases with increasing concentration of nongraphitic N (Fig. 2A and table S1), we believe the redox reaction previously proposed for pseudocapacitance in N-containing polypyrrole (*22*) and carbon nanotubes (*8*, *9*)—that each pyrrolic (N-5) and pyridine (N-6) nitrogen can incorporate an electron and a proton—is also operational here: It fits all of the above descriptions. According to N 1s XPS that can "see" through tubes less than 2 nm thick, there is 8.2 at% N in OMFLC-N (S1), which may store an additional faradaic charge of 660 F g^{-1}. This is more than enough to account for the storage difference (390 F g^{-1}) between OMFLC-N (S1) and OMFLC.

The proposed N-H mechanism dictates that an acidic condition is more favorable for redox reactions. This was verified for S1 in the three-electrode CC test at 1 A g^{-1}: It has a larger capacitance in 0.5 M H_2SO_4 (715 F g^{-1}, Fig. 2B) than in 1 M KOH (pH 14) electrolyte (405 F g^{-1}; fig. S7, A to D, also confirmed by the CV tests). In contrast, OMFLC, which solely relies on EDLC, has very similar capacitances in the two electrolytes (fig. S7E). These results lend further support to the proposed N-H redox mechanism that makes OMFLC-N a superior supercapacitor.

Hoping to reduce these new mechanisms into practice, we investigated whether the three-electrode performance of OMFLC-N can be translated to electrochemical cells. Carbon-based electrodes are special in that they can be used as both cathodes and anodes in symmetric electrochemical cells, with a per-electrode specific capacitance nearly the same as that measured in the three-electrode test. This was confirmed for YP-50, OMC, and OMFLC (table S2). Here, we multiply the nominal specific capacitance of a symmetric EC by 4 to obtain the per-electrode specific capacitance (*23*). In contrast, as mentioned before, pseudocapacitive materials with a pronounced redox peak are usually inefficient electrodes in symmetric electrochemical cells (*23*, *24*) because their two differential capacitances at the two electrodes, C_1 and C_2, are different. (Under the normal circumstance when one electrode has a suitable potential for the major redox peak and thus a larger differential capacitance, the other electrode is at a potential away from the major redox peak, hence having a smaller differential capacitance.) So their total capacitance $C_1C_2/(C_1 + C_2)$ is lower than the maximum, which is $\frac{1}{2}C_1 = \frac{1}{2}C_2$ when $C_1 = C_2$. In contrast, despite predominant contributions of redox reactions, our SM electrode maintains a nearly rectangular CV curve (Fig. 2A)—that is, a constant differential capacitance—in the three-electrode test. So we expect its symmetric electrochemical cell to satisfy $C_1 = C_2$, thus to provide a per-electrode specific capacitance identical to that measured in the three-electrode test. Indeed, its symmetric-cell CV curve (Fig. 3A) in 0.5 M H_2SO_4 electrolyte is rectangular and rather symmetric, and its symmetric-cell CC test (Fig. 3B) gives a per-electrode capacitance of 840 F g^{-1} at 1 A g^{-1}—within 2% of the three-electrode capacitance of 855 F g^{-1} (see table S2). In comparison, other OMFLC-N electrodes (S1 to S3) each having a distinct redox peak in the CV curve all suffered from capacitance losses of 10 to 15% when used in a symmetric electrochemical cell (table S2). All the symmetric-cell electrochemical measurements were conducted in 0.5 M H_2SO_4 electrolyte using an operating voltage of 1.2 V, which did not cause any detectable H_2 or O_2 evolution (fig. S8A).

The performance of OMFLC-N SM electrodes in symmetric aqueous electrochemical cells was further confirmed using another electrolyte, Li_2SO_4, which helps prevent carbon-electrode corroding and allows a higher operating voltage up to 1.9 V (*25*). Indeed, in 2 M Li_2SO_4 electrolyte at pH 1.8, a symmetric electrochemical cell with SM electrodes had a threshold water-splitting voltage of 1.8 V; at 1.6 V there was no detectable H_2 or O_2 evolution after 24 hours (fig. S8B). In acidic (pH 1.8) but not basic (pH 9.2) Li_2SO_4, pronounced redox was confirmed by the CV test (fig. S9). With this electrolyte, symmetric electrochemical cells obtained a specific capacitance of 740 F g^{-1} at 1 A g^{-1} from the CV and CC tests (Fig. 3, A and B), just 5% below the three-electrode capacitance of 780 F g^{-1} (table S2).

Having established the robust redox bipolar activities of OMFLC-N SM as both cathode and anode, we further evaluated its suitability for practical applications, starting with their stability in sustained and cyclic loading (Fig. 3C). After 100 hours of sustained loading, the capacitance retention was 93% at 1.2 V in 0.5 M H_2SO_4 electrolyte and 92% at 1.6 V in 2 M Li_2SO_4 electrolyte. The symmetric electrochemical cell withstood 50,000 cycles between 0 and 1.2 V in 0.5 M H_2SO_4 electrolyte with 82% of the capacitance remaining; a similarly cycled device between 0 and 1.6 V in 2 M Li_2SO_4 (pH 1.8) electrolyte retained 80%.

To pack more energy and power into the device, we increased the mass loading to the limit of not sacrificing full electrochemical efficiency. (To aid electrode formation at >2.0 mg cm^{-2} OMFLC-N SM loading, we added 5 wt% PVDF to the OMFLC-N powders.) Up to 6.0 mg cm^{-2} (~0.69 g cm^{-3}), the gravimetric specific capacitance of the symmetric electrochemical cell changed minimally (Fig. 3D), indicating that OMFLC-N powders had full access to the electrolyte without geometric or electric hindrance or diffusion limitation. Such increased loading benefits the volumetric capacitance, which is important for practical applications. Peaking at 6.0 mg cm^{-2}, the volumetric capacitance increases by more than a factor of 8, so that OMFLC-N SM can reach 560 F cm^{-3} and 810 F g^{-1} in 0.5 M H_2SO_4, and 490 F cm^{-3} and 710 F g^{-1} in 2 M Li_2SO_4 (pH 1.8).

The merit of our material relative to existing battery and supercapacitor materials was evaluated using Ragone plots (specific power versus specific energy) for symmetric electrochemical cells on both the device gravimetric basis (Fig. 3E) and the device volumetric basis (Fig. 3F). In 0.5 M H_2SO_4 electrolyte, our device has a specific energy E of 24.5 Wh kg^{-1} based on the device weight (corresponding to 39.5 Wh $kg_{OMFLC\text{-}N}{}^{-1}$ based on the active-material weight) or 12.0 Wh $liter^{-1}$ based on the device volume (or 27.0 Wh $liter_{OMFLC\text{-}N}{}^{-1}$ based on the electrode volume). The specific power P is 26.5 kW kg^{-1} (42.5 kW $kg_{OMFLC\text{-}N}{}^{-1}$) or 13.0 kW $liter^{-1}$ (29.0 kW $liter_{OMFLC\text{-}N}{}^{-1}$), with a current-drain time (E/P) of 3.4 s. In 2 M Li_2SO_4 electrolyte, E increases to 41.0 Wh kg^{-1} (63.0 Wh $kg_{OMFLC\text{-}N}{}^{-1}$) and 19.5 Wh $liter^{-1}$ (43.5 Wh $liter_{OMFLC\text{-}N}{}^{-1}$) and P stays at 26.0 kW kg^{-1} (44.0 kW $kg_{OMFLC\text{-}N}{}^{-1}$) and 12.5 kW $liter^{-1}$ (30.0 kW $liter_{OMFLC\text{-}N}{}^{-1}$), with a drain time of 5.7 s. For supercapacitor applications, these properties are notable in that high specific power can be simultaneously achieved along with high specific energy, thus making carbon-based supercapacitors potentially competitive against batteries, such as lead-acid batteries (*3*, *26*), nickel metahydride batteries (*27*), and perhaps even lithium batteries (*28*) on a gravimetric basis.

Simplified fabrication of N-doped mesoporous few-layer carbon (omitting the sacrificial silica template and post–carbon deposition etching as described in supplementary materials) was finally implemented by combining chemical vapor deposition with a sol-gel process of inexpensive, environmentally friendly, Si-free precursors/catalysts. The material obtained is made of highly conductive (σ = 360 S/cm) mesoscopically ordered few-layer carbon with a large surface area (1900 m^2 g^{-1}). In 0.5 M H_2SO_4 electrolyte, its electrode has a specific capacitance of 790 F g^{-1} at 1 A g^{-1}, and its packaged device has a specific energy of 23.0 Wh kg^{-1} and a specific power of 18.5 kW kg^{-1} based on the device weight; in 2 M Li_2SO_4 (pH 1.8) electrolyte, the corresponding values are 720 F g^{-1}, 38.5 Wh kg^{-1}, and 22.5 kW kg^{-1}. Indeed, in all important respects (figs. S10 to S13), this material behaves within ~10% of the best OMFLC-N SM described above, thus providing an outstanding low-cost carbon-based material for electrochemical cells for electric power applications.

REFERENCES AND NOTES

1. J. Chmiola *et al.*, *Science* **313**, 1760–1763 (2006).
2. Y. Zhu *et al.*, *Science* **332**, 1537–1541 (2011).
3. P. Simon, Y. Gogotsi, *Nat. Mater.* **7**, 845–854 (2008).
4. X. Yang, C. Cheng, Y. Wang, L. Qiu, D. Li, *Science* **341**, 534–537 (2013).
5. J. Xia, F. Chen, J. Li, N. Tao, *Nat. Nanotechnol.* **4**, 505–509 (2009).
6. M. F. El-Kady, V. Strong, S. Dubin, R. B. Kaner, *Science* **335**, 1326–1330 (2012).
7. J. Huang, B. G. Sumpter, V. Meunier, *Angew. Chem. Int. Ed.* **47**, 520–524 (2008).
8. L. L. Zhang *et al.*, *Energy Environ. Sci.* **5**, 9618–9625 (2012).
9. G. Lota, B. Grzyb, H. Machnikowska, J. Machnikowski, E. Frackowiak, *Chem. Phys. Lett.* **404**, 53–58 (2005).
10. H. Li *et al.*, *J. Power Sources* **190**, 578–586 (2009).
11. D. Zhao *et al.*, *Science* **279**, 548–552 (1998).
12. P. M. Vora *et al.*, *Phys. Rev. B* **84**, 155114 (2011).
13. J. Casanovas, J. M. Ricart, J. Rubio, F. Illas, J. M. Jiménez-Mateos, *J. Am. Chem. Soc.* **118**, 8071–8076 (1996).
14. D. Wei *et al.*, *Nano Lett.* **9**, 1752–1758 (2009).
15. D. W. Wang *et al.*, *Chem. Eur. J.* **18**, 5345–5351 (2012).

16. T. Brezesinski, J. Wang, S. H. Tolbert, B. Dunn, *Nat. Mater.* **9**, 146–151 (2010).
17. K. Brezesinski *et al.*, *J. Am. Chem. Soc.* **132**, 6982–6990 (2010).
18. X. Lang, A. Hirata, T. Fujita, M. Chen, *Nat. Nanotechnol.* **6**, 232–236 (2011).
19. V. Augustyn *et al.*, *Nat. Mater.* **12**, 518–522 (2013).
20. S. Ardizzone, G. Fregonara, S. Trasatti, *Electrochim. Acta* **35**, 263–267 (1990).
21. Y. Surendranath, M. W. Kanan, D. G. Nocera, *J. Am. Chem. Soc.* **132**, 16501–16509 (2010).
22. G. A. Snook, P. Kao, A. S. Best, *J. Power Sources* **196**, 1–12 (2011).
23. M. D. Stoller, R. S. Ruoff, *Energy Environ. Sci.* **3**, 1294–1301 (2010).
24. V. Khomenko, E. Frackowiak, F. Béguin, *Electrochim. Acta* **50**, 2499–2506 (2005).
25. Q. Gao, L. Demarconnay, E. Raymundo-Piñero, F. Béguin, *Energy Environ. Sci.* **5**, 9611–9617 (2012).
26. A. F. Burke, Advanced batteries for vehicle applications. In *Encyclopedia of Automotive Engineering*, D. Crolla, D. E. Foster, T. Kobayashi, N. Vaughan, Eds. (Wiley, New York, 2014), pp. 1–20.
27. A. Burke, M. Miller, *J. Power Sources* **196**, 514–522 (2011).
28. D. Linden, T. B. Reddy, *Handbook of Batteries* (McGraw-Hill, New York, ed. 3, 2001).

ACKNOWLEDGMENTS

Supported by National Natural Science Foundation of China grants 51125006, 91122034, 61376056, and 51402336 and Science and Technology Commission of Shanghai grant 14YF1406500. I.W.C. was supported by U.S. Department of Energy BES grant DE-FG02-11ER46814 and used the facilities (Laboratory for Research on the Structure of Matter) supported by NSF grant DMR-11-20901.

SUPPLEMENTARY MATERIALS

www.sciencemag.org/content/350/6267/1508/suppl/DC1
Materials and Methods
Figs. S1 to S14
Tables S1 and S2
References (*29*–*32*)

20 April 2015; accepted 13 November 2015
10.1126/science.aab3798

NANOMATERIALS

Synthesis of borophenes: Anisotropic, two-dimensional boron polymorphs

Andrew J. Mannix,[1,2] Xiang-Feng Zhou,[3,4] Brian Kiraly,[1,2] Joshua D. Wood,[2] Diego Alducin,[5] Benjamin D. Myers,[2,6] Xiaolong Liu,[7] Brandon L. Fisher,[1] Ulises Santiago,[5] Jeffrey R. Guest,[1] Miguel Jose Yacaman,[5] Arturo Ponce,[5] Artem R. Oganov,[8,9,3]* Mark C. Hersam,[2,7,10]* Nathan P. Guisinger[1]*

At the atomic-cluster scale, pure boron is markedly similar to carbon, forming simple planar molecules and cage-like fullerenes. Theoretical studies predict that two-dimensional (2D) boron sheets will adopt an atomic configuration similar to that of boron atomic clusters. We synthesized atomically thin, crystalline 2D boron sheets (i.e., borophene) on silver surfaces under ultrahigh-vacuum conditions. Atomic-scale characterization, supported by theoretical calculations, revealed structures reminiscent of fused boron clusters with multiple scales of anisotropic, out-of-plane buckling. Unlike bulk boron allotropes, borophene shows metallic characteristics that are consistent with predictions of a highly anisotropic, 2D metal.

Bonding between boron atoms is more complex than in carbon; for example, both two- and three-center B-B bonds can form (*1*). The interaction between these bonding configurations results in as many as 16 bulk allotropes of boron (*1*–*3*), composed of icosahedral B_{12} units, small interstitial clusters, and fused supericosahedra. In contrast, small ($n < 15$) boron clusters form simple covalent, quasiplanar molecules with carbon-like aromatic or anti-aromatic electronic structure (*4*–*7*). Recently, Zhai *et al.* have shown that B_{40} clusters form a cage-like fullerene (*6*), further extending the parallels between boron and carbon cluster chemistry.

To date, experimental investigations of nanostructured boron allotropes are notably sparse, partly owing to the costly and toxic precursors (e.g., diborane) typically used. However, numerous theoretical studies have examined two-dimensional (2D) boron sheets [i.e., borophene (*7*)]. Although these studies propose various structures, we refer to the general class of 2D boron sheets as borophene. Based upon the quasiplanar B_7 cluster (Fig. 1A), Boustani proposed an Aufbau principle (*8*) to construct nanostructures, including puckered monolayer sheets (analogous to the relation between graphene and the aromatic ring). The stability of these sheets is enhanced by vacancy superstructures (*7*, *9*) or out-of-plane distortions (*10*, *11*). Typically, borophene is predicted to be metallic (*7*, *9*–*12*) or semimetallic (*10*) and is expected to exhibit weak binding (*13*) and anisotropic growth (*14*) when adsorbed on noble-metal substrates. Early reports of multiwall boron nanotubes suggested a layered structure (*15*), but their atomic-scale structure remains unresolved. It is therefore unknown whether borophene is experimentally stable and whether the borophene structure would reflect the simplicity of planar boron clusters or the complexity of bulk boron phases.

We have grown atomically thin, borophene sheets under ultrahigh-vacuum (UHV) conditions (Fig. 1B), using a solid boron atomic source (99.9999% purity) to avoid the difficulties posed by toxic precursors. An atomically clean Ag(111) substrate provided a well-defined and inert surface for borophene growth (*13*, *16*). In situ scanning tunneling microscopy (STM) images show the emergence of planar structures exhibiting anisotropic corrugation, which is consistent with first-principles structure prediction. We further verify the planar, chemically distinct, and atomically thin nature of these sheets via a suite of characterization techniques. In situ electronic characterization supports theoretical predictions that borophene sheets are metallic with highly anisotropic electronic properties. This anisotropy is predicted to result in mechanical stiffness comparable to that of graphene along one axis. Such properties are complementary to those of existing 2D materials and distinct from those of the metallic boron previously observable only at ultrahigh pressures (*17*).

During growth, the substrate was maintained between 450° and 700°C under a boron flux between ~0.01 to ~0.1 monolayer (ML) per minute [see supplementary materials for details (*18*)]. After deposition, in situ Auger electron spectroscopy (AES; Fig. 1C) revealed a boron KLL peak at the standard position (180 eV) superimposed on the clean Ag(111) spectrum. We observed no peaks due to contaminants, and none of the distinctive peak shifts or satellite features characteristic of compound or alloy formation (fig. S1).

After boron deposition at a substrate temperature of 550°C, STM topography images (Fig. 1D) revealed two distinct boron phases: a homogeneous phase and a more corrugated "striped" phase (highlighted with red and white arrows, respectively). Simultaneously acquired dI/dV maps (where I and V are the tunneling current and voltage, respectively) of the electronic density of states (DOS), given in Fig. 1E, showed strong electronic contrast between boron sheets and the Ag(111) substrate and increased differentiation between homogeneous and striped islands. The relative concentration of these phases depends upon the deposition rate. Low deposition rates favored the striped phase and resulted in the

[1]Center for Nanoscale Materials, Argonne National Laboratory, 9700 South Cass Avenue, Building 440, Argonne, IL 60439, USA. [2]Department of Materials Science and Engineering, Northwestern University, 2220 Campus Drive, Evanston, IL 60208, USA. [3]Department of Geosciences, Center for Materials by Design, and Institute for Advanced Computational Science, Stony Brook University, Stony Brook, NY 11794, USA. [4]School of Physics, Nankai University, Tianjin 300071, China. [5]Department of Physics, University of Texas San Antonio, San Antonio, TX 78249, USA. [6]NU*ANCE* Center, Northwestern University, 2220 Campus Drive, Evanston, IL 60208, USA. [7]Applied Physics Graduate Program, Northwestern University, 2220 Campus Drive, Evanston, IL 60208, USA. [8]Skolkovo Institute of Science and Technology, Skolkovo Innovation Center, 5 Nobel Street, Moscow 143026, Russia. [9]Moscow Institute of Physics and Technology, 9 Institutskiy Lane, Dolgoprudny City, Moscow Region, 141700, Russia. [10]Department of Chemistry, Northwestern University, 2220 Campus Drive, Evanston, IL 60208, USA.
***Corresponding author. E-mail: nguisinger@anl.gov (N.P.G.); m-hersam@northwestern.edu (M.C.H.); artem.oganov@stonybrook.edu (A.R.O.)**

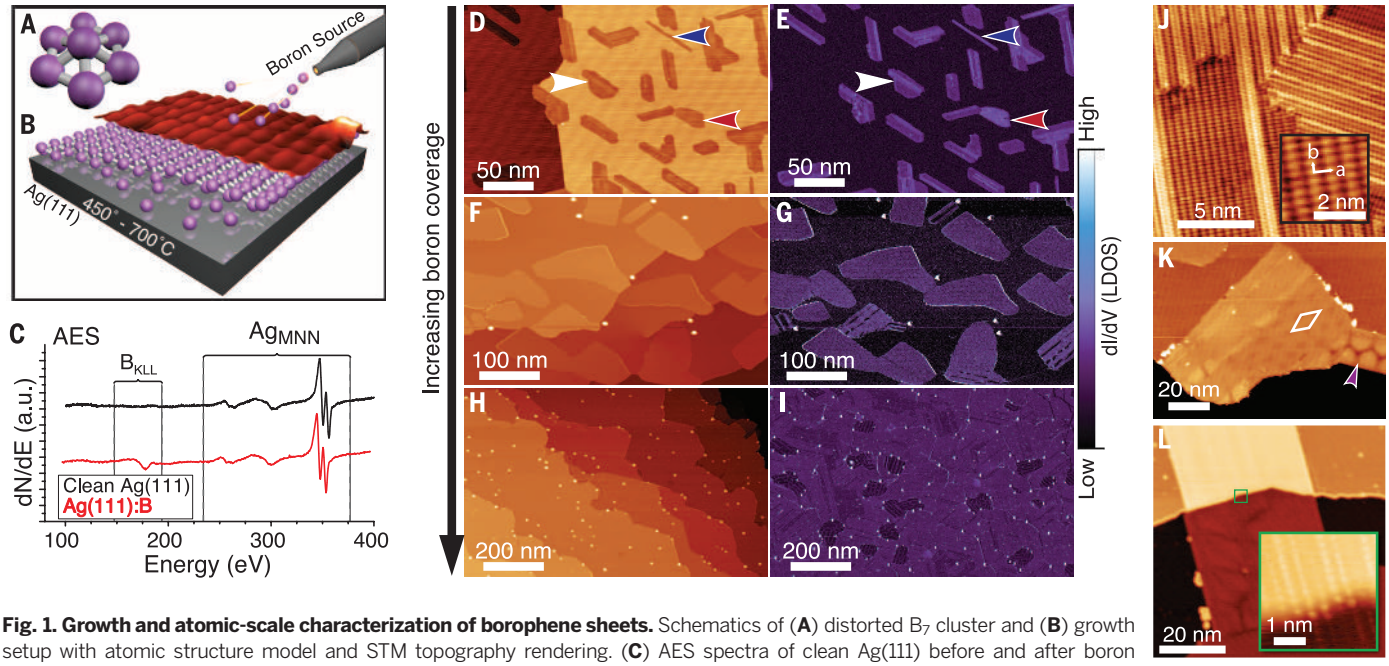

Fig. 1. Growth and atomic-scale characterization of borophene sheets. Schematics of (**A**) distorted B_7 cluster and (**B**) growth setup with atomic structure model and STM topography rendering. (**C**) AES spectra of clean Ag(111) before and after boron deposition. (**D** to **I**) Series of large-scale STM topography (left) and closed-loop *dI/dV* (right) images of borophene sheets, showing (D and E) low coverage (V_{sample} = 2.0 V, I_t = 100 pA), (F and G) medium coverage (V_{sample} = 3.5 V, I_t = 100 pA), and (H and I) high coverage (V_{sample} = 3.5 V, I_t = 100 pA). Regions of homogeneous-phase, striped-phase island, and striped-phase nanoribbon are indicated with red, white, and blue arrows, respectively. (**J** to **L**) STM topography images showing (J) striped-phase atomic-scale structure (V_{sample} = 0.1 V, I_t = 1.0 nA). Inset shows rectangular lattice with overlaid lattice vectors. (K) Striped phase with rhombohedral (indicated by white rhombus) and honeycomb (indicated by purple arrow) Moiré patterns (V_{sample} = 3.5 V, I_t = 100 pA). (L) Striped-phase island, demonstrating carpet-mode growth (V_{sample} = 3.5 V, I_t = 100 pA). Inset shows atomic continuity across the Ag(111) step (V_{sample} = −0.5 V, I_t = 700 pA).

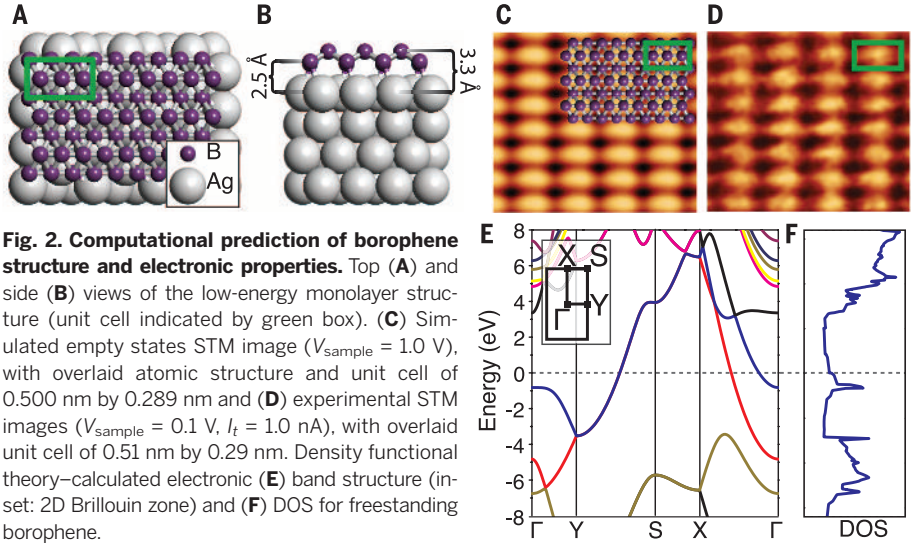

Fig. 2. Computational prediction of borophene structure and electronic properties. Top (**A**) and side (**B**) views of the low-energy monolayer structure (unit cell indicated by green box). (**C**) Simulated empty states STM image (V_{sample} = 1.0 V), with overlaid atomic structure and unit cell of 0.500 nm by 0.289 nm and (**D**) experimental STM images (V_{sample} = 0.1 V, I_t = 1.0 nA), with overlaid unit cell of 0.51 nm by 0.29 nm. Density functional theory–calculated electronic (**E**) band structure (inset: 2D Brillouin zone) and (**F**) DOS for freestanding borophene.

growth of striped-phase nanoribbons (blue arrow, also fig. S2). At higher deposition rates, we observed more of the homogeneous islands (Fig. 1, F and G). Increasing growth temperatures favored the striped phase, suggesting that the homogeneous phase is metastable relative to the striped phase. Both phases exhibited threefold orientation degeneracy with respect to the substrate, as confirmed by low-energy electron diffraction (fig. S3). The island size for both phases resembles that of graphene grown on Ag(111) (*19*).

At boron coverage approaching 1.0 ML, the substrate is completely covered by boron sheets and sparse clusters (Fig. 1, H and I).

High-resolution STM images show anisotropic atomic-scale features for both phases. The homogeneous phase (fig. S4) appears as atomic chains (0.30 nm periodicity) with periodic vertical buckling, a short-range rhombohedral Moiré pattern, and a longer-range 1D Moiré pattern (fig. S4). The striped phase (Fig. 1J) consists of a rectangular lattice commensurate with regions of striped corrugation. The rectangular structure (inset) is defined by vectors **a** and **b** of lengths 0.51 nm (±0.02 nm) and 0.29 nm (±0.02 nm), respectively. Within the striped regions, the in-plane periodicity parallel to the **a** vector is reduced by the increased out-of-plane corrugation associated with the stripes. However, the periodicities along the stripes match those of the rectangular lattice in the **b** direction. Further analysis [see supplementary text (*18*)] shows that the striped regions are simple distortions of the rectangular lattice that maximize the number of ideal boron adsorption sites (fig. S5). The formation of these stripes was temperature-dependent, with fewer stripes observed at 450°C and almost complete stripe coverage at 700°C. This is consistent with a progressive, thermally driven relaxation of the rectangular lattice into more favorable adsorption sites.

Rotationally misaligned striped-phase islands coalesce via defects that accommodate the anisotropic corrugations to form a complete monolayer (fig. S5). As shown in Fig. 1K, the striped regions exhibited Moiré patterns with rhombohedral (~8 nm period, marked by white rhombus) or, far less commonly, honeycomb (indicated by purple arrow) symmetry. These observations indicate the possibility of at least two well-defined long-range structural relationships between borophene and Ag(111). The borophene superstructure is evidently more complex than planar 2D materials such as BN, which forms a well-defined nanomesh on transition metals (*20*, *21*) due to substrate interactions. The mildly attractive B-Ag

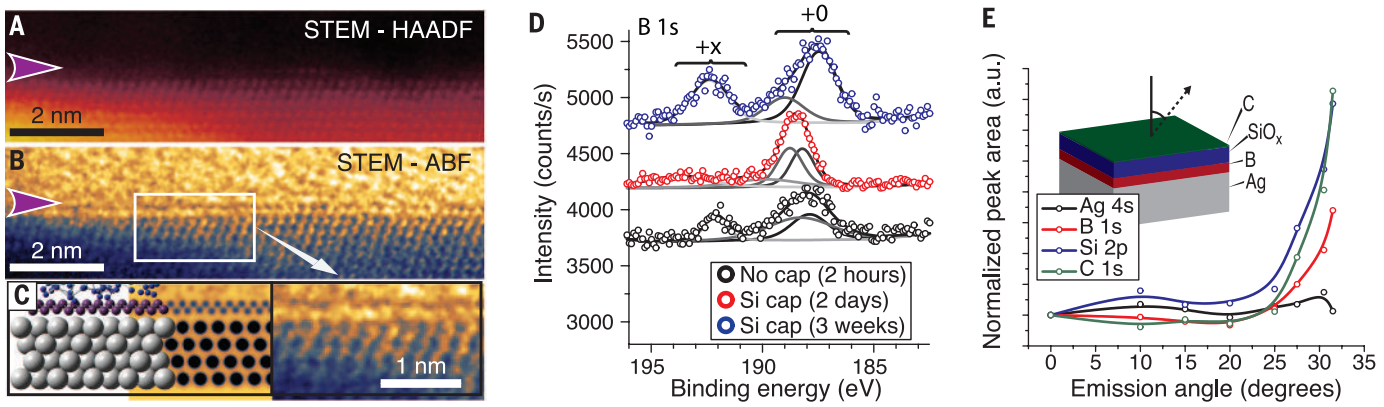

Fig. 3. Borophene structural and chemical characterization. Cross-sectional AC-STEM images from (**A**) HAADF and (**B**) ABF detectors. (C) Juxtaposition (left to right) of Si-capped borophene structure model, simulated ABF image, and magnified ABF image. (**D**) XPS B 1s core–level spectra and fitted components for samples with and without Si capping layers. (**E**) Angle-resolved XPS data acquired on Si-capped samples. Inset: schematic showing measurement angle and sample structure determined by angle-resolved XPS.

interactions, (*21*) result in enhanced corrugation and substrate-stabilized structural variation in borophene, providing additional degrees of freedom for functionality beyond those of conventional 2D materials.

Frequently, borophene growth over the substrate step edges is observed [i.e., "carpet mode" growth (*22*)], as in Fig. 1L. This continuity of the atomic-scale structure over the step (inset) suggests that the borophene is structurally distinct from the underlying substrate.

These experimental results are further elucidated by ab initio evolutionary structure prediction with the USPEX algorithm (*23*, *24*), which minimizes the thermodynamic potential of the system using density functional theory (DFT). Structures calculated with varying concentrations of Ag and B atoms on the Ag(111) substrate show surface segregation of B (fig. S6), indicating that the formation of a B-Ag surface alloy or boride is highly improbable (*16*, *25*). Additional calculations predict likely monolayer (fig. S7) and bilayer (fig. S8) borophene structures on Ag(111), although height measurements (see following discussion) supported a monolayer model.

The lowest-energy monolayer structure is shown in Fig. 2, A and B, and is constructible from distorted B_7 clusters using the Aufbau principle proposed by Boustani (*8*). The symmetry (space group *Pmmn*) and calculated lattice constants agree well with the STM data, with **a** and **b** equal to 0.500 nm and 0.289 nm, respectively. Comparison between simulated (Fig. 2C) and experimental STM topography images (Fig. 2D, also fig. S7) gives excellent agreement, as do electron diffraction data (fig. S3). Freestanding relaxation of this structure removes the slight corrugations along the **a** direction, but preserves the buckling along the **b** direction (fig. S7). The freestanding sheet may exhibit instability against long-wavelength transversal thermal vibrations (fig. S7), which may contribute to the observed stripe formation and would likely distort the structure of the borophene sheet upon removal from the growth substrate. This substrate-induced stability frames borophene as an intermediate class of templated, covalently bound sheets with properties distinct from those of conventional 2D materials and more consistent structure than that of supported silicon phases (*26*).

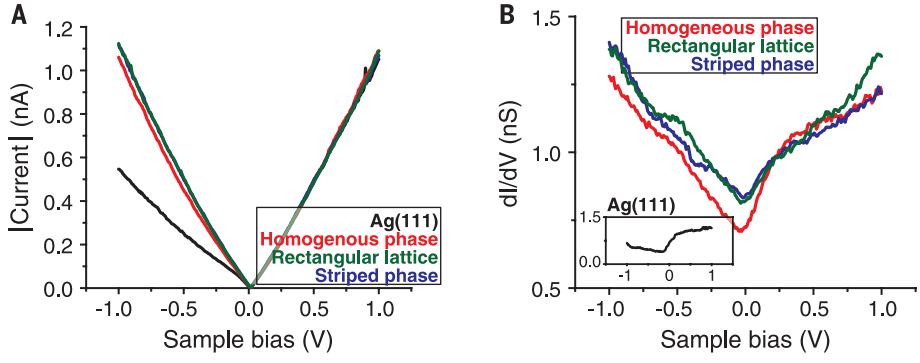

Fig. 4. Scanning tunneling spectroscopy of borophene. (**A**) STS *I-V* curves and (**B**) STS *dI/dV* spectra [inset: clean Ag(111) dI/dV spectrum] from the borophene sheets, which demonstrate metallic characteristics (feedback loop opened at V_{sample} = 1.0 V, I_t = 1.0 nA).

Electronic band structure calculations (Fig. 2E) within the 2D Brillouin zone of the relaxed, freestanding monolayer (inset) predict metallic conduction (i.e., bands crossing the Fermi level) along the Γ-*X* and *Y*-*S* directions (parallel to the uncorrugated **a** direction). However, the out-of-plane corrugation along the **b** direction opens a band gap along the Γ-*Y* and *S*-*X* directions. As a result, borophene is a highly anisotropic metal, where electrical conductivity is confined along the chains. The calculated DOS (Fig. 2F) is likewise metallic (*9*, *11*).

This structure also results in substantial mechanical anisotropy (fig. S7). Owing to the strong, highly coordinated B-B bonds, the in-plane Young's modulus (a measure of stiffness) is equal to 170 GPa·nm along the **b** direction, and 398 GPa·nm along the **a** direction, which potentially rivals graphene, at 340 GPa·nm (*27*). Furthermore, the out-of-plane buckling results in negative values for the in-plane Poisson's ratio (equal to –0.04 along **a** and –0.02 along **b**), resulting in unusual properties, such as in-plane expansion under tensile strain.

The apparent topographic height of the boron islands in STM depended upon scanning parameters, with the islands appearing as depressions for sample biases <3.2 V (compare the images in Fig. 1, D and F). This observation is attributed to the inherent convolution between topography and electronic structure in STM measurements. Similar inversion is observed for NaCl islands (*28*) and graphene (*19*) on Ag(111). However, cross-sectional, aberration-corrected scanning transmission electron microscopy (AC-STEM) unambiguously shows that the boron phase is atomically thin and structurally distinct from the Ag(111) growth substrate. AC-STEM sample preparation is detailed in fig. S9. Images acquired with the high-angle annular dark field (HAADF) detector (Fig. 3A) are sensitive to the atomic number *Z* (contrast ~ $Z^{3/2}$) and show minimal contrast at the interface between the Ag(111) substrate and amorphous SiO_x capping layer, which is consistent with the lack of electron scattering from the low-*Z* boron. Nevertheless, electron energy-loss spectra confirm that the boron lies at the Ag(111) surface (fig. S11). Annular bright field (ABF) images (Fig. 3B and fig. S10), which are

sensitive to light elements such as boron (*29*), revealed a planar structure (indicated by a purple arrow) at this interface. The observed contrast and structure are consistent with a simulated ABF image of the borophene structure model (Fig. 3C). Measured sheet thicknesses of ~0.27 to ~0.31 nm match both the monolayer structure model and multiwalled boron nanotubes (*15*).

X-ray photoelectron spectroscopy (XPS) measures both sample composition and the oxidation state of the species present. Although the borophene islands persisted under ambient conditions (fig. S12), the emergence of higher–binding energy features in the XPS B 1s core-level spectra (Fig. 3D) demonstrate that bare samples (black curve) were partially oxidized within several hours in ambient conditions. However, this oxidation was impeded by an amorphous silicon/silicon oxide capping layer (red curve), which delayed oxidation for several weeks (blue curve). The unoxidized, capped sample is fit by two Voigt components, which reflect the differences in chemical environment between the low- and high-buckled atoms. Increasing the photoelectron detector angle from the sample normal enhances XPS surface sensitivity, thereby selectively probing the surface and subsurface. The normalized, integrated components of angle-resolved XPS spectra on silicon-capped borophene are plotted in Fig. 3E. With increasing emission angle, the relative intensities of the carbon, silicon, and boron peaks increased, whereas the silver peak diminished. These results confirm the structure shown in the inset schematic, corroborating our AES, STM, and STEM results. Additional XPS data are given in fig. S13.

As shown above, theoretical predictions of the borophene structure forecast metallic characteristics. However, all known bulk boron allotropes are semiconductors at standard conditions, only becoming metallic at extremely high pressures (*17*). Scanning tunneling spectroscopy (STS) confirms the metallic characteristics of borophene through *I*–*V* curves (Fig. 4A) and *dI*/*dV* spectra (which measure the local electronic DOS, Fig. 4B). These show gapless (i.e., metallic) behavior consistent with the superposition between the Ag(111) surface (*30*) and the predicted filled-state population in borophene (Fig. 2G). These observations are likely to motivate and inform further studies of metallicity and related phenomena in 2D boron polymorphs.

REFERENCES AND NOTES

1. T. Ogitsu, E. Schwegler, G. Galli, *Chem. Rev.* **113**, 3425–3449 (2013).
2. B. Douglas, S.-M. Ho, *Structure and Chemistry of Crystalline Solids* (Springer Science & Business Media, New York, 2007).
3. A. R. Oganov *et al.*, *Nature* **457**, 863–867 (2009).
4. H.-J. Zhai, B. Kiran, J. Li, L.-S. Wang, *Nat. Mater.* **2**, 827–833 (2003).
5. A. P. Sergeeva *et al.*, *Acc. Chem. Res.* **47**, 1349–1358 (2014).
6. H.-J. Zhai *et al.*, *Nat. Chem.* **6**, 727–731 (2014).
7. Z. A. Piazza *et al.*, *Nat. Commun.* **5**, 3113 (2014).
8. I. Boustani, *Phys. Rev. B* **55**, 16426–16438 (1997).
9. H. Tang, S. Ismail-Beigi, *Phys. Rev. Lett.* **99**, 115501 (2007).
10. X.-F. Zhou *et al.*, *Phys. Rev. Lett.* **112**, 085502 (2014).
11. K. C. Lau, R. Pandey, *J. Phys. Chem. C* **111**, 2906–2912 (2007).
12. E. S. Penev, S. Bhowmick, A. Sadrzadeh, B. I. Yakobson, *Polymorphism of Two-Dimensional Boron.* **12**, 2441–2445 (2012).
13. Y. Liu, E. S. Penev, B. I. Yakobson, *Angew. Chem. Int. Ed.* **52**, 3156–3159 (2013).
14. H. Liu, J. Gao, J. Zhao, *Sci. Rep.* **3**, 3238 (2013).
15. F. Liu *et al.*, *J. Mater. Chem.* **20**, 2197 (2010).
16. H. Okamoto, *J. Phase Equilibria* **13**, 211–212 (1992).
17. M. I. Eremets, V. V. Struzhkin, H. Mao, R. J. Hemley, *Science* **293**, 272–274 (2001).
18. Additional supplementary text and data are available on *Science* Online.
19. B. Kiraly *et al.*, *Nat. Commun.* **4**, 2804 (2013).
20. S. Berner *et al.*, *Angew. Chem.* **46**, 5115–5119 (2007).
21. F. Müller *et al.*, *Phys. Rev. B* **82**, 113406 (2010).
22. H. I. Rasool *et al.*, *J. Am. Chem. Soc.* **133**, 12536–12543 (2011).
23. A. R. Oganov, C. W. Glass, *J. Chem. Phys.* **124**, 244704–244716 (2006).
24. Q. Zhu, L. Li, A. R. Oganov, P. B. Allen, *Phys. Rev. B* **87**, 195317 (2013).
25. A. Kolmogorov, S. Curtarolo, *Phys. Rev. B* **74**, 224507 (2006).
26. B. Feng *et al.*, *Nano Lett.* **12**, 3507–3511 (2012).
27. C. Lee, X. Wei, J. W. Kysar, J. Hone, *Science* **321**, 385–388 (2008).
28. Q. Guo *et al.*, *Surf. Sci.* **604**, 1820–1824 (2010).
29. R. Ishikawa *et al.*, *Nat. Mater.* **10**, 278–281 (2011).
30. J. Kliewer *et al.*, *Science* **288**, 1399–1402 (2000).

ACKNOWLEDGMENTS

This work was performed, in part, at the Center for Nanoscale Materials, a U.S. Department of Energy Office of Science User Facility under Contract No. DE-AC02-06CH11357. This work was also performed, in part, at the NUANCE Center, supported by the International Institute for Nanotechnology, Materials Research Science and Engineering Centers (NSF DMR-1121262), the Keck Foundation, the State of Illinois, and Northwestern University. A.J.M., B.K., J.D.W., X.L., J.R.G, M.C.H., and N.P.G acknowledge support by the U.S. Department of Energy SISGR (contract no. DE-FG02-09ER16109), the Office of Naval Research (grant no. N00014-14-1-0669), and the National Science Foundation Graduate Fellowship Program (DGE-1324585 and DGE-0824162). X.-F.Z thanks the National Science Foundation of China (grant no. 11174152), the National 973 Program of China (grant no. 2012CB921900), and the Program for New Century Excellent Talents in University (grant no. NCET-12-0278). U.S. thanks the National Council of Science and Technology, CONACyT (proposal no. 250836). A.R.O acknowledges support fromthe Defense Advanced Research Projects Agency (grant no. W31P4Q1210008) and the Government of Russian Federation (no. 14.A12.31.0003). D.A., M.J.Y, and A.P. acknowledge support by the National Institute on Minority Health and Health Disparities (NIMHD) in the program Research Centers in Minority Institutions Program (RCMI) Nanotechnology and Human Health Core (grant G12MD007591), the NSF PREM DMR (grant no. DMR-0934218), the Welch Foundation (grant no. AX-1615), and the Department of Defense (grant no. 64756-RT-REP).

SUPPLEMENTARY MATERIALS

www.sciencemag.org/content/350/6267/1513/suppl/DC1
Materials and Methods
Supplementary Text
Figs. S1 to S13
References (*31*–*57*)

27 July 2015; accepted 28 October 2015
10.1126/science.aad1080

BATTERIES

Visualization of O-O peroxo-like dimers in high-capacity layered oxides for Li-ion batteries

Eric McCalla,[1,2,3,4] Artem M. Abakumov,[5,6] Matthieu Saubanère,[2,3,7] Dominique Foix,[2,3,8] Erik J. Berg,[9] Gwenaelle Rousse,[1,3,10] Marie-Liesse Doublet,[2,3,7] Danielle Gonbeau,[2,3,8] Petr Novák,[9] Gustaaf Van Tendeloo,[5] Robert Dominko,[4] Jean-Marie Tarascon[1,2,3,10]*

Lithium-ion (Li-ion) batteries that rely on cationic redox reactions are the primary energy source for portable electronics. One pathway toward greater energy density is through the use of Li-rich layered oxides. The capacity of this class of materials (>270 milliampere hours per gram) has been shown to be nested in anionic redox reactions, which are thought to form peroxo-like species. However, the oxygen-oxygen (O-O) bonding pattern has not been observed in previous studies, nor has there been a satisfactory explanation for the irreversible changes that occur during first delithiation. By using Li_2IrO_3 as a model compound, we visualize the O-O dimers via transmission electron microscopy and neutron diffraction. Our findings establish the fundamental relation between the anionic redox process and the evolution of the O-O bonding in layered oxides.

Because lithium-ion (Li-ion) batteries have the highest energy density of all commercially available batteries, they are able to power most consumer electronics and have emerged as the technology of choice for powering electric vehicles. Li-ion batteries may also be used for grid storage and load-leveling for renewable energy. Current state-of-the-art positive electrodes use layered rock salt oxides ($LiCoO_2$ and its derivatives), spinel ($LiMn_2O_4$), or polyanionic compounds such as olivine-type $LiFePO_4$ (*1*). One push to increase the practical capacity limit of $LiCoO_2$ is via chemical substitution aimed at stabilizing the layered framework. The partial replacement of Co^{3+} with Ni^{2+} and Mn^{4+} has led to the $Li(Ni_xMn_yCo_{1-x-y})O_2$ layered oxides being coined as stoichiometric nickel manganese cobalt (NMC) oxides. These compounds have improved safety and capacities approaching 200 mA·hour/g. Further substitution of the transition metals by Li results in capacities exceeding 270 mA·hour/g. These materials are referred to as Li-rich layered

oxides, as some Li ions now occupy crystallographic sites in the transition metal layers in the ordered rock salt structure (*2*, *3*). During the first charge, these compounds undergo a transformation such that subsequent charge-discharge curves take an S shape without clear redox plateaus (as seen for $Li_2Ir_{0.75}Sn_{0.25}O_3$ in Fig. 1C). Partial oxidation of the oxygen sublattice upon Li removal, leading to an increased capacity, has been conjectured (*4*–*12*). The high capacity is rooted in the cumulative reversibility of both cationic and anionic redox processes ($2O^{2-} \rightarrow O_2^{n-}$, where n = 1, 2, or 3) (*13*–*15*). We speculated, but did not observe, that this oxidation of oxygen results in the formation of peroxo-like species with shortened O-O distances. Nevertheless, such studies demonstrate that the Li-(de)intercalation chemistry does not rely solely on cationic redox reactions as the source of energy storage; the oxygen sublattice is active as well.

Such O-O pairing in the oxygen lattice, resulting from the formation of O_2^{n-} species, predominantly occurs in compounds that have highly covalent metal-oxygen bonding—that is, systems showing a high degree of M(d)-O(sp) band overlap (*13*–*16*). Although this description of the oxidation of the oxygen sublattice is relatively new, the activity of the anionic network for chalcogenide (Ch)–based electrodes has long been recognized (*17*). By properly selecting cation-anion pairs, Rouxel showed the feasibility of tuning the degree of the metal M(3d)-Ch(sp) band mixing so as to trigger the formation of S-S dimers or Te-Te-Te trimers, as observed for iridium tellurides (*17*). Moreover, by performing a survey of various compounds such as $Li_2Ru_{1-x}Sn_xO_3$ (*13*), $Li_{4.27}Fe_{0.56}TeO_6$ (*16*), Li_4NiTeO_6 (*18*), and Li_4FeSbO_6 (*19*), we have demonstrated that the stability of the oxygen close-packed framework against O_2 evolution at high potential is highly tunable with composition. This finding is particularly important because this process leads to large irreversible capacities and poor long-term cycling (*16*, *19*, *20*). Layered compounds containing 4d metals have recently been shown to have reversible capacities of 300 mA·hour/g that involve a reversible anionic redox process (*21*). There is no direct structural evidence for the presence of peroxo-like species in any layered oxide, nor is it clear to what extent oxygen can be reversibly oxidized (i.e., the value of n in O_2^{n-} remains an enigma).

We address these questions via a model system consisting of a Li-rich layered phase with Ir as a 5d metal so as to increase the covalency and minimize the unwanted cationic migration during charge-discharge cycling with the larger Ir atoms. $Li_2Ir_{1-x}Sn_xO_3$ compounds with x = 0, 0.25, and 0.5 were prepared as described in the supplementary materials (*22*). Figure 1A (left) shows the structure of pristine Li_2IrO_3, which displays the cubic close-packed O3 stacking of the Li layers and the $Li_{1/3}Ir_{2/3}O_2$ slabs, where each Li cation is surrounded by six Ir cations to form a honeycomb-like ordering pattern. Figure 1B and fig. S1 show x-ray powder diffraction (XRD) patterns of the pristine $Li_2Ir_{1-x}Sn_xO_3$ materials and demonstrate typical shifts in peak positions consistent with a solid solution, confirmed by the progression of lattice parameters seen in table S1. Figure 1, C and D, and fig. S2 show the electrochemical performance of the x = 0, 0.25, and 0.5 materials. The x = 0.25 and 0.5 samples show cycling behavior typical of Li-rich oxides: two plateaus on first charge in the graphs of voltage versus y in $Li_yIr_{1-x}Sn_xO_3$, with a transformation taking place such that the second charge cycle is markedly different from the first, with an S shape now visible.

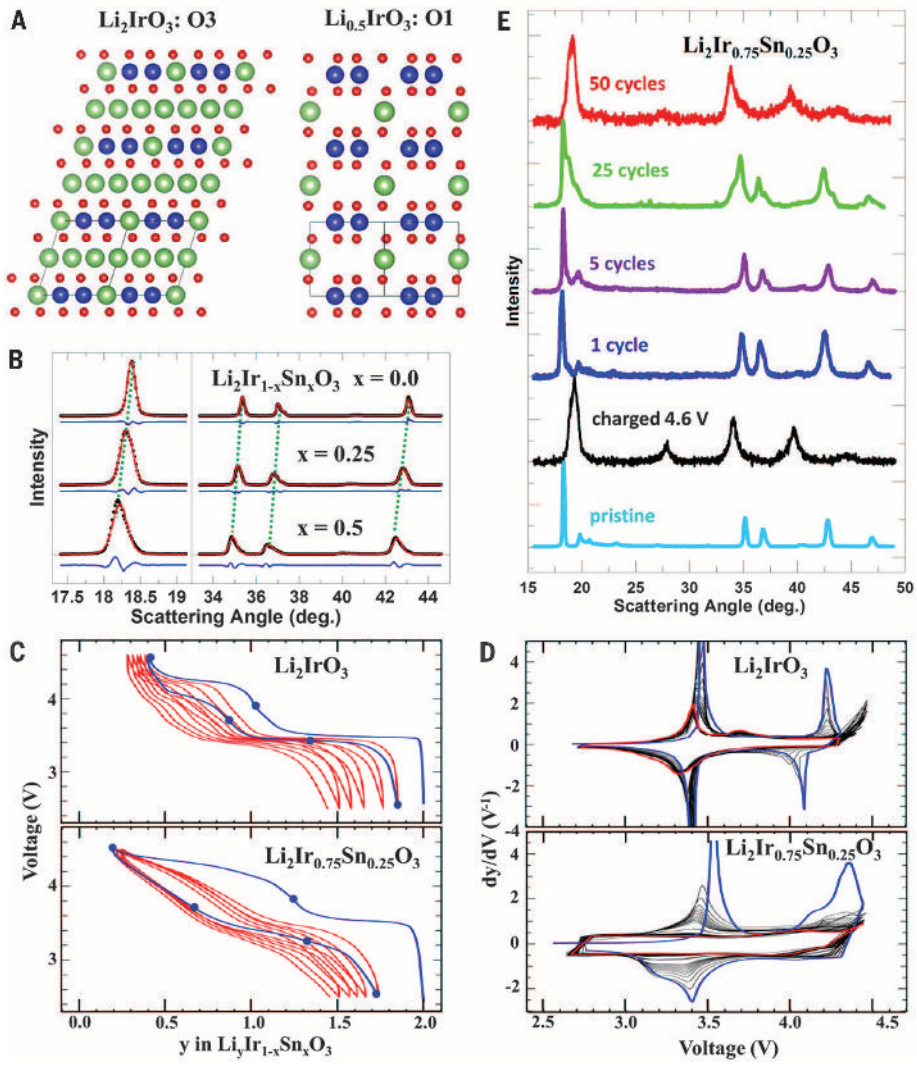

Fig. 1. Structural transformations and electrochemical cycling of Li-Ir-Sn-O materials. (**A**) (Left) Structure of the pristine Li_2IrO_3 material, showing the O3 stacking. (Right) Structure of the fully charged material, showing the O1 stacking. Both structures are shown in the [110] projection. Throughout the figures Ir is blue, Li is green, and O is red. (**B**) XRD patterns for the pristine materials with varying Sn content, fitted by taking stacking faults into account with the FAULTS software. Green dashed lines show peak shifts, consistent with an increase in cell volume as Sn content increases. Complete patterns are included in fig. S1. (**C**) Voltage curves showing the first 10 cycles at C/10 between 2.5 and 4.6 V. The first cycle shown in blue, and blue circles represent specific compositions, as referred to in Fig. 2D. (**D**) Derivative curve showing the evolution of the redox peaks between the first (blue) and 50th (red) cycles. (**E**) XRD patterns for $Li_2Ir_{0.75}Sn_{0.25}O_3$ after various electrochemical tests, showing a gradual conversion during extended cycling until the final scan looks similar to that of the first charged sample.

[1]Collège de France, Chimie du Solide et de l'Energie, FRE 3677, 11 Place Marcelin Berthelot, 75231 Paris Cedex 05, France. [2]ALISTORE–European Research Institute, FR CNRS 3104, 80039 Amiens, France. [3]Réseau sur le Stockage Electrochimique de l'Energie (RS2E), FR CNRS 3459, France. [4]National Institute of Chemistry, Hajdrihova 19, SI-1000 Ljubljana, Slovenia. [5]Electron Microscopy for Materials Science (EMAT), University of Antwerp, Groenenborgerlaan 171, B-2020, Antwerp, Belgium. [6]Center for Electrochemical Energy Storage, Skolkovo Institute of Science and Technology, 3 Nobel Street, 143026 Moscow, Russia. [7]Institut Charles Gerhardt, CNRS UMR 5253, Université Montpellier, Place Eugène Bataillon, 34 095 Montpellier, France. [8]IPREM/ECP (UMR 5254), University of Pau, 2 Avenue Pierre Angot, 64053 Pau Cedex 9, France. [9]Electrochemistry Laboratory, Paul Scherrer Institut, CH-5232 Villigen PSI, Switzerland. [10]Sorbonne Universités–UPMC Univ Paris 06, 4 Place Jussieu, F-75005 Paris, France.
***Corresponding author. E-mail: jean-marie.tarascon@college-de-france.fr**

This transformation indicates the presence of either a solid solution during the removal of lithium or a broad energy distribution of the lithium sites. By contrast, the Li_2IrO_3 sample shows that the plateaus seen on first charge are far more robust, as reported by Kobayashi *et al.* (*23*). However, the *dy/dV* curves show a steady decrease in the size of the redox peaks with extended cycling, yielding a substantial capacity fade for both samples; the $x = 0$ composition in particular shows none of the voltage fade seen in many Li-rich oxides (*3*, *14*).

Because the $x = 0$ and 0.25 samples behave differently, the structural evolution was studied in detail for both systems. Figure 1E shows the associated changes in the XRD patterns for the $x = 0.25$ sample during extended cycling. At the end of charge, the XRD pattern indexes to that of an O1-type structure with a hexagonal close-packed stacking (right image in Fig. 1A). After the first cycle, the XRD pattern returns primarily to that of the pristine O3 structure, though with the appearance of a few small new peaks. These peaks grow with extended cycling until only they remain after 50 cycles, and the peaks attributed to the O3 structure are no longer present. This same process occurs in Li_2IrO_3 samples (fig. S3).

Figure 2 covers the redox processes that occur during electrochemical cycling. The x-ray photoelectron spectroscopy (XPS) results shown in Fig. 2, A and B, and fig. S4 are consistent with previous results for Ru-based systems (*13*–*15*) wherein both metal and oxygen oxidations take place during charge. Here, Ir begins in the 4+ state and is oxidized during the first plateau, which ends at 3.9 V. This represents the greatest positive shift in the Ir 4f peak, and it is tempting to attribute this shift to Ir^{5+}, based on the fact that nearly 1 Li atom is removed from Li_2IrO_3 ($x = 0$) and 0.75 is removed from $Li_2Ir_{0.75}Sn_{0.25}O_3$ ($x = 0.25$), as shown in Fig. 1C. However, unlike in Ru-based systems, we can already detect the presence of peroxo-like species in the O 1s peaks in the XPS spectra at mid-charge, as shown in Fig. 2A ($x = 0$) and fig. S4 ($x = 0.25$). This suggests a mixed redox process, such that Ir is not strictly in the 5+ state but instead the electron being removed during charge is taken from both Ir and O, which is expected given the highly covalent Ir-O bond. Figure 2C shows the progression of the fraction of oxygen in the peroxo-like species during cycling for both samples. In each case, the fully charged state contains nearly half of the sample's oxygen in the peroxo-like species O_2^{n-}. Upon discharge, the peroxo-like species is reduced back to O^{2-} between 3.7 and 2.5 V for both samples, though it occurs slightly earlier in discharge for the Sn-containing material where the peroxo-like species is reduced by the time a lithium content of 1.33 atoms is reached. This difference suggests that Sn promotes the reversibility of the anionic redox process over a wider potential window (3.7 to 3.25 V) with less hysteresis. This change may be attributed to added flexibility in the oxygen network due to the presence of Sn, as previously proposed (*13*). The Li_2IrO_3 sample is therefore a Li-rich oxide, where the peroxo-like species are seen by XPS without immediate conversion to an S curve in the cycling data. We therefore have the opportunity to study anionic redox and the conversion to S curve independently and to establish the true cause of the transformations seen in other Li-rich oxides. Figure 2D shows the change in Bader charge calculated with density functional theory (DFT) as Li is removed from Li_2IrO_3. This also shows mixed redox throughout the Li extraction, in agreement with the XPS results.

These results imply that the local distortions in the oxygen lattice associated with the formation of peroxo-like species can be observed directly by transmission electron microscopy (TEM). The reason such information is available for the Li_2IrO_3 system is that the charged sample takes an O1 structure (Fig. 1A, refinements shown in fig. S5, and structure given in table S2) such that the projection of the oxygen columns becomes available along the *c* axis without overlapping with the columns of Ir or Li. The [010], [100], and [001] high-angle annular dark-field scanning transmission electron microscopy (HAADF-STEM) images of the charged $Li_{0.5}IrO_3$ sample show the highly ordered O1 structure viewed across (Fig. 3A and fig. S6, left) and along (Fig. 3B and fig. S6, right) the *c* axis. These images demonstrate perfect honeycomb ordering of the Ir cations on the transition metal layer and very little migration of Ir to the now nearly empty Li layer. This highly ordered structure is very unusual for this class of Li-rich layered oxides and allows for visualization of the oxygen columns using annular bright field STEM (ABF-STEM) imaging (Fig. 3, B and C, and fig. S7). The ABF-STEM technique has been proven to accurately reveal the positions of "light" elements (such as Li, O, and even H) in the presence of atomic entities with much higher scattering power (*24*–*27*). The correspondence between the experimental [001] HAADF- and ABF-STEM images and the crystal structure projection was established with the help of the simulated

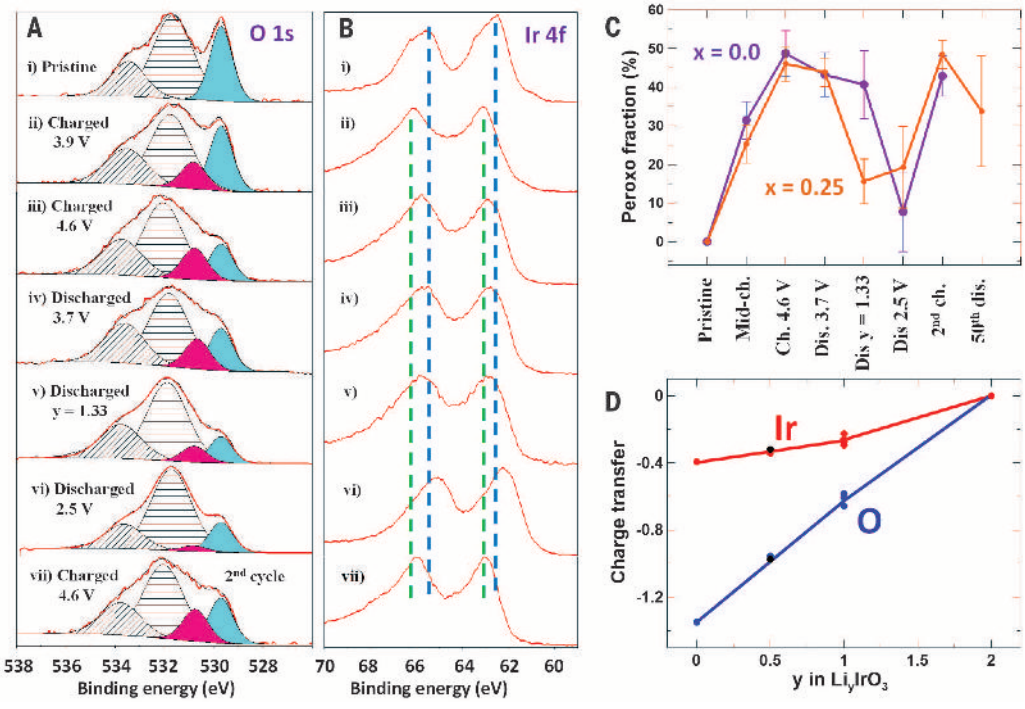

Fig. 2. Changes in cationic and anionic oxidation states during Li_2IrO_3 cycling. (**A**) Oxygen 1s core XPS peaks at various points after electrochemical cycling. The O^{2-} (blue) and O_2^{n-} (red) peaks are attributed to the sample, whereas the two gray striped peaks represent the surface species and electrolyte decomposition products, as described in (*13*). (**B**) Iridium 4f core XPS peaks. The dashed lines are guides for the eye indicating the position of the pristine (4+) peaks (blue) and the highest oxidation state (5+) (green). (**C**) Fraction of lattice oxygen attributed to peroxo for $Li_yIr_{1-x}Sn_xO_3$ samples. The samples discharged to $y = 1.33$ were stopped at 3.4 V for Li_2IrO_3 and 3.25 V for $Li_2Ir_{0.75}Sn_{0.25}O_3$, as shown in Fig. 1C. (**D**) Results for change in Bader charge with respect to the pristine sample obtained from DFT calculations. These are consistent with the XPS results showing mixed redox throughout the charge process. All calculations were performed on the O3 structure, except for the black points at $y = 0.5$, which were obtained for the O1 structure. The red and blue lines are guides for the eye and illustrate continuous mixed redox during charge.

images, using the crystallographic data in table S2 (fig. S8). The projected symmetry of the IrO_6 octahedra is expected to be close to sixfold symmetry, corresponding to all nearly equal O-O separations. However, the shape of these octahedra in the experimental [001] ABF-STEM image is clearly driven toward threefold symmetry due to the formation of shortened (black dumbbells) and lengthened (left blank) projected O-O separations (Fig. 3C). The distinct difference in the short and long O-O projected separations is evident from a comparison of the corresponding ABF intensity profiles (Fig. 3D). The values of the projected O-O separations were estimated from the analysis of a histogram of their distribution (fig. S11), which demonstrates peaks centered at 1.56 and 1.83 Å, reflecting the average values of the shortened and lengthened projected O-O distances (Table 1).

The observed distortion of the oxygen sublattice is in line with the atomic arrangement obtained from ab initio calculations. Figure 3E shows the [001] projection, as obtained on the basis of DFT calculations for the charged $Li_{0.5}IrO_3$ sample. This calculation shows shortened projected O-O distances for pairs of oxygen atoms (joined by red lines) lying between two Ir atoms. Figure 3E also shows the Fukui function, which probes the change in the electron density as a result of an infinitesimal change in the total number of electrons. The Fukui function can be used to probe the redox-active center (atomic and/or molecular entities affected by the charge variation; i.e., where the electronic charge is varying) in an electrochemical reaction. Here, the Fukui function shows changes in electron density around both Ir and O. The shape of the Fukui function around the oxygen atom shows overlapping lobes along the axis joining the O-O pairs with short separations, consistent with the expectation of partially empty antibonding σ* orbitals if peroxo-like species are formed. By contrast, fig. S9 shows no such orbital overlap in the pristine material.

The distortion pattern observed on a local scale was confirmed using the structural refinements of the bulk structure from neutron powder diffraction (NPD) data for the pristine and fully charged Li-Ir-O samples (included in figs. S5 and S10). The [001] projections of the refined structures are shown overlaid in Fig. 3F (for this image, the unit cell of the pristine structure was shrunk slightly to overlap but the aspect ratio was not changed). This shows the displacement in the oxygen lattice taking place during the formation of the peroxo-like species and is consistent with the ABF-STEM image. This also serves to show that changes seen in projected distance with ABF-STEM do in fact correspond to actual atomic displacements.

Table 1 presents a summary of the O-O distances determined with different methods, all confirming a distortion in the lattice such that oxygen atoms approach each other to form O-O pairs lying between two adjacent Ir atoms. By contrast, no such distortions have been seen for materials that do not involve anionic redox [e.g., the stoichiometric NMC compounds given in Table 1 with values based on neutron diffraction (*28*)]. However, the O-O distances measured here do not approach the ~1.5 Å O-O distances seen for peroxide species in highly ionic compounds, such as Li_2O_2, or in systems where oxygen pairs lie in cavities within the cationic network, as seen in a few perovskite materials (*29*). In more covalent systems, such as those discussed here, the formation

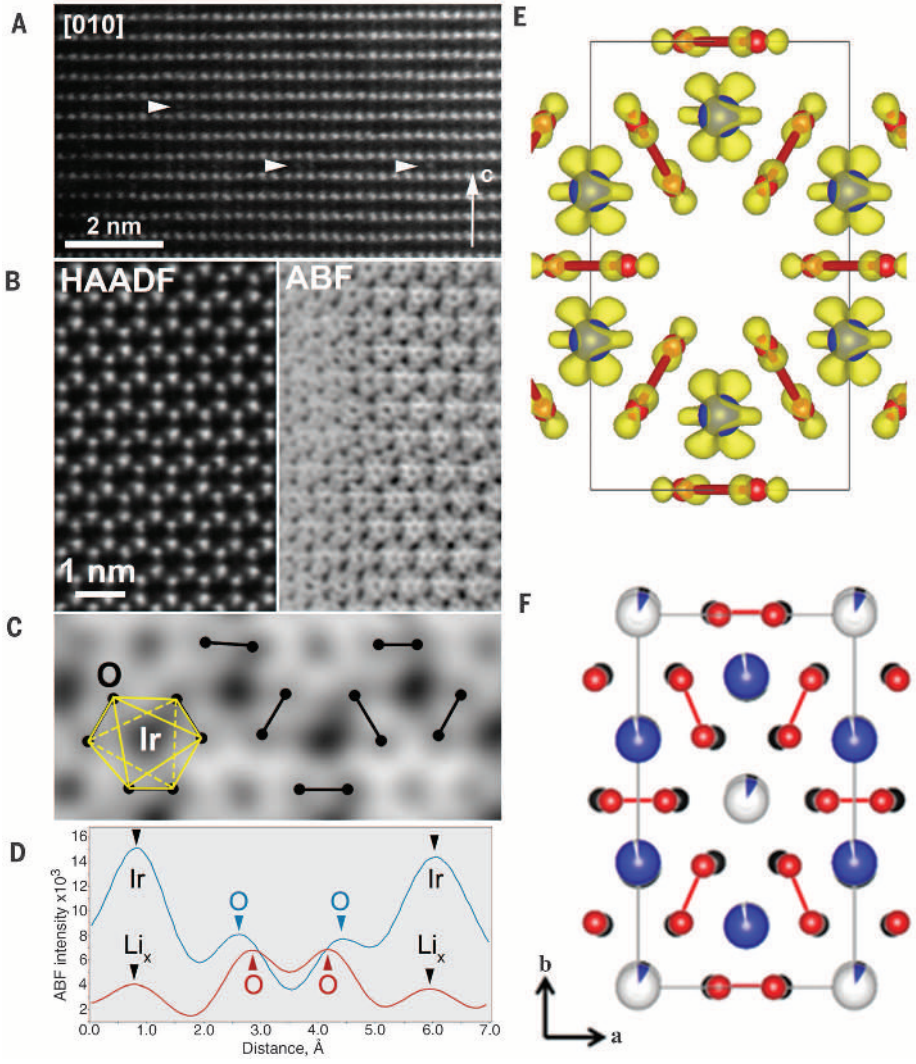

Fig. 3. Structural changes in the oxygen sublattice. (**A**) [010] HAADF-STEM image of the charged $Li_{0.5}IrO_3$ sample, demonstrating the ordered sequence of the Ir layers corresponding to the O1-type structure. The hexagonal close-packing is evident from the absence of the lateral displacement of layers. Virtually no migration of the Ir cation to the Li layers is observed; a few antisite point defects are marked with arrowheads. (**B**) [001] HAADF-STEM and ABF-STEM images of the same sample (taken from different areas; the noise in the ABF-STEM image is suppressed by applying a low-pass Fourier filter). (**C**) Enlarged ABF-STEM image. O-O pairs with short projected distances are marked with dumbbells. The O-O pairs arise from twisting the opposite triangular faces of the IrO_6 octahedra (shown in yellow). (**D**) ABF intensity profiles along the O-O pairs with long (blue) and short (red) projected distances. (**E**) [001] projection of the $Li_{0.5}IrO_3$ in the O1 stacking configuration, obtained with DFT calculations. Li atoms are omitted for clarity, oxygen atoms are shown in red, and Ir atoms are in blue. The yellow surfaces are the Fukui orbitals. (**F**) Structure of the charged Li-Ir-O material, as obtained from neutron powder diffraction (fit shown in fig. S5), overlaid on the pristine structure (fit in fig. S10) shown in black, clearly illustrating the formation of O-O dimers. The overlay required shrinking the pristine structure slightly, but the aspect ratio was unaltered.

of peroxo species therefore manifests itself as a distortion of the oxygen framework with the formation of shorter and longer O-O distances.

An important aspect of these materials is the extent to which they allow O_2 recombination and subsequent oxygen gas release during oxidation, which must be minimized to reduce the irreversible capacity loss. Figure S12 shows that the oxygen release here is relatively small, especially for Li_2IrO_3, and only occurs at voltages above 4.3 V versus Li/Li^+, consistent with our previous studies (*13*, *16*, *19*). This voltage corresponds to ~1.3 V versus standard hydrogen electrode, very close to the potential at which water is split (1.23 V). Our value is a rough estimate, but it does suggest that peroxo-species will be stable against formation of oxygen gas if they form below 4.3 V. This explains why irreversible capacities have plagued the Li-rich NMC materials, which must be oxidized up to 4.5 V to convert to an S curve.

Figure 4A shows a steady decrease in capacity (with no associated voltage fade) during extended cycling, with ~50% retention after only 50 cycles. This fade coincides with the structural variations resulting in the changes to the XRD patterns in Fig. 1. Figure 4 shows the structural changes that occur during extended cycling, as visualized with HAADF-STEM imaging. The image collected after 50 cycles is very unusual, with an apparent nanoscale intergrowth of two distinct structures. The structural changes during electrochemical cycling that involve the gliding of $(Ir_{1-x}Sn_x)_{2/3}O_2$ slabs against each other are ultimately detrimental to the long-term cycling of this material, thus giving rise to capacity fade without any of the voltage fade seen in other Li-rich materials. This demonstrates that these two parameters for evaluating battery performance are not directly related here and that although the transformation from O3 to O1 structures prevents voltage fade, it still results in detrimental capacity fade.

Our NPD and DFT results suggest that peroxo-like dimers form uniformly throughout the bulk in the fully charged $Li_{0.5}IrO_3$ material, allowing us to determine the possible limits on the value of the formal charge n for peroxo-like O_2^{n-} dimers. The lower bound can be set by assuming that all of the 1.5 Li atoms transferred per O_3 unit are attributed to oxygen redox only; this yields $n = 3.0$. The upper bound is set by assuming the mixed redox obtained by DFT calculations (and confirmed qualitatively with XPS), in which case the oxygen lattice accounts for ~1.0 Li atom removed per O_3 unit, resulting in $n = 3.3$. This study therefore suggests the formation of predominantly O_2^{3-} species in Li-rich layered oxides, which explains why all of the lithium cannot be systematically removed from these materials simply by fully oxidizing the oxygen, as would be the case if $n = 2$ was accessible. This also explains why the peroxo-like species were detected by electron paramagnetic resonance (EPR) (*13*, *30*), given that O_2^{2-} is EPR silent whereas O_2^{3-} is active.

The fact that the formation of peroxo-like dimers does not necessarily imply antisite cation disordering has a few consequences. In Li_2IrO_3, the displacement of oxygen atoms during first charge results in confining the space around the iridium atom (Fig. 3F). This results in less free volume around each iridium atom and more tight binding to the surrounding oxygen atoms, therefore lending support to the fact that little migration of iridium takes place and no conversion to the S curve is seen. By contrast, the disorder caused by the addition of tin locally disrupts the pattern of the O_2^{n-} species promoting such migration, which results in a far greater abundance of the antisite defects in the [010] HAADF-STEM images of the charged $x = 0.25$ sample (fig. S13). Thus, conversion to an S curve is seen. More generally, once the Li is removed from the transition metal layers in all Li-rich oxides, the created free volume promotes migration to the Li layer. The microscopy images for this model system also show that these high capacities can be achieved for single-phase layered materials and do not necessarily require structural intergrowth of two layered phases, as proposed in the past (*3*). Lee *et al.* (*31*) showed Li-rich Li-Cr-Mo-O materials that convert toward a disordered rock salt structure during charge (corresponding to massive cation migration such that the transition metal and lithium layers are indistinguishable). Unfortunately, this study did not examine the redox processes involved, and we propose that this material is simply another example of the Li-rich oxides where oxygen participation in the redox process leads to high capacities.

Table 1. Average O-O distances obtained by DFT, NPD, and TEM. "Short" refers to two oxygen atoms between two nearest-neighbor Ir atoms, as viewed in the [001] projection in Fig. 3, E and F. "Long" refers to distances at which the oxygen atoms lie between an Ir atom and a vacancy. In all cases, the distances are averages for the structure. Projected distances are shown for the O1 structure only. N/A, not applicable; ND, not determined.

Sample	O-O distance (Å)		O-O distance in [001] projection (Å)	
	Short	Long	Short	Long
Li_2IrO_3				
Neutron	2.77(2)	2.84(2)	N/A	N/A
DFT	2.74	2.89	N/A	N/A
$Li_{0.5}IrO_3$				
Neutron	2.45(2)	2.73(4)	1.42(1)	1.86(3)
DFT	2.54	2.77	1.51	1.88
TEM	ND	ND	1.56	1.83
$LiNi_{1/3}Mn_{1/3}Co_{1/3}O_2$*	2.686	2.686	N/A	N/A
$Li_{0.04}Ni_{1/3}Mn_{1/3}Co_{1/3}O_2$*	2.553	2.553	N/A	N/A

*From (*28*), as an indication of behavior in systems where redox involves the cationic species only.

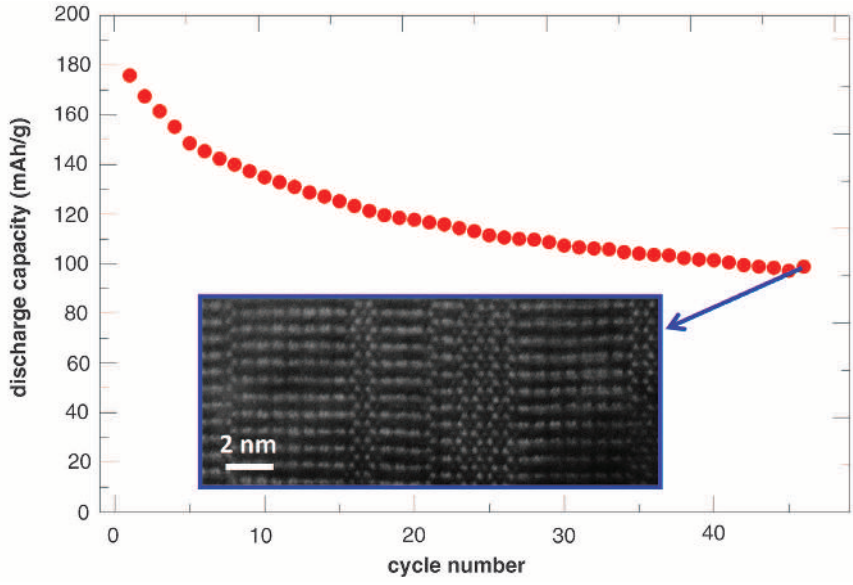

Fig. 4. Long-term cycling performance. Discharge capacity during extended cycling for $Li_2Ir_{0.75}Sn_{0.25}O_3$. (**Inset**) [100] HAADF-STEM image of a particle obtained after 50 cycles, showing complex nanoscale structuring.

Metal substituents can be used to tune the physical properties of these Li-rich phases because they affect the $(O_2)^{n-}$ stability against oxygen recombination or voltage fade, as previously demonstrated for $Li_2Ru_{1-x}M_xO_3$ (M = Sn, Ti, Mn). The benefits of Sn, in that it limits both $O_{2(g)}$ release and voltage fade, are preserved in the $Li_2Ir_{1-y}Sn_yO_3$ system but are mitigated by the emergence of a capacity fade mechanism that is linked to the emergence and accumulation of stacking faults. This finding emphasizes that the origins of voltage and capacity fading in these Li-rich layered phases are different, a point that has previously been a source of confusion.

In summary, combined TEM, neutron diffraction, and ab initio studies on high-capacity Li-rich $Li_2Ir_{1-x}Sn_xO_3$ layered phases permitted the atomic-scale visualization of the $(O\text{-}O)^{n-}$ peroxo-like dimers responsible for the capacity gain in Li-rich layered electrode materials. These observations lead to a better understanding of peroxo formation and localization, O_2 recombination, and the effect of the transition metal substituents. Additionally, these findings provide a chemical handle for tuning the performances of Li-rich layered materials.

REFERENCES AND NOTES

1. B. L. Ellis, K. T. Lee, L. F. Nazar, *Chem. Mater.* **22**, 691–714 (2010).
2. Z. Lu, L. Y. Beaulieu, R. A. Donaberger, C. L. Thomas, J. R. Dahn, *J. Electrochem. Soc.* **149**, A778 (2002).
3. M. M. Thackeray, C. S. Johnson, J. T. Vaughey, N. Li, S. A. Hackney, *J. Mater. Chem.* **15**, 2257–2267 (2005).
4. J. M. Tarascon *et al.*, *J. Solid State Chem.* **147**, 410–420 (1999).
5. G. Ceder *et al.*, *Nature* **392**, 694–696 (1998).
6. M. K. Aydinol, A. F. Kohan, G. Ceder, K. Cho, J. Joannopoulos, *Phys. Rev. B* **56**, 1354–1365 (1997).
7. C.-C. Chang, O. I. Velikokhatnyi, P. N. Kumta, *J. Electrochem. Soc.* **151**, J91–J94 (2004).
8. J. Graetz, C. C. Ahn, R. Yazami, B. Fultz, *J. Phys. Chem. B* **107**, 2887–2891 (2003).
9. S. Laha *et al.*, *Phys. Chem. Chem. Phys.* **17**, 3749–3760 (2015).
10. H. Koga *et al.*, *J. Phys. Chem. C* **118**, 5700–5709 (2014).
11. M. Oishi *et al.*, *J. Power Sources* **276**, 89–94 (2015).
12. W.-S. Yoon *et al.*, *J. Phys. Chem. B* **106**, 2526–2532 (2002).
13. M. Sathiya *et al.*, *Nat. Mater.* **12**, 827–835 (2013).
14. M. Sathiya *et al.*, *Nat. Mater.* **14**, 230–238 (2015).
15. M. Sathiya *et al.*, *Chem. Mater.* **25**, 1121–1131 (2013).
16. E. McCalla *et al.*, *J. Electrochem. Soc.* **162**, A1341–A1351 (2015).
17. J. Rouxel, *Chem. Eur. J.* **2**, 1053–1059 (1996).
18. M. Sathiya *et al.*, *Chem. Commun.* **49**, 11376–11378 (2013).
19. E. McCalla *et al.*, *J. Am. Chem. Soc.* **137**, 4804–4814 (2015).
20. A. R. Armstrong *et al.*, *J. Am. Chem. Soc.* **128**, 8694–8698 (2006).
21. N. Yabuuchi *et al.*, *Proc. Natl. Acad. Sci. U.S.A.* **112**, 7650–7655 (2015).
22. Materials and methods are available as supplementary materials on *Science* Online.
23. H. Kobayashi, M. Tabuchi, M. Shikano, H. Kageyama, R. Kanno, *J. Mater. Chem.* **13**, 957–962 (2003).
24. S. D. Findlay *et al.*, *Ultramicroscopy* **110**, 903–923 (2010).
25. R. Ishikawa *et al.*, *Nat. Mater.* **10**, 278–281 (2011).
26. L. Gu, D. Xiao, Y.-S. Hu, H. Li, Y. Ikuhara, *Adv. Mater.* **27**, 2134–2149 (2015).
27. D. Batuk, M. Batuk, A. M. Abakumov, J. Hadermann, *Acta Crystallogr. B* **71**, 127–143 (2015).
28. S. C. Yin, Y. H. Rho, I. Swainson, L. F. Nazar, *Chem. Mater.* **18**, 1901–1910 (2006).
29. F. Grasset, C. Dussarrat, J. Darriet, *J. Mater. Chem.* **7**, 1911–1915 (1997).
30. M. Sathiya *et al.*, *Nat. Commun.* **6**, 6276 (2015).
31. J. Lee *et al.*, *Science* **343**, 519–522 (2014).

ACKNOWLEDGMENTS

E.M. thanks the Fonds de Recherche du Québec–Nature et Technologies and ALISTORE–European Research Institute for funding this work, as well as the European community I3 networks for funding the neutron scattering research trip. This work was also funded by the Slovenian Research Agency research program P2-0148. This work is partially based on experiments performed at the Institut Laue Langevin. We thank J. Rodriguez-Carvajal for help with neutron scattering experiments and for fruitful discussions. We also thank M. T. Sougrati for performing the Sn-Mössbauer measurements. Use of the Advanced Photon Source at Argonne National Laboratory was supported by the U.S. Department of Energy, Office of Science, Office of Basic Energy Sciences, under contract no. DE-AC02-06CH11357. M.S. and M.-L.D. acknowledge high-performance computational resources from GENCI-CCRT/CINES (grant cmm6691). J.-M.T. acknowledges funding from the European Research Council (ERC) (FP/2014-2020)/ERC Grant-Project670116-ARPEMA.

SUPPLEMENTARY MATERIALS

www.sciencemag.org/content/350/6267/1516/suppl/DC1
Materials and Methods
Figs. S1 to S13
Tables S1 and S2
References (*32*–*43*)

19 June 2015; accepted 6 November 2015
10.1126/science.aac8260

PLANT SYMBIOSES

Rice perception of symbiotic arbuscular mycorrhizal fungi requires the karrikin receptor complex

Caroline Gutjahr,[1,2]* Enrico Gobbato,[3]* Jeongmin Choi,[3] Michael Riemann,[4,5] Matthew G. Johnston,[3] William Summers,[3] Samy Carbonnel,[2] Catherine Mansfield,[3] Shu-Yi Yang,[1] Marina Nadal,[1] Ivan Acosta,[6] Makoto Takano,[4] Wen-Biao Jiao,[6] Korbinian Schneeberger,[6] Krystyna A. Kelly,[3] Uta Paszkowski[1,3]†

In terrestrial ecosystems, plants take up phosphate predominantly via association with arbuscular mycorrhizal fungi (AMF). We identified loss of responsiveness to AMF in the rice (*Oryza sativa*) mutant *hebiba*, reflected by the absence of physical contact and of characteristic transcriptional responses to fungal signals. Among the 26 genes deleted in *hebiba*, *DWARF 14 LIKE is*, the one responsible for loss of symbiosis. It encodes an alpha/beta-fold hydrolase, that is a component of an intracellular receptor complex involved in the detection of the smoke compound karrikin. Our finding reveals an unexpected plant recognition strategy for AMF and a previously unknown signaling link between symbiosis and plant development.

Most land plants establish symbioses with arbuscular mycorrhizal fungi (AMF) of the phylum *Glomeromycota* (*1*). These symbioses contribute to global carbon and mineral nutrient cycles, because AMF provide mineral nutrients to the plant and receive carbohydrates in return. Colonization of plant roots by AMF requires reciprocal recognition initiated by diffusible molecules before fungal attachment to the root surface and root penetration via hyphopodia (*2*). Diffusible precolonization signals include strigolactones, released from plant roots that activate the fungus before physical interaction (*3*), and fungal (lipo)chitooligosaccharides and chitotetraose, secreted by AMF that trigger plant calcium signaling, gene expression, and lateral root formation (*4*, *5*). Plant LysM receptor-like kinases (*6*) are required for perception of chitinaceous microbial molecules that trigger either symbiosis or defense signaling (*7*–*9*). Plant signaling mutants impaired in root colonization by both AMF and nitrogen-fixing bacteria still exhibit transcriptional responses to fungal signaling molecules (*10*–*12*). Therefore, additional signaling modules have been postulated (*12*). We identified the rice receptor for karrikin, a plant growth regulator first identified in smoke (*13*–*16*), as a necessary signaling component for establishment of arbuscular mycorrhizal (AM) symbiosis.

We found that the jasmonate-deficient rice (*Oryza sativa*) mutant *hebiba* (*17*) was unable to

[1]Department of Plant Molecular Biology, University of Lausanne, Biophore Building, 1015 Lausanne, Switzerland. [2]Faculty of Biology, Genetics, University of Munich, Biocenter Martinsried, Grosshaderner Straße 2-4, 82152 Martinsried, Germany. [3]Department of Plant Sciences, University of Cambridge, Downing Street, Cambridge CB2 3EA, UK. [4]Division of Plant Sciences, National Institute of Agrobiological Sciences, 2–1–2 Kannondai, Tsukuba, Ibaraki 305–8602, Japan. [5]Botanical Institute, Molecular Cell Biology, Karlsruhe Institute of Technology, Kaiserstraße 2, 76131 Karlsruhe, Germany. [6]Max Planck Institute for Plant Breeding Research, Carl-von-Linné-Weg 10, D-50829 Cologne, Germany.
*These authors contributed equally to this work.
†Corresponding author. E-mail: up220@cam.ac.uk

establish symbiosis with either of two AMF—*Rhizophagus irregularis* and *Gigaspora rosea*—as reflected by the absence of hyphopodia, intraradical colonization, and induction of colonization marker genes (Fig. 1, A to C) (*10*). The lack of fungal interaction persisted upon increased inoculum strength imposed by growing *hebiba* alongside colonized wild-type plants (Fig. 1D). This suggested that the mutant is compromised at a very early stage of the interaction, during presymbiotic signaling.

The *hebiba* mutant is due to a genomic deletion of 169 kb, which contains 26 annotated genes (*17*, *18*). One of the genes encodes allene oxide cyclase (AOC), part of the jasmonate biosynthetic pathway, loss of which leads to jasmonate deficiency (*17*). However, transgenic complementation of *hebiba* with *AOC* (*hebiba*^{AOC}) did not restore AM symbiosis (fig. S1) (*17*, *19*). Therefore, another gene contained within the deleted interval must be required for AM development.

We identified the gene responsible for AM symbiosis by transforming *hebiba*^{AOC} with genomic clones of individual genes from the deleted interval (table S1) (*17, 18*). Reintroduction of the *LOC_Os03g32270* gene restored fungal colonization of *hebiba*^{AOC} roots in independent rice transformants (Fig. 2, A and B, and table S1). Quantitative measurements of colonization correlated (R^2 = 0.84) with the amount of transcript accumulation from the *LOC_Os03g32270* transgene (Fig. 2C). Transgenic lines such as C10 (Fig. 2B), with transgene mRNA levels below the detection limit, retained the *hebiba* mutant phenotype. *LOC_Os03g32270* encodes the alpha/beta-fold hydrolase DWARF14LIKE (D14L), homologous to *Arabidopsis thaliana* KARRIKIN INSENSITIVE2/HYPOSENSITIVE TO LIGHT (KAI2/HTL). This hydrolase acts together with the F-box protein DWARF3/MORE AXILLIARY GROWTH2 (D3/MAX2) in the perception of karrikins, a group of butenolide compounds found in smoke that induce seed germination in fire-chasing plants (*13*–*16*). The structurally related strigolactones are perceived by a receptor complex involving D3 and the alpha/beta-fold hydrolase DWARF14 (D14), the paralog of D14L (*20*–*22*). However, the strigolactone-insensitive rice mutant *d14* is not perturbed in AM symbiosis (*23*) (Fig. 3A); thus, the strigolactone receptor gene *D14* is not required for establishment of the interaction. A rice *d3* mutant was also severely impaired in AM colonization and marker gene induction (Fig. 3, A and B) (*23*), revealing the importance of the karrikin receptor complex for the earliest stages of AM development. We further confirmed the requirement of D14L in AM development by using a set of RNA interference (RNAi) lines generated in the *Oryza sativa* cv. Nipponbare background. The RNAi lines displayed diverse levels of AM suppression that correlated (R^2 = 0.69) with the degree of down-regulation of endogenous *LOC_Os03g32270* (fig. S2, A to C). The *D14L* RNAi line Ri43 supports AMF colonization (*23*); however, we found a decrease (P = 0.047) in total fungal colonization relative to wild type in this line. The phenotypic diversity among the *D14L* RNAi lines suggests a low transcript threshold for AM symbiosis establishment.

In *Arabidopsis*, *KAI2*/*HTL* controls hypocotyl elongation in response to light and karrikin (*13*, *24*). Overexpression of rice *D14L* in an *Arabidopsis htl-2* mutant restored wild-type hypocotyl length in two independent F_3 populations homozygous for *htl-2* (fig. S3A). Mesocotyl elongation assays in rice demonstrated that *hebiba*^{AOC} is insensitive to karrikin but responds to the synthetic strigolactone GR24 (fig. S3B). In contrast, mutations of *D14* specifically compromised strigolactone but not karrikin responses in rice, whereas mutation of the F-box protein encoding *D3* resulted in insensitivity to both (fig. S3B). Thus, in rice, D14L and D14 mediate perception specificity to karrikin versus strigolactone in an overall similar manner to *Arabidopsis* (*13*). However, the partial response of *Arabidopsis d14* to racemic

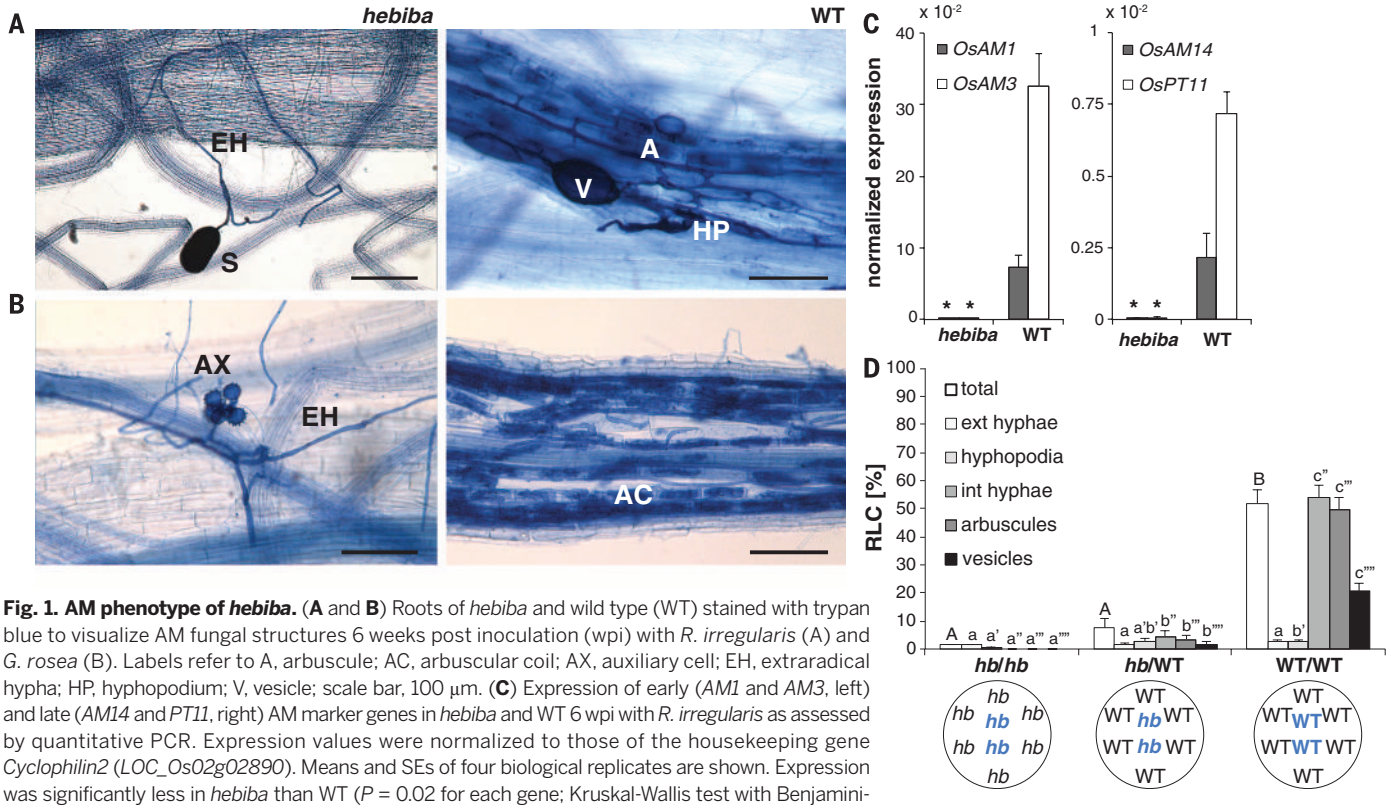

Fig. 1. AM phenotype of *hebiba*. (**A** and **B**) Roots of *hebiba* and wild type (WT) stained with trypan blue to visualize AM fungal structures 6 weeks post inoculation (wpi) with *R. irregularis* (A) and *G. rosea* (B). Labels refer to A, arbuscule; AC, arbuscular coil; AX, auxiliary cell; EH, extraradical hypha; HP, hyphopodium; V, vesicle; scale bar, 100 μm. (**C**) Expression of early (*AM1* and *AM3*, left) and late (*AM14* and *PT11*, right) AM marker genes in *hebiba* and WT 6 wpi with *R. irregularis* as assessed by quantitative PCR. Expression values were normalized to those of the housekeeping gene *Cyclophilin2* (*LOC_Os02g02890*). Means and SEs of four biological replicates are shown. Expression was significantly less in *hebiba* than WT (P = 0.02 for each gene; Kruskal-Wallis test with Benjamini-Hochberg adjustment for multiple testing). (**D**) Percentage of root length colonization (RLC) by *R. irregularis* of two central "tester" surrounded by six "donor" plants at 7 wpi. Means and standard errors of five biological replicates are shown. ext hyphae, extraradical hyphae; int hyphae, intraradical hyphae. For each of the six fungal structures in the figure, separate Kruskal-Wallis tests were performed, using the Benjamini-Hochberg adjustment for the post hoc tests. The P values were as follows: P (total) ≤ 0.01, P (ext. hyphae) = 0.43, P (hyphopodia) ≤ 0.05, P (int. hyphae, arbuscules, vesicles) ≤ 0.001. The letters above each bar indicate growth conditions that were not significantly different in the post hoc pairwise comparisons. The comparisons are for bars with the same case and number of apostrophes.

GR24 (*13*, *25*) was not reproduced in rice *d14* mutants (fig. S3B) (*26*), suggesting that D14L has less redundant activity in rice. Fluorescently tagged D14L in *Arabidopsis* (*24*) and rice localized to both nucleus and cytoplasm (Fig. 2E). D14L in rice (Fig. 2D) as in *Arabidopsis* (*24*) is expressed in all rice organs, and transcript accumulation in roots is not altered during AM colonization.

We asked whether D14L is required for suppression of defense responses against AMF. We found no evidence for increased activation of selected defense marker genes (*27*) during the early stages of mycorrhizal colonization (fig. S4, A and B). Moreover, *hebiba*^{AOC} was susceptible to colonization by the root endophyte *Piriformospora indica* and the pathogen *Magnaporthe oryzae* (fig. S4, C and D), implicating D14L in symbiotic compatibility.

On the basis of the early and pronounced *hebiba* mutant phenotype, we hypothesized that functional D14L is required for the perception of AM fungi before contact. Germinated spore exudates (GSEs) of AMF activate precontact plant responses (*28*). Therefore, we used RNA sequencing (RNA-seq) to monitor the transcriptional changes of *hebiba*^{AOC} and wild-type roots in response to GSEs over the first 24 hours post treatment (hpt) (supplementary materials, tables S2 and S3). Overall 140 genes showed statistically significant differences in average expression upon GSE treatment in wild-type plants (Fig. 4A and tables S4 and S5). In *hebiba*^{AOC} plants, six genes responded significantly to GSEs, of which two genes (predicted to encode an expressed and a hypothetical protein) overlapped with the genes responding in wild type (Fig. 4A and table S4), suggesting that the transcriptional response observed in the wild-type relied on functional D14L. Time-resolved gene ontology (GO) analyses of genes differerentially regulated in response to GSEs in wild type but not in *hebiba*^{AOC} demonstrated an overrepresentation of terms associated with responses to extracellular and biotic stimuli. Genes were induced or repressed at the earliest time points, 3 and 6 hpt, and in a *D14L*-dependent fashion, consistent with D14L playing a role in early signaling activation (Fig. 4B and table S6, A and B). The expression pattern of representative genes was validated by quantitative reverse transcription polymerase chain reaction (RT-PCR) on the same RNA used for the RNA-seq experiment (fig. S5A) and on RNA from two additional biological replicates, which included the complemented line C11 (fig. S5B). Thus, D14L is required to support initial colonization events by AMF. Despite its effect on mesocotyl elongation, treatment with karrikin did not induce significant gene expression changes in roots of wild-type rice (table S4). Also, the exogenous application of karrikin did not stimulate colonization of wild-type roots by *R. irregularis* (fig. S6).

We found that a total of 104 transcripts differed significantly between untreated *hebiba*^{AOC} and wild-type roots (table S4) derived from genes with borderline GO-term enrichment for metabolic processes (table S6C). Whereas mRNA levels of known genes essential for AM symbiosis accumulated independently of functional D14L, transcript levels of the rice homolog of *DWARF 14 LIKE 2* (*13*), *LOC_Os05g51240*, depended on D14L, as earlier observed in *Arabidopsis* (*13*) (table S4). In

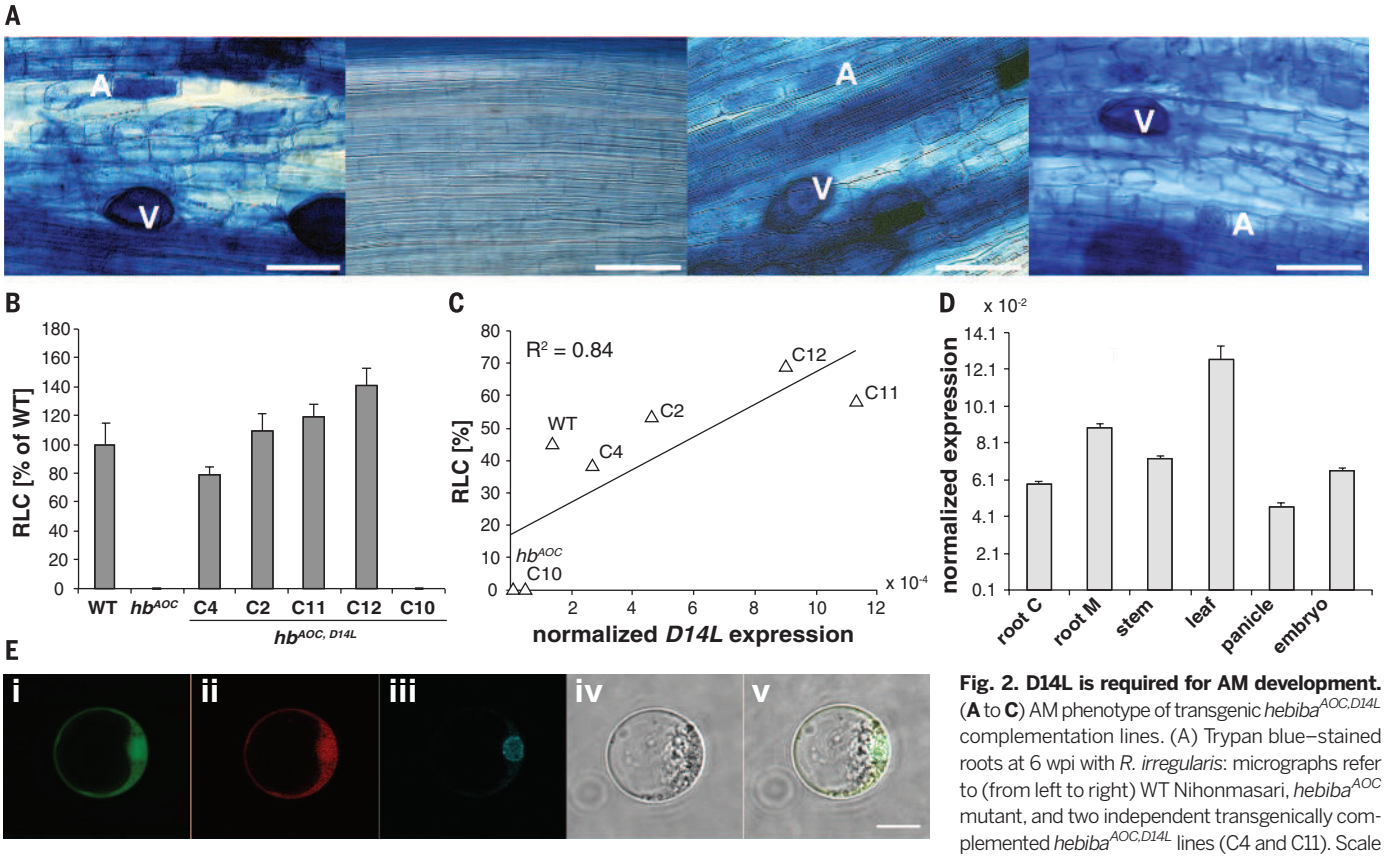

Fig. 2. D14L is required for AM development. (**A** to **C**) AM phenotype of transgenic *hebiba*^{AOC,D14L} complementation lines. (A) Trypan blue–stained roots at 6 wpi with *R. irregularis*: micrographs refer to (from left to right) WT Nihonmasari, *hebiba*^{AOC} mutant, and two independent transgenically complemented *hebiba*^{AOC,D14L} lines (C4 and C11). Scale bar, 50 μm. (B) RLC expressed as % of WT colonization at 6 wpi for independent *hebiba*^{AOC,D14L} complementation lines. Values represent means and SEs from two to five replicate plants. (C) *D14L* transcript levels were assessed by real-time RT-PCR in the independent transgenic complementation lines. The averages for the WT, *hebiba*^{AOC}, and the complementation *hebiba*^{AOC,D14L} lines were plotted against the corresponding averages for total RLC. The Spearman rank correlation was calculated and squared to give the proportion of the variation accounted for by the correlation. (**D**) Real-time RT-PCR–based expression of *D14L* in control root (C), mycorrhizal roots (M), stem, leaf, panicle, and embryo of Nipponbare rice. Expression values were normalized to those of the constitutively expressed gene *Cyclophilin2* (*LOC_Os02g02890*). Means and SDs of three technical replicates are shown. (**E**) Subcellular localization of D14L. A plasmid containing a *D14L* overexpression construct (i) maize ubiquitin promoter:*D14L* cDNA:green fluorescent protein was co-transfected with the plasmid containing a genomic clone of *D14L* driven by its native promoter (ii) p*D14L*:*gD14L*:*RFP* in rice root protoplasts. (iii) DAPI staining. (v) Overlay of all channels, including bright field (iv). Scale bar, 10 μm.

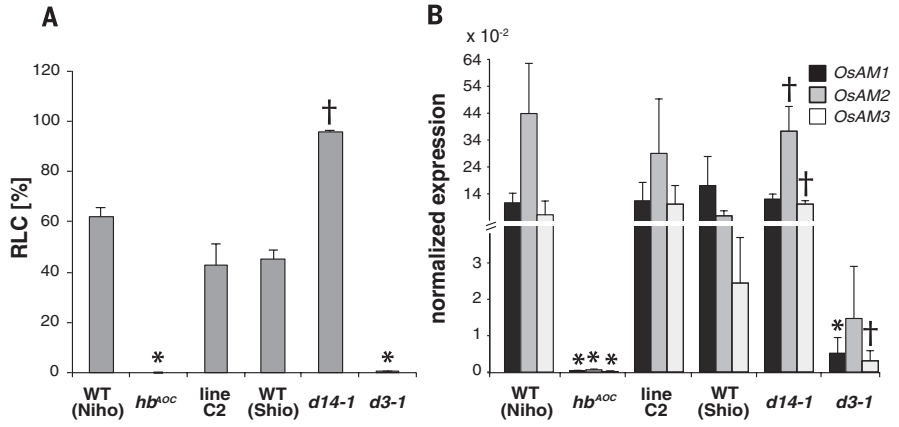

Fig. 3. AM phenotype of *d3* relative to *hebiba*^{AOC}, *d14*, and corresponding WT cultivars. (**A**) Percentage of RLC and (**B**) induction of AM early marker genes at 7 wpi with *R. irregularis* of *d3*, *d14*, *hebiba*^{AOC}, *hebiba*^{AOC,D14L} complementation line C2, and corresponding WT background Nihonmasari (Niho) and Shiokari (Shio), respectively. Expression values were normalized to those of the constitutively expressed gene *Cyclophilin2* (*LOC_Os02g02890*). Values represent means and SEs from three biological replicates (A and B). The mutants and complementation line were compared with the appropriate WT by using the Kruskal-Wallis test. Symbols above the bars indicate statistical significance with respect to the WT (†P < 0.10; *P < 0.05).

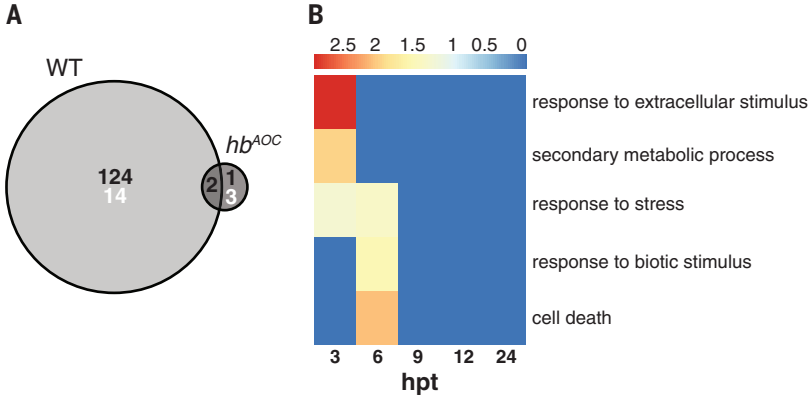

Fig. 4. GSE-induced transcriptional responses of WT and *hebiba*^{AOC}. (**A**) Venn diagram depicting the number of transcripts induced (black) and repressed (white) in WT and *hebiba*^{AOC} plants treated with GSEs in comparison to plants receiving a mock treatment. (**B**) Time-resolved GO-term enrichment analysis ($P \leq 0.001$) for genes differentially regulated in response to GSEs in WT but not in *hebiba*^{AOC}. The color code represents odds ratios.

contrast to *Arabidopsis*, karrikin treatment of rice roots did not induce this gene. Because D14L is found in genomes of plants that germinate without fire stimulation and because *Arabidopsis* mutants lacking D14L show developmental phenotypes, we hypothesize that an endogenous ligand exists and is required for wild-type seedling development (*29*). In rice, the differences in transcriptomes between GSEs and mock or karrikin-treated wild-type plants indicate either that this ligand is not karrikin or that D14L acts upstream of the GSE response, thereby possibly creating a condition permissive for AM symbiosis.

We show that the karrikin receptor complex is central to the everyday interaction of plants with AMF, involving more than 80% of all plant species as opposed to 1200 smoke-responsive plant species (*30*). Conservation of D14L in early land plants, such as liverworts (*31*), suggests that it has served this purpose since AMF started supporting terrestrial plant life. On poor natural soils, plants rely on AMF for mineral nutrient supply and need to coordinate AMF development with their physiological and developmental needs. The karrikin receptor complex may represent a node in the cross-talk between plant development and AM signaling.

REFERENCES AND NOTES

1. S. Smith, D. Read, *Mycorrhizal Symbiosis* (Academic Press, London, ed. 3, 2008).
2. C. Gutjahr, M. Parniske, *Annu. Rev. Cell Dev. Biol.* **29**, 593–617 (2013).
3. K. Akiyama, K. Matsuzaki, H. Hayashi, *Nature* **435**, 824–827 (2005).
4. F. Maillet *et al.*, *Nature* **469**, 58–63 (2011).
5. A. Genre *et al.*, *New Phytol.* **198**, 190–202 (2013).
6. C. Gough, J. Cullimore, *Mol. Plant Microbe Interact.* **24**, 867–878 (2011).
7. G. E. Oldroyd, *Nat. Rev. Microbiol.* **11**, 252–263 (2013).
8. X. Zhang *et al.*, *Plant J.* **81**, 258–267 (2015).
9. K. Miyata *et al.*, *Plant Cell Physiol.* **55**, 1864–1872 (2014).
10. C. Gutjahr *et al.*, *Plant Cell* **20**, 2989–3005 (2008).
11. C. Camps *et al.*, *New Phytol.* **208**, 224–240 (2015).
12. M. Nadal, U. Paszkowski, *Curr. Opin. Plant Biol.* **16**, 473–479 (2013).
13. M. T. Waters *et al.*, *Development* **139**, 1285–1295 (2012).
14. Y. Guo, Z. Zheng, J. J. La Clair, J. Chory, J. P. Noel, *Proc. Natl. Acad. Sci. U.S.A.* **110**, 8284–8289 (2013).
15. S. Toh, D. Holbrook-Smith, M. E. Stokes, Y. Tsuchiya, P. McCourt, *Chem. Biol.* **21**, 988 (2014).
16. G. R. Flematti, E. L. Ghisalberti, K. W. Dixon, R. D. Trengove, *Science* **305**, 977 (2004).
17. M. Riemann *et al.*, *Plant J.* **74**, 226–238 (2013).
18. K. J. V. Nordström *et al.*, *Nat. Biotechnol.* **31**, 325–330 (2013).
19. C. Gutjahr, H. Siegler, K. Haga, M. Iino, U. Paszkowski, *PLOS ONE* **10**, e0123422 (2015).
20. T. Arite *et al.*, *Plant Cell Physiol.* **50**, 1416–1424 (2009).
21. C. Hamiaux *et al.*, *Curr. Biol.* **22**, 2032–2036 (2012).
22. L.-H. Zhao *et al.*, *Cell Res.* **25**, 1219–1236 (2015).
23. S. Yoshida *et al.*, *New Phytol.* **196**, 1208–1216 (2012).
24. X.-D. Sun, M. Ni, *Mol. Plant* **4**, 116–126 (2011).
25. A. Scaffidi *et al.*, *Plant Physiol.* **165**, 1221–1232 (2014).
26. Z. Hu *et al.*, *Plant Cell Physiol.* **51**, 1136–1142 (2010).
27. S. Marcel, R. Sawers, E. Oakeley, H. Angliker, U. Paszkowski, *Plant Cell* **22**, 3177–3187 (2010).
28. M. Chabaud *et al.*, *New Phytol.* **189**, 347–355 (2011).
29. M. T. Waters, A. Scaffidi, Y. K. Sun, G. R. Flematti, S. M. Smith, *Plant J.* **79**, 623–631 (2014).
30. S. D. S. Chiwocha *et al.*, *Plant Sci.* **177**, 252–256 (2009).
31. P.-M. Delaux *et al.*, *New Phytol.* **195**, 857–871 (2012).

ACKNOWLEDGMENTS

We thank J. Gheyselinck for technical assistance; P. Nick (Karlsruhe Institute of Technology, Germany) for providing *hebiba* and Nihonmasari wild-type seeds; M. Nakazono (University of Nagoya, Japan) for providing *d3* and Shiokari wild-type seeds; J. Kyozuka (Graduate School of Agriculture and Life Sciences, University of Tokyo) for *d14* seeds and the *D14L* RNAi line Ri43; and M. Ni (University of Minnesota, USA) for providing *Arabidopsis htl-2* seeds. T. Hardcastle helped by enhancing R/Bioconductor or package baySeq to enable the RNA-seq time course analysis. M. Meyer instructed the carbon-dioxide treatment of *R. irregularis*. C.G. received Ph.D. fellowships from the German National Academic Foundation (Studienstiftung des Deutschen Volkes), the Roche Research Foundation, and the German Research Council (DFG) (GU1423/1-1). E.G. was supported by the Isaac Newton Trust grant RG74108. J.C. is a European Molecular Biology Organization Long-Term Fellow (ALTF 117-2014), and W.S. is a UK Biotechnology and Biological Sciences Research Council–Doctoral Training Partnership scholar, supported by grant PDAG/223 T39. S.C. was funded by the Collaborative Research Center SFB924 "Molecular mechanisms regulating yield and yield stability in plants" of the German Research Council (DFG). Research in the U.P. laboratories was supported by the Swiss National Science Foundation "professeur boursier" grants PP00A-110874 and PP00P3-130704, and by the Gatsby Charitable Foundation grant RG60824. C.G., E.G., J.C., K.A.K., and U.P. designed the experiments. C.G., E.G., J.C., M.G.J., W.S., S.C., C.M., S.-Y.Y. M.N., and I.A. performed the experiments. K.A.K., W.-B.J., and K.S. performed bioinformatics and statistical analysis of the RNA-seq data. M.R. and M.T. provided access to unpublished mapping information. C.G., E.G., K.A.K., and U.P. wrote the manuscript. The supplementary materials contain additional data. The RNA-seq data have been deposited in ArrayExpress with accession number E-MTAB-4072. The authors declare no conflict of interest.

SUPPLEMENTARY MATERIALS

www.sciencemag.org/content/350/6267/1521/suppl/DC1
Materials and Methods
Figs. S1 to S6
Tables S1 to S7
References (*32*–*49*)

7 July 2015; accepted 16 November 2015
10.1126/science.aac9715

NEURODEVELOPMENT

Loss of motoneuron-specific microRNA-218 causes systemic neuromuscular failure

Neal D. Amin,[1,2,3] Ge Bai,[1]* Jason R. Klug,[4] Dario Bonanomi,[1] Matthew T. Pankratz,[1] Wesley D. Gifford,[1,2,5] Christopher A. Hinckley,[1] Matthew J. Sternfeld,[1,6] Shawn P. Driscoll,[1] Bertha Dominguez,[7] Kuo-Fen Lee,[7] Xin Jin,[4] Samuel L. Pfaff[1]†

Dysfunction of microRNA (miRNA) metabolism is thought to underlie diseases affecting motoneurons. One miRNA, miR-218, is abundantly and selectively expressed by developing and mature motoneurons. Here we show that mutant mice lacking miR-218 die neonatally and exhibit neuromuscular junction defects, motoneuron hyperexcitability, and progressive motoneuron cell loss, all of which are hallmarks of motoneuron diseases such as amyotrophic lateral sclerosis and spinal muscular atrophy. Gene profiling reveals that miR-218 modestly represses a cohort of hundreds of genes that are neuronally enriched but are not specific to a single neuron subpopulation. Thus, the set of messenger RNAs targeted by miR-218, designated *TARGET*^{218}, defines a neuronal gene network that is selectively tuned down in motoneurons to prevent neuromuscular failure and neurodegeneration.

Motoneurons are a specialized neuronal subpopulation within the central nervous system (CNS) that establish synaptic connections with muscles to regulate movement. Diseases such as amyotrophic lateral sclerosis (ALS) and spinal muscular atrophy (SMA), which affect motoneurons, appear to share a common pathogenic mechanism based on defective RNA metabolism and biogenesis of microRNAs (miRNAs) (*1*–*5*). Consistent with earlier descriptions of miR-218 expression in embryonic motoneurons (*6*, *7*), we found that miR-218 was the most abundant motoneuron miRNA and was enriched ~27-fold, as determined by small RNA sequencing (RNA-seq) of embryonic mouse spinal cord *Hb9::gfp*$^{+}$ motoneurons purified by fluorescence-activated cell sorting (FACS) (Fig. 1A and supplementary materials and methods). The spinal cord is composed of many interneuron subtypes (*8*). We found that V2a and V3 ventral spinal interneurons did not express a single characteristic miRNA (fig. S1A), indicating that motoneurons may be distinctly reliant on cell type–specific miRNA expression.

We detected miR-218 within visceral and somatic spinal (Fig. 1B and fig. S1B) and brainstem motoneurons (fig. S1C). Robust miR-218 expression was detected postnatally in choline acetyltransferase (ChAT)–positive α and γ motoneurons (Fig. 1C and fig. S1D) but not ChAT^{+} interneurons (fig. S1E). Likewise, miR-218 was selectively expressed in human embryonic motoneurons (fig. S1F). Compared with the extensive catalog of protein markers that delineate motoneuron subtypes (*8*), miR-218 is notable for its expression spanning motoneuron classes from embryonic stages into adulthood (fig. S1G) and its undetectable expression in other tissues.

Two mammalian paralogs of miR-218, *miR-218-1* and *miR-218-2*, are embedded within homologous introns of the *Slit2* and *Slit3* genes, respectively. It has been suggested that the motoneuron-specifying transcription factors Isl1 and Lhx3 up-regulate miR-218 by increasing transcription of *Slit2* and *Slit3* (*6*). We used RNA-seq to investigate Slit2 and Slit3 mRNA expression in motoneurons and discovered that both genes were transcribed using start sites located upstream of exon 6 (Fig. 1D and fig. S2, A and B). This intronic start site was not used by adjacent floor-plate glial cells expressing *Slit2* and *Slit3*. Previously mapped Isl1/2, Lhx3, and Phox2a chromatin immunoprecipitation (ChIP) peaks (*9*) were observed at conserved hexamer DNA response elements (HxREs) proximal to exon 6 (Fig. 1E), suggesting the presence of intragenic motoneuron-specific promoters (Fig. 1F). To test this hypothesis, we generated a transgenic mouse line, *tg(218-2::eGFP)*, with a 7.4-kb sequence containing putative regulatory elements (fig. S2C). In vivo, enhanced green fluorescent protein (eGFP) was expressed in *tg(218-2::eGFP)* spinal and cranial motoneurons, reproducing the endogenous expression pattern of miR-218 (Fig. 1, G and H, and fig. S2C). These findings demonstrate that primary miR-218 transcripts are under independent activation in motoneurons by promoters distinct from those that generate *Slit2* and *Slit3* full-length transcripts in other tissues.

Studies in vitro and in chick embryos have suggested that miR-218 may contribute to motoneuron specification (*6*). However, such miRNA knockdown and overexpression studies can yield nonphysiological effects (*10*). To determine the biological effect of miR-218 disruption in vivo, we used clustered regularly interspaced short palindromic repeats (CRISPR)–Cas9 gene editing (*11*) to create microdeletions of *miR-218-1* and *miR-218-2* precursor sequences in mice (Fig. 2A and fig. S3, A to D). miR-218 expression was detected in miR-218-1$^{-/-}$ and at lower levels in miR-218-2$^{-/-}$ motoneurons but was undetectable in miR-218-1$^{-/-}$2$^{-/-}$ double knockout (218^{DKO}) motoneurons (Fig. 2B and fig. S3, E to H). We found that the number and spatial organization of motoneurons in embryonic day 12.5 (E12.5) spinal cords of 218^{DKO} mutants were unchanged compared to controls (fig. S4, A to F). Subsequent developmental events—including axonal exit from the spinal cord, outgrowth, and peripheral pathfinding—were indistinguishable between Hb9::*gfp*$^{+}$ control and 218^{DKO} embryos (fig. S4G). 218^{DKO} mutants displayed none of the phenotypes characteristic of *Slit2* and *Slit3* disruption (fig. S4, H and I) (*12*, *13*), indicating that *Slit2* and *Slit3* function is unaffected by the intronic microdeletions. We conclude that miR-218 is dispensable for in vivo fate specification and gross early development of motoneurons.

However, 218^{DKO} mice were never viable (fig. S5A). 218^{DKO} embryos exhibited akinesia, kyphosis, and weak or absent responses to pain stimulation after caesarean delivery at E18.5 and died within minutes due to an apparent lack of respiration (Fig. 2C and movie S1). These phenotypic defects are similar to those observed in mice carrying null alleles of Agrin, MuSK, ChAT, and other components required for neuromuscular transmission (*14*). Consequently, we investigated whether the loss of miR-218 affects neuromuscular synaptogenesis, an intricate process in which motor nerves first innervate muscle and subsequently form presynaptic specializations with postsynaptic acetylcholine receptors (AChRs) expressed by developing muscle (*15*). We examined glycerol-cleared *tg(218-2::eGFP)* embryos and found that the motor nerves of 218^{DKO} motoneurons reached E14.5 limb tissue (fig. S5B). However, motor axons appeared to lack penetrating, fine intramuscular branches in limbs, the diaphragm, and intercostal muscles (Fig. 2, D and E, and fig. S6, A and B). At E18.5, the majority of α-bungarotoxin–labeled AChR^{+} clusters lack motor innervation in 218^{DKO} limb muscles (Fig. 2F and fig. S6C), reflecting a gross failure of motoneurons to establish the neuromuscular junctions (NMJs) needed to control body movements.

Although 218^{DKO} mutants had normal numbers of motoneurons at E12.5 (Fig. 2G), 218^{DKO} mutants had 18 to 36% fewer motoneurons at cervical, thoracic, and lumbar spinal cord segments at E18.5, indicating neurodegenerative cell loss (Fig. 2H and fig. S7, A and B). To examine whether the physiology of the remaining motoneurons

[1]Howard Hughes Medical Institute and Gene Expression Laboratory, Salk Institute for Biological Studies, 10010 North Torrey Pines Road, La Jolla, CA 92037, USA. [2]Medical Scientist Training Program, University of California, San Diego (UCSD), 9500 Gilman Drive, La Jolla, CA 92037, USA. [3]Biomedical Sciences Graduate Program, UCSD, 9500 Gilman Drive, La Jolla, CA 92037, USA. [4]Molecular Neurobiology Laboratory, Salk Institute for Biological Studies, 10010 North Torrey Pines Road, La Jolla, CA 92037, USA. [5]Neurosciences Graduate Program, UCSD, 9500 Gilman Drive, La Jolla, CA 92037, USA. [6]Biological Sciences Graduate Program, UCSD, 9500 Gilman Drive, La Jolla, CA 92037, USA. [7]Peptide Biology Laboratory, Salk Institute for Biological Studies, 10010 North Torrey Pines Road, La Jolla, CA 92037, USA.
*Present address: Department of Chemical Physiology, The Scripps Research Institute, La Jolla, CA 92037, USA. †Corresponding author. E-mail: pfaff@salk.edu

was altered in mice lacking miR-218, we assessed fictive locomotion (*16*) and performed intracellular recordings of *Hb9::gfp*$^{+}$ lateral motor column α motoneurons from E18.5 lumbar spinal slices (fig. S8A). Left-right and flexor-extensor activation of motor roots were normal in 218^{DKO} spinal cords, and motoneuron resting membrane potentials, capacitances, resistances, and holding currents were similar between control and 218^{DKO} motoneurons (fig. S8, B to J). However, action potentials were elicited by a rheobase current that was 4.4 times lower in 218^{DKO} motoneurons than in controls (Fig. 2, I and J), indicating membrane hyperexcitability. Thus, miR-218 does not appreciably contribute to early motoneuron development, but it is critical for the regulation of neuromuscular synapses, membrane excitability, and motoneuron survival.

These phenotypic defects suggest that motoneuron-specific gene regulation depends on the post-transcriptional repression of miR-218 target mRNAs. To extend beyond miRNA target identification studies performed in vitro using cancer cell lines (*6*, *17*), we identified miR-218 gene targets within motoneurons by performing polyadenylated (polyA^{+}) RNA-seq of FACS-isolated Hb9::*gfp*$^{+}$ motoneurons from wild-type (WT) and 218^{DKO}

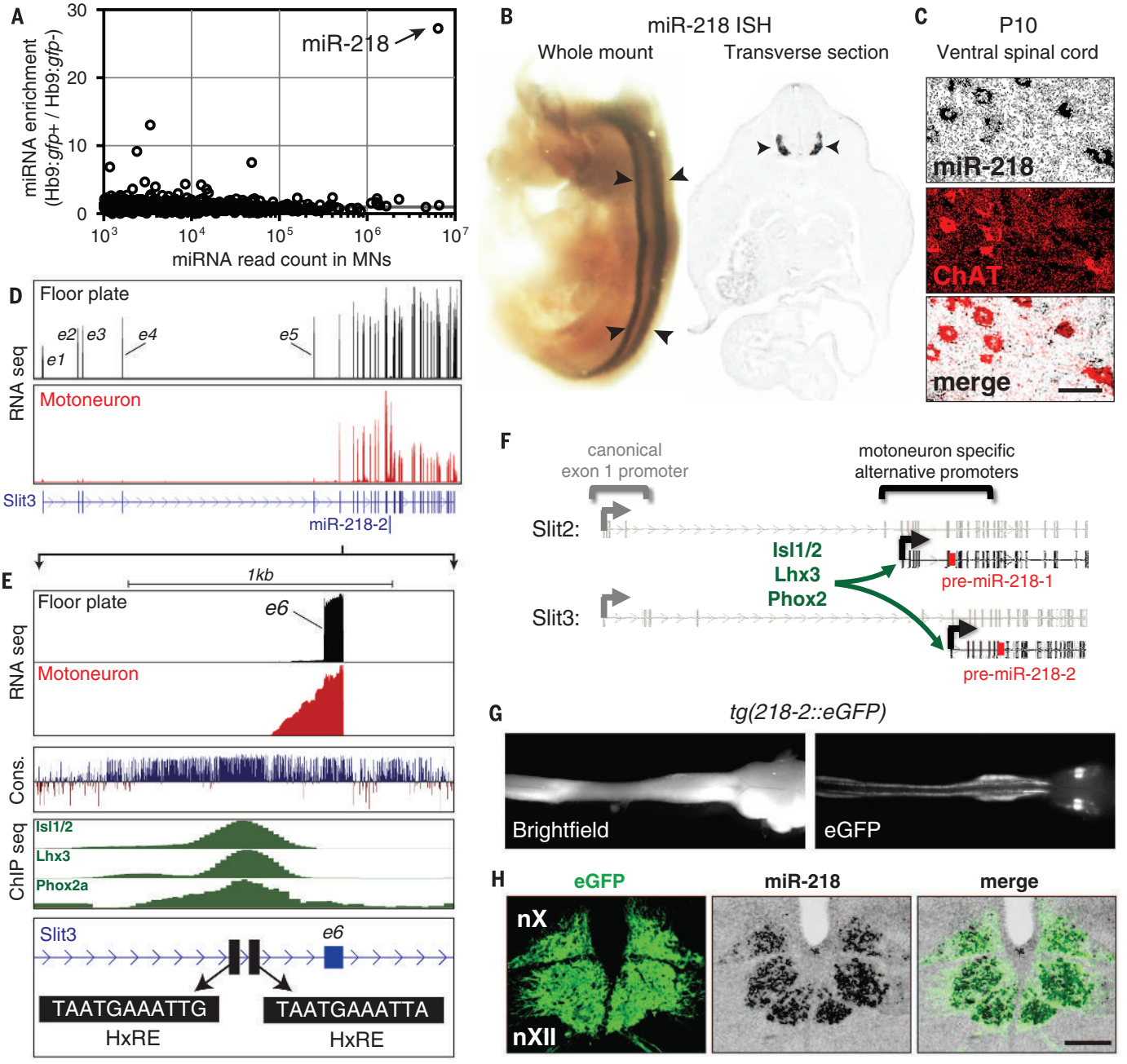

Fig. 1. Abundant and specific expression of miR-218 in spinal and cranial motoneuron subtypes. (**A**) Murine miRNA expression (*x* axis) versus enrichment [E10.5 Hb9::*gfp*$^{+}$ motoneurons (MNs) versus Hb9::*gfp*$^{-}$ non-motoneurons, *y* axis] (n = 2 sorting and sequencing experiments). (**B**) miR-218 in situ hybridization (ISH) in whole-mount and transverse sections at E11.5 (arrowheads identify motor columns). (**C**) miR-218 colocalizes with ChAT^{+} motoneurons at P10. (**D** and **E**) PolyA^{+} RNA-seq reads from E12.5 floor plate and motoneurons, evolutionary conservation (Cons.), and motoneuron-specifying transcription factor ChIP peaks and HxRE DNA binding motifs at the *Slit3* locus containing *pre-miR-218-2*. (**F**) Transcription of miR-218 in motoneurons by alternative promoters. (**G** and **H**) Images from *tg(218-2::eGFP)* mice. (G) Expression of eGFP in spinal and brainstem motoneurons of the CNS and (H) in miR-218^{+} motor nuclei nX and nXII. Scale bars: (C) 50 μm; (H) 200 μm.

E12.5 spinal cords, before the apparent onset of defects (fig. S9A). Using Sylamer (*18*), we determined that 6-, 7-, and 8–base pair (bp) 3′ untranslated region (3′UTR) complementary seed matches to miR-218 were enriched within genes expressed higher in 218^{DKO} motoneurons versus controls (fig. S9, B to E). This finding reflects the widespread derepression of miR-218 target genes in 218^{DKO} motoneurons.

We identified 333 genes with predicted miR-218 binding sites [TargetScan 6.2 (*19*)] that were significantly derepressed in 218^{DKO} versus WT motoneurons (Fig. 3A). We name this coordinately regulated gene set, likely to be under direct miR-218–mediated repression, $_{TARGET}{}^{218}$. $_{TARGET}{}^{218}$ genes are enriched for neurotransmission and neurotransmitter transport processes (fig. S9, F and G). The most highly up-regulated $_{TARGET}{}^{218}$ gene, *Slc1a2* (266% increase), is a glutamate reuptake transporter known to be modulated by riluzole, the only medication approved for the treatment of ALS (*20*). On average, $_{TARGET}{}^{218}$ genes were expressed 61.1% higher in 218^{DKO} motoneurons, and 47 of these genes were expressed at least twofold higher (table S1). The wide breadth of target genes affected in 218^{DKO} motoneurons suggests that miR-218 shapes expression of an extensive genetic network rather than merely modulating a small group of individual genes within a single molecular pathway.

Other miRNA gene regulatory networks have been shown to reinforce the repression of

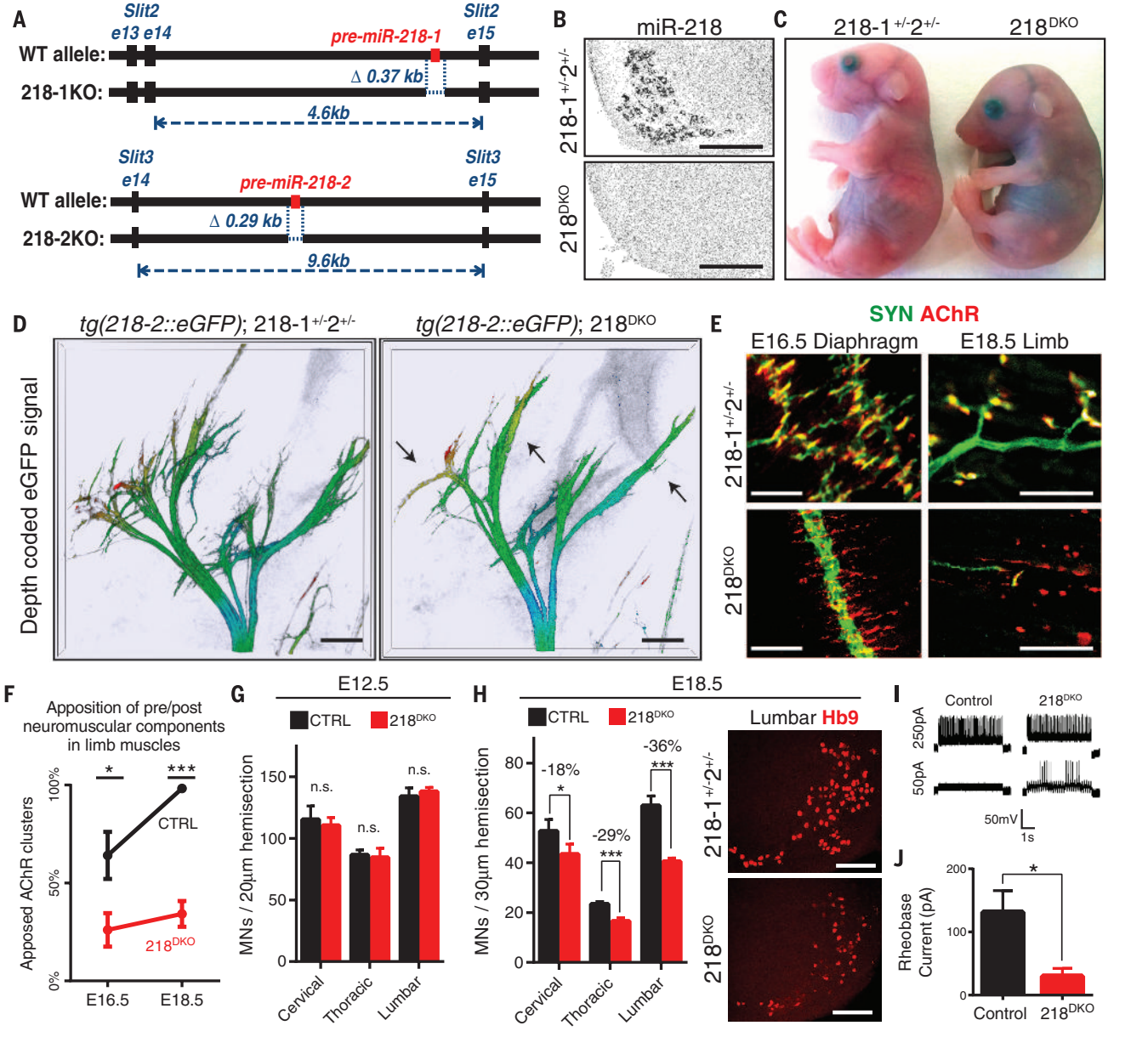

Fig. 2. The loss of miR-218 results in systemic neuromuscular failure, motoneuron cell loss, and hyperexcitability. (**A**) CRISPR-Cas9–mediated multiplexed microdeletions of *pre-miR-218-1* and *pre-miR-218-2* from the mouse genome. (**B**) miR-218 in situ hybridization signal in control and 218^{DKO} E18.5 spinal cords. (**C**) Cesarean-delivered 218^{DKO} E18.5 embryos exhibit flaccid paralysis and die within minutes. (**D**) Decreased intramuscular branching (arrows) of E14.5 motor nerves in *tg(218-2::eGFP)*;218^{DKO} embryos (deep peroneal nerve). (**E** and **F**) In 218^{DKO} embryos, (E) NMJs exhibit abnormal morphology, and (F) most limb $AChR^{+}$ clusters are aneural (n = 3 embryos). (**G** and **H**) Motoneuron counts at E12.5 (n = 4 and 3 embryos) and E18.5 (n = 4 embryos) across spinal segments. (**I**) Representative traces of control and 218^{DKO} motoneurons after intracellular current injection. (**J**) Rheobase quantification (n = 9 and 5 motoneurons). Statistics: In (F), (G), and (H), error bars indicate SD, and results of two-tailed t tests are shown. In (J), error bars indicate SEM, and nonparametric Mann-Whitney t test results are shown. $^{*}P < 0.05$; $^{***}P < 0.001$; n.s., not significant. Scale bars: (B), (D), and (H) 150 µm; (E) 50 µm.

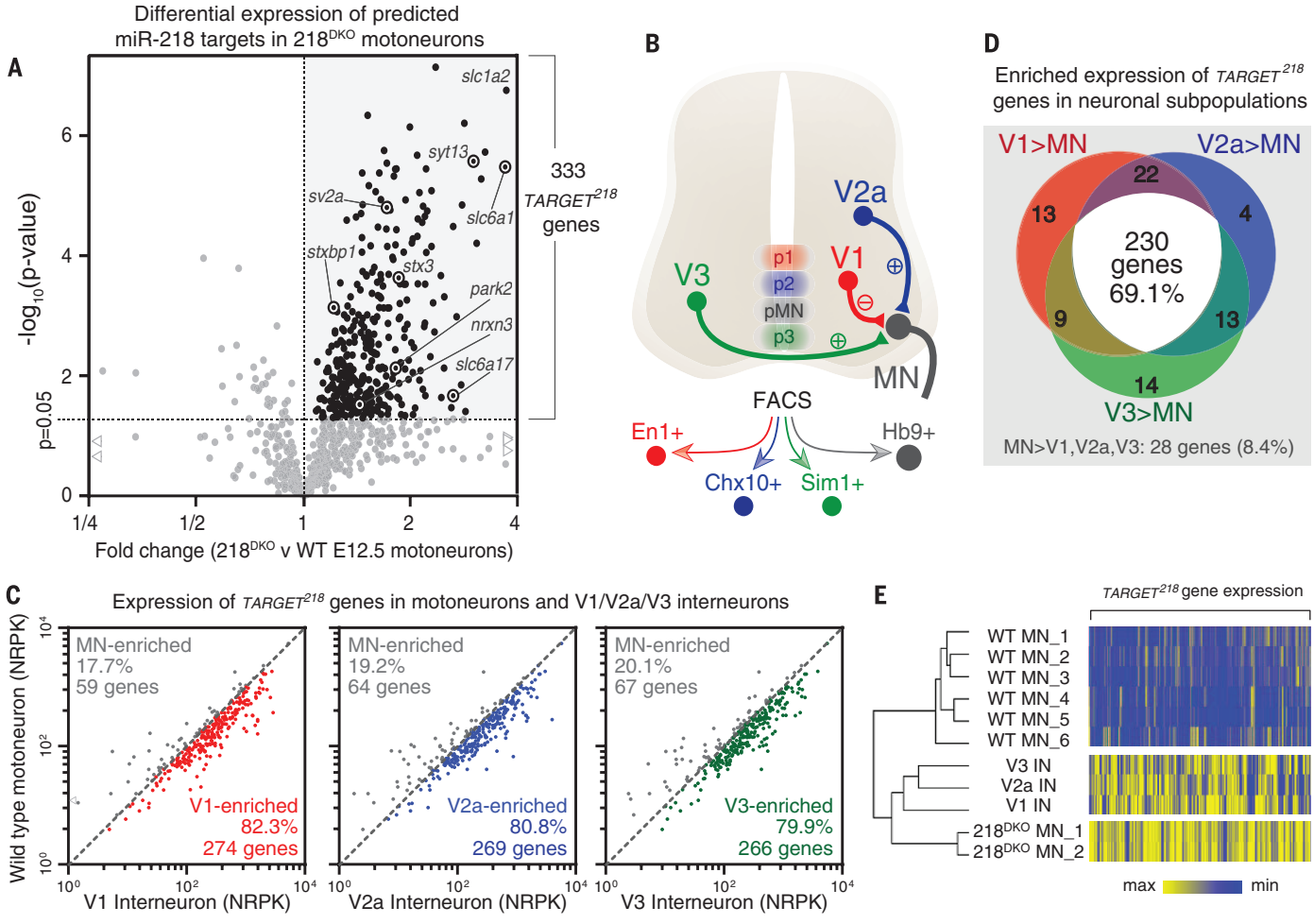

Fig. 3. miR-218 represses an extensive genetic network in motoneurons. (**A**) Volcano plot (mRNA fold difference versus *P* value) of 218^{DKO} versus WT motoneurons of genes expressing at least 10 normalized reads per kilobase and possessing strong miR-218 binding sites [context + score ≤ −0.15, TargetScan6.2 (*19*)] (n = 6 and 2 sorting and sequencing experiments). Of these genes, 333 (designated *TARGET*^{218} genes) are significantly derepressed in 218^{DKO} motoneurons. *TARGET*^{218} genes involved in neurotransmitter transport are labeled. (**B**) Motoneurons and V1, V2a, and V3 interneuron subpopulations derive from adjacent progenitor domains (p1, p2, pMN, p3) and were labeled with transgenes or Cre-reporters for FACS-isolation and RNA-seq. (**C**) *TARGET*^{218} genes are expressed at low levels in motoneurons relative to each of V1, V2a, and V3 interneurons. NRPK, normalized reads per kilobase. (**D**) Most *TARGET*^{218} genes are expressed lower in motoneurons versus V1, V2a, and V3 interneurons. (**E**) Hierarchical clustering of *TARGET*^{218} gene expression in WT motoneurons (WT MN, six replicates), 218^{DKO} motoneurons (218^{DKO} MN, two replicates), and interneuron subpopulations (V1 IN, V2a IN, and V3 IN).

differentiation programs to confer robustness to cell fate decisions (*21*–*23*). However, the lack of cell specification errors in 218^{DKO} embryos suggests that miR-218 might have a previously unrecognized regulatory role. To evaluate whether the *TARGET*^{218} gene network was expressed higher or lower in motoneurons compared with other spinal neuronal subpopulations, we performed gene profiling of FACS-purified interneuron subpopulations labeled by genetic reporters: GABAergic-V1 (En1:Cre), glutamatergic-V2a (Chx10:Cre), and glutamatergic-V3 (Sim1:Cre) spinal interneurons (Fig. 3B and fig. S10, A to C). We found that ~80% of *TARGET*^{218} genes are expressed lower in WT motoneurons versus each of the V1, V2a, and V3 interneurons (Fig. 3C). Moreover, the majority (69.1%) of *TARGET*^{218} genes are expressed lower in WT motoneurons versus all three spinal interneuron subpopulations (Fig. 3D). These findings suggest that miR-218 represses a gene network shared across interneuron subpopulations but not specific to a single one. Furthermore, hierarchical clustering revealed that 218^{DKO} motoneurons express *TARGET*^{218} genes at levels closer to those of V1, V2a, and V3 interneurons than to those of WT motoneurons (Fig. 3E). Thus, rather than reinforcing a preexisting low target gene expression in motoneurons, miR-218 establishes the low *TARGET*^{218} expression observed in motoneurons relative to interneurons.

To evaluate miRNA-mediated repression in an unbiased manner, we bioinformatically evaluated the statistical enrichment of binding sites for all miRNAs across the transcriptome of investigated cell types. Using Sylamer (*18*), we determined the hypergeometric statistical enrichment of 7-bp 3′UTR sequences complementary to known miRNA seed sequences (miRNA seed matches) in transcripts expressed higher or lower in motoneurons versus interneurons (Fig. 4A). We found that 3′UTR seed matches to miR-218 are significantly enriched in transcripts expressed lower in WT motoneurons versus pooled interneurons (Fig. 4A), individual spinal interneuron subpopulations, and even distantly located cortical neuron subpopulations (Fig. 4B) (*24*). 3′UTR seed matches to miR-218 were not found to be enriched in genes expressed higher or lower in 218^{DKO} motoneurons (Fig. 4C). The 3′UTR seed match to miR-124 [a pan-neuronal miRNA abundantly expressed in motoneurons and other CNS neurons (*25*)], but not 3′UTR seed matches to miR-218, was overrepresented in transcripts expressed lower in motoneurons versus purified motoneuron progenitors differentiated from embryonic stem cells (Fig. 4, B and C). We conclude

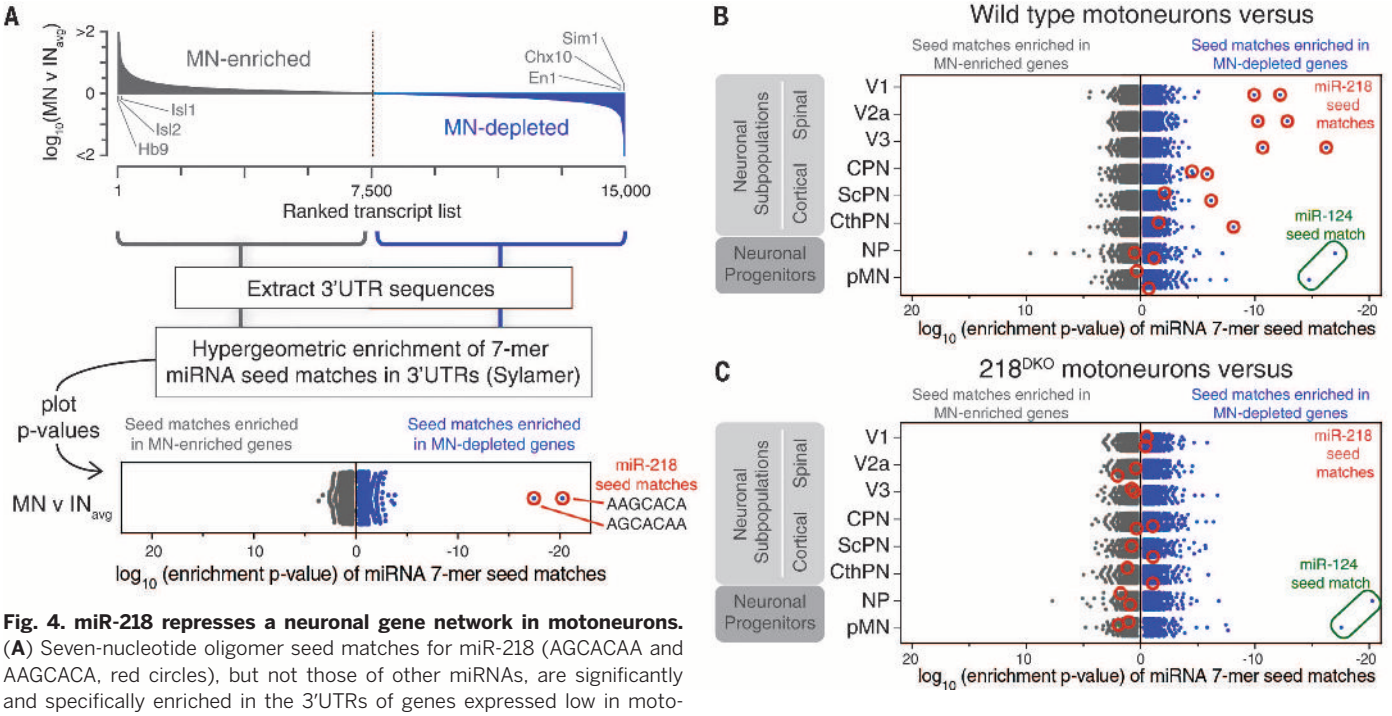

Fig. 4. miR-218 represses a neuronal gene network in motoneurons. (**A**) Seven-nucleotide oligomer seed matches for miR-218 (AGCACAA and AAGCACA, red circles), but not those of other miRNAs, are significantly and specifically enriched in the 3′UTRs of genes expressed low in motoneurons relative to an average of V1, V2a, and V3 interneuron populations (IN_{avg}). (**B**) Genes expressed lower in WT motoneurons versus individual spinal and cortical (*24*) neuronal subpopulations were most enriched for miR-218 seed matches. (**C**) miR-218 seed matches are not enriched in genes expressed higher or lower in 218^{DKO} motoneurons versus other neuronal populations. Genes expressed lower in WT (B) or 218^{DKO} (C) motoneurons versus neuronal progenitors were most enriched for the seed match to miR-124 (GTGCCTT). CPN, callosal; ScPN, subcerebral; CthPN, subplate neurons; NP, mouse embryonic stem (mES) cell–derived neuronal progenitors; pMN, FACS-purified $Olig2^{+}$ mES cell–derived neuronal progenitors.

that: (i) miR-218 targets a genetic network shared across functionally and spatially distinct neuronal cell types; (ii) the low relative expression of this gene network in motoneurons is established by miR-218; and (iii) although miR-124 and miR-218 are coexpressed in motoneurons, their regulatory roles differ—miR-124 represses a neuronal progenitor–associated gene network, whereas miR-218 represses a gene network coordinately expressed by other spinal and cortical neuronal subpopulations.

We have identified a neuronal gene network, $_{TARGET}{}^{218}$, that is selectively repressed in motoneurons by a single miRNA. When this network is derepressed in 218^{DKO} mice, motoneurons exhibit severe NMJ defects, hyperexcitability, and cell loss—the pathological hallmarks of motoneuron diseases such as ALS and SMA (*1*, *26*–*28*). The link between miR-218 and motoneuron diseases likely extends beyond phenotypic similarities. Patients suffering from motoneuron diseases carry genetic mutations in ubiquitously expressed RNA processing factors (e.g., TDP-43, FUS, SMN) or expansion repeats in C9ORF72 that sequester RNA binding proteins (*1*, *2*), but the biological mechanisms that magnify the effects of these changes on motoneurons are unclear. miRNA-dependent regulation—and specifically the repression of miR-218's genetic network—might be particularly sensitive to defects in these RNA metabolic pathways thought to underlie motoneuron disease. Investigations of the pathways affecting miR-218's biogenesis and the modulation of its genetic network may be critical to understand and tackle these devastating diseases.

REFERENCES AND NOTES

1. X. Paez-Colasante, C. Figueroa-Romero, S. A. Sakowski, S. A. Goutman, E. L. Feldman, *Nat. Rev. Neurol.* **11**, 266–279 (2015).
2. C. Volonte, S. Apolloni, C. Parisi, *CNS Neurol. Disord. Drug Targets* **14**, 194–207 (2015).
3. M. Morlando *et al.*, *EMBO J.* **31**, 4502–4510 (2012).
4. Y. Kawahara, A. Mieda-Sato, *Proc. Natl. Acad. Sci. U.S.A.* **109**, 3347–3352 (2012).
5. S. Haramati *et al.*, *Proc. Natl. Acad. Sci. U.S.A.* **107**, 13111–13116 (2010).
6. K. P. Thiebes *et al.*, *Nat. Commun.* **6**, 7718 (2015).
7. M. Kapsimali *et al.*, *Genome Biol.* **8**, R173 (2007).
8. W. A. Alaynick, T. M. Jessell, S. L. Pfaff, *Cell* **146**, 178–178.e1 (2011).
9. E. O. Mazzoni *et al.*, *Nat. Neurosci.* **16**, 1219–1227 (2013).
10. J. A. Vidigal, A. Ventura, *Trends Cell Biol.* **25**, 137–147 (2015).
11. H. Wang *et al.*, *Cell* **153**, 910–918 (2013).
12. L. Ma, M. Tessier-Lavigne, *J. Neurosci.* **27**, 6843–6851 (2007).
13. H. Long *et al.*, *Neuron* **42**, 213–223 (2004).
14. B. Turgeon, S. Meloche, *Physiol. Rev.* **89**, 1–26 (2009).
15. H. Darabid, A. P. Perez-Gonzalez, R. Robitaille, *Nat. Rev. Neurosci.* **15**, 703–718 (2014).
16. A. C. Kwan, S. B. Dietz, W. W. Webb, R. M. Harris-Warrick, *J. Neurosci.* **29**, 11601–11613 (2009).
17. Y. F. Lu, L. Zhang, M. M. Waye, W. M. Fu, J. F. Zhang, *Exp. Cell Res.* **334**, 173–182 (2015).
18. S. van Dongen, C. Abreu-Goodger, A. J. Enright, *Nat. Methods* **5**, 1023–1025 (2008).
19. D. M. Garcia *et al.*, *Nat. Struct. Mol. Biol.* **18**, 1139–1146 (2011).
20. B. C. Cheah, S. Vucic, A. V. Krishnan, M. C. Kiernan, *Curr. Med. Chem.* **17**, 1942–1959 (2010).
21. D. P. Bartel, *Cell* **136**, 215–233 (2009).
22. J. Tsang, J. Zhu, A. van Oudenaarden, *Mol. Cell* **26**, 753–767 (2007).
23. H. Herranz, S. M. Cohen, *Genes Dev.* **24**, 1339–1344 (2010).
24. B. J. Molyneaux *et al.*, *Neuron* **85**, 275–288 (2015).
25. E. V. Makeyev, J. Zhang, M. A. Carrasco, T. Maniatis, *Mol. Cell* **27**, 435–448 (2007).
26. L. R. Fischer *et al.*, *Exp. Neurol.* **185**, 232–240 (2004).
27. B. J. Wainger *et al.*, *Cell Reports* **7**, 1–11 (2014).
28. H. Liu *et al.*, *Sci. Rep.* **5**, 12189 (2015).

ACKNOWLEDGMENTS

We thank K. Lettieri, N. White, and M. Gullo for mouse husbandry; Y. Dayn at the Salk Transgenic Core for oocyte injections; C. O'Connor and C. Fitzpatrick at the Salk Flow Cytometry Core for cell sorting; and M. Ku at the Salk Next Generation Sequencing Core for RNA-seq. Salk Core facilities are supported by the National Cancer Institute (grant P30 CA014195), the National Institute of Neurological Disorders and Stroke (NINDS) (grant P30 NS072031), The Leona M. and Harry B. Helmsley Charitable Trust, and the H.A. and Mary K. Chapman Charitable Foundation. N.D.A. is supported by a NINDS fellowship (F31-NS080340-03) and the UCSD Medical Scientist Training Program (grant T32-GM007198). S.L.P. is a Howard Hughes Medical Institute investigator and the Benjamin H. Lewis chair in neuroscience at the Salk Institute. This research is supported by grants from the NIH (R01GM088278, R21NS084254, R01NS054154, R01NS044420, R01NS060833, and R01AG0476669), The Marshall Heritage Foundation, Sol Goldman Trust, and The Clayton Foundation. The Gene Expression Omnibus accession number is GSE75601. N.D.A., S.L.P., and the Salk Institute have filed the following U.S. provisional patent applications: no. 62/168,755 (30 May 2015) and no. 62/166,677 (26 May 2015). The supplementary materials contain additional data.

SUPPLEMENTARY MATERIALS

www.sciencemag.org/content/350/6267/1525/suppl/DC1
Materials and Methods
Figs. S1 to S10
Tables S1 and S2
References (*29*, *30*)
Movie S1

28 September 2015; accepted 11 November 2015
10.1126/science.aad2509

PHYTOPLANKTON

Millennial-scale plankton regime shifts in the subtropical North Pacific Ocean

Kelton W. McMahon,[1,2]* Matthew D. McCarthy,[1] Owen A. Sherwood,[3] Thomas Larsen,[4] Thomas P. Guilderson[1,2,5]

Climate change is predicted to alter marine phytoplankton communities and affect productivity, biogeochemistry, and the efficacy of the biological pump. We reconstructed high-resolution records of changing plankton community composition in the North Pacific Ocean over the past millennium. Amino acid–specific $\delta^{13}C$ records preserved in long-lived deep-sea corals revealed three major plankton regimes corresponding to Northern Hemisphere climate periods. Non–dinitrogen-fixing cyanobacteria dominated during the Medieval Climate Anomaly (950–1250 Common Era) before giving way to a new regime in which eukaryotic microalgae contributed nearly half of all export production during the Little Ice Age (~1400–1850 Common Era). The third regime, unprecedented in the past millennium, began in the industrial era and is characterized by increasing production by dinitrogen-fixing cyanobacteria. This picoplankton community shift may provide a negative feedback to rising atmospheric carbon dioxide concentrations.

Gone is the paradigm of the oligotrophic subtropical gyres as vast oceanic deserts. In the recent instrumental record, a new picture has emerged of substantial dynamics in plankton community structure, biogeochemical cycling, and export production (*1*–*4*). Numerous lines of evidence suggest that shifts in phytoplankton community regimes are intimately connected to oceanographic conditions (*2*, *4*, *5*). For instance, the 1976 polarity reversal of the Pacific Decadal Oscillation caused a shoaling of the mixed layer and subsequent declines in available nutrients to the North Pacific Subtropical Gyre (NPSG); these conditions probably promoted the food-web regime shift from a eukaryotic to a prokaryotic, cyanobacteria-dominated system (*2*). Such changes are superimposed on secular shifts associated with the areal increase of subtropical gyres that has been ongoing for at least 25 years (*6*). In the face of increasing climate change, it is imperative to understand recent changes at the base of the NPSG food web in the context of longer-term trends. However, our understanding of how NPSG plankton communities have shifted on centennial time scales has been limited by a lack of available methods and paleoarchives of sufficient length and resolution.

Hawaiian gold corals (*Kulamanamana haumeaae*) are extraordinarily long-lived deep-sea organisms that record the biogeochemical signatures of recently exported production in their proteinaceous skeletons (*7*, *8*). We generated millennial-length records of bulk stable carbon isotopes ($\delta^{13}C_{bulk}$) from specimens of *K. haumeaae* collected from the top of the mesopelagic zone at two sites in the Hawaiian archipelago (Fig. 1). The $\delta^{13}C_{bulk}$ records showed remarkable congruence, characterized by a gradual increase of ~1.0 per mil (‰) from ~1000 to ~1850 CE, followed by a rapid decrease of –1.0‰ from ~1850 to the present, after correcting for the Suess effect (Fig. 2A) (*9*–*11*). These changes in $\delta^{13}C_{bulk}$ imply multicentennial-scale shifts in $\delta^{13}C$ values associated with primary production, which we hypothesize reflect major changes in plankton community structure over the past 1000 years.

Bulk $\delta^{13}C$ records integrate the combined influences of the $\delta^{13}C$ value of inorganic carbon utilized during carbon fixation, shifts in plankton community structure, trophic changes, and biochemical fractionation. To isolate plankton source signatures within this signal, we applied a powerful fingerprinting approach to the sampled deep-sea corals, based on the normalized $\delta^{13}C$ values of essential amino acids ($\delta^{13}C_{EAA}$) in primary producers (*11*). These $\delta^{13}C_{EAA}$ fingerprints reflect the substantial metabolic diversity in EAA synthesis pathways and associated isotope effects among evolutionarily distinct primary producers (*12*, *13*). We found diagnostic multivariate patterns in literature values of normalized $\delta^{13}C_{EAA}$ among four key source end-members relevant to the NPSG [eukaryotic microalgae, dinitrogen (N_2)–fixing and non–N_2-utilizing cyanobacteria, and heterotrophic bacteria] (fig. S2). Because animals cannot synthesize the carbon skeletons of EAAs (*14*), these $\delta^{13}C_{EAA}$ fingerprints are incorporated, virtually unmodified, into upper-trophic-level consumers, including gorgonin corals (*15*). Furthermore, $\delta^{13}C_{EAA}$ fingerprints are robust to the many factors affecting bulk $\delta^{13}C$ values, such as environmental and growth conditions (*13*, *16*).

A subset of the deep-sea coral samples spanning the entire 1000-year record was analyzed for $\delta^{13}C_{EAA}$ at ~20-year resolution (table S1). $\delta^{13}C_{EAA}$ values were strongly correlated with $\delta^{13}C_{bulk}$ (fig. S1), indicating that trends in $\delta^{13}C_{bulk}$ can be attributed to changes in source carbon at the base of the food web (*15*). For example, the $\delta^{13}C_{EAA}$ of

[1]Department of Ocean Sciences, University of California–Santa Cruz, Santa Cruz, CA 95064, USA. [2]Institute for Marine Sciences, University of California–Santa Cruz, Santa Cruz, CA 95064, USA. [3]Institute of Arctic and Alpine Research, University of Colorado–Boulder, Boulder, CO 80309, USA. [4]Leibniz Laboratory for Radiometric Dating and Stable Isotope Research, Christian-Albrechts-Universität zu Kiel, 24118 Kiel, Germany. [5]Lawrence Livermore National Laboratory, Livermore, CA 94550, USA.
*Corresponding author. E-mail: kemcmaho@ucsc.edu

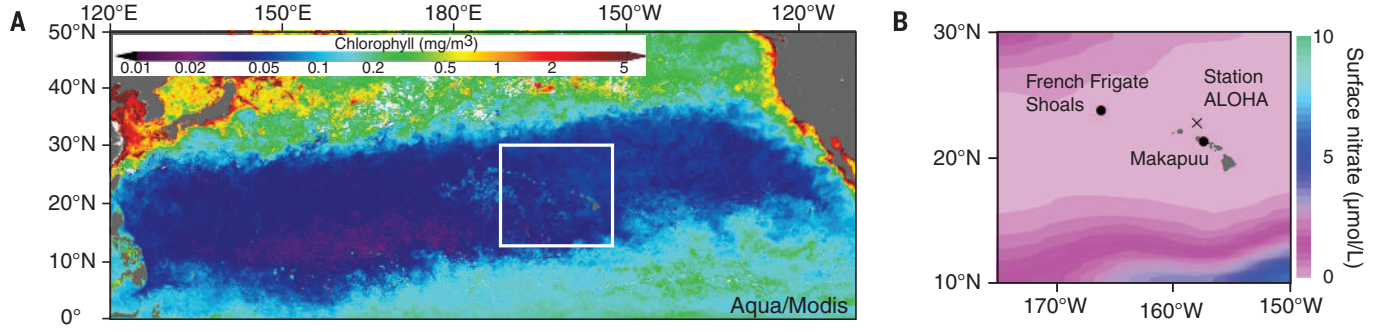

Fig. 1. NPSG productivity distribution, with sample locations. (**A**) Spatial extent of the oligotrophic NPSG, determined from spring 2012 chlorophyll a concentrations measured remotely by NASA's Aqua/MODIS (Moderate Resolution Imaging Spectroradiometer). The white box indicates the area shown in (B). [Image courtesy of NASA Goddard's Ocean Biology Processing Group] (**B**) *K. haumeaae* sampling locations at Makapuu and French Frigate Shoals relative to the oceanographic station ALOHA (indicated by the X), overlain on ocean surface nitrate concentrations (National Oceanographic Data Center, 2013; https://www.nodc.noaa.gov/cgi-bin/OC5/woa13/woa13oxnu.pl?parameter=n).

phenylalanine (Fig. 2B) mirrored that of $\delta^{13}C_{bulk}$ (Fig. 2A); however, the magnitude of change was 10 times larger than in $\delta^{13}C_{bulk}$. This suggests that isotopic contributions from other macromolecules had a strong muting effect on $\delta^{13}C_{bulk}$ values, and thus $\delta^{13}C_{EAA}$ is likely a more sensitive record of changes in primary producer $\delta^{13}C$ than $\delta^{13}C_{bulk}$ is (*15*). Our results indicate that variability in $\delta^{13}C$ values of exported production was much larger than would be inferred from coral $\delta^{13}C_{bulk}$ records alone, and strongly suggest broad changes in the sources of exported primary production through time.

To reconstruct past shifts in the relative contributions of major phytoplankton groups to export production in the NPSG, we applied a Bayesian stable isotope–mixing model to published source end-member $\delta^{13}C_{EAA}$ fingerprints (*11*) and the $\delta^{13}C_{EAA}$ records of *K. haumeaae*, normalized to their respective means (fig. S2 and table S2). Over the entire 1000-year record, photoautotrophic carbon dominated the corals' sinking particulate organic matter (POM) food source (mean, 87 ± 6%), with a relatively small heterotrophic bacterial contribution (13 ± 6%) (Fig. 3). Likewise, prokaryotic cyanobacterial sources dominated photoautrophic carbon (63 ± 14%), with a moderate mean contribution from eukaryotic microalgae (24 ± 10%) (Fig. 3). On centennial time scales, however, relative contributions from photoautotrophic end-members shifted dramatically. For example, between 1000 and 1850 CE, cyanobacteria decreased from 80 to 50% of total exported production, offset by an equivalent increase in eukaryotic microalgae up to a peak contribution of ~45% in the early 1800s. Although previous studies have noted enhanced diatom abundances in the NPSG associated with mesoscale oceanographic features (*17*), such a sustained high level of eukaryotic microalgal production has never been observed in the modern instrumental record. The most conservative explanation of our data is that the changes in the phylogenetic identity of sources contributing to export production reflect changes in the relative community composition of surface plankton through time. An alternate, albeit highly unlikely, hypothesis is that surface plankton community composition has remained relatively constant through time, and instead the degree of decoupling between surface and export production has undergone dramatic changes as a function of climate shifts (*11*).

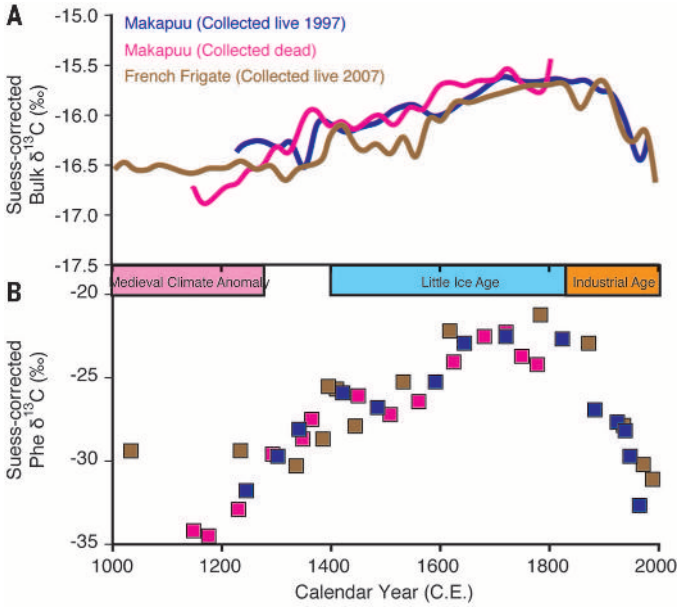

Fig. 2. 1000-year bulk and essential amino acid $\delta^{13}C$ records from deep-sea corals in the NPSG. *K. haumeaae*–derived records of (**A**) $\delta^{13}C_{bulk}$ (solid lines show the 20-year average; analytical error, 0.05‰) and (**B**) $\delta^{13}C_{Phe}$ (Phe, phenylalanine; squares; analytical error, 0.2‰) from Makapuu live coral (purple), Makapuu fossil coral (magenta), and French Frigate Shoals live coral (brown). All records have been corrected for the oceanic Suess effect since 1860 (*10*, *11*). Well-known Northern Hemisphere climate phenomena are overlaid for reference (*18*).

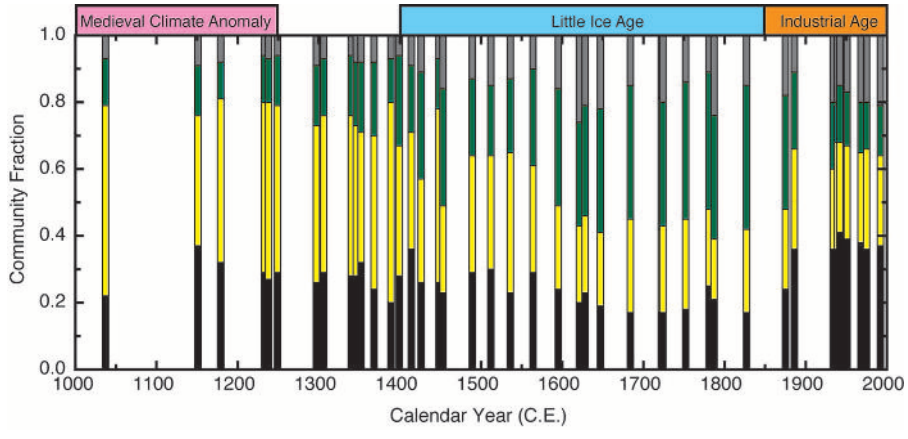

Fig. 3. Millennial record of relative carbon contributions from different primary producers recorded in deep-sea corals. Shown are the relative contributions of carbon from N_2-fixing cyanobacteria (black), non–N_2-utilizing cyanobacteria (yellow), eukaryotic microalgae (green), and heterotrophic bacteria (gray), recorded in deep-sea corals over the past 1000 years. Corals were collected at 450 m depth in the Hawaiian archipelago in the NPSG. Relative contributions are based on a compound-specific Bayesian stable isotope–mixing model of normalized phytoplankton end-member and coral $\delta^{13}C_{EAA}$ values.

To better constrain the patterns of changing plankton community composition, we applied a hierarchical cluster analysis to the normalized $\delta^{13}C_{EAA}$ data (*11*). This approach identified three distinct plankton community regimes that corresponded temporally to well-known Northern Hemisphere climate phenomena (Fig. 4). The first regime corresponded to the Medieval Climate Anomaly [MCA; 950–1250 CE (*18*)], with $\delta^{13}C_{EAA}$ fingerprints indicative of export production dominated by nitrate (NO_3^-)–utilizing cyanobacteria. There is general consensus that the putative MCA in the northern mid-latitudes was similar to the climate of the mid-20th century (*18*, *19*), implying relatively warm sea surface temperatures, weak winds, shallow mixed-layer depths, and resultant nutrient limitation, all favoring a microbial loop–dominated community (*2*). The second regime corresponded to the Little Ice Age [LIA; 1400–1850 CE (*18*)]. In this regime, the plankton assemblage contributing to export production transitioned from a cyanobacteria-dominated community to one far more strongly influenced by eukaryotic microalgae (Fig. 3). This shift probably reflects a transition in the LIA to cooler sea surface temperatures, a reduction in stratification, an increase in mixed-layer depth, and an inferred increase in the supply of inorganic nitrate from depth (*4*, *20*).

The third and current regime began at the end of the LIA and at the onset of the modern industrial age (~1850 CE) (Fig. 4). This regime is distinguished by a transition back to a cyanobacteria-dominated system. However, unlike the MCA period, the current regime is characterized by a biogeochemically distinct group of cyanobacteria, the N_2-fixing diazotrophs. Historically, the availability of inorganic nitrogen (N) and/or phosphorus (P) was thought to limit plankton production in the NPSG (*21*). Since ~1850 CE, however, sea surface temperatures have increased, accompanied by a likely decrease in the trade winds concomitant with gyre expansion, as a result of Northern Hemisphere warming. The resulting increase in stratification and decrease in nutrient availability may have selected for a N_2-fixing cyanobacterial community, as observed in the instrumental record over

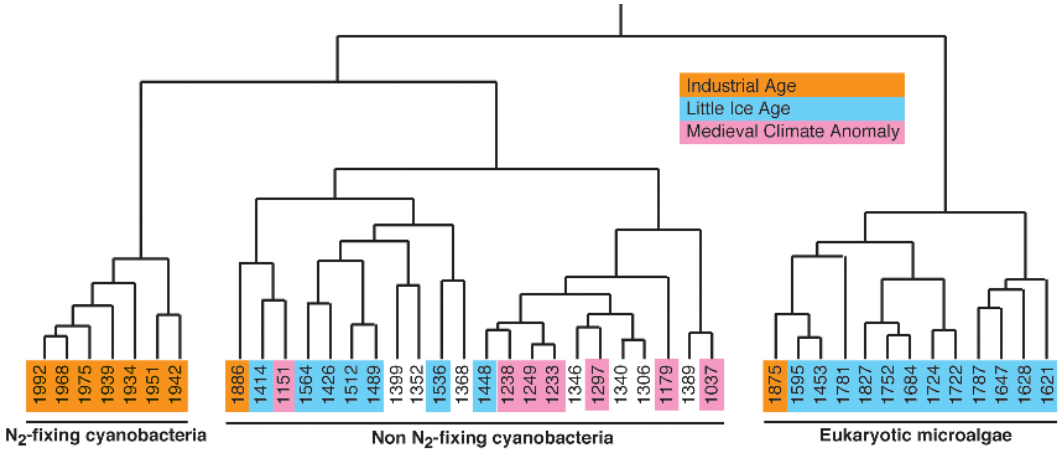

Fig. 4. Phytoplankton regime shifts recorded in deep-sea corals. Shown is a dendrogram of similarity in exported plankton carbon utilized by deep-sea corals over the past 1000 years, based on an average-link hierarchical cluster analysis. The dendrogram is separated into three significantly different clusters according to multiscale bootstrapping with approximately unbiased *P* values >0.95. The dates (CE) are colored based on overlap with well-known Northern Hemisphere climate phenomena (*18*).

the past ~20 years (*2*, *22*). Currently declining P inventories and increasing N:P ratios in the mixed layer at the HOT-ALOHA (Hawaiian Ocean Time-series–A Long-Term Oligotrophic Habitat Assessment) oceanographic station are thought to reflect this decades-long increase in N_2 fixation (*1*, *2*, *8*), an idea that is further supported by recent literature suggesting that canonical Redfield ratios in the NPSG may be more plastic than previously realized (*23*, *24*).

Our $\delta^{13}C_{EAA}$ fingerprinting data, which show a 47% increase in N_2-fixing cyanobacteria carbon in exported POM since the end of the LIA, correspond well with recent evidence of a 17 to 27% increase in NPSG N_2-fixation since ~1850 CE, determined from amino acid–specific nitrogen isotopes ($\delta^{15}N_{AA}$) in the same suite of *K. haumeaae* specimens as used in this study (*8*). These studies represent fully independent lines of evidence supporting the hypothesis that recent decreases in $\delta^{15}N_{bulk}$ values of exported POM in the NPSG are related to increases in diazotrophic plankton within a microbial loop–driven system (*11*).

By offering the first direct phylogenetic context for long-term shifts in isotopic records of exported POM, our data provide a major new constraint in understanding the evolution of NPSG biogeochemistry. For example, a recently proposed alternate hypothesis contends that advection of ^{15}N-depleted nitrate from the Eastern Tropical Pacific, associated with a reduction in denitrification (*25*), might explain recent low $\delta^{15}N$ values in the NPSG; similarly, Kim *et al.* (*26*) suggested that atmospheric N deposition is the dominant factor driving increases in values of N* (a nitrate- and phosphate-based tracer of N_2 fixation and denitrification) across the Pacific. However, the $\delta^{15}N$ value of N entrained in the mixed layer should not, by itself, affect planktonic community structure. Our new evidence for a profound phylogenetic community shift is fully consistent with increasing N_2 fixation, probably linked to overall increased stratification and reductions in upwelled nitrate, over the past 100 years.

Taken together, our data show that phytoplankton community structure in the NSPG is subject to multicentennial shifts that are broadly linked to climate conditions. They also reveal that the present-day cyanobacterial community, which is characterized by strongly enhanced N_2 fixation, is unprecedented within at least the past 1000 years. The transition to the current cyanobacterial regime (<200 years) was much faster than the transition from cyanobacterial dominance during the MCA to eukaryotic dominance during the LIA (>600 years). Both the nature and the rate of change of the current dominant autotrophic assemblage strongly suggest continuing rapid changes in NPSG plankton community structure associated with anthropogenic climate change and are consistent with the predicted expansion of N_2-fixing cyanobacteria habitat (*27*).

Regime shifts in plankton community composition have far-reaching implications for productivity, food-web dynamics, biogeochemical cycling, and the efficacy of the biological pump (*22*, *28*, *29*). The fact that dominant cyanobacterial signatures were recorded in deep-sea corals from the mesopelagic zone strongly suggests that continuing shifts to an N_2-fixing prokaryotic regime have fundamentally altered the main sources of exported POM. These observations also support recent evidence (*3*, *30*) that small-cell picoplankton production, free-living and/or in cyanobacteria-diatom symbioses (*11*, *22*), may be a more important component of export production in oligotrophic gyres than traditionally recognized. Further, recent studies have shown that plankton elemental stoichiometry is more variable than previously assumed under the classical Redfield paradigm, with C:P ratios being several times higher in the oligotrophic gyres than in upwelling regions (*23*, *24*). This suggests that carbon export could actually be more efficient (per mole of P) in the oligotrophic gyres, despite their lower overall productivity, and, furthermore, that increasing nutrient limitation in warmer and more stratified oceans over the past 100 years may have served as a major negative feedback on rising CO_2 concentrations (*23*, *24*). Our finding that the phylogenetic origin of export production in the NPSG has trended toward N_2-fixing prokaryotes over the past century strongly supports this idea. If small-cell export does in fact act as a more efficient carbon pump, our new records suggest that this carbon cycle feedback has already been operating for the past 100 years. For this feedback loop to persist into the future, the system cannot become phosphate-limited.

REFERENCES AND NOTES

1. D. M. Karl, *Ecosystems* **2**, 181–214 (1999).
2. D. M. Karl, R. R. Bidigare, R. M. Letelier, *Deep Sea Res. Part II Top. Stud. Oceanogr.* **48**, 1449–1470 (2001).
3. T. L. Richardson, G. A. Jackson, *Science* **315**, 838–840 (2007).
4. J. E. Dore, R. M. Letelier, M. J. Church, R. Lukas, D. M. Karl, *Prog. Oceanogr.* **76**, 2–38 (2008).
5. G. C. Hays, A. J. Richardson, C. Robinson, *Trends Ecol. Evol.* **20**, 337–344 (2005).
6. J. J. Polovina, E. A. Howell, M. Abecassis, *Geophys. Res. Lett.* **35**, L03618 (2008).
7. T. P. Guilderson, M. D. McCarthy, R. B. Dunbar, A. Englebrecht, E. B. Roark, *Biogeosciences* **10**, 6019–6028 (2013).
8. O. A. Sherwood, T. P. Guilderson, F. C. Batista, J. T. Schiff, M. D. McCarthy, *Nature* **505**, 78–81 (2014).
9. R. J. Francey *et al.*, *Tellus B Chem. Phys. Meteorol.* **51**, 170–193 (1999).
10. P. Quay, R. Sonnerup, T. Westby, J Stutsman, A. McNichol, *Global Biogeochem. Cycles* **17**, 4-1–4-20 (2013).
11. Materials and methods are available as supplementary materials on *Science* Online.
12. J. H. Scott *et al.*, *Astrobiology* **6**, 867–880 (2006).
13. T. Larsen *et al.*, *PLOS ONE* **8**, e73441 (2013).
14. K. W. McMahon, L.-L. Hamady, S. R. Thorrold, *Oceanogr. Mar. Biol. Annu. Rev.* **51**, 327–374 (2013).
15. J. T. Schiff *et al.*, *Mar. Chem.* **166**, 82–91 (2014).
16. T. Larsen *et al.*, *Biogeosciences* **12**, 4979–4992 (2015).
17. R. Scharek, M. Latasa, D. M. Karl, R. R. Bidigare, *Deep Sea Res. Part I Oceanogr. Res. Pap.* **46**, 1051–1075 (1999).
18. M. E. Mann *et al.*, *Science* **326**, 1256–1260 (2009).
19. V. Trouet *et al.*, *Science* **324**, 78–80 (2009).
20. G. Corno *et al.*, *J. Geophys. Res.* **112**, C04021 (2007).
21. R. W. Eppley, E. H. Renger, E. L. Venrick, M. M. Mullin, *Limnol. Oceanogr.* **18**, 534–551 (1973).
22. D. M. Karl, M. J. Church, J. E. Dore, R. M. Letelier, C. Mahaffey, *Proc. Natl. Acad. Sci. U.S.A.* **109**, 1842–1849 (2012).
23. A. C. Martiny *et al.*, *Nat. Geosci.* **6**, 279–283 (2013).
24. Y. C. Teng, F. W. Primeau, J. K. Moore, M. W. Lomas, A. C. Martiny, *Nat. Geosci.* **7**, 895–898 (2014).
25. C. Deutsch *et al.*, *Science* **345**, 665–668 (2014).
26. I. N. Kim *et al.*, *Science* **346**, 1102–1106 (2014).

27. P. Flombaum *et al.*, *Proc. Natl. Acad. Sci. U.S.A.* **110**, 9824–9829 (2013).
28. P. G. Falkowski, R. T. Barber, V. Smetacek, *Science* **281**, 200–206 (1998).
29. P. W. Boyd, P. P. Newton, *Deep Sea Res. Part I Oceanogr. Res. Pap.* **46**, 63–91 (1999).
30. H. G. Close *et al.*, *Proc. Natl. Acad. Sci. U.S.A.* **110**, 12565–12570 (2013).

ACKNOWLEDGMENTS

All methods, additional figures, and source data are available in the supplementary materials. K.W.M., T.P.G., and M.D.M. conceived the project. K.W.M. prepared samples, performed bulk and compound-specific $\delta^{13}C$ analyses, and wrote the manuscript. O.A.S. and T.L. assisted in data analysis and commented on the manuscript. T.P.G. and M.D.M. supervised this project, discussed the results, and commented on the manuscript. We thank M. Hanson, S. Fauqué, and J. Liu for assistance in the laboratory. This work would not have been possible without the captain and crew of the research vessel *Ka'imikai-o-Kanaloa* and the pilots and engineers of the Hawaii Undersea Research Laboratory's Pisces IV and V submersibles. We also thank three anonymous reviewers for valuable feedback on the manuscript. Funding for sample collection was provided by the National Oceanic and Atmospheric Administration's National Undersea Research Program and the National Geographic Society (grant 7717-04). A portion of this work was performed under the auspices of the U.S. Department of Energy (grant DE-AC52-07NA27344). The majority of the work presented here was funded by NSF (grant OCE-1061689). T.L. was supported by The Future Ocean, a program funded by the German Research Foundation.

SUPPLEMENTARY MATERIALS

www.sciencemag.org/content/350/6267/1530/suppl/DC1
Materials and Methods
Figs. S1 and S2
Tables S1 and S2
References (*31*–*68*)

25 February 2015; accepted 6 November 2015
Published online 26 November 2015
10.1126/science.aaa9942

MARINE CALCIFERS

Multidecadal increase in North Atlantic coccolithophores and the potential role of rising CO_2

Sara Rivero-Calle,[1,2]* Anand Gnanadesikan,[1]* Carlos E. Del Castillo,[1,3] William M. Balch,[4] Seth D. Guikema[5]

As anthropogenic carbon dioxide (CO_2) emissions acidify the oceans, calcifiers generally are expected to be negatively affected. However, using data from the Continuous Plankton Recorder, we show that coccolithophore occurrence in the North Atlantic increased from ~2 to more than 20% from 1965 through 2010. We used random forest models to examine more than 20 possible environmental drivers of this change, finding that CO_2 and the Atlantic Multidecadal Oscillation were the best predictors, leading us to hypothesize that higher CO_2 levels might be encouraging growth. A compilation of 41 independent laboratory studies supports our hypothesis. Our study shows a long-term basin-scale increase in coccolithophores and suggests that increasing CO_2 and temperature have accelerated the growth of a phytoplankton group that is important for carbon cycling.

Marine organisms that produce external features made of calcium carbonate are susceptible to harmful consequences from ocean acidification (*1*). Coccolithophores, the main calcifying phytoplankton, are unicellular algae surrounded by calcite plates called coccoliths, whose photosynthesis is strongly carbon-limited (*2*). Coccoliths are a major source of oceanic particulate inorganic carbon (PIC) and serve as ballast for sinking aggregates (*3*), thus accelerating carbon export (*4*). Given increasing partial pressures of atmospheric CO_2 (pCO_2), global warming, and ocean acidification, it is expected that coccolithophores will be affected, producing concomitant effects on ocean carbon fluxes, dimethyl sulfide fluxes (*5*), carbonate geochemistry (*6*), and phytoplankton community structure (*6*). Current evidence regarding how increased pCO_2 will affect coccolithophores is contradictory (*7*–*10*). Most laboratory manipulations study how coccolithophores respond to the increased pCO_2 levels predicted for the end of the century rather than to the CO_2 changes observed in the past five decades.

Here, we report changes in the occurrence of coccolithophores in the North Atlantic during the past 45 years and use random forest (RF) statistical models to evaluate the importance of various environmental drivers for these changes.

The in situ Continuous Plankton Recorder (CPR) surveys were developed to sample plankton in the North Atlantic using ships of opportunity. The surveys have followed the same methodology since 1946 (*11*). Sample preservation methods (using Borax-buffered formalin) and analysis have remained unchanged since 1958 (*12*), producing a unique, consistent, multidecadal data set. Although the CPR filtering system was designed to sample larger microplankton, coccolithophores are trapped, particularly in the intersection of the silk fibers (*12*). It is not possible to accurately quantify organisms that are smaller than the mesh size, but we can use the data set to estimate the probability of coccolithophore occurrence. Although our sampling underestimates natural abundances, this probability is a proxy for changes in coccolithophore abundance (fig. S1).

We calculated the annual probability of coccolithophore occurrence as the fraction of samples per year containing coccolithophores. The CPR data show an increase in occurrence of coccolithophores across the North Atlantic from ~2% of samples in the 1960s to more than 20% of samples with coccolithophores in the 2000s (Fig. 1, A to F, and fig. S2). Regional abundances of coccolithophores in the 2000s are at least 10 times higher than those observed at the beginning of the data record. Our observations are supported by a shift in the opal:carbonate ratio in sediment traps in the Atlantic from the 1990s (*13*), satellite evidence of global poleward expansion of *Emiliania huxleyi* (*14*), and recurring blooms in areas where coccolithophores were previously absent or sparse (*14*–*17*).

To evaluate possible top-down and bottom-up drivers for the increase in coccolithophore occurrence in the North Atlantic, we investigated factors that could affect coccolithophore growth rates and biogeography. Temperature, nutrient availability, light levels, competition, and predation are critical on a local scale. In turn, these may be affected by large-scale processes such as climate modes, global warming, and increases in CO_2. The CPR sampling survey is irregular in time and space, making classic time series analysis inappropriate for this data set. Additionally, the effects of different environmental forcings on phytoplankton groups are nonlinear and interdependent. After evaluating a suite of statistical methods (see the supplementary materials), we selected RF models (*18*), an increasingly popular method in ecology that characterizes structure in high dimensional data while making no distributional assumptions about the response variable or predictors. RF has the advantage of allowing for nonlinearities, geographically and temporally discontinuous data, and the ability to model complex interactions among predictor variables without overfitting the data.

Our RF model predicted the probability of coccolithophore occurrence, defined as the percentage of samples containing coccolithophores in a 1°-by-1° area each month, as a function of more than 20 biological and physical predictors. Because the CPR data set is already complex and discontinuous, we only used in situ measurements of biological and physical parameters without interpolating data. The complete data set included 81,340 observations from 1965 to 2010. The importance of each variable in predicting coccolithophore

[1]Department of Earth and Planetary Sciences, The Johns Hopkins University, Baltimore, MD, USA. [2]Applied Physics Laboratory, The Johns Hopkins University, Baltimore, MD, USA. [3]Goddard Space Flight Center, National Aeronautics and Space Administration, Greenbelt, MD, USA. [4]Bigelow Laboratory for Ocean Sciences, East Boothbay, ME, USA. [5]Department of Industrial and Operations Engineering, The University of Michigan, Ann Arbor, MI, USA.
*Corresponding author. E-mail: sara.rivero@jhu.edu (S.R.-C.); gnanades@jhu.edu (A.G.)

occurrence is ranked in a variable importance plot. Importance is measured as the percentage increase of mean squared error (MSE) in the prediction due to that variable. Partial dependence plots graphically represent the marginal effect of each variable on the response variable. Here, we discuss the top predictors and how these could have driven the observed increase in coccolithophore occurrence.

The evaluation of CO_2 as a driver for observed increases in coccolithophore occurrence required special attention. Although pCO_2 and CPR data were not collected simultaneously, there is information about spatial and long-term CO_2 variability. We created three random forest models, each with a different predictor for pCO_2: (i) global pCO_2, estimated from Mauna Loa, which varies only in time ("Global_pCO_2" variable in the RF_GLOBAL model); (ii) climatological ΔpCO_2, from Takahashi *et al.* (*19*), which has no interannual variability ("delta_pCO_2" variable in the RF_CLIM model); and (iii) local pCO_2, estimated as the sum of the Mauna Loa and Takahashi data set varying in time and space ("Local_pCO_2" variable in the RF_LOCAL model). Local pCO_2 in the North Atlantic can be lower than the global atmospheric pCO_2 by 100 parts per million (ppm) in certain months (fig. S3).

Local and global pCO_2 were the best predictors of coccolithophore occurrence in our RF models (Fig. 2, A and B). In the RF_GLOBAL analysis, the partial dependence plot shows low coccolithophore occurrence (3 to 5%) at pCO_2 ranges between 320 and 360 ppm. This corresponds to atmospheric CO_2 observed at Mauna Loa from 1960 to ~1996. The increase in coccolithophore probability accelerated at $pCO_2 > 370$ ppm (~1997), reaching 22% at 400 ppm. In the RF_LOCAL model (Fig. 2, B and E, and fig. S4), the partial dependence plot shows a threefold range, with the largest coccolithophore probabilities corresponding to the highest CO_2 values. Maximum probabilities of finding coccolithophores coincided at global and local CO_2 levels above 360 ppm (Fig. 2, D and E). As discussed below, such dependence falls within the envelope of laboratory responses of coccolithophore growth rates to increased CO_2.

Within RF_CLIM, the climatological "delta_pCO_2" variable is not a strong predictor (Fig. 2, C and F). Instead, the Atlantic Multidecadal Oscillation (AMO) becomes the top predictor in this model, and other climate modes [Arctic Oscillation (AO) and Multivariate ENSO Index (MEI)] rise in their ranking relative to RF_LOCAL and RF_GLOBAL, reflecting the importance of interannual variability. Recent studies have linked the AMO with phytoplankton (*20*) and coccolithophore variability (*15*). The AMO index tracks temperature anomalies in the North Atlantic, and its positive trend in recent decades could mask global warming or enhance CO_2 effects (Fig. 3). AMO ranked 13th in the RF_GLOBAL model, second in RF_LOCAL, and first in the RF_CLIM analyses (Fig. 2, A to C, respectively). We propose two explanations: Either AMO has a true effect on coccolithophore

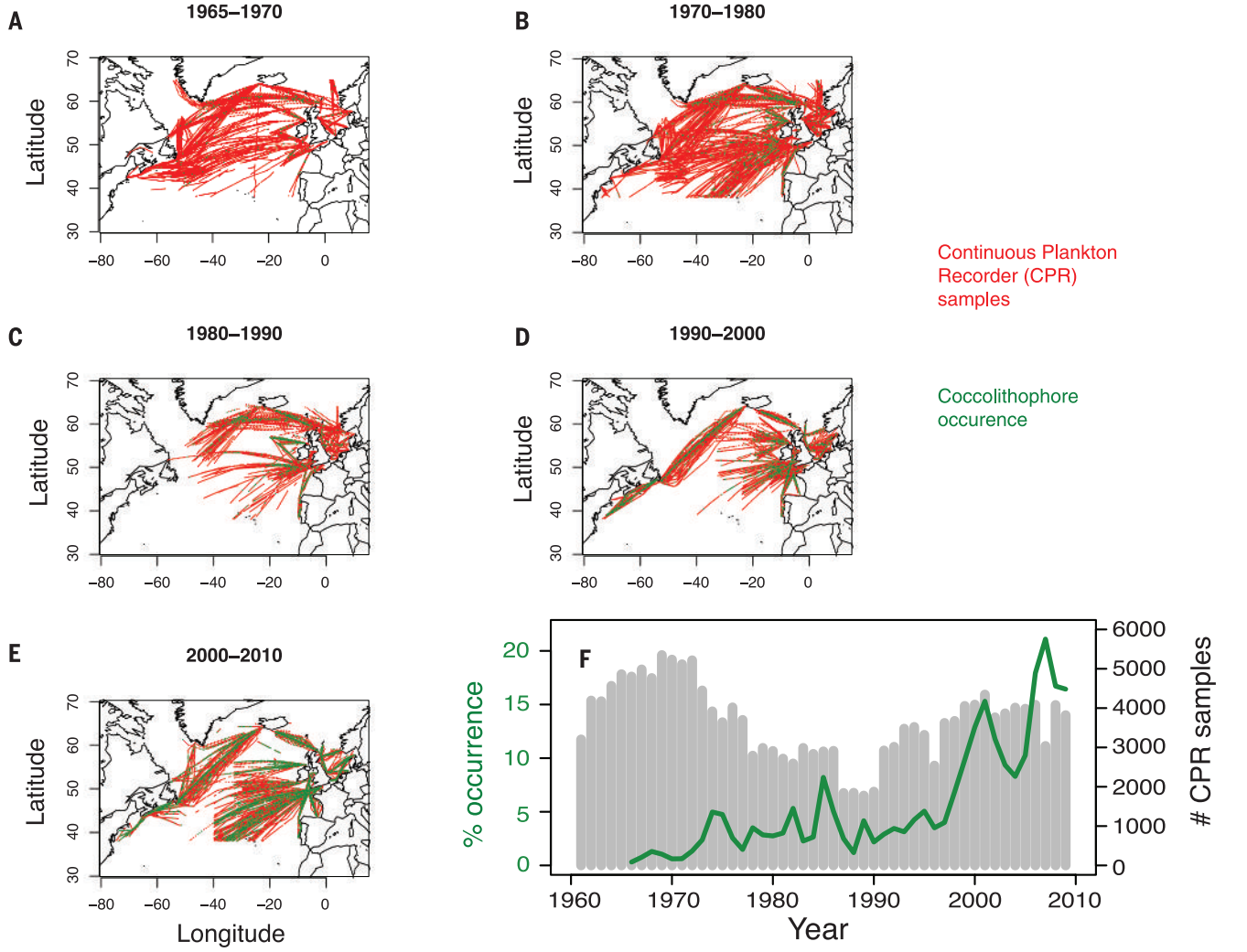

Fig. 1. Distribution of CPR samples (red) and coccolithophore observations (green) per decade. (**A**) 1960s, (**B**) 1970s, (**C**) 1980s, (**D**) 1990s, (**E**) 2000s, and (**F**) comparison of annual sampling effort (total number of samples per year in the North Atlantic) versus average probability of coccolithophore occurrence in raw data (sum of samples with coccolithophore records per year/total number of samples per year × 100). Each sample corresponds to observations found in 10 cm of CPR silk (or ~3 m^3 of water).

abundance or, in the absence of "global CO_2" or "local CO_2," AMO is the only other variable with a similar long-term trend in the past two decades (Fig. 3). The highest coccolithophore probabilities are found during the recent positive AMO phases (Fig. 2G). If the coccolithophore increase were due to positive AMO, their occurrence should have been high during previous positive phases—i.e., the 1960s (Fig. 3). Unfortunately, the scarce information before 1965 limits our ability to draw strong conclusions, but, based on the variability explained and the ranking in partial dependence plots (Fig. 2, A to G), we propose that AMO could be an important secondary driver. AMO has been related to changes in the Meridional Overturning Circulation that would alter nutrient supply (*21*). Positive AMO periods are associated with greater upward transport of nutrients in convective regions but lower upward transport elsewhere. If AMO were the only mechanism responsible for the coccolithophore increase, it would be expected to produce opposite effects in the northwestern and eastern regions. Instead, all regions show increasing trends (fig. S2).

We hypothesize that synergistic effects due to CO_2, AMO, and global warming differentially accelerated coccolithophore growth rates, driving recent increases in their occurrence. Compared to other phytoplankton groups, coccolithophore photosynthesis is severely carbon-limited (*2*), and sedimentary records show a predominance of coccolithophores during warm interglacial (*22*) and high CO_2 periods (*23*). Many studies agree that coccolithophores respond to an increase in CO_2 by decreasing PIC and increasing particulate organic carbon (POC), but there is disagreement with respect to the effects on growth rates (see the supplementary materials). We assembled a compendium of published growth rates as a function of CO_2 (41 laboratory experiments from 16 independent publications) (Fig. 4, fig. S5, and supplementary materials). Results show a quasi-hyperbolic increase in coccolithophore growth rates with pCO_2, with scatter partly produced by differences in experimental treatments: temperature, species, strain, nutrients, and irradiance. Our local pCO_2 estimates between 1965 and 2010 (blue box in Fig. 4) correspond to the ranges in pCO_2 where, based on Fig. 4, we would expect changes in coccolithophore growth rates. This compilation reconciles previous contradictory conclusions on the effects of CO_2 on coccolithophore growth rates (supplementary materials), buttressing our hypothesis that CO_2 enhances coccolithophore growth. Additional RF analyses of other top-down and bottom-up processes (e.g., grazing, nutrients, and temperature) are included in the supplementary materials.

To project future coccolithophore abundances under elevated CO_2 levels, we need to reassess the baseline. Our results show that today's numbers are an order of magnitude greater than those in the 1960s and will likely continue to increase before growth rates stabilize at ~500 ppm. This is critical for understanding changes in the export ratio, biological pump, and alkalinity pump. Our compilation suggests that the changes seen

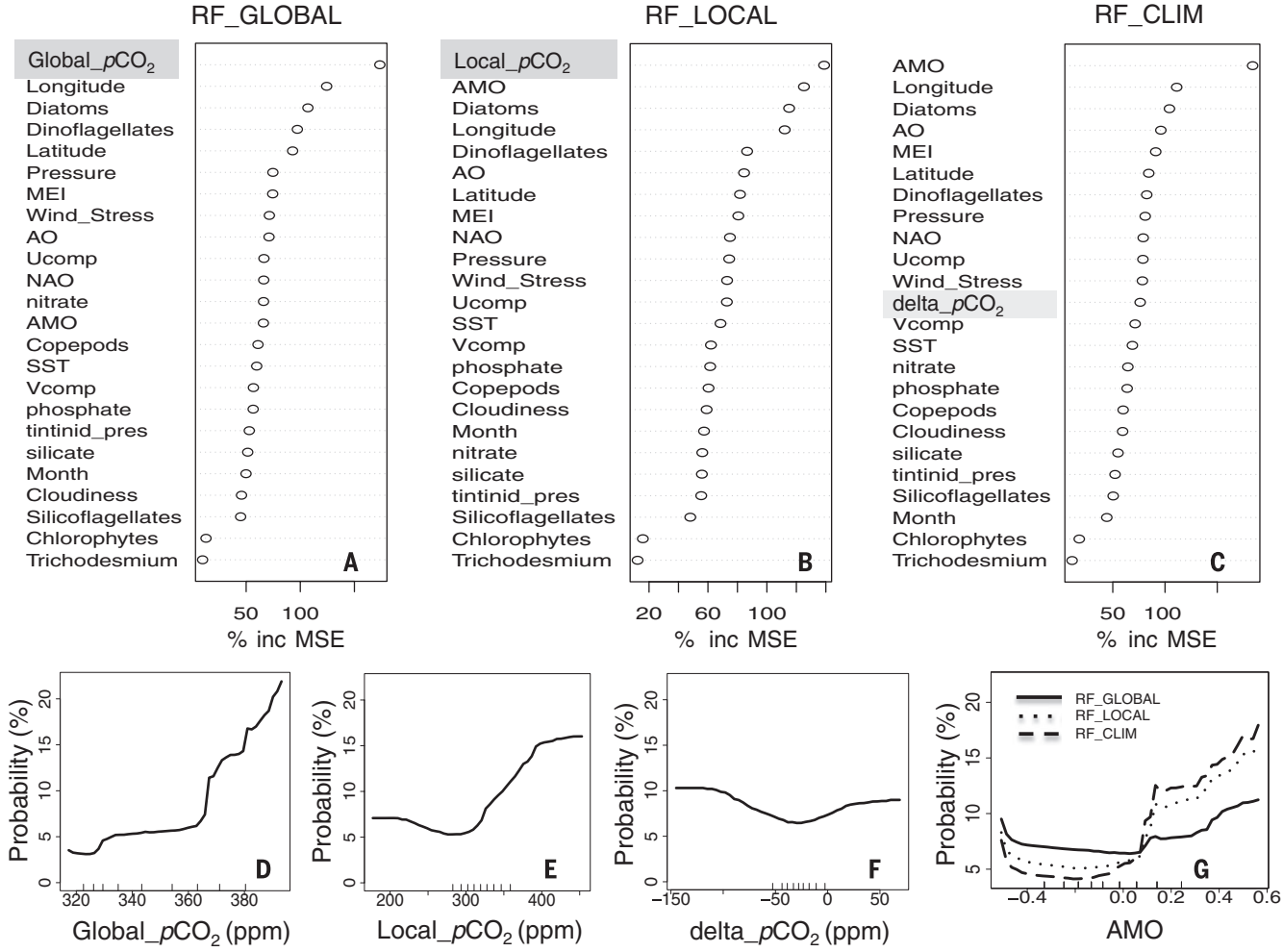

Fig. 2. RF analyses. (**A** to **C**) Variable importance plots for RF_GLOBAL, RF_LOCAL, and RF_CLIM models, respectively. A large increase in percentage MSE (%inc MSE) means that a variable is a better predictor of coccolithophore occurrence). Boxes highlight the ranking of CO_2 parameters within each model. This is the marginal effect of the predictor on coccolithophore probability. (**D** to **F**) Partial dependence plots for CO_2 parameters in RF_GLOBAL, RF_LOCAL, and RF_CLIM models, respectively. (**G**) Partial dependence plot for AMO, based on the probability of coccolithophore occurrence in each of the RF models. Global_pCO_2, atmospheric pCO_2 based on Mauna Loa records; delta_pCO_2, climatological ΔpCO_2 (*19*); local_pCO_2, estimate of local pCO_2 based on the sum of spatial and long-term trends. U and Vcomp, zonal and meridional wind components; SST, sea surface temperature; tintinnid_pres, tintinnid occurrence.

Fig. 3. Long-term trends. (**A**) Annual basin-averaged coccolithophore probability in CPR samples (sum of samples with coccolithophore records per year/total number of samples per year x 100). (**B**) Global atmospheric CO_2 measured from Mauna Loa. (**C**) AMO. (**D** and **E**) Annual mean basin-averaged diatom and dinoflagellate counts in CPR samples per year. Vertical lines marking years 1965 and 1997 are included for reference.

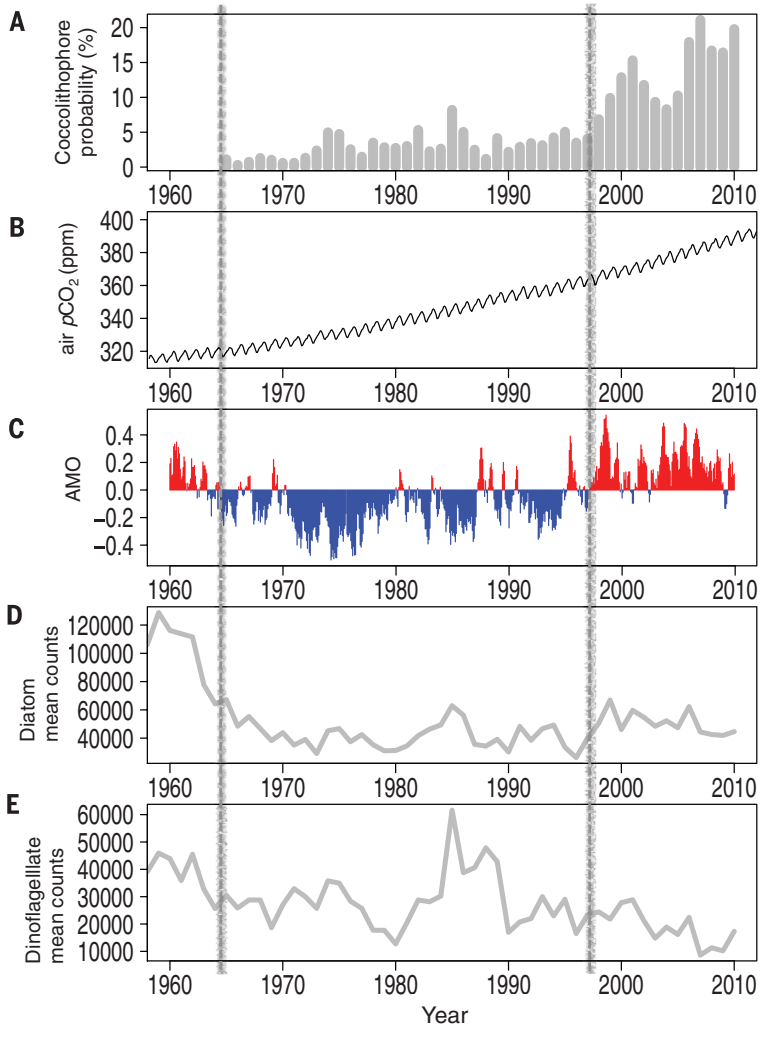

Fig. 4. Relationship between CO_2 and coccolithophore growth rates based on 41 experiments from 16 publications and four species (details in the supplementary materials). Results are binned in 50-ppm intervals, with minimum, quartiles, median, and maximum per interval used to construct box-and-whisker plots. Discontinuous lines represent schematic boundaries of this relationship depending on irradiance, nutrient, and temperature levels. Blue box, range of local oceanic pCO_2 values observed across the North Atlantic during this time period; red arrow, corresponding global atmospheric range.

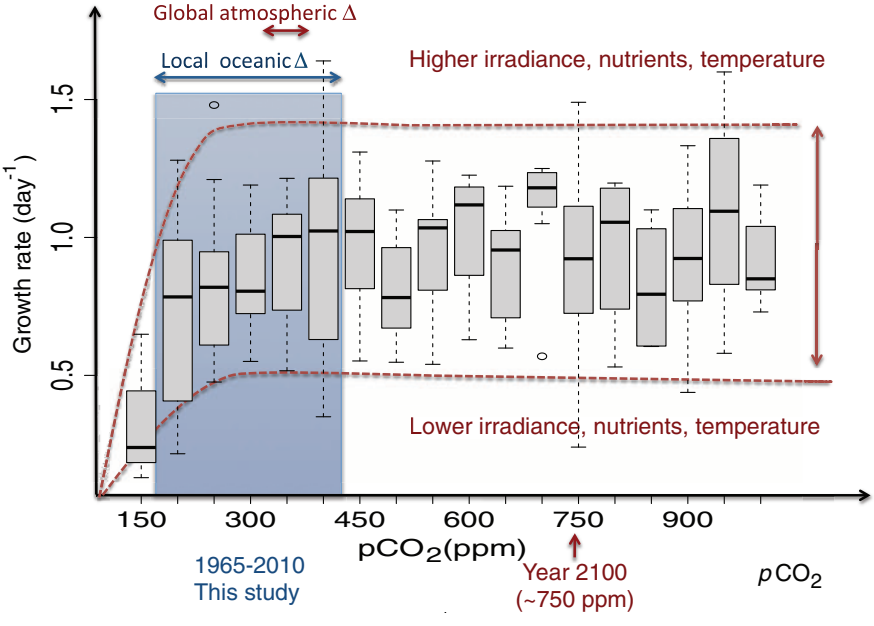

in the North Atlantic may represent a global trend. Contrary to the generalized assumption of negative effects of ocean acidification on calcifiers, coccolithophores may be capable of adapting to a high-CO_2 world (*24*), especially given evidence of highly calcified coccolithophores in areas with seasonally high pCO_2 or low pH (*7*, *8*). Coccolithophores show outstanding competitive abilities under the stratified, warm, nutrient-depleted conditions projected for the future ocean (*6*). Nevertheless, with increasing pCO_2, we might expect changes in community composition and a decrease in calcification, leading to changes in rain ratio, export efficiency, and trophic effects higher in the marine food web.

REFERENCES AND NOTES

1. J. C. Orr *et al.*, *Nature* **437**, 681–686 (2005).
2. B. Rost, U. Riebesell, S. Burkhardt, D. Sultemeyer, *Limnol. Oceanogr.* **48**, 55–67 (2003).
3. R. Francois, S. Honjo, R. Krishfield, S. Manganini, *Global Biogeochem. Cycles* **16**, 34-1–34-20 (2001).
4. R. A. Armstrong, C. Lee, J. I. Hedges, S. Honjo, S. G. Wakeham, *Deep Sea Res. Part II Top. Stud. Oceanogr.* **49**, 219–236 (2002).
5. P. Matrai, M. Vernet, P. Wassmann, *J. Mar. Syst.* **67**, 83–101 (2007).
6. B. Rost, U. Riebesell, Coccolithophores and the biological pump: Responses to environmental changes, in *Coccolithophores: From Molecular Processes to Global Impact*, H. R. Thierstein, J. R. Young, Eds. (Springer, 2004), pp. 99–125.
7. L. Beaufort *et al.*, *Nature* **476**, 80–83 (2011).
8. H. E. K. Smith *et al.*, *Proc. Natl. Acad. Sci. U.S.A.* **109**, 8845–8849 (2012).
9. M. D. Iglesias-Rodriguez *et al.*, *Science* **320**, 336–340 (2008).
10. U. Riebesell, A. Körtzinger, A. Oschlies, *Proc. Natl. Acad. Sci. U.S.A.* **106**, 20602–20609 (2009).
11. A. J. Richardson *et al.*, *Prog. Oceanogr.* **68**, 27–74 (2006).
12. G. C. Hays, A. J. Warner, A. W. G. John, D. S. Harbour, P. M. Holligan, *J. Mar. Biol. Assoc. U. K.* **75**, 503–506 (1995).
13. A. N. Antia *et al.*, *Global Biogeochem. Cycles* **15**, 845–862 (2001).
14. A. Winter, J. Henderiks, L. Beaufort, R. E. M. Rickaby, C. W. Brown, *J. Plankton Res.* **36**, 316–325 (2014).
15. E. K. Hovland, H. M. Dierssen, A. S. Ferreira, G. Johnsen, *Mar. Ecol. Prog. Ser.* **484**, 17–32 (2013).
16. T. J. Smyth, T. Tyrrell, B. Tarrant, *Geophys. Res. Lett.* **31**, L11302 (2004).
17. J. C. Cubillos *et al.*, *Mar. Ecol. Prog. Ser.* **348**, 47–54 (2007).
18. L. Breiman, *Mach. Learn.* **45**, 5–32 (2001).
19. T. Takahashi *et al.*, *Deep Sea Res. Part I Oceanogr. Res. Pap.* **56**, 2075–2076 (2009).
20. M. Edwards, G. Beaugrand, P. Helaouët, J. Alheit, S. Coombs, *PLOS ONE* **8**, e57212 (2013).
21. A. Gnanadesikan, J. P. Dunne, R. Msadek, *J. Mar. Syst.* **133**, 39–54 (2014).
22. A. McIntyre, A. W. H. Be, *Deep-Sea Res.* **14**, 561 (1967).
23. B. Hannisdal, J. Henderiks, L. H. Liow, *Glob. Change Biol.* **18**, 3504–3516 (2012).
24. K. T. Lohbeck, U. Riebesell, T. B. H. Reusch, *Nat. Geosci.* **5**, 346–351 (2012).

ACKNOWLEDGMENTS

We thank D. Johns, the Sir Alister Hardy for Ocean Science (SAHFOS) Associated External Researcher fund, and everyone involved in the CPR survey. We thank the Johns Hopkins University and the Applied Physics Laboratory for financial support and B. Zaitchik, D. Waugh, J. Dunne, and three anonymous reviewers for helpful comments. Funding for S.D.G. was from NSF-1149460. Support for W.B. came from NSF (Division of Ocean Sciences) and NASA (Ocean Biology and Biogeochemistry Program). CPR data used in this study can be obtained from SAHFOS upon request.

SUPPLEMENTARY MATERIALS

www.sciencemag.org/content/350/6267/1533/suppl/DC1
Materials and Methods
Supplementary Text
Figs. S1 to S7
Table S1
References (*25*–*47*)

30 January 2015; accepted 11 November 2015
Published online 26 November 2015
10.1126/science.aaa8026

PALEOCEANOGRAPHY

Dynamical excitation of the tropical Pacific Ocean and ENSO variability by Little Ice Age cooling

Gerald T. Rustic,[1,2]*† Athanasios Koutavas,[1,2,3] Thomas M. Marchitto,[4] Braddock K. Linsley[3]

Tropical Pacific Ocean dynamics during the Medieval Climate Anomaly (MCA) and the Little Ice Age (LIA) are poorly characterized due to a lack of evidence from the eastern equatorial Pacific. We reconstructed sea surface temperature, El Niño–Southern Oscillation (ENSO) activity, and the tropical Pacific zonal gradient for the past millennium from Galápagos ocean sediments. We document a mid-millennium shift (MMS) in ocean-atmosphere circulation around 1500–1650 CE, from a state with dampened ENSO and strong zonal gradient to one with amplified ENSO and weak gradient. The MMS coincided with the deepest LIA cooling and was probably caused by a southward shift of the intertropical convergence zone. The peak of the MCA (900–1150 CE) was a warm period in the eastern Pacific, contradicting the paradigm of a persistent La Niña pattern.

The tropical Pacific Ocean exerts a major influence on global climate through the interannual El Niño–Southern Oscillation (ENSO) (*1*) and Pacific Decadal Oscillation (PDO) (*2*). However, its role on centennial to millennial time scales remains unclear. Recent evidence that a cool eastern equatorial Pacific (EEP) played a key role in the global warming slowdown of the past ~15 years (*3*, *4*) emphasizes the need to understand tropical Pacific climate in the recent past. During the last millennium, Northern Hemisphere (NH) climate evolved from a warm Medieval Climate Anomaly (MCA) (~900–1450 CE) into a substantially colder Little Ice Age (LIA) (~1450–1850 CE), followed by modern warming (*5*–*7*). In the tropics, the MCA-to-LIA transition exhibited a weakening of the East Asian summer monsoon (*8*, *9*), a southward shift of the Atlantic and Pacific intertropical convergence zones (ITCZs) (*10*, *11*), and sea surface cooling in the western Pacific warm pool (WPWP) (*12*, *13*). Notably absent, however, are contemporaneous records of sea surface temperature (SST) from the ENSO-sensitive and dynamically important cold tongue of the EEP. Without such records, any dynamical connections between basin-scale tropical Pacific processes and NH climate cannot be properly diagnosed.

It has been hypothesized that an "ocean dynamical thermostat" (*14*) response of the EEP to solar and volcanic forcing induced a cool, La Niña–like mean state during the MCA and a warmer, El Niño–like state during the LIA (*6*). This hypothesis has found some support in central Pacific corals (*15*), North American tree rings documenting medieval megadroughts (*16*), and multiproxy climate field reconstructions (*6*). In each of these cases, however, direct confirmation from the EEP has been lacking. Insights into past ENSO variability have also remained elusive and are mostly based on discontinuous corals and remote tree-ring records (*15*–*18*). Here we address these data limitations with climate reconstructions from the heart of the EEP cold tongue. We present continuous, multidecadally resolved estimates of local SST, basin-wide zonal SST gradient, and ENSO activity from Galápagos marine sediments over the period ~1000–2009 CE.

Our primary data sets were developed from an ocean multicore (KNR195-5 MC42C) retrieved in 2009 near Española Island in the Galápagos (01°15.18′S, 89°41.13′W, 615 m depth) (Fig. 1). Undisturbed recovery of the sediment-water interface and detection of bomb radiocarbon confirm that the core top is modern (*19*). Sedimentation rates averaged 13 cm/ky over the past millennium. Detection of a modern 0.3–per mil (‰) carbon isotope ($\delta^{13}C$) depletion, or Suess effect (fig. S9), further corroborates the presence of a modern core top and core integrity and argues against substantial signal attenuation by bioturbation (*19*). The core was slabbed continuously in subcentimeter slices representing ~20- to 80-year periods. We analyzed Mg/Ca ratios of the mixed-layer foraminifera *Globigerinoides ruber* (white) as a proxy for mean SST. We also analyzed $\delta^{18}O_c$ (calcite) of individual *G. ruber* shells (~60 individual *G. ruber* analyses per sample horizon) to quantify population-level $\delta^{18}O_c$ variance related to ENSO activity (*20*, *21*). Benchmark tests comparing modern samples with instrumental data support the use of single-shell $\delta^{18}O_c$ variance ($\delta^{18}O_cV$) as a proxy of the monthly SST variance of the real ocean and further show that large

[1]Department of Engineering Science and Physics, College of Staten Island, City University of New York, Staten Island, NY 10314, USA. [2]Doctoral Program in Earth and Environmental Sciences, Graduate Center of the City University of New York, New York, NY 10016, USA. [3]Lamont–Doherty Earth Observatory of Columbia University, 61 Route 9W, Palisades, NY 10964, USA. [4]Department of Geological Sciences and Institute of Arctic and Alpine Research, University of Colorado, Boulder, CO 80309, USA.
*Corresponding author. E-mail: grustic@ldeo.columbia.edu
†Present address: Lamont–Doherty Earth Observatory of Columbia University, 61 Route 9W, Palisades, NY 10964, USA.

ENSO events are consistently captured by isotopic outliers (*19*).

Our Mg/Ca record reveals systematic changes in eastern Pacific SST of ~1°C (Figs. 2C and 3D). Warm SSTs characterize the peak of the MCA (~900–1150 CE), coeval with NH warmth (Fig. 3C). The timing of this warm period is firmly constrained by a calibrated ^{14}C age at 1139 CE (1108–1172 CE, 1σ range) (Fig. 2). This finding contrasts with a previously hypothesized dynamical La Niña state for the MCA (*6*). To further test this hypothesis, we used reconstructed WPWP SSTs (Fig. 3E) and our Galápagos record to compute the zonal SST gradient. During ~900–1150 CE, the zonal gradient was similar to that of the 20th century. This finding does not support an anomalous La Niña–like state; instead, warm SSTs were generally present during this period in both the east and west, in phase with NH warmth.

After peak MCA warmth, Galápagos SSTs cooled by ~1°C (±0.3°C, 1σ) between ~1150 and ~1500 CE. An anomalous strong zonal SST gradient became established during this period (Fig. 3F), largely due to more rapid cooling in the east versus the west. This enhanced zonal gradient is evidence of dynamical changes in Pacific circulation and supports the notion of a cool, La Niña–like mean state. However, the timing of this anomalous tropical Pacific mean state (~1150–1500 CE, ±30 years, 1σ) postdated peak NH MCA warmth and was instead associated with transitional NH cooling into the LIA. The origin of this dynamical anomaly remains unclear. Volcanic and solar forcing (Fig. 3, A and B) indicate an increase in volcanism in the late 12th century followed by a decrease in solar activity in the 13th century, but overall correlations between these forcings and SSTs are poor. In light of decreasing external forcing, the observed EEP cooling and enhanced zonal gradient are not consistent with an ocean dynamical thermostat mechanism (*6*, *14*).

After ~1500 CE, the EEP cooling trend ended and local SSTs began to increase and become more volatile, signaling a shift in the dynamical character of the EEP (Fig. 3D). Beginning in the 16th century, an anomalous weak zonal gradient was established as the WPWP continued to cool but the EEP trend reversed from cooling to warming (Fig. 3, D to F). This reversal occurred as the NH descended into the coldest portion of the LIA in the 16th and 17th centuries (Fig. 3C) and lasted into the mid-19th century. Throughout most of the LIA, the zonal gradient remained reduced, evoking an extended El Niño–like mean state (*6*). This state appears to have ended with renewed WPWP warming in the early 20th century.

The record of $\delta^{18}O_c$ from single-shell *G. ruber* allows us to test for ENSO modulation in association with the above mean state shifts. Figure 2A shows $\delta^{18}O_c$ measurements of individual shells (n = 1325 shells) from 24 samples spanning the entire past millennium. By virtue of the short foraminiferal life cycle (1 month or less), single-shell $\delta^{18}O_c$ responds to seasonal and interannual signals, the latter of which dominate the tails of the $\delta^{18}O_c$ distribution through the presence or absence of outliers. Explicit identification of ENSO

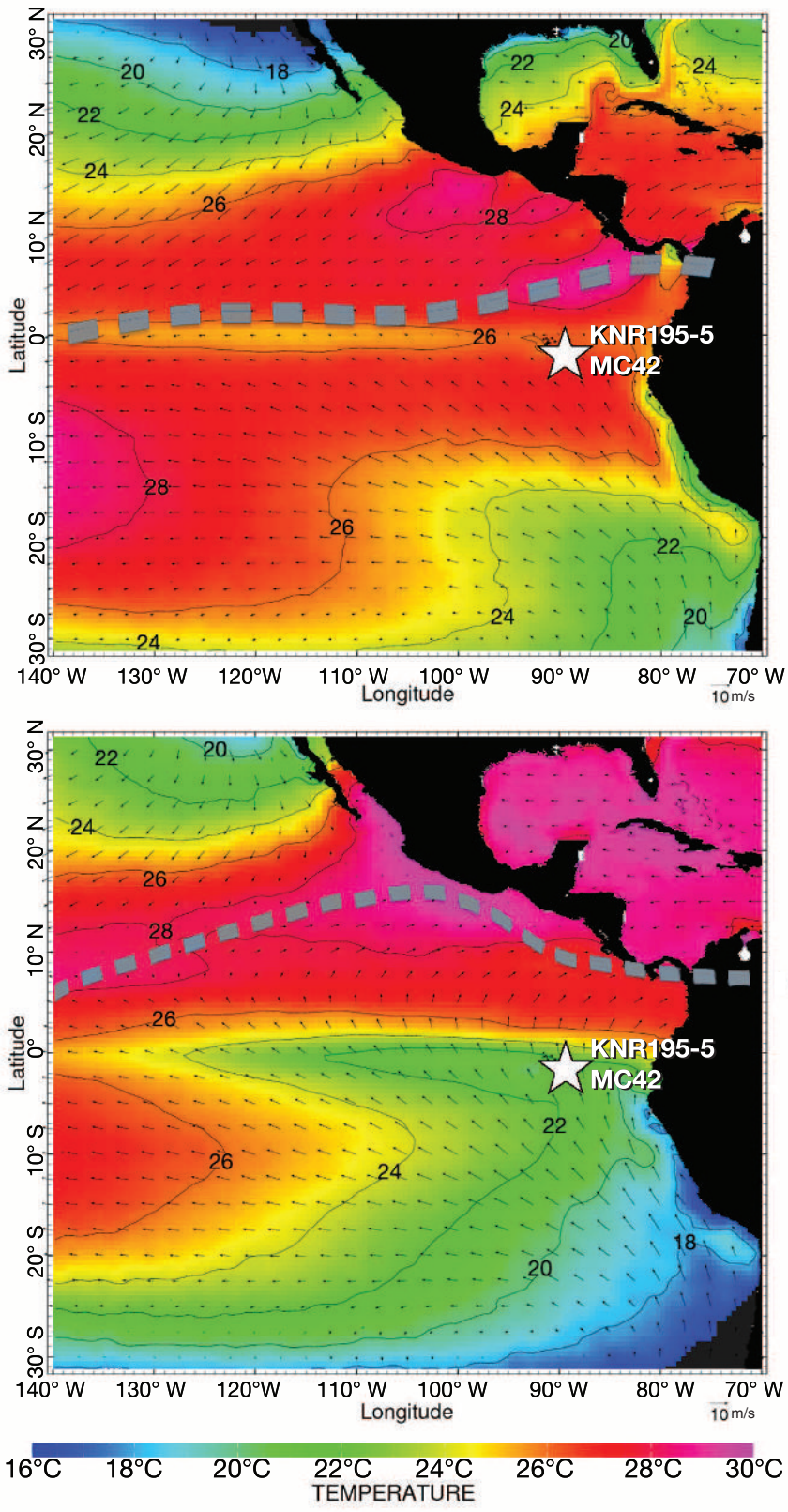

Fig. 1. Average tropical Pacific SST and 1000-mbar winds over the period 1981–2008. (**Top**) Data for March; (**bottom**) data for September. The KNR195-5 MC42 core location is denoted by a white star. Mean SST values are from the Simple Ocean Data Assimilation (SODA) analysis, release 2.1.6 (1981–2008) (*30*); 1000-mbar winds are from the National Oceanic and Atmospheric Administration (NOAA) National Centers for Environmental Prediction–National Center for Atmospheric Research Climate Data Assimilation System (1981–2009) (*31*). The position of the ITCZ is indicated by the gray dashed lines where wind vectors converge.

events in these data is possible only for very strong negative (El Niño) and positive (La Niña) outliers. For example, our data identified strong negative outliers suggestive of the historic El Niños of 1997–1998, 1982–1983, and 1876–1877 (Fig. 2A), although one-to-one correspondence of any of our data with specific events is beyond the method's capability (*19*). For more modest anomalies, however, we can only assign probabilities that they represent ENSO events. To this end, we used historical ENSO events and monthly reanalysis data to calculate that $\delta^{18}O_c$ values exceeding a ±1‰ departure from the mean have a >87% probability of occurring during El Niño and a 100% probability of occurring during La Niña (Fig. 2A) (*19*). The frequency of these high-probability ENSO outliers shows clear modulation through time. For example, warm and cold outliers from the period 1500–1850 CE occurred 2.3 times more frequently than those from the period 1150–1500 CE (normalized to sample size). Bootstrap analysis with varying sample size confirms significant differences in outlier frequency between these two periods (fig. S7). Such high-probability ENSO outliers are the largest driver of the integrated $\delta^{18}O_cV$ signal (Fig. 2B), justifying its interpretation as an ENSO index.

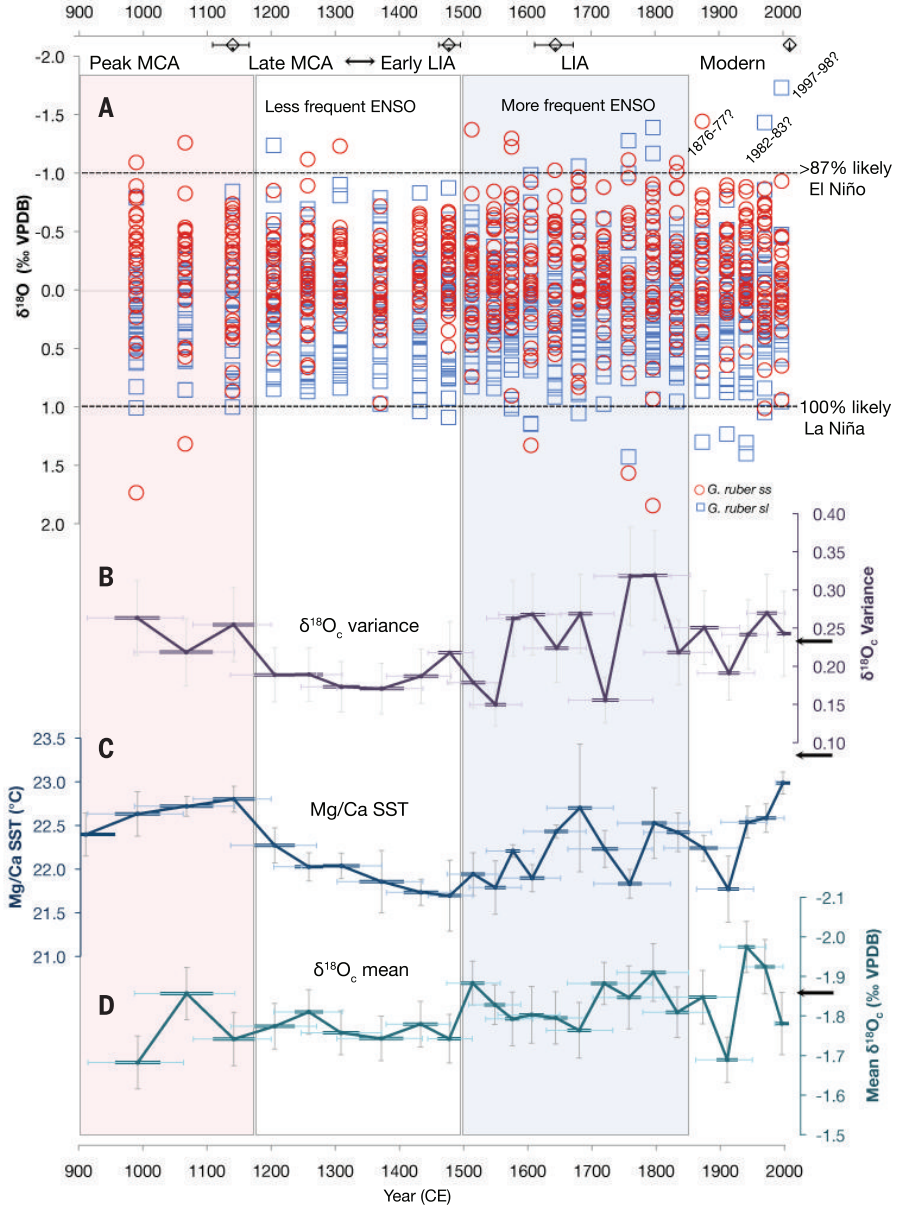

Fig. 2. Climatic proxies measured on Galápagos multicore KNR195-5 MC42C. (**A**) Individual *G. ruber* $\delta^{18}O_c$ in 24 contiguous samples after removing the sample means [shown in (D)]. Red circles denote sensu stricto (*ss*) and blue squares sensu lato (*sl*) morphotypes, which together capture the correct mean, variance, and skewness of historical SST data (*19*). Age control points are represented by black diamonds (top), with black whiskers denoting 1σ age uncertainty for ^{14}C ages. The multicore top is assumed to be modern (2009). Horizontal dashed lines at ±1.0‰ from the mean denote high-probability El Niño and La Niña events outside this range. $\delta^{18}O_c$ values consistent with historical strong El Niño events at 1876–1877, 1982–1983, and 1997–1998 are indicated. VPDB, Vienna Pee Dee belemnite. (**B**) *G. ruber* $\delta^{18}O_c$ variance ($\delta^{18}O_cV$) for each of the 24 sample intervals. Vertical error bars show SE of the variance. (**C**) *G. ruber* Mg/Ca SST. Each datum is the average of triplicate analyses. Vertical error bars indicate SD of the replicates. (**D**) Mean *G. ruber* $\delta^{18}O_c$. Vertical bars indicate SEM. For (B), (C), and (D), the horizontal bars denote the duration of each sample interval and horizontal whiskers show the 1σ age uncertainty. Modern values computed from SODA 2.1.6 are indicated by arrows on the right.

The pattern of $\delta^{18}O_cV$ during the millennium (Fig. 2B) shows marked similarity with Mg/Ca SSTs (correlation coefficient $R = -0.43$, $P < 0.05$) (Fig. 2C), considering that these data sets are entirely independent and based on different geochemical proxies and separate foraminifera samples. A conspicuous feature of both is a mid-millennium (~1500 CE) change in the proxy character. When $\delta^{18}O_cV$ is compared with the reconstructed SST gradient (Fig. 3, F and G), an inverse correlation is evident. Taking into account our age-model uncertainty, Monte Carlo analysis shows an average correlation of $R = -0.55$ with $P < 0.05$ in >95% of realizations (fig. S8). This result implies a fundamental association between a weaker zonal gradient and strong ENSO variability, and vice versa. The LIA (~1500–1850 CE) stands out as a period with high $\delta^{18}O_cV$ and, by inference, greater ENSO activity. The LIA also shows unusual general volatility with large century-scale swings in mean EEP SST (Fig. 3D) and $\delta^{18}O_cV$ (Fig. 3G). In contrast, the preceding period (1150–1500 CE) had the lowest ENSO activity of the millennium and was less volatile. Compared with the LIA, this state had 20% less $\delta^{18}O_c$ variance (*F* test: $P < 0.05$; Brown-Forsythe test: $P < 0.05$) and a 1.0° to 1.5°C stronger zonal gradient. Because the ENSO variance in our data is superimposed on a large annual cycle, this 20% change in $\delta^{18}O_cV$ potentially signifies a much greater change in ENSO variability. To further quantify this, we modeled the effect of ENSO on $\delta^{18}O_cV$. By holding the seasonal cycle constant to its modern value and varying the amplitude of ENSO anomalies in the instrumental era, we calculated that a 20% decrease in total variance required a ~55% decrease in ENSO amplitude. We conclude from these comparisons that the ~350-year periods preceding and following ~1500 CE represent fundamentally different dynamical states. The basin-wide tropical Pacific appears to have toggled between these states during a mid-millennium shift (MMS) that unfolded over the 16th and early 17th centuries.

The MMS occurred as the NH descended into the coldest portions of the LIA, leading us to consider a NH trigger through atmospheric mechanisms. The tropical atmosphere is dominated by the seasonally migrating ITCZ. Evidence linking the ITCZ to hemispheric warming and cooling cycles is widespread throughout the last glacial period (*22*) and implicates southward ITCZ displacements during NH cold periods, consistent with theory and models (*22*, *23*). We propose

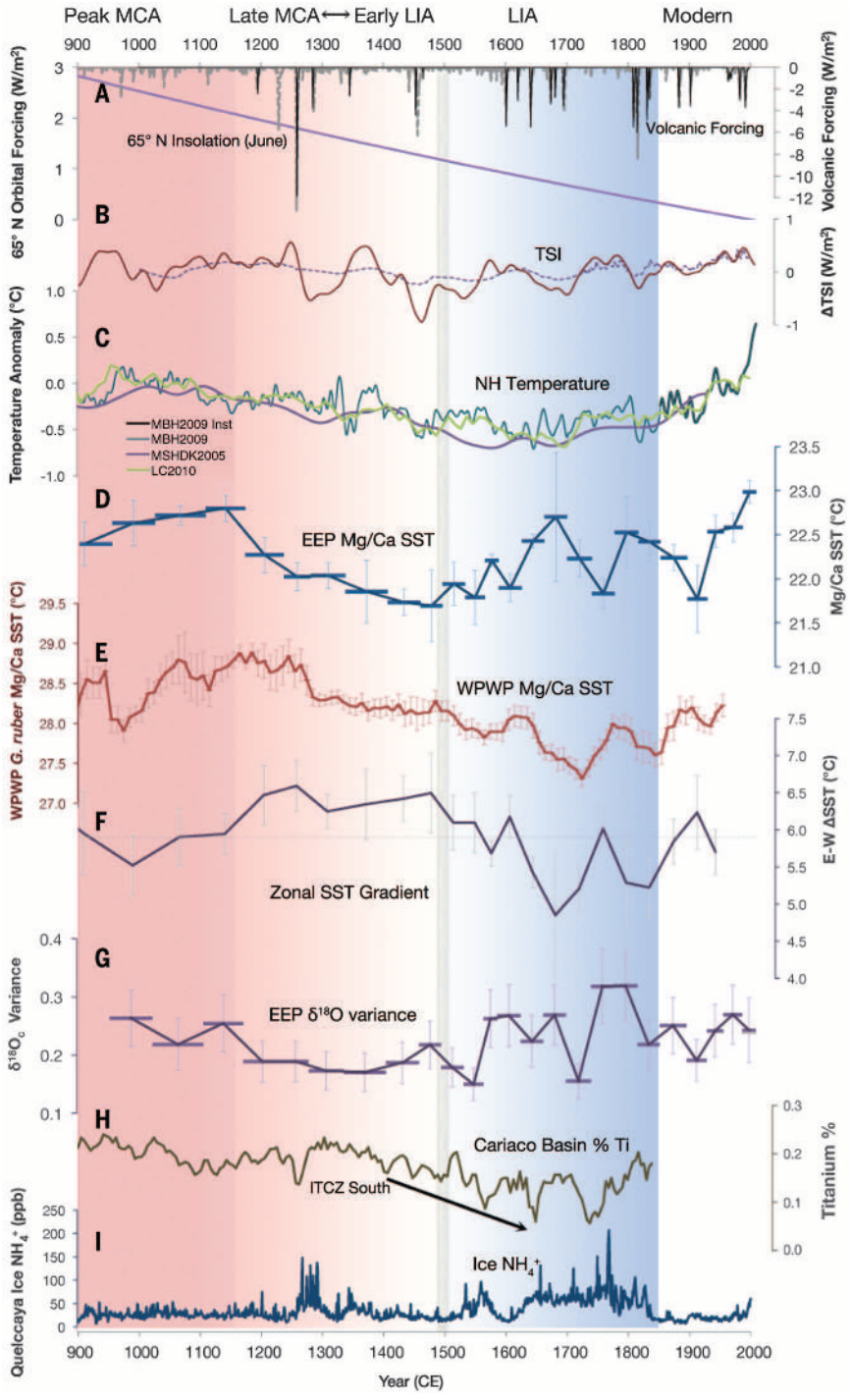

Fig. 3. Climatic evolution of the tropical Pacific in a broader context. (**A**) Volcanic forcing [dotted gray line from (*32*); black solid line from (*6*)] and 65°N June orbital forcing (*33*), as anomalies from the present. (**B**) Total solar irradiance (TSI) anomaly [solid red line from (*34*); dotted purple line from (*6*)]. (**C**) NH temperature reconstructions [MSHDK2005 (*5*) in purple; LC2010 (*7*) in green; MBH2009 (*6*) in blue; instrumental record (MBH2009 Inst) (*6*) in black]. (**D**) EEP Mg/Ca SSTs from KNR195-5 MC42C. Horizontal bar widths represent interval duration. Vertical whiskers show analytical uncertainty. (**E**) WPWP *G. ruber* Mg/Ca SSTs from four Makassar Straight cores (*13*). Vertical whiskers show analytical error. (**F**) Zonal SST gradient [difference between (E) and (D)] computed at the lower resolution of the EEP record. (**G**) EEP $\delta^{18}O_c$ variance from individual *G. ruber*, as in Fig. 2B. Horizontal bar widths show interval duration. Vertical whiskers show SE of the variance. (**H**) Percentage of titanium in the Cariaco Basin (*10*). (**I**) NH_4^+ [parts per billion (ppb)] from the Quelccaya ice core (*24*), interpreted as southward movement of the ITCZ at ~1500 CE.

that the same mechanism operated during the MMS as LIA cooling intensified. A southward shift of the ITCZ during the MCA-LIA transition has been proposed for the Atlantic (*10*), western Pacific (*12*), central Pacific (*11*), and the Peruvian Andes (*24*). Evidence for increasing precipitation off the coast of Panama after 1700 CE likely signals the northward return of the ITCZ (*25*) from its more southerly LIA position. A southward ITCZ shift at ~1500 CE naturally integrates these observations with our findings of EEP warming and reduced zonal gradient across the Pacific. This is fundamentally the same type of ocean-atmosphere adjustment that accompanies individual El Niño events as the ITCZ shifts south over anomalous equatorial surface ocean warming. Under a more southerly ITCZ, cross-equatorial southeast trade-wind stress in the EEP diminishes, leading to weaker cold-tongue development (Fig. 1A) and reduced zonal gradient. Our results suggest that the onset of similar conditions during the MMS was accompanied by dynamical excitation of ENSO activity, a finding that is corroborated by coral ENSO evidence from the 17th century (*15*). The relationship between the zonal SST gradient and ENSO variability is central to the understanding and modeling of basin-scale tropical Pacific dynamics. Some models support an intrinsic relationship between a weak zonal gradient and high ENSO variance (*26*), in accordance with our results. However, a general divergence of ENSO and tropical Pacific climate responses in 21st-century model simulations (*27*) highlights the need for further insight from past reconstructions.

Our reconstruction extends into the 21st century and offers a millennial-scale perspective on modern conditions. Modern SSTs are the highest of the millennium, yet they are within error of peak MCA values and thus are not unprecedented. Modern $\delta^{18}O_c$V values are intermediate between the millennium maxima and minima and therefore do not support unusual ENSO activity. The event tentatively matched to the 1997–1998 El Niño has no precedent in the earlier part of the millennium (Fig. 2A), but as a single event it does not establish a pattern. A warming trend in the EEP appears to have followed the end of the LIA (~1850 CE), although it is coarsely resolved in our sediment record and must be viewed cautiously. Such warming is not evident in gridded instrumental data for our site; however, these data are subject to considerable ambiguity (*28*, *29*). The warming trend now places the EEP on a parallel trajectory with NH climate since 1850 CE, in contrast with its out-of-phase relationship during the LIA. Thus, the EEP-NH in-phase relationship that existed during peak MCA warmth appears to be reestablished. The factors that induced dynamical changes in the Pacific's zonal gradient between 1150 and 1850 CE were seemingly not at play during peak MCA and may have again become disengaged in modern times. The in-phase relationship between the EEP and NH during the warmest times of the millennium (peak MCA and present) requires an explanation and may simply mean that the ITCZ is too far removed from the equator to

exert dynamical influence, allowing broader-scale thermodynamics to become dominant.

REFERENCES AND NOTES

1. M. J. McPhaden, S. E. Zebiak, M. H. Glantz, *Science* **314**, 1740–1745 (2006).
2. N. J. Mantua, S. R. Hare, *J. Oceanogr.* **58**, 35–44 (2002).
3. Y. Kosaka, S.-P. Xie, *Nature* **501**, 403–407 (2013).
4. M. H. England *et al.*, *Nat. Clim. Change* **4**, 222–227 (2014).
5. A. Moberg *et al.*, *Nature* **433**, 613–617 (2005).
6. M. E. Mann *et al.*, *Science* **326**, 1256–1260 (2009).
7. F. C. Ljungqvist, *Geogr. Ann. Ser. A* **92**, 339–351 (2010).
8. P. Zhang *et al.*, *Science* **322**, 940–942 (2008).
9. J. E. Tierney, D. W. Oppo, Y. Rosenthal, J. M. Russell, B. K. Linsley, *Paleoceanography* **25**, PA1102 (2010).
10. G. H. Haug, K. A. Hughen, D. M. Sigman, L. C. Peterson, U. Röhl, *Science* **293**, 1304–1308 (2001).
11. J. P. Sachs *et al.*, *Nat. Geosci.* **2**, 519–525 (2009).
12. A. Newton, R. Thunell, L. Stott, *Geophys. Res. Lett.* **33**, L19710 (2006).
13. D. W. Oppo, Y. Rosenthal, B. K. Linsley, *Nature* **460**, 1113–1116 (2009).
14. A. C. Clement, R. Seager, M. A. Cane, S. E. Zebiak, *J. Clim.* **9**, 2190–2196 (1996).
15. K. M. Cobb, C. D. Charles, H. Cheng, R. L. Edwards, *Nature* **424**, 271–276 (2003).
16. E. R. Cook, C. A. Woodhouse, C. M. Eakin, D. M. Meko, D. W. Stahle, *Science* **306**, 1015–1018 (2004).
17. J. Li *et al.*, *Nat. Clim. Change* **1**, 114–118 (2011).
18. J. Emile-Geay, K. M. Cobb, M. E. Mann, A. T. Wittenberg, *J. Clim.* **26**, 2329–2352 (2013).
19. Supplementary materials are available on *Science* Online.
20. A. Koutavas, P. B. deMenocal, G. C. Olive, J. Lynch-Stieglitz, *Geology* **34**, 993–996 (2006).
21. A. Koutavas, S. Joanides, *Paleoceanography* **27**, PA4208 (2012).
22. T. Schneider, T. Bischoff, G. H. Haug, *Nature* **513**, 45–53 (2014).
23. J. C. H. Chiang, C. M. Bitz, *Clim. Dyn.* **25**, 477–496 (2005).
24. L. G. Thompson *et al.*, *Science* **340**, 945–950 (2013).
25. B. K. Linsley, R. B. Dunbar, G. M. Wellington, D. A. Mucciarone, *J. Geophys. Res.* **99**, 9977–9994 (1994).
26. K. B. Karnauskas, J. E. Smerdon, R. Seager, J. F. Gonzalez-Rouco, *J. Clim.* **25**, 5943–5961 (2012).
27. M. Collins *et al.*, *Nat. Geosci.* **3**, 391–397 (2010).
28. G. A. Vecchi, A. Clement, B. J. Soden, *Eos* **89**, 81–83 (2008).
29. C. Deser, A. S. Phillips, M. A. Alexander, *Geophys. Res. Lett.* **37**, L10701 (2010).
30. J. A. Carton, B. S. Giese, *Mon. Weather Rev.* **136**, 2999–3017 (2008).
31. E. Kalnay *et al.*, *Bull. Am. Meteorol. Soc.* **77**, 437–471 (1996).
32. T. J. Crowley, M. B. Unterman, *Earth Syst. Sci. Data* **5**, 187–197 (2013).
33. J. Laskar *et al.*, *Astron. Astrophys.* **428**, 261–285 (2004).
34. F. Steinhilber, J. Beer, C. Fröhlich, *Geophys. Res. Lett.* **36**, L19704 (2009).

ACKNOWLEDGMENTS

Funding support was provided by the Lamont–Doherty Earth Observatory Climate Center, Professional Staff Congress–City University of New York, a Provost's Research Award to A.K. from the College of Staten Island, and NSF grant OCE-1103482 to T.M.M. We thank T. Herbert and the crew of R/V *Knorr* during cruise KNR195-5 for core collection. Data from this study are available through the NOAA National Centers for Environmental Information World Data Center for Paleoclimatology.

SUPPLEMENTARY MATERIALS

www.sciencemag.org/content/350/6267/1537/suppl/DC1
Materials and Methods
Supplementary Text
Figs. S1 to S10
Tables S1 and S2
References (*35*–*55*)

10 July 2015; accepted 18 November 2015
Published online 3 December 2015
10.1126/science.aac9937

MICROBIAL METABOLISM

A protein trisulfide couples dissimilatory sulfate reduction to energy conservation

André A. Santos,[1]* Sofia S. Venceslau,[1]* Fabian Grein,[1]† William D. Leavitt,[2]‡ Christiane Dahl,[3] David T. Johnston,[2] Inês A. C. Pereira[1]§

Microbial sulfate reduction has governed Earth's biogeochemical sulfur cycle for at least 2.5 billion years. However, the enzymatic mechanisms behind this pathway are incompletely understood, particularly for the reduction of sulfite—a key intermediate in the pathway. This critical reaction is performed by DsrAB, a widespread enzyme also involved in other dissimilatory sulfur metabolisms. Using in vitro assays with an archaeal DsrAB, supported with genetic experiments in a bacterial system, we show that the product of sulfite reduction by DsrAB is a protein-based trisulfide, in which a sulfite-derived sulfur is bridging two conserved cysteines of DsrC. Physiological studies also reveal that sulfate reduction rates are determined by cellular levels of DsrC. Dissimilatory sulfate reduction couples the four-electron reduction of the DsrC trisulfide to energy conservation.

The biogeochemical sulfur cycle is driven by microbial processes, the most prominent of which is dissimilatory sulfate (SO_4^{2-}) reduction (DSR) by marine microorganisms. DSR imparts a strong signature in the stable sulfur isotopes that is commonly used to trace sulfur cycling and Earth's relative redox state in both ancient and modern environments (*1*). This respiratory microbial process, performed only by sulfate-reducing bacteria and archaea, has similarity to assimilatory sulfate reduction performed by many prokaryotic and eukaryotic organisms. Both pathways of sulfate reduction (fig. S1) include (bi)sulfite (HSO_3^-/SO_3^{2-}) reduction as a critical step, performed by siroheme sulfite reductases (*2*, *3*). The dissimilatory sulfite reductases, the most widespread of which is DsrAB (*3*–*5*), are found in prokaryotes with a sulfur-based energy metabolism.

DsrAB is a heterodimer of the phylogenetically related DsrA and DsrB subunits. In vitro, sulfite reduction by DsrAB produces a mixture of products, including trithionate ($S_3O_6^{2-}$), thiosulfate ($S_2O_3^{2-}$), and sulfide (HS^-/S^{2-}) (*6*). Whether DSR involves the direct six-electron reduction of sulfite to sulfide by DsrAB, or whether trithionate and thiosulfate are necessary intermediates (fig. S2) (*6*), remains an open question. This key question shapes both biochemical and geochemical models of sulfur cycling (*7*, *8*) because DsrAB is believed to be a major player in determining sulfur isotope fractionations associated with DSR (*9*). Furthermore, sulfite reduction is coupled to chemiosmotic energy transduction, harnessing the free energy of reducing sulfite to sulfide ($\Delta G^{o'}$ = –172 kJ/mol for HSO_3^-/HS^- reduction with H_2). However, DsrAB is not a membrane-associated protein, leaving the mechanism by which energy is conserved during sulfite reduction unresolved.

The crystal structure of DsrAB from *Desulfovibrio vulgaris* (*10*) revealed a complex with DsrC, a small protein with a highly conserved C-terminal arm that inserts into a cleft between DsrA and DsrB. The arm contains two strictly conserved cysteines: the penultimate residue (Cys_A), and another located 11 residues before (Cys_B) (fig. S3) (*11*). Cys_A was found positioned next to the DsrAB substrate-binding site, suggesting a role in catalysis (*10*). Moreover, all genomes containing the *dsrAB* genes also encode *dsrC* (*11*), which is among the most highly expressed sulfur energy metabolism genes in isolated organisms (*12*) and metatranscriptomes (*13*, *14*). DsrC is also closely related to TusE, a sulfur-trafficking protein involved in persulfide-driven thiolation of tRNAs (*11*, *15*). Together, these observations strongly suggest that DsrC plays a central role in DSR.

Here, we report biochemical, genetic, and physiological evidence that elucidates the role of DsrC. For the in vitro experiments, we used DsrAB and DsrC from the thermophilic archaeon *Archaeoglobus fulgidus* because DsrAB can be isolated from this organism separate from DsrC (*16*, *17*), unlike in *Desulfovibrio* (*10*). In these experiments, reduced DsrC causes a strong increase

[1]Instituto de Tecnologia Química e Biológica António Xavier, Universidade Nova de Lisboa, Oeiras, Portugal. [2]Department of Earth and Planetary Science, Harvard University, Cambridge, MA, USA. [3]Institut für Mikrobiologie & Biotechnologie, Rheinische Friedrich-Wilhelms-Universität Bonn, Germany.
*These authors contributed equally to this work. †Present address: Institut für Pharmazeutische Mikrobiologie, Rheinische Friedrich-Wilhelms-Universität Bonn, Germany. ‡Present address: Department of Earth and Planetary Sciences, Washington University, St. Louis, MO, USA; and Department of Earth Sciences, Dartmouth College, Hanover, NH, USA. §Corresponding author. E-mail: ipereira@itqb.unl.pt

in DsrAB sulfite-reduction activity (Fig. 1A), inducing an initial fast reaction rate, which then slows to a rate similar to when DsrC is absent (*18*). The duration of the fast phase correlates with the amount of reduced DsrC added, with a sulfite-reduction rate (1278 ± 2 mU/mg at 80°C) that is 15-fold higher than in its absence (82 ± 2 mU/mg at 80°C) (Fig. 1B). The Michaelis constant (K_m) for sulfite is not affected (11 ± 4 μM without and 12 ± 3 μM with DsrC). When the DsrC cysteines are alkylated or oxidized to a disulfide state, no effect on DsrAB rate is observed. Sequential addition of reduced DsrC in the slow phase induces another fast reaction phase (Fig. 1C), confirming that the transition to the slow phase is caused by consumption (oxidation) of DsrC. Further, the sulfite consumed in the fast phase shows a clear one-to-one relationship to added DsrC (Fig. 1D). The ratio of methyl viologen oxidized relative to sulfite consumed is 1.8 ± 0.3 in the fast phase and 4.1 ± 1.2 in the slow phase. This indicates that only two electrons are being used to reduce sulfite in the presence of DsrC. In its absence, the number of electrons is higher and more variable, agreeing with the mixture of products formed (trithionate, thiosulfate, and sulfide) with different degrees of reduction. No effect of DsrC is observed for reduction of thiosulfate or trithionate (fig. S5). These results clearly indicate that DsrC is a cosubstrate for sulfite reduction by DsrAB.

The consumption of sulfite and production of thiosulfate and sulfide were measured across the fast and slow phases. In the absence of DsrC, sulfide and thiosulfate are produced from the start of the reaction (Fig. 2A), whereas in the presence of DsrC, almost no sulfur products are detected (except a small amount of sulfide) until the reaction enters the slow phase (Fig. 2B). Similar results were observed for trithionate in experiments with higher DsrC concentration (fig. S6, A and B). The redox state of DsrC recovered after reaction was analyzed with a gel-shift assay from parallel experiments with different concentrations of DsrC (Fig. 3A). At time zero (T_0), DsrC is reduced, as revealed by the shift for one (Cys_A) and two labeled cysteines (Cys_A and Cys_B). During the reaction, an oxidized form is produced (no shift) (Fig. 3, B and C). In both experiments, all DsrC is converted to this oxidized form at the end of the fast phase. In a control experiment without DsrAB, DsrC remains reduced (Fig. 3D).

Mass spectrometry of DsrC after the fast phase (15,477 daltons) showed a mass increase of 29 daltons relative to the initial value (15,448 daltons), suggesting the binding of one sulfur to DsrC. For better mass accuracy, we performed peptide mass fingerprinting of DsrC, with and without alkylation, focusing on its C-terminal peptide (table S1 and fig. S7). At T_0, alkylation confirmed the presence of two reduced Cys (figs. S7A and S7C). After the fast phase, the C-terminal peptide shows a precise mass increase of 32 daltons (fig. S7B) and no reactivity with alkylating agents (fig. S7D). In control experiments with no DsrAB, the C-terminal peptide is unaltered (fig. S8). These

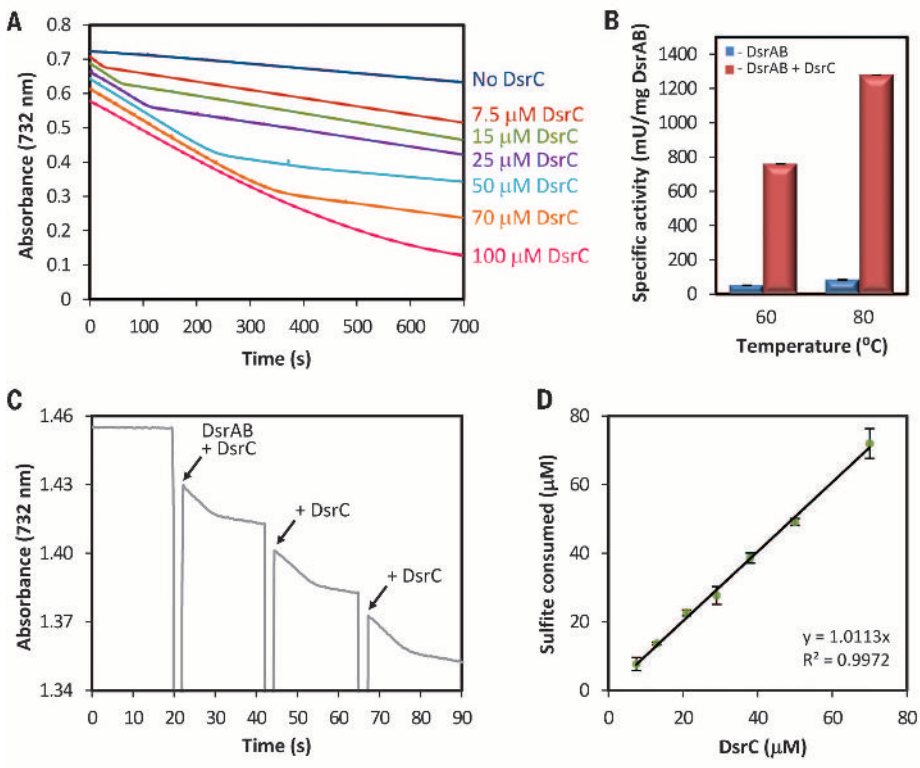

Fig. 1. Effect of DsrC on sulfite reduction by DsrAB. (**A**) Sulfite reduction activity of *A. fulgidus* DsrAB in the presence of different *A. fulgidus* DsrC concentrations. Representative traces are shown. (**B**) Specific activity of DsrAB in the absence and presence of DsrC (7.5 μM). Data points are mean ± SD, $n = 3$ independent experiments. (**C**) Sulfite-reduction activity upon successive additions of DsrC (7.5 μM). (**D**) Sulfite consumed in the fast phase versus DsrC concentration (data are mean ± SD, $n = 3$ independent experiments).

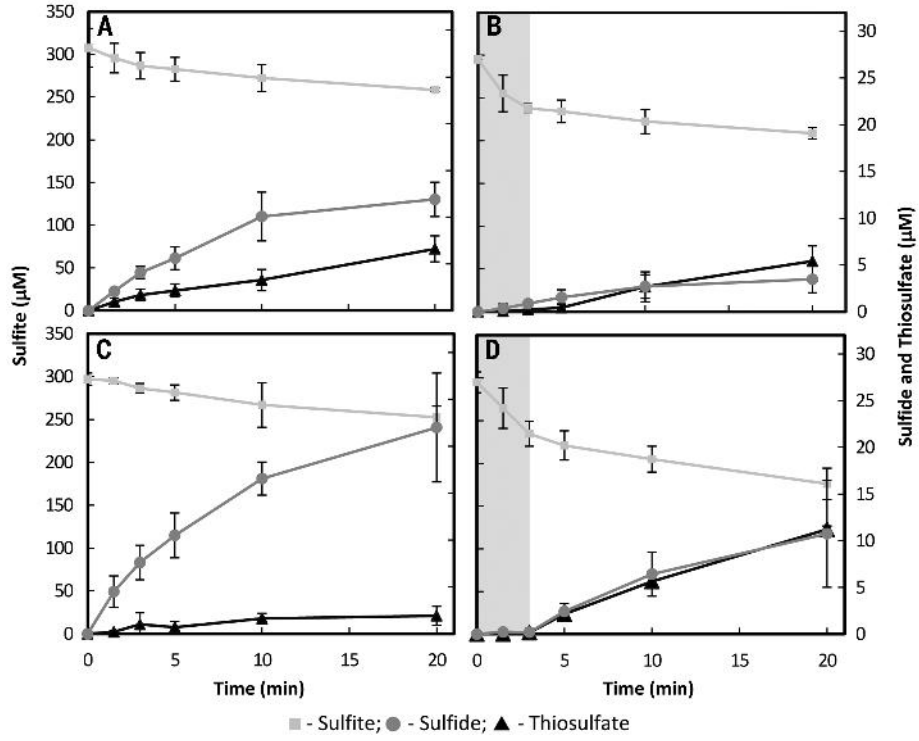

Fig. 2. Sulfite consumption and thiosulfate and sulfide production by *A. fulgidus* DsrAB ± DsrC. (**A**) No DsrC. (**B**) Wild-type DsrC (50 μM). (**C**) DsrC Cys_AAla (C114A) variant (50 μM). (**D**) DsrC Cys_BAla (C103A) variant (50 μM). Data are mean ± SD, $n = 3$ independent experiments. The gray areas highlight the fast phase.

results nullify our prior model, which suggested a DsrC persulfide as the product of sulfite reduction by DsrAB/DsrC (*10*, *11*) because a persulfide would react with both the alkylating and gel-shift reagents (not observed). Together, these results reveal that the product of sulfite reduction by DsrAB/DsrC is a DsrC-bound trisulfide, in which a zero-valent sulfur originating from sulfite forms a bridge between the C-terminal cysteines (Fig. 4).

To probe the reaction mechanism, we produced two DsrC variants lacking each C-terminal Cys. The protein lacking Cys_A (Cys_AAla variant) did not increase the rate of sulfite reduction (Fig. 2C), but substantially altered the product composition; sulfide became the major product, with negligible production of thiosulfate or trithionate (Fig. 2C and fig. S6C). In contrast, the protein lacking Cys_B (Cys_BAla variant) had a similar effect on activity as that of wild-type DsrC, both in terms of rate and absence of sulfur products in the fast phase (Fig. 2D and fig. S6D). Gel-shift assay (Fig. 3E) and mass spectrometry (table S1 and fig. S9) showed no change in the Cys_AAla variant after reaction. The Cys_BAla variant showed a mixture of two products in the gel-shift assay: an oxidized form and a product with one free Cys (Fig. 3E). Intact mass analysis of this variant showed a mass increase of 52 daltons, which agrees with a persulfide sulfenate (SOH) of Cys_A. Peptide mass fingerprinting revealed the presence of a major product with no mass increase, and a minor product offset by 32 daltons (table S1 and fig. S10B). Alkylation revealed the presence of one free Cys at the start and end of the experiment (table S1 and fig. S10CD). On the basis of these results, we propose a previously unidentified mechanism for DsrAB/DsrC sulfite reduction (Fig. 4A). This is supported by a report that the DsrC C-terminal arm can adopt a retracted conformation while still bound to DsrAB, where the two Cys are in close proximity (*19*). This mechanism can explain the results for the DsrC variants. In the absence of Cys_A, the first Cys to react, there is no increase in the reaction rate, and DsrC is not modified (fig. S11). In the absence of Cys_B, the S^I intermediate with a persulfide sulfenate is produced, which cannot react further and is released as a product (mass increase of 52 daltons). This is likely unstable and decomposes to a mixture of the persulfurated (+32 daltons) and the unmodified protein, as detected by means of peptide mass fingerprinting and alkylation.

The in vitro production of thionates ($S_3O_6^{2-}$ and $S_2O_3^{2-}$) by DsrAB in the absence of DsrC can be explained by further reaction of the partially reduced S^{II} and S^0 intermediates with excess sulfite, yielding trithionate and thiosulfate, respectively (fig. S12B). In the absence of DsrC, the siroheme active site of DsrAB is directly accessible through a wide cleft where the DsrC arm usually docks (fig. S13). This cleft is distinct from the much narrower substrate channel (*10*). This different substrate accessibility in the presence and absence of DsrC explains the product composition observed for the Cys_AAla DsrC variant. With this variant, the C-terminal arm blocks the DsrC cleft, with access of sulfite occurring exclusively through the narrower substrate channel. This likely slows down the reaction of additional sulfite with semireduced intermediates, allowing for complete reduction to sulfide. Therefore, previous reports of thiosulfate and trithionate production as in vitro products of DsrAB (*6*) were the result of nonphysiological in vitro conditions [absence of reduced DsrC and unrealistically high (bi)sulfite concentrations].

To complement these results, we performed in vivo studies on the physiological role of DsrC, using *D. vulgaris* Hildenborough—a model sulfate-reducing deltaproteobacterium for which genetic tools are available. Multiple attempts to produce a *dsrC* deletion mutant proved unsuccessful. We undertook a different approach and first provided the wild type with a second copy of *dsrC* in trans on a plasmid, resulting in strain IPFG06 (fig. S14). This strain produces native chromosomally encoded DsrC (c-DsrC), plus a lower amount of plasmid-encoded DsrC (p-DsrC) (fig. S15). The chromosomal *dsrC* gene was then deleted in strain IPFG06 to generate strain IPFG07, containing only the plasmid *dsrC* copy transcribed from a relatively weaker promoter. The same strategy was applied to generate strain IPFG09, in which a plasmid *dsrC* copy encoding a Cys_BAla exchange is present (p-Cys_BAla-DsrC). As expected, Western blot revealed reduced levels of DsrC in strains IPFG07 and IPFG09 (fig. S15). In the case of DsrC lacking Cys_A, despite numerous attempts, it was not possible to delete the chromosomal copy and generate the strain with only p-Cys_AAla-*dsrC*, even with selection under pyruvate fermentation. This strongly indicates that Cys_A is essential for functional DsrC. Growth studies of the variant strains in lactate/sulfate respiration (Fig. 4B) showed a small increase in doubling time for IPFG06 relative to the wild-type. In contrast, IPFG07 containing only p-DsrC had a significant increase in doubling time and reached a lower cell density. This effect was even more pronounced for IPFG09 containing p-Cys_BAla-DsrC. The differences in growth rate were also reflected in sulfate consumption rates (fig. S16). These in vivo studies show that DsrC and its Cys_A are essential for sulfate reduction, as well as cell viability. Cys_B, though not strictly essential, also plays an important role. Thus, the genetic studies in this bacterial system corroborate the biochemical studies with the archaeal proteins, confirming the metabolic importance of DsrC.

Overall, our in vitro and in vivo studies demonstrate that DsrC is a substrate for DsrAB, with production of a trisulfide. Our data places a zero-valent protein trisulfide as a key metabolite in this ancient biological reaction, likely present before the divergence of the Bacteria and Archaea domains (*5*, *20*). Zero-valent sulfur, in the form of protein polysulfides and persulfides, has also been proposed as the activated sulfur currency involved in key cellular functions, such as H_2S

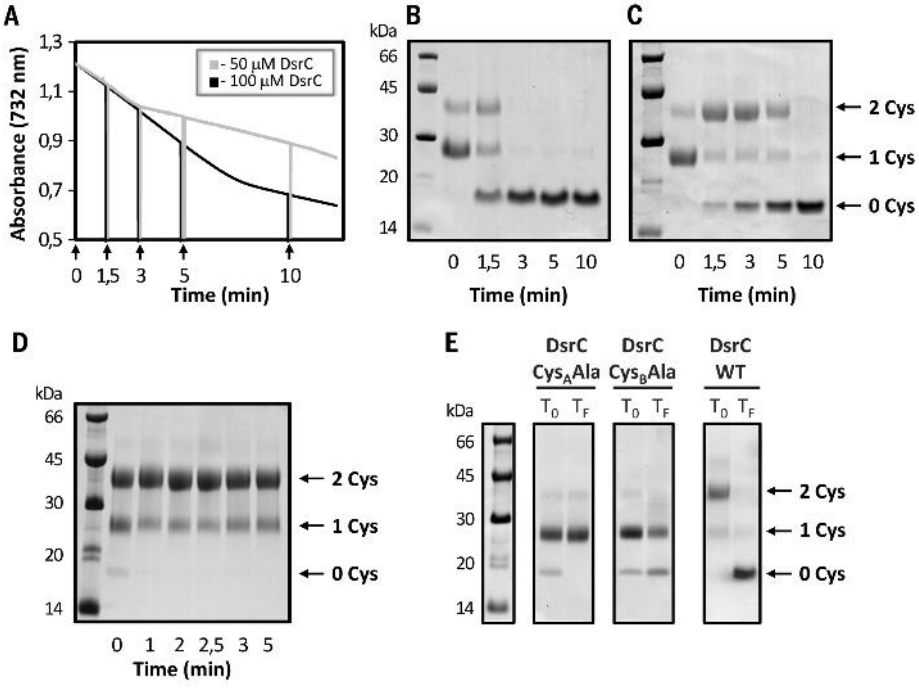

Fig. 3. Redox state of DsrC upon reaction with *A. fulgidus* DsrAB and sulfite. (**A**) Experiments with 50 µM (gray) and 100 µM DsrC (black). Samples were taken at the time points indicated. (**B** to **D**) Gel-shift analysis of MalPEG-labeled DsrC from (B) the 50 µM assay, (C) the 100 µM assay, and (D) a control assay without DsrAB. (**E**) Gel-shift analysis of MalPEG-labeled DsrC from assays with wild-type DsrC (WT) and Cys_AAla (C114A) and Cys_BAla (C103A) variants. Samples were taken after reaching the slow phase.

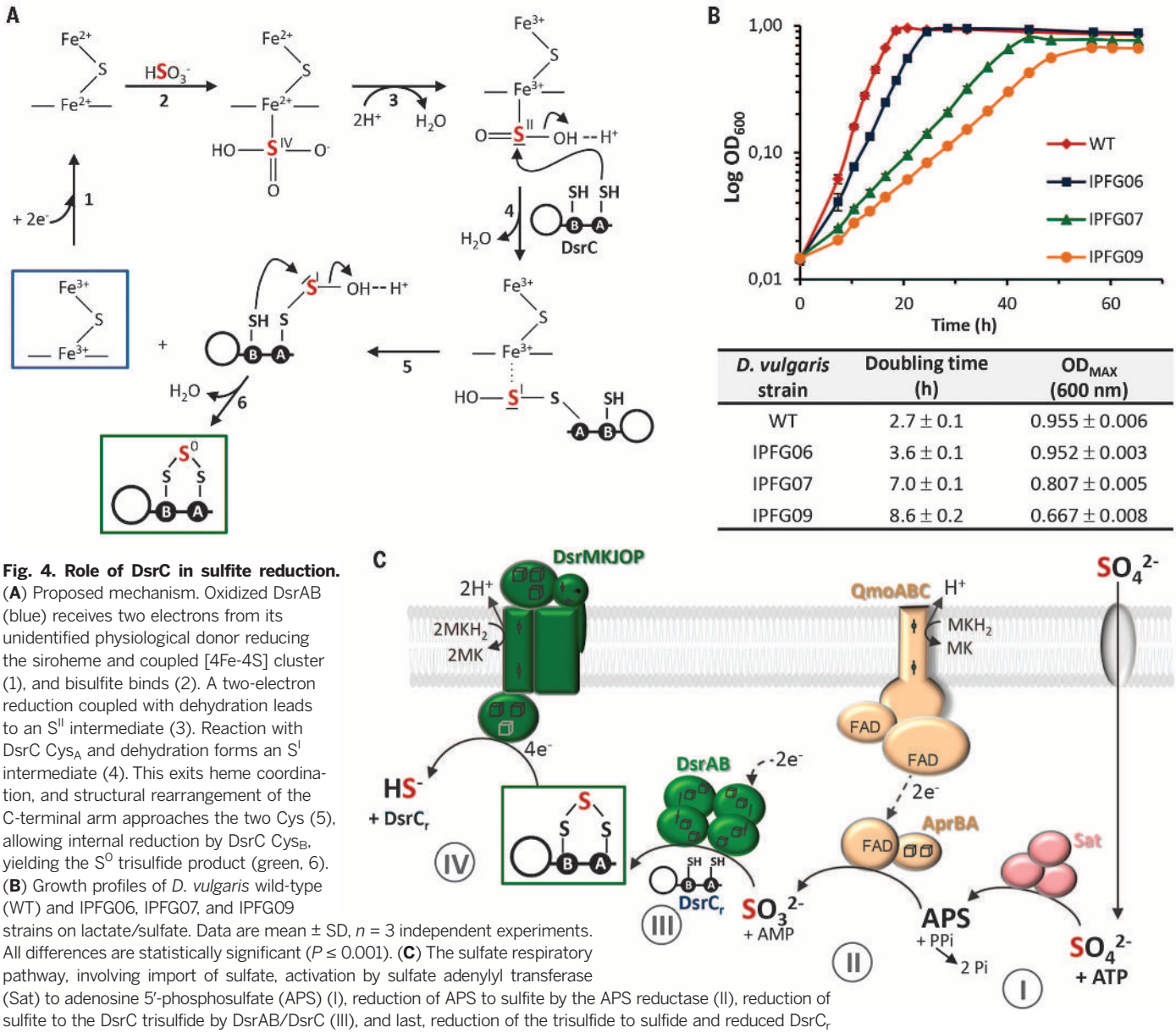

D. vulgaris strain	Doubling time (h)	OD_{MAX} (600 nm)
WT	2.7 ± 0.1	0.955 ± 0.006
IPFG06	3.6 ± 0.1	0.952 ± 0.003
IPFG07	7.0 ± 0.1	0.807 ± 0.005
IPFG09	8.6 ± 0.2	0.667 ± 0.008

Fig. 4. Role of DsrC in sulfite reduction. (**A**) Proposed mechanism. Oxidized DsrAB (blue) receives two electrons from its unidentified physiological donor reducing the siroheme and coupled [4Fe-4S] cluster (1), and bisulfite binds (2). A two-electron reduction coupled with dehydration leads to an S^{II} intermediate (3). Reaction with DsrC Cys_A and dehydration forms an S^{I} intermediate (4). This exits heme coordination, and structural rearrangement of the C-terminal arm approaches the two Cys (5), allowing internal reduction by DsrC Cys_B, yielding the S^0 trisulfide product (green, 6). (**B**) Growth profiles of *D. vulgaris* wild-type (WT) and IPFG06, IPFG07, and IPFG09 strains on lactate/sulfate. Data are mean ± SD, $n = 3$ independent experiments. All differences are statistically significant ($P \leq 0.001$). (**C**) The sulfate respiratory pathway, involving import of sulfate, activation by sulfate adenylyl transferase (Sat) to adenosine 5′-phosphosulfate (APS) (I), reduction of APS to sulfite by the APS reductase (II), reduction of sulfite to the DsrC trisulfide by DsrAB/DsrC (III), and last, reduction of the trisulfide to sulfide and reduced $DsrC_r$ by the DsrMKJOP complex (IV).

signaling, protein and tRNA sulfuration, biosynthesis of sulfur cofactors, redox homeostasis, and enzymatic modulation (*21*, *22*). Further, protein trisulfides have been reported in proteins involved in tRNA sulfuration (*23*) and antibodies (*24*). Formation of a trisulfide is a superior solution to our previous proposal of a persulfide (*10*, *11*), both in chemical and biological terms. As a consequence, DsrAB (bi)sulfite reduction involves only two electrons, with other two originating from reduced DsrC. Critically, the DsrC trisulfide will be reduced in a fourth step to produce the final product sulfide and recycle DsrC (Fig. 4C). This new step in the sulfate-reduction pathway is likely performed by the membrane DsrMKJOP complex, which includes the DsrK subunit, whose characteristic electron paramagnetic resonancesignature indicates a [4Fe-4S] cluster known to perform disulfide reductions (*4*, *11*, *25*). DsrK is closely related to methanogenic HdrD heterodisulfide reductase (*26*) and has been shown to interact with DsrC (*11*, *27*).

The existence of a fourth step in the dissimilatory sulfate-reduction pathway has far reaching implications for the bioenergetics of this microbial process. It means that four of the six electrons for (bi)sulfite reduction likely originate from the menaquinol pool, enabling coupling of ΔpH generation across the membrane directly to sulfite reduction and energy conservation. Therefore, the production of a DsrC trisulfide, and subsequent reduction by DsrK, allows for the soluble process at DsrAB to couple to energy conservation. The DsrC trisulfide may have a low redox potential, precluding direct reduction by menaquinol, suggesting that a more complex process (such as quinone electron bifurcation) may occur at DsrMKJOP (*11*). These insights into the mechanism of sulfate reduction should be incorporated in models for interpreting reaction rates and isotopic fractionations, which are important for our understanding of the biogeochemical sulfur cycle and its evolution. They also require a greater focus on DsrC in metatranscriptomic/proteomic studies because cellular levels of this protein are likely to determine sulfite, and net sulfate, reduction rates.

REFERENCES AND NOTES

1. D. E. Canfield, *Nature* **396**, 450–453 (1998).
2. B. R. Crane, E. D. Getzoff, *Curr. Opin. Struct. Biol.* **6**, 744–756 (1996).
3. J. Simon, P. M. H. Kroneck, *Adv. Microb. Physiol.* **62**, 45–117 (2013).

4. F. Grein, A. R. Ramos, S. S. Venceslau, I. A. C. Pereira, *Biochim. Biophys. Acta* **1827**, 145–160 (2013).
5. A. L. Müller, K. U. Kjeldsen, T. Rattei, M. Pester, A. Loy, *ISME J.* **9**, 1152–1165 (2015).
6. H. D. Peck Jr., J. LeGall, J. VanBeeumen, *Philos. Trans. R. Soc. Lond., B* **298**, 443–466 (1982).
7. A. S. Bradley, W. D. Leavitt, D. T. Johnston, *Geobiology* **9**, 446–457 (2011).
8. B. Brunner, S. M. Bernasconi, *Geochim. Cosmochim. Acta* **69**, 4759–4771 (2005).
9. W. D. Leavitt, A. S. Bradley, A. A. Santos, I. C. Pereira, D. T. Johnson, *Front. Microbiol.* **6**, 1392 (2015).
10. T. F. Oliveira *et al.*, *J. Biol. Chem.* **283**, 34141–34149 (2008).
11. S. S. Venceslau, Y. Stockdreher, C. Dahl, I. A. C. Pereira, *Biochim. Biophys. Acta* **1837**, 1148–1164 (2014).
12. K. L. Keller *et al.*, *Appl. Environ. Microbiol.* **80**, 855–868 (2014).
13. D. E. Canfield *et al.*, *Science* **330**, 1375–1378 (2010).
14. F. J. Stewart, O. Dmytrenko, E. F. Delong, C. M. Cavanaugh, *Front. Microbiol.* **2**, 134 (2011).
15. Y. Ikeuchi, N. Shigi, J. Kato, A. Nishimura, T. Suzuki, *Mol. Cell* **21**, 97–108 (2006).
16. K. Parey, E. Warkentin, P. M. H. Kroneck, U. Ermler, *Biochemistry* **49**, 8912–8921 (2010).
17. K. Parey, G. Fritz, U. Ermler, P. M. H. Kroneck, *Metallomics* **5**, 302–317 (2013).
18. Materials and methods are available as supplementary materials on *Science* Online
19. Y. C. Hsieh *et al.*, *Mol. Microbiol.* **78**, 1101–1116 (2010).
20. M. Wagner, A. J. Roger, J. L. Flax, G. A. Brusseau, D. A. Stahl, *J. Bacteriol.* **180**, 2975–2982 (1998).
21. T. Ida *et al.*, *Proc. Natl. Acad. Sci. U.S.A.* **111**, 7606–7611 (2014).
22. B. D. Paul, S. H. Snyder, *Nat. Rev. Mol. Cell Biol.* **13**, 499–507 (2012).
23. Y. Liu *et al.*, *J. Biol. Chem.* **287**, 36683–36692 (2012).
24. R. W. Nielsen, C. Tachibana, N. E. Hansen, J. R. Winther, *Antioxid. Redox Signal.* **15**, 67–75 (2011).
25. R. H. Pires *et al.*, *Biochemistry* **45**, 249–262 (2006).
26. R. Hedderich, N. Hamann, M. Bennati, *Biol. Chem.* **386**, 961–970 (2005).
27. F. Grein, I. A. C. Pereira, C. Dahl, *J. Bacteriol.* **192**, 6369–6377 (2010).

ACKNOWLEDGMENTS

We thank R. Soares for the mass spectrometry measurements, C. Leitão for HPLC technical support, and H. Santos and L. Gafeira for providing *A. fulgidus*. We also thank J. Wall for plasmids for genetic manipulation of *D. vulgaris*, A. Ramos for technical assistance, A. Masterson for synthesis of the trithionate standard, A. Bradley for detailed discussions, and W. Martin for critical reading of the manuscript. This work was funded by grants from NSF-EAR (1225980 to D.T.J. and I.A.C.P.), from Fundação para a Ciência e a Tecnologia (FCT), Portugal (UID/Multi/04551/2013, PTDC/QUI-BIQ/100591/2008, and PTDC/BBB-BQB/0684/2012) and Deutsche Forschungsgemeinschaft, Germany (Da 351/6-2). A.S. and S.S.V. are recipients of FCT fellowships (SFRH/BD/77940/2011 and SFRH/BPD/79823/2011). W.D.L. acknowledges support by an NSF–Graduate Research Fellowship Program and the Fossett Fellowship from Washington University in St. Louis. The data reported in this paper are provided in the supplementary materials.

SUPPLEMENTARY MATERIALS

www.sciencemag.org/content/350/6267/1541/suppl/DC1
Materials and Methods
Figs. S1 to S15
Tables S1 to S3
References (*28*–*41*)

2 September 2015; accepted 4 November 2015
10.1126/science.aad3558

ECOTOXICOLOGY

Algal toxin impairs sea lion memory and hippocampal connectivity, with implications for strandings

Peter F. Cook,[1,2]* Colleen Reichmuth,[2] Andrew A. Rouse,[2] Laura A. Libby,[3] Sophie E. Dennison,[4] Owen T. Carmichael,[5] Kris T. Kruse-Elliott,[4] Josh Bloom,[4] Baljeet Singh,[3] Vanessa A. Fravel,[6] Lorraine Barbosa,[6] Jim J. Stuppino,[4] William G. Van Bonn,[7] Frances M. D. Gulland,[6] Charan Ranganath[3]

Domoic acid (DA) is a naturally occurring neurotoxin known to harm marine animals. DA-producing algal blooms are increasing in size and frequency. Although chronic exposure is known to produce brain lesions, the influence of DA toxicosis on behavior in wild animals is unknown. We showed, in a large sample of wild sea lions, that spatial memory deficits are predicted by the extent of right dorsal hippocampal lesions related to natural exposure to DA and that exposure also disrupts hippocampal-thalamic brain networks. Because sea lions are dynamic foragers that rely on flexible navigation, impaired spatial memory may affect survival in the wild.

Domoic acid (DA) is an amino acid neurotoxin that causes neurological symptoms in marine animals, most visibly California sea lions (CSLs, *Zalophus californianus*) (*1*). As a result of environmental change and human impacts on marine systems, the size and frequency of DA-producing *Pseudonitszchia* algal blooms are increasing (*2*), and toxic exposure is widespread in CSLs (*3*). Although exposed CSLs show a reliable and specific pattern of seizures and hippocampal lesions (*4*), the sublethal effects on behavior are unclear. In rodents and humans, the hippocampus is necessary for spatial memory (*5*, *6*). As dynamic central-place foragers (*7*), CSLs may be especially vulnerable to spatial memory deficits, and anecdotal data from postrehabilitation tracking show unusual movement patterns in exposed animals (*8*). Together, these observations suggest that DA exposure in CSLs and resultant hippocampal damage could be associated with impaired spatial memory. In this study, we used controlled behavioral studies, integrated with prerelease veterinary care and structural and functional neuroimaging, to directly test this hypothesis in wild sea lions.

Between April 2009 and November 2011, we studied 30 wild CSLs undergoing veterinary care and rehabilitation (table S1). Drawing from the literature on hippocampal function in rodents, we developed two spatial memory assays and compared performances with hippocampal volumes, measured using in vivo magnetic resonance imaging (MRI). The hippocampus was manually traced (fig. S1), and structural volumes were calculated as percentages of total brain volume for each animal (*9*). Veterinary diagnosis predicted hippocampal volume [repeated measures analysis of variance (ANOVA): $F = 16.25$, df = 1, $P < 0.001$] (*9*), justifying the use of volume as the primary independent variable. Given the magnitude and range of hippocampal volumes across the sample, subsequent analyses treated volume as a continuous variable.

Because lesions are typically unilateral in this population (*3*), and because other species show lateralization of hippocampal function (*10*), right and left hippocampal volumes were regressed separately with behavioral performance. In some species, spatial memory is more reliant on the septal (dorsal) than on the temporal (ventral) hippocampus (*11*). Accordingly, we divided the hippocampi in half by length and conducted follow-up regression analyses with ventral and dorsal hippocampal volumes (*9*). We report these results when they differ from those expected based on analyses of the entire longitudinal extent of the hippocampus. Rodent data suggest that the dorsal third of the hippocampus may be sufficient to support spatial memory (*11*), so in cases where the dorsal half was a significant predictor of behavior, we conducted follow-up analyses that

[1]Center for Neuropolicy, Emory University, Atlanta, GA 30322, USA. [2]Pinniped Cognition and Sensory Systems Laboratory, Institute of Marine Sciences, University of California–Santa Cruz, Santa Cruz, CA 95060, USA. [3]Dynamic Memory Lab, Center for Neuroscience, University of California–Davis, Davis, CA 95618, USA. [4]AnimalScan Advanced Veterinary Imaging, Redwood City, CA 94063, USA. [5]Pennington Biomedical Research Center, Baton Rouge, LA 70808, USA. [6]The Marine Mammal Center, Sausalito, CA 94965, USA. [7]Shedd Aquarium, Chicago, IL 60605, USA.
*Corresponding author. E-mail: pfcook@emory.edu

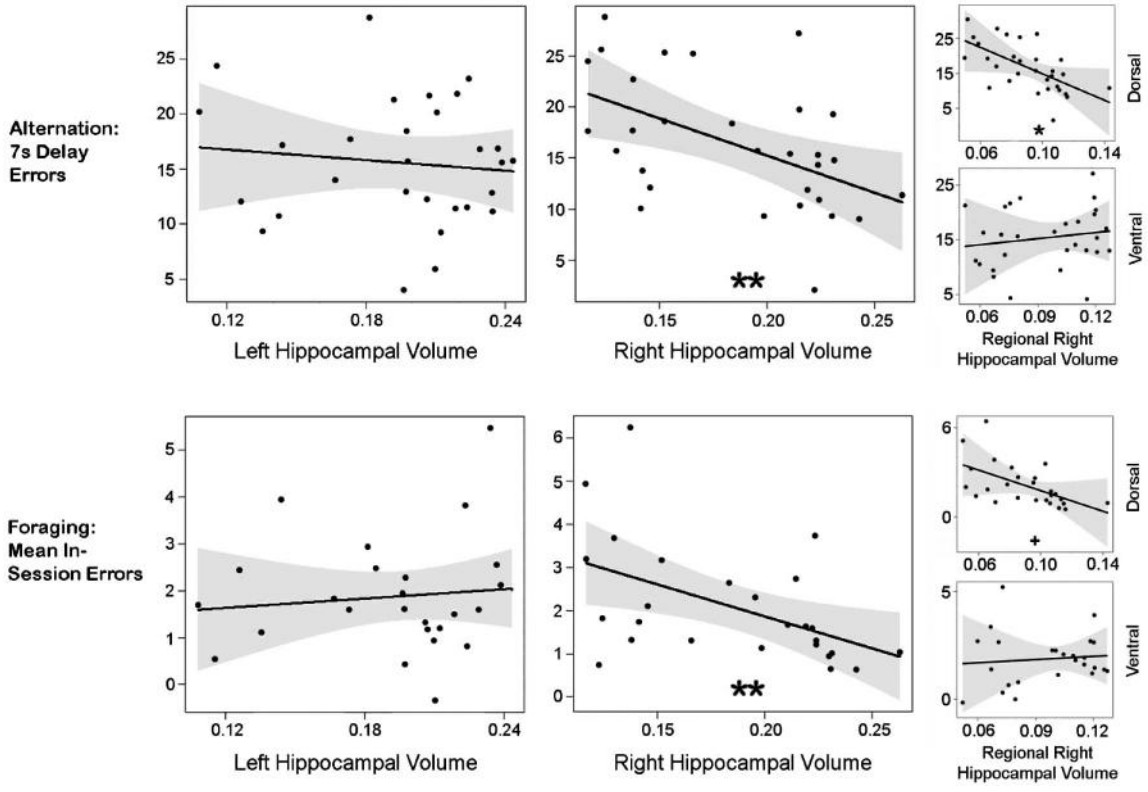

Fig. 1. Spatial memory is related to the integrity of the right hippocampus. The conditional scatterplots show correlations between left and right hippocampal volumes (as a percentage of total brain volume; *x* axes) and performance measures (*y* axes) related to behavioral alternation and foraging tasks, after regressing out other dependent variables. Regression analyses for alternation included no-delay test errors as an independent variable to control for variance in test performance that was unrelated to memory. Alternation, right: $t = -2.82$, df = 27, $P < 0.01$. Alternation, left: $t(0.54) < 1$, df = 27. Foraging, right: $t = -2.66$, df = 23, $P < 0.01$. Foraging, left: $t(0.5) < 1$, df = 23. The insets on the right show correlations of ventral and dorsal right hippocampal volumes with performance measures after regressing out other dependent variables. Alternation, dorsal: $t = -2.05$, df = 27, $P < 0.05$. Alternation, ventral: $t(0.235) < 1$, df = 27. Foraging, dorsal: $t = -1.72$, df = 23, $P < 0.1$. Foraging, ventral: $t(0.33) < 1$, df = 23. Confidence bands for fit lines are shown in gray. Each point represents one animal. $^{+}P < 0.1$; $^{*}P < 0.05$; $^{**}P < 0.01$.

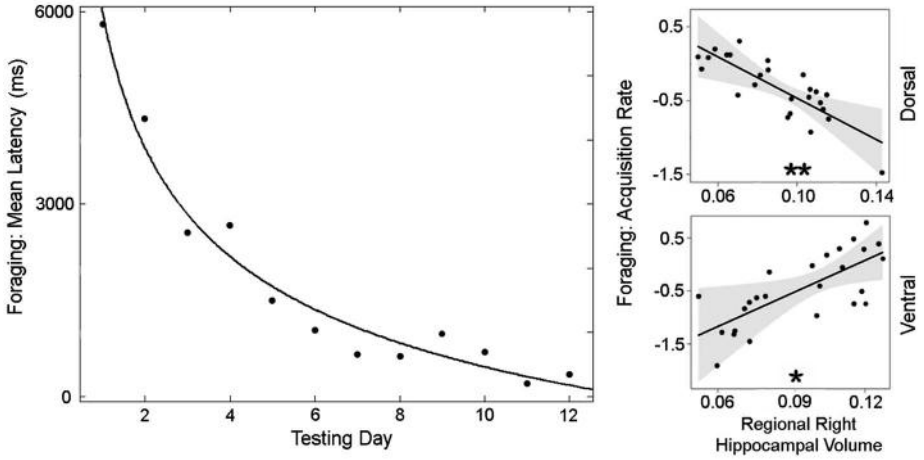

Fig. 2. Dissociable contributions of the dorsal and ventral right hippocampus to long-term spatial memory. Mean latency (to finding a reward) across all subjects is shown as a function of testing day [curve: $y = a*x^b + c$, coefficient of determination (R^2) = 0.97]. The inset conditional plots (right) show correlations between dorsal and ventral right hippocampal volume (as a percentage of total brain volume; *x* axes) and the foraging acquisition rate [log-transformed latency per testing day, *y* axes; represented as the slope of the logged power curve, with the steeper negative slope (faster acquisition) lower on the axis] after regressing out other dependent variables. Dorsal: $t = -3.21$, df = 21, $P < 0.005$. Ventral: $t = 2.44$, df = 21, $P < 0.05$. $^{*}P < 0.05$; $^{**}P < 0.01$.

substituted the volume of the dorsal third. Results were comparable to the dorsal half analyses (*9*).

The first behavioral task involved spatial alternation in a two-choice maze (fig. S2). Delayed alternation performance is impaired by hippocampal lesions in rodents (*12*) and is believed to rely on the role of the hippocampus in representing and sequencing memory for recent navigational episodes (*6*). After training to a baseline success rate of 85% on free-running left-right alternation (movie S1) (*9*), each sea lion was presented with 40 delay trials, in which the animals had to wait for 7 s at the beginning of each trial before entering the maze (movie S2). Delay trials were paired with 40 no-delay comparison trials. Right, but not left, hippocampal volume positively correlated with performance on delay trials. In addition, dorsal, but not ventral, right hippocampal volume positively correlated with performance (Fig. 1).

The second behavioral assessment was a spatial foraging task in which four possible food locations (opaque buckets) were made available once every 24 hours in the animals' enclosure (fig. S3 and movie S3). For each animal, one set location always contained food, while the others did not. At the beginning of a test session, subjects received fish at a central location while the buckets were simultaneously presented. Latency to the correct location across sessions and mean within-session errors (revisits to previously visited locations) were recorded (*9*). Rodent data indicate that within-session errors in similar spatial choice tasks track hippocampal damage (*13*). In our subjects,

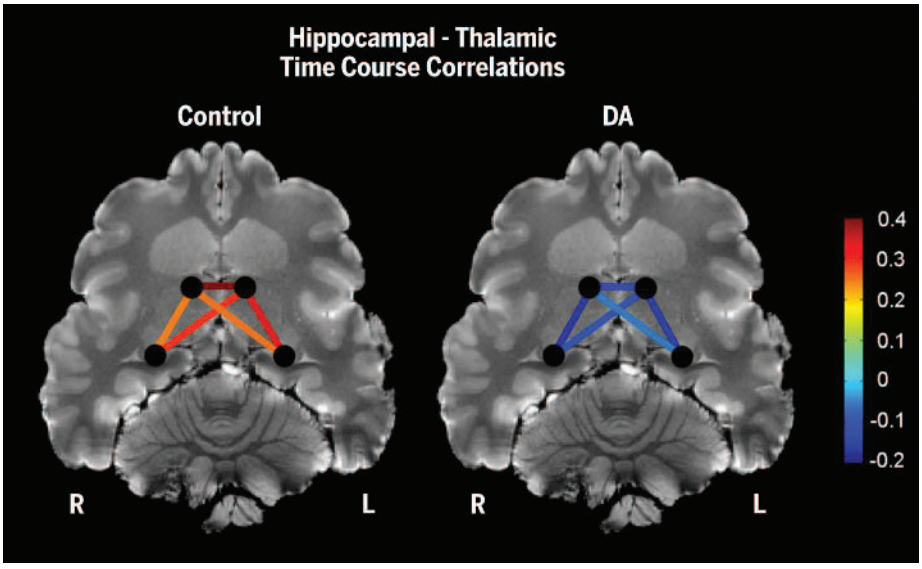

Fig. 3. Altered hippocampal-thalamic connectivity in animals with hippocampal lesions. Shown are maps of hippocampal-thalamic correlation coefficients, averaged for five brains with hippocampal lesions (right) and six without (left). The colors of the lines connecting regions of the brain represent the correlation strength of their respective time courses, with warmer colors indicating higher correlations.

right, but not left, hippocampal volume was positively correlated with within-session performance (Fig. 1).

To assess longer-term spatial memory, an additional performance measure was extracted from the foraging task. Because the mean cross-session learning curve for all animals was fit nearly perfectly by a power function (Fig. 2), the slope of the logged power curve for each animal was used to index the cross-session learning rate (table S3). Neither right nor left hippocampal damage was predictive of learning rate across all sessions (table S4). However, individual learning rates correlated positively with dorsal right hippocampal volumes and negatively with ventral right hippocampal volumes (Fig. 2).

The data reviewed thus far suggest a direct relationship between right hippocampal structure and spatial memory in sea lions. Spatial memory also depends on dynamic interactions between the hippocampus and other brain regions (*14*), with the hippocampal-thalamic axis being particularly relevant (*15*). CSLs with DA toxicosis present with seizures (*3*), which alter hippocampal networks in rodents (*16*). Accordingly, we used functional MRI to examine hippocampal-thalamic functional connectivity (*17*) in 11 CSLs undergoing rehabilitation between August and October 2012 (table S2). Five of the 11 showed volumetric evidence of gross hippocampal lesions (*9*). The other six animals served as a provisional control group. Although their complete ecotoxicant exposure history was not available, independent assessment by a veterinary radiologist and veterinarian found no evidence of neurological abnormality (*9*).

Animals with hippocampal lesions showed reduced hippocampal-thalamic connectivity (repeated measures ANOVA: $F = 22.3$, df = 1, $P < 0.001$) (Fig. 3). Reductions in connectivity were bilateral, with no statistical interaction between group (DA versus control) and laterality [$F(0.003) < 1$, df = 1] (*9*). A subsequent voxel-wise test showed high hippocampal-thalamic connectivity in controls (fig. S5) (*9*).

These data combining behavioral and neural measures in wild sea lions suggest that spatial memory is impaired and hippocampal-thalamic connectivity is disrupted as a result of DA-related hippocampal damage. The functional lateralization matches that found in humans (*10*) and may be consistent with findings of functional cortical asymmetry in sea lions (*18*). Because we examined wild CSLs, the effects of non–DA-related neurological insults were not fully controlled. This limitation is also a strength, because our results directly generalize to wild individuals.

Impairment in short- and long-term spatial memory as a result of hippocampal lesions and altered hippocampal networks probably interferes with foraging in CSLs and could partly explain maladaptive navigational behavior and consequent mortality. Because chronic exposure to DA is widespread in CSLs, these impairments could have population-level consequences, particularly in combination with changing ocean conditions that lead to less reliable foraging conditions (*7*, *19*). In addition, these findings have practical application in the veterinary and rehabilitation setting. Given the negative correlation that we found between navigational memory and the extent of hippocampal damage, in vivo measurements of hippocampal volume in stranded sea lions may be useful markers of prognosis and postrelease outcomes. Specifically, animals with right dorsal hippocampal lesions might be at increased risk in the wild. More generally, these results, obtained from an ecologically valid sample of wild animals that were naturally exposed to DA, may be applicable to other affected species, including sea birds and cetaceans, that are less accessible for neurobehavioral study.

REFERENCES AND NOTES

1. C. A. Scholin *et al.*, *Nature* **403**, 80–84 (2000).
2. M. W. Silver *et al.*, *Proc. Natl. Acad. Sci. U.S.A.* **107**, 20762–20767 (2010).
3. T. Goldstein *et al.*, *Proc. Biol. Sci.* **275**, 267–276 (2008).
4. P. A. Silvagni, L. J. Lowenstine, T. Spraker, T. P. Lipscomb, F. M. D. Gulland, *Vet. Pathol.* **42**, 184–191 (2005).
5. J. O'Keefe, "Nobel lecture: Spatial cells in the hippocampal formation" (Nobel Media AB, 2014); www.nobelprize.org/nobel_prizes/medicine/laureates/2014/okeefe-lecture.html.
6. N. J. Fortin, K. L. Agster, H. B. Eichenbaum, *Nat. Neurosci.* **5**, 458–462 (2002).
7. M. J. Weise, D. P. Costa, R. M. Kudela, *Geophys. Res. Lett.* **33**, L22S10 (2006).
8. K. Thomas, J. T. Harvey, T. Goldstein, J. Barakos, F. M. D. Gulland, *Mar. Mamm. Sci.* **26**, 36–52 (2010).
9. Materials and methods are available as supplementary materials on *Science* Online.
10. V. D. Bohbot *et al.*, *Neuropsychologia* **36**, 1217–1238 (1998).
11. M. B. Moser, E. I. Moser, *Hippocampus* **8**, 608–619 (1998).
12. W. W. Roberts, W. N. Dember, M. Brodwick, *J. Comp. Physiol. Psychol.* **55**, 695–700 (1962).
13. S. B. Floresco, J. K. Seamans, A. G. Phillips, *J. Neurosci.* **17**, 1880–1890 (1997).
14. H. Eichenbaum, *Nat. Rev. Neurosci.* **1**, 41–50 (2000).
15. D. S. Olton, J. A. Walker, F. H. Gage, *Brain Res.* **139**, 295–308 (1978).
16. J. M. Parent *et al.*, *J. Neurosci.* **17**, 3727–3738 (1997).
17. B. Biswal, F. Z. Yetkin, V. M. Haughton, J. S. Hyde, *Magn. Reson. Med.* **34**, 537–541 (1995).
18. O. I. Lyamin, I. S. Chetyrbok, *Neurosci. Lett.* **143**, 263–266 (1992).
19. S. C. Doney *et al.*, *Ann. Rev. Mar. Sci.* **4**, 11–37 (2012).

ACKNOWLEDGMENTS

This research was conducted under authorization granted to the Marine Mammal Health and Stranding Response Program by the National Marine Fisheries Service under scientific research permit 932-1489-10, and it has been approved by the Institutional Animal Care and Use Committees at the University of California–Santa Cruz (UCSC) and The Marine Mammal Center (TMMC). We thank D. Casper and staff members at both UCSC's Pinniped Laboratory and TMMC for contributions to data acquisition and logistical support. Behavioral data are in the supplementary materials; imaging data are archived on Dryad at http://dx.doi.org/10.5061/dryad.0279k. None of the authors claim any competing financial interests.

SUPPLEMENTARY MATERIALS

www.sciencemag.org/content/350/6267/1545/suppl/DC1
Materials and Methods
Supplementary Text
Figs. S1 to S5
Tables S1 to S5
References (*20*–*23*)
Movies S1 to S3

13 May 2015; accepted 9 November 2015
Published online 14 December 2015
10.1126/science.aac5675

MEMBRANE REMODELING

Structure and membrane remodeling activity of ESCRT-III helical polymers

John McCullough,[1]* Amy K. Clippinger,[2]* Nathaniel Talledge,[1,3] Michael L. Skowyra,[2] Marissa G. Saunders,[1] Teresa V. Naismith,[2] Leremy A. Colf,[1] Pavel Afonine,[4] Christopher Arthur,[5] Wesley I. Sundquist,[1]† Phyllis I. Hanson,[2]† Adam Frost[1,3]†

The endosomal sorting complexes required for transport (ESCRT) proteins mediate fundamental membrane remodeling events that require stabilizing negative membrane curvature. These include endosomal intralumenal vesicle formation, HIV budding, nuclear envelope closure, and cytokinetic abscission. ESCRT-III subunits perform key roles in these processes by changing conformation and polymerizing into membrane-remodeling filaments. Here, we report the 4 angstrom resolution cryogenic electron microscopy reconstruction of a one-start, double-stranded helical copolymer composed of two different human ESCRT-III subunits, charged multivesicular body protein 1B (CHMP1B) and increased sodium tolerance 1 (IST1). The inner strand comprises "open" CHMP1B subunits that interlock in an elaborate domain-swapped architecture and is encircled by an outer strand of "closed" IST1 subunits. Unlike other ESCRT-III proteins, CHMP1B and IST1 polymers form external coats on positively curved membranes in vitro and in vivo. Our analysis suggests how common ESCRT-III filament architectures could stabilize different degrees and directions of membrane curvature.

The endosomal sorting complexes required for transport (ESCRT) pathway is best known for facilitating membrane remodeling and fission for processes such as the endosomal intralumenal vesicle (ILV) formation, enveloped virus budding, nuclear envelope closure, and cytokinetic abscission (*1*–*3*). In these reactions, the ESCRT machinery assembles on the interior of a negatively curved, cytoplasm-filled membrane neck and pulls the membrane toward itself to the fission point. These fission reactions are topologically distinct from reactions in which cytoplasmic BAR domain–containing proteins and dynamin-family guanosine triphosphatases assemble around and constrict positively curved membrane tubules.

ESCRT components are recruited to different membranes by site-specific adaptors that ultimately recruit ESCRT-III subunits and their binding partners, including VPS4-family adenosine triphosphatases (ATPases). ESCRT-III assemblies promote membrane constriction and fission, possibly in concert with VPS4. Humans express 12 related ESCRT-III proteins, called charged multivesicular body proteins (CHMPs) 1A-7 and increased sodium tolerance 1 (IST1) (*1*–*3*). Crystal structures of CHMP3 and IST1 show a common structure in which the first two helices form a long hairpin, the shorter helices 3 and 4 pack against the open end of the hairpin, and helix 5 folds back and packs against the closed end of the helical hairpin (*4*–*6*). This "closed" conformation appears to autoinhibit ESCRT-III membrane binding and oligomerization (*4*, *7*, *8*). ESCRT-III subunits can also adopt a second, more extended "open" conformation that has been characterized biochemically, but not visualized in molecular detail. The open conformation appears to be the active, polymerization-competent state because mutations or solution conditions that favor this conformation typically promote polymerization (*1*–*3*). Many ESCRT-III subunits form spiraling homo- and heteromeric filaments, both in vitro (*4*, *9*–*15*) and in cells (*10*, *16*–*19*), but the structural basis for filament assembly is unclear.

We used cryogenic electron microscopy (cryo-EM) to determine the molecular structure of a helical copolymer comprising human IST1 and CHMP1B. Full-length IST1 and CHMP1B spontaneously coassembled under low ionic strength conditions into well-ordered helical tubes. Helical order was further enhanced by using a truncated IST1 construct that spanned residues 1 to 189, hereafter termed $IST1_{NTD}$, and by including small, acidic unilamellar vesicles (SUVs) to nucleate polymer formation. The resulting $IST1_{NTD}$-CHMP1B tubes were long, straight, and 24 nm in diameter (Fig. 1A). The three-dimensional (3D) structure of $IST1_{NTD}$-CHMP1B assemblies was determined to a resolution of ~4 Å by real-space helical reconstruction (supplementary materials, materials and methods, and figs. S1 to S4). Each tube comprised a right-handed one-start helical filament that packed with an interfilament spacing of 5.1 nm per turn (Fig. 1, B to D, and movie S1). Each filament was double-stranded, with distinct inner and outer strands (at 7.7 and 10.2 nm radii, respectively). Segmented densities from subunits in the outer strand corresponded well to the crystal structure of $IST1_{NTD}$ in its closed conformation [Protein Data Bank (PDB) 3FRR] (*5*), with only minor refinements required to optimize the position of helix A (Fig. 1E and movie S2). In contrast, the CHMP1B subunits of the inner strand adopted a very different, open conformation. These subunits were almost entirely α-helical, and side chain densities were clearly evident in the EM density (Fig. 1, B, D, and F; and movie S3). The open CHMP1B conformation resembled an arm, with helices 1 to 3 forming the upper arm and biceps, helix 4 and helix A forming the forearm, and helix 5 forming the hand. Joints between helices 3 and 4 and between helices A and 5 correspond to the elbow and wrist, respectively (Fig. 1, F and G).

High-ionic-strength conditions (*4*, *8*) typically favor the monomeric, closed ESCRT-III subunit conformation (*4*, *8*, *20*, *21*), and CHMP1B also remained monomeric under high-ionic-strength conditions (fig. S5). Lowering the ionic strength triggered coassembly of IST1 and CHMP1B, implying that CHMP1B subunits are captured as they open. To visualize this conformational change, we generated a structure-based homology model for the CHMP1B closed state (supplementary materials, materials and methods). In comparison with the modeled closed state, the helix 5 hand is displaced by ~100 Å when CHMP1B opens. This global reorganization requires only three local rearrangements: The elbow angle between helices 3 and 4 must change, and the loops that connect helix 2/3 and helix 4/A must become helical to create the longer, continuous helices that extend the upper arm to the elbow and create the forearm in the open state (Figs. 1, F and G, and 2A and movie S4).

In the filament, the open CHMP1B conformation is stabilized by extensive intersubunit interactions along the inner strand (Fig. 2B). Each CHMP1B molecule interacts with four other CHMP1B subunits that pack together and cross the forearm of the original subunit. In addition, the helix 5 hand grasps the shoulder of the hairpin four subunits away, making a domain-swapped contact that is analogous to the intrasubunit interaction between the hairpin and helix 5 in the closed ESCRT-III conformations (Fig. 2, A and B). Opening and assembly reduces the total solvent-accessible surface area of CHMP1B from ~10,720 to ~6,350 $Å^2$. The $IST1_{NTD}$-CHMP1B assembly is further stabilized by three additional types of interactions, which differ completely from crystallized contacts for soluble IST1-CHMP1B heterodimers (Fig. 2, C to F, and figs. S6 and S7) (*6*).

A final notable feature of the IST1-CHMP1B tube is the remarkably cationic interior. This surface is created by a series of conserved basic residues from helix 1 of CHMP1B (Fig. 2, D and F), which forms the principal membrane-binding site in other ESCRT-III proteins (*5*, *22*). Its position inside the IST1-CHMP1B copolymer was

[1]Department of Biochemistry, University of Utah, Salt Lake City, UT 84112, USA. [2]Department of Cell Biology and Physiology, Washington University School of Medicine, St. Louis, MO 63110, USA. [3]Department of Biochemistry and Biophysics, University of California, San Francisco, San Francisco, CA 94158, USA. [4]Physical Bioscience Division, Lawrence Berkeley National Laboratory, Berkeley, CA 94720, USA. [5]FEI Company, Hillsboro, OR 97124, USA.
*These authors contributed equally to this work. †Corresponding author. E-mail: wes@biochem.utah.edu (W.I.S.); phanson22@wustl.edu (P.I.H.); adam.frost@ucsf.edu (A.F.)

unexpected because well-characterized ESCRT-mediated membrane remodeling events require that membranes interact with the exterior surface of coiled ESCRT-III filaments, such as in the neck of a nascent ILV or viruses. The functional roles of IST1 and CHMP1B in such canonical ESCRT activities have been enigmatic, however, because neither protein is required for ILV biogenesis (*23*–*26*) or virus budding (*27*). Moreover, IST1

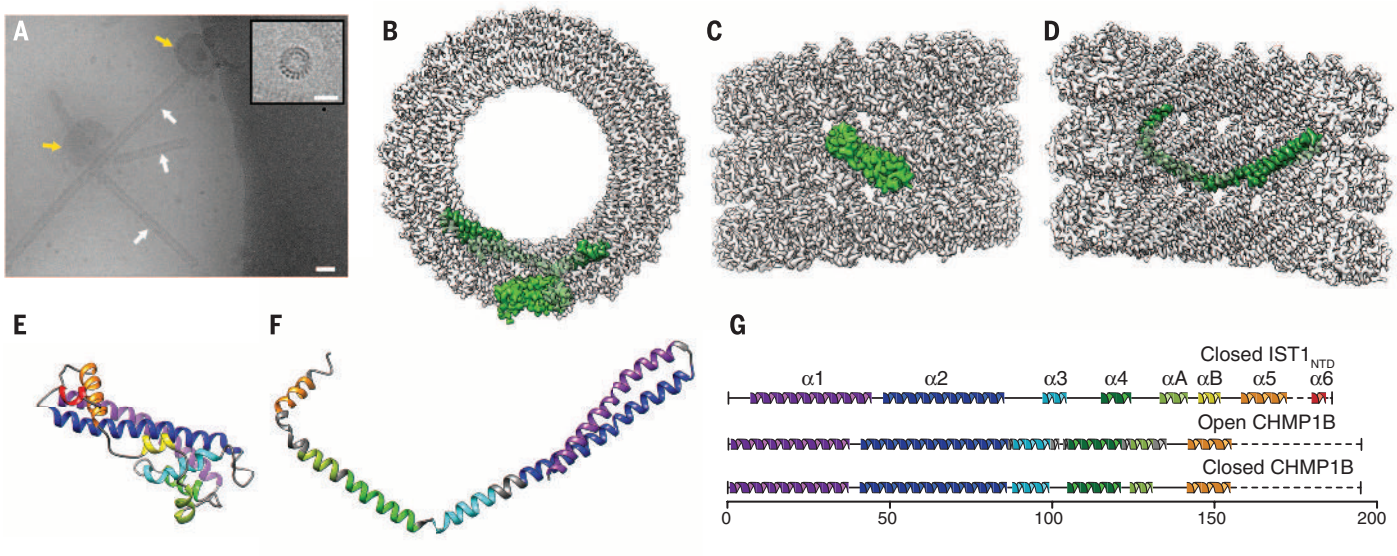

Fig. 1. $IST1_{NTD}$ and CHMP1B copolymerized into helical tubes comprising polar, double-stranded helical filaments. (**A**) Electron cryomicrograph showing $IST1_{NTD}$-CHMP1B tubes (white arrows) assembled by incubating equimolar $IST1_{NTD}$ and CHMP1B in the presence of polymer-nucleating small acidic unilamellar vesicles (SUVs; yellow arrows). (Inset) End-on view of a short $IST1_{NTD}$-CHMP1B tube. Scale bars, 40 nm (A) and 20 nm (inset). (**B**) End-on view of the reconstructed $IST1_{NTD}$-CHMP1B tube highlighting single subunits of $IST1_{NTD}$ (light green, outer strand) and CHMP1B (dark green, inner strand). (**C**) External view of the reconstructed helix with a highlighted $IST1_{NTD}$ subunit. (**D**) Internal cutaway view of the reconstructed helix, with a highlighted CHMP1B subunit. (**E**) Ribbon diagram of the modeled $IST1_{NTD}$ subunit (closed conformation). (**F**) Ribbon diagram of the modeled CHMP1B subunit (open conformation). (**G**) Secondary structure diagrams for closed $IST1_{NTD}$ (top), open CHMP1B (middle), and closed CHMP1B (bottom).

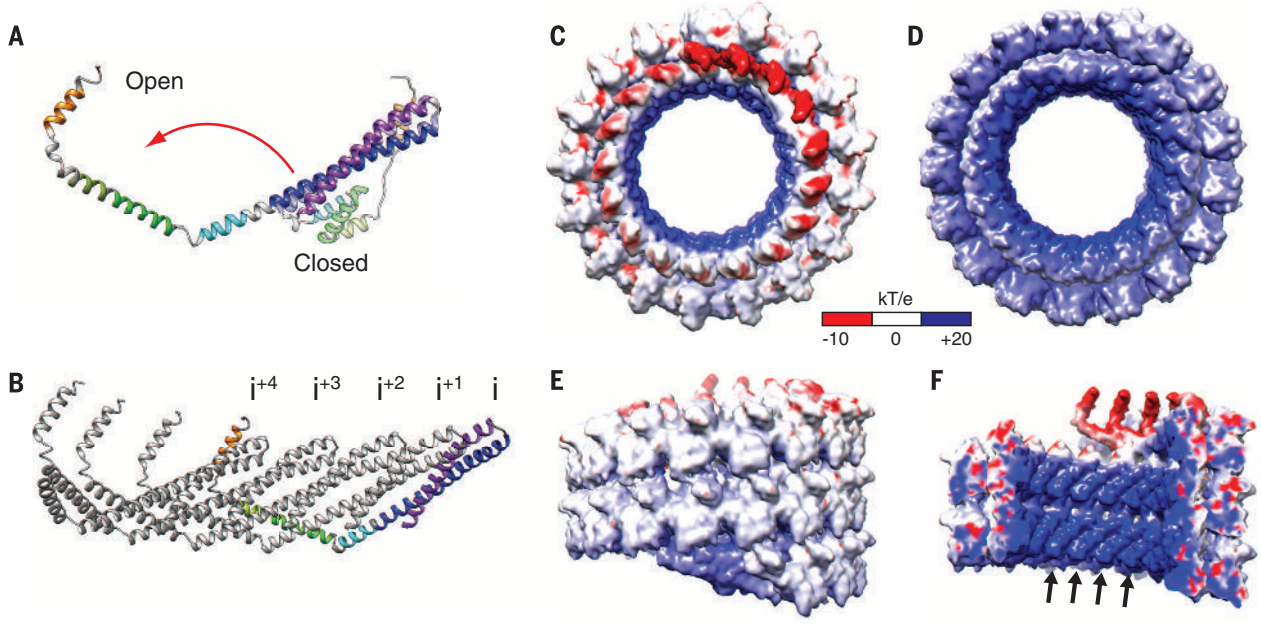

Fig. 2. CHMP1B opening, strand structure, and electrostatic surface potentials of the $IST1_{NTD}$-CHMP1B assembly. (**A**) Superposition of the open and closed CHMP1B conformations. (**B**) Five interlocked CHMP1B molecules from the inner strand of the filament. (**C**) "Top-end," electrostatic surface view of the $IST1_{NTD}$-CHMP1B tube, highlighting the acidity of the CHMP1B inner strand (including Glu^{130}, Asp^{131}, Asp^{147}, Glu^{152}, Asp^{155}, Glu^{156}, and Asp^{160}) and the $IST1_{NTD}$ outer strand (including Asp^{49}, Glu^{50}, Glu^{57}, Glu^{163}, Glu^{168}, Glu^{178}, Asp^{180}, and Glu^{186}). (**D**) "Bottom-end," electrostatic surface view of the $IST1_{NTD}$-CHMP1B tube, highlighting the strongly basic characters of the CHMP1B inner strand (including Lys^{3}, Lys^{87}, Lys^{94}, Lys^{101}, Lys^{107}, and Lys^{114}) and the $IST1_{NTD}$ outer strand (including Lys^{7}, Arg^{10}, Lys^{90}, Arg^{109}, Lys^{118}, Lys^{127}, Lys^{130}, Lys^{134}, and Arg^{137}). (**E**) Exterior, electrostatic surface view of the $IST1_{NTD}$-CHMP1B tube, revealing the modestly basic character of the $IST1_{NTD}$ outer strand. (**F**) Internal cutaway electrostatic surface view of the $IST1_{NTD}$-CHMP1B tube, revealing the strongly basic character of the lumenal surface, contributed primarily by basic residues in CHMP1B helix 1 (arrows), including Lys^{3}, Lys^{13}, Arg^{17}, Lys^{20}, Lys^{21}, Lys^{24}, Lys^{32}, and Lys^{35}.

functions in the resolution of endosomal tubules that project into the cytoplasm and recycle cargoes back to the plasma membrane (*28*). Looking in cells, we found that moderately overexpressed CHMP1B polymerized into elongated cytoplasmic structures (fig. S8). Deep-etch EM of the plasma membranes revealed filaments that were similar to those of CHMP4A and other well-studied ESCRT-III proteins (*17*), except that CHMP1B filaments coated tubules ~35 to 60 nm in diameter that extended into rather than away from the cytoplasm (Fig. 3, A to D) (*17*, *18*). Replicas of cells transfected and immunolabeled for CHMP1B alone, or with IST1, also revealed immunodecorated organelles and tubules that were not attached to the plasma membrane but again had recognizable striations (Fig. 3, E to K). The resemblance of these organelles to early endosomes (*29*), including the occasional presence of clathrin-coated buds (Fig. 3, J and K), indicates that CHMP1B and IST1 can coat and potentially remodel endosomal tubules.

To determine whether distinct membrane remodeling topologies are intrinsic properties of different ESCRT-III filaments, we compared the structures induced by spirals of CHMP1B with those induced by the prototypical ESCRT-III protein CHMP4A. In earlier studies, CHMP4 proteins only deformed the membrane when bound to ATPase-deficient VPS4B (*17*) or an activated CHMP2A mutant (*18*). We found that deleting C-terminal sequences yielded a mutant CHMP4A that formed tight, membrane-deforming spirals (Fig. 4A). The deformations induced by CHMP4A spirals were directed away from the cytoplasm, as expected (*17*, *18*). Comparable views of cells transfected with full-length and C-terminal truncations of CHMP1B confirmed that CHMP4A and CHMP1B induced cellular membranes to tubulate in opposite directions (Fig. 4B and fig. S9).

We also tested how CHMP1B polymers bind and remodel liposomal membranes in vitro. Under physiological solution conditions, CHMP1B formed single- and double-stranded one-start helices and spirals around membrane tubules, with interstrand spacing of 4.7 ± 0.1 nm (Fig. 4C and figs. S10 and S11). Adding IST1 to CHMP1B-induced membrane tubules generated copolymeric helices that were structural analogs of the membrane-free IST1-CHMP1B assemblies described above, as judged by their interstrand spacing (5.1 ± 0.1 nm versus 5.2 ± 0.1 nm) and by the similarities of 2D class averages of the two assemblies (Fig. 4D and figs. S10 and S11). The positively curved membrane tubules within the protein coats could be visualized with negative staining of the CHMP1B and IST1-CHMP1B assemblies (Fig. 4, C and D, and fig. S10), in cryo-EM images, and in 2D class averages of the molecules along the tangential surface of the bilayer (fig. S11). Thus, CHMP1B and IST1 form external coats on positively curved membranes in vitro and in cells.

Our analyses also provide insight into how ESCRT-III filaments can assemble conical spirals of decreasing diameter, as might be required to draw membranes together to the fission point.

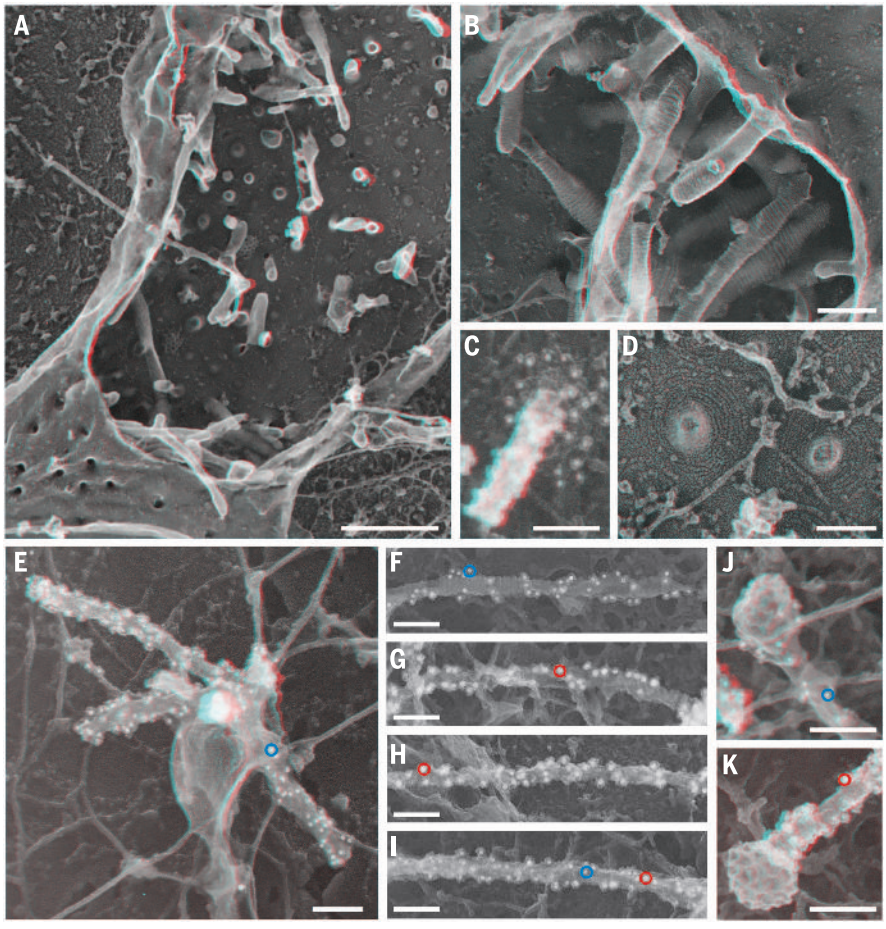

Fig. 3. CHMP1B and IST1 tubulated cellular membranes. (**A**) Survey view of the cytoplasmic surface of the plasma membrane in an unroofed COS-7 cell expressing FLAG-CHMP1B. Tubular invaginations extending into the cell interior are apparent along the exposed plasma membrane and as stabilized openings at the edges of the cell. Use view glasses for 3D viewing of anaglyphs (left eye, red). (**B**) Higher-magnification view of tubular invaginations induced and coated by FLAG-CHMP1B filaments. (**C**) Immunodecoration confirmed the presence of CHMP1B around and along a tubule in a cell expressing untagged CHMP1B. Antibody detected with 12 nm gold is white in these contrast-reversed EM images. (**D**) Higher-magnification view of FLAG-CHMP1B filament spirals on exposed plasma membrane. (**E**) CHMP1B-immunoreactive organelle in an unroofed COS-7 cell expressing untagged CHMP1B. Antibody detected with 12 nm gold is white in these contrast reversed EM images; a representative gold particle is circled in blue. (**F** to **I**) Representative internal tubules from cells coexpressing untagged CHMP1B (12 nm gold; example circled in blue) and IST1-myc (18 nm gold; examples circled in red). (**J** and **K**) Clathrin-coated bud capping the end of (J) CHMP1B and (K) IST1-myc immunolabeled tubules from cotransfected cells. Measurements of filament diameter (and interstrand spacing) showed that when apparently unitary filaments were resolvable, their diameter varied from 5 to 10 nm, including platinum. These measurements are generally consistent with the dimensions of IST1-CHMP1B and CHMP1B filaments formed in vitro. Scale bars, 500 nm (A) and 100 nm (B) to (K).

In addition to uniform 24-nm helices, we frequently observed conical spirals of membrane-associated CHMP1B and $IST1_{NTD}$-CHMP1B (Fig. 4, C and D, and figs. S10 and S11), as well as conical IST1-CHMP1B filaments assembled in the absence of nucleating vesicles (fig. S12). One class of membrane-free $IST1_{NTD}$-CHMP1B cones was sufficiently common to be reconstructed at low resolution, which confirmed that the cones are composed of the same double-stranded filaments as those seen in the $IST1_{NTD}$-CHMP1B helices (Fig. 4D; figs. S1, S11, and S12; and movies S5 and S6). Within the conical spiral, both the degree of filament curvature and the lateral interactions between adjacent filaments varied continuously. Small changes in filament curvature are likely accommodated by altering the angles of the "elbow" and "wrist" joints. Larger changes could, in principle, be accommodated (or even driven) by ratcheting the buttressing intersubunit interactions made by the "forearm" and "hand." For example, changing the connectivity from i+4 to i+5 would tend to straighten the CHMP1B filament. The required continuum of differing lateral interactions in the $IST1_{NTD}$-CHMP1B spirals is apparently accommodated by small shifts in ionic interstrand interactions, which is plausible because the basic charges are distributed

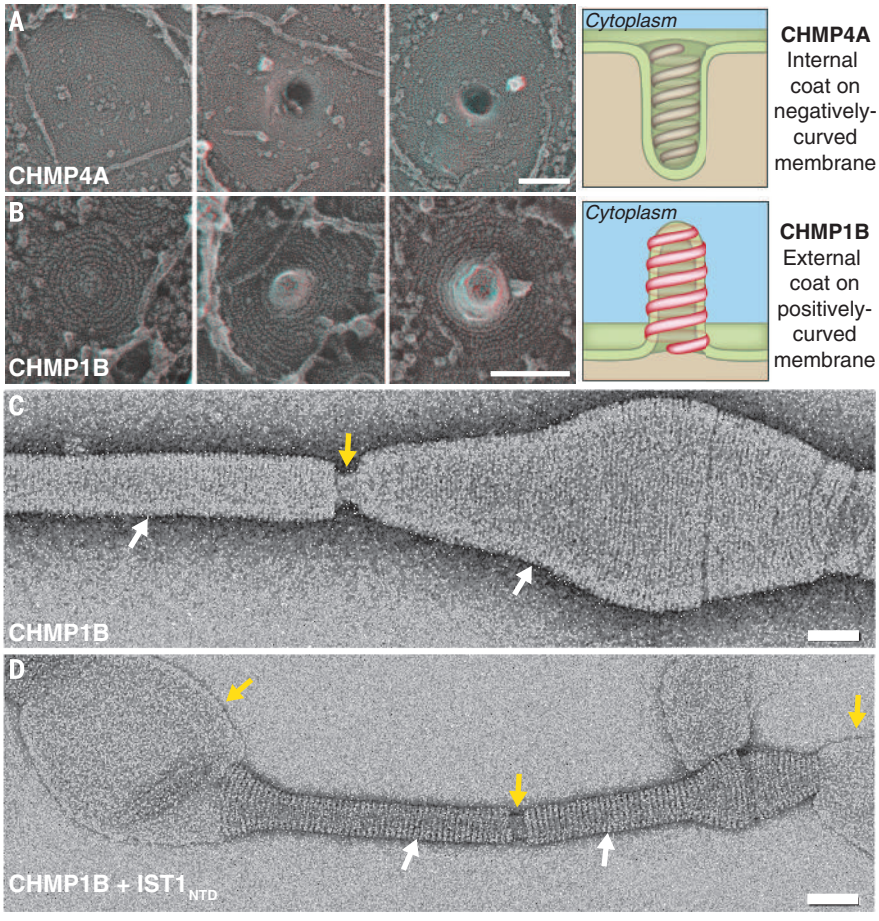

Fig. 4. Topology of ESCRT-III membrane deformation in cells and in vitro. (**A**) Series of filament spirals on the plasma membrane of COS-7 cells expressing $CHMP4A_{1\text{-}164}$ show development of the outwardly directed protrusions previously associated with ESCRT-III filaments (*15*, *16*). Drawing highlights relationship between a CHMP4A conical spiral and a negatively curved plasma membrane tubule. (**B**) Series of filament spirals on the plasma membrane of COS-7 cells expressing FLAG-CHMP1B show development of invaginations directed into the cell. Drawing highlights relationship between a CHMP1B conical spiral and a positively curved plasma membrane tubule. (**C**) Negative stain electron micrograph showing that CHMP1B tubulates liposomes and forms a filamentous coat on the outside of the tubule. White arrows highlight regions coated by the CHMP1B helices, and the yellow arrow highlights a break in the coat where the internal lipid is visible. (**D**) Negative stain electron micrograph showing that the $IST1_{NTD}$-CHMP1B copolymer forms on the outside of membrane tubules. White arrows highlight regions coated by the $IST1_{NTD}$-CHMP1B copolymer, and the yellow arrows highlight breaks in the helical coat or uncoated regions of the liposome where the internal membrane is visible. Scale bars, 100 nm (A) and (B), 50 nm (C) and (D).

almost uniformly along one edge of the double strand (Fig. 2, C and D). Wider IST1-CHMP1B spirals will tend to propagate toward their preferred 24-nm diameter. At this diameter, the narrow lumen (~10 nm) would force internal opposing lipid bilayers (each ~4.7 nm wide) toward hemi-fission (*30*, *31*), potentially providing a driving force for membrane constriction and fission. Last, we note that other ESCRT-III subunits, such as CHMP4A, tubulate membranes in the opposite direction to that seen with CHMP1B. Such stabilization of negative, rather than positive, membrane curvature could be achieved simply by altering the intrinsic degree and direction of filament curvature while retaining an analogous membrane-binding surface and subunit connectivity.

REFERENCES AND NOTES

1. J. H. Hurley, *EMBO J.* **34**, 2398–2407 (2015).
2. P. I. Hanson, A. Cashikar, *Annu. Rev. Cell Dev. Biol.* **28**, 337–362 (2012).
3. J. McCullough, L. A. Colf, W. I. Sundquist, *Annu. Rev. Biochem.* **82**, 663–692 (2013).
4. M. Bajorek *et al.*, *Nat. Struct. Mol. Biol.* **16**, 754–762 (2009).
5. T. Muziol *et al.*, *Dev. Cell* **10**, 821–830 (2006).
6. J. Xiao *et al.*, *Mol. Biol. Cell* **20**, 3514–3524 (2009).
7. Y. Lin, L. A. Kimpler, T. V. Naismith, J. M. Lauer, P. I. Hanson, *J. Biol. Chem.* **280**, 12799–12809 (2005).
8. S. Lata *et al.*, *J. Mol. Biol.* **378**, 818–827 (2008).
9. W. M. Henne, N. J. Buchkovich, Y. Zhao, S. D. Emr, *Cell* **151**, 356–371 (2012).
10. M. J. Dobro *et al.*, *Mol. Biol. Cell* **24**, 2319–2327 (2013).
11. G. Effantin *et al.*, *Cell. Microbiol.* **15**, 213–226 (2013).
12. S. Ghazi-Tabatabai *et al.*, *Structure* **16**, 1345–1356 (2008).
13. C. Moriscot *et al.*, *PLOS ONE* **6**, e21921 (2011).
14. Q.-T. Shen *et al.*, *J. Cell Biol.* **206**, 763–777 (2014).
15. S. Lata *et al.*, *Science* **321**, 1354–1357 (2008).
16. G. Bodon *et al.*, *J. Biol. Chem.* **286**, 40276–40286 (2011).
17. P. I. Hanson, R. Roth, Y. Lin, J. E. Heuser, *J. Cell Biol.* **180**, 389–402 (2008).
18. A. G. Cashikar *et al.*, *eLife* **3**, e02184 (2014).
19. J. Guizetti *et al.*, *Science* **331**, 1616–1620 (2011).
20. A. Zamborlini *et al.*, *Proc. Natl. Acad. Sci. U.S.A.* **103**, 19140–19145 (2006).
21. S. Shim, L. A. Kimpler, P. I. Hanson, *Traffic* **8**, 1068–1079 (2007).
22. N. J. Buchkovich, W. M. Henne, S. Tang, S. D. Emr, *Dev. Cell* **27**, 201–214 (2013).
23. D. P. Nickerson, M. West, R. Henry, G. Odorizzi, *Mol. Biol. Cell* **21**, 1023–1032 (2010).
24. C. Dimaano, C. B. Jones, A. Hanono, M. Curtiss, M. Babst, *Mol. Biol. Cell* **19**, 465–474 (2008).
25. D. P. Nickerson, M. West, G. Odorizzi, *J. Cell Biol.* **175**, 715–720 (2006).
26. S. M. Rue, S. Mattei, S. Saksena, S. D. Emr, *Mol. Biol. Cell* **19**, 475–484 (2008).
27. E. Morita, *FEBS J.* **279**, 1399–1406 (2012).
28. R. Allison *et al.*, *J. Cell Biol.* **202**, 527–543 (2013).
29. W. Stoorvogel, V. Oorschot, H. J. Geuze, *J. Cell Biol.* **132**, 21–33 (1996).
30. Y. Kozlovsky, M. M. Kozlov, *Biophys. J.* **85**, 85–96 (2003).
31. Materials and methods are available as supplementary materials on *Science* Online.

ACKNOWLEDGMENTS

Electron microscopy was performed at the University of California, San Francisco, the University of Utah, and the Oregon Health & Science University (OHSU) Multiscale Microscopy Core with technical support from the FEI Living Lab and the OHSU Center for Spatial Systems Biomedicine (OCSSB). We thank B. Carragher, C. Potter, and the National Resource for Automated Molecular Microscopy—which is supported by the National Institutes of Health (NIH) through the National Center for Research Resources (NCRR) P41 program (RR17573)—where some initial imaging studies were performed. We also thank B. Bammes and Direct Electron, LP (San Diego, CA), W. Chiu, and J. Jakana at the National Center for Macromolecular Imaging at Baylor College of Medicine (Houston, Texas), where other images were collected. Computing support was provided by the Center for High Performance Computing at the University of Utah and the NSF Extreme Science and Engineering Development Environment consortium. We also thank C. Hill, F. Whitby, H. Schubert, B. Barad, and J. Fraser for guidance regarding model refinement and validation; D. Eckert for performing analytical ultracentrifugation experiments; J. Iwasa for artwork; M. LaLonde, C. Rodesch, G. Mercenne, and M. Gudheti for help with supporting experiments; and T. Goddard for Chimera 2 developments. We thank R. Roth for deep-etch EM replicas, J. Heuser for sharing deep-etch EM with us and advice, E. Clipperton for CHMP4A mutants, M. Pretz for IST1-myc constructs, and M. Hartstein for artwork. We thank K. Blumer, M. Babst, and other members of our laboratories and colleagues for helpful discussions. This research was supported by the Searle Scholars Program (A.F.); the Jane Coffin Childs Foundation (M.G.S.); the Phenix Industrial Consortium (P.A.); American Cancer Society grant PF-11-279-01-CCG (L.A.C.); U.S. Department of Energy contract DE-AC02-05CH11231 (P.A.); NIH grants 2P50GM082545-06 (A.F.), 1DP2GM110772-01 (A.F.), R01GM112080 (W.I.S. and A.F.), R01AI051174 (W.I.S.), 1P01 GM063210 (P.A.), R01GM076686 (P.I.H.), and R01NS050717 (P.I.H.); and NSF fellowship DGE-1143954 (A.K.C.). All of the expression constructs used in our study have been or will be deposited in the public DNASU plasmid repository (http://dnasu.org/DNASU/Home.jsp). The density map has been deposited in the Electron Microscopy Data Bank (EMD-6461), and the fitted models were deposited in the PDB (3JC1).

SUPPLEMENTARY MATERIALS

www.sciencemag.org/content/350/6267/1548/suppl/DC1
Materials and Methods
Figs. S1 to S12
Tables S1 and S2
References (*32*–*70*)
Movies S1 to S6

14 September 2015; accepted 16 November 2015
Published online 3 December 2015
10.1126/science.aad8305

EVOLUTIONARY GENETICS

An essential cell cycle regulation gene causes hybrid inviability in *Drosophila*

Nitin Phadnis,[1]† EmilyClare P. Baker,[2]* Jacob C. Cooper,[1] Kimberly A. Frizzell,[1] Emily Hsieh,[2] Aida Flor A. de la Cruz,[2] Jay Shendure,[3,4] Jacob O. Kitzman,[3,5] Harmit S. Malik[2,6]†

Speciation, the process by which new biological species arise, involves the evolution of reproductive barriers, such as hybrid sterility or inviability between populations. However, identifying hybrid incompatibility genes remains a key obstacle in understanding the molecular basis of reproductive isolation. We devised a genomic screen, which identified a cell cycle–regulation gene as the cause of male inviability in hybrids resulting from a cross between *Drosophila melanogaster* and *D. simulans*. Ablation of the *D. simulans* allele of this gene is sufficient to rescue the adult viability of hybrid males. This dominantly acting cell cycle regulator causes mitotic arrest and, thereby, inviability of male hybrid larvae. Our genomic method provides a facile means to accelerate the identification of hybrid incompatibility genes in other model and nonmodel systems.

Genetic crosses between *Drosophila melanogaster* females and males from its closest sister species, *D. simulans*, produce only adult hybrid F_1 females (*1*, *2*). These unisexual broods are a result of hybrid F_1 male inviability between these species, which manifests during larval stages of development. Despite decades of investigation, the genetic basis of this hybrid F_1 male inviability remains incompletely resolved (*3*, *4*). A series of x-ray mutagenesis experiments previously revealed that a complex interaction between the *D. melanogaster* X-chromosome and dominant alleles from the *D. simulans* second and third chromosomes is necessary to kill hybrids (*5*, *6*). The isolation of hybrid rescue strains that produce viable hybrid F_1 males led to the identification of two causal elements of this hybrid incompatibility: *Hybrid male rescue* (*Hmr*) on the *D. melanogaster* X-chromosome (*7*, *8*) and *Lethal hybrid rescue* (*Lhr*) on the *D. simulans* second chromosome (*9*, *10*). The absence of either Lhr^{sim} or Hmr^{mel} results in viable hybrid males (fig. S1). However, *D. melanogaster* males that carry transgenic copies of *D. simulans Lhr* are viable despite carrying both the Hmr^{mel} and Lhr^{sim} incompatible alleles (*9*). These results suggest that the presence of at least one additional unidentified hybrid incompatibility gene is necessary to cause hybrid male inviability.

Traditional genetic approaches have failed to identify this missing hybrid incompatibility gene for several reasons. First, hybrid sterility and inviability between *D. melanogaster* and *D. simulans* hinder recombination-based methods for gene identification. Second, genetic disruptions in *D. melanogaster* do not assist in identifying this gene because it is a dominantly acting *D. simulans* factor. Third, the lack of efficient balancer chromosomes in *D. simulans* prevents the construction and maintenance of mutation-accumulation lines that could help identify this missing incompatibility gene. Finally, all known naturally occurring hybrid rescue alleles are mutations of either *Hmr* or *Lhr;* no new rescue alleles have been identified that may correspond to a third gene. Together, these roadblocks have prevented the identification of this missing hybrid incompatibility gene.

Because no null alleles for the missing *D. simulans* hybrid incompatibility gene have been isolated from natural populations, we speculated that—in contrast to *Hmr* and *Lhr*—this gene might be essential for viability. We reasoned that the complex epistatic interaction underlying hybrid F_1 male inviability is analogous to a multicomponent toxin; reconstitution of this toxin requires the simultaneous presence of all components. Under this model, hybrid inviability does not occur when even one of the components or hybrid incompatibility genes is missing (e.g., loss of either Lhr^{sim} or Hmr^{mel} rescues hybrid males). Extending this analogy, we sought other genes whose ablation results in viable hybrid males using a simple genomics-based approach (Fig. 1A).

We mutagenized 55,000 *D. simulans* males by feeding adults with ethyl methane sulfonate (EMS) and crossed these males to *D. melanogaster* females. All resulting progeny inherit one mutagenized complement of the *D. simulans* genome and one intact complement from *D. melanogaster*. When *D. simulans* sperm carrying null mutations at any F_1 hybrid incompatibility gene fertilize *D. melanogaster* eggs, the resulting hybrid male progeny are predicted to be viable. This strategy allows us to survey mutations in all *D. simulans* genes that may be involved in the F_1 hybrid incompatibility, even those in essential genes; however, haploinsufficient genes (i.e., genes that require two copies for viability) would not be sampled.

We recovered 32 viable hybrid F_1 males from these crosses (compared with >300,000 hybrid F_1 females). Of these, 26 males were the result of a nondisjunction event that led to their inheriting a *D. simulans* X-chromosome (*11*); these males were viable, as shown previously (*2*). Further tests confirmed that we had recovered six independently produced rescue hybrid F_1 males, each of which is viable because of mutations at a locus different from Lhr^{sim} (*11*).

Because rescue hybrid F_1 males isolated from these crosses are sterile, they cannot be used in genetic crosses to map the causal gene. Instead, we performed high-throughput sequencing to obtain whole-genome sequences of each of the six independently derived rescue hybrid males and of both parental strains. We then compared the *D. simulans*–derived component of the genomes of rescue hybrid F_1 males to the unmutagenized *D. simulans* parental strain. This allowed us to identify all new mutations in each of the rescue males (*11*) (table S1 and fig. S2). As expected, most of the EMS-induced mutations were point substitutions (Fig. 1B). However, we also identified two large partially overlapping deletions, which mapped to the *D. simulans*–derived chromosomal arm *3R* (Fig. 1B and fig. S3). Each of the six rescue males carried between 600 and 1200 new mutations, as expected, on the basis of the random mutagenesis strategy. Only one *D. simulans* gene, however, was disrupted across all six rescue hybrid males (Fig. 1C). This gene was *Suppressor of Killer-of-prune* [*Su*(*Kpn*)]–*glutathione-S-transferase–containing FLYWCH zinc finger protein* (*gfzf*) (we refer to this as *gfzf*) (*12*, *13*).

The *gfzf* gene encodes two alternative transcripts. The longer transcript encodes a polypeptide with four FLYWCH zinc finger domains and one glutathione-*S*-transferase (GST) domain, whereas the shorter transcript encodes a polypeptide with only the GST domain. The *D. simulans* allele of *gfzf* (i.e., $gfzf^{sim}$) incurred unique mutations (two nonsense, one frameshift, two deletions, and one missense mutation in a highly conserved residue) in each of the six rescue hybrid F_1 males (Fig. 1D and table S2). Four of these mutations only disrupt the longer of the two alternate transcripts encoded by *gfzf* (Fig. 1D and table S2). These results suggest that the longer $gfzf^{sim}$ transcript is involved in hybrid incompatibility. None of the rescue hybrid F_1 males we collected had mutations in the *Lhr* gene, which suggested that our genetic screen did not achieve saturation. We attribute this to the fact that the coding sequence of Lhr^{sim} [1188 base pairs (bp)] is smaller and may present a smaller mutagenesis target than $gfzf^{sim}$ (3117 bp).

[1]Department of Biology, University of Utah, Salt Lake City, UT 84112, USA. [2]Basic Sciences Division, Fred Hutchinson Cancer Research Center, Seattle, WA 98109, USA. [3]Genome Sciences, University of Washington, Seattle, WA 98195, USA. [4]Howard Hughes Medical Institute, University of Washington, Seattle, WA 98195, USA. [5]Department of Human Genetics, University of Michigan, Ann Arbor, MI 48109, USA. [6]Howard Hughes Medical Institute, Fred Hutchinson Cancer Research Center, Seattle, WA 98109, USA.
*Present address: Department of Genetics, University of Wisconsin-Madison, Madison, WI 53706, USA. †Corresponding author. E-mail: nitin.phadnis@utah.edu (N.P.); hsmalik@fhcrc.org (H.S.M.)

Consistent with our predictions (*6*), *gfzf*^{sim} resides on the *D. simulans* third chromosome and is essential for viability (*13*). To circumvent the difficulty of testing the contribution of an essential gene in hybrid inviability, we depleted (knocked down) the expression of the *gfzf*^{sim} longer transcript in F_1 hybrids using RNA interference (RNAi) knockdown constructs (*pValium20-gfzf*^{sim}) that target only *gfzf*^{sim} but not *gfzf*^{mel} (*11*) (figs. S4 and S5). We produced transgenic *D. melanogaster* strains that carry these constructs under the control of the inducible promoter upstream activating sequence (UAS), inserted on the *D. melanogaster* X-chromosome (fig. S6).

We crossed these transgenic flies to a heterozygous *D. melanogaster* strain carrying a *CyO* balancer and a ubiquitously expressing *GAL4* driver *P{Act5C-GAL4}* on the second chromosome. This cross produces two types of daughters. The first set inherits the *CyO* balancer chromosome but not the *Actin5C-GAL4* driver and, therefore, does not express the knockdown construct. When these *D. melanogaster* females are crossed to *D. simulans* males, the resulting hybrid F_1 males are inviable, as expected, because they do not express the knockdown construct ("RNAi off," Fig. 2A). The second set of daughters inherits one copy each of the *Act5C-GAL4* driver and the RNAi construct. In crosses between these *D. melanogaster* females and *D. simulans* males, one out of four hybrid F_1 sons inherit both the RNAi construct and the *Act5C-GAL4* driver and therefore robustly express the RNAi construct. We found that these hybrid F_1 males are viable ("RNAi on," Fig. 2A and figs. S7 to S9). Thus, knocking down the expression of only the long transcript of *gfzf*^{sim} in hybrid F_1 males is sufficient to reverse hybrid inviability. These results confirm that *gfzf*^{sim} is the missing hybrid incompatibility gene.

In contrast to our results with *gfzf*^{sim} knockdown, we found that disrupting *gfzf*^{mel} does not rescue the viability of F_1 hybrid males (table S3). Thus, allelic differences between *gfzf*^{mel} and *gfzf*^{sim} are important for hybrid inviability as are both *Hmr* and *Lhr*, with the limitation of comparing results between *gfzf*^{sim} knockdown and *gfzf*^{mel} disruption. Because positive selection likely resulted in the divergent functional properties of *Hmr* and *Lhr* orthologs (*9*, *14*), we tested whether *gfzf* had also been subject to positive selection. We obtained *gfzf* sequences from 9 *D. melanogaster* and 13 *D. simulans* strains (table S4). Using a McDonald-Kreitman test and an outgroup species *D. yakuba*, we found that an excess of fixed nonsynonymous changes had occurred leading up to the hybrid inviability–associated *gfzf*^{sim},

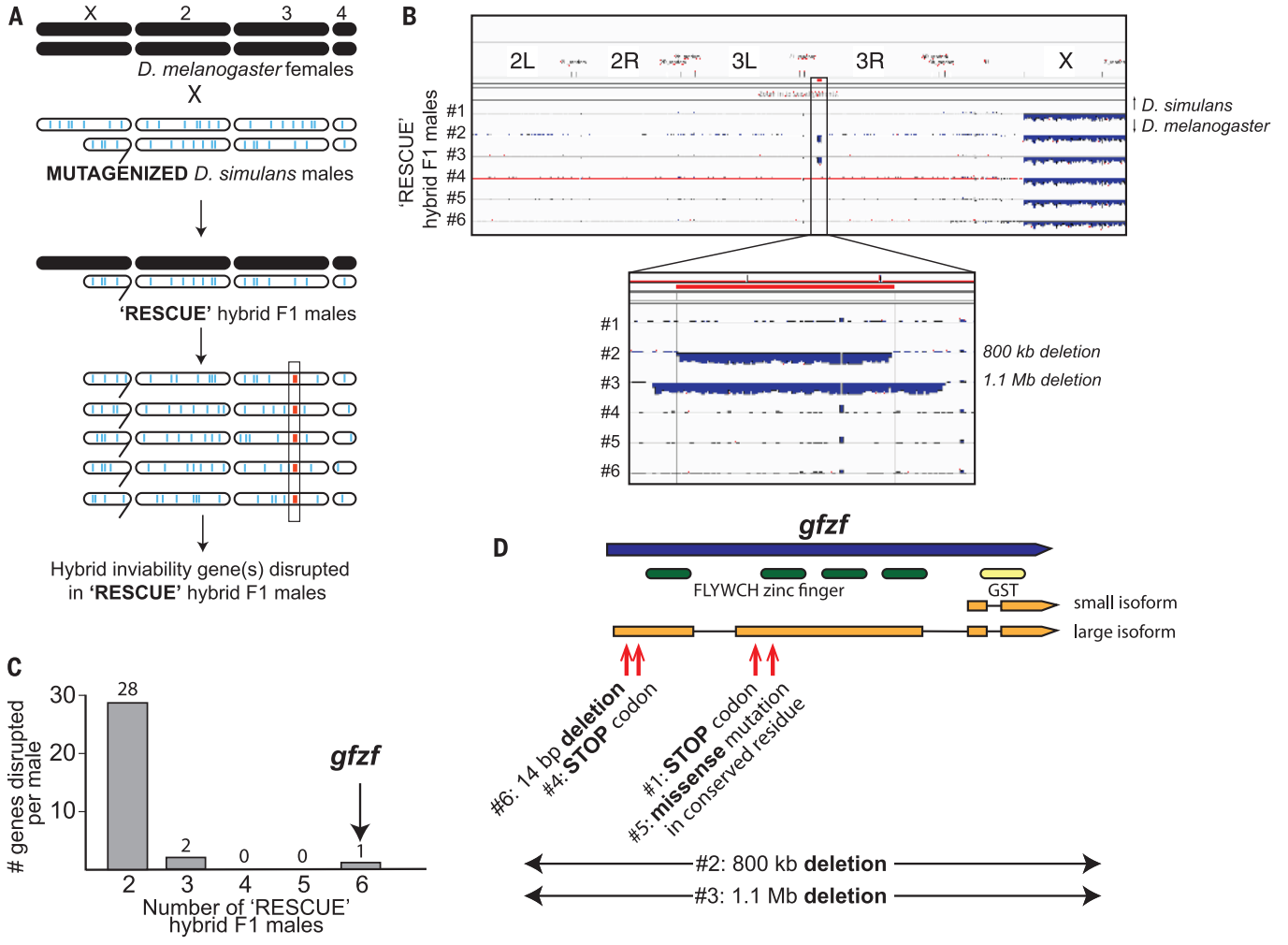

Fig. 1. A genomics screen identifies *gfzf*^{sim} as a hybrid inviability gene. (**A**) We mutagenized *D. simulans* males (new mutations shown in blue) and crossed them with *D. melanogaster* females. When a *D. simulans* sperm carrying a mutation at a hybrid incompatibility gene fertilizes a *D. melanogaster* egg, a viable "rescue" hybrid F_1 male is produced. Sequencing the genomes of multiple "rescue" hybrid males identify the causative hybrid incompatibility gene mutated across these rescue males (shown in red and outlined). (**B**) Single-fly genome sequencing of all "rescue" hybrid males allows assignment of new mutations (including large deletions in two of the males) to the *D. simulans*–derived component of hybrid genomes. (**C**) A single gene, *gfzf*^{sim}, is mutated across all six "rescue" hybrid F_1 males. The *x* axis represents the number of genes mutated across all six males, any five males, and so on. The *y* axis represents the number of genes mutated across these males. (**D**) *gfzf* encodes two alternative transcripts. The larger transcript encodes FLYWCH zinc finger domains along with a GST domain, whereas the shorter transcript encodes only the GST domain.

especially in the FLYWCH zinc finger domains (fig. S10). In contrast, we found no evidence for positive selection along the *D. melanogaster* lineage.

Although our results demonstrate the role of *gfzf*^{sim} in hybrid male inviability between *D. melanogaster* and *D. simulans*, previous studies have found that *gfzf*^{mel} also affects dominant genetic incompatibility between strains of *D. melanogaster* (*13*). Indeed, *gfzf*^{mel} plays an essential role in potentiating inviability seen in crosses between *D. melanogaster* females homozygous for the eye color mutation *prune* (*pn*), and *D. melanogaster* males carrying *Killer-of-prune* (*Kpn*) (*13*) [hence, the name *Su*(*Kpn*), or *Suppressor of Killer of prune*]. The essential, dominant role of *gfzf* in lethal incompatibilities within and between species suggests that there may be limited genetic paths to the evolution of dominant lethal incompatibilities.

The ability of *gfzf* in mediating dominant lethal incompatibilities may stem from its role in the DNA damage–induced G_2-M cell cycle–checkpoint mechanism, where it can potentiate the dE2F2/RBF pathway to block cell proliferation (*15*, *16*). In contrast, *gfzf* has also shown to be required for cell proliferation by transcriptionally regulating the RAS/MAPK pathway (*17*). Despite its essential role in both cell cycle arrest and regulation of cell proliferation, the precise molecular function of *gfzf* is still uncharacterized. Moreover, the biological consequence of *gfzf*^{sim} activity on hybrid male viability is unknown. Nevertheless, the developmental timing and consequences of either *gfzf* deficiency or *gfzf*-mediated dominant lethality are suggestive of a common mechanism that manifests in the larval-pupal transition. Larval tissues in *Drosophila* mostly consist of polyploid cells, whereas the larval nervous system and imaginal discs are composed of diploid cells. During pupation, the polyploid tissues are degraded, and the diploid imaginal discs proliferate to produce the adult body form. Individuals that lack proper imaginal discs can survive and continue to grow as larvae but die during the larval-pupal transition. Notably, homozygous *gfzf*^{mel} null mutants, *gfzf*^{mel}*-pn-Kpn* males, and *gfzf*^{sim}-expressing hybrid males, all lack imaginal discs and die as larvae (*13*, *18*, *19*). This phenotype of lethality during the larval-pupal transition along with an absence of imaginal discs is diagnostic of dysfunction in cell cycle–regulation mechanisms (*20*).

We hypothesized that the *gfzf*^{sim}-associated hybrid male lethality was due to cell proliferation defects in hybrid larvae. We therefore drove the expression of our *gfzf*^{sim} knockdown construct in hybrid F_1 males with a *T80-GAL4* driver, which is expressed ubiquitously in early embryonic stages but specifically in the nervous system and imaginal discs in late larval stages (*21*). We found that *T80-GAL4* mediated *gfzf*^{sim} knockdown robustly rescued the viability of hybrid F_1 males to adulthood (Fig. 2B and fig. S11). This result suggests that the primary defect in hybrid F_1 males produced in *D. melanogaster* × *D. simulans* crosses

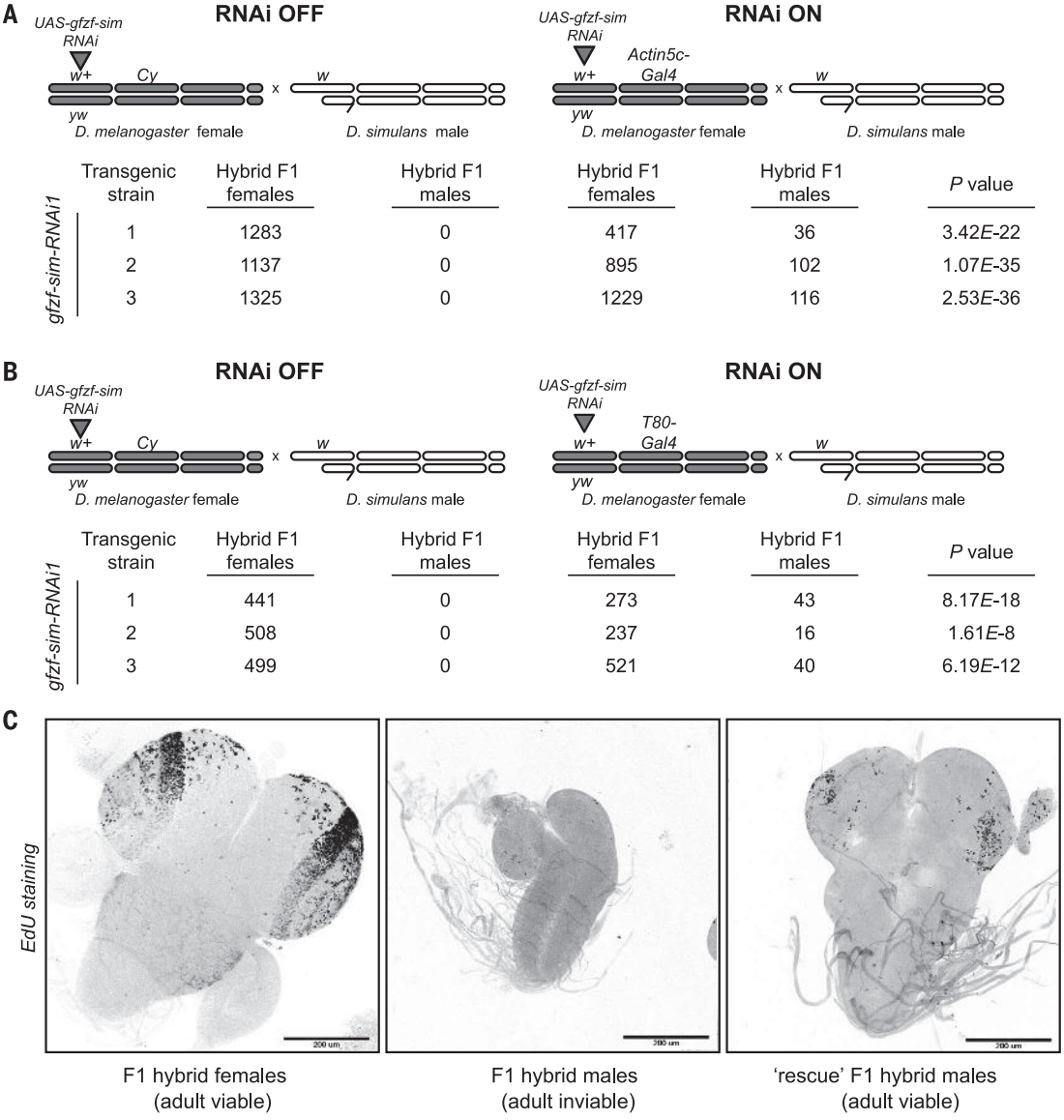

	Transgenic strain	Hybrid F1 females	Hybrid F1 males	Hybrid F1 females	Hybrid F1 males	*P* value
gfzf-sim-RNAi1	1	1283	0	417	36	3.42*E*-22
	2	1137	0	895	102	1.07*E*-35
	3	1325	0	1229	116	2.53*E*-36

	Transgenic strain	Hybrid F1 females	Hybrid F1 males	Hybrid F1 females	Hybrid F1 males	*P* value
gfzf-sim-RNAi1	1	441	0	273	43	8.17*E*-18
	2	508	0	237	16	1.61*E*-8
	3	499	0	521	40	6.19*E*-12

Fig. 2. Knockdown of *gfzf*^{sim} rescues cell proliferation defects and restores hybrid male viability. (**A**) No hybrid males are recovered in crosses where the *pValium20- gfzf*^{sim} RNAi construct is not expressed (no GAL4 driver, "RNAi OFF"). In crosses between *D. simulans* males and *D. melanogaster* females carrying one copy each of *pValium20-gfzf*^{sim} and a ubiquitously expressing Actin5C-GAL4 driver, one out of four possible hybrid male progeny inherit both *pValium20-gfzf*^{sim} and the Actin5C-GAL4 driver ("RNAi ON") and produce viable F_1 hybrid male progeny. *P* values were calculated using Fisher's exact test. (**B**) RNAi knockdown of *gfzf*^{sim} by a T80-GAL4 driver, more specific to larval neuroblasts and imaginal discs, successfully restores the viability of F_1 male hybrids. (**C**) EdU staining shows the diminutive larval brains and cell proliferation defects in "inviable" hybrid males compared with viable F_1 hybrid female larvae. These cell proliferation defects are also partially rescued in hybrid males upon *gfzf*^{sim} knockdown.

may be in diploid tissue proliferation. Indeed, previous studies on larval brains have shown both cell cycle arrest and profound mitotic defects in hybrid F_1 male larvae. These larvae also display diminutive imaginal discs and reduced larval brain sizes due to cell cycle arrest (*22*, *23*). Using 5-ethynyl-2′-deoxyuridine (EdU) to track DNA synthesis in proliferating cells, we found that cell proliferation is restored in larval brains from hybrid F_1 males upon $gfzf^{sim}$ knockdown, which indicates a relief from cell cycle arrest (Fig. 2C and fig. S12). Thus, $gfzf^{sim}$ knockdown relieves both cell cycle arrest and hybrid F_1 male inviability. Together, these results support the model that *gfzf* is a cell cycle regulator of diploid tissues in larvae. Furthermore, they implicate the arrest of cell proliferation as the cause of hybrid F_1 male inviability at this late-larval stage of *Drosophila* development.

Although Hmr and Lhr physically interact with each other (*9*), there is no evidence of a direct physical interaction between gfzf and either Hmr or Lhr. Both Hmr and Lhr proteins localize to centromeres and pericentric heterochromatin, where they play a role in mitotic chromosome segregation (*24*) and the suppression of transposable elements (*25*). These findings have led to a model in which incompatibility between Lhr^{sim} and Hmr^{mel} and their expression levels may cause dysfunction at centromeres or pericentric heterochromatin (*24*). Although the molecular nature of this dysfunction is still unclear, we speculate that the direct engagement of $gfzf^{sim}$ arrests the proliferation of dysfunctional diploid imaginal discs, which leads to hybrid inviability. Under this scenario, ablation of Lhr^{sim} or Hmr^{mel} removes the primary dysfunction, whereas ablation of $gfzf^{sim}$ removes the cell cycle arrest. Alternatively, $gfzf^{sim}$ may act indirectly by contributing to the sensitization of the hybrid genetic background, making it susceptible to the defects caused by the incompatibility between Lhr^{sim} and Hmr^{mel} that leads to hybrid inviability. In both scenarios, removal of any one of these three genes would restore hybrid viability. Thus, the same checkpoints that normally ensure the correction of mitotic errors may be also responsible for the inviability of hybrid males in the *D. melanogaster* × *D. simulans* interspecies cross.

The discovery of hybrid rescue genes, with mutations that reverse hybrid sterility or inviability, has meaningfully advanced our understanding of the genetic mechanisms that underlie the evolution of reproductive isolation during or following speciation. The identification of *gfzf*, in particular, emphasizes the role of cell cycle–regulation mechanisms in the evolution of hybrid incompatibilities (*22*, *23*) and the complex epistatic interactions that underlie dominant hybrid incompatibilities in F_1 hybrids. Our genomics-based approach may also allow mapping of genes that underlie hybrid incompatibilities and other phenotypes even when they lie within chromosomal inversions, which often impedes their precise genetic identification. Although this method requires that there be a single incompatibility separating two species, recently diverged species are likely to meet this criterion (*26*). Our approach may help accelerate the discovery of genes and genetic mechanisms underlying hybrid dysfunction in multiple taxa, shedding light on how reproductive isolation evolves.

REFERENCES AND NOTES

1. L. S. Quackenbush, *Science* **32**, 183–185 (1910).
2. A. H. Sturtevant, *Genetics* **5**, 488–500 (1920).
3. D. A. Barbash, *Genetics* **186**, 1–8 (2010).
4. W. B. Provine, *Genetics* **129**, 1–5 (1991).
5. H. J. Muller, G. Pontecorvo, *Nature* **146**, 199–200 (1940).
6. G. Pontecorvo, *J. Genet.* **45**, 51–66 (1943).
7. D. A. Barbash, D. F. Siino, A. M. Tarone, J. Roote, *Proc. Natl. Acad. Sci. U.S.A.* **100**, 5302–5307 (2003).
8. P. Hutter, M. Ashburner, *Nature* **327**, 331–333 (1987).
9. N. J. Brideau *et al.*, *Science* **314**, 1292–1295 (2006).
10. T. K. Watanabe, *Jpn. J. Genet.* **54**, 325–331 (1979).
11. Materials and methods are available as supplementary materials on *Science* Online.
12. M.-S. Dai, X.-X. Sun, J. Qin, S. M. Smolik, H. Lu, *Gene* **342**, 49–56 (2004).
13. E. Provost *et al.*, *Genetics* **172**, 207–219 (2006).
14. S. Maheshwari, J. Wang, D. A. Barbash, *Mol. Biol. Evol.* **25**, 2421–2430 (2008).
15. A. M. Ambrus, V. I. Rasheva, B. N. Nicolay, M. V. Frolov, *Genetics* **183**, 79–92 (2009).
16. S. Kondo, N. Perrimon, *Sci. Signal.* **4**, rs1 (2011).
17. D. Ashton-Beaucage *et al.*, *PLOS Biol.* **12**, e1001809 (2014).
18. L. Sanchez, A. Dubendorfer, *Rouxs Arch. Dev. Biol.* **192**, 48 (1983).
19. T. Seiler, R. Nothiger, *Experientia* **30**, 709 (1974).
20. M. Gatti, B. S. Baker, *Genes Dev.* **3**, 438–453 (1989).
21. B. J. Loveall, D. L. Deitcher, *BMC Dev. Biol.* **10**, 92 (2010).
22. B. J. Bolkan, R. Booker, M. L. Goldberg, D. A. Barbash, *Genetics* **177**, 2233–2241 (2007).
23. H. A. Orr, L. D. Madden, J. A. Coyne, R. Goodwin, R. S. Hawley, *Genetics* **145**, 1031–1040 (1997).
24. A. W. Thomae *et al.*, *Dev. Cell* **27**, 412–424 (2013).
25. P. R. V. Satyaki *et al.*, *PLOS Genet.* **10**, e1004240 (2014).
26. N. Phadnis, *Genetics* **189**, 1001–1009 (2011).

ACKNOWLEDGMENTS

We thank T. Levin, M. Levine, M. Patel, Naina Phadnis, B. Ross, and S. Zanders for their comments on the manuscript and members of the Malik, Peichel, and Phadnis labs for discussions. This work was supported by a Howard Hughes Medical Institute–Life Sciences Research Foundation (HHMI-LSRF) postdoctoral fellowship (N.P.); a Mario Cappecchi–endowed assistant professorship (N.P.); an NIH Developmental Biology Training Grant 5T32 HD0741 (J.C.C.); graduate research fellowship DGE-071824 from the NSF (J.O.K.); grants from the NIH: R01 GM115914 (N.P.), HG006283 (J.S.), and R01 GM074108 (H.S.M.); and especially a grant from the Mathers Foundation (H.S.M.). J.S. and H.S.M. are investigators of HHMI. The data reported in this paper are tabulated in the supplementary materials and archived at the following databases: primary read data at the Sequence Read Archive under accession number PRJNA290665 and *gfzf* sequences at GenBank under accession numbers KU064780 to KU064795.

SUPPLEMENTARY MATERIALS

www.sciencemag.org/content/350/6267/1552/suppl/DC1
Materials and Methods
Tables S1 to S4
Figs. S1 to S12
References (*27*–*32*)

8 June 2015; accepted 13 November 2015
10.1126/science.aac7504

BOYALIFE & Science Science Translational Medicine Award in Stem Cell and Regenerative Medicine

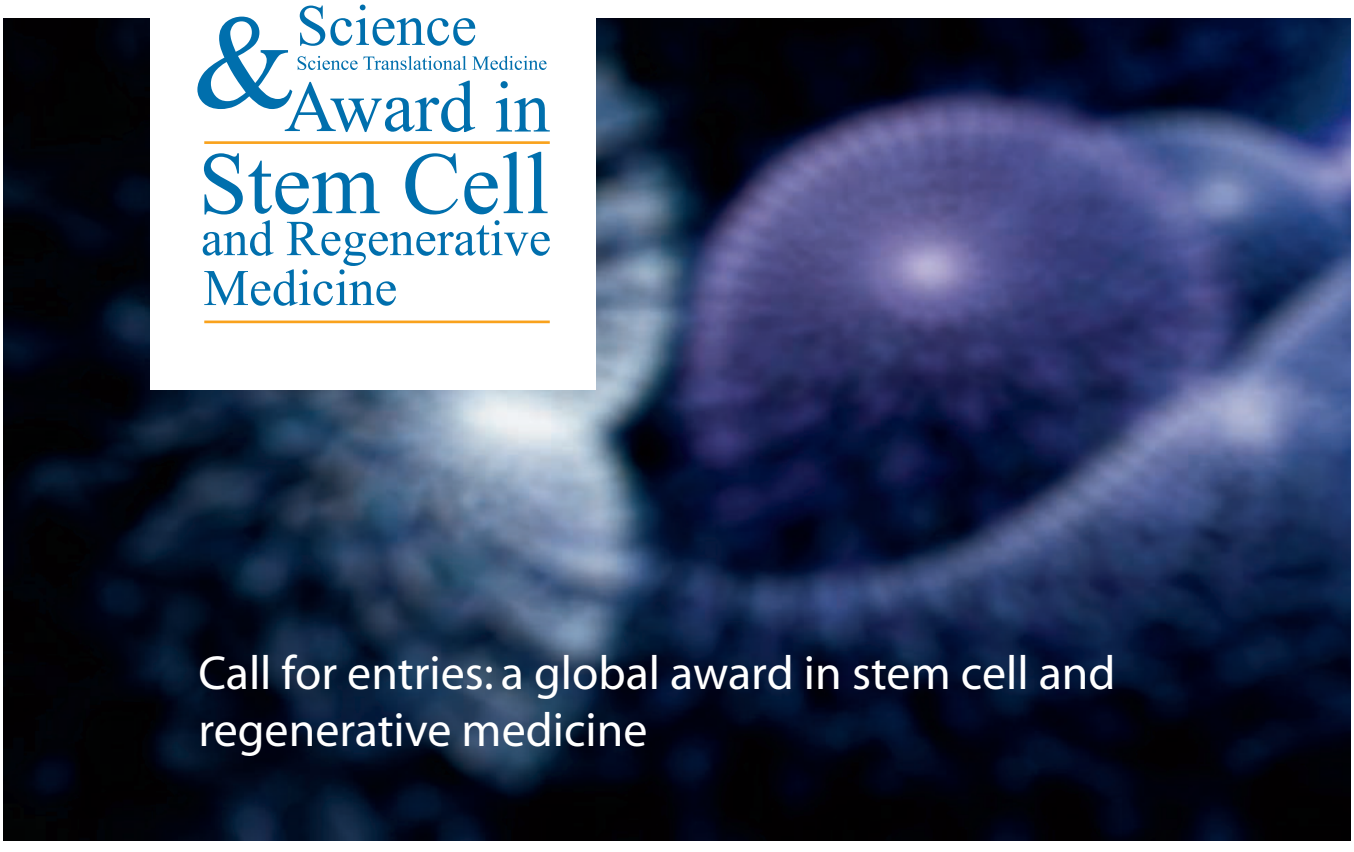

Stem cell and regenerative medicine is the new frontier in life sciences.
Boyalife, Science and Science Translational Medicine jointly establish a global award to recognize significant contributions in advancing basic science to clinical applications in this field.

The award is to recognize and reward scientists in the fields of stem cell and/or regenerative medicine with a focus on developing cell-based treatments for cancer, degenerative disorders, immunotherapy and stem cell transplantation.

You could be next to win this prize and to receive

- A Grand Prize of **$25,000** and a Runner-Up Prize of **$5,000** will be awarded.
- The Grand Prize Winning Essay will be published in Science; a brief abstract of the Runner-Up Essay will be published in Science.

The 2016 Award is now open. The deadline for submissions is March 1, 2016
For more information, please visit : *http://bitly.com/BoyalifeSciencePrize*

BOYALIFE For Better Health | Science AAAS | Science Translational Medicine AAAS

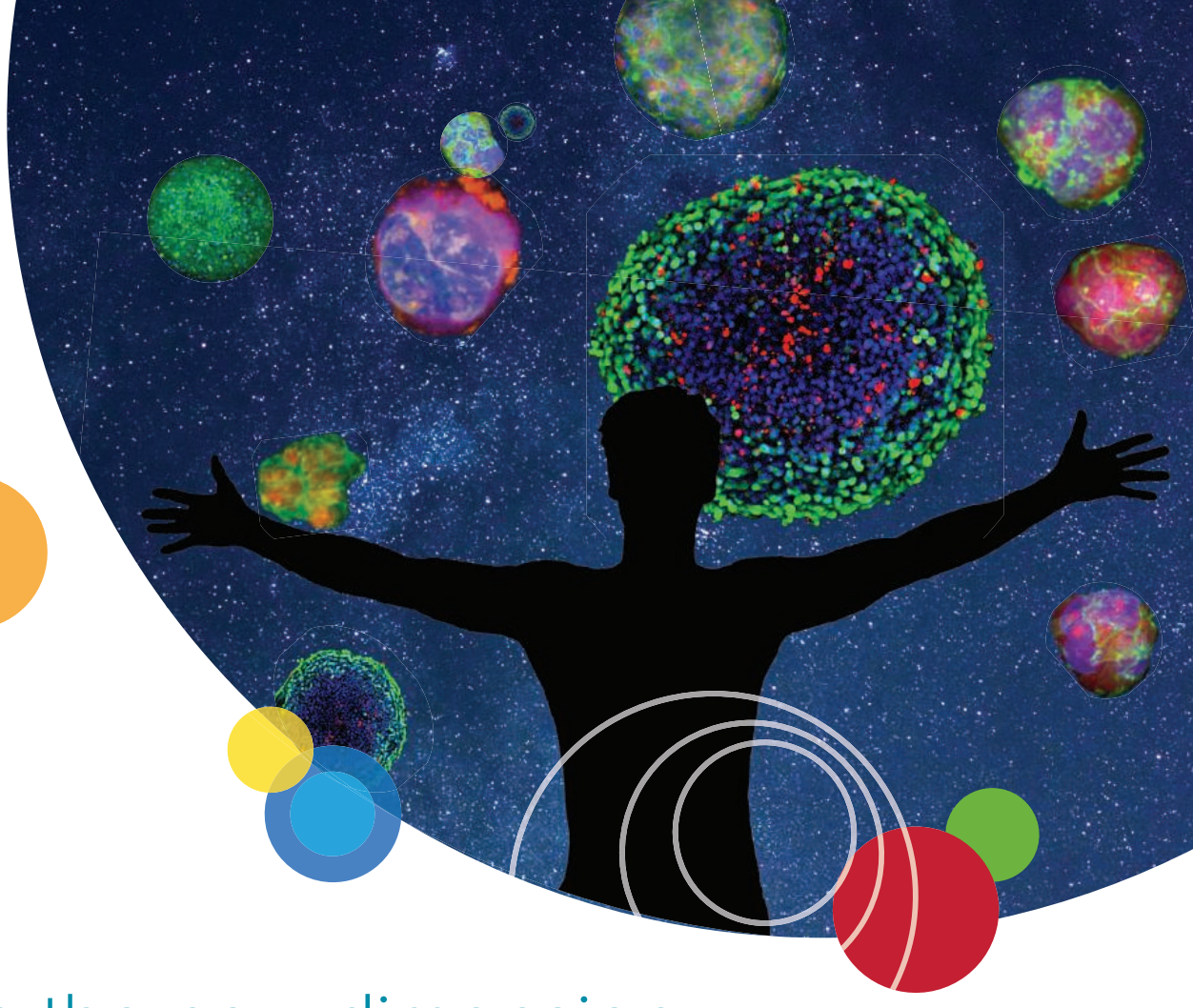

Explore the new dimension

The confocal system for your complex biology

Explore the complexities of biology faster while generating better results. With our new ImageXpress® Micro Confocal High-Content Imaging System, you can run 3D cellular assays and obtain confocal results—at a speed you'd only expect from widefield screening. Easily quantify images and generate statistically relevant data by selecting an optical geometry from crisp confocal or whole-well widefield options to match your application requirements. Built on the reliable, field-proven ImageXpress Micro platform, the ImageXpress Micro Confocal is our most versatile system yet.

ImageXpress® Micro Confocal system

Discover more.

moleculardevices.com/IXMConfocal

MOLECULAR DEVICES

Unleash your brilliance™

For Research Use Only. Not for use in diagnostic procedures.
© 2015 Molecular Devices, LLC. All Rights Reserved. The trademarks mentioned herein are the property of Molecular Devices, LLC or their respective owners.

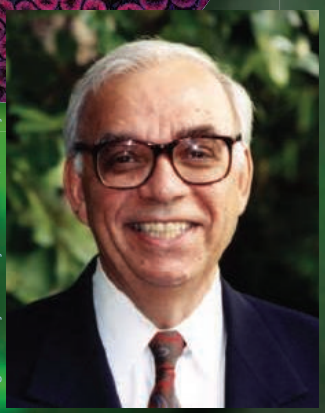

Image courtesy University of California, Berkeley.

Nicholas R. Cozzarelli,
former PNAS Editor-in-Chief.

Call for 2015 Cozzarelli Prize Nominations

The PNAS Editorial Board is now accepting nominations through January 8, 2016 for the 2015 Cozzarelli Prize. This award recognizes scientific excellence and will be given to six papers published in PNAS during 2015.

Nominations should be sent to pnas@nas.edu and should include a citation and brief explanation of the merits of the work. The award recipients will be recognized during the PNAS Editorial Board Meeting and the NAS Annual Meeting Awards Ceremony on May 1, 2016 in Washington, DC.

PNAS
www.pnas.org

For more information and a list of previous winners visit www.pnas.org/site/misc/cozzarelliprize.xhtml.

Thank You

The American Association for the Advancement of Science gratefully acknowledges the individuals whose generosity has established them as founding members of our Edison Society. These leaders in giving play a critical role in advancing science, engineering, and innovation around the world for the benefit of all people.

Lewis & Connie Branscomb
Kenneth A. Cowin
Denise N. & Gary S. David
Gregory S. Ferriss
Stephen & Janelle Fodor
Sibyl R. Golden & the Golden Family
Benjamin C. Hammett
Ellen Scherl Harbus, MD
Rush Holt & Margaret Lancefield
Alice S. Huang & David Baltimore
Pauline P. Lee in memory of Bernard S. Lee
Alan & Agnes Leshner
Lawrence H. Linden
Dennis Liotta
Marion T. M. Mason*
Gilbert S. Omenn & Martha A. Darling
Daniel Pinkel
Carol T. Raugust*
John W. Rowe, MD
Phillip A. & Ann H. Sharp
David Evans Shaw
William F. Ward*

These donors' pledges and contributions were received between October 21, 2014 and November 20, 2015.

** Bequest*

AAAS

To learn more about how a gift to AAAS can advance science and serve society, visit us at **www.aaas.org/giving.**

AAAS *Travels*

Discover **Antarctica!**
& the Annular Solar Eclipse
February 23–March 9, 2017

Considered to be one of the last pristine regions and Earth's most inhospitable habitats, Antarctica offers the most magnificent wilderness with icebergs and breathtaking scenery plus the Annular Solar Eclipse over Patagonia—a once-in-a-lifetime adventure! From $8,695 + air.

For a detailed brochure, call (800) 252-4910
All prices are per person twin share + air

BETCHART EXPEDITIONS Inc.
17050 Montebello Rd, Cupertino, CA 95014
Email: AAASInfo@betchartexpeditions.com
www.betchartexpeditions.com

AAAS is here –
bringing scientific expertise to policy making.

Good science policy is the result of politicians understanding science and scientists understanding policy. Toward this end, AAAS manages the Science & Technology Policy Fellowships program, which embeds scientists and engineers in the federal government for up to two years. From Congress to the State Department, each class of Fellows contributes to the policy-making process while getting hands-on experience at the intersection of science and policy. As a AAAS member your dues support these efforts. If you're not yet a AAAS member, join us. Together we can make a difference.

To learn more, visit aaas.org/plusyou/fellows

AAAS + U = Δ

CALL FOR PAPERS! MANUSCRIPTS DUE MAY 1, 2016.

WE'VE GOT A **MATERIAL INTEREST** IN YOU

Publish in our Special Series,
Materials By Design. We'll waive all APCs.

Science Advances, the new, open-access journal from AAAS, is accepting papers for an exciting Special Series, Materials By Design, that showcases work in material science and engineering with potential global impact. Submit your research today, and if our guest editors select your manuscript for publication, we'll waive all APCs!

Time sequence of buckling silicon microwires.

Manuscripts due by May 1, 2016
Learn more and submit your research at ScienceAdvances.org

ScienceAdvances | AAAS
SIGNIFICANT RESEARCH, GLOBAL IMPACT

want new technologies?

antibodies
apoptosis
biomarkers
cancer
cytometry
data
diseases
DNA
epigenetics
genomics
immunotherapies
medicine
microbiomics
microfluidics
microscopy
neuroscience
proteomics
sequencing
toxicology
transcriptomics

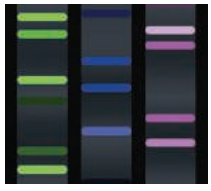

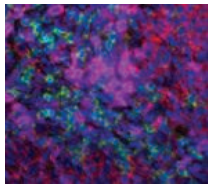

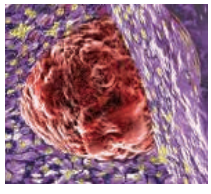

watch our webinars

Learn about the latest breakthroughs, new technologies, and ground-breaking research in a variety of fields. Our expert speakers explain their quality research to you and answer questions submitted by live viewers.

VIEW NOW!
webinar.sciencemag.org

Science
AAAS

Brought to you by the *Science*/AAAS Custom Publishing Office

@SciMagWebinars

UHPLC System

A new ultra-high-performance liquid chromatography (UHPLC) system delivers exceptional performance and reliable separations with the flexibility required for labs developing methods ranging from high-throughput analyses to pharmaceutical quality-control applications. The Vanquish Flex UHPLC system is designed for high speed, resolution, and sensitivity, allowing users to perform biocompatible analysis to obtain high quality and consistent data. The system's integrated modular design allows customers to mix and match modules depending on the demands of the application. Throughout the biopharmaceutical workflow, data integrity is essential to ensure the best decisions can be made, from drug discovery and development to batch release in quality control. The Vanquish Flex system is designed to provide sharp peaks at high throughputs, allowing more data to be analyzed in less time. Data quality is ensured via the system's robustness and repeatability, ensuring that large sample sets can be analyzed for comparison during quality control protocols.

Thermo Fisher Scientific
For info: 800-556-2323
www.thermoscientific.com/vanquish

Western Blot Imaging System

The Omega Lum G from Aplegen is the ideal package for those looking for a gel and Western blot imaging documentation system. Simply unpack it to get started capturing images of your gels and blots. As with all Aplegen systems, it is powered by the intelligent SmartCapture Technology, which simplifies imaging to the point where the user just has to pick an application and the image is automatically captured with the optimum exposure. This automatically controlled system even takes care of filter selection and focusing, so the user will have a publication-quality image at the click of a button. It can be used for fluorescent gels and chemiluminescent blots. Additionally, the Omega Lum G's multiple excitation sources make it suitable for nucleotide and protein stains. The system is compatible with an extensive range of dyes and includes a 6 million pixel resolution camera that is cooled to an impressive –35°C.

Gel Company/Aplegen
For info: 415-247-8760
www.gelcompany.com

Conjugated Antibodies

A new, unique range of conjugated antibodies leverages Innova's Lightning-Link and InnovaCoat bioconjugation technologies to provide customers with antibodies conjugated to an extensive range of enzymes, fluorescent dyes, and colloidal gold, for improved flexibility in experimental design. The new range comprises 200 antibodies to nearly 30 different cardiac biomarkers, each available directly conjugated to 24 different enzymes, fluorescent dyes, or nanoparticles. Innova intends to expand the range into other key research areas in the near future, catering to an increasingly wide scientific audience. In conjunction with its new range of antibodies, Innova has launched a new corporate website to provide customers with easier online ordering facilities as well as access to a range of resources and support materials.

Innova Biosciences
For info: +44-1223-496170
www.innovabiosciences.com

Microbiological Systems

The next generation Chromogenic ID software module, for the ProtoCOL 3 and Protos 3 colony counters, analyzes chromogenic agars from major media supplier E&O Laboratories, which means microbiologists can now use ProtoCOL 3 and Protos 3 systems to quickly and easily identify and count pathogens cultured on chromogenic plates from both E&O Laboratories and CHROMagar. The new Chromogenic ID software module ensures that the ProtoCOL 3 and Protos 3 systems can, in seconds, precisely identify and count any bacteria or yeast cultured on E&O chromogenic or Colorex plates, saving microbiologists time examining colonies and ensuring that critical microbial identification results are consistent from one microbiologist to another. The ProtoCOL 3 and Protos 3 systems allow precise chromogenic colony identification by capturing true-to-life color images of colonies on chromogenic plates utilizing their patented red, blue, and green lighting.

Synbiosis
For info: +44-(0)-1223-727125
www.synbiosis.com/chromogenic-id

Motorized Stage System

The OptiScan III is the newest generation of the OptiScan system. The OptiScan III is an affordable, accurate stage and focus system for routine microscopy procedures requiring high precision. The OptiScan III offers the user full control in the *x*, *y*, and *z* axes via compatibility with OptiScan motorized stages for both inverted and upright microscopes and for Prior's non-encoded focus motors and FB series motorized focus blocks. The system offers an *xy* step size of 1.0 µm and a *z*-axis step size of 0.1 µm, providing excellent precision for a wide variety of potential applications. Its S-curve acceleration curve provides smooth and almost vibration-free movement of the stage. Both the focus and stage can be controlled by joystick or via computer using an RS232 or USB connection. The OptiScan III system is fully compatible with the vast majority of common imaging software. A software development toolkit is also provided with the system.

Prior Scientific
For info: 800-877-2234
www.prior.com

Monoclonal Antibody

A new immunohistochemistry (IHC)-approved, human-specific, VISTA rabbit monoclonal antibody (mAb) is now available for use in biomedical research. VISTA (V-domain Ig suppressor of T-cell activation, C10orf54, GI24, SISP1) is a negative checkpoint control protein that regulates T-cell activation and immune response. Its role in negative checkpoint control has made it an important target in the field of tumor immunology, a field that seeks to develop better therapeutic options by dismantling the mechanisms tumors use to generate and thrive in their own immunosuppressive microenvironments. VISTA (D1L2G) XP Rabbit mAb #64953 is validated using Cell Signaling Technology's rigorous standards, to recognize human VISTA in IHC and Western blot research applications.

Cell Signaling Technology
For info: 877-616-2355
www.cellsignal.com

Electronically submit your new product description or product literature information! Go to www.sciencemag.org/products/newproducts.dtl for more information.

Newly offered instrumentation, apparatus, and laboratory materials of interest to researchers in all disciplines in academic, industrial, and governmental organizations are featured in this space. Emphasis is given to purpose, chief characteristics, and availability of products and materials. Endorsement by *Science* or AAAS of any products or materials mentioned is not implied. Additional information may be obtained from the manufacturer or supplier.

Join AAAS. Get instant access to *Science*. Support all of the sciences.

When you subscribe to *Science*, you become part of the American Association for the Advancement of Science (AAAS), a nonprofit community of more than 100,000 members worldwide who believe in the power of science to make the world a better place. AAAS is hard at work promoting science in government, schools, and in the public commons around the globe.

AAAS's award-winning journal *Science* offers the top peer-reviewed research across multiple disciplines. With your subscription, you'll get:

- 51 weeks of home delivery of *Science*
- Instant online retrieval of every *Science* article ever published, dating back to 1880
- Full access to the *Science* mobile site and apps
- Career advice, webinars, blogs and fascinating features exclusively for AAAS members
- Members-only newsletters, and much more

With increasing public skepticism about science–and public funding for research more uncertain than ever–our work has never been more important. Join hands with us today!

Visit promo.aaas.org/joinaaas. Together, we can make a difference.

Science
AAAS

“A multi-course meal for the mind”

– The Globe and Mail

NAUTILUS

Save 37% on *Nautilus* Prime
Use Coupon Code: **AAAS9**

nautil.us/aaas/9

AAAS 2016 ANNUAL MEETING | WASHINGTON, DC FEBRUARY 11–15

Global Science Engagement

Register now to use funds from fiscal year 2015. Reduced rates are available until January 19, 2016. AAAS members are eligible for further discounts.

aaas.org/meetings

AAAS, publisher of *Science*, thanks the sponsors and supporters of the 2016 Annual Meeting

European Commission

SUBARU

RESEARCH COUNCILS UK

HELMHOLTZ ASSOCIATION

THE KAVLI FOUNDATION

for its generous support of the Science Journalism Awards

NANYANG TECHNOLOGICAL UNIVERSITY

As of December 2, 2015

applied biosystems

Discovery. **Applied.**

Identifying meaningful biological variants is what you do. Genetic analysis is how you get there. Robust chemistries, reliable instruments – and scalable informatics – your research demands nothing less. And it all must work together. Seamlessly and consistently. Because when the right tools are applied, discovery is not far behind.

Explore your path to discovery at **thermofisher.com/appliedbiosystems**

ThermoFisher SCIENTIFIC

For Research Use Only. Not for use in diagnostic procedures. © 2015 Thermo Fisher Scientific Inc. All rights reserved.
All trademarks are the property of Thermo Fisher Scientific and its subsidiaries unless otherwise specified. **CO125174 0715**

Science Careers Advertising

For full advertising details, go to ScienceCareers.org and click For Employers, or call one of our representatives.

Tracy Holmes
Worldwide Associate Director
Science Careers
Phone: +44 (0) 1223 326525

THE AMERICAS

E-mail: advertise@sciencecareers.org

Fax: +1 (202) 289 6742

Tina Burks
Phone: +1 (202) 326 6577

Nancy Toema
Phone: +1 (202) 326 6578

Online Job Posting Questions
Phone: +1 (202) 312 6375

EUROPE / INDIA / AUSTRALIA / NEW ZEALAND / REST OF WORLD

E-mail: ads@science-int.co.uk

Fax: +44 (0) 1223 326532

Sarah Lelarge
Phone: +44 (0) 1223 326527

Kelly Grace
Phone: +44 (0) 1223 326528

Online Job Posting Questions
Phone: +44 (0) 1223 326528

JAPAN

Katsuyoshi Fukamizu (Tokyo)
E-mail: kfukamizu@aaas.org
Phone: +81 3 3219 5777

Hiroyuki Mashiki (Kyoto)
E-mail: hmashiki@aaas.org
Phone: +81 75 823 1109

CHINA / KOREA / SINGAPORE / TAIWAN / THAILAND

Ruolei Wu
Phone: +86 186 0082 9345
E-mail: rwu@aaas.org

All ads submitted for publication must comply with applicable U.S. and non-U.S. laws. *Science* reserves the right to refuse any advertisement at its sole discretion for any reason, including without limitation for offensive language or inappropriate content, and all advertising is subject to publisher approval. *Science* encourages our readers to alert us to any ads that they feel may be discriminatory or offensive.

ScienceCareers
FROM THE JOURNAL SCIENCE AAAS

ScienceCareers.org

Auburn University's College of Agriculture invites applications for the following tenure-track faculty positons

The Department of Animal Sciences is seeking candidates for the position of **Assistant Professor of Metabolomics**. This is a 9-month tenure-track position with 75% research and 25% instruction responsibilities. The successful candidate will play a leading role in metabolomics research at Auburn University and collaborate with researchers conducting complementary studies in genomics, transcriptomics, proteomics and bioinformatics. For a complete job description and/or to apply, please visit: **http://aufacultypositions.peopleadmin.com/postings/1348**. Review of applications will begin **January 1, 2016** and continue until the position is filled.

The Department of Biosystems Engineering is seeking applications for the position of **Assistant Professor of Bioprocess Engineering**. This is a 9-month, tenure-track position with a 60% research and 40% teaching appointment. The successful candidate for this position will be expected to participate actively in the Auburn University multidisciplinary Cluster Hires Initiative in the cluster of Scalable Energy Conversion-Science and Technology. For a complete job description and/or to apply, please visit: **http://aufacultypositions.peopleadmin.com/postings/1362**. Review of applications will begin **February 1, 2016** and continue until the position is filled.

The Department of Crop, Soil and Environmental Sciences is seeking candidates for the position of **Assistant Professor- Agroclimatologist**. This is a 9-month tenure-track position with 75% research and 25% instruction responsibilities. The successful candidate will be expected to participate actively in the Auburn University multidisciplinary Cluster Hires Initiative in the cluster of Climate, Human, and Earth System Sciences. For a complete job description and/or to apply, please visit: **http://aufacultypositions.peopleadmin.com/postings/1346**. Review of applications will begin **January 4, 2016** and continue until the position is filled.

The Department of Entomology and Plant Pathology is seeking candidates for the position of **Assistant Professor- Molecular Ecology of Plant and Soil Systems**. This is a 9-month tenure-track position with 75% research and 25% instruction responsibilities. The successful candidate for this position will be expected to participate actively in Auburn University multidisciplinary Cluster Hires Initiative in the cluster of Omics and Informatics. For a complete job description and/or to apply, please visit: **http://aufacultypositions.peopleadmin.com/postings/1354**. Review of applications will begin **February 1, 2016** and continue until the position is filled.

Auburn University is an EEO/Vet/Disability Employer.

SCHOOL OF OPTOMETRY
INDIANA UNIVERSITY
BLOOMINGTON

Tenured or Tenure-Track Faculty Position, Open Rank

Indiana University School of Optometry and Vision Science program seek candidates for a tenured or tenure-track faculty position. Applications are invited from scientists using innovative approaches to study human visual function, with expertise in a combination of visual psychophysics, oculomotor function and/or visual neuroscience. The successful candidate will enhance the existing strengths of the School's visual optics, retinal imaging, neuroscience, clinical translational and ocular biology groups, as well as campus strengths in psychological and brain sciences, cognitive science and neuroscience. A Ph.D. or equivalent degree is required. Responsibilities will include developing or maintaining an independent research program, attracting extramural funding, and teaching in the professional and graduate programs. Both research preeminence and superior quality teaching are high priorities in these programs. Depending on the candidate's interests and needs, there is the possibility of a joint appointment with another department (**www.indiana.edu/about/a-z-list/index.html**).

Indiana University is a major research University founded in 1820. It currently enrolls over 32,000 undergraduates and 7,500 graduate and professional students on the Bloomington campus with over 110,000 students in the University system. The School of Optometry has very active research and graduate programs with numerous collaborations with other disciplines within the university. The School has several major teaching clinics as well as outreach affiliations. Bloomington is a relaxed community located in a beautifully wooded and hilly area of the state where cultural and recreational opportunities abound, housing costs are low, schools are excellent, and commuting time is short. More information about the School is available at **www.optometry.iu.edu**, and about the University at **www.indiana.edu**.

For consideration, please submit a letter of application, curriculum vitae, statement of research and teaching interests, and names and contact information of at least three references.

Interested candidates should review the application requirements and submit their application at: **http://indiana.peopleadmin.com/postings/2120.** Questions regarding the position or application process can be directed to: Dr. Rowen Candy at **rcandy@indiana.edu** or submitted via postal mail at Indiana University School of Optometry, Attn: OAA# **21511-11**, c/o Dr. Rowen Candy, 800 E. Atwater Ave., Bloomington, IN 47405.

Applications received by March 1, 2016, will be assured consideration. The search will remain open until the position is filled. Salary and rank will be commensurate with qualifications and experience.

Indiana University is an equal employment and affirmative action employer and a provider of ADA services. All qualified applicants will receive consideration for employment without regard to age, ethnicity, color, race, religion, sex, sexual orientation or identity, national origin, disability status or protected veteran status.

Think beyond.
Make a difference.

8.9 billion Swiss francs in core research and development expenditure in 2014 makes Roche one of the most research focused companies worldwide.

Our 120 year heritage and a stable shareholder structure ensure a long-term view and a strong and stable commitment to researching and developing novel treatments in the areas of oncology, immunology, infectious diseases, ophthalmology and neuroscience in order to improve the lives of patients all over the world.

Because it's not just a job.
It's a responsibility.
A big one.

The next step is yours.
careers.roche.ch/research

Roche

ScienceCareers online @sciencecareers.org

UNIVERSITY OF CAMBRIDGE

www.jobs.cam.ac.uk

University Lecturer

Department of Physiology, Development and Neuroscience • £38,896-£49,230

Applications are invited for a research-oriented, tenure-track University Lectureship in Physiology, available from 1 October 2016 or as soon as possible thereafter. Based in central Cambridge, we are searching for an outstanding scientist, with an excellent publication record, undertaking fundable work in a field which complements our world class programme in physiology (http://www.pdn.cam.ac.uk/research/). We are particularly interested in candidates who work at the cellular and molecular level or who use cutting edge post-genomic or imaging technologies to investigate fundamental issues in systems physiology.

The successful applicant will have a PhD in a relevant subject area, will have an aptitude and enthusiasm for teaching, and be willing to contribute effectively to our undergraduate programmes in preclinical medicine, preclinical veterinary science, and natural sciences (http://www.pdn.cam.ac.uk/teaching). He/she will be expected to contribute to the design and delivery of undergraduate and graduate lecture courses and to perform other academic duties including administration, examining and assessment.

We welcome applications from all qualified candidates and we strongly encourage women to apply. We will shortly be recruiting a neuroscientist but, on this occasion, we are not looking to strengthen this area of our research portfolio. Appointment will be based on merit alone.

Informal enquiries may be made to Professor Bill Harris, Head of Department (wah20@cam.ac.uk; +44 (0) 1223 766137/333772).

Appointment will be made at University Lecturer level with a probationary period of five years, with appointment to the retirement age thereafter. The pensionable salary scale starts at £38,896 to £49,230 per annum. Once an offer of employment has been accepted, the successful candidate will be required to undergo a health assessment, with a satisfactory outcome determined by the University.

To apply online for this vacancy and to view further information about the role, please visit: http://www.jobs.cam.ac.uk/job/8816.

Please complete the online application as fully as possible.

The closing date for applications is midnight on Sunday 7 February 2016.

Please quote reference PM07714 on your application and in any correspondence about this vacancy.

The University values diversity and is committed to equality of opportunity.

The University has a responsibility to ensure that all employees are eligible to live and work in the UK.

UNIVERSITY OF CAMBRIDGE

www.jobs.cam.ac.uk

Herchel Smith Postdoctoral Research Fellowships (Fixed Term)

Academic Division, Central Cambridge • £28,982-£37,768

Fixed-term: Funding is available for a maximum period of three years.

The Managers of the Herchel Smith Postdoctoral Research Fellowships Fund invite applications for these Fellowships within the Biological Sciences (particularly in fields at the interface with the physical sciences); and within the following fields in the Physical Sciences: Organic Chemistry, Biological Chemistry and related areas of Chemistry; any area within Experimental Solid State Physics. Further details can be found at www.herchelsmith.cam.ac.uk, where details can also be found of comparable Fellowships in Astronomy and in Pure Mathematics.

The Managers expect to offer four Fellowships in the Biological Sciences and three in the Physical Sciences.

The Fellowships are intended to enable a small number of outstanding and highly motivated scholars who have demonstrated a capacity for individual research to devote themselves exclusively to research at an early stage in their careers, to develop their academic potential, and to produce work of an international standard within their field.

All Fellowships are to be held from 1 October 2016 or otherwise by negotiation. Fellowships are available for between two and three years. Fellows will usually work in close collaboration with an established research group. Fellows are required to pursue their research on a full-time basis in Cambridge.

In accordance with Dr Smith's will, candidature is limited to candidates who have obtained their PhD degree, or equivalent, within the last three years at any university but normally excluding Cambridge and Harvard. Fellowships can only be offered to those with less than three years postdoctoral experience by the time the Fellowship is taken up. In addition to holding a PhD or equivalent, candidates should provide evidence of: outstanding academic excellence; a high quality and original research proposal; and evidence of their capabilities as an independent researcher.

The stipend will be on the University's Postdoctoral Research Associate scale, currently between £28,982 to £37,768 per annum, with an annual research allowance of £15,000.

Further details are available at http://www.herchelsmith.cam.ac.uk/fellowships/ or from the Secretary to the Fund Managers, Tel. +44 (0)1223 332283, e-mail: duncan.mccallum@admin.cam.ac.uk

Please quote reference AK07732 on your application and in any correspondence about this vacancy.

Closing Date: 11 January 2016

The University values diversity and is committed to equality of opportunity.

The University has a responsibility to ensure that all employees are eligible to live and work in the UK.

Labex IBEID Institut Pasteur

International call for candidates to head a 5-year group in Basic and Translational Medical Entomology at the Institut Pasteur of French Guiana.

To strengthen its basic research in entomology, and to improve its preparedness to respond to newly emerging infectious agents, Institut Pasteur calls for applications by outstanding young scientists to head a Young Investigator's Group.

The successful junior candidate* will be appointed on the basis of a tenure track position, as head of a group of 6 persons in the newly-created Amazonian Vectopole of the Institut Pasteur of French Guiana, city of Cayenne (http://www.pasteur-cayenne.fr/la-recherche/nos-equipes/uem/vectopole/). This group will be created for a period of 5 years and may thereafter compete for a full research group. It will also be affiliated to the Laboratory of Excellence (LabEx) "Integrative Biology of Emerging Infectious Diseases" (http://www.pasteur.fr/labex/ibeid).
Priority topics include basic and translational entomology, insect microbiota and vector competences. However, all aspects of medical entomology will be considered, and outstanding candidates with an ambitious and original basic research project and taste for translational research are strongly encouraged to apply.

A highly attractive package matching the experience of the successful candidate will be provided, including salaries (principal investigator, technician, post-doctoral fellowship), a substantial contribution to laboratory equipment and to annual running costs, as well as support for relocation expenses.
The deadline for applications is February 15th, 2016. Short-listed candidates will be invited in Paris for interview in April 2016 and decisions will be announced by the end of June 2016.

Candidates should send their formal applications by E-mail to the Director of Scientific Evaluation, Prof. Alain Israël, at Institut Pasteur (ibeid-g5@pasteur.fr).

The Application shall comprise the following information (in order), in a single pdf file:

1. A brief introductory letter of motivation, including the name of the proposed group [candidates are encouraged to contact the coordinators of the LabEx, Pascale Cossart (pascale.cossart@pasteur.fr) or Philippe Sansonetti (philippe.sansonetti@pasteur.fr)].
2. A Curriculum Vitae and a full publication list.
3. A description of past and present research activities (up to 5 pages with 1.5 spacing, Times 11 font size).
4. The proposed research project (up to 6 pages with 1.5 spacing, Times 11 font size) highlighting how it would fit in the defined topic.
5. The names of 3 scientists from whom letters of recommendation can be sought, together with the names of scientists with a potential conflict of interest from whom evaluations should not be requested.

** Institut Pasteur is an Equal Opportunity Employer. Junior group leaders should be less than 8 years after PhD at the time of submission. Women are eligible up to 11 years after their PhD if they have one child and up to 14 years after their PhD if they have two or more children.*

NOW HIRING
300
LADDER FACULTY

Join us in defining the new American research university

clusterhiring.ucr.edu

SCHOOL OF MEDICINE
CASE WESTERN RESERVE UNIVERSITY

Chair and Professor
Department of Neurosciences

The School of Medicine at Case Western Reserve University (CWRU) invites applications and nominations for the position of chair of the department of neurosciences. The department has a long-standing history of success, and the institution seeks an outstanding scientist with the leadership and vision necessary for developing and strengthening an innovative research program that integrates basic neuroscience research with other School of Medicine and university departments, as well as affiliate hospital programs. The department's research strengths include cellular and molecular neurobiology, neurodegeneration and regeneration, and systems and computational neuroscience. In addition, the department has an exceptional graduate program that provides high-quality interdisciplinary training in modern neuroscience. The new chair will be supported by a highly competitive recruitment package including an Endowed Professorship.

The unified campus at CWRU encourages and facilitates collaborative interactions among scientists in the Schools of Medicine, Engineering, Nursing, Dentistry, and Arts and Sciences. Beyond the core campus, the neurosciences department and the School of Medicine serve as hubs for initiatives and programs with other School of Medicine faculty at our four affiliated hospitals: University Hospitals Case Medical Center, Cleveland Clinic, MetroHealth Medical Center, and the Louis Stokes Cleveland VA Medical Center.

The new chair will be expected not only to lead the department's local research and teaching programs but also to draw on diverse city-wide resources and opportunities to catalyze new enterprises with both basic science and clinical science faculty at affiliated hospitals, including collaborative, city-wide programs in Autism, Brain Health and Alzheimer Disease. Research missions are supported by excellent core facilities that incorporate a broad spectrum of basic science and translational neuroscience research including, but not limited to: high-throughput drug screening, genomics, proteomics, metabolomics, transgenic animal model development, behavioral testing, human and small animal neuroimaging, super-resolution light microscopy, flow cytometry, structural biology, and bioinformatics pipelines that support efficient data analysis.

Applicants for this position must have a Ph.D. and/or an M.D. degree with a distinguished record of scientific achievement, demonstrated leadership skills, and a commitment to the education and mentorship of both students and faculty. Appointment as a Professor of Neurosciences with tenure is anticipated and requires evidence of a productive and excellent research program recognized at the national/international level. The capacity for imaginative programming and a vigorous collaborative spirit are also essential characteristics.

Applicants should submit a curriculum vitae, a letter of interest addressing research, educational, administrative and leadership goals and vision to: Anthony Wynshaw-Boris, M.D, Ph.D., Neuroscience Chair Search Committee, c/o Michelle Yanick (**neuroscience-chair-search@case.edu**).

In employment, as in education, Case Western Reserve University is committed to Equal Opportunity and Diversity. Women, veterans, members of underrepresented minority groups, and individuals with disabilities are encouraged to apply.

Case Western Reserve University provides reasonable accommodations to applicants with disabilities. Applicants requiring a reasonable accommodation for any part of the application and hiring process should contact the Office of Inclusion, Diversity and Equal Opportunity at 216-368-8877 to request a reasonable accommodation. Determinations as to granting reasonable accommodations for any applicant will be made on a case-by-case basis.

Get a job on the go.
Search worldwide for thousands of scientific jobs in academia, industry, and government. The application process is seamless, linking you directly to job postings from your customized push notifications.

Scan this code to download app or visit **apps.sciencemag.org** for information.

ScienceCareers | AAAS
FROM THE JOURNAL SCIENCE

ScienceCareers.org

THE FOUNDATION FOR POLISH SCIENCE, THE LARGEST NON-PROFIT ORGANIZATION IN POLAND DEDICATED SOLELY TO THE DEVELOPMENT OF SCIENCE, HAS FOR THE 24TH TIME GRANTED THE FOUNDATION FOR POLISH SCIENCE PRIZES, CONSIDERED TO BE POLAND'S MOST IMPORTANT SCIENTIFIC AWARDS.

FNP
Foundation for Polish Science

Prof. Jerzy Jedlicki from the Tadeusz Manteuffel Institute of History of the Polish Academy of Sciences in Warsaw received the Prize in the field of the humanities and social sciences for fundamental studies on the phenomenon of the intelligentsia as a social stratum and its role in modernization processes in Central & Eastern Europe.

Prof. Kazimierz Rzążewski from the Centre for Theoretical Physics of the Polish Academy of Sciences received the Prize in the field of mathematical, physical and engineering sciences for discovery of the phenomenon of magnetostriction in ultra-cold gases with dipole forces.

Prof. Stanisław Penczek from the Centre for Molecular and Macromolecular Studies of the Polish Academy of Sciences in Łódź received the Prize in the field of chemical and material sciences for elaboration of the theory of ring-opening polymerization and its use for synthesis of biodegradable polymers.

www.fnp.org.pl

HUMAN FRONTIER SCIENCE PROGRAM

CALL FOR LETTERS OF INTENT FOR RESEARCH GRANTS: AWARD YEAR 2017

HFSP supports **international** preferably **intercontinental** collaborations in **basic** life science research. Applications are invited for grants to support **innovative** approaches to understanding **complex mechanisms of living organisms**. Applicants are expected to develop **novel** lines of research distinct from their ongoing research. Preliminary results are not required.

Program Grants are for independent scientists at all stages of their careers while **Young Investigators' Grants** are for teams of scientists who are **all** within 5 years of establishing an independent laboratory and within 10 years of obtaining their PhDs. Both provide 3 years support for 2 – 4 member teams, with not more than one member from any one country, unless critical for the **innovative** nature of the project. Awards are dependent upon team size and successful teams will receive up to $450,000 per year. The principal applicant must be located in one of the **HFSP** member countries but co-investigators may be located in any country.

Please read the guidelines on the HFSP web site (www.hfsp.org). Teams must register via the web site by March 21, 2016 so as to submit a letter of intent online by the March 31, 2016 deadline.

Specific enquiries: **grant@hfsp.org**

MONASH University | ARMI AUSTRALIAN REGENERATIVE MEDICINE INSTITUTE

Key Research Opportunity at the Australian Regenerative Medicine Institute for an established Multiple Sclerosis research scientist/clinician scientist

As a result of a significant philanthropic gift and contribution from Monash University, The Australian Regenerative Medicine Institute is now recruiting Faculty who wish to establish/relocate their research group to the Institute's new research facilities. We seek a dynamic, independent scientist with an outstanding MS research track record, and a desire to work in a multidisciplinary environment.

The successful candidate will bring a strong track record for attracting independent funding and is expected to initiate and maintain a successful MS research program synergising with the Monash research environment, taking an active part in collaborative research. Clinician researchers or biomedical researchers particularly interested in regenerative medicine as it applies to the analysis or treatment of MS are strongly encouraged to apply. This fixed appointment will be for an initial five years with extension possible upon review.

About the Australian Regenerative Medicine Institute (ARMI): Monash University, the Victorian State Government and the Australian Commonwealth Government have invested over $AUD150m in ARMI, a new research institute for regenerative medicine, focused on unraveling basic mechanisms of the regenerative process and developing clinical applications. Situated on the Monash University Clayton campus in Melbourne, ARMI is a research Institute within the Faculty of Biomedical and Psychological Sciences located in new, state of the art laboratories with well-equipped common facilities creating a framework for a creative, interdisciplinary and highly interactive environment.

A key objective of ARMI is to enhance the field of regenerative medicine by promoting the career opportunities for young scientists. As the headquarters for EMBL Australia the Institute oversees the operation of a networked series of research groups within Australia that is operated according to the EMBL research model and philosophy.

ARMI has a vibrant research program in regenerative medicine and has established state of the art core research facilities with access to various animal models including zebrafish, axolotls, rodents and nonhuman primates. The Institute leadership is also keen to hear from researchers interested in using these animal models for their research and wishing to relocate to ARMI to take advantage of this world leading facility.

Further details are available from:

Prof. Peter Currie, Deputy Director
peter.currie@monash.edu

Prof Claude Bernard
claude.bernard@monash.edu

www.armi.org

To Apply: Applicants should submit an expression of interest including a cover letter, curriculum vitae, a list of publications (indicating ten most significant publications), a statement of previous research achievements, a research plan (maximum 8 pages/font 12), a financial plan, and a list of at least three reference persons, all in a .pdf binder. Your complete submission, referenced "ARMI Group Leader in MS Research" should be sent to **laura.crilley@monash.edu** by **January 28th 2016**.

We look forward to receiving your application!

ScienceCareers online @sciencecareers.org

Two Faculty Clusters in Soft Matter and Energy
Department of Applied Physical Sciences
University of North Carolina at Chapel Hill

The newly launched Department of Applied Physical Sciences (APS) invites applications for the founding cluster hires in Soft Matter and Energy. The positions are open rank, including the possibility of endowed professorships. The goal of APS is to bridge fundamental research and training in materials science and engineering with translational impact on society's most challenging problems. APS partners with all STEM and Health Affairs departments toward multidisciplinary, team-based research, education, and entrepreneurship. This hiring initiative continues an aggressive strategy to build a pre-eminent Department of Applied Physical Sciences, aiming for 20 new hires, including new clusters, together with joint appointments from existing programs. UNC-Chapel Hill is a Top-Ten public research university, ranking 6th nationally in R&D expenditures, including public and private institutions.

The initial clusters build upon existing strengths and target international prominence and leadership. The cluster in soft matter will focus on hires at the interface between the physical and life sciences, while the cluster in energy targets expertise to solve challenges ranging from energy storage to membrane technologies.

All candidates should have an established record of research excellence and clear potential for multidisciplinary collaboration, extramural funding including industry, and translational impact in education and entrepreneurship. Excellence and commitment to education are essential qualities for these recruitments. A PhD in disciplines that contribute to Soft Matter and Energy is required.

Applicants' cover letters must succinctly state their relevance to the Soft Matter or Energy clusters. Applications will only be accepted online: **http://unc.peopleadmin.com/postings/88874**

Review of completed applications will begin **January 1, 2016**, and will continue until the initial clusters are completed; additional clusters will be identified in future announcements.

Questions should be directed to: **E. T. Samulski, Chair, Department of Applied Physical Sciences, University of North Carolina at Chapel Hill, Chapel Hill, NC 27599-3287, et@unc.edu**.

The University of North Carolina at Chapel Hill is an Equal Opportunity Employer that welcomes all to apply, including protected veterans and individuals with disabilities.

Stony Brook University

Assistant/Associate or Full Professor Biomedical Engineering

The Department of Biomedical Engineering is inviting applications for an Assistant, Associate or Full Professor tenure-track faculty position in any BME area. Candidates must have a Ph.D. in BME or related field. A minimum of two years of postdoctoral experience is preferred.

Outstanding candidates wishing to be considered at the Associate or Full Professor level must have active, funded research programs in their area of expertise. Candidates are expected to develop and maintain competitive extramurally funded interdisciplinary research programs and to excel in teaching at both the graduate and undergraduate levels. For more information, visit **http://www.bme.stonybrook.edu**.

Those interested in this position should submit a State employment application, resume/CV, statement of research and teaching interests, and contact information of three references in a single PDF file electronically utilizing the Blue Resources box at the bottom of the posting (**highly preferred**).

Alternatively, submit above materials to:

Stefan Judex, Department of Biomedical Engineering, Bioengineering Building, Room 213, Stony Brook University, Stony Brook, NY 11794-5281.

For a full position description, or to apply online, visit: **www.stonybrook.edu/jobs** (**Ref. # F-9468-15-11-F**).

Equal Opportunity Employer, females, minorities, disabled, veterans

UCLA

Assistant Professor in Plant Diversity and Evolution

The University of California, Los Angeles (UCLA) Department of Ecology and Evolutionary Biology (EEB) seeks an organismal biologist with a focus on plant diversity and/or evolution. UCLA has a rich history of work in plant ecology and evolution, and we seek an individual who will help us maintain and grow this critical component of our program. Qualified candidates must have a Ph.D. in a related field of biological sciences, and the search is restricted to the Assistant Professor level. The position is defined broadly within evolution and ecology, but preference will be given to candidates whose research/teaching interests would utilize, at least in part, the UCLA Mildred E. Mathias Botanical Garden and associated UCLA Herbarium. The successful candidate will be expected to establish an internationally recognized and externally funded research program and contribute to EEB's teaching needs at the introductory undergraduate level. There are many opportunities for collaboration across a broad group of partners on and off campus, including the UC NRS Stunt Ranch Reserve and White Mountains Research Center, the UCLA La Kretz Center for California Conservation Science, the UCLA Center for Tropical Research, and our Institute of Environment and Sustainability. Information about the Department and the Botanical Garden and may be found at http://www.eeb.ucla.edu and http://www.botgard.ucla.edu/.

Applicants should submit materials online to **https://recruit.apo.ucla.edu/apply/JPF01858** and include (1) a cover letter, (2) curriculum vitae, (3) personal statement that describes current and future research and teaching, a vision of how the candidate's research, teaching and/or outreach might include and enhance the Botanical Garden, (4) a summary of ongoing and anticipated activities to promote gender and racial diversity, and (5) names and contact information of three references. Review of candidates will begin on **18 January 2016** and continue until the position is filled. Please use job number **JPF01858** in all correspondence.

Individuals with a history of mentoring students under-represented in the sciences are encouraged to apply and to describe their experience in a cover letter

Inquiries regarding the position should be directed to **Grace Angus** (**gracea@lifesci.ucla.edu**) or the **Search Chair, Professor Brad Shaffer** (**brad.shaffer@ucla.edu**).

As a campus with a continually growing diverse student body, we encourage applications from women, minorities, and individuals with a commitment to mentoring under-represented demographics in the sciences. The University of California is an Equal Opportunity/Affirmative Action Employer. All qualified applicants will receive consideration for employment without regard to race, color, religion, sex, sexual orientation, gender identity, national origin, disability, age or protected veteran status. For the complete University of California nondiscrimination and affirmative action policy see: UC Nondiscrimination and Affirmative Action Policy (http://policy.ucop.edu/doc/4000376/NondiscrimAffirmAct).

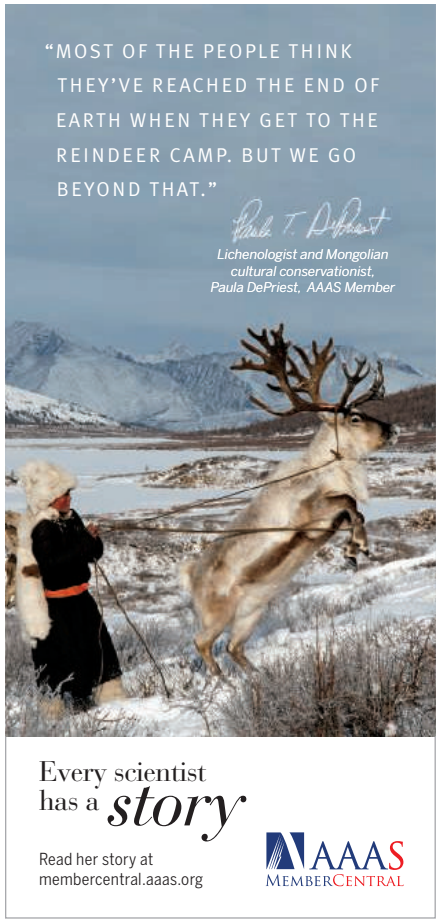

NEBRASKA NANOSCIENCE FACILITY POSITIONS
NATIONAL NANOTECHNOLOGY COORDINATED INFRASTRUCTURE

The Nebraska Nanoscale Facility (NNF) and Nebraska Center for Materials and Nanoscience (NCMN) at the University of Nebraska-Lincoln (UNL) are seeking several high-level science/engineering personnel. The NNF (http://nanoscale.unl.edu) is part of the NSF-supported National Nanotechnology Coordinated Infrastructure (NNCI) consisting of a number of sites distributed across the United States to provide the nation with outstanding facilities for synthesis, fabrication and characterization of nanoscale materials and structures, and to promote research, education and outreach in the field. The NNF contains Central and Shared Laboratory Facilities that together contain more than 50 major research instruments and occupy about 20,000 sq. ft. of laboratory space in the new Voelte-Keegan Nanoscience Research Center. Many researchers from UNL and other institutions use these facilities each year, and additional information is available at http://www.unl.edu/ncmn/.

NNF Facilities Coordinator: We seek an energetic and enterprising individual to serve as NNF Facilities Coordinator. The coordinator's prime responsibility is to proactively establish new and foster existing contacts to facility users from industry and academia. In addition, the coordinator will be responsible for logistical aspects of the facilities, including physical space and daily operations; develop collaborations between users and research groups; assist in proposal writing for new equipment and programmatic reviews; and advancing the strategic goals of NNF.

NNF Research Technologists (2): We seek highly motivated individuals capable of performing experimental work in nanofabrication and characterization of a wide variety of materials. The NNF strives for excellence in service to users from industry and academia. To fulfill this mission, the research technologists will assist and train graduate students and other users in the use of sophisticated equipment, repair and upgrade instruments in the facilities, and develop protocols for safe usage of the equipment.

Candidates for all positions must have a Ph.D. in Materials Science, Nanoscience, Condensed Matter Physics or Chemical Sciences. They also should have a successful record of research and/or facility experience in a university, national laboratory or industry. Candidates must have a broad understanding of materials and nanotechnology fabrication and characterization techniques, excellent communication skills and the ability to effectively interact with students and faculty from a broad set of disciplines.

These positions are full-time professional appointments with salary commensurate with experience and qualifications. Application review will begin by **January 15, 2016** and will continue until the positions are filled. To view full details and to apply, go to **http://employment.unl.edu** (Requisition **F_150280** for the **Facilities Coordinator position** or **F_150281** for the **Research Technologist positions**). Applicants should submit a cover letter, brief statement of their experience and views on user facility operations, CV, and contact information for four references as single PDF files.

The University of Nebraska-Lincoln is committed to a pluralistic campus community through affirmative action, equal opportunity, work-life balance, and dual careers. See http://www.unl.edu/equity/notice-nondiscrimination.

POSITIONS OPEN

Group leader positions at the *Imagine* Institute for Genetic Diseases

The *Imagine* Institute for Genetic Diseases, located in the Necker Enfants malades Hospital campus in the heart of Paris, is inviting applications for group leader positions. *Imagine* is an interdisciplinary research centre with excellent core facilities for genomics, cell imaging, flow cytometry, bioinformatics, pathophysiology and animal housing for transgenic mice and zebra fish. *Imagine* is affiliated with Paris Descartes University, the INSERM national institute for medical research and the Paris Public Hospitals Group (*Assistance Publique-Hôpitaux de Paris*). The Institute focuses on rare diseases, their genetic architecture and life-long outcomes. *Imagine* intends to address unmet basic and clinical research questions related to rare diseases, in order to increase knowledge in a major medical field that is currently insufficiently covered. The Institute is currently composed of 350 staff members from 24 labs and 3 associated labs in the fields of genetics, immunology, infectious diseases, haematology, nephrology, developmental defects, metabolic diseases/encephalopathy, dermatology and gastroenterology. Applications may focus on any field directly linked or related to the basis, pathophysiology and treatment of genetic diseases, with special emphasis on:

- Neuroscience, Development and stem cells and computational biology.

Appointments will be made at a junior or senior level, depending on experience.

Applications should be submitted to the Executive Committee to **newgroups@institutimagine.org** and must include:

- a full CV, including a list of publications
- past and current research interests (2 pages)
- future research proposals (5 pages)
- letters of recommendation by referees (3 pages in all) should be submitted with the application.

Further information can be found on **www.institutimagine.org/en**

Applications must be received by **May 15th, 2016**.

Imagine Institute
24 boulevard du Montparnasse,
75015 Paris, France

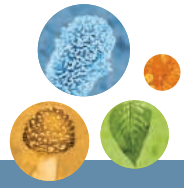

THE 11TH ANNUAL
DOE Joint Genome Institute
Genomics of Energy & Environment Meeting

March 21–24, 2016 • Walnut Creek, CA

This vibrant scientific gathering features presentations on metagenomics, microbial, fungal and plant genomics; genome editing; secondary metabolites; pathway engineering; synthetic biology; high-throughput functional genomics; and high-performance computing applications.

Additional short talks will be selected from poster abstracts, due March 7, 2016. Genomic technologies and informatics workshops precede the main meeting on March 21–22.

Confirmed speakers include:

Chris Bowler
École Normale Supérieure (France)

Charles Chiu
University of California, San Francisco

Manpreet Dhami
Stanford University

José Dinneny
Carnegie Institution for Science

Tim Donohue
Great Lakes Bioenergy Research Center

Kirsten Hofmockel
Iowa State University

Steve Kay
University of Southern California

Sarah Lebeis
University of Tennessee

Christopher Mason
Weill Cornell Medical College

Margaret McFall-Ngai
University of Hawaii

Gene Myers
Max Planck Institute of Molecular Cell Biology and Genetics (Germany)

Dianne Newman
California Institute of Technology

Christine Queitsch
University of Washington

Jeffrey Ross-Ibarra
University of California, Davis

Reshma Shetty
Ginkgo Bioworks

Hamilton Smith
JCVI

Mary Voytek
NASA

Kelly Wrighton
The Ohio State University

Register here: http://bit.ly/2016-JGI

JGI JOINT GENOME INSTITUTE
A DOE OFFICE OF SCIENCE USER FACILITY

BERKELEY LAB

U.S. DEPARTMENT OF ENERGY
Office of Science

16-JGI-2220

Science Careers online @sciencecareers.org

Yale SCHOOL OF PUBLIC HEALTH

Tenure Track Assistant or Associate Professor
Department of Environmental Health Sciences
New Haven, Connecticut

The Department of Environmental Health Sciences at the Yale School of Public Health is seeking to recruit an outstanding environmental epidemiologist with expertise in population genomics for a tenure-track faculty position at the level of Assistant or Associate Professor. Areas of specialization include, but are not limited to, cutting-edge analyses of large, population-scale GWAS, exome, whole genome, and metagenomic sequencing datasets, as well as epigenomic data management. Candidates with a background in environmental epidemiology, population genomics and gene-environment interactions who can integrate with metabolomics, transcriptomics, and exposure phenotypes are particularly encouraged to apply.

Candidates must have a doctoral degree in an appropriate field by the start of appointment, postdoctoral experience, and a strong record of research accomplishments. The ability to obtain external research funding and publish in highly-ranked, peer-reviewed journals is expected. The successful candidate would also be expected to contribute through research, teaching, and outreach, and to perform research in an area that develops and complements ongoing efforts in the Department of Environmental Health Sciences at the Yale School of Public Health.

Applicants are asked to submit PDF files that contain a cover letter, curriculum vitae, concise statements of research and teaching interests, and copies of up to five recent publications. In addition, applicants should arrange to have at least three letters of reference uploaded as a PDF document on letterhead with signature. Applications will be considered immediately and will continue until the position is filled.

Please apply online at: **https://academicjobsonline.org/ajo/jobs/6844**. For additional information and inquiries please contact: **Dr Vasilis Vasiliou**, Chair of the Department of Environmental Health Sciences. Email correspondence: **vasilis.vasiliou@yale.edu**. Website: **www.publichealth.yale.edu**

Yale University is an Affirmative Action/Equal Opportunity Employer. Yale values diversity in its faculty, students, and staff and especially encourages applications from women, persons with disabilities, protected veterans, and underrepresented minority scholars.

LOYOLA MEDICINE

Loyola University Chicago Stritch School of Medicine

Co-Director of Cardiovascular Research Institute, Loyola Stritch School of Medicine; Departments of Molecular Pharmacology and Therapeutics and Medicine (Division of Cardiology)

The Departments of Molecular Pharmacology and Therapeutics and Medicine and the Division of Cardiology at Loyola University Chicago, Stritch School of Medicine seek applicants for the Cardiovascular Research Institute Co-Directorship, a joint leadership position with a Basic Scientist leader in the Institute. This position is for a physician/scientist with an M.D. or M.D./Ph.D. who is actively engaged as a clinician and also directs a basic and/or translational research program in the area of Cardiovascular Disease. The appointment will be approximately 50% in each of the two aforementioned Departments with protected time for research, depending on extramural funding. Applicants should currently hold a faculty appointment at the rank of Associate Professor or Professor.

The faculty applicant will be expected to have and sustain an independent, externally funded research program, contribute to scholarship, graduate, and medical education and to the Translational Research mission that binds the two academic units. The Department of Molecular Pharmacology and Therapeutics is developing a pre-clinical Translational Research Laboratory, with which this faculty member will also be affiliated. The applicant is expected to participate in the vigorous collaborative academic environment that exists between these entities and the Cardiovascular Research Institute at Loyola University Chicago's Health Sciences campus. Finally, there is an expectation that the Co-Director assist with the operations of the Institute and mentorship of junior physicians/scientists in the group. A generous salary and research startup package are available. Applicants should have a strong record of research productivity and funding as well as successful teaching and mentorship experience. Leadership experience is desirable.

Interested candidates should email a single PDF file which includes a cover letter, CV, statement of research interests, and contact information of four references (two within and two outside of your current institution) to **pharmrecruit@luc.edu** as well as apply online at **www.careers.luc.edu** (search for position # **S141016-N**).

Loyola University Chicago is an Equal Opportunity/Affirmative Action Employer.

For recruitment in science, there's only one Science

Two Fantastic Recruiting Opportunities!

FACULTY CAREERS | January 29, 2016

Gear up to recruit for the faculty positions at your university with this much anticipated issue that reaches thousands of Ph.D. scientists looking for positions in academia.

Reserve ads by Jan 12 to guarantee space.

POSTDOC CAREERS | March 25, 2016

Be sure to promote your openings to the thousands of scientists who will be reading *Science* to find out about the latest postdoc opportunities.

Reserve ads by March 8 to guarantee space.

To book your ad: **advertise@sciencecareers.org**

The Americas
202-326-6582

Europe/RoW
+44 (0) 1223-326500

Japan
+81-3-3219-5777

China/Korea/Singapore/Taiwan
+86-186-0082 9345

Produced by the *Science*/AAAS Custom Publishing Office.

SCIENCECAREERS.ORG

ScienceCareers
FROM THE JOURNAL SCIENCE AAAS

RECRUIT AND PROMOTE YOUR BRAND ALL YEAR

Science **Careers will publish the 2016 issue of its annual Career Directory, which is promoted and distributed all year long.**

Reserve space by January 8
Ad materials due by January 15

BENEFITS TO YOUR COMPANY

- Opportunity to brand your organization to scientists beyond your normal reach.
- Print bonus distribution of 3,000 copies to career fairs and meetings around the globe.
- Booklet PDF e-mailed to 100,000 scientists including all *Science* Careers registrants.

To book your ad:
advertise@sciencecareers.org

The Americas
202-326-6577

Europe/RoW
+44 (0) 1223-326500

Japan
+81-3-3219-5777

China/Korea/Singapore/Taiwan
+86-186-0082 9345

SCIENCECAREERS.ORG

ScienceCareers
FROM THE JOURNAL SCIENCE AAAS

WE MAKE LIVES BETTER
UT HEALTH SCIENCE CENTER®
SAN ANTONIO

THE ROBERT A. WELCH DISTINGUISHED CHAIR IN CHEMISTRY
School of Medicine
Department of Biochemistry
The University of Texas Health Science Center at San Antonio

We are seeking outstanding candidates at the Professor or senior Associate Professor level who utilize structural and biophysical approaches (X-ray, NMR, computation) to understand basic biological mechanisms and/or develop novel therapeutics. Special areas of interest include cancer, neuroscience, aging and metabolic disorders. In addition to the Welch Chair endowment and its associated newly renovated space, significant resources from the Institution, UT System (UT STARS) and State agencies such as the Cancer Prevention and Research Institute of Texas (CPRIT) are available to outstanding candidates.

The selected candidate will be expected to play a leadership role, including involvement in the hiring of several junior faculty within the department in the coming years. Currently, the Department has 16 primary faculty covering a broad range of research interests (**http://www.biochem.uthscsa.edu**). There is a significant structural biology focus, which is supported by uniquely integrated core facilities in X-ray crystallography, NMR spectroscopy, Mass Spectrometry, AUC, SPR, ITC, and a new Center for Innovative Drug Discovery (CIDD).

UTHSCSA is located northwest of downtown San Antonio in the South Texas Medical Center, gateway to the scenic Texas Hill Country, with its many recreational opportunities. UTHSCSA consists of five schools: Medical, Graduate, Dental, Nursing and Health Professions. San Antonio is the 7th largest city in the U.S. with a beautiful, historical downtown area featuring the Riverwalk with its diverse entertainment, and fine restaurants.

Please submit by e-mail to Esther James at **jamese@uthscsa.edu** a Curriculum Vita, description of research interests, list of four referees and a cover letter addressed to **Dr. P. J. Hart, Chair of Welch Search Committee, MSC 7760, UTHSCSA, 7703 Floyd Curl Dr., San Antonio, TX 78229-3900.**

The University of Texas Health Science Center at San Antonio is an Equal Employment Opportunity/Affirmative Action Employer including protected veterans and persons with disabilities. All faculty appointments are designated as security-sensitive positions.

Postdoctoral Fellowships in Genomic Biology
at the University of Illinois at Urbana-Champaign

The Carl R. Woese Institute for Genomic Biology at the University of Illinois at Urbana-Champaign offers a number of fellowships for truly exceptional young scholars who have completed their Ph.D. within the last several years, and are looking for a stimulating and supportive interdisciplinary environment to carry out independent and collaborative research in the field of genomic biology. IGB Fellows will typically spend two years conducting research in one of several research themes in the Institute, and ideally this research will also overlap with two or more of these thematic areas. A personalized mentoring plan will be developed for each Fellow. Annual salary is $50,000. **Applicants should submit their information and letter of intent to aweckle@illinois.edu. The closing date for all positions is January 29, 2016. Fellows will be announced on or about February 15, 2016.**

Computing Genomes for Reproductive Health

We seek an individual with both a computational and a clinical background to conduct research on the evolution of pregnancy and the development of human obstetrical syndromes. The Fellow will lead interactions between clinical service providers and basic scientists. They will conduct independent research while working with study coordinators, electronic medical records, and multi-omics high dimensional datasets. The ideal candidate will strengthen a multidisciplinary team working to drive advances in the field of reproductive medicine through the study of interactions among genes, their products, organisms, and environments. The theme takes a precision medicine-based approach to research obstetrical syndromes and the developmental origins of health and disease. (Derek Wildman, Theme Leader). MD, PhD or MD/PhD required.

The University of Illinois is an Affirmative Action/Equal Opportunity Employer. The Carl R. Woese Institute for Genomic Biology is a pioneer in advancing life sciences research with program areas in systems biology, cellular and metabolic engineering, and genome technology. Visit www.igb.illinois.edu for additional information.

暨南大學 JINAN UNIVERSITY

百年暨大，诚聘英才
携手暨大，共创未来

Faculty Positions Available at Jinan University Guangzhou

Description

Jinan University, Guangzhou, P.R. China is an institution of higher education under the direct administration of the Overseas Chinese Affairs Office of the State Council in China, being selected as one of the universities given priority in construction in the “211 Project”.In 2015, Jinan University becomes one of seven high-level universities under construction in Guangdong Province. The key disciplines in College of Information Science and Technology are currently under rapid development, and have the prioritized funding and human resource support.

The College of Information Science and Technology (http://xxxy.jnu.edu.cn/) is recruiting outstanding academics and researchers in the following and related fields: Cryptography and Information Security, Computer Science, Mathematics, Electrical and Electronic Engineering.

Successful candidates will be expected to develop thriving, well-funded research programs and contribute to both undergraduate and graduate education.Positions will be for a three-year period with extensions to long-term positions based on performance. Successful candidates will be provided with attractive annual salary (300,000-1,000,000RMB), start-up fund, housing allowance and others based on your records.

Qualifications

Applicants must hold a Ph.D.degree with strong record of research publications.

Application

The recruitment is available for a long term. Please send a cover letter, a full CV with a publication list in a single pdf. Please arrange three reference letters sent directly to the following email address:

Email: 171088944@qq.com, cryptjweng@gmail.com
Contact Person: Lijun Zhu
Phone (O): +86-85222933, 86-13642666576

Interested candidates could visit the website (http://personal.jnu.edu.cn or http://xxxy.jnu.edu.cn/) for application details.

暨南大學 JINAN UNIVERSITY

百年暨大，诚聘英才
携手暨大，共创未来

Jinan University implements Jinan Double Hundred Talents Plan to recruit global talents

Jinan University, first university of overseas Chinese founded by the state, with the largest foreign student among the country currently, is the national "211 Project" of key comprehensive university directly under the guidance of Overseas Chinese Affairs Office of State Council. Jinan University, known as "Chinese top university".
According to the school discipline construction and innovative platform construction, Jinan University now recruiting global talents and will provide favorable working and living condition. There are multiple positions open at Economics College (applied economics, statistics, finance, regional economics) / Science and Technology College (Optical Engineering, Mechanical Engineering, Materials Science and Engineering, Physics, Food Science and Engineering) / Information Science and Technology College (Information & Communication Engineering, Electronic Science and Technology, Computer Science and Technology, Basic Mathematics, Computational Mathematics, Applied Mathematics, Cyberspace Security) / Life Science and Technology College (Chemical, Biological Engineering, Biochemistry and Molecular Biology, Cell Biology, Biology, Medical Engineering, Ecology, Developmental and Regenerative Biology, Immunobiology, Red Tide and Marine Biology)

Candidate material

a. A resume
b. Assumed research projects of nearly five years , published papers (specify the collection situation, journal impact factor and the number of papers he cited of SCI, EI, SSCI, CSSCI), the list of award-winning achievements;
c. Copy of Degree Certificates/Diploma, all research projects, awards and patents;
d. The full text of 2-5 representative papers;
e. Copy of certificate and incumbents certificate of holding an important position in the foreign office or in the domestic one;
f. Work plan after coming to school.

Treatments provided

Jinan University provides 300,000-1,100,000 RMB annual salary for successful candidates, with 500,000-10,000,000 RMB research start-up fund and 1,000,000-5,000,000 RMB settling-in allowance.

Contact

Personnel department home page: http: //personal.jnu.edu.cn/
Tel: 0086-20-85227283 (including fax), 0086-20-85223525
Contact: Mr. Tong, Mr. Liu
E-mail: otalents@jnu.edu.cn
Address: Human Resources Development and Management Service of Jinan University,
No. 601, Huangpu Road West, Guangzhou.
Postal Code: 510632

赛尔互联 CERNET

赛尔互联——为中国大陆高校倾力打造海内外高层次人才引进服务

请访问 Sciencecareers.org/CER 获取全国各地联系信息

赛尔互联为您量身打造
海外人才引进解决方案

广告联系：赵佳 zhaojia@cernet.com
+86 10 62603373

中国教育在线 www.eol.cn 是赛尔互联旗下品牌

Shanghai Jiao Tong University Seeking Global Talents

Established in 1896, Shanghai Jiao Tong University (SJTU) is one of the oldest and most prestigious universities in China, which is located in Shanghai, a famous dynamic city in the world. Today, bearing the responsibility of invigorating the Chinese nation and developing for the benefits of mankind, she is sailing for the new aim as a comprehensive, research-oriented and internationalized world-class university.

Driven by the national strategic demands and aiming at global scientific frontiers, SJTU is actively engaged in problem-oriented research. During six consecutive years, SJTU ranked first in total number of NSFC projects, ranked second in the number of SCI papers in all Chinese universities. In 2014, SJTU ranked third in the number of papers appeared in SCI journals with top 10% Impact Factor (IF), and ranked fourth in the number of papers published in *Science, Nature, Cell* and *PNAS* among all Chinese universities.

SJTU is a multi-disciplinary institution covering such diverse fields such as mechanical engineering, naval architecture, electronic information, electrical engineering, computer science, ocean engineering, civil engineering, material science & engineering, aeronautics & astronautics, physics & astronomy, chemistry & chemical engineering, environment science & engineering, life sciences, medicine, pharmacy, agriculture, economics, management, law, humanities and arts, etc.. According to Thomson Reuter's Essential Science Indicator (ESI), SJTU has 16 academic Programs entering ESI World Top 1%, in which engineering, materials science, mathematics and computer science are in the World Top 100.

Based on the world university standard, SJTU is striving to set up the tenure system to develop the top-tier faculty led by international academic masters. On the time of the 120th Anniversary of SJTU in coming 2016, SJTU sincerely invites applicants from global outstanding scientists for tenured and tenure-track faculty positions in various academic disciplines. Successful applicants will be offered highly competitive salary and startup funding.

Please submit application files including a cover letter, curriculum vita, publications list and five representative publications to *faculty@sjtu.edu.cn*, and indicate the position you are applying for.

SJTU is the right place where your dreams start to fly. For more information, please visit us at http://hr.sjtu.edu.cn/

Disciplines	Positions	Number of job vacancies
1.Mechanical Engineering 2.Electronic Information & Electrical Engineering 3.Computer Science	Chair Professor	10
4.Naval Architecture & Ocean Engineering 5.Civil Engineering 6.Materials Science & Engineering	Distinguished Professor	20
7.Aeronautics and Astronautics 8. Environmental Science & Engineering 9. Physics and Astronomy	Tenured Full Professor	30
10.Chemistry and Chemical Engineering 11. Life Sciences 12. Agriculture	Tenured Associate Professor	40
13.Economics & Management 14.Law 15.Humanities and Arts	Tenure-track Assistant Professor	60

Contact

Division of Human Resources
Shanghai Jiao Tong University
Email: faculty@sjtu.edu.cn
Tel:+86 21 34206732 http://hr.sjtu.edu.cn/

OPPORTUNITIES IN CHINA
Science Careers online @sciencecareers.org

南京郵電大學 Nanjing University of Posts and Telecommunications

NUPT Recruits High-level Talents with High Salaries All Over the World

Under the co-administration by the Jiangsu Government and Ministry of Industry and Information Technology, Nanjing University of Posts and Telecommunications (NUPT) is a key university with a glorious traditaion. With engineering being its major body and IT subjects being its specialties, NUPT embraces a history of 73 years. It ranks 57 on the NPI (Nature Publishing Index) List of Top 100 Chinese Universities, lists the 80th among Top Chinese Institutes according the Special Edition of Nature Magazine and ranks 100 on the ESI (Essential Science Indicators) list of Chinese University (Institutes).

NUPT is among the first group of academic members of the International Telecommunication Union (ITU), With Material Science, Engineering and Chemistry topping 1% on ESI's International List of Subjects. The subjects of Information and Telecommunications Engineering and Optical Engineering are among Top 20 in China, while Communication Engineering, Electronic Information Engineering and Electronic Information Science and Technology are among the top 15.

Professor Yang Zhen, the president of NUPT, is issuing the letter of appointment to Professor Peter Grünberg, the winner of Nobel Prize in Physics in 2007 (Left)

NUPT embraces several prestigious faculties. In recent years, NUPT has hosted one Nobel Prize Laureate, members of Academy of Sciences from other countries and IEEE Fellows. NUPT boasts high-end talents on its panel; there are members of the Chinese Academy of Sciences (CAS), Chang Jiang Scholars from the Ministry of Education and the One Thousand Talents Program. NUPT has also fostered ten Innovatiion research teams on provincial level. It is a key member of a National Collaborative Innovation Center. NUPT has a National University Science Park in the field of the internet of things, which is the onlyone of its kind nationwide. In recent years, NUPT has published numerous papers in sister journal to Nature Magazine.Moreover, Quite a few research papers by NUPT professors have been listed among the top100 Most Influential International Academic Papers of China, and have been acknowledged by ESI as "Hot Papers".

NUPT is recognized as the Cradle of Chinese IT Elites. It has outstanding alumni like Houlin Zhao, Secretary-General of ITU, Hao Yin, Academician of CAS and Xiaobing Cao, Chairman of the China Telecom Corporation, all of whom are among the thousands of talents in the field of posts and telecommunications. NUPT shares vast mutual cooperation with renowned companies like Huawei, ZTE, China Mobile and China Telecom in terms of cultivation of talents, scientific researches and employment of its graduates. Meanwhile, NUPT has been a training center for the Asia-Pacific Telecommunity (APT) since 1990.

Overseas high-level talents are intended to be recruited in such disciplines as Optical Engineering, Electronic Science and Technology, Information and Communication Engineering, Education, Instrument Science and Technology, Control Science and Engineering, Computer Science and Technology, Software Engineering, Cyberspace Security, Management Science and Engineering, and Business Administration, with 2-3 talents to be employed for each discipline.

Applicants are required to obtain a doctorate degree in prestigious universities abroad and have at least 2 years' working experience abroad in well-known universities or research institutions, and serve abroad as an associate professor in famous universities or as an equivalent expert and scholar in research institutes; be the top-notch talent in the peers in this field of scientific research or obtain an internationally recognized academic achievements or potential to be the academic or technical leader in the field.

Salaries and Housing Subsidies for the High-level Talents (Individual Income Taxes on Talents' Own)

Salaries for the first-level talents in science and engineering will be negotiated face to face, and housing subsidies will be 10 million RMB. Salaries for the second-to fourth-level talents will be 0.25 to 1 million RMB, and housing subsidies will be 0.8 to 2.5 million RMB.

Salaries for the first- level talents in economy and management will be negotiated face to face, and housing subsidies will be 7 million RMB. Salaries for the second-to fourth-level talents will be 0.2 to 0.8 million RMB, and subsidies will be 0.6 to 1.5 million RMB.

Salaries for the first- level talents in liberal arts will be negotiated face to face, and housing subsidies will be 5 million RMB. Salaries for the second-to fourth-level talents will be 0.2 to 0.7 million RMB, and housing subsidies will be 0.5 to 1.3 million RMB.

There is no age limit for the first-level talents, while the second-level talents are supposed to be below 50 years old, the third-level talents below 45 years old, the fourth-level talents below 40 years old. NUPT will adopt various modes of job arrangements for the spouse of the recruited talent.

Research Funds for the Recruitment of High-level Talents

According to the research objectives, achievements, the implementation of the programs and the needs, NUPT will provide the start-up research funds, mainly for laboratory construction.

Research funds for the first-level talents in science and engineering will be negotiated face to face, and research funds for the second-to the fourth-level talents will be 0.5 to 3 million RMB.

Research funds for the first-level talents in economy and management will be negotiated face to face, and research funds for the second-to the fourth-level talents will be 0.5 to 2 million RMB.

Research funds for the first-level talents in liberal arts will be negotiated face to face, and research funds for the second-to the fourth-level talents will be 0.1 to 0.5 million RMB.

Contact:

Mr. ZHOU Jian
Phone: 18951896185
E-mail: jzhou@njupt.edu.cn
Website:www.njupt.edu.cn

中国•北京高校招聘

Recruitment for Universities in Beijing, China

www.edu.cn/zhaopin

SCAN
北京理工大學
www.bit.edu.cn

SCAN
華北電力大學
www.ncepu.edu.cn

北京郵電大學
www.bupt.edu.cn

北京工業大學
www.bjut.edu.cn

北京工商大學
www.btbu.edu.cn

SCAN
首都師范大學
www.cnu.edu.cn

Looking for more positions? Please send your CV to
acabridge@163.com or call the direct line: 86-10-62603334

中国华南高校招聘

Recruitment for Universities in Southern China

秀美河山，旅游胜地

改革开放的先行者

The beautiful rivers and mountains, tourist attractions,
the pioneer of reform and opening up.

中山大學 www.zsu.edu.cn

華南理工大學 www.scut.edu.cn

廣東海洋大學 www.gdou.edu.cn

海南大學 www.hainu.edu.cn

廣西大學 www.scut.edu.cn

Looking for more positions? Please send your CV to
acabridge@163.com or call the direct line: 86-10-62603334

www.edu.cn/hnzp

中国西北高校招聘

Recruitment for Universities in Northwest China

一帶一路：中國夢與世界夢的交滙橋梁

One Belt and One Road:The bridge between the Chinese dream and the world dream

西安交通大學
www.xjtu.edu.cn

陕西師范大學
www.snnu.edu.cn

西安電子科技大學
www.xidian.edu.cn

西北工業大學
www.nwpu.edu.cn

Looking for more positions? Please send your CV to acabridge@163.com or call the direct line: 86-10-62603334

www.edu.cn/xbzp

中国西南高校招聘

Recruitment for Universities in Southwest China

钟灵毓秀，杰归西南

Welcome your joining in southwest China's colleges and universities

西南大學
www.nefu.edu.cn

重庆大学
www.cqu.edu.cn

电子科技大学
www.uestc.edu.cn

四川農業大學
www.sicau.edu.cn

Looking for more positions? Please send your CV to acabridge@163.com or call the direct line: 86-10-62603334

www.edu.cn/xnzp

Cold Spring Harbor Laboratory

2016 Meetings & Courses

125th anniversary celebration on CSHL sandspit

Meetings

Spring 2016

Systems Biology: Global Regulation of Gene Expression
Evolutionary Biology of Nematodes
Neuronal Circuits
The PARP Family & ADP-ribosylation
Protein Homeostasis in Health & Disease
Gene Expression & Signaling in the Immune System
Nuclear Organization & Function
The Biology of Genomes
The Cell Cycle
Retroviruses
81st Cold Spring Harbor Symposium: Targeting Cancer

Summer | Fall 2016

Glia in Health & Disease
Genome Engineering: The CRISPR/Cas Revolution
Regulatory & Non-Coding RNAs
The PI3K-mTOR-PTEN Network in Health & Disease
Translational Control
Epigenetics & Chromatin
Axon Guidance, Synapse Formation & Regeneration
Mechanisms of Aging
Germ Cells
Biological Data Science
Neurodegenerative Diseases: Biology & Therapeutics
Blood Brain Barrier

Cold Spring Harbor Laboratory
Meetings & Courses Program
1 Bungtown Road, Cold Spring Harbor, NY 11724
www.cshl.edu/meetings

Courses

Spring 2016

Workshop on Leadership in Bioscience
Cell & Developmental Biology of Xenopus
Expression, Purification & Analysis of Proteins & Protein Complexes
Quantitative Imaging: From Cells to Molecules

Summer | Fall 2016

Workshop on Schizophrenia & Related Disorders
Single Cell Analysis
Advanced Bacterial Genetics
Ion Channels & Synaptic Transmission
Mouse Development, Stem Cells & Cancer
Proteomics
Statistical Methods for Functional Genomics
Advanced Techniques in Molecular Neuroscience
Drosophila Neurobiology: Genes, Circuits & Behavior
Frontiers & Techniques in Plant Science
Metabolomics
Computational Neuroscience: Vision
Eukaryotic Gene Expression
Imaging Structure & Function in the Nervous System
Yeast Genetics & Genomics
Genetics & Neurobiology of Language
Brain Tumors
Programming for Biology
X-Ray Methods in Structural Biology
Computational & Comparative Genomics
Antibody Engineering & Phage Display
Advanced Sequencing Technologies & Applications

POSITIONS OPEN

FACULTY POSITIONS - MEDICAL SCHOOL

The Saint James School of Medicine, an international medical school (website: **www.sjsm.org**), invites applications from candidates with teaching and/or research experience in any of the basic medical sciences for its Caribbean campuses. A faculty position teaching Histology at our Anguilla campus is currently available. Applicants must be M.D., D.O., and/or Ph.D.

Teaching experience in the U.S. system is desirable but not required. Retired persons are encouraged to apply. Attractive salary and benefits. Submit curriculum vitae by email to **jobs@mail.sjsm.org** or online at **website: www.sjsm.org.**

Postdoctoral Associate MS/Proteomics
Yale University

The Yale/NIDA Neuroproteomics Center (website: http://medicine.yale.edu/keck/nida/index.aspx) has an opening for a postdoctoral associate in the area of "proteomics of altered signaling in addiction". The incumbent will work with Center investigators and Dr. TuKiet Lam, Director of the MS and Proteomics Resource of the Keck Laboratory, and of the Discovery Proteomics Core of the Yale/NIDA Neuroproteomics Center. Responsibilities will include implementing emerging and developing new MS/proteomics biotechnologies and applying these biotechnologies to research carried out by Center investigators. Requirements include: Ph.D. degree in analytical chemistry, biochemistry, or a related field; thorough understanding of mass spectrometry; extensive hands-on experience with tandem LC MS/MS instruments; strong publication record in the above areas; and the ability to excel in a team-oriented environment. Experiences with Top-Down, Middle-up, and/or quantitative proteomics technologies will be an advantage. Interested candidates should email a cover letter and Curriculum Vitae in PDF format to emails: **angus.nairn@yale.edu**, **kenneth.williams@yale.edu**, and **tukiet.lam@yale.edu**. *Yale is an Equal Opportunity, Affirmative Action Employer.*

ENDOWED FACULTY CHAIR POSITION

Montana State University-Bozeman and the Department of Animal and Range Sciences is proud to announce the Nancy Cameron Endowed Chair Beef Physiology position. This endowed faculty chair position is bolstered by an endowment that supports both research and graduate student training. We believe that this is an exciting opportunity for an accomplished researcher to perform cutting-edge scientific research on Beef Physiology, while developing a nationally recognized program at Montana State University. We encourage all those with a Ph.D. in Animal Science or closely related field, preferably those with an emphasis in physiology to apply. The successful applicant should have post-graduate experience, a record of publishing high-quality original research, a demonstrated ability to obtain competitive grants, a record of training graduate students, teaching experience, and have an established, independent research program. Please review the position description for additional information on the required and preferred qualifications and application process at this website: **http://jobs.montana.edu:80/postings/2622.**

Postdoctoral Associate

Doctoral Degree or foreign equivalent degree in Biochemistry or Cell Biology. Experience in protein purification and characterization, experience with mammalian cell culture and established track record of publishing in peer-reviewed international journals. Experience in studying protein phosphorylation is preferred. Eligibility to apply for NIH Fellowships would be an advantage.

For a full position description, or to apply online, visit website **www.stonybrook.edu/jobs** (Req. # 1502709). *Affirmative Action/Equal Opportunity Employer.Female/Minority/Disabled/Veteran.*

POSITIONS OPEN

The Forest and Wildlife Ecology department at the University of Wisconsin-Madison seeks applicants for a tenure-track **ASSISTANT PROFESSOR** of Forest Economics and Risk Management. Full position vacancy listing found here website: **http://www.ohr.wisc.edu/Weblisting/External/PVLSummaryApply.aspx?pvl_num=84696.**

SUNY GENESEO ASSISTANT PROFESSOR POSITIONS

State University of New York at Geneseo Department of Biology invites applications for two tenure track faculty positions at the rank of Assistant Professor in the areas of: (1) genetics/molecular and (2) ecology to begin in August 2016. The duties of the positions include teaching courses at the undergraduate level, conducting research, advising students, and providing service to the department and college. For details and to apply, submit an online faculty application at website **https://jobs.geneseo.edu**. Review of completed applications will begin upon receipt. To be guaranteed consideration, applications must be completed by January 4, 2016. The final date that letters of reference will be accepted is January 11, 2016. If using Interfolio to submit letters of reference, please follow the special instructions at this website: **https://help.interfolio.com/hc/en-us/articles/203701096-Upload-Letters-to-an-Online-Application-System**

AAAS is here –
helping scientists achieve career sucess.

Every month, over 400,000 students and scientists visit ScienceCareers.org in search of the information, advice, and opportunities they need to take the next step in their careers.

A complete career resource, free to the public, *Science* Careers offers hundreds of career development articles, webinars and downloadable booklets filled with practical advice, a community forum providing answers to career questions, and thousands of job listings in academia, government, and industry. As a AAAS member, your dues help AAAS make this service available to the scientific community. If you're not a member, join us. Together we can make a difference.

To learn more, visit
aaas.org/plusyou/sciencecareers

AAAS + U = Δ

Post Your Jobs
1 million candidates*
151,000 job applications*
Reach Scientists. Fill Positions.
ScienceCareers
employers.sciencecareers.org
*Jan–Dec 2014

Join the Conversation!

Twitter is a great way to connect with AAAS members and staff about the issues that matter to you most. Be a part of the discussion while staying up-to-date on the latest news and information about your personal member benefits.

Follow us @AAASmember and join the conversation with #AAAS

AAAS MemberCentral
MemberCentral.aaas.org

Advance your career with expert advice from *Science* Careers.

Download Free Career Advice Booklets!

ScienceCareers.org/booklets

Featured Topics:

- Networking
- Industry or Academia
- Job Searching
- Non-Bench Careers
- And More

ScienceCareers

FROM THE JOURNAL SCIENCE AAAS

KANSAS STATE UNIVERSITY

Director of the
Terry C. Johnson Center for Basic Cancer Research

The Terry C. Johnson Center for Basic Cancer Research (JCRC) at Kansas State University invites applications and nominations for the position of Director, to begin on July 7, 2016. KSU is a Carnegie "Very High Research" and "Engaged" University serving 25,000 students. The mission of JCRC is to advance the understanding of cancer by funding research, higher education, training and outreach, including education of the public about cancer and cancer research. It currently engages nearly 100 faculty and staff affiliates, and it is poised to respond to the challenge of finding cures for cancer. The JCRC has more than $12 million in endowments that it uses to provide seed funding for faculty affiliates, support for undergraduate and graduate student research, scholarships for pursuit of careers in biomedical sciences, graduate student or faculty travel awards, and extensive outreach activity.

The next director of the JCRC will be a person with outstanding scientific skills, whose personality and experience make her or him an effective administrator, a skilled communicator, an enthusiastic fund-raiser, a catalyst for collaborative initiatives, and a central figure in creating conceptual and experimental networks across disciplines. Candidates must have a Ph. D., M.D., D.V.M. or equivalent degree, a record of leadership in cancer or cancer-related research, experience in mentoring young investigators in grant-writing for public or private support, and in assisting faculty with intellectual property development.

K-State is located in Manhattan, in the rolling Flint Hills of northeast Kansas, 125 miles west of Kansas City via Interstate 70. The Tuttle Creek Reservoir, one of the largest in the Midwest, sits five miles north of the city. The 668-acre campus is conveniently situated near both business and residential areas. More information about Manhattan may be found at: http://www.k-state.edu/admissions/life/manhattan.html; information about JCRC may be found at: http://cancer.k-state.edu/.

Applicants must submit a single PDF file via email, that includes: (i) an application letter describing their qualifications related to the expectations noted above, their views on program development within the JCRC and their leadership philosophy; (ii) a detailed *curriculum vitae*; (iii) a description of their cancer-related research experience. Please send applications and the names and email addresses of three references (at least one from outside your own institution) to: **Dr. Phillip E. Klebba**, c/o **Karen Solt**, **solt@ksu.edu**. Screening will begin on **March 31, 2016**, and continue until the position is filled.

Kansas State University is an EOE of individuals with disabilities and protected veterans. Kansas State University actively seeks diversity among its employees.

AAAS

ADVANCING SCIENCE. SERVING SOCIETY

Editor, *Science* Immunology

The *Science* family of journals is seeking a full-time Editor for our new journal, *Science* Immunology. We are looking for an exceptional scientific editor with broad interests in immunology, a lively curiosity, and experience with peer review of scholarly research in the sciences. Responsibilities include executing the editorial mission of the journal and hiring and managing the editorial team. The Editor will also handle the review, selection, and editing of manuscripts, working with authors on revisions, soliciting reviews and special issues, and fostering contacts and communication with the scientific community. Candidates are expected to travel to scientific meetings. Postdoctoral experience, multiple publications and at least 7 years of editorial experience are required, as is the ability to work constructively as a member of a team.

For this position, we require a Ph.D. in a scientific discipline plus postdoctoral experience and at least 5 years of editorial experience. Excellent written and oral communications skills essential.

Science is published by the AAAS, the world's largest scientific membership organization. Visit us at **www.aaas.org**.

Please visit our job information website **http://www.aaas.org/page/employment-aaas** to get more information, and to apply to AAAS online.

AAAS is an EO Employer. All qualified applicants will receive consideration for employment without regard to race, color, religion, sexual orientation, gender identity, national origin, age, disability, veteran status, or other protected category. AAAS uses E-Verify to confirm the employment eligibility of all newly hired employees.

ScienceCareers online @sciencecareers.org

By **Elizabeth Pennisi**

Beetle horns and book writing

By day, Douglas Emlen studies insect weaponry, but at night, military history is his preferred reading. Eight years ago, these interests merged unexpectedly. As a professor of ecology and biology at the University of Montana in Missoula, he had spent 20 years examining the mating and territorial behavior of dung and rhinoceros beetles, well known for their very large horns, to understand why some insects spend so much energy building big weapons. Asked to write a review about weapons systems across the animal kingdom, he dug into the file cabinets full of papers on the subject that he had collected over the years. The more he read about tusks, horns, claws, antlers, and other weapons, the more enthralled he became. So, when the journal made him cut 10,000 words from the manuscript, he decided it was time to branch out and write a book for a general audience.

"I wanted to do something different, something fun and accessible," Emlen recalls. He gathered up the material that didn't make it into the review, wrote a book proposal, found an agent, and got a contract. It was a far more momentous decision than he realized at the time, one that would sweep him in new directions, both in his writing and his research.

Writing a popular book while running a lab was a challenge. He scrambled to write grants, publish papers, and handle his teaching and administrative responsibilities while also squeezing in the many rewrites his editor requested to make him sound more like a storyteller than a scientist. "I thought I was a good writer, but I was in for a pretty rude awakening," he says. His graduate students and colleagues took up the slack in the day-to-day operation of the lab, but he fell behind on reading about evolutionary development, his lab's current focus. One summer, he shelved research altogether and devoted his time to the book. His routine was to get out of bed, head for a coffee shop or the university library, work until he couldn't see straight, get home after dark, spend some time with his children, and then crash. Support from his colleagues, students, and family made it all possible, he says.

Yet far from compromising his science, Emlen says writing the book has enriched it. The book "started out as a way to tell the story of the science that I already knew to try to get people jazzed about science," he explains. But as he wrote, he realized there are commonalities between animals' weapon systems and humanmade ones. History shows that war technologies—be they knights' armor, battleships, or missiles—got bigger and more expensive until new weapons, such as guns, submarines, and computer hackers, undermined them. After writing the book, he says, "I look at my science totally differently." For example, it helped him see how, in his beetles, "sneaky" males that lack big horns and instead gain access to females by digging tunnels past the big-horned males guarding them could eventually make horns obsolete. In fact, he says, that's exactly what may have happened in some beetle species that have lost their horns.

"I wanted to do something different, something fun and accessible."

Working on *Animal Weapons: The Evolution of Battle*, which earned Emlen the 2015 Phi Beta Kappa Award in Science, has also changed how he writes and edits. In his papers, he now aims for "crisp and clean, quick and active" writing. He keeps waiting for a journal editor to push back on this new style, but it hasn't happened yet. Meanwhile, all else is getting back to normal. He says it will take about a year to catch up on the research literature he missed while working on the book, but the grant he rewrote five times is now in hand, so the lab is bigger than it's ever been. His primary research goals are unchanged, but some of his fieldwork is inspired by the book, he notes, as is a more interdisciplinary approach overall.

He doesn't know if he will write another book like it, but, he says, "it's the most important thing that I've ever done, and the most fun thing." And, by showing how animal studies can help us understand when and why our own weapons work—or don't work—as deterrents, it drove home the importance of basic research. "You never know where it will lead." ■

Elizabeth Pennisi is a senior correspondent for Science. *Send your story to SciCareerEditor@aaas.org.*

ILLUSTRATION: ROBERT NEUBECKER

Published by AAAS